Faculty of Chemical Engineering
University of Chemistry and Technology Prague
Technická 3, 166 28 Prague 6, Czech Republic

MOLECULAR BEAM INVESTIGATIONS OF FREE CLUSTERS AND NANOPARTICLES: PROCESSES OF ATMOSPHERIC AND BIOPHYSICAL RELEVANCE

Habilitation Thesis
by

Michal Fárník

J. Heyrovský Institute of Physical Chemistry, v.v.i.
Czech Academy of Sciences
Dolejškova 3, 182 23 Prague 8, Czech Republic

Prague, 2015

Laß die Moleküle rasen
was sie auch zusammenknobeln!
Laß das Tüfteln, laß das Hobeln
heilig halte die Ekstasen!

Christian Morgenstern: *Alle Galgenlieder*
Insel Verlag Wiesbaden, 1972

Acknowledgements

Ten years ago I was returning back to the J. Heyrovský Institute of Physical Chemistry in Prague from my ten years long postdoctoral stay abroad in several laboratories in Germany and USA. During my last research stay at the Max-Planck Institute in Göttingen I worked with Prof. Udo Buck, who donated me the experimental apparatus which after some upgrades became our present CLUB apparatus described in this work. Therefore, first I would like to express my sincere thanks to Udo, not only for the apparatus which helped me to have a head start in Prague with my research, but also for the good time which I had working with him.

My thanks also go to all the members, past and current, of our group at the J. Heyrovský Institute, who contributed to the research presented here. First to mention is my dear colleague and friend Viktoriya Poterya, who joined me at the end of 2005 as my first postdoc and contributed most significantly to the formation our new experiments and our group. My second postdoc Juraj Fedor came in 2009 and built the first version of our VMI system and introduced a lot of new ideas and new experiments. He also helped to recruit our first Ph.D. student Jaroslav Kočisek. Both, Juraj and Jaro, have returned recently in 2015 from abroad, are became my collaborators in our institute. Our complex and complicated experiments would not work without the many skills of Andriy Pysanenko. Recently we have had a brief but valuable help of Peter Rubovič. The driving force behind a lot of research everywhere in the world are the students. A great deal of the work presented here was helped by a very talented Ph.D. student Jozef Lengyel, and other master and Ph.D. students: Kateryna Grygoryeva, Daniela Šmídová and Pavla Svrčková. Former students should be remembered: Václav Profant, Ondřej Tkáč and Pavel Koštál. Help is provided also from Ondřej Votava and his lab. Also a close collaboration with Petr Slavíček at the University of Chemistry and Technology Prague is highly appreciated.

All these people generate not only the great scientific results in our lab, but especially a pleasant and enthusiastic working environment without which it would be difficult for me to do the work which I am doing and how I am doing it. Indeed, there is not enough space to mention here the help and support of all the colleagues and collaborators both here and abroad, the referees of our papers, and others, who all help to shape and move forward our research, yet my sincere thanks goes to all of them.

Last but not least I really appreciate the cordial and comforting support and understanding of my family.

This work would be impossible without a financial support. My return to the J. Heyrovský Institute was facilitated by the institute and award of the J. E. Purkyně Fellowship of the Academy of Sciences of the Czech Republic, and several grants supported our research since then, the current ones are: projects Nos.: 15-12386S, 1414082S and 14-08937S of the Czech Science Foundation.

Abstract

In this work, I have summarized the most recent research of my Group of Molecular and Cluster Dynamics at the J. Heyrovský Institute of Physical Chemistry, the Czech Academy of Sciences. Out of our recent publications, I have selected 16 papers, 11 of them from the last years 2014 and 2015, to illustrate the different research topics investigated in our laboratory.

Our general topic is to study elementary chemical and physical processes at a detailed molecular level. Examples of such processes can be photodissociation of molecules; photoionization and electron ionization or electron attachment; pickup, coagulation and clustering of molecules on nanoparticles, etc. We elucidate the role played by solvent molecules in these elementary processes. Therefore we study these processes in isolated molecular clusters under vacuum as a function of the cluster sizes and compositions. In principle, we can follow an evolution of a certain process from the monomers to conglomerates of thousands of molecules. Thus our investigations bridge the gap between individual molecules in the gas phase all the way to their behaviour in the bulk.

From a more practical point of view, we focus especially on two areas: (1) Clusters, nanoparticles and processes relevant to atmospheric chemistry; (2) Processes relevant to biophysics. Within the first topic we investigate various processes on/in ice nanoparticles which play an important role in the atmosphere, e.g., in the process of the ozone hole generation above Antarctic. Within the latter topic we study some essential building blocks of biomolecules, namely their UV photostability, hydrogen bond (generation and breaking), and how are these processes influenced by a solvent. The investigated processes are briefly outlined in Chapter 1 *Introduction.*

Experimentally, our tools are isolated clusters and nanoparticles generated in molecular beams in vacuum. We investigate the clusters by various methods, e.g., UV laser spectroscopy and photofragment velocity map imaging (Sec. 2.2.1); mass spectrometry after electron and/or photoionization and other special mass spectrometric methods such as Na doping and photodetachment (Sec. 2.2.2); pickup of molecules and cluster velocity measurements by means of time-of-flight technique (Sec. 2.2.3) etc. These methods are briefly introduced in the Chapter 2 *Experiment.*

The investigations in the above mentioned fields are accompanied by the development and implementation of new experimental techniques in our group. Therefore Chapter 3 *Results*

has two sections illustrating two new methods which we have introduced in our experiments: In the first Sec. 3.1 we introduce the *Velocity map imaging as a tool for cluster dynamics investigations.* The second Sec. 3.2 *Na-doping and solvated electron reactivity* introduces a new powerful method for cluster mass spectrometry implemented in our laboratory in 2014 and we analyze and discuss its different advantages and drawbacks for the cluster studies. In the following three sections we focus on the results in various topics investigated in our laboratory. Two chapters summarize some of our investigations of atmospherically relevant processes on ice nanoparticles, namely Sec. 3.3 *Photochemistry of molecules in ice nanoparticles*, and Sec. 3.4 *Nucleation and growth of ice nanoparticles.* Finally, some of our biologically relevant studies are discussed in the last Sec. 3.5 *Solvation effects on essential building blocks of biomolecules.* Each of these result sections is accompanied by 2-4 published articles attached in Appendices A-E, and the individual sections summarize the context of these papers and outlines the major conclusions. The collection closes with Chapter 4 *Outlook* where some of our current experiments and future plans are outlined.

Contents

Chapter 1

Introduction

1.1 Molecular beams and clusters: A tool for understanding chemistry at the molecular level

Even in the simplest of chemical reactions many elementary processes take place. Dozens of reactions and other processes between molecules can occur in parallel. To understand the details of the chemistry at the molecular level is certainly a scientific challenge. The situation of a chemist struggling to unravel the mystery of a chemical process from the initial reactants and the final products has been compared with that *"of a spectator of a drastically shortened version of a classical drama - Hamlet say - where he or she is only shown the opening scenes of the first act and the last scene of the finale. The main characters are introduced, then the curtain falls for change of scenery and as it rises again we see on the scene floor a considerable number of dead bodies and a few survivors. Not an easy task for the inexperienced to unravel what actually took place in between"* [1].

When physicists developed atomic and molecular beam techniques [2, 3, 4], they presented chemists a unique and extremely useful tool for investigating elementary chemical processes [5, 6]. For the first time chemists could observe and gain fundamental insights into the mechanism and dynamics of elementary chemical reactions in crossed-beam scattering experiments, i.e., the collision of two molecules and the resulting exchange of atoms, independent of secondary processes [7, 8]. In 1986 D.R. Herschbach and Y.T. Lee received the Nobel Prize in chemistry together with J.C. Polanyi for their outstanding contribution towards *"understanding the dynamics of chemical elementary processes"*, which were studied experimentally in the crossed molecular beams. Combination of molecular beams with lasers allowed, not only to study reactions between individual molecules, but also reactions between molecules in prepared individual quantum states while probing the quantum states of the products, i.e., paving the way to the ideal chemist-purist world of well defined state-to-state reactions. Further development of the laser techniques to short (femtosecond) pulses in combination with molecular beams allowed direct tracking of chemical reactions in real time. For this development another

Nobel Prize was awarded in 1999 to A.H. Zewail.[1]

All these developments represented a huge leap forwards in detailed understanding of chemistry at the molecular level. Yet, a question can be posed by a hard-core macroscopic chemist: Do we really learn something about the bulk chemistry once we void the studied system of its environment? The major advantage of the molecular beams, i.e., the possibility to study the reaction independent of secondary processes, may become the major flaw of the method in the eyes of a chemical engineer. His chemistry happens in the bulk where the processes are strongly influenced by the solvent molecules.

By the way of example, let us consider the acidic dissociation of hydrogen chloride HCl molecule in water to halide anion and proton. Indeed, the way we usually write this reaction: $HCl+H_2O \rightarrow Cl^- + H_3O^+$, it actually never happens. A single HCl molecule cannot react with a single water molecule this way. A collective action of hydrogen bonds of several water molecules is necessary to break the H–Cl bond. Thus a crossed-beam study of HCl with H_2O would yield absolutely no products. Similar conclusions were also drawn for another very reactive system: $Na+H_2O$. No products were observed in crossed molecular beam studies [9]. And yet we learn, and often eye-witness already in freshmen's chemistry courses, how reactive this system is.

The question arises: Can we study the elementary processes in the presence of solvent molecules without increasing the complexity of the system so that we would have to recede from the molecular level understanding of the studied processes? Is there a middle ground between the macroscopic bulk-chemistry and the individual molecule-molecule elementary collisions? The answer to these questions is *clusters*.

Clusters are weakly bound aggregates of molecules which can be generated in molecular beams. We can study elementary chemical and physical processes, in them, thus investigating the processes with the molecule in an environment of a finite size. The Cluster Isolated Chemical Reaction (CICR) method was advocated in late 1990s [10], in which the elementary processes between molecules were studied on large mainly rare-gas clusters. In addition, the clusters can, in principle, allow observation of the solvent effects on the studied process by adding the solvent molecules subsequently one-by-one. By the way of example, for the above mentioned acidic dissociation of hydrogen halides in water, experiments with $HBr(H_2O)_n$ clusters revealed that for n=5 the so called zwitterionic structure $H_3O^+(H_2O)_{n-1}Br^-$ was generated, i.e., that the acidic dissociation occurred [11, 12]. Similarly, the reaction $Na+H_2O$ was studied in $Na_m(H_2O)_n$ clusters [13].

The topicality of molecular beams combined with laser techniques and clusters has been underlined above. This is the general subject of our present work: the investigation of molecular dynamics in clusters generated in molecular beams and probed by various methods including lasers, mass spectrometers, and other special techniques. These experimental techniques will be introduced in the present work, and then several examples of atmospherically and biologically

---

[1] A number of Nobel Prize awards was connected with the molecular beam methods, which underlines their importance: O. Stern (1943), I. I. Rabi (1944), P. Kusch (1955), A. Zewail (1999), and J. B. Fenn (2002).

relevant investigations will be discussed.

1.2 Clusters and their relevance to the fundamental research, atmospheric chemistry and biology

The term *molecular clusters* denotes aggregates of molecules ranging from dimers to conglomerates of thousands or even more constituents. The molecules in clusters are typically bound together by weak van der Waals interactions or by hydrogen bonds. Energetically these interactions are of the order of ~0.1 eV and less, i.e., more than an order of magnitude weaker than the covalent chemical bonds in the constituent molecules which are several electronvolts. Since the typical dimensions of the larger clusters consisting roughly of 10-10^3 molecules are of the order of nanometers, they are often called *nanoparticles*. Work in the field of cluster and nanoparticles in general is relevant to solid state physics, molecular, atomic and even nuclear physics and chemistry and has practical implications for many areas, e.g., nanoelectronics, surface science, catalysis, environmental studies, biology or even medicine [14, 15]. The particles found in the atmosphere in the nanometer size region have been termed *aerosols*.[2] Thus we use all three terms *clusters/nanoparticles/aerosols* in this work to denote the investigated species.

In this collection we will be concerned with free clusters generated in vacuum in molecular beams [16, 6]. Essentially three motivations can be put forward for such cluster investigations:
(1) the fundamental understanding of bulk properties based on the properties of the individual constituent molecules;
(2) the unique properties of the clusters, which promote their use as *nano-laboratories* for investigations of various physical and chemical processes at a detailed molecular level;
(3) the practical role which the clusters and nanoparticles play in nature, e.g., in atmospheric chemistry or astrochemistry.

The first point was one of the original motivations for cluster studies in molecular beams. Clusters can provide the link between properties of an individual molecule and the properties of the bulk material composed of these molecules by investigating physical and chemical properties as a function of the cluster size, ultimately resulting in understanding the transition from a molecule, to bulk.

In addition, the clusters possess many unique properties. Just to mention a few, they exhibit a large number of (i) isomeric structures, (ii) internal degrees of freedom, and (iii) closely spaced energy levels. These make them a very efficient heat bath and they can cool down in vacuum by evaporation of their constituents from the surface to very low internal temperatures T_C ~0.1-100 K. Besides, the surface-to-volume ratio in clusters is large, while the volume molecules quickly converge to the bulk behaviour at the same time. Another peculiarity of the

---

[2] Strictly speaking, *aerosol* is the mixture of gas pas phase molecules with solid or liquid particles of nm to μm size range. However, the term *aerosols* is often used to denote just the aerosol particles, and here we concentrate on the small particles from ≤1 nm to ~5 nm.

molecular clusters is the dual character of bonding: strong intramolecular bonds (∼1-10 eV) vs. weak intermolecular interactions (∼0.1 eV). All these properties have recently promoted their use as *nanolaboratories* for investigations of various processes. For example large He_n–clusters ($n \geq 10^3$), so called *He-nanodroplets*, provide ultracold He (0.37 K) superfluid (i.e., non-perturbing) matrices for spectroscopy of molecules [17]. Even complex spectra of large biomolecules could be resolved in He-droplets due to their very low temperature attained by the molecule [18].

The photodissociation of molecules in rare-gas clusters, which was studied previously with our original experimental apparatus in Göttingen, may serve as another example [19] of how the clusters can be exploited as *nanolaboratories* for studying the photochemical processes in solvent environment. The understanding of photochemical processes in condensed media is one of the current challenges in chemical physics both for fundamental and technological reasons. A molecular level understanding is difficult to achieve due to the many-body nature of the interactions leading to inseparable dynamics on a wide range of time and length scales. A photodissociation process of a diatomic HX molecule is schematically represented in Fig 1.1. In the gas phase the isolated molecule is promoted by the UV radiation to an excited (HX)* PES which is repulsive and the system evolves on this surface unperturbed by other interactions so that the hydrogen atom departs with the kinetic energy E_{kin}=$h\nu$-D_0, Fig 1.1 (a) ($h\nu$ is the UV-photon energy and D_0 is the HX dissociation limit in the particular electronic state, and the heavy X-atom is -in the first approximation- assumed to remain at rest after the photodissociation due to its much higher mass $m_X \gg m_H$ -more rigorous treatment of the fragment kinetic energy will be given in Sec. 2.1.2). The solvent molecules surrounding the HX molecule in the condensed phase can be represented in the simplified picture by a wall in the way of the departing H-fragment, Fig 1.1 (b). However, in this representation the wall would be partly transparent and some fragments could pass through and leave with their E_{kin}

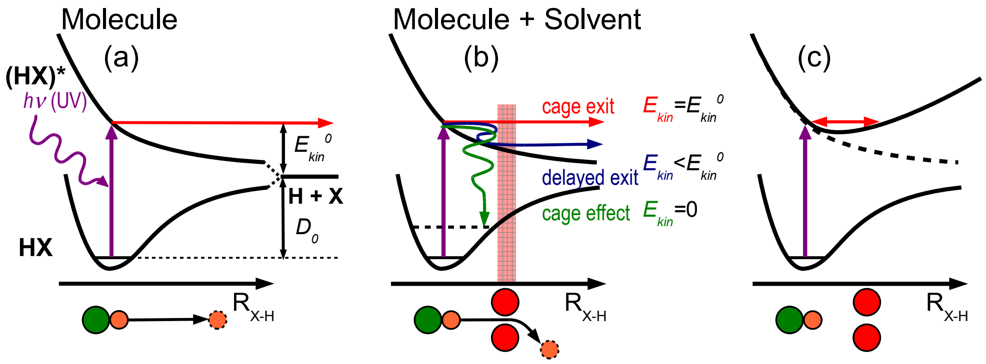

Figure 1.1: Schematic representation of photodissociation of an isolated HX molecule (a), and the possible effects of the solvent molecules on the photodissociation process: mechanical (b) and electronic interaction (c).

unchanged. Some fragments can loose part of their kinetic energy in inelastic collisions with the solvent cage molecules but they still leave the cage with somewhat lower energy. Other fragments, on the other hand, can loose their energy entirely and the HX molecule can be recreated, possibly in some higher excited state. To overcome the simplification of this "wall" approach one should take into account the electronic structure of the solvent molecules and their interaction with the HX molecule which may change the PESs substantially. Thus the dissociative PES of the excited state (HX)* of an isolated molecule can be changed into a bound state by the presence of the solvent species, Fig 1.1 (c). Examples of such such changes of PES from a dissociative to a bound state by the presence of solvent molecule were discussed in some of our studies [20, 21, 22, 23, 24, 25]. In other words, some photodissociation channels of the bare molecule may be closed in the bulk and some new ones may open by the presence of the solvent. The situation is even more complicated by the possibility of chemical reactions between the departing fragment and the solvent molecules. It is extremely challenging to study all these processes at the molecular level in the bulk. At this point the free clusters as *flying nano-laboratories* can help.

When the molecule is photolyzed in a cluster the initial dynamics of the process is essentially the same as in the condensed phase, since the molecule is surrounded by the solvent. Nevertheless, while in the condensed phase the fragments usually do not leave the bulk and are, therefore, often lost from detection, the clusters decay during the process and the escaping fragments can be detected. Thus, in the cluster experiments, observables can be measured not accessible in the bulk studies, e.g., the kinetic energy of the fragments after the photodissociation. This energy carries the information about the fragment interaction with the solvent cage after the photodissociation. Besides, investigating the process as a function of the cluster size, i.e., as a function of the number of solvent molecules, brings the information about the role of the solvent in the photodissociation. Last but not least, the finite size of the clusters allows theoretical treatments at a level of theory which would be too demanding for the non-periodic condensed matter. Altogether detailed information about the dynamics of the process in the molecule-solvent system can be gained from such studies, as will be shown in this work.

Finally, the third motivation for cluster studies revealed above were practical implications which some clusters and nanoparticles have in the nature. By the way of example the ice nanoparticles play an important role in the interstellar space, where the density of chemical species and temperatures are too low for chemistry and the microscopic particles can accumulate the impinging molecules for a very long time and provide the necessary catalytic surfaces for their chemistry to occur. In addition, water clusters and ice nanoparticles are also key players in atmospheric chemistry. This example will be further detailed in the following section. Subsequently two other major areas of our cluster research covered in this work, will be briefly introduced.

1.2.1 Atmospheric chemistry

Stratospheric ice particles play a key role in the *ozone depletion* process. Many details of the ozone chemistry in the stratosphere still elude the very detailed understanding. Yet, it has been well established already in 1980s, soon after the striking discovery of the ozone hole above Antarctica, that the chemistry leading to the ozone depletion in the stratosphere is not a pure gas-phase chemistry but a heterogeneous chemistry involving reactions and processes on the surface and in the bulk of ice particles in the polar stratospheric clouds (PSCs) [26, 27, 28, 29, 30]. The stratosphere, which is generally very dry, is not easily prone to cloud formation. Therefore, the PSCs can only form in the extremely cold conditions of the polar winter stratosphere. These cloud particles provide the necessary heterogeneous surfaces for the fast chemistry in the stratosphere. Above Antarctica the PSCs generation and evolution is assisted by other atmospheric conditions such as lower temperatures and polar vortex (huge masses of cold air circling near poles).

Many different reactions were proposed to proceed in the course of the heterogeneous chemistry assisted by the ice particles in PSCs. Essentially these reactions lead to conversion of so called *reservoir species* relatively harmless to ozone (e.g., HCl, HBr, $ClONO_2$) to the *active species* (e.g., Cl_2, Br_2, BrCl, HOCl, HOBr), which can be readily photolyzed by the sun UV radiation and release halogen radicals that destroy ozone directly in catalytic cycles [31]. The active species are generated in the PSCs in these reactions during the cold polar winter and their photolysis starts releasing the halogen radicals in the Antarctic spring when the sun radiation reaches the Antarctic region. The molecular precursors for the above mentioned reservoir species are freons: chlorofluorocarbon (CFC) molecules , e.g., CCl_2F_2. The ozone depletion chemistry is illustrated by a simplified cartoon in Fig. 1.2.

More recently alternative reaction models have been proposed, which lead to halogen radical generation directly from these CFCs, bypassing the necessity of generating the reservoir species from CFCs [32, 33]. Nevertheless, the key role of PSCs is preserved in these models, since the essential step is a dissociative attachment of the *solvated electron* generated by cosmic radiation in PSC particles to the CFC molecules adsorbed on the particle surface [34].

From the above it is obvious that the chemistry and photochemistry of the ice particles in the PSCs with the adsorbed pollutant molecules such as hydrogen halides and freons play a key role in the ozone depletion process. The ice nanoparticles (large water clusters), which can be generated in the molecular beams in our apparatus with different molecules attached to them can mimic the stratospheric particles in the laboratory conditions. Interacting these species with UV laser beams can then reveal their photochemistry. Results of such experiments with hydrogen halides and freons are presented in Sec. 3.3.

Since we do not only investigate the atmospherically processes but also design and develop new experimental methods for these studies, Sec. 3.1 reviews our studies concerned with the implementation of velocity map imaging technique for the photodissociation studies in our ex-

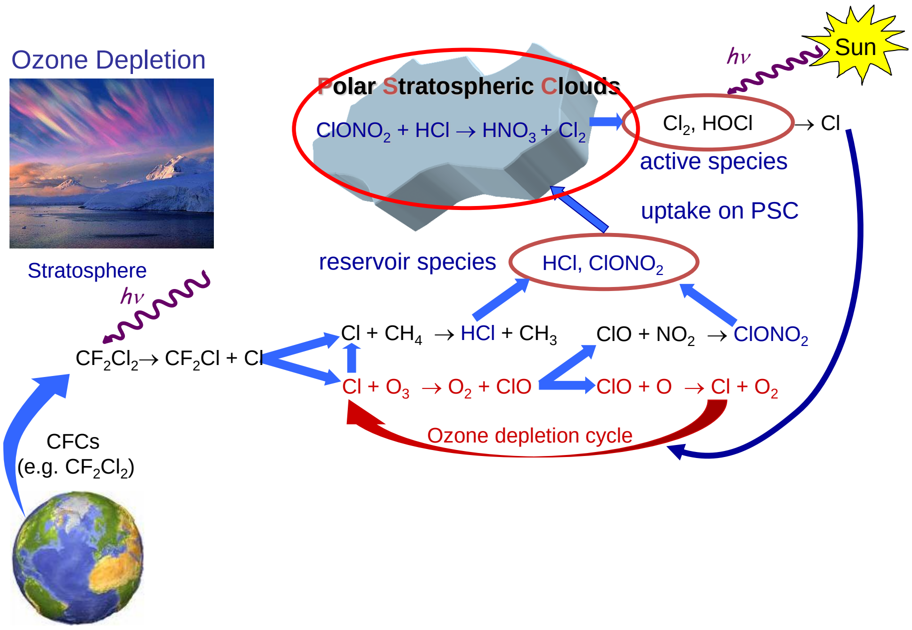

Figure 1.2: A simplified schematic cartoon of the ozone depletion chemistry.

periments. This techniques is indeed also relevant for the biologically relevant studies discussed below.

Another partly instrumentally oriented series of publications concerned the doping of the ice nanoparticles with sodium atoms. From the point of view of the instrumental development, this method was designed as a non destructive ionization method for the nanoparticle mass spectrometry. In terms of atmospheric chemistry relevance, this method was used to generate solvated electrons in the ice nanoparticles, and we have investigated the solvated electron dynamics and reactivity in the nanoparticles using this method. The solvated electrons generated by cosmic radiation in PSC particles have been mentioned above as possible important players in the ozone depletion processes [32, 33, 34]. Our publications concerning the sodium doping and solvated electron reactivity are discussed in Sec. 3.2.

In our studies we also address the question of the ice particle generation, their sizes and shapes, and also the interaction and behaviour of the adsorbed molecules on these ice nanoparticles. The latter subject is not related only to the atmospheric chemistry but also to the astrochemistry as mentioned above: the ability of the ice grains in the space to collect and accumulate molecules is the necessary condition for the radiation induced chemistry on ice grains to happen, however, another inevitable condition is the mobility and interaction between the individual molecules. We have addressed the questions of the ice nanoparticle nucleation and growth, and also the behaviour of the embedded molecules on the ice nanoparticles in the articles reviewed in Sec. 3.4.

1.2.2 Biomolecules in clusters

Biological systems involve rather complex molecules. The understanding of chemistry and physics in these species at the molecular level is correspondingly complicated. Therefore, often smaller functional units of the larger biomolecules are investigated in the gas phase. This *bottom-up approach* in the studies of biomolecules means that if we want to understand the photochemistry of the larger biomolecules, we start from the essential building blocks of these molecules. This is illustrated in Fig. 1.3 on the example of pyrrole molecule, which is a building block of the porphyrin ring. The porphyrin ring is a part of many biomolecules such as hemoglobin or chlorophyll. Pyrrole is not only a part of these biomolecules, but it is also the UV-active chromophore, i.e., the unit where the UV photon is absorbed and the photochemistry is initiated. This was the motivation for many studies devoted to the photochemistry of the isolated pyrrole molecule in the gas phase [35, 36, 37, 38, 39, 40, 41, 42]. However, it turns out that the photoinduced processes are often controlled by the environment of the chromophores. This can be demonstrated on the example of nucleic acid photochemistry [43, 44]. Therefore, also here the clusters can provide model systems. Increasing the complexity of the studied systems by adding various solvents to the simple molecules such as pyrrole can allow for answering the essential questions as: Are the molecules intrinsically photostable or is the photostability provided via the solvation? Do specific interactions (e.g., hydrogen bonds) play a defining role in the photochemistry of these molecules in biological systems? We concentrate on the cluster studies and we have addressed these questions for pyrrole and other essential building blocks of biomolecules (imidazole, pyrazole, phenol, aniline) in our laboratory previously [20, 45, 21, 46, 22, 23, 24, 25]

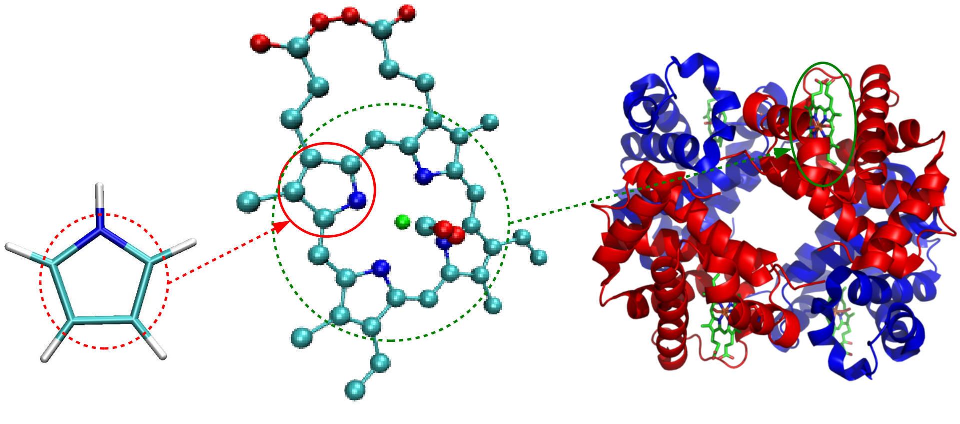
(a) Pyrrole (b) Hem (c) Hemoglobin

Figure 1.3: Pyrrole molecule as a basic functional unit of biomolecules illustrating the *bottom-up approach*: the pyrrole molecule (a) is a building block of porphyrins, which are the essential units of biomolecules such as hem (b), which in turn is a basic functional unit of hemoglobin (c).

Hydrogen bond is very important in biological matter. The most prominent examples of its significance in biology are the pairing of base pairs in nucleic acids, molecular recognition or enzyme catalysis. All these examples are related to essential conditions of life. For this reason, hydrogen bonding phenomena became a subject of extensive studies. Experimental studies of hydrogen bonding in the ground state are relatively straightforward, e.g., using vibrational spectroscopy, which provides a very detailed information about this type of bonding [47, 48, 49].

Experimental investigation of hydrogen bonding in the excited state is more complicated. While photochemistry of systems with intramolecular hydrogen bonds was studied for a relatively long time (e.g., in a context of sunscreen protection or fluorescence spectroscopy), photochemistry of intermolecular hydrogen bond has become only recently a major research subject [50]. There are interesting questions to be addressed: Is there any photochemistry specific for hydrogen bonded systems? And if the answer is yes, is the different photochemistry related to biophysically relevant processes? The answer to the first question is affirmative, photoinduced processes are controlled by the ground state structure and the X–H$\cdots$Y structural motif implies ultrafast excited state hydrogen (or proton) transfer as a typical reaction of hydrogen bonded systems. The hydrogen bond was suggested to be a key component in protecting nucleic acids against radiation damage [51, 52, 53].

Since the absorbed photon triggers ultrafast dynamical processes, various time resolved experiments, based on photoabsorption, fluorescence or photoionization can be used to study the excited state dynamics [54]. The dynamical processes occur often on the edge of the time resolution of the respective experiments. In our studies, we concentrate on the experiments in the energy domain. In particular we detect the kinetic energy distribution of the atomic fragments released from the studied system. The natural choice for the study of hydrogen bonded systems is to detect the kinetic energy of the hydrogen atoms. If the detected hydrogen atom was released from the molecule participating in the hydrogen bonding, we obtain information about the character of this bond both in the ground and in the excited states.

The above mentioned hydrogen transfer and proton transfer processes in the hydrogen bonded cluster systems can be addressed not only by the photodissociation studies but also by mass spectrometry. Our experimental setup provides the unique option of different ionization methods applied to the same clusters beam. Already our previous preliminary investigations [46] showed that quite different mass spectra of hydrogen bonded clusters can be obtained by electron ionization versus photoionization. New mass spectrometer and new ionization options have been implemented in our apparatus in the mean time, and subsequently the new mass spectrometric investigations of the hydrogen bonded clusters of biologically relevant molecules presented in this work [55, 56] provide more detailed insights into the hydrogen and proton transfer processes in these systems upon the excitation with electrons and photons. The results of our photodissociation and mass spectrometric studies of small essential building blocks of biomolecules in clusters will be presented in Sec. 3.5.

Chapter 2

Experiment

The experiments covered in this work were carried out on two molecular beam setups in the Group of Molecular and Cluster Dynamics at the J. Heyrovský Institute of Physical Chemistry in Prague: the *CLUster Beam (CLUB)* apparatus and the *Apparatus for IMaging (AIM)*. The CLUB apparatus was originally built and used in the group of U. Buck at the Max-Planck-Institute for Dynamics and Selforganization in Göttingen and dedicated to studies of photodissociation of molecules in cluster environments [19]. I joined Buck's group in 2002 and started to work on this experiment. In 2005 I have moved the apparatus to the J. Heyrovský Institute in Prague. In the period 2010-2012 we have significantly upgraded the CLUB apparatus and the present work contains the results obtained with the new experiments implemented on the CLUB apparatus in Prague.

The above mentioned upgrade resulted in a world-wide unique and very versatile experimental setup. The versatility of the present setup allows to perform various independent experiments with the same molecular beam, thus assuring that the same species are investigated in different experiments and their results can be compared directly yielding a complex information about the nature of investigated species and processes. For example, in the CLUB apparatus different mass spectra can be measured for the same clusters: (i) after electron ionization (EI) with different electron energies; (ii) after a photoionization (PI); (iii) after sodium doping and photodetachment of electron (NaPI); (iv) and even negatively charged clusters after the electron attachment have recently been measured. Thus we can obtain up to four mass spectra which are very often all different but correspond to the same neutral species. In addition, the dependence of these spectra on electron and photon energies can be measured. From these different spectra a reliable information about the original neutral cluster size and composition can be reconstructed. In the literature, the information about the cluster size and composition is often concluded from a single type of mass spectra, very often without any ionizing species energy dependence. However, we have shown (see e.g. Ref. [57]) that such information derived from a single mass spectrometric technique can be quite misleading.

Similarly, the combination of velocity map imaging (VMI) for photodissociation studies and mass spectrometric techniques on our CLUB apparatus is unique. Very often the VMI experiments are performed on a dedicated apparatus without the mass spectrometry option or with a very rough and insensitive TOF mass spectrometry. This may be sufficient for investigations of isolated molecules, however, for the clusters their amount, size, and composition in the molecular beam are essentially unknown in such experiments. Our combination of VMI and various mass spectrometric techniques allows to determine unambiguously the nature of the species which are investigated in the photodissociation VMI experiments. We have illustrated this unique feature of our CLUB apparatus, e.g., in Refs. [58, 25]. The above mentioned different experiments are usually performed on dedicated setups with different molecular beam sources and thus their results often cannot be compared directly, since they probe different species.

Our apparatus in the original configuration in Göttingen was described in some of the earlier publications [59, 60, 61] and a comprehensive account can be found in the Ph.D. Thesis of H. N. Nahler [62]. A detailed description of the CLUB apparatus after the new installation and smaller modifications in Prague can be found in my DSc. Thesis [63]. Our recent upgrades of the CLUB apparatus have been partly covered in our publications [64, 65, 66, 57, 67, 68] and in the Ph.D. Thesis of J. Kočišek [69] and J. Lengyel [70].

The second experimental apparatus in our laboratory, *Appartus fo IMaging (AIM)*, was entirely built by our group in Prague [71]. Originally this apparatus was dedicated to the development and testing of the VMI technique before its implementation on the CLUB apparatus, so that the CLUB experiments could go on uninterrupted while the VMI was being developed in our laboratory. However, the AIM proved to be a very useful tool for photodissociation investigations of isolated molecules and small clusters. Therefore, after the VMI implementation on the CLUB apparatus, the AIM was extended as a VMI dedicated setup. It is relatively simpler and significantly smaller experiment compared to the CLUB, yet it provides interesting new results, see e.g. [71, 72, 73]. It was described in more details in Ref. [71] and in the Ph.D. Thesis of J. Kočišek [69].

These two experimental setups, CLUB and AIM, are complemented by several UV pulsed laser systems in our laboratory. The laser beams can be switched and directed into different input ports of both machines for different experiments outlined below.

In the next part first we outline some general principles of our experiments in Sec. 2.1: 2.1.1 describes the supersonic expansions for molecular beams and cluster generation, and 2.1.2 introduces the photodissociation. Then the CLUB apparatus is described in general in Sec. 2.2, and a brief account of the individual experiments follows: 2.2.1 describes the photodissociation experiment and VMI; 2.2.2 outlines the mass spectrometry experiments with electron- and photo-ionization, and NaPI ; 2.2.3 explains the pickup experiment and clusters cross section measurements. Subsequently the AIM will be described in Sec. 2.3. Finally, the account of the laboratory laser systems will be given in Sec. 2.4.

2.1 Physical principles

2.1.1 Supersonic expansions, molecular beams

Molecular beams are generated by *supersonic* – so called *free-jet* – expansions of molecules in the gas phase into the vacuum. The overview of the technique can be found in many reviews and textbooks, e.g., in Refs. [5, 6]. Generally, the gas expansion can be characterized by the Knudsen number K_n=λ/d, where λ is the mean free path of the molecules in the reservoir and d is the nozzle diameter. For $K_n \geq 1$ the molecules do not collide frequently in the nozzle vicinity and an effusive molecular beam is generated characterized by the Maxwell-Boltzmann distribution of molecular velocities, low intensity, and wide angular distribution. In this regime the expansion can be treated within the gas kinetic theory.

On the other hand, for $K_n \ll 1$ the supersonic expansions can be achieved resulting in faster molecular beams with narrow velocity distribution, high particle densities and small angular divergence. The condition $\lambda \ll d$ implies many collisions during the expansion establishing a local equilibrium at each point along the expansion, which can be then treated as an adiabatic process. The molecules, which are accelerated by the pressure difference, reach the local sonic speed at the nozzle throat and further exceed it – therefore the term *supersonic expansion*. The continuous flow in the expansion in this regime can be described by flow dynamic and thermodynamic equations.

The free-jet expansion is illustrated schematically in Fig. 2.1. The internal thermal energy of the gas is turned into the kinetic energy of the molecular flow with velocity u during the

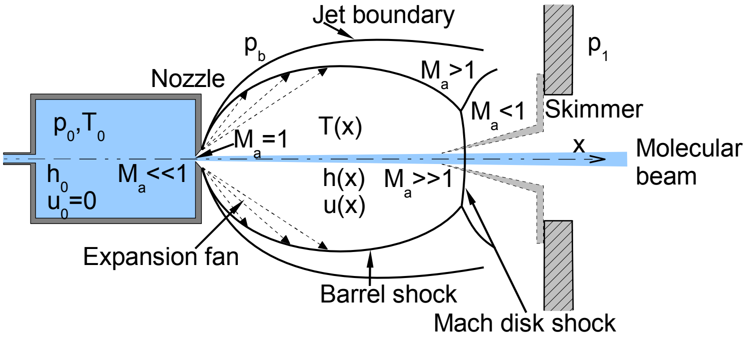

Figure 2.1: Schematic illustration of the supersonic expansion of a gas through a nozzle. The various regions of the free-jet expansion are labelled. The gas expands from the stagnation temperature T_0 and pressure p_0 through the nozzle into a background vacuum p_b. The various free-jet expansion regions are characterized by the Mach number M_a which is the ratio of the particle speed to the local speed of sound, i.e. $M_a \gg 1$ means that highly supersonic speeds are achieved. The molecular beam is formed by inserting a skimmer into the free-jet expansion before the Mach disk shock and the expansion enters another differentially pumped chamber. The skimmer interference with the expansion should be minimized by its shape and position.

expansion. Assuming a one-dimensional flow in the direction x from the nozzle throat the total energy per molecule, which is the sum of the enthalpy $h(x)$ and the kinetic energy, i.e. $e(x)=h(x)+\frac{m}{2}u^2(x)$, has to be conserved along x. Thus

$$h_0 = \frac{m}{2}u^2(x) + h(x), \tag{2.1}$$

where h_0 is the enthalpy of the molecule in the source. The enthalpy is a function of temperature and for an ideal gas can be written as

$$h_0 - h = \int_T^{T_0} \frac{c_p}{N_a} dT' = \frac{c_p(T_0 - T)}{N_a}, \tag{2.2}$$

where N_a is the Avogadros constant and c_p is the molar heat capacity at a constant pressure, $c_p=N_a k_B \frac{\gamma}{\gamma-1}$, where k_B is the Boltzmann constant, and γ is the heat capacity ratio c_p/c_V (γ=5/3 for an ideal gas). The thermal motion of the molecules in the beam is given by the local temperature $T(x)$ which is cooled down during the expansion. If the entire enthalpy is transformed into the kinetic energy of the molecule the terminal temperature will be $T = T_\infty$=0 after the expansion process is finished. In this case Eqs. 2.1 and 2.2 yield for the terminal velocity

$$u = u_\infty = \sqrt{\frac{2k_B T_0}{m}\frac{\gamma}{\gamma - 1}}. \tag{2.3}$$

In reality the molecules maintain a certain rest thermal velocity $\alpha = \sqrt{\frac{2k_B T}{m}}$ corresponding to a finite final temperature T. The molecular cooling, i.e. the quality of the expansion can be characterized by the *speed ratio* $S = u/\alpha$. it can be shown that the speed ratio can be determined experimentally as

$$S \approx 2\sqrt{\ln 2}\frac{u_e}{\Delta u_e}, \tag{2.4}$$

where u_e is the experimentally determined velocity of the molecules and Δu_e is the full width at half maximum (FWHM) of the measured velocity distribution. Typically the speed ratio reaches values of 10 to 100, i.e., the thermal speed of the molecules is one or two orders of magnitude smaller than the beam speed. Despite many approximations in the derivation of Eq. 2.3, the measured beam velocities agree surprisingly well with u_∞ especially for rare gas expansions. By the way of example the calculated terminal velocity for He and Ar expansions at room temperature (300 K) u= 1767 ms^{-1} and 559 ms^{-1}, respectively, usually agree with the measured velocities within a few percent.

Due to the assumption T=0 the terminal velocity u_∞ should be the upper limit. However, in the cluster beams the condensation energy released upon molecule clustering can accelerate the species and even faster beams than the calculated u_∞ can be obtained. It should be noted that the above derivation of u_∞ assumed c_p being temperature independent, which is a rough approximation. By the way of example for He, which is usually considered to be closest to the ideal gas behaviour, c_p changes by factor of four in the temperature range between 3 K and 300 K. A more rigorous treatment of the supersonic expansions can be found in the above mentioned textbooks [5, 6] and in [74, 75].

The molecules cool down in the expansion cooling the various degrees of freedom at various rates depending on the energy transfer collision cross sections for the various energy modes. Therefore the different energy modes of the molecules can be characterized by different temperatures. The translational temperature of the random molecular motion α around the beam velocity u can correspond to very low temperatures T_{tr} ~1-10 K. The rotational relaxation leads to very low temperatures typically T_{rot} ~10 K. This strong cooling is largely exploited in various rotational and ro-vibrational spectroscopies. On the other hand, vibrational relaxation requires typically 10^4 collisions, while in usual expansions the molecules undergo 10^2-10^3 collisions, leading to only moderate vibrational cooling and consequently the vibrational modes usually freeze out in the expansion without converting their energy into the directional velocity of the beam. The low temperatures, the long interaction time between molecules moving in the same direction with the same velocity, and the numerous collisions in the expansion can lead to the cluster generation in the beam.

Molecular clusters are often produced in *seeded expansions*. The molecules are added in small concentrations ($\leq$10 %) to the expansion of a carrier gas, typically rare gas such as He or Ar. To calculate the beam velocity for such expansions, Eq. 2.3 can be modified by using a weighted average mass $m = C_M \cdot m_M + (1 - C_M) \cdot m_B$, where C_M is the relative concentration of molecules M, m_M is their mass, and m_B is the mass of carrier (buffer) gas. As long as the concentration of molecules is small, the expansion parameters, i.e., the velocity u and speed ratio S, are mostly determined by the carrier gas. Thus the heavy molecules coexpanded with helium can reach high speeds and velocity ratios. Helium also does not tend to generate clusters with the molecules due to its very weak interactions and a beam of isolated molecules or small pure molecular clusters are generated. Argon, due to its higher mass, can carry away more energy from the system in three-body collisions, i.e. the clustering of molecules in Ar expansions is more efficient. This results in larger clusters generated in Ar than in He under the same expansion conditions. However, the somewhat stronger interaction of argon with the molecules can also lead to the generation of mixed clusters with Ar [65, 66]. The differences between He and Ar expansions are exploited in our experiments with clusters discussed in this work.

The clusters generated in free jets exhibit a certain size distribution. If small clusters are produced, e.g., in He-expansions under normal conditions[1], the size distributions usually assume an exponential shape, the molecular beam being dominated by the monomers and falling off exponentially towards lager cluster sizes.

A typical example of the larger clusters discussed in this work are the rare gas and water clusters. Their size distribution can be characterized mathematically by a log-normal distribution, the width of which roughly corresponds to its mean value [77]. The mean cluster size can be determined from the expansion pressure p_0 and temperature T_0 according to the empirical

---

[1] It should be mentioned that under high enough pressures (several tens bars) and low enough temperatures (typically around 10 K and below) even helium can generate large clusters of 10^3-10^8 atoms, so called He nanodroplets [76].

formula (Hagena's scaling law) [78, 79, 80, 81]:

$$\bar{n} \;=\; K \cdot \left(\frac{\Gamma^*}{1000}\right)^{\zeta}, \tag{2.5}$$

where $K = 38.4$ was determined from diffractive He atom scattering on large Ar_n clusters [81]. The dimensionless parameter Γ^* introduced by Hagena [79] allows to compare various expansions independent of nozzle and gas parameters:

$$\Gamma^* \;=\; \frac{p_0[mbar] \cdot d_e[\mu m]^{0.85}}{T_0[K]^{2.2875}} \cdot K_c, \tag{2.6}$$

where K_c is characteristic constant of the expanding gas (e.g., $K_c = 1646\ \mathrm{K}^{2.2875}\mathrm{mbar}^{-1}\mu\mathrm{m}^{0.85}$ for Ar) and d_e is the equivalent nozzle diameter, which is for the present nozzles of conical shape with diameter d and opening angle α_D:

$$d_e \;=\; k \cdot \frac{d}{\tan(\alpha_D/2)}, \tag{2.7}$$

where $k = 0.736$. For example, in the present experiments under typical expansion conditions p_0= 3 bar and T_0= 210 K the argon expansion through the typical nozzle of d= 60 μm diameter and α_D= 30° opening angle results in the mean Ar_n cluster size $\bar{n}$=100.

The other example of the large clusters discussed in this work are the water clusters (ice nanoparticles). These can be produced by pure or Ar-seeded expansion of water vapour in a special cluster source with a heated reservoir attached directly to the nozzle inside the vacuum chamber. The reservoir can be filled with water from outside the vacuum and heated to a temperature T_R ($\sim$300-470 K) to generate sufficient water vapour pressure expanded through the nozzle, which is heated independently to a temperature $T_0 \geq T_R$ to prevent condensation in the nozzle. The size distributions of large water clusters $\bar{n}$=10-1750 have been studied previously in the group of U. Buck with the present water cluster source [82]. Their size distributions were measured directly by fragmentation free methods, namely by doping with Na atoms followed by single photon ionization [83] which will be explained in Sec. 2.2.2. The resulting average sizes could be again correlated with the source parameters based on Eq. 2.5. The resulting parameters are available for water clusters in Refs. [82, 83]:

$$\Gamma^* \;=\; \frac{n_0 \cdot d_e^q \cdot T_0^{q-3}}{K_{ch}}, \tag{2.8}$$

where the characteristic constant $K_{ch} = r_{ch}^{q-3} T_{ch}^{q-3}$ for H_2O derives from the molecular parameters r_{ch} = 3.19 Å, and T_{ch} = 5684 K. The stagnation pressure p_0 and gas density n_0 can be connected through ideal gas law. The parameters $K = 11.6$, $\zeta = 1.886$ (Eq. 2.5) and $q = 0.634$ (and $k = 0.933$ in Eq. (2.7) for d_e) were determined from fitting the measured size distributions of large $(H_2O)_n$ clusters. [82]

A highly relevant general question is the one of the internal cluster temperatures, yet it is difficult to access experimentally. Two approaches have been exploited so far: (1) electron diffraction, which reflects the thermal motion of the particles forming the cluster [84, 85]; (2) rovibrational spectroscopy of a molecule embedded in the cluster. The later method works only for very weakly interacting large helium clusters, which turned out to be superfluid and thus not hindering the motion of the molecule. Therefore rotationally resolved spectra of, e.g., SF_6 and OCS molecules were obtained in helium nanodroplets and their rotational temperature was determined to be 0.37 K [17]. This is probably the most accurately determined cluster temperature. For the other rare gas clusters the temperatures determined by the first method range from approximately 10 K for Ne_N and 37 K for Ar_N to 80 K for Xe_N with some dependence on the cluster size [84, 85].

For water clusters still some ambiguity exists. The electron diffraction yielded the temperature of 180 ± 20 K for $(H_2O)_N$, $N \leq 200$ [86]. Besides the cluster temperatures can be estimated based on model calculations. A relaxation model calculations delivered temperatures of approximately 70 K and 190 K for $(H_2O)_9$ [87]. An estimate based on the same model results in temperatures in the range 100-130 K for clusters of several hundreds water molecules [88]. Some discussion of cluster temperatures can be found in the reviews [10, 89, 90].

It has been mentioned above that the coexpansion (e.g., HBr with Ar) can lead to the clusters with foreign molecules embedded inside. To prepare mixed clusters with molecules or small host clusters adsorbed on the surface of the larger clusters the so-called pick-up technique introduced by Scoles and coworkers [91] is applied. The cluster is passed through a scattering cell filled with the molecular vapour with a variable pressure. The number of captured molecules depends sensitively on this pressure and follows a Poisson distribution [92]. By a suitable choice of the pick-up pressure, one can arrange conditions at which only one or a few molecules are adsorbed on the surface of the cluster. The probability of the molecule to penetrate inside the cluster depends on the parameters of the local interactions between the deposited molecule and the cluster molecules. By the way of example, it has been shown by a series calculations [93] that, e.g., the HBr molecule deposited on Ar_n in the pick-up process stays near the surface in the first and second shells. Similarly, if more than one molecule is coadsorbed on the cluster, they can coagulate to generate small clusters on the nanoparticle, again depending on the nature of intermolecular interactions. The pickup processes will be explained in more details in Sec. 2.2.3, and the results based on this technique are presented in Sec. 3.4.

2.1.2 Photodissociation

In this section the general physics of the photodissociation process is briefly outlined. The basic idea of photodissociation has been mentioned in the introduction Sec. 1.2. Here, the photodissociation is illustrated on the example of the HBr molecule. Fig. 2.2 shows schematically the potentials involved in the photodissociation process: the ground state $X^1\Sigma_0^+$, and the repulsive excited electronic states $A^1\Pi_1$, $a^3\Pi_1$ and $a^3\Pi_0^+$.[2] The $A^1\Pi_1$ and $a^3\Pi_1$ states correlate with the

---

[2] It should be mentioned that alltogether 12 electronically excited states are involved in the photodissociation processes of hydrogen halides in general. For HBr only the 3 excited states discussed above can be excited directly from the

Br atom in the ground $^2P_{3/2}$ state in the dissociation limit, while the $a^3\Pi_0^+$ potential leads to the spin-orbit excited state Br*($^2P_{1/2}$). The excitation $X^1\Sigma_0^+ \rightarrow a^3\Pi_0^+$ is a parallel transition, while the transitions to the $A^1\Pi_1$ and $a^3\Pi_1$ states are perpendicular[3]. The underlying mechanism of HBr photodissociation has been studied and understood in detail [94, 95, 96] also in Buck's laboratory with the original version of the present apparatus [97]. At 243 nm used in our experiment the dissociation to the Br ground state proceeds through the excitation to the $A^1\Pi_1$ state which is a perpendicular transition, and the excited Br* state can be populated in a parallel transition via the $a^3\Pi_0^+$ state.

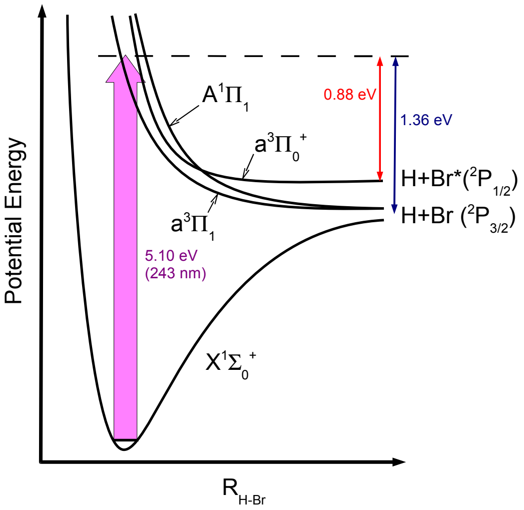

Figure 2.2: PESs involved in photodissociation of the HBr molecules. The vertical excitation with 243 nm (5.10 eV) is shown by the broad vertical arrow. The excited states $a^3\Pi_1$ and $A^1\Pi_1$ correlate with the ground state Br($^2P_{3/2}$) in the dissociation limit, while the dissociation in $a^3\Pi_0^+$ state leads to the spin-orbit excited state Br*($^2P_{1/2}$). In the former process 0.88 eV excess energy is relesed into the relative kinetic energy of the fragments, while in the latter one it is 1.36 eV.

The kinetic energy of the H fragment $E_{kin}(H)$ measured in our experiment can be interpreted in terms of the energy balance equation

$$h\nu + E_{int}(HBr) = D_0 + E_{int}(Br) + E_{kin}(Br) + E_{kin}(H), \tag{2.9}$$

where the laser energy $h\nu$ and the dissociation energy D_0(HBr)= 3.745 eV are known. The Br fragment kinetic energy $E_{kin}(Br)$ follows from the conservation of momentum. The HBr molecule dissociates to the Br atom either in the ground $^2P_{3/2}$ or the excited $^2P_{1/2}$ state with the excitation energy $E_{int}(Br)$ of 0.475 eV. The electronic excitation of the Br atom is reflected

---

electronic ground state due to the selection rules for electronic dipole transition.

[3] In principle parallel (perpendicular) transition means that the transition dipole moment of the molecule is parallel (perpendicular) to the molecular axis. In other words, the parallel (perpendicular) transition can be excited with a linearly polarized light oriented with the polarization electric field $\vec{E_L}$ vector parallel (perpendicular) to the molecular axis.

by the energy loss of the H atom. On the other hand an initial internal excitation of the HBr molecule $E_{int}(HBr)$ is reflected as a kinetic energy gain of the H fragment. Thus at the wavelength of our laser 243 nm (5.10 eV) the photodissociation from the v=0 vibrational level of the ground electronic state will yield H atoms with $E_{kin}(H)$= 1.34 eV and 0.87 eV corresponding to the generation of Br atom in the ground or excited state, respectively.[4] An example of such H-fragment kinetic energy distribution after HBr photodissociation will be presented in Sec. 2.2.1.

Besides the fragment kinetic energy, additional information, which can be obtained from our experiment, is the H-fragment angular distribution. The distribution $I(\theta)$ is a product of $\vec{E}$–$\vec{\mu}$–$\vec{v}$ vector correlation, where $\vec{E}_L$ is the electric field vector of the linearly polarized laser, $\vec{\mu}$ is the transition dipole moment for the excitation driven by the laser field, and $\vec{v}$ is the resulting fragment velocity. For diatomic molecules $\vec{\mu}$ can be either parallel or perpendicular to the molecular axis. If the photodissociation is fast compared to the molecular rotation $\tau_{dis} \ll \tau_{rot}$, the fragment velocity vector $\vec{v}$ lies in the molecular axis. This situation is illustrated in Fig. 2.3. It can be shown that the resulting fragment angular distribution is given by

$$I(\theta) = \frac{\sigma_0}{4\pi}(1 + \beta P_2(\cos\theta)), \tag{2.10}$$

where σ_0 is the photodissociation cross section and $P(x) = 1/2(3x^2 - 1)$ is the second order Legendre polynomial. The anisotropy parameter β assumes values between -1 and +2 for perpendicular and parallel transitions, respectively. Fig. 2.3 shows the corresponding $I(\theta)$ distributions.

Now the photodissociation of the HBr molecule in the cluster environment can be discussed. The kinetic energy of the H fragment $E_{kin}(H)$ will be given by energy balance similar to the Eq. 2.9 for the single molecule

$$h\nu + E_{int}(HBr) = D_0 + E_{int}(Br) + E_{kin}(Br) + E_{kin}(H) + E_{clu}. \tag{2.11}$$

The influence of the cluster is included by the term E_{clu}, which expresses a continuous energy loss of the H atom caused by collisions and capturing processes by the cluster cage. Thus we can distinguish essentially three cases of photofragment behavior in the cluster which have already been illustrated pictorially in Fig. 1.1: (i) The H-atom leaves the cluster after the photolysis without loosing any energy in interactions with the cage atoms, i.e. $E_{clu} = 0$ (*direct cage exit*). (ii) In the other extreme case the H fragment can loose all of its kinetic energy in the collisions with the cage atoms, i.e. $E_{kin}(H) = 0$ (*cage effect*). (iii) Finally, in an intermediate case the fragment looses part of its energy in collisions and escapes the cage (*delayed cage exit*).

In the clusters it can be also noted that some fragments appear at energies exceeding the maximum available energy. From Eq. 2.11 it follows that these fragments have to originate from

---

[4] The total energy, E_{tot}= 1.36 eV and 0.88 eV, released in the photodissociation process is partitioned between the kinetic energy of H and Br fragments. Thus, considering the momentum conservation, the kinetic energy of H-fragment is $E_{kin}(H)$=$E_{tot} \times \frac{m_{Br}}{m_H + m_{Br}}$.

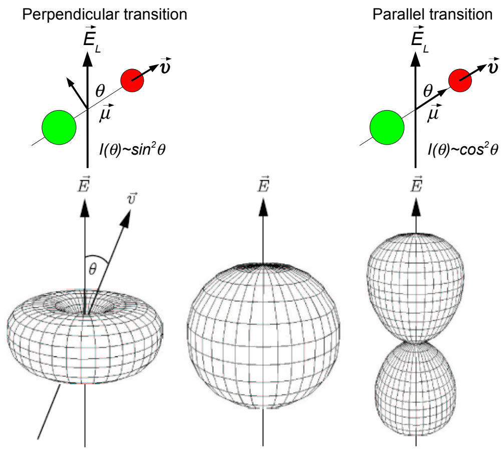

Figure 2.3: Top panel: illustration of the $\vec{E}$–$\vec{\mu}$–$\vec{v}$ vector correlation ($\vec{E}_L$–laser electric field vector, $\vec{\mu}$–transition dipole moment, $\vec{v}$–fragment velocity). Lower panel: the fragment angular distributions for a perpendicular transition ($I(\theta) \propto \sin^2\theta$, $\beta = -1$, left), parallel transition ($I(\theta) \propto \cos^2\theta$, $\beta = +2$, right), and isotropic distribution ($\beta = 0$, center).

initially vibrationally excited molecules. The mechanism of vibrational excitation of a molecule by frustrated dissociation in clusters was revealed in our experiment with photodissociation of acetylene molecules in various clusters [98]. It has been found that the C_2H_2 molecules can be initially excited into a dissociative state but caged by the cluster and recombined to the electronic ground state, yet vibrationally excited. These vibrationally excited molecules were then photodissociated by the next photon yielding the faster fragments.

We have increased the average time delay between the subsequently arriving photons by decreasing the laser photon fluence and thus the excited molecule could dissipate more energy into the cluster before absorbing the dissociating photon, which led to less amount of the faster fragments. This is schematically illustrated in Fig. 2.4. It is interesting to note that this way, we were actually able to obtain information about the cluster dynamics in the time domain from the measurements in the energy domain (i.e. the measurements of the kinetic energy of the H-fragments). Indeed, such measurements cannot substitute the time-resolved experiments [99, 54] but can provide an interesting alternative to study the dynamics in clusters and are capable of delivering a complementary information.

2.2 CLUB: CLUster Beam apparatus

The CLUB apparatus is schematically depicted in Figure 2.5: it represents a unique and versatile apparatus for variety of experiments with clusters. The molecular beam is produced by continuous supersonic gas expansions through a conical nozzle into vacuum, as described in Sec. 2.1. The mean cluster sizes can be controlled by the expansion conditions: pressure,

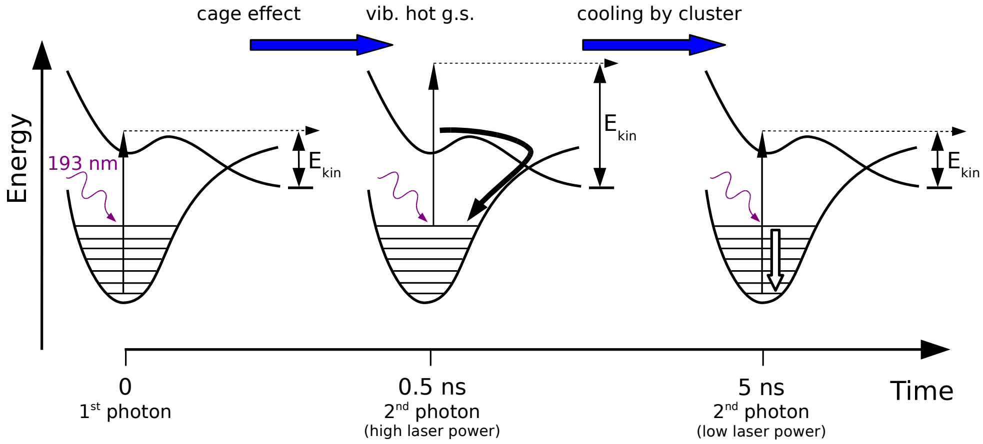

Figure 2.4: Schematic illustration of the photodissociation dynamics reflected by the fragment kinetic energy measurements: The molecule is promoted to an excited dissociative state but can be caged by the cluster environment and undergo a transition through a conical intersection to a vibrationally excited electronic ground state. The next arriving photon can excite the vibrationally hot molecule resulting in the fragments with higher kinetic energy E_{kin}. If the delay between the successive photons is increased by using lower laser intensities, the vibrational relaxation of the molecule by cluster cooling can result in less energetic fragments. (Adopted from photodissociation measurements of C_2H_2 in clusters [98])

temperature and nozzle geometry. The clusters can be doped with foreign molecules either in coexpansion or by passing them through a pickup cell filled with the molecular gas. Up to three different pickup cells can be used in the CLUB simultaneously as will outlined in Sec. 2.2.3.

After passing through several differentially pumped high vacuum chambers the cluster beam enters the chamber where the photodissociation experiments are performed. The molecules in clusters are excited with nanosecond UV laser pulses. The desired photofragments are then selectively photoionized by resonance enhanced multiphoton ionization (REMPI) method and their kinetic energies are recorded. The time-of-flight (TOF) technique was used to measure the fragment velocity previously. Recently we have implemented the velocity map imaging (VMI) technique[100, 101, 102, 103]. In this technique the ionized photofragments are detected with a large-area position sensitive detector with phosphor screen and the resulting images are recorded with a fast CCD camera. The image processing delivers a detailed 3D information about the photofragment velocities from which the photodissociation dynamics can be learned. The technique will be explained in Sec. 2.2.1.

The next chamber along the beam path contains a new reflectron TOF mass spectrometer (RTOF) with electron- and/or photo- ionization options. It has been first implemented and described in our recent studies by [104] and [65] and it will be described in some detail in Sec. 2.2.2. At the end of the apparatus, the clusters can be also detected and analysed by a quadrupole mass spectrometer after electron ionization. This option serves the beam alignment

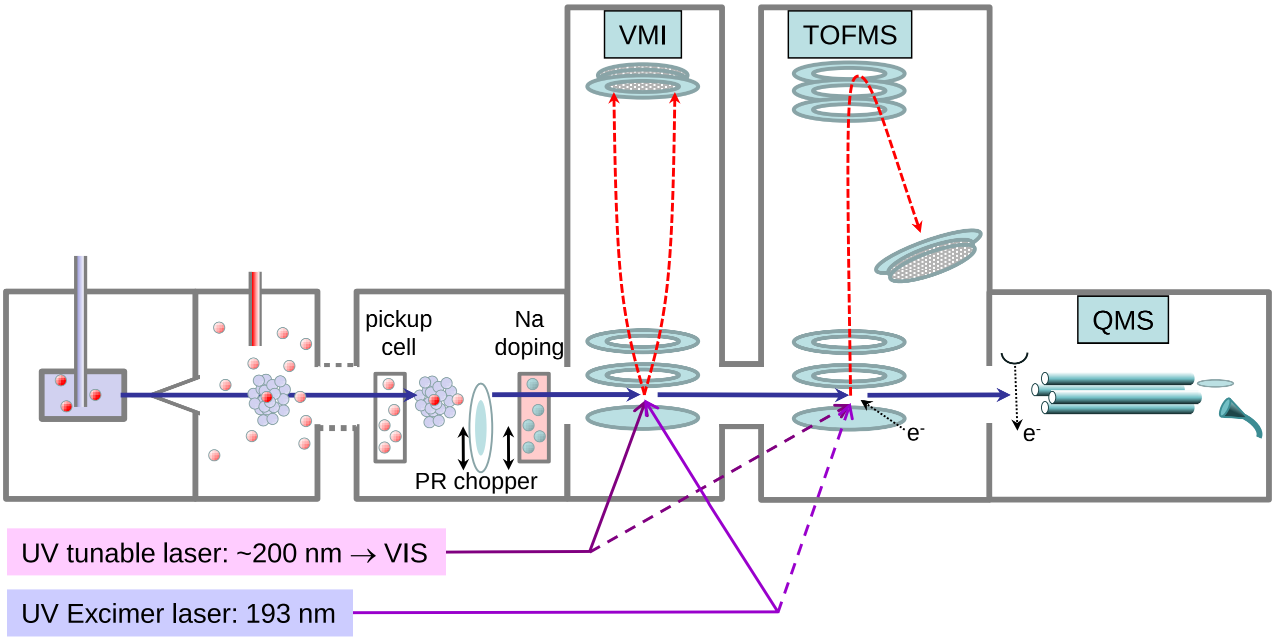

Figure 2.5: The schematic picture of the present experiment: VMI–velocity map imaging; TOFMS–reflectron time-of-flight mass spectrometer, where the clusters can be ionized by electrons (EI) or photons (PI); QMS–quadrupol mass spectrometer, where clusters are ionized by EI.

and analysis. Also cluster velocities can be measured using a pseudorandom (PR) chopper and the quadrupole detection to measure the cluster flight-times. Subsequently the cluster pickup cross sections can be evaluated from change in the cluster velocity in the pickup experiments. This method was exploited in many of our studies [64, 105, 106, 67, 107, 108] and will be described in Sec. 2.2.3.

It should be mentioned that the CLUB apparatus poses one additional experimetal option which has not been used in the works outlined within this collection. After passing the skimmer, the cluster beam can be crossed at right angles by a secondary beam. This crossed beam arrangement can be implemented for cluster-molecule reaction investigation, or for a neutral cluster size selection in elastic scattering. For this purpose the cluster beam is elastically scattered with a beam of He atoms produced in the secondary nozzle. The principle of the size selection method is described in [109, 110] and we have exploited this method in several of our earlier studies in Prague [111, 45, 112], however, we will not discuss this method here.

A more detailed description of the individual parts of the experiment will follow in the next sections.

2.2.1 Velocity map imaging

The up-to-date method for photodissociation investigation is the velocity map imaging (VMI) and its various modifications such as various slicing methods. All these methods have been summarized in recent textbook [103] and review article [113], and for the local community we have recently described this method in detail in Czechoslovak Physics Journal [114]. Therefore it will be only briefly outlined below.

The ion imaging technique was introduced by Chandler and Houston in 1987 [100]. However, it became the major method for the photodissociation studies after the introduction of VMI by Eppink and Parker in 1997 [101] and especially with the various slicing methods reviewed in [113].

The VMI principle is schematically depicted in Fig. 2.6. Generally, in the imaging of a photodissociation process, the expanding Newton sphere of fragments is projected after a certain flight time onto a position sensitive detector -typically a large area multi-channel plate with a phosphorous screen. The image of the phosphorous screen is recorded with a charge-coupled device (CCD) camera. The complete information about the fragment velocity obtained from the image yields a very detailed insight into the dynamics of the photodissociation process. This is supported also by a state-selective photoionization (REMPI) providing a single quantum state specificity.

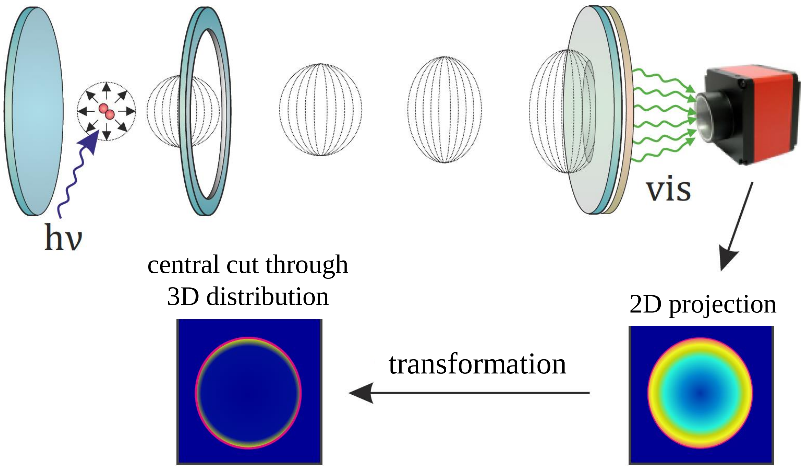

Figure 2.6: The schematic picture of the velocity map imaging principle. The photofragments after the photodissociation generate the so called Newton sphere in the space. They are REMPI ionized and extracted towards a position sensitive detector (e.g., a multichannel plate with a phosphor screen). The expanding Newton sphere is projected onto the detector generating a 2D projection of a 3D velocity distribution of the photofragment. From this 2D projection a slice through the 3D distribution can be reconstructed mathematically.

Fig. 2.7 illustrates the VMI results on the example of the HBr molecule dissociation, which was discussed above in Sec. 2.1. It shows the H-fragment image after the 193 nm photodissociation of HBr molecule. The image shows the central slice through the 3D velocity distribution obtained by Abel transformation of the measured raw image. Two sets of doublets of concentric rings can be seen in the images: the inner one corresponds to the 243 nm photodissociation (in addition to the 193 nm also 243 nm has to be used in the experiment for the H-fragment REMPI) and the outer doublet originates from the 193 nm photodissociation. Always the inner circle of the doublet corresponds to the photodissociation process yielding the Br fragment in the spin-orbit excited state Br$^*(^2P_{1/2})$, and the outer ring to the ground state Br$(^2P_{3/2})$, see the corresponding PES on the left in Fig. 2.7 and Sec. 2.1. Integrating the images along circles corresponding to a constant fragment velocity (constant kinetic energy) yields the kinetic energy distribution (KED) shown at the bottom in Fig. 2.7. The anisotropy of the observed processes with respect to the laser polarization (vertical) is obvious from the images on the first sight (anisotropy of the corresponding circles). The angular distributions for the individual processes can be evaluated by integrating the images along angle directions in a certain energy range corresponding to the studied process as illustrated at the bottom right graph.

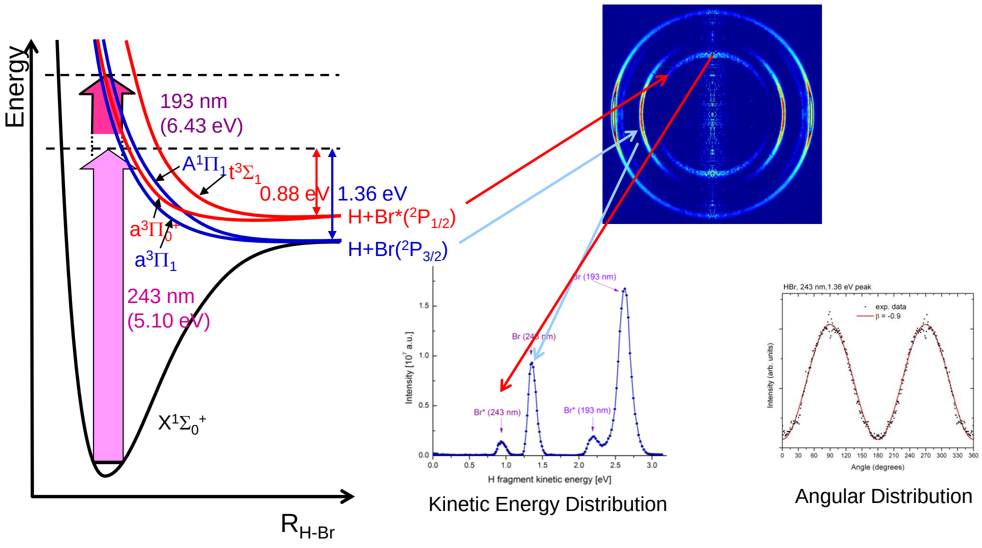

Figure 2.7: The illustration of VMI on the example of HBr photodissociation. Potential energy curves relevant for HBr photodissociation at 193 nm and 243 nm are shown left (see Sec. 2.1). The shown central slice through 3D velocity distribution of H fragments was obtained by Abel transformation of the measured raw image. Integration of the image yields the fragment kinetic energy distribution (bottom left) and angular distribution (bottom right). See text for details.

Fig. 2.8 shows the clustering effects exhibited in the VMI images of HBr molecules photodissociated at 243 nm in large Ar clusters. As discussed above in Sec. 2.1, the image shows a strong central peak corresponding to the zero kinetic energy fragments generated by the *cage effect*. Indeed, the fast H-fragments corresponding to the *direct exit* are also present, and some intensity in between (clearly seen in KED) corresponds to the *delayed exit*. Finally, some faster fragments due to the HBr vibrational excitation after caging are also discernible in the images and KED. More detailed discussion can be found in the attached Ref. [71].

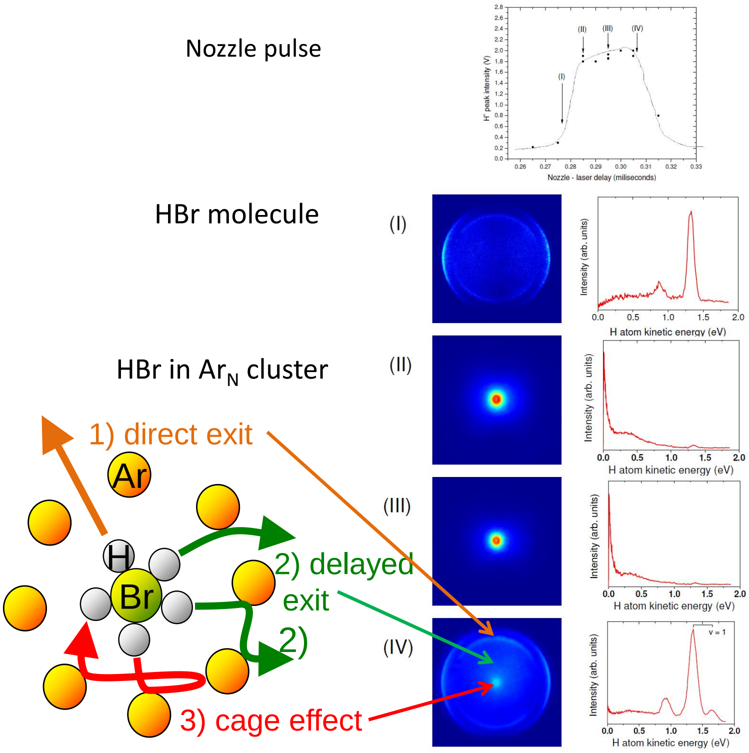

Figure 2.8: The illustration of the clustering effects exhibited in the VMI images of HBr molecules photodissociated at 243 nm in large Ar clusters.

The main advantage of the VMI method for our experiment is the collection efficiency: while the originally used TOF method harvested essentially only the fragments flying either directly to the detector or in the opposite direction and all the other fragments also carrying information about the studied process escaped the detection, the imaging methods collects essentially all the fragments flying in any direction after the photodissociation. The spectra equivalent to the TOF spectra can be obtained by data processing as cuts through the measured images. Therefore the VMI method was introduced in the CLUB apparatus, however, first we have developed and tested the technique on the AIM. The VMI systems on the CLUB and AIM are essentially identical, and a detailed technical description of our particular VMI follows by the AIM setup in Sec. 2.3.

2.2.2 Mass spectrometry experiments

RTOF Mass Spectrometer

The RTOF MS is a double stage reflectron system with Willey-McLaren ion extraction, custom built by Stefan Kaesdorf. [115] The molecular beam passes directly through the extraction region of the mass spectrometer to ensure the highest possible sensitivity. Clusters are ionized by a pulsed electron gun at 10 kHz frequency. Electron energy can be varied in 1–90 eV range with a resolution of ≈0.7 eV. Produced ions are extracted by 10 kV pulse and accelerated into the final kinetic energy of 8 kV. After passing 0.95 m effective flight path the ions are detected on 4 cm in diameter Photonics MCP detector in chevron configuration. The mass resolution $\frac{M}{\Delta M} \geq 5000$ can be achieved where ΔM is measured as the full width at half maximum (FWHM) of a single mass peak at around 500 Da. The time-to-digital conversion (TDC) method is employed for data acquisition with 0.5 ns or 0.25 ns step.

The ion signal can be measured as the function of two parameters: m/z ratio and electron energy. Particular mass spectra and electron energy dependent ion yields were then extracted from the obtained 3D data and analysed using Origin program (OriginLab, Northampton, MA). Appearance energies of particular ions are derived from power law fits of the measured ion yields near the threshold using the functional form: $y = (x - AE)^p + b$, according to Wannier. [116] The free parameters AE, b, and p represent appearance energy, background, and power dependence, respectively. This approach was successfully used for the appearance energy measurements [65, 66]. The electron energy axis has to be calibrated with a suitable peak of known appearance energy, e.g. H_2O signal with IE= 12.621 eV.

In addition to the electron ionization also photoionization can be used to charge the clusters. For this purpose, any of the UV lasers in our laboratory can be directed into the RTOF chamber and focused between the repeller and extractor plates of the RTOF ion source. Care must be taken not to strike the metal plates, since the UV light would release electrons from the metal which could be accelerated by the extraction voltage and ionize the clusters. The UV ionization of the clusters is a non-resonant multiphoton process in our case. Usually we employ ArF_2 laser with the wavelength of 193 nm (6.4 eV) but other lasers and wavelengths could be used too, e.g. 315 nm for NaPI and also for a direct two-photon ionization of hydroxypyridine in clusters.

Na-doping and photoionization

Various mass spectrometric methods represent indispensable tools for characterization of clusters, free nanoparticles and aerosol particles especially in atmospherically relevant investigations [117, 118, 119]. They can provide an insight into the size, structure and chemical composition of studied species. A major drawback of mass spectrometry is the necessity of cluster ionization which often leads to a significant fragmentation, especially in the case of the weakly bound cluster species. In 2002 the group of U. Buck introduced Na-doping and subsequent photoionization (NaPI) as a fragmentation-free cluster ionization method for large water and ammonia clusters [82]. Applying this ionization method, the mass spectrometry revealed the original neutral cluster size distributions of water and ammonia clusters.

The essential idea in this method was that a Na atom releases an electron generating Na^+ ion and so called *solvated electron* e_s^- in the cluster. The binding energy of the solvated electron was approximately 3.2 eV and 1.8 eV in large water and ammonia clusters, respectively [120, 90]. Thus low energy UV photons could be used to photodetach e_s^- from these clusters and the photodetachment did not lead to any significant cluster fragmentation. The principle of the NaPI method is schematically depicted in Fig. 2.9 The same group has also obtained essentially fragmentation-free mass spectra of rare gas clusters by Na-doping [83]. In this case, however, the ionization mechanism did not involve any solvated electron - the Na atoms with low ionization energy of approximately 5.1 eV were ionized directly in the clusters by 193 nm (6.1 eV) photons.

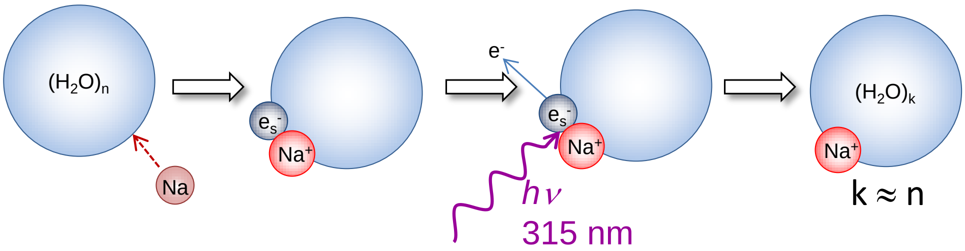

Figure 2.9: The schematic illustration of the NaPI method: Na doping of the water clusters $(H_2O)_n$ leads to the Na^+ ion and solvated electron e_s^- generation in the cluster. The e_s^- is subsequently photodetached by a low energy UV photon (315 nm in our case) leaving the positively charged $(H_2O)_kNa^+$ cluster behind. This method has been proved to be essentially fragmentation-free $k \approx n$.

Later on, the group of R. Signorell proposed the NaPI method as a “sizer for weakly bound ultrafine aerosol particles” due to the fragmentation-free ionization [119, 121]. They have implemented the method to investigate different large homogeneous clusters [122, 123, 124]. They have also revealed the nature of the solvated electron in various clusters using photoelectron velocity map imaging after Na doping [125, 126]. The group of T. Zeuch used Na-doping for investigations of vibrational spectroscopy of size selected large clusters [127, 128, 129, 130]. More details about the NaPI and its different aspects and applications can be found in two recent comprehensive reviews [90, 89]. However, we have shown in several publications covered within this collection that the application of the NaPI to aerosol particles and mixed clusters is more complicated and can yield completely different results than expected [57, 131, 132].

In the CLUB apparatus we have implemented the Na-oven in the vacuum chamber before the VMI chamber. The Na-oven was used previously in the Buck’s group [82]. An important extension worth mentioning is a motorized motion of the oven inside vacuum chamber which allows to remove the oven from the beam path and measure the direct unattenuated molecular beam without the necessity of cooling down the oven. The second important improvement was a shielding box around the oven with an entrance and exit holes for the beam, which shields the vacuum chamber from the deposition of the Na-vapour and helps to improve the background vacuum. The operating conditions of the Na-oven can be found in the corresponding publications [57, 131, 132]. The conditions can be set so that the clusters undergo mostly single or multiple pickup processes as they pass through the oven. This is an important factor discussed in our Ref. [132].

A unique combination of NaPI and EI methods for detection applied to a single molecular beam allows for investigations of the Na reactivity in clusters [104, 131, 132]: while the EI ionizes all cluster species, the NaPI requires the presence of solvated electron which is lost if a molecule reacts in the cluster with the Na atom or with the solvated electron. In Sec. 3.2 we demonstrate a few cases especially of mixed clusters where NaPI method cannot provide a real picture of the neutral cluster size distribution and composition. A detailed understanding of the underlying processes is necessary for an implementation of NaPI method for studying of the mixed clusters representing atmospheric aerosols.

2.2.3 Pickup experiment

The principle of the experiment can be briefly summarized as follows: clusters are doped with the guest molecules in a pickup chamber and two characteristics of the cluster beam are measured as a function of the pickup gas pressure -the neutral beam velocity and the fragment ion mass spectra.

Several pickup cells were built and can be implemented in the pickup vacuum chamber of the CLUB apparatus. Up to three different cells can be used in series in our experiments. There is the original T-shaped 50 mm long pickup cell right at the entrance to the pickup vacuum chamber. This cell can be used to introduce molecules from an outside inlet system either in the gas phase, or highly volatile substances if the inlet is heated. Recently we have built another heated pickup cell which can be mounted in the pickup vacuum chamber, which is dedicated to pickup of substances introduced into the cell in liquid or solid phase, and their vapour pressure is controlled by heating the cell in the vacuum during the experiment. This cell was used in our recent experiment with the pickup of aniline molecules on water clusters [25]. Finally, there is the above mentioned Na-oven at the end of the pickup vacuum chamber, which can be also filled with other substances than Na.

In addition, in many quantitative experiments we filled directly the scattering chamber (right after the skimmer from the source chamber) with gas molecules from an outside inlet system and used the whole scattering chamber as the pickup cell. The advantage of this arrangement was that the much longer effective capture length of L= 170 mm allowed to operate the chamber at much lower pickup pressures which were still measurable with a calibrated ionization gauge even for a pickup of larger number of molecules on the clusters. The pressure in the chamber was monitored by Bayard-Alpert ionization gauge (Varian type 571), which was calibrated for the specific gases by comparing the measured pressures to the values of a capacitance gauge pressure (Pfeiffer CMR 365). The background pressure in the pickup chamber was $\leq 1\times10^{-6}$ mbar, and the pressure with the pickup gas went up to 7×10^{-4} mbar.

For the velocity measurements the cluster beam was modulated by a pseudorandom mechanical chopper [133] (PR) in the next differentially pumped chamber. The chopper contained two pseudorandom sequences of 127 elements and its rotation with frequency of 492.1 Hz corresponded to a single opening time window of 8 μs. After the chopper the beam passed the flight path of 1510 mm through the photodissociation and RTOF chambers (955 mm in some older experiments before the RTOF chamber insertion in the CLUB) to the ion source of a quadrupole mass spectrometer (QMS) with an electron multiplier detector at the end. The arrival time to the detector was measured. The total flight time was properly corrected for the time spent by the ion fragment in the quadrupole and for any electronic delay of the trigger signals and converted to the beam velocity distribution. The velocity distribution was evaluated from the measured data by the cross-correlation mathematical method. [133] Usually the quadrupole mass spectrometer was set on an ionization fragment of the clusters, and the velocity was measured for several cluster fragments to check for consistency.

By the way of an example, the maximum velocity of the Ar_N clusters (without any pickup gas) measured at the nozzle temperature T_0= 223 K was 490 ms^{-1} with a speed-ratio of S=35. This corresponds to the theoretical maximum beam velocity given by Eq. 2.3, v_∞= 481 ms^{-1}. The slightly higher measured beam velocity can be due to the condensation effect which provides an additional heating of the beam during the expansion as outlined in 2.1.

The clusters in the beam are slowed down by the pickup due to the momentum transfer and the velocity change increases with the number of guest molecules. Let us assume a M_N cluster of a size N with an initial velocity v_i colliding with k stationary molecules in the pickup cell which stick to the cluster. Then the momentum conservation yields for the cluster final velocity v_f the equation:

$$Nm_{Ar}v_i = (Nm_M + km_X)v_f, \tag{2.12}$$

where m_M is the cluster constituent mass and m_X is the mass of the guest molecule. It assumes that no considerable evaporation of cluster constituents occurs upon the pickup. This assumption has been justified by the molecular dynamics simulations outlined in our publications [64, 105, 106]. The simulations also show that the molecule remains on the cluster if a considerable momentum transfer between the molecule and the cluster occurs. Thus this simple model describes the final velocity dependence sufficiently well.

The number of picked up molecules along the path-length L in a gas at a pressure p (corresponding to the number density n_g=p/k_BT) can be expressed as

$$k = n_g\sigma_e L = \frac{p}{k_BT}\sigma_e L, \tag{2.13}$$

where σ_e is the pickup cross section. The measured effective cross section σ_e incorporates the velocity-averaging correction factor [134, 135, 6] into the cross section $\sigma_e = \sigma_0 \cdot F_{a0}(\infty, x)$. Combining equations (2.12) and (2.13), the relative change in the cluster velocity is directly proportional to pickup cell pressure

$$\frac{\Delta V}{V} \equiv \frac{v_i - v_f}{v_f} = \frac{m_X}{N m_{Ar}} \frac{L\sigma_e}{k_B T} p. \tag{2.14}$$

Thus, from the slope of the relative velocity change dependence on the pressure the pickup cross section σ_e can be evaluated.

Since the pickup of the k-th molecule is assumed to be a random process independent of the previous (k-1) events, its probability follows the Poisson distribution: [136]

$$P_k(p) = \frac{1}{k!}(\sigma_e L n_g)^k e^{-\sigma_e L n_g} = \frac{1}{k!}(\frac{\sigma_e L}{k_B T} p)^k e^{-\frac{\sigma_e L}{k_B T} p}. \tag{2.15}$$

Thus the pickup cross section σ_e can be obtained by measuring the dependence of a fragment ion intensity (corresponding to, e.g., pickup of k=1 molecule) on the pickup pressure, and fitting this dependence with the corresponding Poisson distribution. [137]

By a comparison of the two above mentioned methods and their detailed analysis and theoretical simulations we have shown that the method based on the Poisson distribution measurements did not deliver reliable pickup cross sections [64]. Therefore the former method based on the velocity change Eq. 2.14 was used in our publications [105, 106, 107, 67, 108]

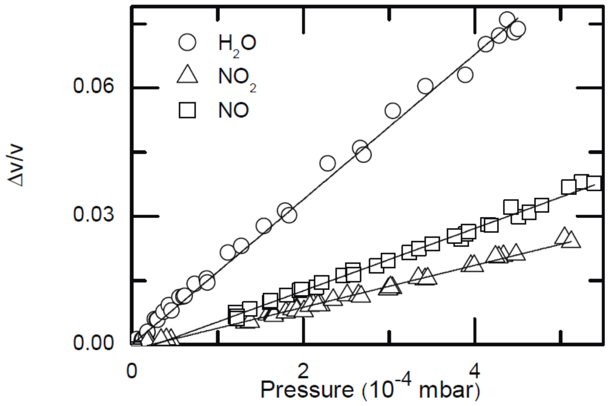

Figure 2.10: The liner dependence of the relative velocity change of the cluster as a function of the pickup pressure for pickup on water clusters $(H_2O)_N$, $\bar{N} \approx 260$.

We plot the relative velocity change as a function of the pressure and fit a linear dependence $\frac{\Delta V}{V} = \alpha \cdot p$. Examples of such plots are shown in Fig. 2.10 From the slope α the pickup cross section σ_e can be evaluated as

$$\sigma_e = \alpha \cdot \frac{m_C N}{m_X} \cdot \frac{k_B T}{L}. \tag{2.16}$$

The quantity that is evaluated directly from the experimental data is the effective cross section

$$\sigma_e = \sigma_0 \cdot F_{a0}(\infty, x), \tag{2.17}$$

which incorporates the velocity-averaging correction factor F_{a0} due to the velocity distribution of the target molecules. [134, 135, 6] Label ∞ denotes the hard sphere potential approximation, and $x = \frac{v_i}{\alpha_g}$ where v_i is the cluster beam velocity and α_g is the most probable velocity in the Maxwellian distribution of the scattering gas. These correction factors were tabulated in the literature. [134, 135]

2.3 AIM: Apparatus for IMaging

The newly-constructed experimental setup AIM (Apparatus for IMaging) is shown schematically in figure 2.11. It consists of two differentially pumped vacuum chambers: a molecular beam source chamber and an interaction chamber. In the interaction chamber the molecular beam is crossed at 90 degrees with a laser beam used for photodissociation and photoionization. The ionic products are analyzed in the velocity map imaging detection system positioned perpendicularly to the molecular and laser beams.

The molecular beam is produced by gas expansion through a pulsed solenoid valve (General valve) with a nozzle of 0.6 mm diameter. The valve is driven by a home-build pulse generator with a tunable nozzle opening time. The nozzle is placed approximately 20 mm in front of the skimmer (0.55 mm openning diameter, 30 deg opening angle) on a movable stage which allows to ajust the nozzle-skimmer distance from outside vacuum. Since this distance is critical for a good quality of the molecular beam, [6] it was optimized for given expansion conditions to signal intensity and image resolution usually moving the nozzle by ±20 mm.

The skimmer separates the source chamber from the interaction chamber. The former is evacuated by a diffusion pump (Balzers, 650 l/s) to the background pressure of $\approx 5\times10^{-6}$ mbar, and the later by a turbomolecular pump (Pfeiffer Vacuum, 520 l/s) to $\approx 7\times10^{-8}$ mbar (without the gas pulse). In the interaction chamber the molecular beam is crossed with a laser beam in the center of the interaction chamber about 12 cm downstream from the skimmer orifice.

The interaction point is in the center of the ion electrostatic lens system which extracts the ionic photoproducts towards a position sensitive detector. The design of the ion lens system approximately follows the original velocity map imaging designed by Eppink and Parker. [101] The velocity mapping condition is achieved by three electrodes: repeller, extractor and ground with grid-less arrangement. The outer diameter of the electrodes is 63 mm and the spacing between them is 10 mm. The holes in the extractor and ground electrode have 20 mm diameter. Typical voltages at which velocity mapping conditions are achieved are 1.8 kV on repeller and 1.4 kV on extractor. Our system is additionally equipped with a three-electrode Einzell lens, however, the lens was not used during the present experiments (all electrodes were kept at the ground potential). All electrodes are manufactured from stainless steel. The trajectory of ions in the field-free region is electrostatically shielded with a thin copper sheet. The front plate of the position sensitive detector is placed approximately 50 cm from the interaction point.

The detector itself consists of two multichannel plates with 56 mm diameter (Topag AG)

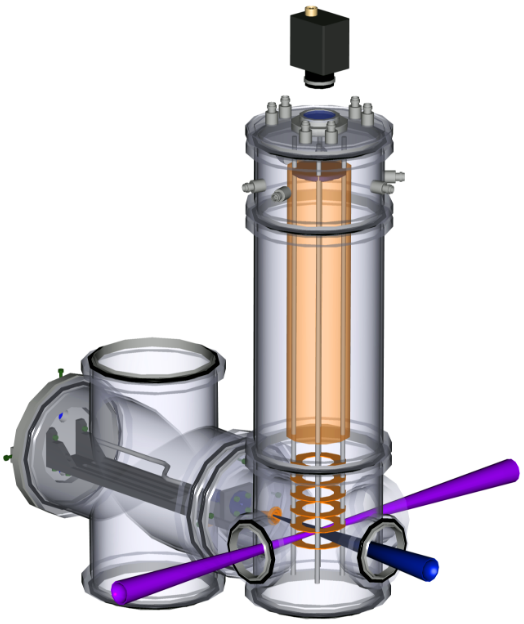

Figure 2.11: Schematic drawing of the new experimental apparatus for implementation of velocity mapping methods AIM. The molecular beam (blue), UV laser beam (violet), and imaging detection system (gold) are mutually perpendicular.

in chevron configuration and the phosphor screen (Proxitronic AG, phosphorus P43). The detector can be operated in two modes –either continuous when all ion masses are detected, or gated when a short voltage pulse is applied to the front plate and the detector is active only during this pulse. In the continuous mode the typical voltages on the input side of the front MCP, output side of the back MCP and phosphorus screen are 0, 1.5 and 5 kV, respectively. In the pulsed mode, the output side is kept at 1.2 kV and a negative pulse of 300 V is applied to the input side. The typical length of the pulse (detection window) is 50 ns. This enables imaging of only single ion mass.

The phosphor screen is followed by a glass window and the outside-of-vacuum 8-bit grayscale CCD camera (Unibrain Fire-i 702b) with imaging lens (25 mm,$f/1.6$), connected to the acquisition computer via a FireWire interface. The camera shutter is opened typically for 400 ms (four laser pulses) and then the accumulated image is transfered to the computer. The camera is controlled via a LabView program. Simultaneously, the rear side of the second multichannel plate is capacitively coupled to an oscilloscope and TOF mass spectra can be recorded.

A series of operations is performed on the images - the center of the image is found based on symmetry considerations and the inverse Abel transform is performed on the image in order to reconstruct the 3D distribution from the 2D projection of the photofragment sphere. We use the the Hankel method for reconstruction of the images [103]. The kinetic energy distribution is obtained from the Abel-inverted image as described elsewhere [103].

2.4 Laser systems

Several pulsed UV-laser systems are available in the laboratory: a fixed wavelength (193 nm) excimer laser; and two tunable systems (∼200-700 nm) consisting of Nd:YAG lasers, dye lasers and frequency mixing units. In addition, a tunable IR OPO/OPA system can be also used. The laser beams from all these systems can be directed into different viewports in CLUB and AIM apparatus for the various experiments.

A typical wavelength used in our experiments is 243 nm which can photodissociate the molecules and subsequently photoionize the H-fragment by resonance enhanced multiphoton ionization (REMPI) in a 2+1 excitation scheme[5] This wavelength is generated by sum frequency mixing (SFM) the 1064 nm fundamental of a Nd:YAG laser (Quanta Ray GCR-5) with 315 nm produced by frequency doubling the output of a dye laser (DL) operated at 630.3 nm. The DL is pumped by the second harmonic of the Nd:YAG laser, i.e. 532 nm. Fig. 2.12 depicts schematically this frequency generation scheme in our older laser system based on Spectra Physics Quanta Ray GCR-5 Nd: YAG laser, LAS LDL 20505 dye laser and Spectra physics WEX wavelength extender. The new UV laser systems is analogical and consists of Innolas Spitlight 1500 Nd: YAG laser, and a custom built Lioptec dye laser with a mixing unit. Both systems work at a frequency of 10 Hz with a pulse length of ≤10 ns and can deliver high energy up to 10 mJ/pulse at 243 nm.

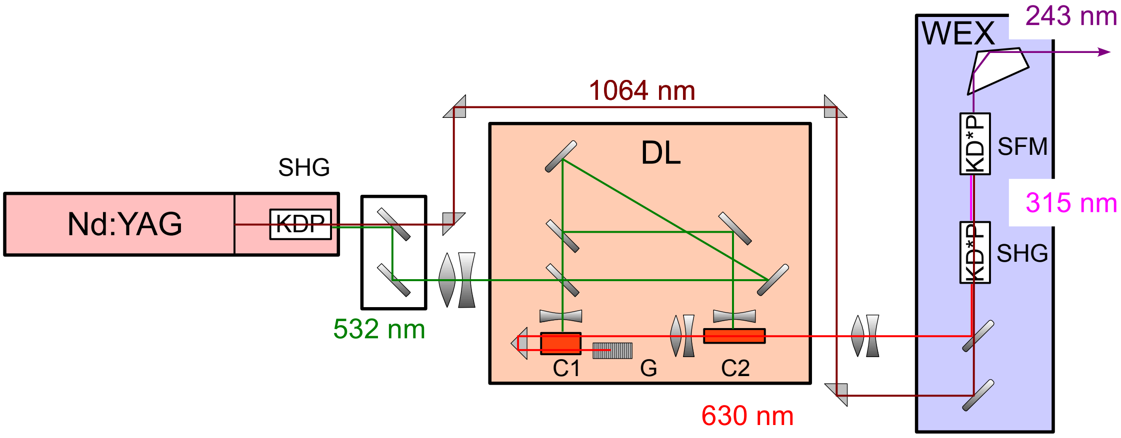

Figure 2.12: Schematic picture of the tunable UV laser system. Nd:YAG laser produces 1064 nm radiation, which is frequency doubled (SHG) in a nonlinear KDP crystal to 532 nm. By this wavelength the dye laser (DL) is pumped producing 630 nm. In the wavelength extender (WEX) the 630 nm is frequency doubled to 315 nm, which is then added with the original 1064 nm (SFM) resulting in 243 nm.

---

[5] The simultaneous two-photon excitation with 243.06 nm wavelength corresponds to the $1s \rightarrow 2s$ transition in the H atom and the additional third photon then brings the electron from the $2s$ level into the ionization continuum resulting in the proton H^+.

Another wavelength of 235 nm used so far in our experiments for REMPI ionization of Cl fragments was produced analogically. In principle, the UV lasers can be tuned in the entire range from 200 nm to the visible region by changing the dye and mixing crystals.

The 193 nm laser light is produced by an ArF/F_2-Excimer laser (LambdaPhysics: LFP 202). The emitted light is unpolarized, and it can be polarized using a thin film polarizer (TFP). Energies up to 200 mJ/pulse can be obtained. However, due to the large beam size and rectangular shape and about 20 ns pulse duration, the photon flux in the apparatus at the focal point is usually about the same order of magnitude as the photon flux from our tunable UV systems, e.g., a typical photon flux of the order of 10^{28} $s^{-1}cm^{-2}$.

All the laser systems can be mutually synchronized for experiments involving one or two lasers (in principle all three of them could be used in one experiment as well). Critical to the two-color experiments is the beam overlap in time and space. The time synchronization of the two laser beams is achieved by triggering the lasers via a pulse delay generator. Experimentally challenging is the spatial overlap of the two laser beams focussed to a tight spot ($\sim 10\mu$m in diameter) with the intersection point of the cluster beam and the VMI or RTOF axis.

Chapter 3

Results

3.1 Velocity map imaging as a tool for cluster dynamics investigations

As outlined already in Chapter 2 *Experiment*, in 2011 we introduced a new method for our photodissociation studies: Velocity Map Imaging (VMI). The method is described in Sec. 2.2.1. First, we built a new molecular beam apparatus AIM (see Sec. 2.3) dedicated to the development and testing of the VMI method in our laboratory, and subsequently the VMI method was also implemented in the CLUB apparatus. In this section we discuss three studies illustrating the development and implementation of the VMI experiment in our laboratory.

Velocity map imaging of HBr photodissociation in large rare gas clusters [71]: This was our first VMI study performed on the AIM. We did numerous investigations of the photodissociation of hydrogen halide molecules in various clusters previously and we understood these processes in great details in the isolated molecules as well as solvated in different rare gas cluster environments [138, 139, 140, 141, 142]. Comprehensive review of hydrogen halide photodissociation in cluster environments can be found in my DSc. Thesis [63]. Therefore HBr molecule represents well studied system, and it was selected to test the performance of the new AIM apparatus. Nevertheless, the AIM experiments provided some new insights into the HBr photodissociation dynamics in rare gas clusters which were outlined in the present article [71].

Several points could be highlighted from this study: First, the VMI technique was implemented to study clustering in the pulsed supersonic expansions of HBr in helium, argon, and xenon. The cluster generation along the gas pulse was probed by the UV photodissociation and photoionization of HBr molecules at 243 nm. The results are illustrated in Fig. 2.8. Two distinct features appeared in the hydrogen atom photofragment images in the clustering regime: (i) photofragments with near zero kinetic energies and (ii) hot photofragments originating from vibrationally excited HBr molecules. The origin of both features is attributed to the fragment caging by the cluster. The latter fragments were generated in two photon processes: an HBr molecule is photodissociated by the first photon, however the cluster cage leads to the fragment recombination recreating the HBr molecule in the cluster in a vibrationally excited state; a second photon then photolyzes the excited molecule yielding the H-fragments with the kinetic energies exceeding the maximum available energy for the ground state photodissociation. Besides, we also showed that the beam velocity distributions in the expansions could be characterized directly by the imaging of non-resonantly ionized parent HBr molecules.

The major message of our study to the molecular beam community is that a great attention must be paid to gas pulse and laser timing when clusters are studied in pulsed expansions, since the clustering during the gas pulse is a highly inhomogeneous process. Therefore continuous expansions - as implemented on our CLUB apparatus - represent a much more viable option for cluster investigations.

Caging of Cl atoms from photodissociation of CF_2Cl_2 in clusters [73]: This investigation of freon CF_2Cl_2 photodissociation was also performed on the AIM. It represented our first photodissociation study in which other photofragments than H-atoms, namely Cl-atoms, were detected. The freon CF_2Cl_2 is indeed the infamous culprit in the stratospheric ozone destruction process. Surprisingly its photodissociation has not been studied by VMI previously, despite its importance in atmospheric chemistry. Besides our study in rare gas clusters served as a necessary prerequisite for the later investigations of CF_2Cl_2 on ice nanoparticles [67] performed on the CLUB apparatus and discussed in Sec. 3.3. For these reasons, the significance of the present investigation was twofold: it was important for the further development of the VMI technique in our laboratory, and also for the atmospheric chemistry related to the ozone depletion process.

The Cl fragment images at 193 nm were recorded in various expansion regimes corresponding to isolated molecules and molecules in rare gas clusters. The obtained images of isolated CF_2Cl_2 molecule photodissociation and photodissociation in smaller Ar_N clusters are illustrated in Fig. 3.1. The molecular kinetic energy distributions were dominated by a peak at $E_{kin}(\mathrm{Cl}) \approx 0.97$ eV corresponding to the direct C–Cl bond dissociation but they also reveal features at lower kinetic energies. Several mechanisms which could lead to these slow Cl atoms were discussed. One of the proposed mechanisms was generation of 2 Cl fragments by one UV photon:

$$\mathrm{CF_2Cl_2} + h\nu \rightarrow \mathrm{CF_2Cl^*} + \mathrm{Cl}, \tag{3.1}$$

$$\mathrm{CF_2Cl^*} \rightarrow \mathrm{CF_2} + \mathrm{Cl}. \tag{3.2}$$

These reactions can either proceed subsequently or in a concerted manner where the two Cl atoms are releases simultaneously. Currently, the UV quantum yield of Cl from CF_2Cl_2 employed in the atmospheric modeling is 1.0 [143], which means that a single Cl atom is released into the stratosphere by one 193 nm photon dissociating the CF_2Cl_2 molecule. Our results suggested that this value could be higher, which would indeed change the atmospheric model outcomes.

The photodissociation in clusters was investigated in two regimes: (i) small Ar clusters with the CF_2Cl_2 molecule embedded in approximately one solvation Ar layer; (ii) large Xe_N,

(a) CF_2Cl_2 molecule

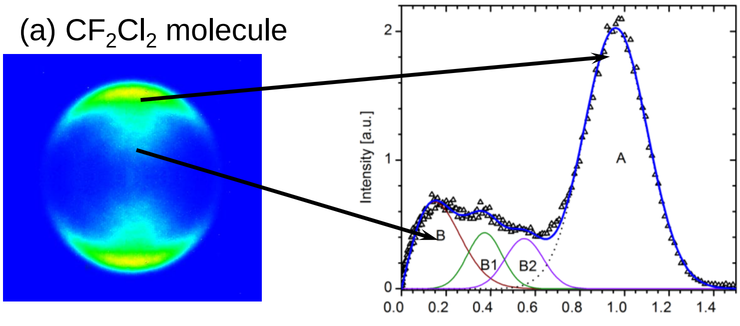

(b) CF_2Cl_2 in Ar_N

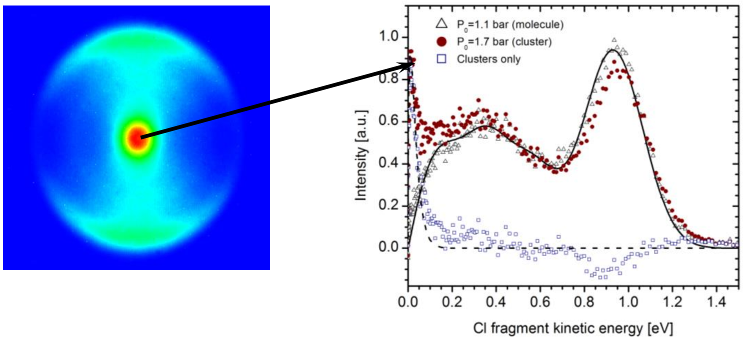

Figure 3.1: (a) The Cl-fragment images from isolated CF_2Cl_2 molecule photodissociation (left) and the corresponding KED (right), and (b) the image and KED from the photodissociation of CF_2Cl_2 in Ar_N clusters.

$\bar{N} \approx 100$ - 500, clusters with embedded CF_2Cl_2 molecules. In the former clusters we observed caging which yielded the Cl fragments with zero kinetic energy, and direct exit resulting in fragments with the kinetic energies corresponding to the fragments from isolated molecules. In the latter case (ii) essentially only the caged Cl fragments were observed.

Photodissociation dynamics of ethanethiol in clusters: complementary information from velocity map imaging, mass spectrometry and calculations [58]: The investigation of ethanethiol CH_3CH_2SH (EtSH) photodissociation in clusters was performed on the CLUB apparatus: This study demonstrates the power of our unique experimental setup for the cluster studies which resides in the combination of the VMI photodissociation experiment with the sophisticated EI mass spectrometry - both methods provide complementary data yielding an information about the cluster nature which cannot be obtained by any of the two methods alone. This synergy of both methods is illustrated schematically in Fig. 3.2.

The H fragment images recorded by VMI at 243 nm for isolated molecules showed a direct S–H bond fission (KED peak at E_{kin}(H)$\approx$ 1.25 eV) with a partly resolved structure corresponding to the vibrational levels of the CH_3CH_2S cofragment, illustrating the resolving power of our VMI. Clusters of different nature ranging from dimers to large $(EtSH)_N$, $\bar{N} \leq 10$, clusters and to ethanethiol clusters embedded in larger argon "snowballs" were generated and proved by the combination of VMI with the EI mass spectrometry using the RTOFMS. Photodissociation in

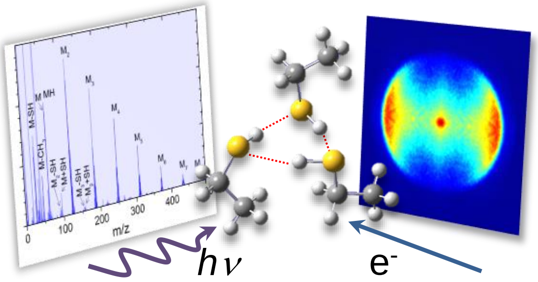

Figure 3.2: Schematic illustration of the complementary information obtained by VMI and mass spectrometry methods on the CLUB apparatus for the clusters of ethanethiol molecules.

the clusters resulted in a sharp peak of near-zero kinetic energy fragments which occurred due to the H-fragment caging. However, the onset of a strong EtSH clustering which was observed in the mass spectra, was not accompanied by the appearance of the strong central peak in VMI images. The strong central peak of caged fragments occurred at lower EtSH concentrations in Ar suggesting that the H-fragments are caged if EtSH molecule are embedded in a larger "Ar-snowball". Cluster ion fragments containing Ar atoms occurred in the mass spectra under these conditions, supporting the idea of EtSH embedded in the "Ar-snowball". The dynamics of the fragment caging was also calculated theoretically in the group of P. Slavíček, University of Chemistry and Technology in Prague.

The articles discussed in this section are attached in Appendix A.

3.2 Na-doping and solvated electron reactivity

In Chapter 2 *Experiment* Sec. 2.2.2, we have introduced a new method for cluster mass spectrometry NaPI which has recently been implemented in our CLUB apparatus. The method has been described in more detail in Sec. 2.2.2. Four of our studies using the NaPI method are discussed below.

Extensive water cluster fragmentation after low energy electron ionization [57]: After the NaPI method implementation in our CLUB apparatus, we first investigated the large water cluster ionization and fragmentation. The comparison between the water cluster mass spectra after electron ionization and after NaPI obtained under identical expansion conditions for $(H_2O)_N$, $\bar{N} \approx$ 10-150, indicated a strong water cluster fragmentation upon EI even at low kinetic energies of the ionizing electrons close to the ionization threshold at ≈13 eV. Specifically, for clusters of an average size $\bar{N} \approx 130$ the average ion fragment size corresponded to only about 10% of the mean neutral cluster size. This is an important message for many researchers who use the water clusters in the laboratory studies (e.g., to mimic ice nanoparticles in the atmosphere), and who rely on a mass spectrometry for the particle characterization: the mass spectra can deliver quite misleading impression about the cluster size. The following three examples, will show that also NaPI can sometimes be quite misleading concerning the cluster size and composition.

Nucleation of mixed nitric acid-water ice nanoparticles in molecular beams that starts with a HNO_3 molecule [104]: We have used a comparison between EI and NaPI method for the first time to study the mixed ice nanoparticles of nitric acid and water. This study yielded very surprising results that some clusters were "invisible" to the NaPI. We performed this study in collaboration with the group of T. Zeuch in Göttingen where we did our NaPI measurements before implementing this method in the CLUB apparatus (above).

We focused on the mixed $(HNO_3)_M{\cdot}(H_2O)_N$ clusters, since the nitric-acid ices represent the most important class of ice particles in the polar stratospheric clouds. Therefore we attempted to generate these clusters in our molecular beam experiment and implemented the mass spectrometry after EI to detect and analyze them. We could derive some interesting conclusions about the acidic dissociation of HNO_3 in water clusters, however, to backup our conclusions we attempted to obtain the mass spectra of the "neutral clusters" using the NaPI method. Since we did not poses the NaPI possibility on the CLUB at that point, we took our cluster source to Göttingen where similar molecular beam apparatus with the NaPI option existed. Transferring the beam source assured the same expansion conditions - i.e., the same clusters - as were generated in Prague. To our surprise we did not see *any* clusters with NaPI despite the fact that the EI mass spectra clearly showed the clusters in the beam. Only when the nitric acid in the source was diluted with water so that pure water clusters were generated, they were detected by the NaPI. The "invisibility" of the mixed clusters for the NaPI was attributed to a fast charge transfer (CT) reaction between Na and HNO_3:

$$\mathrm{Na} + \mathrm{HNO_3} \rightarrow \mathrm{Na}^+ + \mathrm{HNO_3^-}. \tag{3.3}$$

This reaction could be followed by further reactions of the HNO_3^- ion in the cluster as suggested by later theoretical calculations of P. Slavíček. However, as soon as this CT process took place in the cluster, the solvated electron could not be generated, and the cluster could not be detected by the NaPI (the solvated electron could not be photodetached, since it was not present). Fig. 3.3 illustrates schematically the cluster processes in NaPI and EI.

This explanation lead to three major conclusions: (i) The NaPI was previously proposed as a "general method for mass spectrometry of small atmospheric aerosols" [119]. Our results showed that the NaPI cannot be implemented for mixed nitric-acid/water clusters which represent important class of atmospheric aerosols. (In addition, our further studies outlined below could not find any mixed clusters for which the NaPI could be used reliably.) (ii) Although the NaPI failed as a general mass spectrometric method, in combination with EI it provided a new tool for probing the reactivity in aerosol particles (as was also demonstrated in our further studies below). (iii) Since all the clusters in the beam in our experiment were "invisible" for NaPI, it suggested that they all contained an HNO_3 molecule. This in turn demonstrates that HNO_3 is

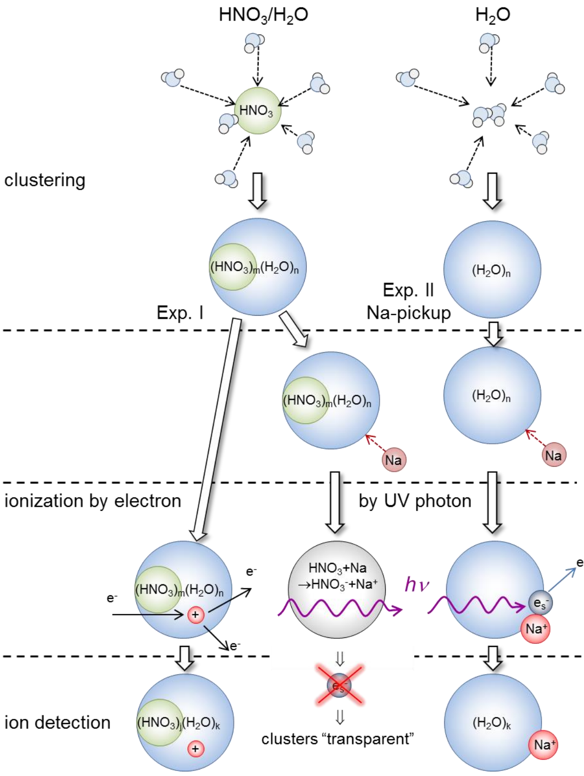

Figure 3.3: Schematic illustration of the processes in the clusters observed during the experiments with the NaPI and EI methods.

a strong nucleation agent in the supersonic expansions, which suggests that this molecule can play the same role of a nucleation center also in the atmosphere.

Reactivity of hydrated electron in finite size system: Sodium pickup on mixed N_2O-water nanoparticles [131]: Recently we have confirmed the "invisibility" of some mixed clusters for the NaPI by another example: the mixed clusters of N_2O and water, and we discussed the reactivity of solvated electron in these clusters which is the reason for this "invisibility". This investigation was done in close collaboration with the theory group of P. Slavíček, who interpreted our experimental results by his theoretical simulations.

As above, the mixed $(N_2O)_M{\cdot}(H_2O)_N$ clusters were not detected by the NaPI method but their generation was proved by the EI spectra. Theoretical simulations of the dynamics in the mixed Na-doped clusters revealed that the solvated electron was generated at first but reacted immediately with an N_2O molecule to form an N_2O^- anion, which made it unavailable for the cluster ionization by electron photodetachment. A further chain of reactions was suggested:

$$N_2O^- \rightarrow N_2 + O^-, \tag{3.4}$$

$$O^- + H_2O \rightarrow OH^- + OH\cdot\,. \tag{3.5}$$

This again disproved the NaPI as a general ionization method for atmospheric aerosols: molecules with a positive electron affinity in the clusters prevent the solvated electron generation and inhibit the cluster ionization by the electron photodetachment. On the other hand, we showed again that the combination of NaPI and EI was a suitable tool for the investigation of the solvated electron reactivity.

Sodium doping and reactivity in pure and mixed ice nanoparticles [132]: Since the NaPI was successfully applied to some homogeneous clusters, however, our studies above demonstrated that the mixed clusters investigated here could not be detected by this method, we questioned the suitability of the NaPI method for the mixed cluster detection in general. The quest for mixed species which could be detected by NaPI led us to the mixed ammonia-water clusters as suitable candidates, since both, water and ammonia, support the solvated electrons.

The obtained results were both, positive and negative: The mixed ammonia-water clusters were detected by the NaPI and EI. However, each method revealed a different cluster composition. Surprisingly, the EI spectra exhibited clusters with higher ammonia content, thus the differences could not be simply attributed to a larger fragmentation upon EI compared to NaPI. Therefore the NaPI method did not provide the real neutral cluster composition for these mixed clusters. The possible scenarios of cluster fragmentation in the NaPI process were proposed and discussed in the paper.

Since all our investigations showed that the Na reactivity in clusters was the key in the NaPI technique, we also investigated the Na reactivity in pure water clusters. A single Na atom in the water cluster generates the ion pair Na^+ and the loosely bound solvated electron. However, if more than two Na atoms were embedded in the cluster, the famous “explosive” reaction generating NaOH and H_2 could occur. This reaction was previously investigated in pure water clusters doped with several Na atoms [120, 144], and our combination of NaPI and EI confirms the reactions occurring in the electronically ground state in ice nanoparticles. Sodium reactions in clusters lead to substantial energy release and subsequently to cluster fragmentation. Therefore, attention must be paid to the single doping if NaPI is used for cluster size analysis in the mass spectrometry.

The papers discussed above are attached in Appendix B.

3.3 Photochemistry of molecules on ice nanoparticles

The photodissociation of molecules, namely hydrogen halides and freons, on ice nanoparticles is relevant to the stratospheric ozone depletion. We have focused on the hydrogen halide photodissociation on ice nanoparticles since the foundation of our laboratory in Prague in 2005. Our very first paper published from the new laboratory in Prague in 2007 [145] was on this subject. Already in this first paper we have revealed experimentally that a neutral H_3O radical was generated after the photoexcitation of an HBr molecule on ice nanoparticle. This idea followed from earlier theoretical predictions of H_3O species in similar systems by Domcke and Sobolewski. In a series of papers [146, 147, 148, 149, 150] they proposed theoretically the excitation of charge separated species such as the small zwitterionic clusters $Cl^{-}\cdot(H_2O)_3\cdot H_3O^{+}$ to lead to the neutral H_3O radicals. Fig. 3.4 depicts the suggested mechanism of the H_3O generation in our experiment: It starts with the acidic dissociation of the HBr molecule, forming a zwitterionic structure $Br^{-}\cdot H_3O^{+}\cdot(H_2O)_{n-1}$, which is then excited by the 193 nm laser to an S_1 state of the charge-transfer-to-solvent (CTTS) character [147]. The system then relaxes into a biradical minimum with Br and H_3O neutral radicals. The H_3O ultimately decays into water and the H atom which is released from the cluster and detected [149, 146]. Several experimental findings and further arguments support this mechanism as was outlined in a series of our studies which followed [23, 142, 145, 151, 152, 153].

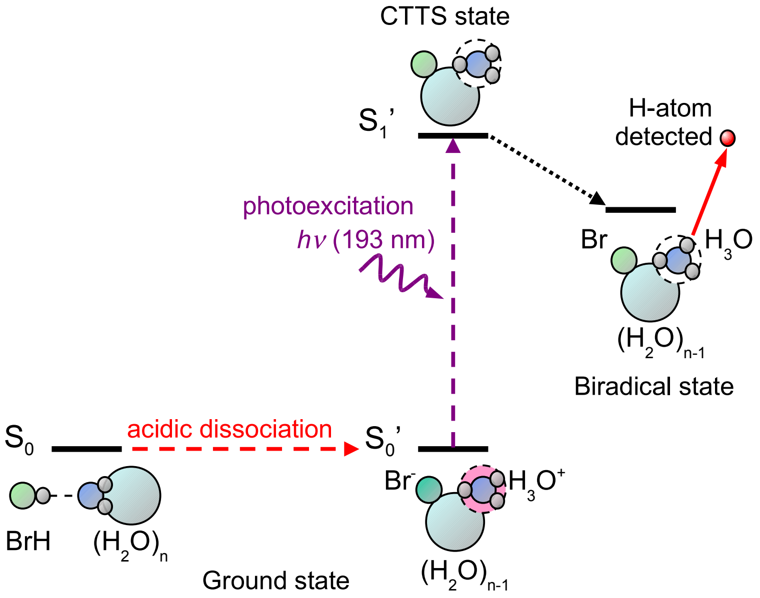

Figure 3.4: Proposed mechanism of the $HBr\cdot(H_2O)_n$ cluster photochemistry: The acidic dissociation takes place in the ground state generating the zwitterionic species $Br^{-}\cdot H_3O^{+}\cdot(H_2O)_{n-1}$, which is excited by the 193 nm laser radiation into the CTTS state and subsequently relaxes to the biradical state $Br\cdot H_3O\cdot(H_2O)_{n-1}$. In this state the observed H-fragment is released from the H_3O radical.

In this section we discuss two of our recent photodissociation studies on ice nanoparticles using the newly implemented VMI method. First, we concentrate on the above discussed photodissociation of hydrogen halides [107], and then we investigate another atmospherically relevant class of molecules: freons CF_2Cl_2 [67].

Imaging of hydrogen halides photochemistry on argon and ice nanoparticles [107]: The hydrogen halide photodissociation on ice nanoparticles was investigated on the CLUB apparatus with the TOF technique previously [142, 145, 151, 152, 153, 23], as discussed above. With the implementation of the new VMI technique we have returned to this subject since it offered benefits for the method development, as well as for a deeper scientific understanding of the investigated process: (i) the familiar system seemed ideal for testing the new VMI system on the CLUB, and (ii) the new VMI was a promising tool to resolve some of the unresolved issues of our previous TOF experiments. The major opened question from our previous photodissociation experiments was, if the nascent Cl radical left the ice nanoparticle or remained bound to it. This was a crucial question from the point of view of the Cl-budged in the stratosphere. We have suggested in one of our previous publications [151] that the photoinduced processes on ice nanoparticles could contribute up to 5% of the total stratospheric Cl budged. However, this proposition assumed that the nascent Cl atoms were released from the ice after the UV excitation. Our new VMI study resolved this question by showing that the Cl-fragments were trapped by the ice nanoparticles.

We investigated the photodissociation of HCl and HBr molecules at 193 nm deposited on large Ar_N and $(H_2O)_N$, $\bar{N} \approx 10^2$ - 10^3, clusters. The photodissociation on Ar_N led to a strong H-fragment caging manifested by the fragment intensity peaking sharply at zero kinetic energy. Some of the Cl-fragments from HCl photodissociation on Ar_N were also caged, while some of them escaped the cluster directly without losing their kinetic energy. The images of H-fragments from HCl and HBr on $(H_2O)_N$ also exhibited a strong central intensity, however, with a different kinetic energy distribution which originated from the above mentioned processes: the HX acidic dissociation followed by H_3O neutral hydronium radical formation after the UV excitation, and the slow H-fragments stem from subsequent decay of the H_3O. The atmospherically important result was that the corresponding Cl-cofragment from the photoexcitation of the HCl on $(H_2O)_N$ was trapped in the ice nanoparticle and therefore could not contribute to the stratospheric Cl budged.

In addition, the time-of-flight mass spectrometry after electron ionization complemented by pickup cross section measurements provided information about the composition and structure of the clusters. It showed that the hydrogen halides coagulated efficiently to generate smaller $(HX)_n$ clusters on Ar_N upon multiple pickup conditions, while the same molecules remained isolated on $(H_2O)_N$. These results were further extended in our follow up studies of molecule clustering on ice nanoparticles [67, 108] outlined in the next section.

Clustering and photochemistry of freon CF_2Cl_2 on argon and ice nanoparticles [67]: CF_2Cl_2 is the infamous freon convicted of the Antarctic ozone hole generation. Therefore we focused on the UV photodissociation and photochemistry of CF_2Cl_2 molecules. In our previous study [73] discussed above in Sec. 3.1 we investigated the photodissociation of isolated CF_2Cl_2 molecules and molecules embedded in Ar and Xe clusters. Here, we aim at its photochemistry on atmospherically relevant ice nanoparticles. Therefore we produced large $(H_2O)_N$ clusters and deposited the CF_2Cl_2 molecules on them in a pickup process. For a comparison, we also investigated the CF_2Cl_2 molecules deposited on large Ar_N clusters by the pickup. We probed the photodissociation dynamics at 193 nm by VMI technique, and complemented the experiments by cluster composition analysis using a mass spectrometry after EI. The molecular beam experiment was also complemented by *ab initio* calculations performed in the collaborating group of P. Slavíček.

The CF_2Cl_2 molecules deposited on large argon clusters were highly mobile and coagulated to form the $(CF_2Cl_2)_n$ clusters on Ar_N. The photodissociation of the CF_2Cl_2 molecules and clusters on Ar_N lead to the caging of the Cl fragment. On the other hand, the CF_2Cl_2 molecules adsorbed on the $(H_2O)_N$ ice nanoparticles did not form clusters, and no Cl fragments were observed from their photodissociation. Since the CF_2Cl_2 molecules were clearly adsorbed on $(H_2O)_N$, the missing Cl signal was interpreted in terms of surface orientation with Cl-atoms towards the ice surface via so-called *halogen bond*. In addition, embedding of the CF_2Cl_2 molecule on the disordered surface of the ice nanoparticles was suggested, which corresponded with our recent discovery that the large ice nanoparticles generated in our experiments poses highly irregular shapes [106] as discussed in the next section. This once again illustrates the complementarity of the various experiments possible on the CLUB, which all are capable of providing different views of the same particles via quite different processes.

The papers discussed in this section are attached in Appendix C.

3.4 Nucleation and growth of ice nanoparticles

In the Chapter 2 *Experiment*, Sec. 2.2.3, we have introduced the pickup technique: briefly, the nanoparticle beam is passed through a chamber filled with molecules in the gas phase and the molecules can be picked up one-by-one by the nanoparticles. The nanoparticles are slowed down by the momentum transfer in the pickup process, and from an accurate measurement of their velocity the pickup cross section of the nanoparticle can be evaluated. Nanoparticles with a well defined number of embedded foreign molecules can be prepared and coagulation leading to the cluster generation on the nanoparticles is investigated. In this section we discuss some of our recent pickup studies.

Cluster cross sections from pickup measurements: Are the established methods consistent? [64]: In our first study of the pickup processes of several molecules on Ar_N clusters in 2011, we have established the method for pickup cross section measurement and confirmed its reliability.

Pickup of several molecules, H_2O, HBr, and CH_3OH, and Ar atoms on free Ar_N clusters was investigated. The pickup cross sections of the clusters with known mean sizes,$\bar{N} \approx 150$ and 260 were measured by two independent methods: (i) the cluster beam velocity decrease due to the momentum transfer of the picked up molecules to the clusters, and (ii) Poisson distribution of a selected cluster fragment ion as a function of the pickup pressure. In addition, the pickup cross sections were calculated using molecular dynamics and Monte Carlo simulations. The simulations supported the results of the velocity measurements. On the other hand, the Poisson distributions yielded significantly smaller cross sections, inconsistent with the known Ar_N cluster sizes. These results were discussed with the conclusion that the velocity measurements could provide reliable results for the cluster pickup cross section or the mean cluster sizes, and the number of picked up molecules. Subsequently we have exploited this method to determine the water cluster pickup cross sections which are important for atmospheric processes (see below).

Uptake of atmospheric molecules by ice nanoparticles: Pickup cross sections [105]: Once the reliable method for the cluster pickup cross section meaurements was established we have measured the pickup of several atmospherically relevant molecules on ice nanoparticles $(H_2O)_N$. As the typical examples were chosen: water, methane, NO_x species (NO, NO_2), hydrogen halides (HCl, HBr), and volatile organic compounds (CH_3OH, CH_3CH_2OH). The cross sections for pickup of these molecules on ice nanoparticles $(H_2O)_N$ with the mean size of $\bar{N} \approx 260$ (diameter 2.3 nm) were measured as outlined in Fig. 3.5.

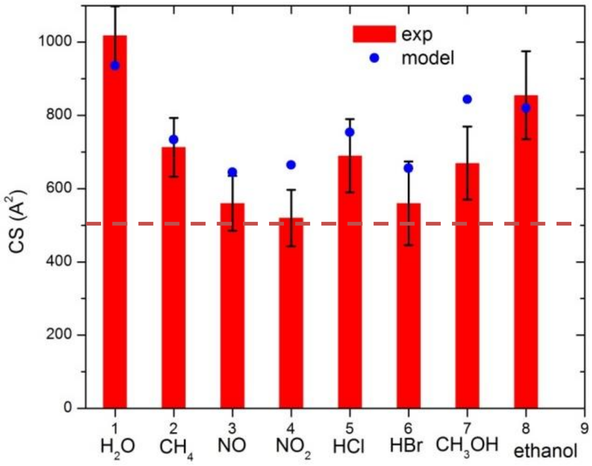

Figure 3.5: Pickup cross sections measured for different molecules on ice nanoparticles $(H_2O)_N$ with the mean size of $\bar{N} \approx 260$ (diameter 2.3 nm). The dashed line corresponds to the geometrical cross section of a spherical $(H_2O)_{260}$ nanoparticle. The blue dots represent calculated cross sections using our model outlined in [105].

The most surprising result was that the pickup cross section for water molecules on ice nanoparticles exceeded substantially the corresponding geometrical cross section of the nanoparticle. Thus for water molecules molecular dynamics simulations were performed to learn the details of the pickup process. The experimental results for water were in good agreement with the simulations. The pickup cross sections of ice particles of several nanometers in diameter can be more than 3 times larger than the geometrical cross sections of these particles. This can have significant consequences in modeling of atmospheric ice nanoparticles and cloud nucleation, where mostly geometrical cross sections have been used so far.

Irregular Shapes of Water Clusters Generated in Supersonic Expansions [106]: Additional measurements of the pickup of water molecules on ice nanoparticles showed that the ice nanoparticles generated in supersonic expansions poses highly irregular shapes, and we termed them *nanosnowflakes*.

We measured the cross sections for pickup of guest molecules on neutral argon and water clusters with the mean sizes in the range from $\bar{N} = 50$ to 600. The experiments were supported by molecular dynamics simulations and analytical models based on the interaction potentials. The cross sections for argon clusters were consistent with their assumed spherical shape and followed approximately the theoretically justified $N^{1/3}$ dependence. On the other hand, the cross sections of water clusters departed from this dependence and were considerably larger starting from $\bar{N} \geq 300$. We interpreted this increase of cross section by the occurrence of highly irregular shapes of water clusters produced in the supersonic expansion of water vapor under the conditions of the large cluster generation. It ought to be mentioned that this result was also in agreement with our photodissociation study of CF_2Cl_2 on these ice nanoparticles [67] which showed evidence for CF_2Cl_2 being embedded in some kind of "pockets" on the surface of the ice nanoparticles as discussed above in Sec. 3.3.

Lack of Aggregation of Molecules on Ice Nanoparticles [108]: In some of our photodissociation studies mentioned above [107, 67] we noticed indications that the molecules embedded on ice nanoparticles tend not to coagulate into the clusters, while the same molecules generated relatively large clusters when picked up on argon nanoparticles. Therefore we have devoted a special attention to these processes: coagulation and non-coagulation of foreign molecules picked up on free nanoparticles. These results are important for atmospheric chemistry, as well as for astrochemistry where ice grain assisted (photo)chemistry was implemented for synthesis of more complex molecules and, e.g., possible origins of life in space.

We deposited a controlled number of guest molecules on the water and argon nanoparticles in a pickup chamber and their aggregation was studied mass spectrometrically. The studied molecules (HCl, CH_3Cl, $CH_3CH_2CH_2Cl$, C_6H_5Cl, CH_4, and C_6H_6) formed large aggregates on argon nanoparticles. On the other hand, no aggregation was observed on ice nanoparticles. Molecular simulations confirmed the experimental results; they revealed a high degree of aggregation on the argon nanoparticles and show that the molecules remained mostly isolated on the water ice surface. This finding would influence the efficiency of ice grain-mediated synthesis (e.g., in outer space) and is also important for the cluster community because it shows some limitations of the pickup experiments on water clusters.

However, it is worth noting, that most recently we have observed coagulation and cluster generation of hydroxypyridine on ice nanoparticles. This recent result from our laboratory which has been currently submitted for publication, was very surprising in the view of the previous experiments. It may suggest, that some molecules which can generate strong hydrogen bonds actually coagulate to form clusters on ice. It is even more interesting, since we see a strong propensity for hydroxypyridine dimer which generates a double hydrogen bond motif known in biology (DNA base pairs). Thus this most recent study justified the possibility of biologically relevant bond generation on ice grains.

The articles discussed in this section are attached in Appendix D.

3.5 Solvation effects on essential building blocks of biomolecules

This last section concerns our recent investigations of essential building blocks of biomolecules. This topic has also been intensely investigated in our laboratory from its foundation in Prague in 2005. The first study of pyrrole molecule photochemistry [20] was published already among the first papers from our new laboratory in 2007. A number of studies followed on the essential building blocks of biomolecules: pyrrole, imidazole, pyrazole and phenol in various clusters [21, 22, 23, 24, 45, 46]. These small heteroaromatic molecules act as UV chromophores in larger biomolecules. Therefore the investigations of photodissociation behavior of the small heteroaromatic molecules in the gas phase can contribute to the understanding of biomolecule UV photostability (e.g. the DNA radiation damage). In these studies we focused namely on the solvent effects on the UV photostability by investigating the photochemistry of these molecules in clusters.

The photophysical behavior of heteroaromatic systems, incuding the above mentioned molecules has been subject of numerous experimental and theoretical papers covered in the recent reviews [154, 155]. A special attention has been paid to the non-radiative relaxation mechanism which utilizes the dissociative $\pi\sigma^*$ channel with the σ^* orbital localized on the X–H bond (X = O or N). This channel has been suggested to provide an effective relaxation route via $\pi\sigma^*/\mathrm{S}_0$ conical intersection (CI) leading either to X–H bond fission or to the original species in the ground state [156]. This "$\pi\sigma^*$ state photochemistry" can be illustrated on the example of the N–H bond photodissociation in pyrrole molecule. The cuts through the potential energy surfaces (PES) of the pyrrole molecule are shown in Fig. 3.6 and the corresponding processes are illustrated schematically in Fig. 3.7. Upon low energy excitation, the photodynamics is dominated by the $\pi\sigma^*$ state. This state is asymptotically dissociative (see Fig. 3.6) and as result, the hydrogen atom is released (hydrogen dissociation, HD, channel). At elongated N–H distances, the $\pi\sigma^*/\mathrm{S}_0$ intersection occurs. It is, therefore, possible that frustrated dissociation (FD) takes place, and the molecular ground state is recreated. At higher photon energies, the $\pi\pi^*$ state is populated. A molecular ring distortion (MRD) reaction channel is opened. Subsequently, the molecule quenches into the vibrationally hot ground state where again the hydrogen atom can dissociate or other molecular fragments can be formed.

This dynamics leads to a bimodal character of the H-fragment KED spectra from the photodissociation of these molecules. These spectra measured for pyrrole molecule at 243 nm and 193 nm are schematically shown on the insets in Fig. 3.7. The relatively narrow peak of *fast fragments* (around 0.8 eV in the particular case of pyrrole) originates from the direct dissociation on the $\pi\sigma^*$ surface. The *slow fragments* exhibit a broad distribution peaking near zero energy. These fragments correspond to statistical decay of the vibrationally hot ground state molecule after the quenching of the $\pi\sigma^*$ or $\pi\pi^*$ state.

Our major contribution to this field was to investigate how these KED spectra changed upon complexation of the molecules in clusters and these changes were rationalized based on

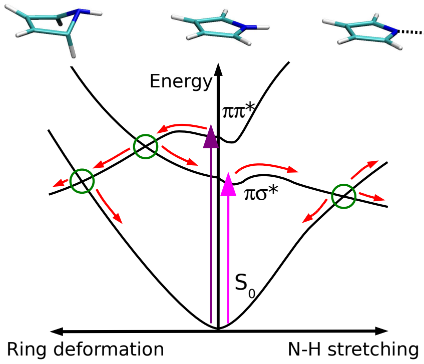

Figure 3.6: Schematic picture of general PES typical for the studied species based on *ab initio* calculations for pyrrole molecule. The cuts through PES along the N-H stretching and ring-deformation coordinates are shown as indicated by the schematic diagrams of pyrrole molecule at the top. The vertical arrows show the UV excitation and the red arrows indicate the possible dissociation pathways. Circles label the conical intersections CI $\pi\sigma^*/\mathrm{S}_0$, $\pi\pi^*/\pi\sigma^*$ and $\pi\pi^*/\mathrm{S}_0$.

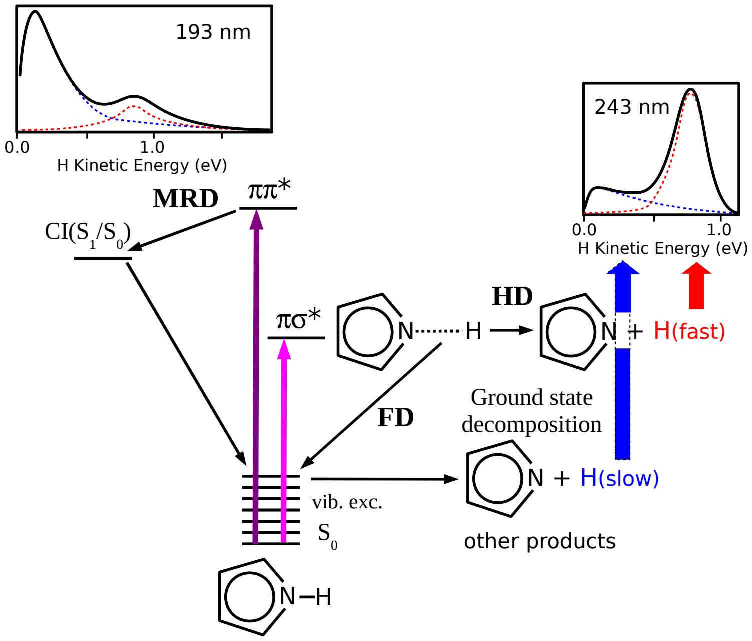

Figure 3.7: Schematic picture of photodissociation processes possible in the molecules (Py, Im, Pz). The excitation of $\pi\sigma^*$ state can lead to the direct hydrogen dissociation (HD) and fast H-atom production. Alternatively, frustrated dissociation (FD) can occur via a $\pi\sigma^*/\mathrm{S}_0$ conical intersection at elongated N-H distances. At higher photon energies, the $\pi\pi^*$ state is populated and molecular ring distortion (MRD) can occur, quenching the molecule into the vibrationally hot ground state, where it can again dissociate yielding the slow H-fragments or other products.

theoretical calculations performed in the group of P. Slavíček. The calculations showed that the electronic interaction with the solvent led to a significant change in the PES along the N-H coordinate (shown in Fig. 3.8), while the PES along the molecular distortion coordinate remained essentially unchanged. The interaction with the solvent pushed the potential along the N-H coordinate higher in energy, which caused the conical intersection between the $\pi\sigma^*$ state and the ground state S_0 along this coordinate to disappear. This in turn closed the dissociation channel to the fast H-fragments.

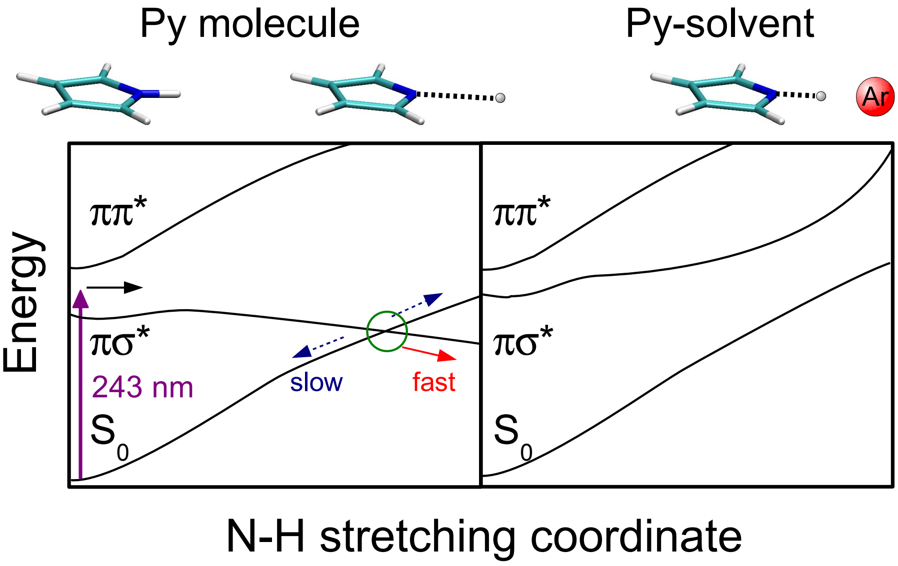

Figure 3.8: Schematic illustration of the influence of a solvent on photodissociation of pyrrole molecule: Left panel shows the PES for photodissociation of the bare molecule indicating the CI (green circle) between the repulsive $\pi\sigma^*$ state and the ground state S_0 leading to the production of the slow (blue arrow) and fast (red arrow) fragments. In the presence of an Ar atom as a prototype of a structureless solvent put into the dissociation pathway the CI along the N–H stretching coordinate disappears, i.e. this dissociation channel is closed. (Note that the slow fragments can be still produced along the other coordinates, e.g., the ring deformation coordinate).

This discussion of pyrrole photochemistry essentially encompassed the major features observed also for the other above mentioned molecules imidazole, pyrazole and phenol. However, each case is indeed specific depending especially on the ordering and relative positions of the $\pi\sigma^*$ and $\pi\pi^*$ states involved in the excitation. These states can also be strongly influenced by the solvent. More detailed discussion of these effects can be found in our previous publications [20, 21, 22, 23, 24, 45, 46].

Below we extend this topic to the aniline ($PhNH_2$) molecule photochemistry in various clusters [25]. Fig. 3.9 illustrates schematically the relevance of aniline clusters to the biological molecules. In addition, in this section we also discuss two investigations performed with our new mass spectrometric tools, where we focus on hydrogen transfer (HT) and proton transfer

(PT) processes in the clusters of aniline [56] and phenol [55] molecules which mimic the HT/PT processes in biologically relevant systems.

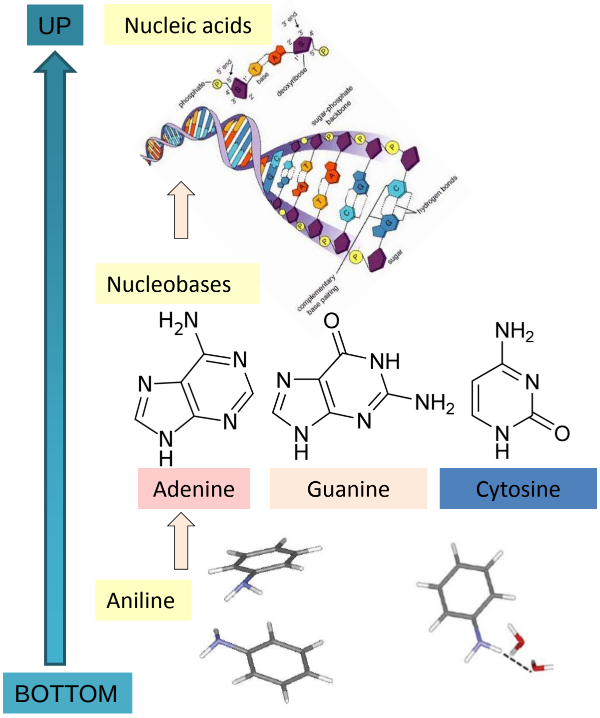

Figure 3.9: Schematic illustration of the aniline molecule and clusters relevance to the biological molecules and the bottom-up approach to its investigation.

Photodissociation of aniline NH bonds in clusters of different nature [25]: Aniline represents a model system for investigations of photochemistry in the purine derived DNA bases, guanine and adenine, see Fig. 3.9 [157, 155]. Therefore we investigated the photodissociation of N–H bond in aniline molecule in various clusters by a combination of VMI and mass spectrometric techniques. The mass spectrometry allowed us to determine various expansion regimes corresponding to different species generated: isolated molecules; small $(PhNH_2)_N$, $N \leq 3$, clusters; larger $(PhNH_2)_N$, $N \geq 10$; small mixed $PhNH_2{\cdot}(H_2O)_N$, $N \leq 10$, clusters; and individual $PhNH_2$ molecules deposited on large $(H_2O)_N$, $\bar{N} = 430$. The H-fragment KEDs exhibited fast fragments around 0.8 eV (A) assigned previously to a direct dissociation along a repulsive $\pi\sigma^*$ state potential, and slow statistical fragments peaking near 0.2 eV (B). In the aniline clusters the contribution of fast fragments (A) decreased relative to (B) with increasing the cluster size. Similar effect was observed when aniline was solvated with water. The experimental data were interpreted with *ab initio* calculations performed by D. Nachtigallová at the Institute of Organic Chemistry and Biochemistry. Cluster structures were calculated with both N–H bonds of an aniline molecule participating in hydrogen bonding, as well as the ones with free N–H bonds. The latter ones yielded preferentially the fast fragments as the isolated molecule. For the N–H engaged in hydrogen bonding a barrier increased along the N–H coordinate on the dissociative $\pi\sigma^*$ state potential surface, and also the energy of $\pi\sigma^*/S_0$ conical intersection increased. Thus the fast dissociation channel was closed stabilizing the molecule in cluster. The population could be funnelled through other conical intersections into the hot ground state which decayed statistically, yielding the slow H-fragments.

This study provided a new detailed molecular-level picture of N–H bond photodissociation in solvated molecules which poses two N–H bonds where either one or both of the bonds can be engaged in hydrogen bonding. Such studies can help to further reveal the detailed molecular mechanism of biomolecule photostability.

Proton transfer and isotope-induced reaction in aniline cluster ions [56]: In the course of the above photodissociation investigation we have performed a detailed mass spectrometric study of aniline clusters in order to define our species in the molecular beams. These mass spectrometric experiments revealed a wealth of information about proton transfer processes in these clusters, namely a very unusual isotopic effect in the PT reactions. These results were not directly relevant to the above discussed photodynamics, and therefore they were discussed separately in [56].

Several fragment ions in the cluster mass spectra were shown to originate from intracluster reactions, namely, $[\mathrm{Ph}]^+$, $[\mathrm{PhNH_3}]^+$ and $[\mathrm{PhNPh}]^+$. Reaction schemes were proposed for these ions starting with the PT process. The mass region beyond the monomer mass was dominated by cluster ions $(\mathrm{PhNH_2})_n^+$ accompanied by satellites with ±H and +2H. In the experiments with deuterated species, new fragment ions were identified. The aniline isotopomer $d5$-$\mathrm{PhNH_2}$ yielded the fragment ions $(\mathrm{PhNH_2})_n\cdot(\mathrm{NPhNH_2})^+$. Analogical series was observed in experiments with $d7$-$\mathrm{PhND_2}$, and additional fragments occurred corresponding to $(\mathrm{PhND_2})_n\cdot(\mathrm{D_2NNDPhNDND_2})^+$ ions. Replacing hydrogen with deuterium usually slows the reaction dynamics, and thus some reaction channels were expected to be closed in the experiments with the deuterated species. Therefore the enrichment of the mass spectra with the new fragments in the experiments with the deuterated species was rather unexpected. The possible complex reaction pathways to these ions and the unusual isotope effects yielding these new products were discussed and explained: the slowing down of the reaction dynamics by deuteration led to the reaction termination at some intermediate complexes.

Proton transfer in hydrogen-bonded network of phenol molecules: intracluster formation of water [55]: We have investigated the photochemistry of phenol (PhOH) in clusters [24], previously. Similarly to the above discussed case of aniline, also here the photodissociation experiment was accompanied by mass spectrometric study to reveal the nature of the clusters under investigation. These original mass spectrometric measurements suggested an interesting effect: water generation after electron ionization of pure phenol clusters. However, the mass spectrometry was done using quadrupole mass spectrometer and the TOF system for photodissociation studies. The resolution, sensitivity and dynamical range of both these mass spectrometers was surpassed by the newly implemented RTOF mass spectrometer on the

CLUB apparatus. Therefore we have revisited the mass spectrometry of phenol clusters with the new mass spectrometer.

Besides $[(\mathrm{PhOH})_n]^+$ cluster ion series, hydrated phenol cluster ions $[(\mathrm{PhOH})_n \cdot x\mathrm{H_2O}]^+$ with up to $x = 3$ water molecules and dehydrated phenol clusters $[(\mathrm{PhOH})_n$ - $\mathrm{H_2O}]^+$ were observed. The hydrated phenol series exhibited minima and maxima that were interpreted as evidence for proton transfer between the hydrogen bonded cluster ions of cyclic structures. The proton transfer lead to a water generation within the clusters, and subsequent elimination of the diphenyl ether molecule(s) from the cluster yielded the hydrated phenol cluster ions. Alternatively, a water molecule release yielded a series of dehydrated phenols $[(\mathrm{PhOH})_n$ - $\mathrm{H_2O}]^+$, among which the case of $n = 2$, i.e. the diphenyl ether ion $[\mathrm{PhOPh}]^+$, constitutes the maximum.

The results summarized in this section have been published in Refs. [25, 55, 56] added in Appendix E.

Chapter 4

Summary and outlook

In this work some recent experiments performed in the Molecule and Cluster Dynamics Group at the J. Heyrovský Institute of Physical Chemistry in Prague have been summarized.

The results were preceded by a brief description of our two experimental setups: CLUB and AIM. The *CLUster Beam (CLUB)* apparatus represents a very versatile worldwide unique experimental setup dedicated to various investigations of clusters, nanoparticles and aerosol particles in molecular beams. It encompass different experiments such as UV laser spectroscopy and photofragment velocity map imaging (Sec. 2.2.1); mass spectrometry after electron and/or photoionization and other special mass spectrometric methods such as Na doping and photodetachment (Sec. 2.2.2); pickup of molecules and cluster velocity measurements by means of time-of-flight technique (Sec. 2.2.3) etc. The second *Appartus fo IMaging (AIM)* is dedicated to the VMI technique only and is used for the photodissociation studies of isolated molecules and small clusters.

In this collection altogether 16 of our recent papers were summarized (most of them from the last two years 2014 and 2015), and divided into 5 Sections to illustrate the various activities in our laboratory. Two of the *Results* sections exemplified the method development performed in our group: Sec. 3.1 explained the *Velocity map imaging as a tool for cluster dynamics investigations*, and Sec. 3.2 *Na-doping and solvated electron reactivity* introduced a new powerful method for cluster mass spectrometry. The following chapters summarized some of our investigations of atmospherically relevant processes on ice nanoparticles, namely Sec. 3.3 *Photochemistry of molecules in ice nanoparticles*, and Sec. 3.4 *Nucleation and growth of ice nanoparticles.* Finally, in the last Sec. 3.5 we have discussed the *Solvation effects on essential building blocks of biomolecules.*

Several future directions of our research build upon the work illustrated in this collection:

Negative ions: First, we have just recently further extended our experimental capabilities on the CLUB by generating and detecting negatively charged clusters. The electron attachment and especially dissociative electron attachment (DEA), are important processes in many areas, namely in atmospheric chemistry and also in radiation damage of biomolecules. The DEA processes have been investigated in great details for isolated molecules, however, so far very little is known about the solvent effects in these processes. Our bipolar RTOF (the polarity of extraction and acceleration voltages can be reversed) with the electron ionization option where the electron energy can be varied essentially from 1 to 90 eV with a reasonable energy resolution ($\leq$0.7 eV) represents an experimental tool for negative ion generation and investigations. This has been proven first by studying DEA on SF_6 molecules and clusters. We have measured the mass spectra of negatively charged clusters as a function of electron energy. This represents 3D data sets from which the ion intensities as a function of mass (mass spectra) or electron energy (ion yield curves) can be evaluated. In addition, by switching the polarity, the positive ion spectra can be recorded as well for the same species. This wealth of information provides insight in the DEA processes in the cluster environments.

This method has been established in our lab first in the fall 2015 and subsequently we have investigated by the same method clusters of nitrophenol which can represent a source of HONO in the atmosphere. This study is currently prepared for publication.

The interest in the negative ions has recently been induced by practical applications of focused electron beam deposition (FEBID). The FEBID is nowadays broadly used in nanofabrication, however, the detailed molecular level understanding of the electron-induced chemistry of molecules that serve as precursors for FEBID is yet lacking. Our ultimate goal is to use the knowledge of the elementary processes in isolated molecules (e.g., fragmentation pathways, cross sections etc.) for optimizing the deposition performance. The biggest drawback of gas phase studies is that they completely ignore the effect of environment that certainly plays a strong role in determining the outcome of electron-induced reactions. We bridge the gap between the gas phase and surface approach by depositing the molecules on the surface of nanoparticles in molecular beams by the pickup technique. The resulting species are ionized either negatively by electron attachment or positively by EI and the mass spectra are recorded and analyzed. Currently we are preparing our first publication on this subject concerning $Fe(CO)_5$ molecules.

The investigation of the negatively charge clusters and nanoparticles represents new vast landscape for our future investigations which is yet relatively unexplored. Thus this is a promising new direction for our future research.

Biomolecules: The successfully developed subject of solvation effects on essential building blocks of biomolecules discussed in Sec. 3.5 will be developed further in our laboratory. It has been already mentioned, that a new study of hydroxypyridine molecules on ice nanoparticles has recently been submitted for publication from our laboratory. There were propositions that the ice grains could represent species where the biologically relevant molecules could be synthesized in the space. However, we have shown in several of our investigations that many molecules generate clusters on argon nanoparticles but they remain as isolated individual molecules on ice nanoparticles. This seemed to somewhat undermine the proposition of reactions between the molecules on ice surfaces. Nevertheless, we have just come across an exception from this behavior: hydroxypyridine. We see in our experiments an unambiguous evidence for generation of clusters, especially dimers, of hydroxypyridine on the ice nanoparticles. Besides, hydroxypyridine dimers represent structural motif of biologically relevant hydrogen bonds similar to e.g. DNA base pairs. We will follow this direction of our research seeking for other molecules clustering on ice nanoparticles. The combination of various mass spectrometric methods present in the CLUB provides a tool to reveal the structure and composition of these clusters.

Another development of our experiment in the field of biomolecules represent introduction of new pickup oven dedicated to evaporation of larger biomolecules for the pickup experiments. This new oven has recently been built and tested in the CLUB. It will allow doping of ice nanoparticles with larger biomolecules for the photodissociation and mass spectrometric experiments. In addition, experiments with pickup of several species in separated pickup cells will be attempted. The idea is to observe reactions of the molecules on ice nanoparticles, either in the ground state or after an excitation by UV photons or electrons.

Atmospheric chemistry: This has been our major subject and it will remain in our focus also in the future. Namely the photochemisty of molecules on ice nanoparticles, which is relevant to the ozone depletion but also to other processes in atmospheric chemistry, will be further investigated. Two interconnected directions of the future research can be outlined. First, we will extend the range of species with which we do our experiments, both in terms of the ice nanoparticles as well as in terms of the embedded molecules. So far we have worked almost exclusively with the pure ice nanoparticles, except for the few studies involving nitric acid/water, N_2O/water and ammonia/water mixtures. Such mixed species represent even better models for the aerosol particles in the atmosphere, therefore we will focus in the future on generating the mixed species involving atmospheric molecules such as HNO_3, H_2SO_4, various amines, etc. Once we learn to generate and characterize such species, we can deposit other atmospheric molecules (e.g. hydrogen halides) on them and investigate their photodissociation and photochemistry. Second direction in these studies represents extending the REMPI detection in our photodissociation studies on phtofragments other than H and Cl atoms detected so far. Possible candidates represent e.g. CH_3 radical (from a CH_3Cl photodissociation), oxygen, OH radical (perhaps the most important radical in atmospheric chemistry) etc. This direction will further widen our horizons concerning possible photochemistry experiments.

Instrumental: One further instrumental enrichment is currently being set up in our laboratory, namely the implementation of a new infrared laser. This laser IR OPO/OPA has been purchased some time ago, unfortunately its installation was hampered by several misfortunate accidents and it has not been brought to full operation yet. However, this work is proceeding approaching its final stage. Once the pulsed IR light will be available, a variety of new experiments can be performed, e.g. IR-UV experiments where the clusters will be first vibrationally excited prior to the UV dissociation of the molecules. One can imagine exciting directly the molecules which are photodissociated, or the surrounding cluster molecules. In both cases the energy flow between the molecule and the solvating environment can be studied (either molecular excitation or de-excitation by the solvent). These experiments will be done on both AIM and CLUB. Another possibility on the CLUB will be the IR excitation of the cluster species in the mass spectrometer and then coupling the EI or PI or NaPI with the IR excitation. All these experiments offer unprecedented wealth of possibilities for the future cluster studies, many of which will be world-wide unique.

As a final remark, in 2011 in my DSc. Thesis, I have summarized the major part of a new research, which we have started in 2005 at the J. Heyrovský Institute in Prague. The present collection outlines some of the newest developments in this fields achieved within the last less than five years. Absolute majority of the papers in this collection stem from the last two years of research. This demonstrates that an interesting and vital field of studying free clusters and nanoparticles in molecular beams has been established in our laboratory, and this last chapter suggests many possibilities and challenges for the future investigations in all the introduced areas.

Chapter 5

Bibliography

References

[1] Forsén, S. In *Nobel Lectures, Chemistry 1981-1990*; Frängsmyr, T., Malmström, B. G., Eds.; World Scientific Publishing Co.: Singapore, 1992.

[2] Stern, O. *Z. Phys.* **1920**, *2*, 49.

[3] Stern, O. *Z. Phys.* **1920**, *3*, 417.

[4] Stern, O.; Gerlach, W. *Z. Phys.* **1922**, *9*, 349.

[5] Scoles, G. *Atomic and Molecular Beam Methods;* Oxford: New York, 1988.

[6] Pauly, H. *Atom, Molecule and Cluster Beams;* Springer: Berlin, 2000.

[7] Bernstein, R. B. *Chemical Dynamics via Molecular Beam and Laser Techniques;* Oxford University Press: Oxford, 1982.

[8] Levine, R. D.; Bernstein, R. B. *Molecular Reaction Dynamics and Chemical Reactivity;* Oxford University Press: Oxford, 19872.

[9] Düren, R.; Lackschewitz, U.; Milošević, S.; Waldapfel, H.-J. *Chem. Phys.* **1990**, *140*, 199.

[10] Mestdagh, J. M.; Gaveau, M. A.; Gée, C.; Sublemontier, O.; Visticot, J. P. *Int. Rev. Phys. Chem.* **1997**, *16*, 215.

[11] Hurley, S. M.; Dermota, T. E.; Hydutsky, D. P.; Castleman, A. W. *Science* **2002**, *298*, 202.

[12] Hurley, S. M.; Dermota, T. E.; Hydutsky, D. P.; Castleman, A. W. *J. Chem. Phys.* **2003**, *118*, 9272.

[13] Buck, U.; Steinbach, C. *J. Phys. Chem. A* **1998**, *102*, 7333.

[14] Castleman, A.; Keesee, R. *Science* **1988**, *241*, 36.

[15] Jena, P.; Castleman, A. W. *Proc. Nat. Acad. Sci. USA* **2006**, *103*, 10560.

[16] Haberland, H. *Clusters of Atoms and Molecules;* Springer: Berlin, 1994.

[17] Toennies, J. P.; Vilesov, A. F. *Angew. Chem. Int. Ed.* **2004**, *43*, 2622.

[18] Dong, F.; Miller, R. E. *Science* **2002**, *298*, 1227.

[19] Buck, U. *J. Phys. Chem. A* **2002**, *106*, 10049.

[20] Poterya, V.; Profant, V.; Fárník, M.; Slavíček, P.; Buck, U. *J. Chem. Phys.* **2007**, *127*, 064307.

[21] Poterya, V.; Profant, V.; Fárník, M.; Šištík, L.; Slavíček, P.; Buck, U. *J. Phys. Chem. A* **2009**, *113*, 14583.

[22] Slavíček, P.; Fárník, M. *Phys. Chem. Chem. Phys.* **2011**, *13*, 12123.

[23] Fárník, M.; Slavíček, P.; Buck, U. In *Hydrogen Bonding and Transfer in the Excited State II*; Han, K.-L., Zhao, G.-J., Eds.; Wiley: Chichester, UK, 2011; pages 865 – 889.

[24] Poterya, V.; Šištík, L.; Lengyel, J.; Slavíček, P.; Fárník, M. *Phys. Chem. Chem. Phys.* **2014**, *12*, 8936 – 8944.

[25] Poterya, V.; Nachtigallová, D.; Lengyel, J.; Fárník, M. *Phys. Chem. Chem. Phys.* **2015**, *17*, 25004 – 25013.

[26] Molina, M. J.; Tso, T. L.; Molina, L. T.; Wang, F. C. Y. *Science* **1987**, *238*, 1253.

[27] Tolbert, M. A.; Rossi, M. J.; Malhotra, R.; Golden, D. M. *Science* **1987**, *238*, 1258.

[28] Tolbert, M. A.; Rossi, M. J.; Golden, D. M. *Geophys. Res. Lett.* **1988**, *15*, 847.

[29] Leu, M.-T. *Geophys. Res. Lett.* **1988**, *15*, 17.

[30] Peter, T. *Ann. Rev. Phys. Chem.* **1997**, *48*, 785–822.

[31] Solomon, S.; Garcia, R. R.; Rowland, F. S.; Wuebbles, D. J. *Nature* **1986**, *321*, 755.

[32] Lu, Q.-B.; Madey, T. E. *J. Chem. Phys.* **1999**, *111*, 2861.

[33] Lu, Q.-B.; Sanche, L. *J. Chem. Phys.* **2004**, *120*, 2434.

[34] Lu, Q.-B.; Sanche, L. *Phys. Rev. Lett.* **2001**, *87*, 078501.

[35] Blank, D. A.; North, S. W.; Lee, Y. T. *Chem. Phys.* **1994**, *187*, 35.

[36] Cronin, B.; Nix, M. G. D.; Qadiri, R. H.; Ashfold, M. N. R. *Phys. Chem. Chem. Phys.* **2004**, *6*, 5031.

[37] Wei, J.; Kuczmann, A.; Riedel, J.; Renth, F.; Temps, F. *Phys. Chem. Chem. Phys.* **2003**, *5*, 315.

[38] Wei, J.; Riedel, J.; Kuczmann, A.; Renth, F.; Temps, F. *Faraday Discuss.* **2004**, *127*, 267.

[39] Papadakis, V.; Kitsopoulos, T. N. *Rev. Sci. Instrum.* **2006**, *77*, 083101.

[40] Lippert, H.; Ritzel, H.-H.; Hertel, I. V.; Radloff, W. *Chem. Phys. Chem.* **2004**, *5*, 1423.

[41] Barbatti, M.; Vazdar, M.; Aquino, A. J. A.; Eckert-Maksić, M.; Lischka, H. *J. Chem. Phys.* **2006**, *125*, 164323.

[42] van den Brom, A. J.; Kapelios, M.; Kitsopoulos, T. N.; Nahler, N. H.; Cronin, B.; Ashfold, M. N. R. *Phys. Chem. Chem. Phys.* **2005**, *7*, 892.

[43] Crespo-Hernandez, C. E.; Arce, R.; Ishikawa, Y.; Gorb, L.; Leszczynski, J.; Close, D. M. *J. Phys. Chem. A* **2004**, *108*, 6373.

[44] Crespo-Hernandez, C. E.; Cohen, B.; Hare, P. M.; Kohler, B. *Chem. Rev.* **2004**, *104*, 1977.

[45] Profant, V.; Poterya, V.; Fárník, M.; Slavíček, P.; Buck, U. *J. Phys. Chem. A* **2007**, *111*, 12477 – 12486.

[46] Poterya, V.; Tkáč, O.; Fedor, J.; Fárník, M.; Slavíček, P.; Buck, U. *Int. J. Mass Spectrom.* **2010**, *2010*, 85 – 93.

[47] Fárník, M.; Davis, S.; Nesbitt, D. J. *Faraday Discuss.* **2001**, *118*, 63.

[48] Fárník, M.; Nesbitt, D. J. *J. Chem. Phys.* **2004**, *121*, 12386.

[49] Fárník, M.; Steinbach, C.; Weimann, M.; Buck, U.; Borho, N.; Suhm, M. A. *Phys. Chem. Chem. Phys.* **2004**, *6*, 4614.

[50] Sobolewski, A. L.; Domcke, W. G. *J. Phys. Chem. A* **2007**, *111*, 11725.

[51] Schultz, T.; Samoylova, E.; Radloff, W.; Hertel, I. V.; Sobolewski, A. L.; Domcke, W. *Science* **2004**, *306*, 1765.

[52] Markwick, P.; Doltsinis, N. *J. Chem. Phys.* **2007**, *126*, 175102.

[53] Schwalb, N.; Temps, F. *J. Am. Chem. Soc.* **2007**, *129*, 9272.

[54] Dermota, T. E.; Zhong, Q.; Castleman, A. W. *Chem. Rev.* **2004**, *104*, 1861–1886.

[55] Lengyel, J.; Gorejová, R.; Herman, Z.; Fárník, M. *J. Phys. Chem. A* **2013**, *117*, 11225 – 11232.

[56] Lengyel, J.; Poterya, V.; Fárník, M. *J. Mass Spectrom.* **2015**, *50*, 643 – 649.

[57] Lengyel, J.; Pysanenko, A.; Poterya, V.; Kočišek, J.; Fárník, M. *Chem. Phys. Lett.* **2014**, *612*, 256 – 261.

[58] Svrčková, P.; Pysanenko, A.; Lengyel, J.; Rubovič, P.; Kočišek, J.; Poterya, V.; Slavíček, P.; Fárník, M. *Phys. Chem. Chem. Phys.* **2015**, *17*, 25734.

[59] Baumfalk, R.; Buck, U.; Frischkorn, C.; Gandhi, S. R.; Lauenstein, C. *Ber. Bunsenges. Phys. Chem.* **1997**, *101*, 606.

[60] Baumfalk, R.; Buck, U.; Frischkorn, C.; Gandhi, S. R.; Lauenstein, C. *Chem. Phys. Lett.* **1997**, *269*, 321.

[61] Lohbrandt, P.; Galonska, R.; Kim, H. J.; Lauenstein, M. S. C.; Buck, U. In *Atomic and Molecular Beams. The State of the Art 2000*; Campargue, R., Ed.; Springer: Berlin, 2001; page 623.

[62] Nahler, N. H. *PhD Thesis, GA Universität Göttingen* **2002**.

[63] Fárník, M. *Molecular Dynamics in Free Clusters and Nanoparticles Studied in Molecular Beams;* ICT Prague Press: Institute of Chemical Technology Prague, 2011.

[64] Fedor, J.; Poterya, V.; Pysanenko, A.; Fárník, M. *J. Chem. Phys.* **2011**, *135*, 104305.

[65] Kočišek, J.; Lengyel, J.; Fárník, M. *J. Chem. Phys.* **2013**, *138*, 124306.

[66] Kočišek, J.; Lengyel, J.; Fárník, M.; Slavíček, P. *J. Chem. Phys.* **2013**, *139*, 214308.

[67] Poterya, V.; Kočišek, J.; Lengyel, J.; Svrčková, P.; Pysanenko, A.; Hollas, D.; Slavíček, P.; Fárník, M. *J. Phys. Chem. A* **2014**, *118*, 4740 – 4749.

[68] Fárník, M.; Poterya, V. *Front. Chem.* **2014**, *2*, 4.

[69] Kočišek, J. *PhD Thesis, Department of Surface and Plasma Science, Faculty of Mathematics and Physics, Charles University, Prague* **2013**.

[70] Lengyel, J. *PhD Thesis, University of Chemistry and Technology, Prague* **2015**.

[71] Fedor, J.; Kočišek, J.; Poterya, V.; Votava, O.; Pysanenko, A.; Lipciuc, L.; Kitsopoulos, T. N.; Fárník, M. *J. Chem. Phys.* **2011**, *134*, 154303.

[72] Fárník, M.; Poterya, V.; Kočišek, J.; Fedor, J.; Slavíček, P. *Mol. Phys.* **2012**, *110*, 2817.

[73] Poterya, V.; Kočišek, J.; Pysanenko, A.; Fárník, M. *Phys. Chem. Chem. Phys.* **2014**, *16*, 421 – 429.

[74] Christen, W.; Rademann, K. *Phys. Rev. A* **2008**, *77*, 012702.

[75] Christen, W.; Rademann, K. *Phys. Scripta* **2008**, *80*, 048127.

[76] Toennies, J. P.; Vilesov, A. F.; Whaley, K. B. *Physics Today* **2001**, *2*, 31.

[77] Póczik, I. *Z. Phys. D* **1991**, *20*, 395.

[78] Hagena, O. F. *Surf. Sci.* **1981**, *106*, 101 – 116.

[79] Hagena, O. F. *Z. Phys. D* **1987**, *4*, 291 – 299.

[80] Hagena, O. F. *Rev. Sci. Instrum.* **1992**, *63*, 2374 – 2379.

[81] Buck, U.; Krohne, R. *J. Chem. Phys.* **1996**, *105*, 5408 – 5415.

[82] Bobbert, C.; Schütte, S.; Steinbach, C.; Buck, U. *Eur. Phys. J. D* **2002**, *19*, 183–192.

[83] Schütte, S.; Buck, U. *Int. J. Mass Spectrom.* **2002**, *220*, 183 – 192.

[84] Farges, J.; de Feraudy, M. F.; Raoult, B.; Torchet, G. *Sur. Sci.* **1981**, *106*, 95.

[85] Torchet, G.; Farges, J.; de Feraudy, M. F.; Raoult, B. In *The Chemical Physics of Atomic and Molecular Clusters*; Scoles, G., Ed.; North-Holland: Amsterdam, 1990; page 513.

[86] Torchet, G.; Schwartz, P.; Farges, J.; de Feraudy, M. F.; Raoult, B. *J. Chem. Phys.* **1983**, *79*, 6196.

[87] Brudermann, J.; Buck, U.; Buch, V. *J. Phys. Chem.* **2002**, *106*, 453.

[88] private communication. Buck, U. **2007**.

[89] Buck, U.; Pradzinski, C. C.; Zeuch, T.; Dieterich, J. M.; Hartke, B. *Phys. Chem. Chem. Phys.* **2014**, *16*, 6859 – 6871.

[90] Zeuch, T.; Buck, U. *Chem. Phys. Lett.* **2013**, *579*, 1 – 10.

[91] Gough, T. E.; Mengel, M.; Rowntree, P. A.; Scoles, G. *J. Chem. Phys.* **1985**, *83*, 4958.

[92] Behrens, M.; Fröchtenicht, R.; Hartmann, M.; Siebers, J. G.; Buck, U. *J. Chem. Phys.* **1999**, *111*, 2436.

[93] Nahler, N. H.; Baumfalk, R.; Buck, U.; Vach, H.; Slavíček, P.; Jungwirth, P. *Phys. Chem. Chem. Phys.* **2003**, *5*, 3394.

[94] Peoux, G.; Monnerville, M.; Duhoo, T.; Pouilly, B. *J. Chem. Phys.* **1997**, *107*, 70.

[95] Pouilly, B.; Monnerville, M. *Chem. Phys.* **1998**, *238*, 437.

[96] Rakitzis, T. P.; Samartzis, P. C.; Toomes, R. L.; Kitsopoulos, T. N. *J. Chem. Phys.* **2004**, *121*, 7222.

[97] Baumfalk, R.; Buck, U.; Frischkorn, C.; Nahler, N. H.; Hüwel, L. *J. Chem. Phys.* **1999**, *111*, 2595.

[98] Fárník, M.; Poterya, V.; Votava, O.; Ončák, M.; Slavíček, P.; Dauster, I.; Buck, U. *J. Phys. Chem. A* **2009**, *113*, 7322.

[99] Zhong, Q.; Castleman, A. W. *Chem. Rev.* **2000**, *100*, 4039.

[100] Chandler, D. W.; Houston, P. L. *J. Chem. Phys.* **1987**, *87*, 1445.

[101] Eppink, A. T. J. B.; Parker, D. H. *Rev. Sci. Instrum.* **1997**, *68*, 3477.

[102] Gebhardt, C. R.; Rakitzis, T. P.; Samartzis, P. C.; Ladopoulos, V.; Kitsopoulos, T. N. *Rev. Sci. Instrum.* **2001**, *72*, 3848.

[103] Whitaker, B. *Imaging in Molecular Dynamics;* Cambridge University Press: Cambridge, 2003.

[104] Lengyel, J.; Pysanenko, A.; Kočišek, J.; Poterya, V.; Pradzynski, C.; Zeuch, T.; Slavíček, P.; Fárník, M. *J. Phys. Chem. Lett.* **2012**, *3*, 3096 – 3109.

[105] Lengyel, J.; Kočišek, J.; Poterya, V.; Pysanenko, A.; Svrčková, P.; Fárník, M.; Zaouris, D.; Fedor, J. *J. Chem. Phys.* **2012**, *137*, 034304.

[106] Lengyel, J.; Pysanenko, A.; Poterya, V.; Slavíček, P.; Fárník, M.; Kočišek, J.; Fedor, J. *Phys. Rev. Lett.* **2014**, *112*, 113401.

[107] Poterya, V.; Lengyel, J.; Pysanenko, A.; Svrčková, P.; Fárník, M. *J. Chem. Phys.* **2014**, *141*, 074309–1 – 10.

[108] Pysanenko, A.; Habartová, A.; Svrčková, P.; Lengyel, J.; Poterya, V.; Roeselová, M.; Fedor, J.; Fárník, M. *J. Phys. Chem. A* **2014**, *119*, 8991 – 8999.

[109] Buck, U.; Meyer, H. *Phys. Rev. Lett.* **1984**, *52*, 109.

[110] Buck, U.; Meyer, H. *J. Chem. Phys.* **1986**, *84*, 4854.

[111] Steinbach, C.; Fárník, M.; Buck, U.; Brindle, C. A.; Janda, K. C. *J. Phys. Chem. A* **2006**, *110*, 9108.

[112] Janeček, I.; Cintavá, S.; Hrivňák, D.; Kalus, R.; Fárník, M.; Gadea, F. X. *J. Chem. Phys.* **2009**, *131*, 114306.

[113] Ashfold, M. N. R.; Nahler, N. H.; Orr-Ewing, A. J.; Vieuxmaire, O. P. J.; Toomes, R. L.; Kitsopoulos, T. N.; Garcia, I. A.; Chestakov, D. A.; Wu, S.-M.; .; Parker, D. H. *Phys. Chem. Chem. Phys.* **2006**, *8*, 26 – 53.

[114] Grygoryeva, K.; poterya, V.; Fárník, M.

[115] Geräte für forschung und industrie, Munich. Kaesdorf, S. **2011**.

[116] Wannier, G. H. *Phys. Rev.* **1953**, *90*, 817.

[117] MacTaylor, R. S.; Castleman, A. W. *J. Atmos. Chem.* **2000**, *36*, 23 – 63.

[118] Laskin, A.; Laskin, J.; Nizkorodov, S. *Environ. Chem.* **2012**, *9*, 163 – 189.

[119] Yoder, B. L.; Litman, J. H.; Forysinski, P. W.; Corbett, J. L.; Signorell, R. *J. Phys. Chem. Lett.* **2011**, *2*, 2623–2628.

[120] Steinbach, C.; Buck, U. *Phys. Chem. Chem. Phys.* **2005**, *7*, 986 – 990.

[121] Schläppi, B.; Ferreiro, J. J.; Litman, J. H.; Signorell, R. *Int. J. Mass Spectrom.* **2014**, *372*, 13 – 21.

[122] Forysinski, P.; Zielke, P.; Luckhaus, D.; Corbett, J.; Signorell, R. *J. Chem. Phys.* **2011**, *134*, 094314.

[123] Litman, J. H.; Yoder, B. L.; Schläppi, B.; Signorell, R. *Phys. Chem. Chem. Phys.* **2013**, *15*, 940.

[124] Schläppi, B.; Litman, J. H.; Ferreiro, J. J.; Stapfer, D.; Signorell, R. *Phys. Chem. Chem. Phys.* **2015**, *17*, 25761.

[125] West, A. H.; Yoder, B. L.; Signorell, R. *J. Phys. Chem. A* **2013**, *113*, 13326 – 13335.

[126] West, A. H.; Yoder, B. L.; Luckhaus, D.; Saak, C.-M.; Doppelbauer, M.; Signorell, R. *J. Phys. Chem. Lett.* **2015**, *6*, 1487 – 1492.

[127] Forck, R. M.; Dauster, I.; Schieweck, Y.; Zeuch, T.; Buck, U.; Rončák, M.; Slavíček, P. *J. Chem. Phys.* **2010**, *132*, 221102.

[128] Forck, R. M.; Pradzynski, C. C.; Wolff, S.; Ončák, M.; Slavíček, P.; Zeuch, T. *Phys. Chem. Chem. Phys.* **2012**, *9*, 3004.

[129] Pradzynski, C. C.; Forck, R. M.; Zeuch, T.; Slavíček, P.; Buck, U. *Science* **2012**, *337*, 1529–1532.

[130] Forck, R. M.; Dieterich, J. M.; Pradzynski, C. C.; Huchting, A. L.; Mata, R. A.; Zeuch, T. *Phys. Chem. Chem. Phys.* **2012**, *14*, 9054–9057.

[131] Šmídová, D.; Lengyel, J.; Pysanenko, A.; Med, J.; Slavíček, P.; Fárník, M. *J. Phys. Chem. Lett.* **2015**, *6*, 2865–2869.

[132] Lengyel, J.; Pysanenko, A.; Rubovič, P.; Fárník, M. *Eur. Phys. J. D* **2015**, page accepted for publication.

[133] Auerbach, D. J. In *Atomic and Molecular Beam Methods, Vol. I*; Scoles, G., Ed.; Oxford: New York, 1988; page 362.

[134] Berling, K.; Belbing, R.; Kramer, K.; Pauly, H.; Schlier, C.; Toschek, P. *Z. Phys.* **1962**, *166*, 406.

[135] Lang, N. C.; Lilenfeld, H. V.; Kinsey, J. L. *J. Chem. Phys.* **1971**, *55*, 3114.

[136] Lewerenz, M.; Schilling, B.; Toennies, J. P. *J. Chem. Phys.* **1995**, *102*, 8191.

[137] Macler, M.; Bae, Y. K. *J. Chem. Phys.* **1997**, *106*, 5785.

[138] Slavíček, P.; Jungwirth, P.; Lewerenz, M.; Nahler, N. H.; Fárník, M.; Buck, U. *J. Phys. Chem. A* **2003**, *107*, 7743.

[139] Nahler, N. H.; Fárník, M.; Buck, U.; Vach, H.; Gerber, R. B. *J. Chem. Phys.* **2004**, *121*, 1293.

[140] Slavíček, P.; Jungwirth, P.; Lewerenz, M.; Nahler, N. H.; Fárník, M.; Buck, U. *J. Chem. Phys.* **2004**, *120*, 4498.

[141] Fárník, M.; Nahler, N. H.; Buck, U.; Slavíček, P.; Jungwirth, P. *Chem. Phys.* **2005**, *315*, 161.

[142] Fárník, M.; Buck, U. *Phys. Scripta: Comm. At. Mol. Opt. Phys.* **2007**, *76*, 73.

[143] IUPAC.

[144] Mundy, C.; Hutter, J.; Parrinello, M. *J. Am. Chem. Soc.* **2000**, *122*, 4837.

[145] Poterya, V.; Fárník, M.; Slavíček, P.; Buck, U.; Kresin, V. V. *J. Chem. Phys.* **2007**, *126*, 071101.

[146] Sobolewski, A. L.; Domcke, W. *Phys. Chem. Chem. Phys.* **2002**, *4*, 4.

[147] Sobolewski, A. L.; Domcke, W. *J. Phys. Chem. A* **2003**, *107*, 1557.

[148] Sobolewski, A. L.; Domcke, W. *Phys. Chem. Chem. Phys.* **2005**, *7*, 970.

[149] Sobolewski, A. L.; Domcke, W. *J. Chem. Phys.* **2005**, *122*, 184320.

[150] Sobolewski, A. L.; Domcke, W. *Phys. Chem. Chem. Phys.* **2007**, *9*, 3818.

[151] Ončák, M.; Slavíček, P.; Poterya, V.; Fárník, M.; Buck, U. *J. Phys. Chem. A* **2008**, *112*, 5344–5353.

[152] Ončák, M.; Slavíček, P.; Fárník, M.; Buck, U. *J. Phys. Chem. A* **2011**, *115*, 6155–6168.

[153] Poterya, V.; Fedor, J.; Pysanenko, A.; Tkáč, O.; Lengyel, J.; Ončák, M.; Slavíček, P.; Fárník, M. *Phys. Chem. Chem. Phys.* **2011**, *13*, 2250 – 2258.

[154] Ashfold, M. N. R.; Cronin, B.; Devine, A. L.; Dixon, R. N.; Nix, M. G. D. *Science* **2006**, *312*, 1637.

[155] Roberts, G. M.; Stavros, V. G. *Chem. Sci.* **2014**, *5*, 1698 – 1722.

[156] Sobolewski, A.; Domcke, W.; Dedonder-Lardeux, C.; Jouvet, C. *Phys. Chem. Chem. Phys.* **2002**, *4*, 1093.

[157] Roberts, G. M.; Williams, C. A.; Young, J. D.; Ullrich, S.; Patterson, M. J.; Stavros, V. G. *J. Am. Chem. Soc.* **2012**, *134*, 12578 – 12589.

Chapter 6

List of abbreviations

AIM	Apparatus for IMaging
CCD	Charge-coupled device (camera)
CFC	Chlorofluorocarbon, freon
CI	Conical intersection
CICR	Cluster isolated chemical reaction
CLUB	CLUster Beam apparatus
CM	Center-of-mass (system)
CT	Charge transfer
CTTS	Charge-transfer-to-solvent (electronic band)
DEA	dissociative electron attachment
EI	Electron ionization
EA	Electron affinity
EtSH	ethanethiol
FEBID	focused electron beam deposition
FT	Fourier transformation
FTIR	Fourier transformation infrared (spectroscopy)
FWHM	Full width at half maximum
HT	hydrogen transfer
IR	Infrared (radiation, laser, etc.)
KED	Kinetic energy distribution
LAB	Laboratory (system, angle, etc.)
MC	Monte-Carlo (simulation)
NaPI	Na-doping and photoionization method
PI	Photoionization
PES	Potential energy surface
PSC	Polar stratospheric cloud
PT	proton transfer

REMPI	Resonce-enhanced multiphoton ionization
RTOF	Reflectron time of flight mass spectrometer
SFM	Sum frequency mixing
SHG	Second harmonic generation
TFP	Thin film polarizer
TOF	Time-of-flight (spectrometer, spectrum, etc.)
UV	Ultraviolet (radiation, laser, etc.)
VMI	Velocity map imaging
WMTOF	Time-of-flight spectrometer of Wiley-McLaren type

Appendix A

Velocity map imaging

THE JOURNAL OF CHEMICAL PHYSICS **134**, 154303 (2011)

Velocity map imaging of HBr photodissociation in large rare gas clusters

J. Fedor,[1] J. Kočišek,[1] V. Poterya,[1] O. Votava,[1] A. Pysanenko,[1] M. L. Lipciuc,[2]
T. N. Kitsopoulos,[3] and M. Fárník[1,a)]
[1]*J. Heyrovský Institute of Physical Chemistry v.v.i., Academy of Sciences of the Czech Republic, Dolejškova 3, 18223 Prague, Czech Republic*
[2]*Chemistry Research Laboratory, Department of Chemistry, University of Oxford, 12 Mansfield Road, Oxford OX1 3TA, United Kingdom*
[3]*Department of Chemistry, University of Crete, Heraklion, Greece and Institute of Electronic Structure and Lasers, Foundation for Research and Technology, Hellas, P.O. Box 1527, 71110 Heraklion, Greece*

(Received 17 February 2011; accepted 26 March 2011; published online 18 April 2011)

We have implemented the velocity map imaging technique to study clustering in the pulsed supersonic expansions of hydrogen bromide in helium, argon, and xenon. The expansions are characterized by direct imaging of the beam velocity distributions. We have investigated the cluster generation by means of UV photodissociation and photoionization of HBr molecules. Two distinct features appear in the hydrogen atom photofragment images in the clustering regime: (i) photofragments with near zero kinetic energies and (ii) "hot" photofragments originating from vibrationally excited HBr molecules. The origin of both features is attributed to the fragment caging by the cluster. We discuss the nature of the formed clusters based on the change of the photofragment images with the expansion parameters and on the photoionization mass spectra and conclude that single HBr molecule encompassed with rare gas "snowball" is consistent with the experimental observations. © *2011 American Institute of Physics*. [doi:10.1063/1.3578610]

I. INTRODUCTION

The field of UV photochemistry and molecular dynamics in general has received an impetus by the introduction of imaging techniques.[1–7] They represent effective tools to study the photodissociation dynamics, since the photofragment images in general contain a complete information about the kinetic energy and angular distributions at the same time. During the last decade numerous experiments have investigated the photodynamics of isolated molecules in molecular beams by means of various ion imaging techniques often providing a detailed insight into the photodissociation process.

The imaging technique is also well suited to study the dynamics in more complex systems, e.g., in various atomic and molecular clusters. The clusters provide an ideal step toward more complicated systems since the basic elements of interest (e.g., noncovalent interactions) are present and, at the same time, the experimental approaches as for isolated molecules can be used: the clusters can be formed in molecular beams, probed by lasers and the kinetics of photofragments can be measured (as opposed to the condensed phase, where the photofragments are usually lost in the bulk). The effect of noncovalent interactions under various cluster formation conditions can be then deduced from the kinetic energy spectra of the photofragments.

Such approach has been adopted in the past, however, usually more traditional detection methods were employed. Often, the kinetic energy of photofragments was measured via the time-of-flight (TOF) technique. For instance, photodissociation of hydrogen halides on/in various large rare gas clusters HX·Rg$_n$ ($\bar{n} \sim 10^2$ atoms) was studied on a versatile cluster beam apparatus in Göttingen.[8–14] When this experiment was moved to our laboratory in Prague, the studies have been extended to other systems, e.g., hydrogen halides on ice nanoparticles[15–17] or clusters of biologically relevant molecules.[18,19]

The application of imaging techniques to cluster studies has been so far very limited and usually restricted to small species. When cluster effects were observed in photofragment images, it has been usually attributed exclusively to dimers, e.g., $(CH_3I)_2$,[20] $(HI)_2$,[21] $(ICN)_2$,[22] and pyrrole-Xe.[23] There were only two recent studies, where also somewhat larger species were considered: e.g., pyrrole-ammonia[24] and N_2O (Ref. 25) clusters. The imaging was also exploited to study photoelectrons from negative metal cluster ions[26,27] and from fullerenes.[28] Recently, imaging of photoelectrons and photoions from species deposited on large argon clusters has been reported.[29] However, we are not aware of any photodissociation imaging study in such clusters.

In this paper we present our new experimental setup that combines pulsed molecular beam, photodissociation and photoionization, and the velocity map imaging techniques. We investigate HBr photodissociation in large clusters of tens to hundreds rare gas atoms. The HBr molecule was chosen since its photodissociation has been studied in great detail by the TOF technique in the gas phase[30–32] and in various clusters,[8–10,13,33–37] and it has also been studied by imaging technique in the gas phase.[38,39] The relative simplicity of

---

[a)] Author to whom correspondence should be addressed. Electronic mail: michal.farnik@jh-inst.cas.cz.

0021-9606/2011/134(15)/154303/7/$30.00

the hydrogen bromide photodissociation dynamics allows to unravel the cluster effects easily. The experiments show that the clustering occurs in expansions with the buffer gas argon and xenon. When helium is used as a buffer gas, a pure molecular beam is obtained. We identify clustering from the distinct changes in the photofragment images and investigate the nature of the formed species. The presence and intensity of cluster-assigned features in the images depends on the buffer gas, mixture composition and it is also very sensitive to the time during the gas pulse at which the laser probes the expansion. A detailed insight into the dynamics of cage effect is obtained from the photofragment images.

II. EXPERIMENT

In the newly constructed experimental setup, Apparatus for IMaging (AIM), the pulsed molecular beam is crossed at 90° with a laser beam and the ionic products are analyzed by the velocity map imaging system, positioned perpendicular to the molecular beam. Only a brief overview of the experiment follows, a more detailed description is available as a supplementary material.[40]

The molecular beam is produced by expanding the mixture of HBr and buffer gas (with a controlled stagnation pressure) via pulsed solenoid valve with a nozzle of 0.6 mm diameter. The expanding gas is skimmed and the resulting beam is crossed at 90° with a laser beam in a second, differentially pumped chamber. In this paper we present a one-color experiment, where 243.07 nm laser light is used for photodissociation of HBr and subsequent effective ionization of hydrogen atom fragments via 2 + 1 REMPI (resonance-enhanced multiphoton ionization). The laser light is linearly polarized with the polarization plane parallel to the position sensitive detector. The laser pulses are repeated at the frequency of 10 Hz with a pulse duration of 5 ns.

The interaction point of the laser with molecular beam is in the center of the electrostatic lens system which extracts the ionic photoproducts toward a position sensitive detector. The design of the ion lens system approximately follows the original velocity map imaging setup of Eppink and Parker.[41] The detector consists of two multichannel plates in chevron configuration and the phosphor screen. The detector can be operated either in a continuous mode when all ion masses are detected, or gated mode when a short voltage pulse is applied to the front plate and the detector is active only during this pulse. The phosphor screen is followed by a glass window and the outside-of-vacuum 8 bit gray scale CCD camera. The camera shutter is opened typically for 400 ms, and then the accumulated image is transferred to the computer. Simultaneously, the rear side of the second multichannel plate is capacitively coupled to an oscilloscope and TOF mass spectra can be recorded.

After the acquisition, the center of the image is found based on symmetry considerations and the inverse Abel transform (using the Hankel method[3]) is performed. The kinetic energy distribution is obtained from the Abel-inverted image as described in Ref. 3.

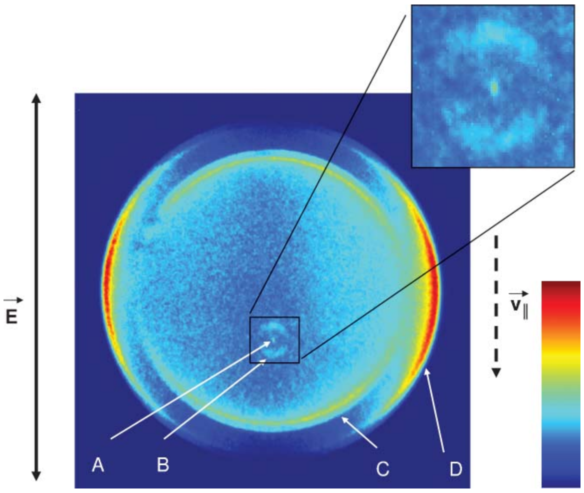

FIG. 1. Raw image of all photofragments in the expansion of 5% HBr in argon with stagnation pressure of 1.5 bar (nonclustering conditions). The detector was not gated therefore all ions are detected. The direction of laser polarization is depicted on the left side, the direction of the molecular beam on the right. The marked features are identified as (A) HBr^+, (B) Br^+, (C) and (D) H^+.

III. EXPERIMENTAL RESULTS

A. HBr photodissociation and molecular beam characterization

In Fig. 1 we present a raw data image of all ions formed after the photodissociation and photoionization of HBr molecule. We used the mixture of 5% HBr seeded in Ar (1.5 bar stagnation pressure). The detector was not gated and therefore there are also other nonresonantly ionized fragments visible. They were identified based on their flight times and are characterized by the distinct features in the image. The feature (A) corresponds to a nonresonantly ionized parent ion HBr^+, the other features belong to ionized products of photodissociation $HBr + \hbar\omega \rightarrow H + Br$: (B) to nonresonantly ionized Br atoms and (C) and (D) to 2 + 1 REMPI ionized hydrogen atoms. The different arrival times of the fragments (0.89 μs for hydrogen and 7.9 μs for heavier fragments HBr and Br) are reflected in the different centers of the individual features—all fragments have approximately the same initial velocities in the direction of the molecular beam ($\vec{v}_{\parallel}$) but due to the different flight times they travel different distances in the detector plane. HBr^+ image shows no kinetic energy release and its shape reflects the velocity spread of the molecular beam.[42] Thus it can be used to extract the molecular beam velocity distribution in both longitudinal and perpendicular directions, which in turn provides information on the nozzle expansion.

As known from the previous studies, photodissociation of HBr at 243 nm occurs predominantly via excitation to three electronic states $^1\Pi_1$, $^3\Pi_1$, and $^3\Pi_0$.[43] The $^1\Pi_1$ and $^3\Pi_1$ states correlate with the ground state asymptotic limit $H + Br(^2P_{3/2})$. The available excess energy is 1.357 eV, and this transition has a perpendicular character (D in Fig. 1). The $^3\Pi_0$ excited HBr state correlates with the asymptotic limit

H + Br*($^2P_{1/2}$) yielding 0.882 eV excess energy. We have used the two H$^+$ rings for the kinetic energy scale calibration. The calibration shows that the Br$^+$ ring (B) originates from the dissociation to the excited Br* asymptotic state. This is confirmed by the fact that both features (B) and (C) exhibit the same parallel character that is associated with the initial excitation to the $^3\Pi_0$ state.

From the diameter of the H$^+$ rings and the time-of-flight of the H$^+$ ions the calibration of velocities in the plane perpendicular to the detector can be done. The HBr$^+$ feature offset with respect to the center of the H$^+$ rings corresponds to the parallel velocity $v_\parallel$ of neutral HBr molecules in the beam. The length of the HBr$^+$ image reflects the velocity spread of the beam $\Delta v_\parallel$ (FWHM of the velocity distribution). A commonly used characteristics of an expansion is the speed ratio $S_\parallel$ which can be determined experimentally as $S_\parallel = 1.66 \times v_\parallel/\Delta v_\parallel$. The translational temperature $T_\parallel$ is related to the speed ratio as

$$T_\parallel = T_0\left(1 + \frac{\gamma - 1}{\gamma}S^2\right)^{-1}, \tag{1}$$

with $T_0 = 295$ K being the stagnation temperature and γ is the ratio of the gas specific heats (adiabatic index $\gamma = 5/3$ for an ideal monoatomic buffer gas).[44]

Table I summarizes the beam characteristics extracted from images for expansion of 1% HBr in helium, argon, and xenon buffer gas at the stagnation pressure of 1.5 bar. The terminal velocity in a supersonic expansion can be calculated as[44]

$$v_\infty = \sqrt{\frac{2k_BT_0}{m}\frac{\gamma}{\gamma - 1}}. \tag{2}$$

Here k_B is the Boltzmann constant, and $m = Cm_X + (1 - C)m_B$, where C is the concentration of the molecules X of mass m_X in the buffer gas of mass m_B. Despite the limited applicability of this ideal gas model,[45,46] the measured beam velocities usually agree very well with the calculated terminal velocities (within ≤10%), which is also the case of the present values.

The beam velocity $v_\parallel$ should be independent of the stagnation pressure according to Eq. (2). In argon and xenon, the beam velocity and the speed ratio changed only slightly with the stagnation pressure, while these parameters were a very sensitive function of the stagnation pressure in helium. This evidence suggests an incomplete cooling during the expansion in helium with our nozzle, which is also consistent with the relatively small speed ratio $S \approx 11$. Extremely high speed ratios $S \gg 100$ can be achieved in high pressure and low temperature helium expansions.[47]

TABLE I. Parameters of the molecular beam for various buffer gases. In all cases, the concentration of HBr in the mixture was 1% and the stagnation pressure was 1.5 bar. The perpendicular beam characteristics $\Delta v_\perp$, $S_\perp$ ($S_\perp = 1.66 \times v_\parallel/\Delta v_\perp$), and $T_\perp$ characterize the strong velocity anisotropy recognizable directly in the raw images by the narrow oval shape of the feature (A) (Ref. 44).

Buffer gas	v_∞ (ms^{-1})	$v_\parallel$ (ms^{-1})	$\Delta v_\parallel$ (ms^{-1})	$\Delta v_\perp$ (ms^{-1})	$S_\parallel$	$S_\perp$	$T_\parallel$ (K)	$T_\perp$ (K)
Helium	1606	1501	227	86.6	11.06	28.8	6.1	0.9
Argon	551	590	40	24	24.5	40	1.2	0.47
Xenon	307	340	48	32	11.8	18.2	5.3	2.24

B. Cluster formation

Adiabatic expansion of gas can lead to cluster formation under certain expansion conditions. Helium due to its low mass and weak interactions is often exploited in expansions when clustering should be inhibited.[48] Indeed, in the present experiments no indication for clustering has been observed in helium under all exploited conditions: stagnation pressure between 0.5 and 2.5 bars, HBr concentration from 1% to 10%. The main features (C) and (D) from Fig. 1 corresponding to the H-fragments from the bare HBr molecule photodissociation remained essentially unchanged. However, the images looked very different for a certain range of experimental conditions in argon and xenon buffer gas.

The results for the expansion of 1% HBr mixture in xenon are shown in Fig. 2. The top panel shows the dependence of the H$^+$ time-of-flight peak intensity on the delay $\Delta\tau_D$ between the start of the nozzle opening current pulse and the laser pulse. There is a pronounced plateau in the gas pulse demonstrating that the nozzle is fully open for about 200 μs. Setting the delay $\Delta\tau_D$ to various values we can probe the molecular beam pulse at different regions. The resulting raw images for the expansion of 1% HBr mixture in xenon taken at the different delays $\Delta\tau_D$ (a)–(d) are shown in Fig. 2. The multichannel plate was gated so that only H$^+$ ions were detected.

The images differ dramatically when probing the molecular beam pulse in different regions. At the rising edge (a) the image closely resembles the image from photodissociation of an isolated HBr molecule. The images with the nozzle fully opened (b) and (c) are dominated by a "blob" in the center of the image. The stronger of the fast fragment peaks [H + Br($^2P_{3/2}$)] is also visible, however, the molecular features are barely discernible when the central peak should not be saturated. At the decreasing edge of the molecular beam (d) the central feature is weaker, the fast fragments are more visible and an additional weak ring appears with kinetic energy of 1.64 eV, i.e., by 0.3 eV higher than the H + Br($^2P_{3/2}$) ring. The central feature has a darker spot in the center on all images where the blob appears.

Figure 3 shows H$^+$ velocity map images taken in the expansion of 1% HBr mixture with argon at two different regions of the molecular pulse: at the rising edge (a) and in the center of the pulse (b). The stagnation pressure was 2.5 bar, since in argon expansions the additional features in the image appeared only at the higher stagnation pressures. In the center of the molecular beam pulse, the central blob and the additional ring with the kinetic energy of ≈1.64 eV appear again. In this case the central blob does not have any darker spot in the center.

The difference between the expansion in argon and xenon becomes apparent in Fig. 4(a) where the intensity profiles along the central cut (perpendicular to the beam

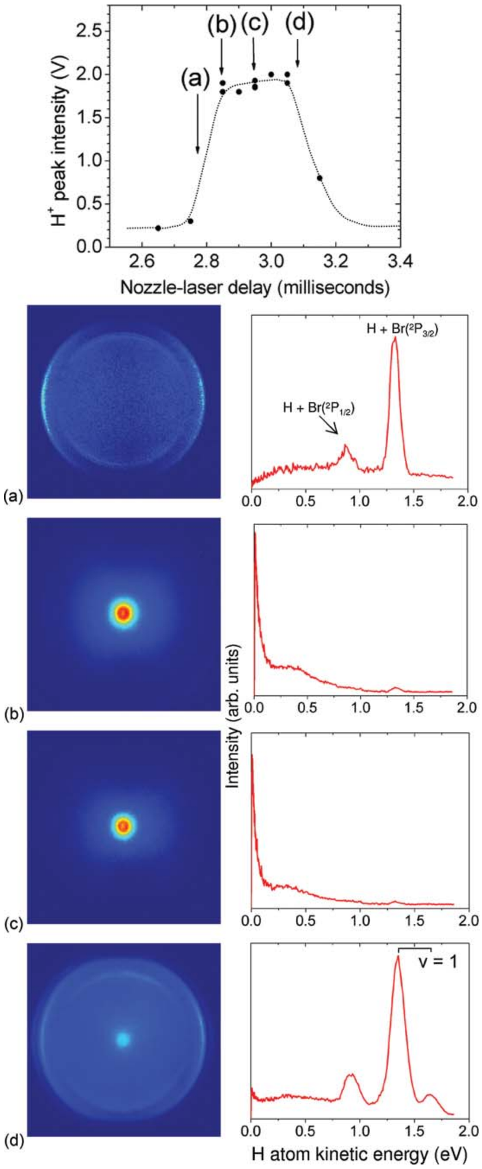

FIG. 2. (Top panel) Intensity of the H^+ signal as a function of the laser-nozzle opening trigger delay $\Delta\tau_D$ in the expansion of 1% HBr/Xe mixture at 1.5 bar. The four raw H^+ images (left column) from HBr photodissociation were taken at the denoted time delays, i.e., the light crossed the molecular pulse in different regions. The corresponding 360° integrated kinetic energy distributions are shown on the right column.

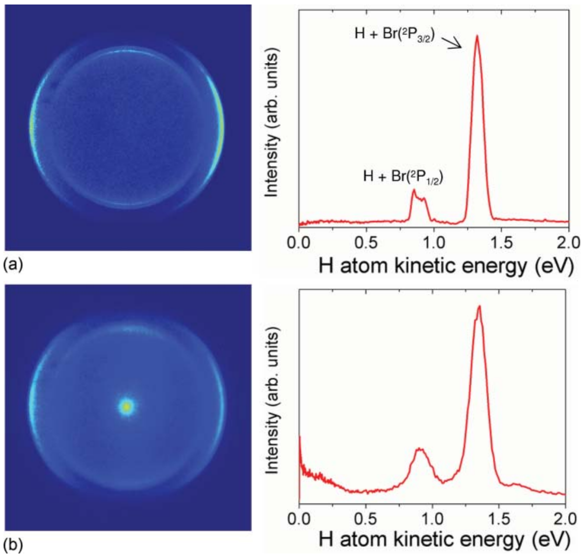

FIG. 3. Raw velocity map images and corresponding kinetic energy distribution for the expansion of 1% HBr mixture with argon buffer gas. Image (a) was taken at the rising edge of the molecular pulse, image (b) in the center. The stagnation pressure was 2.5 bar.

velocity) through the images are shown. The lower intensity at the central spot is certainly not due to an imperfection on the detector, since it appears only in the case of the HBr/Xe expansion while there is a maximum in the center in HBr/Ar expansion. A possible experimental artifact leading to such effect could be a space charge generated in the laser focus, which would remove the slowest ions from the spectra by accelerating them. The dependence on the laser intensity was measured, however, the darker central spot was still visible even at the lowest laser intensity. Therefore, we exclude the space charge as a possible cause of this effect. The central darker spot shifts the maximum of the H^+ KED by approximately 0.01 eV toward higher energies in HBr/Xe expansion when compared to HBr/Ar [Fig. 4(b)].

IV. DISCUSSION

We interpret the dramatic change of the photofragment image throughout the gas pulse duration to be due to the clustering in the beam. At the rising and falling edges of the molecular pulse, the nozzle is not fully opened and the cooling in the expansion is insufficient to cause a significant clustering. The dependence of expansion temperature on time during the nozzle opening in pulsed expansions is known from spectroscopy,[49] the measured rotational temperatures deviate significantly in the middle of the pulse and on its

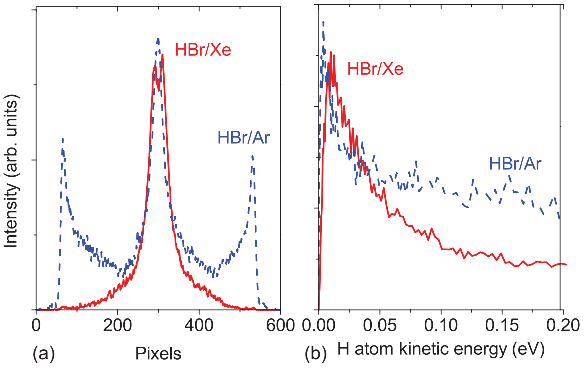

FIG. 4. (a) Intensity profiles along the central cut (perpendicular to the beam velocity) through the images in Fig. 2(b) (Xe expansion, solid line) and in Fig. 3(b) (Ar expansion, dashed line). The profiles were scaled to the same maximum. (b) Low kinetic energy part of the corresponding kinetic energy distributions.

edges. Similarly, variations of speed ratio were measured in short pulses by the imaging technique.[42] Thus in the middle of the pulse when the nozzle is fully opened, the cooling is most effective and also the cluster formation can set on. There are two prominent features in our images in the clustering regime (i) the central feature and (ii) the appearance of the additional outer ring.

The central "blob" is caused by the *cage effect*: The H-fragment after HBr molecule photodissociation in a cluster can loose almost entire kinetic energy in collisions with cluster constituents. It can then either recombine with the bromine to form the HBr molecule or, since the cluster disintegrates during the photodissociation process, the caged atom can remain isolated with the near zero kinetic energy and can be extracted for detection which results in the central peak (see also Ref. 8 and references therein).

The outermost ring appearing in images 2(d) and 3(b) corresponds to the kinetic energy of 1.64 eV, i.e., 0.3 eV above the H + Br($^2P_{3/2}$) channel. The vibrational spacing of the HBr ($X^1\Sigma^+$) ground electronic state is 0.328 eV,[50] thus this ring most probably originates from the photodissociation HBr($v=1$) + $\hbar\omega \rightarrow$ H + Br($^2P_{3/2}$). The origin of the vibrationally excited HBr can be again the cage effect: the caged H-fragment recombines with the bromine to recreate the HBr molecule in a vibrationally excited state. Before the collisional relaxation to the ground ($v=0$) state can takes place, the molecule can absorb another UV photon and release the "superhot" H atom. We have detailed this mechanism in the recent study of acetylene photodissociation in clusters.[51]

Pronounced features corresponding to the "hot" H-fragments were also observed previously in the photodissociation of HBr in $(\mathrm{HBr})_n$ clusters,[32] and on the surface and inside argon clusters.[37] Alternative explanation was proposed: if there are several HBr molecules present in the cluster, the hydrogen fragment from one photodissociated molecule can hit and vibrationally excite second HBr molecule which then absorbs a photon to dissociate and yield the "hot" H-fragment. Both scenarios are energetically possible for $(\mathrm{HBr})_n$. However, in the above mentioned case of acetylene[51] the escaping hydrogen does not have enough kinetic energy to vibrationally excite another acetylene molecule. Thus, only the first scenario—the recombination with the caged atom—is possible in the acetylene case. We propose the caging and recombination to be the source of vibrationally hot HBr molecules also in the present case, because the majority of the present clusters are of the $\mathrm{HBr}\cdot\mathrm{Rg}_n$ character, i.e., large rare gas clusters with only one HBr molecule inside, as argued below.

The occurrence of the large rare gas clusters under our conditions can be expected from the expansion parameters. The clustering in the rare gas expansions was investigated in a great detail and empirical formulas have been derived[52–55] to determine the mean cluster size $\bar{n}$ in dependence on the stagnation pressure p_0 and temperature T_0 and the nozzle shape and diameter d_e:

$$\bar{n} = K\left(\frac{\Gamma^*}{1000}\right)^{\zeta}, \qquad (3)$$

where $K = 38.4$ and $\zeta = 1.64$ apply for rare gas clusters.[55] The dimensionless parameter Γ^* introduced by Hagena[53] allows to compare various expansions independent of nozzle and gas parameters (Hagena's scaling law):

$$\Gamma^* = \frac{p_0[\mathrm{mbar}] \times d_e[\mu\mathrm{m}]^{0.85}}{T_0[K]^{2.2875}} K_c, \qquad (4)$$

where K_c is characteristic constant of the expanding gas (e.g., $K_c = 1646$ and 5554 $\mathrm{K}^{2.2875}\mathrm{mbar}^{-1}\mu\mathrm{m}^{-0.85}$ for Ar and Xe, respectively). The following classification of expansions according to the Γ^* parameter has been proposed: $\Gamma^* \leq 200 \Rightarrow$ no clustering; $200 \leq \Gamma^* \leq 1000 \Rightarrow$ beginning clustering; $1000 \leq \Gamma^* \Rightarrow$ strong clustering resulting in $\bar{n} \gtrsim 100$. In the present case $\Gamma^* \approx 2150$ and 4290 for Ar and Xe, respectively. Therefore, strong clustering can be expected in both cases resulting in the following mean cluster sizes according to the formula (3): $\bar{n} = 131$ for Ar at 2.5 bar, and $\bar{n} = 418$ for Xe at 1.5 bar. The use of the above formula for the pulsed expansions might be limited by the mechanical effects of the nozzle opening, which can influence the expansion and consequently the cluster building. Also the seeding of even a small HBr amount ($\approx$1%) into the rare gas can change the expansion conditions. Thus we can assume $\bar{n}$ to be somewhat smaller than the above numbers following from Eq. (3) for pure rare gas expansions, yet it is probably still of the order of $\sim$10–10^2.

One experimental evidence hinting toward the $\mathrm{HBr}\cdot\mathrm{Rg}_n$ composition of the observed clusters is the dependence of the clustering on the HBr concentration in the mixture with carrier. For both argon and xenon, the clustering appeared only for diluted mixtures $\lesssim$1%. For the higher HBr concentrations (up to 10%) no evidence for cluster formation was observed and only images corresponding to the bare HBr molecules were observed at all exploited expansion pressures ($\sim$0.5 –3.0 bar).

The experience from experiments on our other apparatus, where we use continuous expansions through conical nozzles, suggests that at concentrations $\leq$1% large Ar clusters with HBr molecules embedded inside the "rare-gas snowball" are generated.[35,37] On the other hand, pure $(\mathrm{HBr})_n$ clusters, $n \approx$2–10, with no Ar atoms attached are generated at higher concentrations $\sim$5%.[33] The present measurements show that the situation in our pulsed nozzle is different, since no central feature was observed in the images at the higher concentrations. The previous TOF spectra of both $(\mathrm{HBr})_n$ and $\mathrm{HBr}\cdot\mathrm{Ar}_n$ clusters exhibited the central peak.[33,35,37] Thus we can conclude that the $(\mathrm{HBr})_n$ clusters are not generated at the concentrations above $\approx$1% in the present pulsed expansions. Yet, at low concentrations and higher pressures we definitely produce clusters, which are then presumably of $\mathrm{HBr}\cdot\mathrm{Rg}_n$ nature.

Another evidence for such composition is provided by the time-of-flight photoionization mass spectra. Figure 5 shows the mass spectrum taken in the center of the molecular beam pulse upon expansion of 1% HBr mixture with xenon at the stagnation pressure of 1 bar (middle trace). The wavelength of the laser was lowered by approximately 0.1 nm from the H atom REMPI wavelength in order to prevent the domination of the H^+ peak in the mass spectrum, thus all the species are ionized via nonresonant multiphoton processes. One can clearly see the progression of the Xe_n^+ fragment ions and

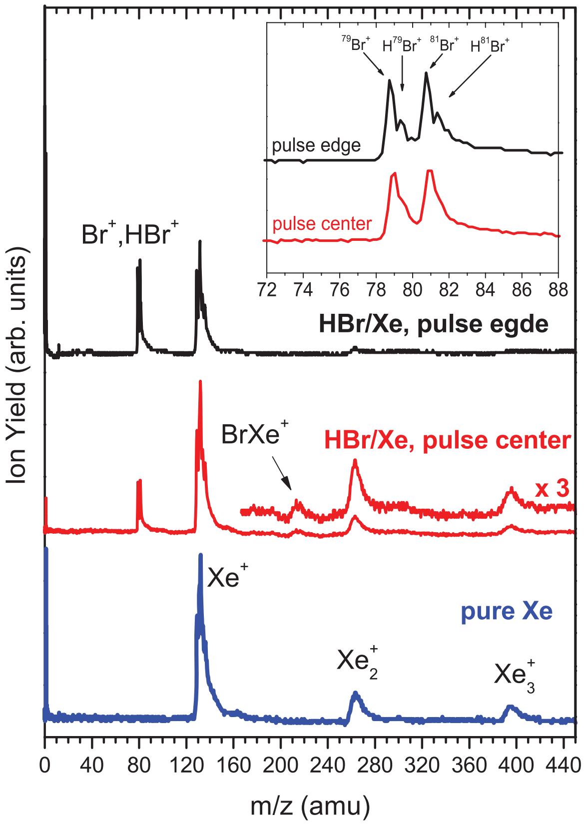

FIG. 5. Photoionization time-of-flight mass spectra. Expansion of 1% HBr mixture in xenon probed at the pulse edge (upper trace) and in the pulse center (middle trace); and expansion of pure xenon (bottom trace). Spectra were measured with stagnation pressure of 1 bar. (Inset) The detail HBr$^+$ peak for the mass spectrum taken in the center of the pulse (clustering conditions) and on the rising edge (no clustering).

mixed dimer ion BrXe$^+$. No evidence for the fragments of the larger (HBr)$_n$ clusters, i.e., (HBr)$_k^+$ or (HBr)$_k$H$^+$, $k \geq 2$ ions, is visible in the spectrum. The inset shows the detail of HBr$^+$ peaks measured in the clustering regime (center of the molecular pulse) and in the molecular beam (rising edge of the pulse). No evidence of (HBr)H$^+$, which is present in the mass spectrum of (HBr)$_n$ clusters,[33] is visible. The Xe$_n^+$ peak progression can also be seen in the expansion of pure Xe gas (bottom trace). We have shown in several recent studies that an extensive fragmentation occurs upon nonresonant multiphoton ionization of clusters due to the dynamical effects.[19,56] The presence of Xe$_n^+$ cluster ion fragments in the present spectra suggests fragmentation of species containing substantially more than ten xenon atoms. This progression disappears when the molecular pulse is probed in its decreasing or increasing edge and the mass spectrum is dominated by HBr$^+$ and Xe$^+$ peaks (top trace in Fig. 5).

The difference between the HBr/Ar and HBr/Xe images also supports the conclusion that we produce HBr·Rg$_n$ species rather than pure HBr$_n$ clusters. The intensity dip in the image center suggests that the near zero velocity fragments are generated only in Ar but not in Xe clusters. One possible reason could be the mass of the cluster constituents. The energy transfer per collision decreases with increasing collision partner mass. A simple estimate assuming central encounters yields $\Delta E/E = 4\times m_{\mathrm{H}}/m_{\mathrm{Rg}}$, i.e., $\Delta E/E = 0.03$ for Xe and 0.10 for Ar. Baumfalk *et al.*[8,36] invoked this effect to explain the photodissociation of single HBr molecule deposited on the surface of large rare gas clusters. They found that while for argon clusters the kinetic energy distribution (KED) peaks at 0 eV, for xenon clusters it peaks around 0.4 eV. This value is much larger than the present shift of about 0.01 eV, which is consistent with the fact, that the H atom undergoes statistically more collisions when the HBr molecule is not on the cluster surface but rather in its center.

An alternative explanation for the dip in intensity in the middle of images with Xe can be a mechanism which removes selectively the near zero velocity fragments in Xe but not in Ar clusters. One possibility is the trapping of zero energy hydrogens by Xe atoms to generate a XeH complex, which is not resonantly ionized to yield H$^+$. The capture cross section for H atom will be larger in xenon and the XeH complex is more stable than the ArH counterpart.[57] A similar process has been observed in our previous cluster studies of Xe-hydrides.[14,58] Still, if the slow neutral H atom is not captured but rather ionized, the nascent H$^+$ ion can react with the rare gas atoms within the decaying cluster to yield RgH$^+$ (or Rg$_k$H$^+$) ions. Again, the reaction cross section is larger in Xe than in Ar.[59]

Another possibility for the selective removal of slow H$^+$ atoms in xenon can be a quenching of H(2s) intermediate state in the (2 + 1) REMPI process by xenon atoms. The (5p^{5}5d) excited state of xenon lies at 10.2 eV (81 926 cm^{-1}) (Ref. 60) close to the H(2s) excitation (82 259 cm^{-1}), while there is no such closely lying state in Ar. If the resonant absorption of the first two photons by hydrogen occurs still in the vicinity of the rare gas atoms (which is the case for the very slow hydrogen fragments), the xenon atoms could effectively quench the population of the H(2s) state.

The present experimental evidence does not provide enough information to decide which of the above-mentioned processes is dominant in causing the difference between the images in Ar and Xe clusters. Therefore, we present the various hypothesis to stimulate further research in this direction.

V. CONCLUSIONS

We have investigated the coexpansion of HBr with three different buffer gases through a pulsed nozzle using a velocity map imaging technique. The orthogonal arrangement of our experiment enabled us to characterize the velocity distribution of the neutral molecules in the molecular beam. Via changing the delay between the nozzle opening and the laser pulse we were able to probe different regions of the molecular beam pulse. In the rising and falling edge of the pulse the beam was mostly molecular. With the nozzle fully opened cluster formation sets on and has been identified via distinct features in the H$^+$ images—a central maximum due to photofragment caging and an additional outer ring due to photodissociation of vibrationally excited HBr molecules, which were also produced by caging and recombination of the fragments in clusters.

The nature of the clusters produced in such expansions is close to a single HBr molecule embedded in the large rare gas cluster. This conclusion is supported by (i) the difference in the low kinetic energy region for expansion in argon and xenon, (ii) the dependence of cluster formation on HBr concentration in the expanding mixture, and (iii) the photoionization time-of-flight ion mass spectra.

In the view of the present discussion it also becomes apparent that care has to be taken when interpreting new features in images taken in expansions of heavier rare gases. A strong clustering can occur in these expansions. One way of avoiding this effect in pulsed expansions is shortening the pulse by not fully opening the nozzle. When cluster formation occurs careful analysis of their size and composition is needed.

ACKNOWLEDGMENTS

This work has been supported by the Grant Agency of the Czech Republic Project No. 203/09/0422. J. Fedor acknowledges the support of the Grant No. 235414 "IPhoN" within FP7-MC-IEF. The work has also been supported by FP7-MC-ITN project No. 238671 "ICONIC."

[1] D. W. Chandler and P. L. Houston, J. Chem. Phys. **87**, 1445 (1987).
[2] C. R. Gebhardt, T. P. Rakitzis, P. C. Samartzis, V. Ladopoulos, and T. N. Kitsopoulos, Rev. Sci. Instrum. **72**, 3848 (2001).
[3] B. Whitaker, *Imaging in Molecular Dynamics* (Cambridge University Press, Cambridge, 2003).
[4] D. Townsend, M. P. Minitti, and A. G. Suits, Rev. Sci. Instrum. **74**, 2530 (2003).
[5] J. J. Lin, J. G. Zhou, W. C. Shiu, and K. P. Liu, Rev. Sci. Instrum. **74**, 2495 (2003).
[6] V. Papadakis and T. N. Kitsopoulos, Rev. Sci. Instrum. **77**, 083101 (2006).
[7] C. Huang, S. A. Lahankar, M. H. Kim, B. Zhang, and A. G. Suits, Phys. Chem. Chem. Phys. **8**, 4652 (2006).
[8] U. Buck, J. Phys. Chem. A **106**, 10049 (2002).
[9] N. H. Nahler, R. Baumfalk, U. Buck, H. Vach, P. Slavíček, and P. Jungwirth, Phys. Chem. Chem. Phys. **5**, 3394 (2003).
[10] P. Slavíček, P. Jungwirth, M. Lewerenz, N. H. Nahler, M. Fárník, and U. Buck, J. Phys. Chem. A **107**, 7743 (2003).
[11] N. H. Nahler, M. Fárník, U. Buck, H. Vach, and R. B. Gerber, J. Chem. Phys. **121**, 1293 (2004).
[12] P. Slavíček, P. Jungwirth, M. Lewerenz, N. H. Nahler, M. Fárník, and U. Buck, J. Chem. Phys. **120**, 4498 (2004).
[13] M. Fárník, N. H. Nahler, U. Buck, P. Slavíček, and P. Jungwirth, Chem. Phys. **315**, 161 (2005).
[14] U. Buck and M. Fárník, Int. Rev. Phys. Chem. **25**, 583 (2006).
[15] V. Poterya, M. Fárník, P. Slavíček, U. Buck, and V. V. Kresin, J. Chem. Phys. **126**, 071101 (2007).
[16] M. Ončák, P. Slavíček, V. Poterya, M. Fárník, and U. Buck, J. Phys. Chem. A **112**, 5344 (2008).
[17] V. Poterya, J. Fedor, A. Pysanenko, O. Tkáč, J. Lengyel, M. Ončák, P. Slavíček, and M. Fárník, Phys. Chem. Chem. Phys. **13**, 2250 (2011).
[18] V. Poterya, V. Profant, M. Fárník, P. Slavíček, and U. Buck, J. Chem. Phys. **127**, 064307 (2007).
[19] V. Poterya, V. Profant, M. Fárník, L. Šištík, P. Slavíček, and U. Buck, J. Phys. Chem. A **113**, 14583 (2009).
[20] K. V. Vidma, A. V. Baklanov, E. B. Khvorostov, V. N. Ishchenko, S. A. Kochubei, A. T. J. B. Eppink, D. A. Chestakov, and D. H. Parker, J. Chem. Phys. **122**, 204301 (2005).
[21] K. V. Vidma, D. H. Parker, G. A. Bogdanchikov, A. V. Baklanov, and S. A. Kochubei, J. Phys. Chem. A **114**, 3067 (2010).
[22] X.-P. Zhang, W.-B. Lee, D.-F. Zhao, M.-K. Hsiao, Y.-L. Chen, and K.-C. Lin, J. Chem. Phys. **130**, 214305 (2009).
[23] L. Rubio-Lago, D. Zaouris, Y. Sakellariou, D. Sofikitis, T. N.Kitsopoulos, F. Wang, X. Yang, B. Cronin, A. L. Devine, G. A. King, M. G. D. Nix, N. M. R. Ashfold, and S. S. Xantheas, J. Chem. Phys. **127**, 064306 (2007).
[24] L. Rubio-Lago, G. A. Amaral, A. N. Oldani, J. D. Rodríguez, M. G. Gonzáles, G. A. Pino, and L. Bañares, Phys. Chem. Chem. Phys. **13**, 1082 (2011).
[25] N. R. Cheong, H. S. Park, S. H. Nam, S. K. Shin, S. G. Cho, H. W. Lee, J. K. Song, and S. M. Park, Bull. Korean Chem. Soc. **30**, 2661 (2009).
[26] B. Baguenard, J. C. Pinaré, C. Bordas, M. Broyer, Phys. Rev. A **63**, 023204 (2001).
[27] C. Bartels, C. Hock, J. Huwer, R. Kuhnen, J. Schwöbel, B. von Issendorff, Science **323**, 1323 (2009).
[28] M. Kjellberg, O. Johansson, F. Jonsson, A. V. Bulgakov, C. Bordas, E. E.B. Campbell, K. Hansen, Phys. Rev. A **81**, 023202 (2010).
[29] A. Masson, L. Poisson, M.-A. Gaveau, B. Soep, J.-M. Mestdagh, V. Mazet, and F. Spiegelman, J. Chem. Phys. **133**, 054307 (2010).
[30] S. R. Langford, P. M. Regan, A. J. Orr-Ewing, and M. N. R. Ashfold, Chem. Phys. **231**, 245 (1998).
[31] P. M. Regan, S. R. Langford, A. J. Orr-Ewing, and M. N. R. Ashfold, J. Chem. Phys. **110**, 281 (1999).
[32] R. Baumfalk, U. Buck, C. Frischkorn, N. H. Nahler, and L. Hüwel, J. Chem. Phys. **111**, 2595 (1999).
[33] R. Baumfalk, U. Buck, C. Frischkorn, S. R. Gandhi, and C. Lauenstein, Ber. Bunsenges. Phys. Chem. **101**, 606 (1997).
[34] R. Baumfalk, U. Buck, C. Frischkorn, S. R. Gandhi, and C. Lauenstein, Chem. Phys. Lett. **269**, 321 (1997).
[35] R. Baumfalk, N. H. Nahler, U. Buck, M. Y. Niv, and R. B. Gerber, J. Chem. Phys. **113**, 329 (2000).
[36] R. Baumfalk, N. H. Nahler, and U. Buck, Faraday Discuss. **118**, 247 (2001).
[37] R. Baumfalk, N. H. Nahler, and U. Buck, Phys. Chem. Chem. Phys. **3**, 2372 (2001).
[38] T. P. Rakitzis, P. C. Samartzis, R. L. Toomes, L. Tsigiridas, M. Coriou, D. Chestakov, A. T. J. B. Eppink, D. H. Parker, and T. N. Kitsopoulos, Chem. Phys. Lett. **364**, 115 (2002).
[39] T. P. Rakitzis, P. C. Samartzis, R. L. Toomes, and T. N. Kitsopoulos, J. Chem. Phys. **121**, 7222 (2004).
[40] See supplementary material at http://dx.doi.org/10.1063/1.3578610 for a detailed description of the experimental setup.
[41] A. T. J. B. Eppink and D. H. Parker, Rev. Sci. Instrum. **68**, 3477 (1997).
[42] D. Irimia, R. Kortekaas, and M. H. M. Janssen, Phys. Chem. Chem. Phys. **11**, 3958 (2009).
[43] A. Smolin, O. Vasyutinskii, G. Balint-Kurti, and A. Brown, J. Phys. Chem. A **110**, 5371 (2006).
[44] H. Pauly, *Atom, Molecule and Cluster Beams* (Springer, Berlin, 2000).
[45] W. Christen and K. Rademann, Phys. Rev. A **77**, 012702 (2008).
[46] W. Christen, K. Rademann, and U. Even, J. Phys. Chem. A **114**, 11189 (2010).
[47] M. Hillenkamp, S. Keinan, and U. Even, J. Chem. Phys. **118**, 8699 (2003).
[48] The obvious exception is the vast field of helium nanodroplets research, where large He$_n$, $\bar{n} \gtrsim 10^3$, clusters are generated in low temperature (typically $\lesssim$20 K) high pressure (typically $\gtrsim$ 10 bar) expansions.
[49] H. W. Lülf and P. Andersen, in *Rarefied Gas Dynamics*, edited by O. M. Belotserkovskii, M. N. Kogan, S. S. Kutateladse, and A. K. Rebrov (Plenum, New York, 1985), p. 911.
[50] D. H. Rank, U. Fink, and T. A. Wiggins, **18**, 170 (1965).
[51] M. Fárník, V. Poterya, O. Votava, M. Ončák, P. Slavíček, I. Dauster, and U. Buck, J. Phys. Chem. A **113**, 7322 (2009).
[52] O. F. Hagena, Surf. Sci. **106**, 101 (1981).
[53] O. F. Hagena, Z. Phys. D: At., Mol. Clusters **4**, 291 (1987).
[54] O. F. Hagena, Rev. Sci. Instrum. **63**, 2374 (1992).
[55] U. Buck and R. Krohne, J. Chem. Phys. **105**, 5408 (1996).
[56] V. Poterya, O. Tkáč, J. Fedor, M. Fárník, P. Slavíček, and U. Buck, Int. J. Mass Spectrom. **2010**, 85 (2010).
[57] T. Kiljunen, J. Eloranta, and H. Kunttu, J. Chem. Phys. **110**, 11814 (1999).
[58] V. Poterya, O. Votava, M. Fárník, M. Ončák, P. Slavíček, U. Buck, and B. Friedrich, J. Chem. Phys. **128**, 104313 (2008).
[59] J. Lundell, J. Mol. Struct. **355**, 291 (1995).
[60] Y. Ralchenko, A. E. Kramida, R. J., and NIST ASD Team (2010), in *NIST Atomic Spectra Database (version 4.0.1)* (National Institute of standards and Technology, Gaithersburg, MD, 2011). Available: http://physics.nist.gov/asd.

PCCP

PAPER

Cite this: *Phys. Chem. Chem. Phys.*, 2014, **16**, 421

Caging of Cl atoms from photodissociation of CF_2Cl_2 in clusters

Viktoriya Poterya,*[a] Jaroslav Kočišek,[ab] Andriy Pysanenko[a] and Michal Fárník*[a]

Received 7th May 2013,
Accepted 20th June 2013

DOI: 10.1039/c3cp51926k

www.rsc.org/pccp

We investigate the photodissociation dynamics of freon CF_2Cl_2 by velocity map imaging at 193 nm. The Cl fragment images are recorded in various expansion regimes corresponding to isolated molecules and molecules in rare gas clusters. The molecular kinetic energy distributions are dominated by a peak at $E_{\mathrm{kin}}(\mathrm{Cl}) \approx 0.97$ eV corresponding to the direct C–Cl bond dissociation but they also reveal features at lower kinetic energies. Possible mechanisms leading to these slow Cl atoms are discussed. The photodissociation in clusters is investigated in two regimes: (i) small Ar clusters with the CF_2Cl_2 molecule embedded in approximately one solvation Ar layer; (ii) large Xe_n, $\bar{n} \approx 100$–500, clusters with embedded CF_2Cl_2 molecules. In the former clusters we observe *caging* yielding the Cl fragments with zero kinetic energy and *direct exit* resulting in fragments with the kinetic energies corresponding to the fragments from isolated molecules. In the latter case (ii) only the caged Cl fragments are observed.

1 Introduction

Since the discovery of the atmospheric ozone hole the chlorofluorocarbon compounds (CFCs or so called ''freons'') have been recognised as one of the major threats to our protective ozone layer.[1–4] The freons are not reactive and not soluble in water and therefore they have long atmospheric residence time and diffuse into the stratosphere where they are photolyzed by UV radiation and the released Cl atoms play a crucial role in the catalytic decomposition of stratospheric ozone. Other key players in these processes are ice particles in polar stratospheric clouds (PSCs). Thus the photochemistry which involves not only the CFC in the gas phase but is also influenced by the environment of the PSC particles needs to be investigated to elucidate the complex process of ozone depletion. In our present paper we investigate the detailed photodissociation dynamics of one of the major freons CF_2Cl_2, and we focus on the question: ''how does the solvation of this molecule in clusters affect the photodissociation dynamics?''

Following the early photodissociation studies,[5–7] the Cl photofragment kinetic energy from CF_2Cl_2 was measured by the time-of-flight (TOF) technique.[8,9] Some inconsistencies can be found between these earlier works: Baum and Huber[8] observed exclusively the $CF_2Cl + Cl$ decay channel at 193.3 nm (6.41 eV) with the total kinetic energy release (TKER) of 1.475 eV. On the other hand, Yen *et al.*[9] reported two other channels resulting in slower fragments (TKER $\approx$ 0.53 eV and 0.12 eV) in addition to the fast Cl fragments (TKER $\approx$ 1.63 eV) at the photodissociation wavelength of 187 nm (6.63 eV). The lowest energy channel was tentatively assigned to the secondary dissociation of the CF_2Cl fragment, while the intermediate energy channel was suggested to belong to the primary dissociation into an excited CF_2Cl^* radical state and an alternative explanation involving concerted three-body dissociation $CF_2 + 2Cl$ was also mentioned.

More recently, the total quantum yield for chlorine atoms from CF_2Cl_2 was measured at 193 nm $\Phi = 1.03$ which suggested that the single C–Cl bond rupture always occurs in the photolysis of CF_2Cl_2.[10] The authors supported their conclusion by agreement with the above mentioned work of Baum and Huber[8] where the components due to the dissociation producing two Cl-atoms were not detected. However, they ignored the study of Yen *et al.*[9] mentioned above which reported the two slow fragment channels. Besides, they mentioned discrepancy with the earlier measurements[5] where formation of two Cl atoms was inferred to occur increasingly as the photolysis wavelength became shorter below 230 nm.

Here we present the photodissociation study of free CF_2Cl_2 molecules in the gas phase, and molecules embedded in Ar and Xe clusters. We adopted a similar approach as in our previous studies of hydrogen halides photodissociation in clusters: first, these processes were studied in rare gas clusters[11–15] to understand the details of the interaction with archetypal non-reacting solvents–rare gas atoms; subsequently the study was extended to atmospherically relevant water clusters.[16–19] Here we

---

[a] J. Heyrovský Institute of Physical Chemistry v.v.i., Academy of Sciences of the Czech Republic, Dolejškova 3, 18223 Prague, Czech Republic. E-mail: michal.farnik@jh-inst.cas.cz, viktoriya.poterya@jh-inst.cas.cz; Fax: +420 2 8658 2307; Tel: +420 2 6605 3206

[b] Department of Surface and Plasma Science, Faculty of Mathematics and Physics, Charles University, V Holešovičkách, 18000 Prague, Czech Republic

investigate the CF_2Cl_2 photodissociation in rare gas clusters as a prerequisite to the future studies of CFC on water clusters.

While the TOF technique was used in the above mentioned studies of hydrogen halides, here we exploit the velocity map imaging (VMI) technique[20] recently introduced in our laboratory and demonstrated on HBr in the rare gas clusters.[21] It is the up-to-date method to reveal the details of the photodissociation process. This work represents the first VMI investigation of CF_2Cl_2, also revealing some details about the photodissociation of isolated molecules, and resolves some of the inconsistencies in the above mentioned studies.[8,9] The photodissociation processes of the free molecule and the molecule embedded in the rare gas clusters are directly compared.

2 Experiment

The present study was performed on Apparatus for IMaging (AIM) introduced and described in more detail in our recent publications.[21,22] The molecular beam is produced by gas expansion through a pulsed solenoid valve (General valve) with a nozzle of 0.6 mm diameter. Various expansion conditions were exploited to obtain distinct "molecular" and "cluster" regimes some of which are summarized in Table 1. Either pure CF_2Cl_2 (Messer, purity DIN 8960) or CF_2Cl_2–Rg (Rg = Ar, Xe) mixtures of various concentrations were expanded at various stagnation pressures and the different regimes were distinguished from the images as outlined in the next section.

After passing through a skimmer the molecular beam enters the interaction chamber where the molecules interact with the laser beams. The interaction point is in the center of the electrostatic lens system which extracts the ionic photoproducts towards a position sensitive detector $\approx$50 cm upwards from the interaction point. The imaging system is perpendicular to the beam axis, and the design of the ion lens system approximately follows the original velocity map imaging of Eppink and Parker.[20] The detector (two multichannel plates 56 mm in diameter in the chevron configuration and the phosphor screen) can be operated in continuous or gated mode which enables imaging of single ion mass.

In the interaction point the molecular beam is crossed with two counterpropagating laser beams: the photodissociation 193.3 nm ArF/F_2-Excimer laser, and 235.336 nm and 235.205 nm laser to ionize the Cl($^2P_{3/2}$) and Cl*($^2P_{1/2}$) using REMPI, respectively. The tunable UV radiation around 235 nm is generated by doubling the 470 nm output of the dye laser (Pulsare-S, Fine Adjustment) pumped by the third harmonics (355 nm) of the Nd:YAG laser (Spitlight 1500, Innolas). The pulsed lasers are operated at 10 Hz frequency in the nanosecond regime. The 193 nm beam is restricted by an orifice and focussed with a 500 mm lens onto a spot $\approx$17 μm in diameter in the interaction region. A thin film polarizer (TFP) selects the horizontal (90°) polarization from the unpolarized laser output. As a result the electric field vector of the radiation is parallel to the molecular beam, *i.e.* perpendicular to the imaging TOF axis. The 235 nm beam is focused into the interaction region with a 200 mm lens onto a spot $\approx$13 μm in diameter. It is also polarized parallel to the molecular beam. The photon fluxes are discussed below.

Table 1 Expansion conditions for the "molecular" and the "cluster" regime

Expanding gas concentration (%)	Stagnation pressure P_0 (bar)	Regime
CF_2Cl_2	1.6	Molecule
CF_2Cl_2–Ar (5%)	1.1	Molecule
CF_2Cl_2–Ar (5%)	1.7	Cluster
CF_2Cl_2–Xe (5%)	1.7	Cluster

The overlap of the molecular beam with the two lasers as well as the overall imaging system performance is aligned on an image of the test system which is the well studied HBr molecule.[21,22] The time overlap of the three beams is adjusted using a delay generator (BNC 575) triggered by the photoionization laser.

The images are recorded using an 8-bit greyscale CCD camera (Unibrain Fire-i 702b) with an imaging lens (25 mm, *f*/1.6), connected to the acquisition computer *via* a FireWire interface and controlled by a LabView program. Also TOF mass spectra can be recorded from the rear side of the second multichannel plate capacitively coupled to an oscilloscope. To process the images the inverse Abel transform is performed. We use the Hankel method for reconstructing the images[23] and the Iterative Inversion method[23] was also implemented to check the consistency of our results. The kinetic energy distribution (KED) of the Cl-fragment is obtained from the images, and the anisotropy parameter β is also evaluated.

3 Experimental results

3.1 Pure CF_2Cl_2 expansions: molecular case

First, we investigate the photodissociation of isolated CF_2Cl_2 molecules. These volatile molecules are not expected to cluster easily. Thus the regime where pure CF_2Cl_2 is expanded is strictly molecular. This is confirmed below by comparison with images generated in Ar expansions where regimes of both bare molecules and clusters are explored.

Fig. 1 shows an example of the raw Cl-fragment image from the CF_2Cl_2 molecule photodissociation at 193 nm. The evaluated KED is shown in Fig. 2. At first sight the spectrum is composed of the fast fragments peaking around $E_{\text{kin}}(\text{Cl}) \approx 0.97$ eV (A), and a broad slow component. Upon more detailed analysis and laser power dependence measurements (below), this slow component could be decomposed to three contributions which are indicated in Fig. 2: the major slow contribution B peaking at a low energy of $\sim$0.17 eV; and peaks B1 and B2 at around $\sim$0.39 eV and $\sim$0.56 eV, respectively. Although the contributions B1 and B2 are not resolved in Fig. 2 they are reproduced in almost all the KEDs measured under various conditions. Therefore we decompose the contribution of the slow fragments into these three components and report their parameters in Table 2. However, it cannot be excluded that just a single process or even more than the three processes contribute

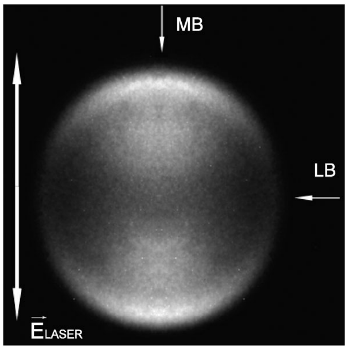

Fig. 1 Example of the Cl-fragment image from CF_2Cl_2 molecule photodissociation at 193 nm. The directions of the molecular beam (MB) dissociation laser beam (LB) and laser polarization (E_{LASER}) are indicated.

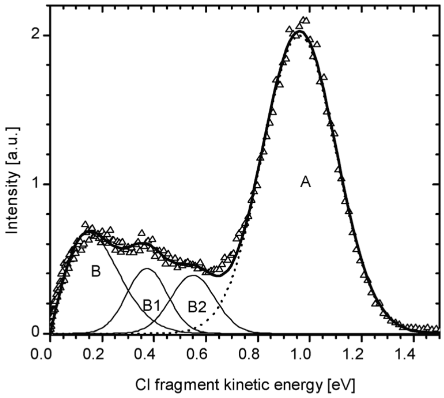

Fig. 2 KED of the Cl-fragment from CF_2Cl_2 molecule photodissociation at low 193 nm corresponding to the image in Fig. 1. The fit (line) is composed of 4 peaks A, B, B1, and B2 (see the text for details).

to the low energy part of KED. The values in Table 2 compile numerous fits to spectra obtained under different expansion conditions including CF_2Cl_2–Ar expansions reported below. The separation of the slow KED part into the three components B, B1 and B2 yields consistently the best fit of all the measured spectra. The peaks A, B1 and B2 were fitted with Gaussian shape; while the peak B was fitted with a functional form of the statistical character $f(E) \propto E{\cdot}e^{-(E/\varepsilon)^2}$

Table 2 Fitted parameters of KEDs and anisotropy parameters β. $\bar{E}_{kin}(Cl)$ is the peak maximum position; ΔE is full width at half maximum (FWHM) of the peak. Reported errors were evaluated from images recorded under various conditions, and approximate values not well determined by the fits are reported without errors

Process	$\bar{E}_{kin}(Cl)$ (eV)	ΔE (eV)	β
A	0.97 ± 0.03	0.33 ± 0.03	1.7 ± 0.3
B	0.17 ± 0.05	0.24 ± 0.05	0.4 ± 0.3
B1	0.38 ± 0.03	0.18 ± 0.05	0.8 ± 0.3
B2	0.55 ± 0.03	0.20 ± 0.05	~0.8
C	~0.00	~0.04	0.0

We present our spectra in terms of the $E_{kin}(Cl)$ Cl-fragment kinetic energy (KE) rather than the total kinetic energy release (TKER), since the $E_{kin}(Cl)$ is obtained directly from the image, while the derivation of TKER requires an assumption that the process is two-body photodissociation $CF_2Cl_2 + h\nu \rightarrow CF_2Cl + Cl$; under this assumption the relation between the TKER and the reported $E_{kin}(Cl)$ is:

$$\mathrm{TKER} = \frac{m(CF_2Cl_2)}{m(CF_2Cl)} E_{kin}(Cl) \approx 1.41 \times E_{kin}(Cl) \qquad (1)$$

Due to the discrepancy between the previously observed spectra,[8,9] the dependence on the dissociation laser intensity was carefully investigated to reveal a possible multiphoton character of the observed processes. Fig. 3 shows two KEDs measured at different photon fluxes of 4.5×10^{27} cm^{-2} s^{-1} (open circles) and 1.4×10^{28} cm^{-2} s^{-1} (closed circles). Since it is difficult to compare the signal intensities from different imaging experiments, the KEDs are arbitrarily scaled to have comparable intensities at maximum B (note that the KEDs at higher laser power are offset by ~0.2 in intensity). We concentrate on the KED shape. There is a clear increase in the A/B peak ratio between the two photon fluxes (confirmed also by measurements at intermediate photon fluxes). In the measurements with the higher photon fluxes up to 8×10^{28} cm^{-2} s^{-1} the KED shapes remain qualitatively the same, *i.e.* the A/B ratio is almost constant.

It ought to be mentioned that no image could be seen with either 193 nm or 235 nm laser alone at the photon fluxes exploited here. On the other hand, all the features (especially the slow components) are present in the KEDs even at the lowest 193 nm photon flux. This suggests that they all correspond to the single 193 nm photon processes. The photon flux of 235 nm photons could not be lowered significantly, since it had to be sufficient for the (2 + 1) REMPI detection of Cl atoms. On the other hand, it was at the upper limit of our current laser possibilities, therefore the power dependence on 235 nm laser

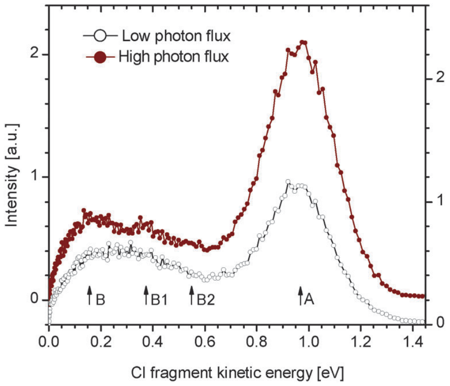

Fig. 3 KED of the Cl-fragment from the CF_2Cl_2 molecule measured at 193 nm photon flux. The spectrum measured at 1.4×10^{28} cm^{-2} s^{-1} (full circles) is offset for clarity (left hand side intensity axis) with respect to the spectrum measured at 4.5×10^{27} cm^{-2} s^{-1} (open circles, right hand side intensity axis).

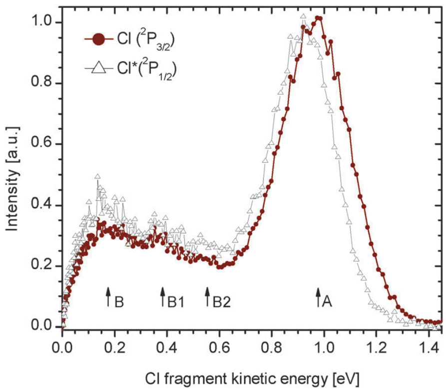

Fig. 4 The KED spectrum of the Cl*($^2P_{1/2}$) fragment (triangles) in comparison with the Cl($^2P_{3/2}$) fragment (circles) normalized to maximum.

could not be investigated in an extended region. Increasing the temporal delays between the lasers did not change the images qualitatively apart from decreasing the intensity.

Fig. 4 shows the KED spectrum of the excited Cl*($^2P_{1/2}$) fragment in comparison with the Cl($^2P_{3/2}$) fragment normalized to the maximum. The total Cl$^+$ signals measured at 235.336 nm and 235.205 nm were in a ratio of about ≈ 3 which agrees with the branching ratio of Cl* fragments to the total chlorine atom yield of 0.2.[10] The Cl* KED is essentially the same as that of Cl. The fast peak A is shifted by ~ 0.07 eV to lower KE which corresponds to the Cl spin–orbit splitting energy of 0.109 eV when translated into the fragment KE. The slow features B, B1 and B2 are reproduced in the Cl* spectrum. Also the dependence of Cl* spectra on the expansion conditions follows the dependence of Cl.

From the images the angular distributions were evaluated by integrating for fragment energies around the corresponding peaks. For the fast process A the anisotropy factor is $\beta = 1.7 \pm 0.3$, suggesting a parallel nature of this process. The slow processes also exhibit some anisotropy (see the image in Fig. 1): $\beta = 0.4 \pm 0.3$ for B integrated between 0.10–0.20 eV, $\beta = 0.8 \pm 0.3$ for B1 (0.36–0.42 eV), and $\beta \sim 0.8$ for B2 (0.52–0.58 eV), see Table 2. The integration intervals were chosen to minimize the overlap between the peaks, however, it is clear from the images as well as the KEDs that distinguishing B1 and B2 is somewhat arbitrary.

3.2 CF_2Cl_2–Ar expansions

We focus on the study of CF_2Cl_2 photodissociation in clusters. Expansions of the 5% mixture of CF_2Cl_2 in Ar and Xe were used to produce the rare gas clusters with CF_2Cl_2 molecules embedded as discussed below. Fig. 5 shows two images obtained in Ar expansions at a low stagnation pressure of $P_0 = 1.1$ bar (a), and higher pressure of $P_0 = 1.7$ bar (b); in the latter image the central intensity due to the clustering effects is clearly observable. Similar images were also recorded by varying mixing ratios, expansion pressures, and laser powers.

Fig. 6 shows the corresponding KEDs. The KED obtained at $P_0 = 1.1$ bar (open triangles) is essentially the same as in the case of pure CFC expansion above – it corresponds to the low laser intensity KED in Fig. 3. This confirms the assignment of similar images to the molecular conditions where no clusters are generated as opposed to the clustering conditions apparent in Fig. 5(b). This and similar molecular KEDs were also fitted with peaks A, B, B1 and B2 (overall fit shown by the solid line) and the parameters of these fits were averaged in Table 2.

On the other hand, the image at the higher pressure $P_0 = 1.7$ bar in Fig. 5(b) shows a clear intensity maximum in the center expressed by the zero KE peak in the corresponding KED in Fig. 6 (full circles). The molecular KED normalized in the region of minimum around 0.7 eV (open triangles in Fig. 6) was subtracted from this KED resulting in the zero KE peak showing the pure contribution from clusters, peak C (open squares). This peak was fitted with the distribution peaking at zero (dashed line), and the fitted parameters are also summarized in Table 2. The low KE fragments generating the central peak are the fingerprints of the photodissociation in clusters as observed previously by the imaging techniques.[21,24] This will be discussed below.

3.3 CF_2Cl_2–Xe expansions: cluster case

The clustering of molecules with Xe is stronger than that with Ar, and therefore Xe was exploited to investigate the clustering effects

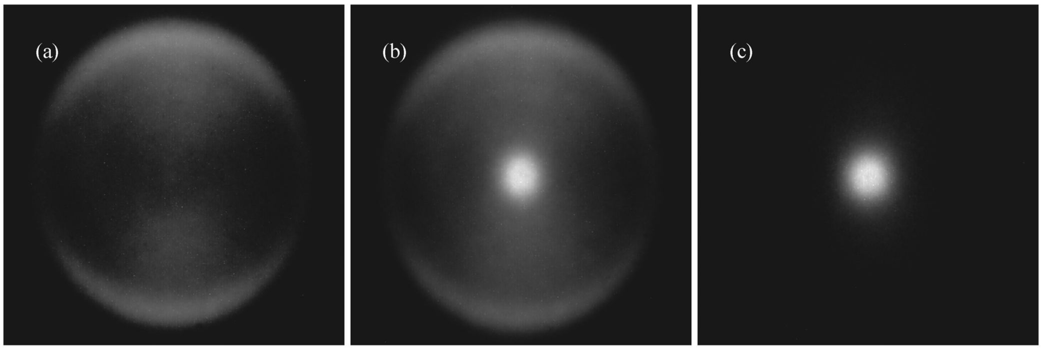

Fig. 5 Image of CF_2Cl_2 photodissociation in 5% CF_2Cl_2–Rg mix expansions: (a) Rg = Ar $P_0 = 1.1$ bar (molecule); (b) Rg = Ar $P_0 = 1.7$ bar (small clusters); (c) Rg = Xe $P_0 = 1.7$ bar (large clusters).

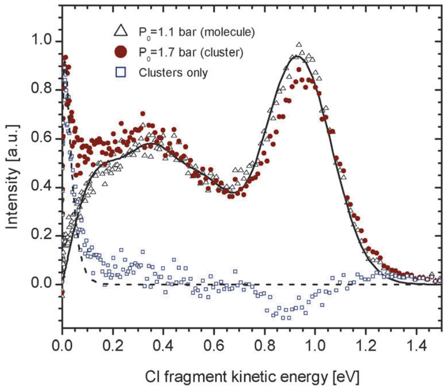

Fig. 6 KEDs obtained from the images in Fig. 5(a) – triangles: molecular case; and Fig. 5(b) – full circles: cluster case. The squares correspond to the pure cluster contribution obtained by subtraction of these KEDs.

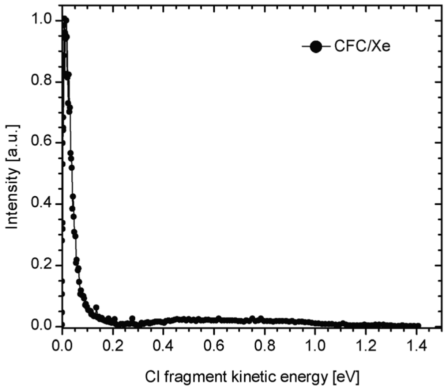

Fig. 7 KED measured in the 5% CF_2Cl_2–Xe mix expansion at the expansion pressure P_0 = 1.7 bar corresponding to the image in Fig. 5(c).

in imaging studies.[21–26] Although we have already observed the clustering effects with Ar, as in the case of our HBr study,[21] we also used Xe for comparison. Fig. 5(c) shows the image measured in the 5% CF_2Cl_2–Xe mix expansion obtained under the same conditions as in Ar expansions: P_0 = 1.7 bar. It exhibits essentially only the central "cluster" maximum as confirmed by the corresponding KED shown in Fig. 7.

4 Discussion

4.1 Photodissociation of the CF_2Cl_2 molecule

First, we discuss our results obtained for the photodissociation of CF_2Cl_2 in comparison with the previous TOF measurements.[8,9] As outlined in the Introduction Baum and Huber[8] reported only the fast photodissociation channel at 193 nm. On the other hand, Yen *et al.*[9] observed two channels resulting in slower fragments at a somewhat shorter wavelength of 187 nm. Our images recorded under the molecular regime also show clear evidence for slow Cl (and Cl*) fragments from CF_2Cl_2 photodissociation at 193 nm.

The analysis of our KEDs yields the fast peak A at 0.97 eV. The fast peak has been assigned to the direct photodissociation process

$$CF_2Cl_2 + h\nu \rightarrow CF_2Cl + Cl. \tag{2}$$

Thus eqn (1) corresponds to a TKER of 1.37 eV. Baum and Huber[8] reported a TKER of 1.475 eV, while Yen *et al.*[9] reported a value of 1.63 eV at 187 nm (*i.e.* at the dissociation energy higher by 0.22 eV). Considering the enthalpy of this process to be 3.48 eV (80.3 kcal mol^{-1}),[10] the above TKER of 1.37 eV represents about 47% of the excess energy and the rest 53% (1.56 eV) must be deposited into the internal excitation of the CF_2Cl radical.

What is the origin of the peak B at the lowest energy $E_{\mathrm{kin}}(\mathrm{Cl}) \approx$ 0.17 eV? The shape of the distribution suggests a statistical character of the corresponding process. Yen *et al.*[9] assigned their lowest energy maximum at TKER ≈ 0.12 eV to the secondary dissociation process

$$CF_2Cl \rightarrow CF_2 + Cl. \tag{3}$$

Since this unimolecular decay requires a dissociation energy of about 2.2 eV (54 kcal mol^{-1}),[8–10] the above internal excitation of 1.56 eV is not sufficient. Only if the Cl fragments from CF_2Cl_2 photodissociation, eqn (2), leave with energies $E_{\mathrm{kin}}(\mathrm{Cl}) \leq 0.5$ eV, would there be enough energy left in the internal excitation of the CF_2Cl radical to release the secondary Cl. However, 0.5 eV corresponds to the very edge of peak A, and therefore there are not many CF_2Cl radicals generated with enough internal energy to undergo the decay (eqn (3)). Also Baum and Huber[8] used similar arguments to conclude that the secondary decay (eqn (3)) does not happen.

If the statistical process (eqn (3)) would contribute to the KED, it would imply that more than one Cl atom could be dissociated from CF_2Cl_2 with one 193 nm photon; *i.e.* the quantum yield $\Phi(\mathrm{Cl})$ would be larger than 1. The quantum yield at 193 nm has been reported $\Phi(\mathrm{Cl}) = 1.03 \pm 0.09$.[10] However, the area of peak B represents about 25% of peak A which would lead to a larger quantum yield ~1.25. Therefore other processes than the secondary decay (eqn (3)) should be responsible for peak B; or an alternative compensating channel must exist which does not yield Cl fragments upon the 193 nm photon absorption.

Another explanation of the slow fragment can involve concerted dissociation of two Cl fragments simultaneously (or nearly simultaneously) also mentioned by Yen *et al.*[9] The excess energy in the case of the process

$$CF_2Cl_2 + h\nu \rightarrow CF_2 + 2Cl \tag{4}$$

would be ~0.7 eV.[10] However, in such a case the assumption of two-body dissociation cannot be implemented and the kinetic energy $E_{\mathrm{kin}}(\mathrm{Cl})$ cannot be simply calculated from the excess energy. Nevertheless, such a process would presumably yield the slow Cl fragments. Nevertheless, in this case one exciting photon yields two Cl fragments again (*i.e.* $\Phi(\mathrm{Cl}) > 1$) and the same arguments should be considered as above.

The two other slow components B1 and B2 are not well resolved, yet they are reproduced in many KEDs measured under various conditions. Yen *et al.*[9] also reported an intermediate process at TKER $\approx$ 0.53 eV. The two maxima B1 and B2 correspond to a TKER of $\sim$0.5 eV and $\sim$0.8 eV, respectively, assuming eqn (1) for two-body dissociation (eqn (2)). However, the excess energy is smaller by 0.22 eV in our experiment. Yen *et al.*[9] proposed the above mentioned ''concerted dissociation'' of two Cl atoms (eqn (4)) as the most likely interpretation of their intermediate fragments.

A hypothetical possibility to generate the slow Cl fragments (peak B, B1 or B2) would be the existence of an electronically excited CF_2Cl^* state (which could also be dissociative). However, no such suitable CF_2Cl^* state has been reported in the literature.

We should also consider the multiphoton processes. We have excluded the photodissociation by more than a single 193 nm photon based on the laser intensity measurements presented above. We also exclude multiphoton processes with 235 nm photons alone, since no signal was observed with 235 nm laser only. Thus the only process involving two photons which can contribute to the Cl fragment yield would involve the combination of 193 nm and 235 nm photons. One possibility is the 193 nm photodissociation of CF_2Cl_2 (eqn (2)) followed by the 235 nm photodissociation of the CF_2Cl radical fragment.

$$CF_2Cl + h\nu\,(235\ \text{nm}) \rightarrow CF_2 + Cl. \tag{5}$$

An indication of such a process came from experiments with cross-polarized dissociation and ionization lasers, however, we could not confirm this process unambiguously. On the other hand, the intensity of the (193 nm + 235 nm) process should increase with the 193 nm photon flux too, which is not the case (see Fig. 3). If this two-photon process happens, its energetics together with the B1 and B2 peak positions would suggest substantial energy left in the internal excitation of the CF_2 fragment of $\sim$2.1–2.4 eV.

Further discussion of the observed processes can be assisted by the transition anisotropy clearly shown by the images: the evaluated anisotropy factor for the direct process A is $\beta \approx 1.7 \pm 0.3$, which can be compared to the previous TOF estimates of 0.65[8] and 0.45.[9] The previous values were based only on the measurements with two different polarizations; in this respect the imaging experiment is superior. Besides, saturation of a transition lowers the anisotropy, since molecules with less favourable orientation with respect to the laser polarization are excited.[23] The smaller β parameters measured previously may suggest that the studies[8,9] were saturating the transitions. We have carefully investigated the 193 nm photon flux dependence and observed the decrease of β with increasing photon flux: *e.g.* $\beta = 0.7$ at the photon flux of 6×10^{28} cm^{-2} s^{-1}.

Based on the CF_2Cl_2 equilibrium geometry with an angle $\alpha = 56.3$ deg between the two C–Cl bonds the anisotropy β could assume a maximum value of 1.08.[8] The anisotropy factor β close to 2 would correspond to a nearly parallel process (in the approximation of diatomic dissociation). This suggests a significant opening of the corresponding bond angle in the excited dissociative state to a nearly linear Cl–C–Cl geometry.

The slow fragments were assigned to the three processes: B, B1, and B2 and the corresponding β-parameters are given in Table 2. The major slow contribution B has been suggested above to correspond to the secondary dissociation of internally excited CF_2Cl, and $\beta \sim 0$ would be expected for the statistical decay. However, $\beta \approx 0.4$ measured for process B suggests a somewhat anisotropic distribution, which is evident even in the image in Fig. 5(a). If these fragments originated from the secondary decay of the internally excited CF_2Cl radical, this dissociation would have to follow quickly the primary dissociation before the molecule can rotate substantially; *i.e.* it would essentially be a concerted dissociation of the two Cl fragments. For comparison, Yen *et al.*[9] assigned their lowest energy maximum at TKER $\approx$ 0.12 eV to the secondary statistical decay process of CF_2Cl; they reported $\beta \approx 0.1$.

For both B1 and B2 we have obtained $\beta \approx 0.8$. The interpretation of these processes as secondary dissociation of the CF_2Cl fragment with 235 nm lasers could be consistent with the essentially parallel nature of these processes. However, we have to consider the large overlap and relative ambiguity of these processes. Yen *et al.*[9] reported $\beta = 0.15$ for their intermediate process at TKER $\approx$ 0.53 eV.

From the above analysis it follows that many details of the CF_2Cl_2 molecule photodissociation dynamics still remain unclear, especially the question: which processes are responsible for the slow Cl fragments (maxima B, B1 and B2)? Nevertheless the present analysis provides a sufficient basis for separation of the solvent effects on photodissociation of the CF_2Cl_2 molecule in clusters, which is our major target here.

4.2 Photodissociation of CF_2Cl_2 in clusters

Fig. 5(b) shows the image measured in a 5% CF_2Cl_2–Ar mix expansion at higher expansion pressure P_0 = 1.7 bar. The strong intensity at the centre is the fingerprint of clustering and fragment *caging* in clusters as observed in imaging experiments previously.[21,24] This central feature becomes even more pronounced in Xe-expansions (see Fig. 5c), however, it has not been observed in pure CF_2Cl_2 expansions even at elevated pressures of up to 2 bar. This suggests that mixed clusters $(CF_2Cl_2)_m{\cdot}Rg_n$ (Rg = Ar, Xe) are generated in CF_2Cl_2–Rg expansions.

It is difficult to determine the neutral cluster sizes and composition, yet we can make some reasonable estimates. We have recorded the mass spectra with the imaging setup but no evidence for ionized cluster species was found. This is not surprising, since the clusters undergo strong fragmentation in the non-resonant multiphoton ionization process.[21,27]

The cluster sizes of rare gas clusters were exploited previously in great details, and they were found in good agreement with the empirical law established by Hagena[28–30] and Buck.[31] The explicit form of Hagena's formula applicable for our expansion conditions can be found in our previous publication on cluster imaging.[21] Hagena's formalism defines a dimensionless parameter Γ^* characterizing the various clustering regimes.[29] For the current expansion conditions (P_0 = 1.7 bar) assuming pure rare gas expansion yields $\Gamma^* \geq 1000$ for both Ar and Xe which implies a strong clustering regime. The mean cluster sizes would correspond to $\bar{n} \sim 70$ and 500 for Ar and Xe, respectively.

Diluting the rare gas with other molecules can change the expansion conditions significantly: for example 5% of HBr in Ar yields pure $(HBr)_n$ clusters under the conditions where large Ar_n clusters would be produced in pure Ar expansion.[32–34] We also pointed out that clustering in pulsed expansions is a very sensitive function of the valve opening and timing throughout the valve opening period.[21,24] Here experimental evidence shows that clusters are generated and they are mixed CF_2Cl_2–Rg species. Besides we know that relatively large Rg_n clusters would be generated in pure rare gas expansion under the present conditions. Therefore, based on analogy with our previous work on HBr in Ar and Xe clusters, we deduce that our present clusters are Rg_n species with CF_2Cl_2 molecules or small clusters embedded inside, *i.e.* $(CF_2Cl_2)_m{\cdot}Rg_n$ where $\bar{m} \sim 1$, and $\bar{n} \leq 70$ and $\bar{n} \leq 500$ for Ar and Xe, respectively (these are the upper boundaries for the mean sizes).

On the other hand, the expansion in Ar at $P_0 = 1.1$ bar yields the *molecular* regime. The modified Hagena's formula for pure Ar expansion under these conditions would yield $200 \leq \Gamma^* \leq 1000$, *i.e.* "beginning of clustering" and the corresponding mean cluster size $\bar{n} \approx 30$. Since the measured images show that the isolated CF_2Cl_2 molecules dominate in the beam under these conditions, it implies that about $k \approx 30$ Ar atoms should be evaporated upon CF_2Cl_2 attachment to the Ar_n; otherwise the mixed $CF_2Cl_2{\cdot}Ar_{n-k}$ clusters would be observed. Under the *clustering* conditions Ar_n clusters with $\bar{n} = 70$ would be generated in pure Ar expansion as outlined above. Assuming the evaporation of 30 Ar atoms from $Ar_{\bar{n}}$ would yield $CF_2Cl_2{\cdot}Ar_{40}$. In the case of Xe much larger species are generated. In summary we generate:

- in Ar expansions: CF_2Cl_2 embedded in Ar_n clusters with $\bar{n} \geq 10$-presumably a single solvation shell ($n = 12$);
- in Xe expansions: large $(CF_2Cl_2)_m{\cdot}Rg_n$, $\bar{m} \sim 1, 100 \leq \bar{n} \leq 500$.

Below we argue that these species are consistent with the observed images and KEDs.

The origin of the strong central intensity in the images and the zero energy peak in KEDs is the fragment caging after the photodissociation. The *cage effect* in rare gas clusters has been studied in detail by the TOF[11–15] and imaging[21] techniques. This process in KED was fitted with peak C centred around zero (see Fig. 6). The central peak is isotropic $\beta \approx 0$ in accordance with the caging process. The rest of the KED corresponds to the photodissociation of bare molecule. Also the anisotropy β parameters for the processes A, B, B1, and B2 evaluated from the images with the "cluster peak" in the centre correspond to the molecular case. This suggests that part of the Cl fragments is unaffected by the clustering: either there is a substantial fraction of non-clustered CF_2Cl_2 molecules in the beam, or a large number of Cl fragments leave the clusters without loosing any kinetic energy and without changing their direction of motion, *i.e.* without undergoing any inelastic or elastic collisions. Assuming the above suggested mean size $\bar{n} \geq 10$ of $CF_2Cl_2{\cdot}Ar_n$ clusters, there cannot be a prevailing fraction of unclustered bare CF_2Cl_2 molecules in the beam. Therefore the latter option is probable.

Thus there are two processes happening in the clusters after the CF_2Cl_2 photodissociation: (1) the Cl fragment is caged in the cluster and looses all its KE in collisions with the cage atoms;† (2) the fragment leaves the clusters essentially without interacting with Ar atoms. This behaviour would be consistent with the CF_2Cl_2 molecule embedded in a small Ar cluster constituting a single solvation layer around the molecule: the Cl fragment either collides with the solvating Ar atom and is caged, or upon favourable orientation it escapes the cage between the neighbouring Ar atoms. Similar behaviour was observed and theoretically simulated for HBr embedded in Ar clusters.[12,35]

The fragment caging in the Xe case is even stronger than in Ar clusters. The images recorded under the same conditions as the Ar-cluster experiment show only the central peak of zero KE fragments (see Fig. 5(c) and the corresponding KED in Fig. 7). The significantly stronger central peak corresponding to the caging in Xe expansions compared with Ar can be explained by the above discussed larger clusters produced in Xe where the Cl fragment is shielded from escaping from the cluster by several solvation layers.

It is instructive to compare the present case to the previously studied photodissociation of hydrogen halides in rare gas clusters.[11–15,21] Analogical processes were observed: caging of H-fragments, namely comparing photodissociation of HBr in Ar and Xe clusters yields much stronger caging in the Xe case.[21] There were also H-fragments leaving even from the large clusters through several solvation layers without loosing their KE, but being elastically scattered by the cluster constituents.[11,14,36]

On the other hand, there are some differences in the present case with respect to the hydrogen halide studies. The H-fragments show some contribution of inelastic scattering at intermediate energies between the fast fragments corresponding to the *cage exit* and the *caged* ones near zero KE; these fragments were termed *delayed cage exit*.[11] The contribution of Cl *delayed exit* fragments in the present spectra is negligible as follows from the comparison between the "molecule" and "cluster" spectra, *e.g.* in Fig. 6. Yet another difference is the presence of the faster H-fragments corresponding to vibrationally excited HBr molecules in the clusters.[21,36] Such faster H-fragments have also been observed from photodissociation of acetylene in clusters.[22,37] However, there is no indication of significantly faster Cl fragments from the photodissociation of the CF_2Cl_2 molecule in the clusters: no significant broadening of peaks or shift towards higher energies with respect to the "molecule" KED is observed in the "cluster" KEDs in Fig. 6 and 7. This suggests that after the primary excitation the CF_2Cl_2 molecule dissociates and does not recombine back to the original molecule in a vibrationally

---

† Note, that the central peak corresponds to the fragments with zero KE which still left the cluster; *i.e.* these fragments were caged, lost their kinetic energy, yet the cluster decayed in this process and left the nearly stationary fragments behind.

hot state even if the Cl fragment is caged, while such processes are feasible for hydrogen from HBr or acetylene.[21,22,37] Yet from another point of view, the absence of faster Cl fragments in the cluster KEDs confirms the single-photon photodissociation conditions in the present experiments.

5 Conclusions

Even though we focus on the photodissociation of CF_2Cl_2 in clusters, some details about the photodissociation dynamics of bare molecule have been revealed by the imaging experiment. We observe the fast Cl fragments (peak A) from the direct CF_2Cl_2 photodissociation and additional contributions of slow fragments (peaks B, B1 and B2). We discuss several possible processes which can yield the slow fragments: (1) statistical decay of the internally excited CF_2Cl fragment radical; (2) "concerted" simultaneous dissociation of two Cl atoms; (3) secondary photodissociation of CF_2Cl fragments with 235 nm photons.

It should be mentioned that the above proposed processes (1) and (2) can have significant consequences for the atmospheric chemistry of ozone depletion. For the purposes of atmospheric photolysis modelling the quantum yield value $\Phi(\mathrm{Cl}) = 1$ is recommended[38] in agreement with $\Phi(\mathrm{Cl}) = 1.03 \pm 0.09$ measured at 193 nm.[10] However, the processes (1) and (2) yield two Cl fragments per one 193 nm photon. Thus it can be considered that these processes would significantly enhance the Cl radical yield in the stratospheric models.

Further investigations, namely theoretical, are needed to answer the remaining questions about the CF_2Cl_2 molecule photodissociation. Nevertheless, the present molecular imaging data also provide a solid basis for our experiments with clusters.

In the rare gas clusters we see evidence for strong *caging* of Cl fragments in the cluster yielding free Cl atoms with near-zero kinetic energy. In Ar clusters significant amount of the fragments escapes the cluster without loosing any kinetic energy. The CF_2Cl_2 molecule surrounded with a single argon solvation layer has been proposed as the prevailing cluster structure. The zero kinetic energy fragments dominate the spectrum in Xe clusters which generate larger species with many solvation layers.

Some differences have been observed for Cl fragments here as opposed to H fragments from hydrogen halides and other molecules studied in the rare gas clusters: no delayed exit and no significantly faster fragments corresponding to the excited molecules have been observed for Cl. These differences between Cl and H atom dynamics after the photodissociation in clusters are worth investigating further, since they are relevant to atmospheric chemistry. Namely to the question if the Cl radicals are released into the gas phase after they have been generated by photodissociation within clusters.

It has been shown previously that even archetype solvents such as the rare gas atoms can change the excited state potential *via* electronic interactions and thus influence the photodissociation dynamics. This behaviour was observed for simple heteroaromatic ring molecules clustered with Ar and Xe.[25,39] On the other hand, the H-fragments from the hydrogen halides in the rare gas clusters exhibit only the mechanistic effects of caging and cage exit.[11] Yet, their photodissociation in water clusters is completely different.[16,18] Here we also observe purely mechanistic effects of caging and cage exit for Cl-fragments from CF_2Cl_2 in rare gas clusters. Will this behaviour be different again in the water clusters? This question remains to be answered by future studies.

Acknowledgements

This work was supported by the Grant Agency of the Czech Republic Project No. P208/11/0161. J.K. acknowledges the support of Grant No. 238671 ICONIC within FP7-MC-ITN. We gratefully acknowledge Petr Slavíček for fruitful discussions of our results.

References

1 M. J. Molina and F. S. Rowland, *Nature*, 1974, **249**, 810.
2 S. Solomon, R. R. Garcia, F. S. Rowland and D. J. Wuebbles, *Nature*, 1986, **321**, 755.
3 S. Solomon, *Rev. Geophys.*, 1999, **37**, 275.
4 B. J. Finlayson-Pitts and J. N. Pitts, *Chemistry of the Upper and Lower Atmosphere*, Academic Press, San Diego, 2000.
5 R. E. Rebbert and P. J. Ausloos, *J. Photochem.*, 1975, **4**, 419.
6 J. J. Tiee, F. B. Wampler and W. W. Rice, *Chem. Phys. Lett.*, 1979, **68**, 403.
7 Y. Matsumi, K. Tonokura, M. Kawasaki, G. Inoue, S. Satyapal and R. Bersohn, *J. Chem. Phys.*, 1991, **94**, 2669.
8 G. Baum and J. R. Huber, *Chem. Phys. Lett.*, 1993, **203**, 261.
9 M. Yen, P. M. Johnson and M. G. White, *J. Chem. Phys.*, 1993, **99**, 126.
10 F. Taketani, K. Takahashi and Y. Matsumi, *J. Phys. Chem. A*, 2005, **109**, 2855.
11 U. Buck, *J. Phys. Chem. A*, 2002, **106**, 10049.
12 N. H. Nahler, R. Baumfalk, U. Buck, H. Vach, P. Slavíček and P. Jungwirth, *Phys. Chem. Chem. Phys.*, 2003, **5**, 3394.
13 P. Slavíček, P. Jungwirth, M. Lewerenz, N. H. Nahler, M. Fárník and U. Buck, *J. Phys. Chem. A*, 2003, **107**, 7743.
14 N. H. Nahler, M. Fárník, U. Buck, H. Vach and R. B. Gerber, *J. Chem. Phys.*, 2004, **121**, 1293.
15 M. Fárník, N. H. Nahler, U. Buck, P. Slavíček and P. Jungwirth, *Chem. Phys.*, 2005, **315**, 161.
16 V. Poterya, M. Fárník, P. Slavíček, U. Buck and V. V. Kresin, *J. Chem. Phys.*, 2007, **126**, 071101.
17 M. Ončák, P. Slavíček, V. Poterya, M. Fárník and U. Buck, *J. Phys. Chem. A*, 2008, **112**, 5344.
18 V. Poterya, J. Fedor, A. Pysanenko, O. Tkáč, J. Lengyel, M. Ončák, P. Slavíček and M. Fárník, *Phys. Chem. Chem. Phys.*, 2011, **13**, 2250.
19 M. Ončák, P. Slavíček, M. Fárník and U. Buck, *J. Phys. Chem. A*, 2011, **115**, 6155.

20 A. T. J. B. Eppink and D. H. Parker, *Rev. Sci. Instrum.*, 1997, **68**, 3477.

21 J. Fedor, J. Kočišek, V. Poterya, O. Votava, A. Pysanenko, L. Lipciuc, T. N. Kitsopoulos and M. Fárník, *J. Chem. Phys.*, 2011, **134**, 154303.

22 M. Fárník, V. Poterya, J. Kočišek, J. Fedor and P. Slavíček, *Mol. Phys.*, 2012, **110**, 2817.

23 B. Whitaker, *Imaging in Molecular Dynamics*, Cambridge University Press, Cambridge, 2003.

24 P. Glodic, A. Kartakoullis, M. Fárník, P. C. Samartzis and T. N. Kitsopoulos, *J. Chem. Phys.*, 2012, **137**, 154306.

25 L. Rubio-Lago, D. Zaouris, Y. Sakellariou, D. Sofikitis, T. N. Kitsopoulos, F. Wang, X. Yang, B. Cronin, A. L. Devine, G. A. King, M. G. D. Nix and M. N. R. Ashfold, *J. Chem. Phys.*, 2007, **127**, 064306.

26 M. L. Lipciuc, F. Wang, X. Yang, T. N. Kitsopoulos, G. S. Fanourgakis and S. S. Xantheas, *ChemPhysChem*, 2008, **9**, 1838.

27 V. Poterya, O. Tkáč, J. Fedor, M. Fárník, P. Slavíček and U. Buck, *Int. J. Mass Spectrom.*, 2010, **2010**, 85.

28 O. F. Hagena, *Surf. Sci.*, 1981, **106**, 101.

29 O. F. Hagena, *Z. Phys. D: At., Mol. Clusters*, 1987, **4**, 291.

30 O. F. Hagena, *Rev. Sci. Instrum.*, 1992, **63**, 2374.

31 U. Buck and R. Krohne, *J. Chem. Phys.*, 1996, **105**, 5408.

32 R. Baumfalk, U. Buck, C. Frischkorn, S. R. Gandhi and C. Lauenstein, *Ber. Bunsen-Ges. Phys. Chem.*, 1997, **101**, 606.

33 R. Baumfalk, U. Buck, C. Frischkorn, S. R. Gandhi and C. Lauenstein, *Chem. Phys. Lett.*, 1997, **269**, 321.

34 R. Baumfalk, U. Buck, C. Frischkorn, N. H. Nahler and L. Hüwel, *J. Chem. Phys.*, 1999, **111**, 2595.

35 R. Baumfalk, N. H. Nahler, U. Buck, M. Y. Niv and R. B. Gerber, *J. Chem. Phys.*, 2000, **113**, 329.

36 R. Baumfalk, N. H. Nahler and U. Buck, *Phys. Chem. Chem. Phys.*, 2001, **3**, 2372.

37 M. Fárník, V. Poterya, O. Votava, M. Ončák, P. Slavíček, I. Dauster and U. Buck, *J. Phys. Chem. A*, 2009, **113**, 7322.

38 IUPAC Subcommittee on Gas Kinetic Data Evaluation, *Data Sheet PCl15*, 15th December 2000, http://www.iupac-kinetic.ch.cam.ac.uk/.

39 V. Poterya, V. Profant, M. Fárník, P. Slavíček and U. Buck, *J. Chem. Phys.*, 2007, **127**, 064307.

PCCP

PAPER

View Article Online
View Journal | View Issue

Cite this: *Phys. Chem. Chem. Phys.*, 2015, **17**, 25734

Photodissociation dynamics of ethanethiol in clusters: complementary information from velocity map imaging, mass spectrometry and calculations†

Pavla Svrčková,[ab] Andriy Pysanenko,[a] Jozef Lengyel,[ab] Peter Rubovič,[a]
Jaroslav Kočišek,[a] Viktoriya Poterya,[a] Petr Slavíček[ab] and Michal Fárník*[a]

Received 20th January 2015,
Accepted 23rd February 2015

DOI: 10.1039/c5cp00367a

www.rsc.org/pccp

We investigate the solvent effects on photodissociation dynamics of the S–H bond in ethanethiol CH_3CH_2SH (EtSH). The H fragment images are recorded by velocity map imaging (VMI) at 243 nm in various expansion regimes ranging from isolated molecules to clusters of different sizes and compositions. The VMI experiment is accompanied by electron ionization mass spectrometry using a reflectron time-of-flight mass spectrometer (RTOFMS). The experimental data are interpreted using *ab initio* calculations. The direct S–H bond fission results in a peak of fast fragments at $E_{kin}(H) \approx 1.25$ eV with a partly resolved structure corresponding to vibrational levels of the CH_3CH_2S cofragment. Clusters of different nature ranging from dimers to large $(EtSH)_N$, $N \geq 10$, clusters and to ethanethiol clusters embedded in larger argon "snowballs" are investigated. In the clusters a sharp peak of near-zero kinetic energy fragments occurs due to the *caging*. The dynamics of the fragment caging is pictured theoretically, using multi-reference *ab initio* theory for the ethanethiol dimer. The larger cluster character is revealed by the simultaneous analysis of the VMI and RTOFMS experiments; none of these tools alone can provide the complete picture.

1 Introduction

The sulphur compounds are important players in aerosol generation and in atmospheric chemistry in general.[1] The ultraviolet (UV) photolysis of various sulphur containing molecules is a key part of the sulphur cycle in the atmosphere. The detailed investigations of the S–H bond photodissociation dynamics in molecules and clusters thus contribute to the understanding of atmospheric sulphur (photo)chemistry.

In our work, we focus on the photodissociation of ethanethiol CH_3CH_2SH (EtSH). Based on the analogy with methanethiol, two reaction channels are expected in the spectral region above 200 nm, the S–H and S–C bond breaking:

$$CH_3CH_2SH + h\nu \rightarrow CH_3CH_2S + H, \tag{1}$$

$$CH_3CH_2SH + h\nu \rightarrow CH_3CH_2 + SH. \tag{2}$$

The present experiment focuses on the S–H bond fission, and we primarily investigate the solvent effects on photodynamics in different types of clusters.

So far, photochemistry of the EtSH molecule was characterized rather incompletely from an experimental point of view. Even the full UV absorption spectrum was not recorded and the UV absorption cross sections were published only for some wavelengths.[2,3] The velocity map imaging[4] (VMI), which is the up-to-date method to investigate the photodissociation dynamics,[5] was used only once to study the S–H photodissociation of EtSH at 243 nm previously.[6] This rather limited information contrasts with the number of studies of the analogical methanethiol molecule which was the subject of numerous experimental[7–15] and theoretical investigations.[14–21] From these studies, the following picture emerged for methanethiol photochemistry. The absorption at around 240 nm (corresponding to the population of the $1A''$ electronic state) leads almost exclusively to the S–H bond rupture. This channel remained dominant even upon the excitation into the $2A''$ state below 220 nm, yet the C–S dissociation channel was observed too. The dissociation was very fast, leading to the high anisotropy of the photofragments.

In relevance to the present mass spectrometry of EtSH clusters, a mass spectrometric study of the molecule should be mentioned.[22] More recently the ionization energy and conformational isomers were revealed using non-resonant two-photon

---

[a] *J. Heyrovský Institute of Physical Chemistry v.v.i., The Czech Academy of Sciences, Dolejškova 3, 18223 Prague, Czech Republic. E-mail: michal.farnik@jh-inst.cas.cz; Fax: +420 2 8658 2307; Tel: +420 2 6605 3206*

[b] *Department of Physical Chemistry, University of Chemistry and Technology Prague, Technická 5, Prague 6, Czech Republic*

† Electronic supplementary information (ESI) available: H-fragment velocity map images, mass spectra from different ethanethiol clusters, and calculated cluster structures. See DOI: 10.1039/c5cp00367a

pulsed field ionization photoelectron spectroscopy,[23] and vacuum ultraviolet mass-analyzed threshold ionization spectroscopy.[24]

Here, we investigate the photochemistry of EtSH by VMI, and cluster structure and composition by electron ionization RTOFMS. We provide new data for the S–H photodissociation in the isolated EtSH molecule at 243 nm with a partly resolved vibrational structure. Our experiment also reveals the origin of the previously observed slow H-fragments[6] as a consequence of multiphoton processes. Then we focus on the photodissociation of ethanethiol in different clusters, ranging from dimers to large $(\mathrm{EtSH})_N$ clusters, and to ethanethiol clusters embedded in larger argon clusters. The detailed photodissociation dynamics is rationalized by *ab initio* calculations for the isolated molecule as well as for clusters.

2 Experiment

The experiments were carried out on the CLUster Beam (CLUB) apparatus which is a very versatile molecular beam setup.[25–29] In the present study we exploited two of the possible different experiments: the VMI and electron ionization RTOFMS.

To generate the beam of the molecules or clusters the carrier gas (He or Ar) was passed through a reservoir filled with liquid EtSH. The reservoir was placed outside the vacuum, and kept at a constant temperature T_R by heating it resistively in the mixture of $\mathrm{CO_2}$ ice and ethylene glycol. The EtSH vapour was transported by the carrier gas at a stagnation pressure P_0 towards a nozzle kept at a temperature $T_0 \approx 313$ K, and expanded into vacuum. Helium was used as the buffer gas for generating isolated molecules and small clusters up to trimers, while the larger $(\mathrm{EtSH})_N$, $N \geq 10$, clusters and Ar-covered species were generated in coexpansions with argon. Table 1 summarizes the expansion conditions.

2.1 Velocity map imaging

The cluster beam was skimmed and passed through two differentially pumped chambers before entering the chamber hosting the VMI assembly mounted perpendicularly to the beam axis. The molecules and clusters interact with the laser in the center of an electrostatic lens system which extracts the ionized photoproducts towards a position sensitive detector 50 cm upwards from the interaction point. The imaging system design follows approximately the original VMI of Eppink and Parker.[4] The detector (two multichannel plates with 56 mm diameter in Chevron configuration and the phosphor screen) was operated in gated mode which enabled imaging of a single ion mass. The gating was triggered by a laser light pulse delayed using a delay generator (BNC 575).

Table 1 Expansion conditions. "Cluster size *n*" denotes the largest $(\mathrm{EtSH})_n^+$ fragment discernible in the mass spectra; "mix" corresponds to the appearance of $\mathrm{Ar}_m{\cdot}(\mathrm{EtSH})_n^+$ fragments in the mass spectra; the arrows indicate a gradual change in the parameter. The nozzle parameters: diameter d = 50 μm, opening angle α = 30°, length l = 2 mm

Buffer gas	Stagnation pressure P_0 (bar)	Reservoir temperature T_R (K)	Concentration C (%)	Cluster size n
He	1	222	1.2	1
	2, 3	263	7.5, 5	3
Ar	2	263	7.5	15
	2 → 5	276	14 → 6	13–15
	5	263 → 220	3 → 0.2	17 → mix

Laser radiation at 243.1 nm was used to dissociate the EtSH molecules and to REMPI ionize the H-atoms. The tunable UV radiation was generated by doubling the 630 nm output of the dye laser (Pulsare-S, Fine Adjustment) pumped by the second harmonics (532 nm) of the Nd:YAG laser (Spitlight 1500, Innolas). The 315 nm wavelength was frequency summed with the fundamental 1064 nm wavelength of the Nd:YAG laser. The lasers were operated at a 10 Hz frequency in the nanosecond regime. The laser beam was focussed with a 700 mm lens onto a spot of radius ≈24 μm in the interaction region. The laser radiation was polarized so that the electric field vector of the radiation was parallel to the molecular beam, *i.e.* perpendicular to the imaging TOF axis. To investigate multiphoton processes the energy at the laser output was varied between 1.2 and 4.4 mJ per pulse corresponding to the photon fluxes at the interaction region ranging between 10^{27} and 10^{28} photons $\mathrm{cm^{-2}\ s^{-1}}$ (using different output powers and neutral density filters).

The images were recorded using a 16-bit greyscale CCD camera (unibrain Fire-i 780b) with the imaging lens (25 mm, f/1.6) connected to an acquisition computer *via* a FireWire interface and controlled by a custom made program. To process the images several reconstruction methods were used to check the consistency of our results: the inverse Abel transform and Hankel method,[30] Iterative Inversion method,[30] and the BASEX.[31] Comparing different evaluation methods was important especially for the search for a narrow zero-kinetic-energy (zero-KE) peak due to the fragment caging in the clusters, and for distinguishing the zero-KE peak from low energy fragments originating from the multiphoton processes. The H-fragment kinetic energy distributions (KEDs) were obtained from the images, and also the anisotropy parameters β were evaluated. The kinetic energy scale was calibrated using H-fragments from HBr photodissociation.[32] More details about our VMI and the measurement procedures can be found in our recent publications.[25,26]

2.2 Reflectron time-of-flight mass spectrometer

After leaving the VMI chamber the molecular beam entered a mass spectrometer chamber with the RTOFMS mounted perpendicularly to the beam. This mass spectrometer offers several ionization options: electron ionization (EI) using an electron gun with 10 kHz repetition frequency and a tuneable electron energy of 5–90 eV with 0.7 eV resolution,[33–35] photoionization exploiting multiphoton ionization with our tuneable UV lasers, and a special method of Na-doping and subsequent photoionization.[27] In the present study we used EI with 70 eV electrons. The ions were extracted perpendicularly to the beam by a 10 kV pulse and accelerated to the final kinetic energy of 8 kV. After passing the effective flight path of 0.95 m length, the ions were detected on the Photonics MCP detector in the Chevron configuration, 40 mm in diameter. The mass spectra were recorded with a resolution of $M/\Delta M \approx 5 \times 10^3$.

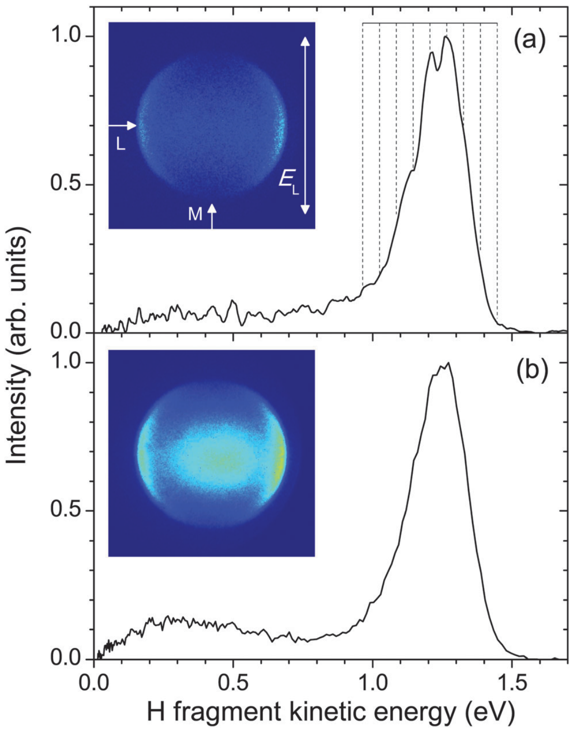

Fig. 1 (a) The H-fragment KED from EtSH molecule photodissociation at 243 nm: P_0 = 1 bar He, EtSH reservoir temperature T_R = 222 K corresponding to the concentration C = 1.2%. The inset shows the raw image with the directions of the molecular (M) and laser (L) beams and the laser polarization (E_L) indicated. (b) The KED and image at an increased photon flux of 8×10^{27} photons cm^{-2} s^{-1} illustrating the multiphoton processes.

3 Theoretical methods

The experiments were complemented by *ab initio* calculations. The theoretical calculations were used (i) to reveal the nature of the bonding in the ethanethiol clusters, (ii) to investigate the nature of the dissociation process of the ethanethiol molecule in an excited state, considering both isolated molecules and ethanethiol clusters, and (iii) to interpret the vibrational resolution of the KED spectra.

The $(EtSH)_N$ (N = 1–4) clusters were optimized using the density functional approach using the B97D3 functional[36] and the aug-cc-pVDZ basis set. The B97D3 functional includes empirical dispersion correction which is important for the present complexes. The excited states of the isolated EtSH molecule were calculated at the CASPT2/aug-cc-pVDZ level, considering the active space of 6 electrons in 7 orbitals. Two states of the A′ symmetry and two states of the A″ symmetry were averaged. For the $(EtSH)_2$ complex, we have used the active space of 12 electrons in 10 orbitals, using averaging over two states. Vibrational frequencies were calculated at the MP2/aug-cc-pVDZ level and scaled with a recommended factor of 0.959.[37]

The ground state calculations (including the frequency calculations) were performed using the Gaussian09 programme,[38] the CASPT2 calculations were executed using the MOLPRO2012 suite of codes.[39]

4 Results and discussion

4.1 Molecule

First, we investigated the photodissociation of isolated EtSH molecules in He-expansions. The molecular conditions were obtained at the expansion of ≈1% EtSH (reservoir temperature T_R = 222 K) in P_0 = 1 bar of He. The example image and corresponding KED are shown in Fig. 1(a). A number of very similar images and mass spectra were recorded for different conditions around the above values; in particular, the reservoir temperature was increased to T_R = 263 K without any significant change in the results.

The KED exhibits a relatively narrow peak at around 1.25 eV corresponding to the fast H-fragments from the direct S–H bond fission; this is supported also by the anisotropy parameter $\beta = -1.0 \pm 0.2$ obtained by fitting the angular distribution corresponding to the fast process, which suggests an immediate dissociation after the perpendicular electronic excitation. The present image and corresponding KED in Fig. 1(a) agree with the previous results of Zhang *et al.*[6] The major difference with respect to the previous results is the resolved structure in the present KED. It ought to be mentioned that our experiment is dedicated to cluster studies where any fine structure in the images is usually blurred by cluster effects, and therefore the VMI setup has not been optimized for high resolution (the perpendicular arrangement is not optimal for the high resolution VMI). More than 10 images similar to the one shown in the inset in Fig. 1(a) were recorded under comparable conditions corresponding to the isolated molecules. They were carefully analyzed, and the present KED represents the average of many spectra exhibiting the same features between ∼0.9 eV and 1.5 eV.

The maxima at approximately 1.27 eV and 1.21 eV and the shoulder at 1.15 eV were reproduced in almost all spectra. In many spectra an additional unresolved structure with the same spacing of 0.06 eV was also observed. Therefore we tentatively indicate a series of positions within the fast fragment peak in Fig. 1(a) with the spacing of 60 meV (484 cm^{-1}). This spacing should correspond to some vibrational levels in the EtS fragment. The observed frequency could correspond to the CH_2 wagging mode: the calculated frequency is 473 cm^{-1} or 453 cm^{-1} upon scaling. This mode changes its frequency during the S–H dissociation (for EtSH, the frequency amounts to 782 cm^{-1}), *i.e.* a large Franck–Condon factor is expected. Alternatively, the spacing could be attributed to the C–S stretching (681 cm^{-1}) which is, however, less probable due to dynamical reasons.

The mass spectrum recorded under the molecular conditions is shown in the ESI† – it corresponds to the well known mass spectrum of the EtSH molecule.[40] The major mass peak is of the parent ion $CH_3CH_2SH^+$ at m/z 62 (M) followed by the fragments (in the order from the most to the least intense): $CH_3CH_2^+$ at m/z 29 (M–SH) resulting from splitting-off the SH group; CH_2SH^+ at m/z 47 (M–CH_3) resulting from splitting-off the CH_3 group; and the H_2S^+ fragment at m/z 34 accompanied by fragments with ±H.

4.1.1 Multiphoton processes. In the previous photodissociation study of EtSH some small fraction of slow hydrogen fragments was observed and tentatively assigned to "a different dynamical channel".[6] Although this slow contribution was rather negligible for C_2H_5SH it was more pronounced for C_3H_7SH. It was argued that the corresponding process "likely occurred on the ground electronic state *via* internal conversion from the excited electronic state". A small contribution due to the slow fragments similar to the previous spectra[6] is also discernible in Fig. 1(a). However, it was possible to obtain the KED without this contribution at low photon fluxes of $\approx 1 \times 10^{27}$ photons cm^{-2} s^{-1}. Some of the KEDs averaged in Fig. 1(a) were recorded at somewhat higher photon fluxes for intensity reasons, therefore the slow fragment contribution appears there. Fig. 1(b) shows the KED with a pronounced contribution of the slow fragments recorded at a higher photon flux of 8×10^{27} photons cm^{-2} s^{-1}. The structure of the fast peak was smeared out, yet an unresolved shoulder structure corresponding to Fig. 1(a) is still discernible in the KED.

The analysis of the multiphoton processes is also important since they often result in slow hydrogens near the image center: the "central blob". However, in clusters the important information about the dissociation dynamics often appears near the center as well, *e.g.*, the fragment caging yields a central peak. Just recently we have demonstrated that the central peak can also reveal information about interesting photochemistry: namely the H_3O radical generation in hydrogen halide photodissociation on ice nanoparticles.[25,41,42] The present photodissociation of EtSH molecules and clusters provides an example where the different effects reflected in the image center can be disentangled, namely the multiphoton processes and the fragment caging. This will be demonstrated further below in the cluster analysis.

4.1.2 Dynamics of EtSH dissociation. The VMI experiments (KEDs and image anisotropy) suggest that the hydrogen dissociation is a direct process. The *ab initio* calculations indeed confirm this assumption: the excited state potential is purely repulsive along the S–H coordinate (see below). We further address the question whether the S–H dissociation is the only possible reaction channel. Similarly as for the methanethiol case,[12] a rupture of both the S–H and C–S bonds can in principle take place. The Potential Energy Surface (PES) is analogical to that of methanethiol, with some important quantitative differences. The two lowest excited states in the Franck–Condon region are of the A″ symmetry lying closer together than in the methanethiol case. While the C–S dissociation is accompanied by a small energy barrier for the 1A″ state in methanethiol,[12] both the C–S and C–H dissociation channels are open for EtSH. This is demonstrated by Fig. 2 displaying a two-dimensional cut through the PES calculated at the CASPT2 level along the two coordinates. The PES seems to be rather symmetric with respect to these two coordinates. A wavepacket promoted from the ground state (1A′) to the 1A″ excited state can thus in principle split into the two possible channels, forming either the SH or H fragments. However, we need to consider the masses connected with the two coordinates, since the true dynamics is reflected rather by the PES in mass weighted coordinates. There the slope towards the C–S dissociation will diminish compared to the S–H slope due to the much heavier S-atom mass compared to the mass of H. Due to these dynamical reasons, the system will follow the H-dissociation pathway which is very fast, while the SH dissociation is much slower.

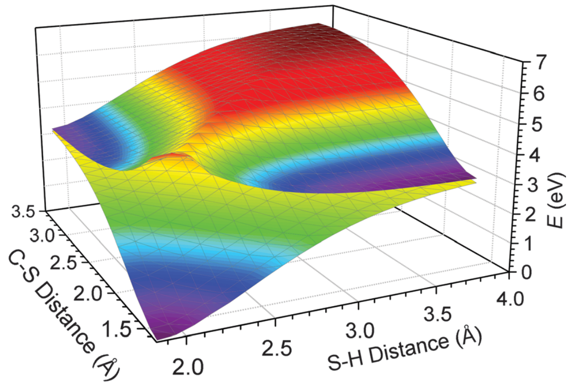

Fig. 2 The calculated PES for EtSH molecule dissociation along the S–H and C–S coordinates (see text for details).

4.2 Clusters

4.2.1 He-expansions. Some small clusters were generated already in He-expansions at elevated pressures P_0 = 2 and 3 bar and the EtSH reservoir temperature T_R = 263 K corresponding to the concentrations $C \approx 7.5\%$ and 5.0%, respectively. The mass spectrum shown in Fig. 3(a) exhibits a relatively strong dimer ion peak $(EtSH)_2^+$ at m/z 124 (M_2) with satellites shifted by ±1 and 2 H-atoms, $EtSH{\cdot}SH^+$ at m/z 95 (M + SH) with satellites, and even a small trimer ion $(EtSH)_3^+$ at m/z 186 (M_3). It is also interesting to note that the protonated monomer $EtSH{\cdot}H^+$ at m/z 63 (MH) becomes larger than the $EtSH^+$ peak and dominates the spectrum. Also protonated hydrogen sulfide H_3S^+ at m/z 35 increases with respect to the spectrum of isolated molecules, *i.e.*, this fragment is generated by intracluster reactions after the EI (compare to the monomer mass spectrum, Fig. S1 in ESI†).

This spectrum suggests that a significant amount of dimers and at least some trimers are present in the neutral beam. However, the hydrogen bonded clusters can fragment substantially upon electron ionization,[27] and thus even larger clusters could be present. On the other hand, the corresponding photodissociation image shown in the inset in Fig. 3(a) is very similar to the monomer images above. Only a very faint "central spot" can be distinguished upon a closer inspection of the image. This central spot is below recognized as the fingerprint of fragment caging in the clusters. Thus the image is dominated

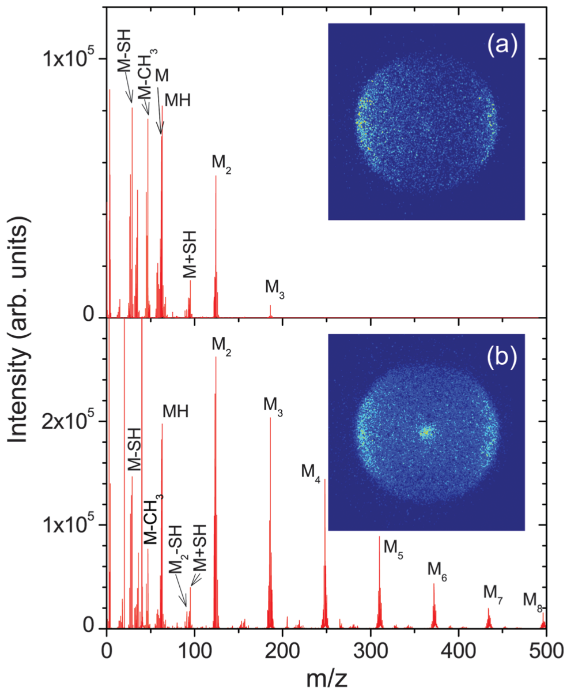

Fig. 3 The RTOFMS mass spectra recorded in expansions of (a) P_0 = 2 bar He, and (b) P_0 = 2 bar Ar, through the EtSH reservoir at T_R = 263 K corresponding to the concentration $C \approx 7.5\%$. The mass peaks corresponding to the $(EtSH)_n^+$ clusters are labeled. The insets show the corresponding velocity map images.

by the photodissociation of the monomers and free S–H bonds in the dimers and very little contribution comes from the larger clusters where the fragment caging is more probable as discussed below. The combined evidence from the mass spectra and images leads to the conclusion that the neutral beam is dominated by isolated molecules and dimers where the free S–H bonds can dissociate.

4.2.2 Ar-expansions. To generate the larger clusters, expansions in argon were exploited. The mass spectra recorded in Ar under the same conditions as He spectra above are shown in Fig. 3(b). The series of mass peaks corresponding to the $(EtSH)_n^+$ clusters up to n = 8 with a maximum at n = 2 is shown and even further peaks up to n = 15 are unambiguously discernible in the spectrum. All the cluster ion peaks are accompanied by smaller satellites shifted by $\pm k \cdot$H, k = 1–3. The dominance of $(EtSH)_n^+$ over the protonated $(EtSH)_n \cdot H^+$ clusters suggests a relatively weak hydrogen bond in the clusters (compared to analogue ethanol EtOH clusters where the mass spectra are dominated by protonated $(EtOH)_n \cdot H^+$ peaks[43]). Only for n = 1 the protonated $(EtSH) \cdot H^+$ peak exceeds the monomer $(EtSH)^+$ peak. There are also some minor fragments in between the major peaks corresponding to $(EtSH)_n \cdot SH^+$ (M_n + SH) at m/z M_n + 33 and $(EtSH)_n \cdot CH_3CH_2^+$ (M_{n+1}–SH) at m/z M_n + 29. These fragments mirror the most abundant (M–SH) fragment of the monomer: the C–S bond in the EtSH molecule is dissociated by EI and either the SH or CH_3CH_2 fragment remains attached to the charged cluster fragment. Thus the EI points to the C–S bond breaking in the EtSH molecule, while the UV photodissociation probes the S–H bond.

The inset in Fig. 3(b) shows the corresponding H-fragment image which now exhibits the clear central spot corresponding to zero-KE fragments. The $(EtSH)_N$ clusters generate cyclic hydrogen bonded structures for $N \geq 3$ as shown by our calculations. In these cyclic structures the released hydrogen dissociates against the neighboring heavy S-atom and can loose part of its energy in the collision. Further inelastic collisions within the cluster eventually slow down the fragment to zero-KE. It will be shown that the KED of the caged fragments peaks very sharply at around zero. Yet, it should be noted that the slow fragments still have to escape the cluster or the cluster has to decay in this process in order for the zero-KE fragments to be detected. Thus the caging for the observed fragments actually means that they are slowed down to $E_{\text{kin}} \approx 0$ eV but still released from the cluster. The calculated caging dynamics is described in the next section.

4.2.3 Cluster structure and caging dynamics. Similarly to hydrogen sulfide which possesses a weaker hydrogen bond compared to water, EtSH is less cohesive than EtOH. The enthalpy of vaporization is 27.2 kJ mol^{-1} for EtSH, which is almost two times smaller than that of the EtOH molecule (42.3 kJ mol^{-1}).[44] The EtSH vaporization enthalpy is consistent with the calculated binding energy of small EtSH clusters found in the range of 0.1–0.3 eV. Calculated structures of the complexes $(EtSH)_N$ are displayed in Fig. 4. The EtSH dimer exhibits a distorted hydrogen bond arrangement which is far from collinearity. In the larger $(EtSH)_N$ clusters the hydrogen bond becomes almost collinear.

Starting from N = 3, all the S–H bonds are involved in the hydrogen bonding, serving both as the hydrogen bond donors and acceptors. It is well known that the hydrogen bond in an excited state has distinctly different properties compared to the ground state.[45,46] The effect of the neighboring molecules on the EtSH dissociation is demonstrated in Fig. 5 where we

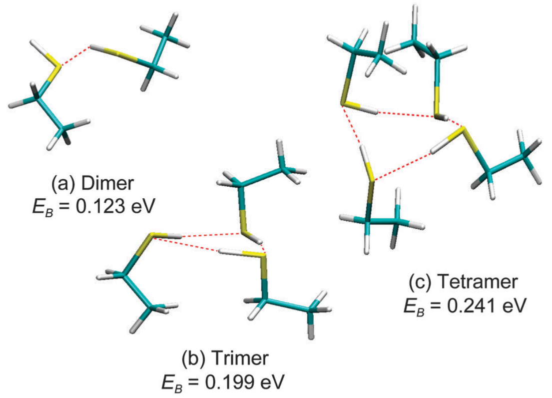

Fig. 4 The calculated structures and energetics of the small $(EtSH)_N$, N = 2–4, clusters. E_B is the binding energy per single molecular unit (the corresponding cartesian coordinates are given in the ESI†).

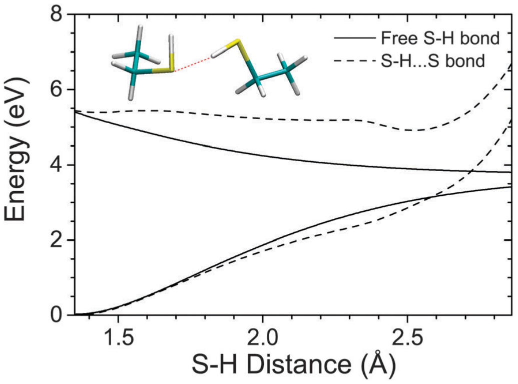

Fig. 5 The calculated PES for $(EtSH)_2$ dimer dissociation along the S–H free and bound coordinates. Structure of the dimer was taken from the larger tetrameric cluster.

compare potential energy curves for the ground and excited states of the EtSH monomer and dimer. The special structure of the dimer allows us to directly compare the dissociation of the free and hydrogen bond donating S–H groups.

If we excite the EtSH unit with the free S–H bond, we observe a direct dissociation, very much like for the isolated molecules (Section 4.1.2). The excess energy available upon the excitation with 5.1 eV photons estimated from this graph is in a good agreement with the KED peak maximum at 1.25 eV. On the other hand, if the hydrogen bond donating EtSH unit is excited, free dissociation is no longer possible. While the details of the potential curve depend on the particular geometrical arrangement (and on the basis set used), the general trends are clear: the ground state potential energy curve is affected only very little by the presence of the solvating molecule, the excited state feels the presence of the neighboring molecule almost immediately. The potential is not dissociative in this configuration and there is much less excess energy available. However, since the free zero-KE H-fragments are observed experimentally from the clusters the dissociation of the bonding hydrogen occurs. This can be facilitated by changing the cluster geometry in the excited state, which can occur upon the UV excitation due to vibrations in the ground state. Fig. S5 in the ESI† shows an example of how the excited state PES depends on the S–H···S bond angle: a small change in the angle can yield a dissociative pathway with very little excess energy.

4.2.4 Mixed clusters. Fig. 6(a) shows the KED and image (inset) obtained at P_0 = 2 bar Ar and T_R = 276 K corresponding to a higher EtSH concentration $C \approx 14\%$. The corresponding mass spectrum exhibits $(EtSH)_n^+$ clusters up to n = 13 (shown in the ESI†). The major difference with respect to Fig. 3(b) is that it is dominated by the monomer rather than the dimer mass peak. The images look also essentially the same except for a higher intensity allowing for a better evaluation of the KED. Although the central peak of caged fragments is clear in the image, the zero-KE fragment contribution in the KED is negligible and the spectrum is dominated by the fast fragments similar to the fragments from isolated molecules. The fast fragments can originate from the photodissociation of the isolated unclustered molecules in the beam as well as from the direct exit of the H-fragments after the EtSH dissociation in the clusters.[47]

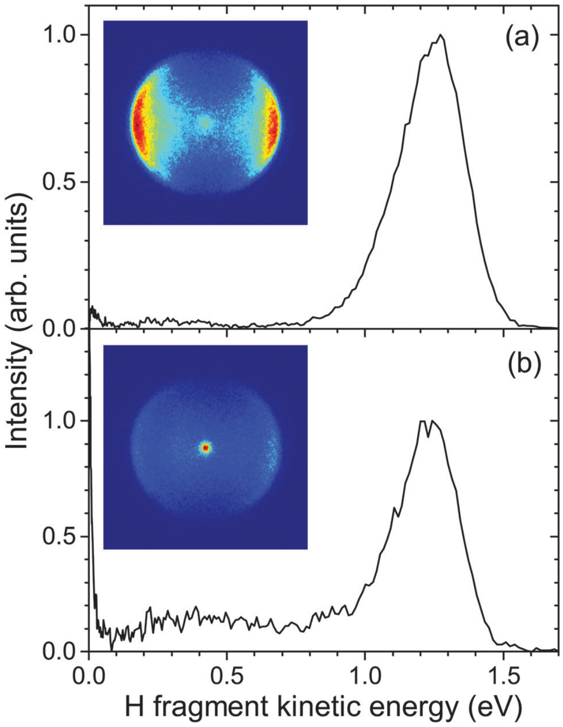

Fig. 6 The H-fragment KED recorded in the expansion of P_0 = 2 bar Ar through the EtSH reservoir at T_R = 276 K corresponding to the concentration $C \approx 14\%$ (a), and T_R = 233 K corresponding to $C \approx 1\%$ (b). The insets show the corresponding velocity map images.

Subsequently we tried to increase the clustering efficiency by increasing the buffer gas pressure to P_0 = 5 bar and then we gradually cooled down the reservoir temperature $T_R = 276 \rightarrow 220$ K, *i.e.* the EtSH concentration dropped from C = 5.6% to 0.2%. The photodissociation behavior and mass spectra gradually changed and several examples are given in the ESI.† Fig. 6(b) exemplifies the change in the H-fragment image and KED at T_R = 233 K (C = 1.0%). The central peak increased in intensity and strongly dominates the image. In the corresponding KED the zero-KE maximum also exceeds the fast fragment peak maximum by a factor of 1.4, although the zero-KE peak is very narrow (see ESI† for an extended part of KED near 0 eV). Upon further decreasing the concentration the peak of caged fragments increases with respect to the fast fragments until the spectrum exhibits essentially only the zero-KE fragments at C = 0.2%.

The mass spectra (see the ESI†) did not change dramatically with the decreasing concentration. The essential pattern of fragments discussed above remained. As the concentration decreased from C = 5.6% to 1.8% ($T_R = 276 \rightarrow 243$ K), the observed maximum cluster fragment ion $(EtSH)_n^+$ increased slightly from $n = 15$ to 17, and then it decreased to $n = 11$ with a further decrease of the concentration to 0.2% (T_R = 220 K). A small but noticeable change in the mass spectra occurred at around $C = 0.4\%$ (T_R = 228 K) where the Ar_m^+ cluster fragments start to appear with $m \leq 5$. Further below at $C = 0.3\%$ (T_R = 224 K) further argon clusters $m \geq 5$ occur in the spectra and additional new mixed peaks $EtSH_n \cdot Ar_m^+$, $n, m = 1, 2$ appear. This points to the generation of the mixed $EtSH_N \cdot Ar_M$ clusters.

We can combine the evidence from the mass spectra and VMI experiment to reveal some information about the size and composition of the neutral clusters:

(1) as the EtSH concentration in argon decreases from about 1.8% (T_R = 253 K), the largest observed $(EtSH)_n^+$ fragment size n decreases, suggesting smaller $(EtSH)_N$ neutral precursors;

(2) at the same time, with the decreasing concentration the zero-KE peak in VMI increases in comparison to the fast fragment peak, suggesting more fragment caging in the clusters, *i.e.* larger neutral cluster precursors;

(3) at low concentrations below 0.3% (T_R = 223 K) there are some mixed $(EtSH)_N \cdot Ar_M$ clusters in the beam;

Apparently (1) and (2) contradict each other and the contradiction can be resolved by assuming that large mixed $(EtSH)_N \cdot Ar_M$ clusters are generated at low EtSH concentrations where smaller $(EtSH)_N$ clusters are encaged in larger argon "snowballs" leading to H-fragment caging. On the other hand, the weakly bound Ar atoms leave the cluster during the EI process and therefore mostly bare $(EtSH)_n^+$ fragment ions occur in the mass spectra.

How large can the argon clusters be? The mean size $\bar{M}$ of Ar_M clusters generated in nozzle expansions can be calculated from the expansion conditions (stagnation pressure, nozzle shape and temperature) using Hagena's formula[48,49] which has recently been outlined explicitly for our apparatus elsewhere.[35] This formula yields $\bar{M} \approx 50$ for the current conditions assuming pure argon expansion. At low EtSH concentrations $\leq 1\%$ the expansion is probably not perturbed significantly by the EtSH molecules and the large Ar_M clusters can be generated. Yet, the condensation most likely starts with EtSH dimers and thus the Ar clusters will grow around the EtSH clusters. Therefore we tentatively propose that the cluster species generated at low EtSH concentrations ($\leq 1\%$) have a structure of about 50 argon atoms creating a "snowball" around about ≤ 10 EtSH molecules. It ought to be mentioned that this is in agreement with the previous experiments with hydrogen halides where for concentrations $\leq 1\%$ molecular species embedded in argon were generated, while at higher concentrations bare $(HX)_N$ clusters were produced.[47]

5 Conclusions

We investigated the photodissociation dynamics of the S–H bond in EtSH at 243 nm. The VMI experiment was accompanied by RTOFMS after EI. The experiments were performed in various expansion regimes corresponding to species ranging from isolated molecules to dimers and large clusters of more than 10 EtSH molecules, to EtSH clusters embedded in larger Ar species. In addition, the cluster nature and photodissociation dynamics were revealed by *ab initio* calculations. From the combination of the experimental results and theory the following picture emerged for the EtSH molecule dissociation:

- The strong anisotropy of the H-fragment suggested a direct dissociation of the S–H bond. While the calculations showed the purely repulsive nature of the potential energy curves along both the S–H and S–C coordinates, the dissociation channel associated with the S–C bond cleavage should be dynamically suppressed.
- The slow H-fragments observed previously[6] were due to the multiphoton processes.
- The fast H-fragment KED reflected the vibrational excitation of the co-fragment, most likely the wagging mode of the EtS fragment.

And for the clusters the following conclusions could be drawn:

- The H-fragments were caged in $(EtSH)_N$ clusters yielding zero-KE fragments beginning from the smallest clusters $N \geq 3$.
- The caging increased with the cluster size and dominated in the mixed Ar coated $(EtSH)_N \cdot Ar_M$ clusters, where essentially no fast H-fragments were observed.
- The caging resulted in very sharp zero-KE H-fragments clearly discernible from the slow fragments due to the multiphoton processes.
- Our *ab initio* calculations demonstrated a very strong effect of the environment on the excited states, rationalizing the efficient caging.

The unique feature of the present experiment is the combination of the VMI in tandem with a high resolution RTOFMS. It was demonstrated that the nature of the generated clusters was reflected in the H-fragment KEDs from the VMI, as well as in the mass spectra. The complete detailed information about the clusters, their approximate size, composition and dynamics was only revealed from the combination of the two experiments performed simultaneously on the same cluster beam, and none of these tools alone could provide the complete picture. In addition, a high level theory was necessary to fully reveal the cluster structure and photodissociation dynamics.

Acknowledgements

This work was supported by the Czech Science Foundation project Nos. 14-14082S and 14-08937S.

References

1 B. J. Finlayson-Pitts and J. N. Pitts, *Chemistry of the upper and lower atmosphere*, Academic Press, San Diego, 2000.
2 L. Bridges, G. L. Hemphill and J. White, *J. Phys. Chem.*, 1972, **76**, 2668.
3 P. H. Wine, R. J. Thompson and D. H. Semmes, *Int. J. Chem. Kinet.*, 1984, **16**, 1623.

4 A. T. J. B. Eppink and D. H. Parker, *Rev. Sci. Instrum.*, 1997, **68**, 3477.

5 M. N. R. Ashfold, N. H. Nahler, A. J. Orr-Ewing, O. P. J. Vieuxmaire, R. L. Toomes, T. N. Kitsopoulos, I. A. Garcia, D. A. Chestakov, S.-M. Wu and D. H. Parker, *Phys. Chem. Chem. Phys.*, 2006, **8**, 26.

6 J. Zhang, B. Jiang, X. Yang and J. Xie, *Chem. Phys. Lett.*, 2002, **364**, 80.

7 J. Segall, Y. Wen, R. Singer, M. Dulligan and C. Wittig, *J. Chem. Phys.*, 1993, **99**, 6600.

8 S. B. Barone, A. A. Turnipseed, T. Gierczak and A. R. Ravishankara, *J. Phys. Chem.*, 1994, **98**, 11969.

9 S. H. S. Wilson, M. N. R. Ashfold and R. N. Dixon, *J. Chem. Phys.*, 1994, **101**, 7538.

10 R. E. Stevens, C. Kittrell and J. L. Kinsey, *J. Phys. Chem.*, 1995, **99**, 11067.

11 L. J. Rogers, M. N. R. Ashfold, Y. Matsumi, M. Kawasaki and B. J. Whitaker, *J. Chem. Soc., Faraday Trans.*, 1996, **92**, 5181.

12 G. A. Amaral, F. Ausfelder, J. G. Izquierdo, L. Rubio-Lago and L. Bañares, *J. Chem. Phys.*, 2007, **126**, 024301.

13 Z. Chen, Q. Shuai, A. T. J. B. Eppink, B. Jiang, D. Dai, X. Yang and D. H. Parker, *Phys. Chem. Chem. Phys.*, 2011, **13**, 8531.

14 E. Jensen, J. S. Keller, G. C. G. Waschewsky, J. E. Stevens, R. L. Graham, K. F. Freed and L. J. Butler, *J. Chem. Phys.*, 1993, **98**, 2882.

15 L. J. Butler, *Annu. Rev. Phys. Chem.*, 1998, **49**, 125.

16 B. Mouflih, C. Larrieu and M. Chaillet, *Chem. Phys.*, 1998, **119**, 221.

17 D. Yarkony, *J. Chem. Phys.*, 1994, **100**, 3639.

18 J. E. Stevens, K. F. Freed, M. F. Arendt and R. L. Graham, *J. Chem. Phys.*, 1994, **101**, 4832.

19 J. E. Stevens, H. W. Jang, L. J. Butler and J. C. Light, *J. Chem. Phys.*, 1995, **102**, 7059.

20 D. Yarkony, *J. Chem. Phys.*, 1996, **104**, 7866.

21 T. Bing and P. Shou-Fu, *Chin. Phys. B*, 2008, **17**, 1501.

22 B. G. Keyes and A. G. Harrison, *J. Am. Chem. Soc.*, 1968, **90**, 5671.

23 Y.-S. Cheung, C.-W. Hsu, J.-C. Huang, C. Y. Ng, W.-K. Li and S.-W. Chiu, *Int. J. Mass Spectrom.*, 1996, **159**, 13.

24 S. Choi, T. Y. Kang, K.-W. Choi, S. Han, D.-S. Ahn, S. J. Baek and S. K. Kim, *J. Phys. Chem. A*, 2008, **112**, 7191.

25 V. Poterya, J. Lengyel, A. Pysanenko, P. Svrčková and M. Fárník, *J. Chem. Phys.*, 2014, **141**, 074309.

26 V. Poterya, J. Kočišek, A. Pysanenko and M. Fárník, *Phys. Chem. Chem. Phys.*, 2014, **16**, 421.

27 J. Lengyel, A. Pysanenko, V. Poterya, J. Kočišek and M. Fárník, *Chem. Phys. Lett.*, 2014, **612**, 256.

28 J. Lengyel, A. Pysanenko, V. Poterya, P. Slavíček, M. Fárník, J. Kočišek and J. Fedor, *Phys. Rev. Lett.*, 2014, **112**, 113401.

29 M. Fárník and V. Poterya, *Front. Chem.*, 2014, **2**, 4.

30 B. Whitaker, *Imaging in Molecular Dynamics*, Cambridge University Press, Cambridge, 2003.

31 V. Dribinski, A. Ossadtchi, V. A. Mandelshtam and H. Reisler, *Rev. Sci. Instrum.*, 2002, **73**, 2634.

32 J. Fedor, J. Kočišek, V. Poterya, O. Votava, A. Pysanenko, L. Lipciuc, T. N. Kitsopoulos and M. Fárník, *J. Chem. Phys.*, 2011, **134**, 154303.

33 J. Kočišek, J. Lengyel and M. Fárník, *J. Chem. Phys.*, 2013, **138**, 124306.

34 J. Lengyel, R. Gorejová, Z. Herman and M. Fárník, *J. Phys. Chem. A*, 2013, **117**, 11225.

35 J. Kočišek, J. Lengyel, M. Fárník and P. Slavíček, *J. Chem. Phys.*, 2013, **139**, 214308.

36 S. Grimme, S. Ehrlich and L. Goerigk, *J. Comput. Chem.*, 2011, **32**, 1456.

37 NIST, Precomputed vibrational scaling factors, http://cccbdb.nist.gov/vibscalejust.asp.

38 M. J. Frisch, G. W. Trucks, H. B. Schlegel, G. E. Scuseria and M. A. Robb, *et al.*, *Gaussian 09 Revision D*, Gaussian Inc., Wallingford, CT, 2009.

39 H.-J. Werner, P. J. Knowles, G. Knizia, F. R. Manby and M. Schütz, *et al.*, *MOLPRO, version 2012.1, a package of ab initio programs*, 2012, see "http://www.molpro.net".

40 NIST Mass Spec Data Center, S.E. Stein, director,"Mass Spectra" in NIST Chemistry WebBook, NIST Standard Reference Database Number 69, ed. P. J. Linstrom and W. G. Mallard, National Institute of standards and Technology, Gaithersburg MD, 20899, http://webbook.nist.gov, June 2005.

41 V. Poterya, M. Fárník, P. Slavíček, U. Buck and V. V. Kresin, *J. Chem. Phys.*, 2007, **126**, 071101.

42 M. Ončák, P. Slavíček, V. Poterya, M. Fárník and U. Buck, *J. Phys. Chem. A*, 2008, **112**, 5344.

43 B. D. Kay and A. W. Castleman, *J. Phys. Chem.*, 1985, **89**, 4867.

44 V. Majer and V. Svoboda, *Enthalpies of Vaporization of Organic Compounds: A Critical Review and Data Compilation*, Blackwell Scientific Publications, Oxford, 1985.

45 P. Slavíček and M. Fárník, *Phys. Chem. Chem. Phys.*, 2011, **13**, 12123.

46 M. Fárník, P. Slavíček and U. Buck, in *Hydrogen Bonding and Transfer in the Excited State II*, ed. K.-L. Han and G.-J. Zhao, Wiley, Chichester, UK, 2011, p. 865.

47 U. Buck, *J. Phys. Chem. A*, 2002, **106**, 10049.

48 O. F. Hagena, *Surf. Sci.*, 1981, **106**, 101.

49 U. Buck and R. Krohne, *J. Chem. Phys.*, 1996, **105**, 5408.

Appendix B

Na-doping and solvated electron reactivity

Chemical Physics Letters 612 (2014) 256–261

Contents lists available at ScienceDirect

Chemical Physics Letters

journal homepage: www.elsevier.com/locate/cplett

Editors Choice

Extensive water cluster fragmentation after low energy electron ionization

Jozef Lengyel[1], Andriy Pysanenko, Viktoriya Poterya, Jaroslav Kočišek, Michal Fárník*

J. Heyrovský Institute of Physical Chemistry v.v.i., Academy of Sciences of the Czech Republic, Dolejškova 3, 18223 Prague, Czech Republic

ARTICLE INFO

Article history:
Received 23 July 2014
In final form 13 August 2014
Available online 19 August 2014

ABSTRACT

Water clusters $(H_2O)_N$ from the size range $\bar{N} \approx 10$–150 have been investigated by electron ionization (EI) and photoionization after Na-doping (NaPI) under identical experimental conditions. The NaPI yields cluster sizes in good agreement with a semiempirical formula derived previously. The EI leads to large cluster fragmentation even at electron energies near the ionization threshold at 13 eV. The fragmentation does not change significantly between 15 eV and 90 eV. For $\bar{N} = 138$ the mean cluster ion fragment size corresponds to only about 10% of the original neutral cluster size.

1. Introduction

Water clusters have been the subjects of intense research activities due to their importance in environmental sciences and biosciences, as well as due to the omnipresence of water as the most important polar solvent [1–3]. Large $(H_2O)_N$ clusters with $\bar{N} \approx 10$–10^3 represent laboratory model to mimic important systems and processes, e.g., cloud particle and aerosol nucleation [4–8], chemistry and photochemistry on ice particles in atmosphere [9–12], processes in radiation chemistry [13], processes in chemistry and biology induced and controlled by solvent [14], etc. In many laboratory studies water clusters are detected by mass spectrometric methods. Therefore the cluster ionization is of prime importance and was investigated by various means [15–21].

The ionization of the water $1b_1$ (HOMO) orbital in the bulk leads ultimately to the hydronium cation H_3O^+ and $OH^\bullet$ radical:

$$H_2O^+ + H_2O \rightarrow H_3O^+ + OH^\bullet. \quad (1)$$

The proton transfer from the H_2O^+ radical occurs with almost 100% efficiency within 40 fs [22,23]. In this process about 1 eV energy is released [23]. This is sufficient to evaporate the $OH^\bullet$ radical from the hydronium in a cluster. Therefore the direct ionization of $(H_2O)_N$ clusters yields typically the protonated $(H_2O)_nH^+$ fragments [24,18,25]. This observation is independent of the ionization method, whether electron- or photoionization is implemented [26]. The non-protonated $(H_2O)_n^+$ ions were observed upon ionization of water clusters solvated with rare gas atoms [20,21,27–29]. Nevertheless, an infrared spectroscopy of the water clusters showed that the non-protonated clusters have the structure $H_3O^+\cdots OH^\bullet$, i.e., the proton transfer still takes place [30,31].

One of the important questions concerning the water cluster ionization is the cluster fragmentation: What was the original neutral cluster size? And intimately related is the question of the energy distribution: What energy is deposited into the cluster in the ionization process? How is it distributed over the cluster degrees of freedom? The water cluster fragmentation and energy transfer processes after the ionization are still not completely understood. In this article we compare the electron ionization (EI) mass spectra of water clusters to the spectra obtained by special ionization method of photoionization after Na-doping (NaPI), which is essentially free of cluster fragmentation [32,33]. This method will be outlined in Section 2.

A comprehensive investigation [17] of the metastable fragmentation of protonated water clusters after a chemical ionization revealed that the cluster decay could be analyzed employing an evaporative cooling model [34]. In this model the fast proton transfer (1) and $OH^\bullet$ radical loss process was followed by slow water molecule evaporation process. The chemical ionization process generated the protonated water clusters with small amounts of internal energy, which was reduced by subsequent evaporation of water molecules. More recently Belau et al. [18] published a comprehensive study of vacuum ultraviolet (VUV) ionization of $(H_2O)_N$ water clusters up to $N = 79$. They measured the appearance energies of different cluster sizes, and analyzed the cluster metastable decay near the threshold. Metastable loss of up to three water molecules was observed.

---

* Corresponding author.
E-mail address: michal.farnik@jh-inst.cas.cz (M. Fárník).

[1] Also at: Department of Physical Chemistry, Institute of Chemical Technology, Technická 5, Prague 6, Czech Republic.

http://dx.doi.org/10.1016/j.cplett.2014.08.038

Table 1
The expansion conditions exploited in the present work. The stagnation pressure p_0 corresponds to the reservoir temperature T_R, and the mean neutral cluster sizes $\bar{N}$ were calculated using Eqs. (2) and (3).

Nozzle parameters	Diameter d	Opening angle α	Length
	100 ± 5 μm	33 ± 1°	2 mm
Nozzle temperature T_0 (K)	423 ± 5 K		
Reservoir temperature T_R (K)	352 ± 5–398 ± 5 K		
Stagnation pressure p_0 (K)	0.45 ± 0.09–2.26 ± 0.35 bar		
Mean cluster size N (K)	8 ± 3–138 ± 26		
Na-oven temperature: 513 K		Cap temperature: 493 K	

Little fragmentation of water cluster after near threshold VUV photoionization was also reported by Signorells' group [33,35]. They compared the VUV ionization mass spectra to the spectra obtained by NaPI. The NaPI method was fragmentation-free, and thus revealed the original neutral cluster size distribution. On the other hand, relatively large difference was observed between the electron ionization and NaPI in Bucks' group [32]. They studied large water clusters of the mean size $\bar{N} \approx 1200$ bombarded by high energy (550 eV) electrons, and measured the loss of ≈280–450 molecules from the $(H_2O)_N$ clusters. A sputtering model rather than evaporation was used to describe the observed large fragmentation. The fragmentation was also analyzed using a theoretical model of cluster heating and molecular dynamics simulations [36].

The main question addressed here is: What is the water cluster fragmentation pattern for low energy electrons? Will the electron ionization at some lower energy become 'soft ionization' similar to the threshold photoionization? We seek the answers by a direct comparison of the water cluster mass spectra after EI and NaPI methods. For the first time such comparison has been possible for low energy electrons near the ionization threshold, enabled by the recent implementation of NaPI in our experiment.

2. Experiment

The present experiment was performed on the CLUster Beam apparatus (CLUB) [37]. The apparatus has recently been extended with further options enabling different experiments with clusters: the photofragment velocity map imaging (VMI), the electron ionization time-of-flight mass spectrometry, and the cluster pickup cross section determination from velocity measurements. The apparatus description can be found in the corresponding publications [38,39]. Here we introduced yet another experimental method: NaPI which further increased the versatility of the present setup.

The clusters were produced by supersonic expansions of pure water vapor under different conditions outlined in Table 1. The clusters passed a skimmer and a differentially pumped vacuum chamber. In the next chamber they could be doped by Na-atoms evaporated in an oven. The oven was the same as used in Refs. [32,40]. Subsequently, the clusters passed through the VMI chamber, and in the next chamber the clusters were analyzed by a reflectron time-of-flight mass spectrometer (RTOF) described in more detail elsewhere [41,21]. The clusters were ionized by electrons with variable energy 5–90 eV with 0.7 eV resolution at 10 kHz repetition frequency (EI). The mass spectra were recorded with the resolution of $M/\Delta M \approx 10^4$. Alternatively, the Na-doped clusters were ionized by 315 nm (3.9 eV) photons with 10 Hz repetition frequency (NaPI). Figure 1 represents a schematic picture of the present ionization experiments.

The 315 nm radiation was produced by frequency doubling output of the dye laser at 630 nm (LAS) pumped with the second harmonics 532 nm of the Nd:YAG laser (Spectra Physics, GCR-4). The typical UV energy at the chamber entrance was 2 mJ/pulse focused by f = 400 mm lens through a fused silica window into the ionization region of the mass spectrometer. Attention was paid to avoid multiphoton ionization, and ionization by electrons emitted from electrodes by the UV radiation.

The NaPI method was first introduced by Bucks' group [32,40]. Later on, it was suggested by Signorells' group as a 'sizer for weakly bound ultrafine aerosol particles' due to the fragmentation-free ionization [33]. It is also used in Zeuchs' group in connection with the vibrational spectroscopy of large size selected clusters [42–44]. Yet, the implementation of this method as the sizer for neutral clusters is still relatively new and scarce. The essential idea is doping the clusters with Na in a pickup process. For water clusters this results in generating Na^+ and an electron, which is generally termed solvated or aqueous electron e^-_{aq} in the literature although it resides on the cluster surface [42]. The weakly bound solvated electrons can be detached by UV photons of relatively low energies 3–4 eV, and the remaining $(H_2O)_N{\cdot}Na^+$ cluster ion can be detected by the mass spectrometer. This method is essentially fragmentation-free due to the very low ionizing photon energy and thus the mass spectrum reflects the original neutral cluster size distribution. Although, we have recently demonstrated that this method is not universal and possible reactions of sodium with cluster constituents can lead to unexpected results [41], for the pure water clusters this method yields the neutral cluster size distributions [32]. More details can be found in [32,33,35,40,43–45].

Based on this method Buck's group measured the cluster size distributions of $(H_2O)_n$ clusters generated in supersonic expansions of pure water vapor. The mean cluster sizes could be obtained using the Hagena's scaling laws [46–49]:

$$\bar{N} = K \cdot \left(\frac{\Gamma^*}{1000}\right)^{\zeta}. \tag{2}$$

The dimensionless parameter Γ^* was derived from the NaPI experiments [32]:

$$\Gamma^* = \frac{n_0 \cdot d_e^q \cdot T_0^{q-3}}{K_{ch}}, \tag{3}$$

where the parameters K = 11.6, ζ = 1.886 and q = 0.634 were determined fitting the measured mean sizes. The equivalent nozzle diameter $d_e = k \cdot (d/(\tan(\alpha/2))$ is given by the nozzle throat diameter d and its opening angle α (d = 100 μm, α = 33° in the present experiments, and k =0.933 for H_2O). The characteristic constant $K_{ch} = r_{ch}^{q-3} T_{ch}^{q-3}$ for H_2O derives from the molecular parameters r_{ch} = 3.19Å, and T_{ch} = 5684 K the meaning of which is explained in [32]. The gas density n_0 can be evaluated from the stagnation pressure p_0 through the ideal gas law. The present expansion conditions are summarized in Table 1.

We concentrate on the size range between 10 and 150 molecules for two reasons. First, this is the size range mostly relevant for our investigations of photochemistry on water clusters. Second, experimental reason is the RTOF mass discrimination. The accommodation of different experiments on CLUB dictates the perpendicular arrangement of the RTOF to the molecular beam. Different clusters attain a uniform velocity in a supersonic expansion (≈1400 ms^{-1} in the present experiments). Thus the different cluster sizes poses largely different kinetic energies, e.g., between 200 meV and 200 eV for $(H_2O)_N$ clusters between N = 1 and 10^3, respectively. To avoid loss of the clusters from the RTOF detector due to their momentum in the beam direction a special design was applied: namely high extraction voltages (≈10 kV) and large area MCP detector (40 mm active area diameter). Yet, the mass spectra which span across a large mass range ≥10^3 amu cannot be all accommodated on the detector, and attention must be paid to the mass discrimination. We have calibrated our RTOF with perfluorotributylamine (FC-43) for which the mass peak intensities in the range 1–500 amu are

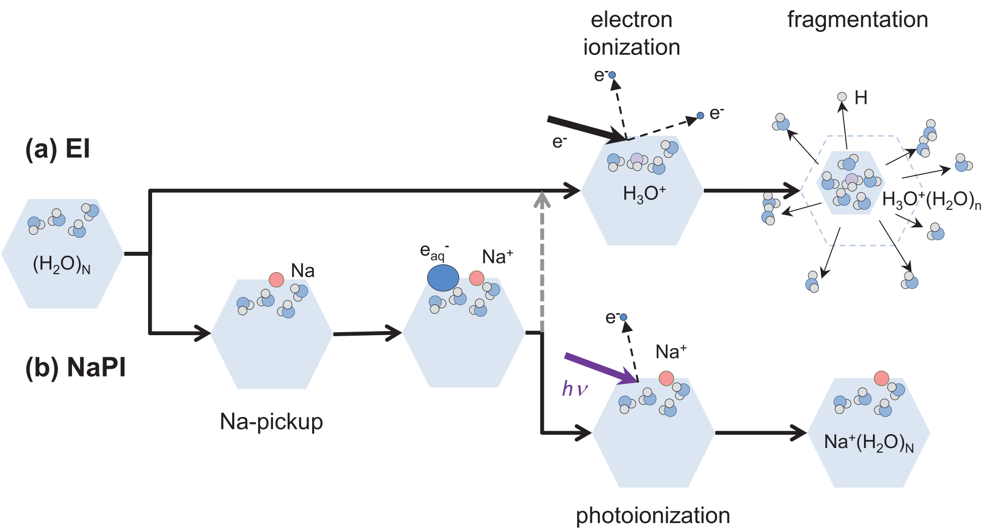

Figure 1. Schematic representation of the present water cluster ionization methods: (a) electron ionization (EI), (b) photoionization after Na-doping (NaPI).

tabulated. In addition, measurements of well known spectra of Ar_N clusters suggest that we can rely on relative intensities in the mass range up to ≈10^3 amu. We could easily set the mass spectrometer to detect much higher masses ≥10^4 amu. Yet, we discriminated the smaller masses upon the corresponding settings. Therefore we concentrated on the clusters below ≈10^3 amu where the RTOF sensitivity was calibrated.

3. Results and discussion

3.1. Electron ionization

First, we compared EI mass spectra for clusters generated under different expansion conditions, i.e., different reservoir temperatures T_R corresponding to different pressures p_0, and resulting in the mean cluster sizes $\bar{N}$ according to Eqs. (2) and (3). Figure 2 shows the electron ionization mass spectra at the typical electron energy of 70 eV. This energy is broadly used in the mass spectrometry due to the maximum ion yield for most species. The calculated $(H_2O)_N$ mean cluster sizes $\bar{N}$ are indicated in the figure. The spectra show the mass peaks of the protonated $(H_2O)_nH^+$ fragments in dependence on n. The insets show the integrated mass peak intensities from which the mean cluster sizes were evaluated as:

$$\bar{n} = \frac{\sum n \cdot I_n}{\sum I_n}, \tag{4}$$

where I_n are the integrated mass peak intensities of the $(H_2O)_nH^+$ clusters. These sizes are indicated in Figure 2 as $\bar{N}_e$.

The results clearly show two major points: (i) $\bar{N}_e$ depends only very slightly on the expansion conditions, although $\bar{N}$ ranges from 8 to 138; (ii) $\bar{N}_e$ is significantly smaller than $\bar{N}$ (with the exception of the smallest clusters). These results indicate an extensive cluster fragmentation upon 70 eV electron ionization.

3.2. Photoionization after Na-doping

The NaPI method serves the purpose to reveal the fragmentation-free mass spectra reflecting the original neutral cluster size distributions. The 'soft' photodetachment of e_{aq}^- from $Na+ \cdot e_{aq}^-$ pair leaves the cluster essentially unperturbed, as outlined in Section 2. Figure 3 shows the mass spectra obtained by 315 nm photoionization of Na-doped water clusters. The spectra show the mass peaks of the doped $(H_2O)_N{\cdot}Na^+$ clusters in dependence on N. The clusters $(H_2O)_N$ were generated under the same expansion conditions as in Figure 2a–c. The spectrum for $\bar{N} = 138$ (Figure 2d) was omitted from Figure 3, since it was already influenced by the mass discrimination.

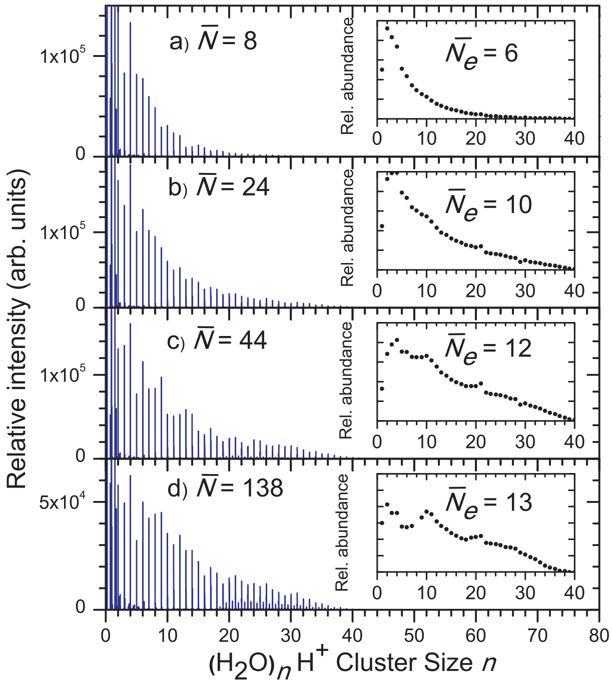

Figure 2. The EI mass spectra measured at $E_e = 70$ eV electron energy for $(H_2O)_N$ with the mean cluster sizes $\bar{N} = 8$ (a), 24 (b), 44 (c), and 138 (d). The axis shows the size n of the protonated $(H_2O)_nH^+$ fragments. The insets show the integrated peak intensities. The mean cluster sizes $\bar{N}_e$ calculated from the integrated spectra are indicated.

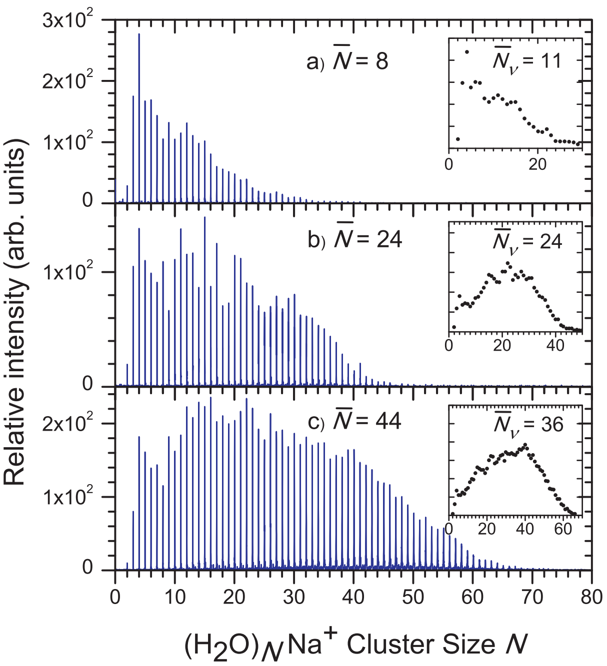

Figure 3. The mass spectra obtained by NaPI method for expansion conditions corresponding to $\bar{N} = 8$ (a), 24 (b), and 44 (c). The axis shows the size N of $(H_2O)_NNa^+$ clusters. The insets show the integrated peak intensities. The mean cluster sizes $\bar{N}_v$ evaluated from the integrated spectra are indicated.

The mean cluster sizes indicated in Figure 3 have been evaluated using Eq. (4). Besides, the integrated intensities were fitted with the log-normal function:

$$f(N) = \frac{A}{\sqrt{2\pi}\sigma N} \exp\left[-\left(\frac{\ln N - \mu}{\sqrt{2}\sigma}\right)^2\right], \tag{5}$$

and the mean sizes evaluated as $\bar{N}_v = e^{\mu}$. The log-normal distributions were derived and tested in Ref. [32] rather for the larger sizes $\bar{N} \geq 100$. Nevertheless the mean cluster sizes derived according to Eq. (5) agreed well with the ones evaluated directly by the spectra integration (4), although the fits were not perfect. The obtained values $\bar{N}_v$ are indicated in Figure 3 and agree well with the mean sizes $\bar{N}$ calculated by formulas (2) and (3).

It ought to be mentioned that in both EI and NaPI spectra the integrated mass peak intensities were used to obtain the mean size rather than just the mass peak maxima, since the peak width increased with the ion fragment size. Also double-peaks were observed originating from a metastable decay of the nascent $(H_2O)_nH^+$ ions in the RTOF. The origin and analysis of such double-peaks (and multiple-peaks) for various clusters was discussed by Castleman's group [17,50]. It also revealed the metastable decay of water cluster ions after the threshold VUV ionization [18]. However, here we concentrate on the total cluster fragmentation upon the electron ionization, therefore we integrate the intensities of the metastable fragments with their parent ions. It is also worth noting that the integrated intensities of EI spectra clearly exhibit the well known special stability peak at $n = 21$ [51].

We can discuss to what extent the cluster size measured by NaPI method reflects the original neutral cluster size. The NaPI can yield somewhat smaller clusters even if the ionization procedure is fragmentation free, since water molecules can be evaporated from the cluster due to the energy deposited in the collision with Na, and due to the solvation of Na in the cluster. Considering the measured cluster beam velocity of 1400 ms^{-1} and neglecting the randomly oriented thermal velocity of Na atom, the energy deposited into the cluster in a sticking collision with Na corresponds to 230 meV. The binding energy of a water molecule to the larger $(H_2O)_N$ cluster exceeds 400 meV. Thus the energy deposited into the cluster in the collision is not sufficient to evaporate water molecules, and the collision energy is assumed to have a negligible effect on the cluster size. We have recently tested this effect also by molecular dynamics simulations of $H_2O + (H_2O)_N$ collisions resulting in no cluster evaporation [7,8]. Another energy contribution is due to the solvation of the Na in water. The solvation energy of an Na atom can be estimated based on the difference between Na atom ionization potential in the gas phase (5.1 eV) and in water clusters (~3 eV) [43], and considering the hydration energy of Na^+ ion in water (4.2 eV) [52]. This yields about 2 eV solvation energy. A more conservative estimate based on the difference between 'intact complex' and 'solvated electron' published in Table 6 of Ref. [43] would yield even less than 1 eV of solvation energy. Thus the solvation energy can evaporate at most 5 water molecules. In addition, this energy can be quickly dissipated over many internal cluster degrees of freedom. Thus, in principle, the Na doping can result in somewhat smaller measured cluster sizes, yet the number of evaporated molecules from the clusters is usually neglected compared to the original cluster size especially for the larger clusters. Besides, it has no influence on the difference in the cluster sizes obtained by EI and NaPI methods presented here.

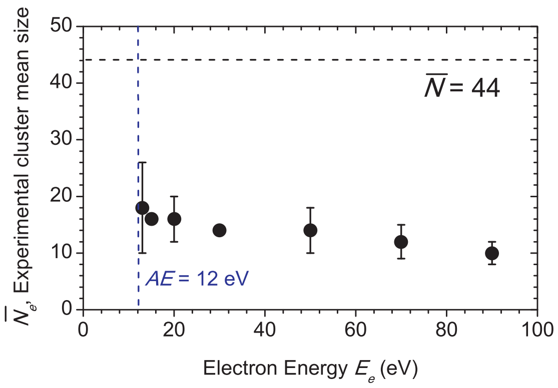

Figure 4. The mean cluster sizes $\bar{N}_e$ measured for the water clusters with the mean size $\bar{N} = 44$ in dependence on the ionizing electron energy from 13 eV to 90 eV.

3.3. *Electron energy dependence*

There is a large difference between the NaPI and EI mass spectra. The electron ionization at 70 eV leads to the extensive fragmentation and the cluster loses most of its constituents. The EI of the largest $(H_2O)_N$ clusters investigated here with the mean size $\bar{N} \approx 138$ resulted in the $(H_2O)_nH^+$ fragments with the mean size $\bar{N}_e \approx 13$, which corresponds to the evaporation of 90% of the ionized cluster. Can the excessive fragmentation be caused by the impinging electron energy? It is known from the electron ionization studies of large molecules and clusters [53–57] that only a small fraction of the electron energy is deposited in the molecule, and most of the energy is carried away by the electrons. Fragmentation measurements of small size selected argon clusters demonstrated that less than 2 eV out of the 70 eV were deposited in the cluster [55].

Thus we investigate the EI mass spectra in dependence on the electron energy E_e. Figure 4 shows the mean cluster size $\bar{N}_e$ evaluated from the spectra as a function of E_e. The spectra change only slightly between 13 eV and 90 eV. Even at the lowest measured energy $E_e = 13$ eV the mean size $\bar{N}_e = 18$ was still significantly

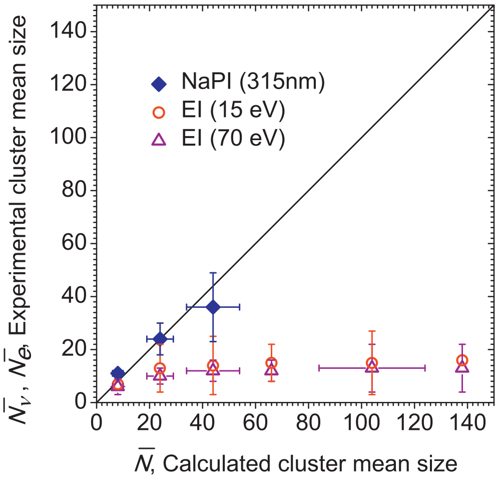

Figure 5. The comparison of the mean cluster sizes measured by EI and NaPI methods, and calculated from scaling formulas.

smaller compared to the neutral cluster size $\bar{N} = 44$. The decreasing error bars with E_e reflect the signal increase with the increasing electron energy. Therefore the integration time required to obtain spectra of comparable intensity at low energies is much longer than at high E_e. Subsequently, more experimental $\bar{N}_e$ measurements were averaged to yield the points at high E_e leading to the smaller error bars. Similar spectra independence of the electron energy was observed also for the other cluster sizes. Thus the strong fragmentation upon EI does not depend significantly on the electron energy.

The ionization potential of an isolated water molecule is 12.6 eV and decreases to less than 11 eV in larger clusters and in the bulk [18]. In our recent electron ionization study [21] we have observed $(H_2O)_nH^+$ appearance energy (AE) 12 ± 0.4 eV. This value has been obtained by averaging AE values for n ranging between 2 and 8. Thus the measurements at 13 eV were done just above this AE. Therefore the signals were relatively low as expressed by the large error bars at $E_e = 13$ eV in Figure 4. Nevertheless, relatively strong spectra showing the large cluster fragmentation were unambiguous already at 15 eV for all investigated cluster sizes. Therefore we claim the fragmentation independence of the electron energy in the region 15–90 eV.

3.4. Cluster fragmentation

The comparison of the mean cluster sizes measured by EI and NaPI methods, and calculated from scaling formulas is summarized in Figure 5. The $\bar{N}_e$ and $\bar{N}_\nu$ values evaluated from EI and NaPI methods, respectively, are plotted as a function of the corresponding cluster mean size $\bar{N}$ calculated from Eqs. (2) and (3). The error bars on the data deserve some discussion. The horizontal errors reflect the uncertainty in determining the calculated size $\bar{N}$ which encompass uncertainties in the determination of nozzle diameter d ($\pm 5\ \mu$m), divergence angle α ($\pm 1^\circ$), and reservoir temperature T_R (± 5 K) (and thus the corresponding pressure p_0). The later is also the reason for displaying a limited number of $\bar{N}$ points for EI. The mass spectra were measured under different temperatures T_R which were grouped by $\Delta T_R = 10$ K. Each group was assigned $\bar{N}$ according to the central T_R, thus each point in Figure 5 is average of 2–10 experimental points. The vertical error bars correspond to the standard deviations of these averages. They also reflect the reproducibility of the mass spectra measurements repeated over an extended time period. Two sets of EI points are plotted in Figure 5 corresponding to 70 eV (triangles) and 15 eV (circles) electron ionization energies. It can be seen that the difference in the fragment mean size is very small and independent of the neutral cluster size $\bar{N}$.

The size range for which the NaPI method can reveal the true neutral cluster size distribution is relatively limited due to the RTOF mass discrimination in the perpendicular arrangement, as discussed above. Nevertheless, in the covered region there is a good agreement between the measured $\bar{N}_\nu$ and calculated $\bar{N}$. The previous comprehensive measurements of Bobbert et al. [32] leading to the formulas (2) and (3) were done mainly for the larger clusters $N \geq 10^2$. The present agreement suggests the applicability of these formulas also for the smaller clusters. We can assume that the NaPI mass spectra reflect approximately the original neutral cluster size distributions.

In the view of the large difference between EI and NaPI spectra, we have to ask if the same species are ionized in both cases. Indeed, both experiments were performed simultaneously with the same cluster beam. However, there was a difference in the probed species between the two ionization methods: while the EI method is universal, NaPI method ionizes only the clusters with Na atoms adsorbed. Therefore we measured also the EI spectra on the clusters doped with Na. These spectra were essentially identical with the pure water cluster spectra obtained under the same conditions, dominated by the protonated $(H_2O)_nH^+$ fragments.

Only when the Na-oven temperature was increased significantly to 633 K, the mixed ion fragments with Na could be detected, namely $(H_2O)_N{\cdot}Na^+$ and even $(H_2O)_N{\cdot}Na_m^+$ with $m \geq 1$. Nevertheless, the fragment distribution after EI did not change with Na-pickup still exhibiting the strong fragmentation. The mass spectra were dominated by $(H_2O)_nH^+$ fragments without Na, even under the conditions when all the clusters are supposed to adsorb some Na atoms (based on the mean geometrical cross-section of the clusters and estimated Na-pressure in the oven). This suggests that the Na atoms (or the Na^+ and e_{aq}^- ion pairs) are evaporated in the EI process.

The large fragmentation of $(H_2O)_N$ clusters $\bar{N} = 10^2$–10^3 at high electron energies of 550 eV was analyzed by a sputtering model [32]: the ionizing electron generates electronic excitations along the penetration path into the target, then the excitation converts into the vibrational excitation of the molecules which is transported to the surface where the molecules evaporate. This process evaporates molecules from the finite size clusters much more efficiently than a bulk solid. Beu et al. [36] analyzed theoretically the fragmentation statistics of the large water clusters using molecular dynamics simulations at different temperatures and percolation theory. The agreement with the experimental data suggested that the interaction of the high energy electrons with the clusters could be described by a fragmentation theory based on cluster heating. The main feature of these models was that the maximum and mean fragment sizes were dependent on the original neutral cluster size. However, the present investigations show rather independence of the fragment sizes from the neutral precursor size $\bar{N}$ as well as from the electron energy. But the fragmentation also does not correspond to the ‘evaporation’ model usually applied at low energies, where only few molecules are evaporated from the large cluster [34,17,18]. Therefore the present data call for a new theoretical model.

4. Conclusions

The electron ionization ($E_e = 13$–90 eV) and photoionization ($\lambda = 315$ nm) after Na-doping have been measured in the same experiment for $(H_2O)_N$ clusters in the size range $\bar{N} \approx 10$–150.

- The NaPI method yields cluster sizes in good agreement with the scaling formula derived previously [32]. The scaling laws were based on the NaPI measurements especially for larger clusters $\bar{N} \geq 10^2$. The validity of these formulas for the smaller clusters is of special interest for our photochemistry investigations.
- The EI leads to a large cluster fragmentation. For $\bar{N} = 138$ the ionized fragment size corresponds to only about 10% of the original neutral cluster. This is important to take into account especially in water cluster studies where the cluster sizes are estimated from the electron ionization spectra typically at 70 eV electron energy.
- The observed cluster fragmentation does not correspond to the metastable evaporation of a few molecules observed in near threshold VUV ionization [18,35]. However, it also does not follow the power law of statistical model [36] or cluster sputtering [32]. Therefore a new theory is required for the present case of the interaction of low energy ($E_e \leq 100$ eV) electrons with water clusters.

In addition, especially for Na-doped clusters the actual detailed mechanism of both electron ionization and photoionization have to be elucidated. More experimental work is under way in our group to explore these processes. Also involvement of theory is highly desirable to elucidate the ionization process of Na-doped water clusters.

Nevertheless, the main message of the present letter remains an unambiguous experimental fact: namely, that the electron ionization of water clusters leads to strong fragmentation even at the electron energies near to the ionization threshold.

Acknowledgment

This work has been supported by the Grant Agency of the Czech Republic project Nos.: 14-08937S and 14-14082S.

References

[1] B.J. Finlayson-Pitts, J.N. Pitts, Chemistry of the Upper and Lower Atmosphere, Academic Press, San Diego, 2000.
[2] R.S. MacTaylor, A.W. Castleman, J. Atmos. Chem. 36 (2000) 23.
[3] P. Jena, A.W. Castleman, Proc. Natl. Acad. Sci. U. S. A. 103 (2006) 10560.
[4] S. Zamith, P. Feiden, P. Labastie, J.-M. L'Hermite, Phys. Rev. Lett. 104 (2010) 103401.
[5] S. Zamith, P. Feiden, P. Labastie, J.-M. L'Hermite, J. Chem. Phys. 133 (2010) 154305.
[6] S. Zamith, G. de Tournadre, P. Labastie, J.-M. L'Hermite, J. Chem. Phys. 138 (2013) 034301.
[7] J. Lengyel, et al., J. Chem. Phys. 137 (2012) 034304.
[8] J. Lengyel, A. Pysanenko, V. Poterya, P. Slavíček, M. Fárník, J. Kočišek, J. Fedor, Phys. Rev. Lett. 112 (2014) 113401.
[9] B.J. Finlayson-Pitts, Phys. Chem. Chem. Phys. 11 (2009) 7760.
[10] J.J. Gilligan, A.W. Castleman, J. Phys. Chem. A 105 (2001) 5601.
[11] V. Vaida, J. Chem. Phys. 135 (2011) 020901.
[12] M. Fárník, V. Poterya, Front. Chem. 2 (2014) 4.
[13] B.C. Garrett, et al., Chem. Rev. 105 (2005) 355.
[14] A. Domaracka, et al., J. Phys.: Conf. Ser. 373 (2012) 012005.
[15] H. Shinohara, N. Nishi, N. Washida, J. Chem. Phys. 84 (1985) 5561.
[16] Z. Shi, J.V. Ford, S. Wei, A.W. Castleman, J. Chem. Phys. 99 (1993) 8009.
[17] S.Q. Wei, A.W. Castleman, Int. J. Mass Spectrom. Ion Processes 131 (1994) 233.
[18] L. Belau, K.R. Wilson, S.R. Leone, M. Ahmed, J. Phys. Chem. A 111 (2007) 10075.
[19] S. Barth, M. Ončák, V. Ulrich, M. Mucke, T. Lischke, P. Slavíček, U. Hergenhahn, J. Phys. Chem. A 113 (2009) 13519.
[20] A. Golan, M. Ahmed, J. Phys. Chem. Lett. 3 (2012) 458.
[21] J. Kočišek, J. Lengyel, M. Fárník, P. Slavíček, J. Chem. Phys. 139 (2013) 214308.
[22] O. Maršálek, C.G. Elles, P.A. Pieniazek, E. Pluhařová, J. VandeVondele, S.E. Bradforth, P. Jungwirth, J. Chem. Phys. 135 (2011) 224510.
[23] O. Svoboda, D. Hollas, M. Ončák, P. Slavíček, Phys. Chem. Chem. Phys. 15 (2013) 11531.
[24] L. Angel, A.J. Stace, Chem. Phys. Lett. 345 (2001) 277.
[25] F. Dong, S. Heinbuch, J.J. Rocca, E.R. Bernstein, J. Chem. Phys. 124 (2006) 224319.
[26] K. Hansen, P.U. Andersson, E. Uggerud, J. Chem. Phys. 131 (2009) 124303.
[27] R.T. Jongma, Y. Huang, S. Shi, A.M. Wodtke, J. Phys. Chem. A 102 (1998) 8847.
[28] S. Denifl, et al., Angew. Chem. Int. Ed. 121 (2009) 9102.
[29] S. Denifl, et al., J. Chem. Phys. 132 (2010) 234307.
[30] G.H. Gardeinier, M.A. Johnson, A.B. McCoy, J. Phys. Chem. A 113 (2009) 4772.
[31] K. Mizuse, A. Fujii, J. Phys. Chem. A 117 (2013) 929.
[32] C. Bobbert, S. Schütte, C. Steinbach, U. Buck, Eur. Phys. J. D 19 (2002) 183.
[33] B.L. Yoder, J.H. Litman, P.W. Forysinski, J.L. Corbett, R. Signorell, J. Phys. Chem. Lett. 2 (2011) 2623.
[34] C.E.J. Klots, J. Chem. Phys. 83 (1985) 5854.
[35] J.H. Litman, B.L. Yoder, B. Schläppi, R. Signorell, Phys. Chem. Chem. Phys. 15 (2013) 940.
[36] T.A. Beu, C. Steinbach, U. Buck, Eur. Phys. J. D 27 (2003) 223.
[37] M. Fárník, Molecular Dynamics in Free Clusters and Nanoparticles Studied in Molecular Beams, ICT Prague Press, Prague, 2011.
[38] V. Poterya, et al., J. Phys. Chem. A 118 (2014) 4740.
[39] V. Poterya, J. Lengyel, A. Pysanenko, P. Svrčková, M. Fárník, J. Chem. Phys. 141 (2014) 074309.
[40] S. Schütte, U. Buck, Int. J. Mass Spectrom. 220 (2002) 183.
[41] J. Lengyel, et al., J. Phys. Chem. Lett. 3 (2012) 3096.
[42] C.C. Pradzynski, R.M. Forck, T. Zeuch, P. Slavíček, U. Buck, Science 337 (2012) 1529.
[43] T. Zeuch, U. Buck, Chem. Phys. Lett. 579 (2013) 1.
[44] U. Buck, C.C. Pradzinski, T. Zeuch, J.M. Dieterich, B. Hartke, Phys. Chem. Chem. Phys. 16 (2014) 6859.
[45] C. Steinbach, U. Buck, Phys. Chem. Chem. Phys. 7 (2005) 986.
[46] O.F. Hagena, Surf. Sci. 106 (1981) 101.
[47] O.F. Hagena, Z. Phys. D 4 (1987) 291.
[48] O.F. Hagena, Rev. Sci. Instrum. 63 (1992) 2374.
[49] U. Buck, R. Krohne, J. Chem. Phys. 105 (1996) 5408.
[50] S.Q. Wei, W.B. Tzeng, A.W. Castleman, J. Chem. Phys. 93 (1990) 2506.
[51] J.A. Fournier, C.J. Johnson, C.T. Wolke, G.H. Weddle, A.B. Wolk, M.A. Johnson, Science 344 (2014) 1009.
[52] J. Burgess, Metal Ions in Solution, Ellis Horwood, Chichester, 1978.
[53] W.A. Chupka, M. Kaminsky, J. Chem. Phys. 35 (1961) 1991.
[54] H. Ehrhardt, F. Linder, Z. Naturforsch 22a (1967) 444.
[55] P. Lohbrandt, R. Galonska, H.J. Kim, M.S.C. Lauenstein, U. Buck, in: R. Campargue (Ed.), Atomic and Molecular Beams. The State of the Art 2000, Springer, Berlin, 2001, p. 623.
[56] V. Profant, V. Poterya, M. Fárník, P. Slavíček, U. Buck, J. Phys. Chem. A 111 (2007) 12477.
[57] V. Poterya, O. Tkáč, J. Fedor, M. Fárník, P. Slavíček, U. Buck, Int. J. Mass Spectrom. 2010 (2010) 85.

THE JOURNAL OF PHYSICAL CHEMISTRY Letters
Letter
pubs.acs.org/JPCL

Nucleation of Mixed Nitric Acid−Water Ice Nanoparticles in Molecular Beams that Starts with a HNO_3 Molecule

Jozef Lengyel,[†,¶] Andriy Pysanenko,[†] Jaroslav Kočišek,[†,§] Viktoriya Poterya,[†] Christoph C. Pradzynski,[‡] Thomas Zeuch,[‡] Petr Slavíček,[†,¶] and Michal Fárník*[,†]

[†]J. Heyrovský Institute of Physical Chemistry, v.v.i., Academy of Sciences of the Czech Republic, Dolejškova 3, 182 23 Prague 8, Czech Republic

[‡]Institut für Physikalische Chemie, Universität Göttingen, Tammannstrasse 6, D-37077 Göttingen, Germany

Supporting Information

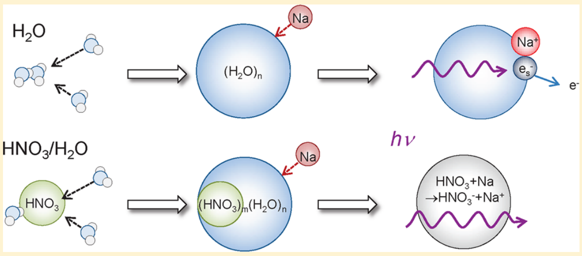

ABSTRACT: Mixed $(HNO_3)_m(H_2O)_n$ clusters generated in supersonic expansion of nitric acid vapor are investigated in two different experiments, (1) time-of-flight mass spectrometry after electron ionization and (2) Na doping and photoionization. This combination of complementary methods reveals that only clusters containing at least one acid molecule are generated, that is, the acid molecule serves as the nucleation center in the expansion. The experiments also suggest that at least four water molecules are needed for HNO_3 acidic dissociation. The clusters are undoubtedly generated, as proved by electron ionization; however, they are not detected by the Na doping due to a fast charge-transfer reaction between the Na atom and HNO_3. This points to limitations of the Na doping recently advocated as a general method for atmospheric aerosol detection. On the other hand, the combination of the two methods introduces a tool for detecting molecules with sizable electron affinity in clusters.

SECTION: Environmental and Atmospheric Chemistry, Aerosol Processes, Geochemistry, and Astrochemistry

There are essentially two major reasons to investigate mixed nitric acid−water clusters; (i) in atmospheric chemistry, particles containing hydrates of nitric acid play an important role, and the nitric acid−water clusters can mimic these particles in laboratory experiments, and (ii) from a fundamental point of view, they represent one of the prototype examples of an acid−base system in which proton transfer can be studied.

The importance of mixed nitric acid−water particles in atmospheric chemistry is derived from the fact that the polar stratospheric clouds (PSCs) of type I consist essentially of the nitric acid hydrates. They play a key role in the stratospheric ozone depletion (see refs 1−3 and references therein). The dissolution of water with hygroscopic species such as H_2SO_4 and HNO_3 substantially speeds up aggregation, leading to the homogeneous heteromolecular nucleation, which plays a key role in aerosol particle production and cloud formation in both the troposphere and stratosphere.[3−7] We have also recently discovered that the uptake cross section for NO_x species that are the precursors for HNO_3 on ice nanoparticles is significantly larger than expected.[8]

The question of the acid dissociation of HNO_3 in water to produce H_3O^+ and NO_3^- ions has been addressed by numerous theoretical and experimental studies (see a recent review in ref 9 and references therein). Theoretical calculations predicted that the acidic dissociation in isolated clusters occurs in $HNO_3(H_2O)_n$ complexes for $n \geq 4$.[10] Partial transfer of the HNO_3 proton to its nearest water molecule was calculated and confirmed experimentally by microwave spectroscopy in the nitric trihydrate complex.[11] Similar results were found in calculations and spectroscopy of deposited films of nitric acid hydrates.[12] The acid dissociation on aqueous surfaces was studied theoretically,[13] and the proton transfer through aqueous surfaces was investigated experimentally upon HNO_3 collision with the water surface.[14] We have studied the general question of acidic dissociation of simple diatomic molecules (hydrogen halides) on ice nanoparticles by photodissociation experiments.[15−18] Here, we employ different experimental methods to address acidic dissociation and other questions for polyatomic HNO_3 molecules in water clusters.

The mass spectrometry of nitric acid−water clusters in molecular beams was studied in Castleman's group.[19] Their mass spectra were similar to our present spectra discussed below. The same group then concentrated on elucidation of solvation mechanism in collisions of protonated water clusters $(H_2O)_kH^+$ with HNO_3 molecules in a fast flow reactor.[20,21] Similar processes were also studied theoretically.[22] Nevertheless, the information on especially the larger nitric acid−water clusters is still limited.

Received: September 11, 2012
Accepted: October 9, 2012

ACS Publications dx.doi.org/10.1021/jz3013886 | J. Phys. Chem. Lett. 2012, 3, 3096−3101

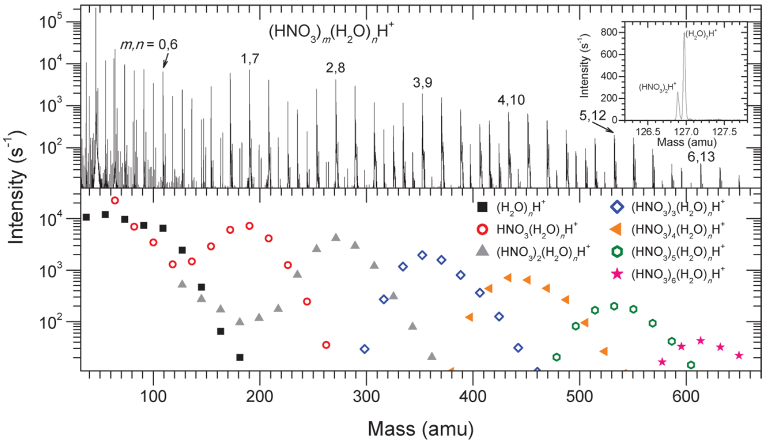

Figure 1. TOFMS spectrum. Expansion of nitric acid vapor in He. The inset illustrates the mass resolution by showing the $(HNO_3)_2H^+$ and $(H_2O)_7H^+$ mass peaks at around 127 amu. Some pronounced $(HNO_3)_m(H_2O)_nH^+$ peaks are labeled with m,n. The lower panel shows the spectra analysis, distinguishing the different groups of mass peaks.

Here, we investigate these clusters generated in supersonic expansions by two different mass spectrometric experiments providing complementary information, (i) on the CLUster Beam (CLUB) apparatus in the group of Fárník in Prague and (ii) on a molecular beam apparatus in the group of Zeuch in Göttingen. In both experiments, the clusters were produced by supersonic expansions of nitric acid vapor seeded in buffer gas, and mass spectra were recorded by a reflectron time-of-flight mass spectrometer (TOFMS). The major difference was the cluster ionization method. In the CLUB apparatus, the clusters were ionized by a variable energy electron gun. In the Göttingen apparatus, the photoionization method after Na pickup was employed.

The photoionization method was developed in Buck's group where it was implemented for clusters of water and ammonia.[23,24] Currently, it is used in Zeuch's group for vibrational spectroscopy of clusters.[25−27] Roughly, the idea is that the sodium releases a solvated electron in the cluster, which has a low ionization energy. The solvated electron is photodetached by the UV laser at photon energies of 3−4 eV, far below the ionization potential of any of the cluster constituents. This results in the soft fragmentation-free ionization of the cluster. Thus, the measured mass spectrum reflects directly the original neutral cluster size distribution. This method was used later in the group of Signorell to analyze for acetic acid clusters the Na pickup efficiency and fragmentation effects in comparison to single VUV photon ionization experiments.[28] Recently, it has been advocated by the same group in this journal as a general method for determination of accurate size distribution and chemical composition of fine aerosol particles.[29] We show principal limitations of the Na doping method, which cannot be applied for the present case of nitric acid−water clusters. Yet, we also show that in combination with the electron ionization, the Na doping can detect species with a sizable electron affinity in clusters.

Figure 1 shows an example of the TOFMS mass spectrum after electron ionization at 70 eV of clusters generated in the expansion from vapor of concentrated (65%) nitric acid seeded in He at 1.8 bar. The nitric acid reservoir was stabilized at 100 °C, which corresponds to the HNO_3 mole fraction of 10.5% in the vapor. The lower panel shows the spectra analysis distinguishing the different groups of mass peaks by different symbols/colors. Similar spectra were recorded under various conditions, employing Ar and He as the buffer gas, changing the nitric acid concentration in the vapor by varying the reservoir and nozzle temperatures and by changing the buffer gas pressure, and also at various ionizing electron energies. The spectra change with the varying conditions, yet some general features remain essentially constant: the major mass peak series correspond to $(HNO_3)_m(H_2O)_nH^+$, $m = 0−6$; $m = 1$ and 2 series both exhibit intensity minima for $n = 3$ followed by an increase to a maximum at $n \approx 7−8$; and all series for $m \geq 3$ show onset sizes $n_0(m)$, such that the mass peaks of clusters with a number of water molecules less than $n_0(m)$ are not observed, and the intensity for $n \geq n_0(m)$ increases significantly, reaching a maximum at some larger $n(\approx n_0(m) + 4)$.

Qualitatively, the same features were observed previously by Kay et al.[19] for clusters of the same deuterated species, with some minor differences. Our minimum for the $HNO_3(H_2O)_nH^+$ series is at $n = 3$ rather than at $n = 4$; we observe a minimum for the $(HNO_3)_2(H_2O)_nH^+$ series at $n = 3$, while an onset at $n = 4$ was reported;[19] all of our onsets $n_0(m)$ for $m \geq 4$ are smaller by one than those in ref 19; and we observe homonuclear species $(HNO_3)_mH^+$ for $m = 2$ and 3, while these were reported as not existing previously.[19] Essentially, all of these differences can be assigned to a higher sensitivity of the present experiment.

The interpretation of the spectra[19] was based on the fact that the position of the $(HNO_3)_m(H_2O)_nH^+$ series minimum for $m = 1$ and onsets for $m \geq 2$ were essentially independent of the expansion conditions. It was concluded that these features arise due to the onset of the acidic dissociation at the critical sizes; the ion pair generation increases the dipole moment of the cluster, which enhances the cross section for water molecule addition, leading to the observed increase in intensity of the corresponding mass peaks. An alternative explanation involved an increase in the electron ionization cross section upon the formation of the zwitterion. In any case, the acidic dissociation was invoked in the neutral clusters larger by one water molecule than the observed minimum and onset mass peak, that is, assuming the following electron ionization: $(HNO_3)_m(H_2O)_n + e^- \rightarrow (HNO_3)_m(H_2O)_{n-1}H^+ + OH + 2e^-$. Under the same assumptions, our present data would place the threshold for the acidic dissociation for a single nitric acid molecule in $HNO_3(H_2O)_n$ at $n = 4$, in agreement with theory.[10]

It should be mentioned that the measurements of the cluster dipole moments by deflection in electric fields did not show any significant increase of the dipole moment at $n = 4$ or 5.[30] Therefore, an alternative interpretation may involve ion−molecule reactions in the cluster after ionization. The experiments in Castleman's group[20,21] showed that at least five water ligands were necessary to solvate the proton before the first nitric acid molecule could be taken up in reactions of protonated water clusters exposed to nitric acid vapors. Switching reactions in which HNO_3 replaces a H_2O molecule were proposed in the interpretation and, more recently, supported by theoretical calculations.[22] Thus, upon ionization of the $HNO_3(H_2O)_n$ cluster with prevailing water content, the $(H_2O)_kH^+$ ion can be initially created, which exchanges H_2O for HNO_3, contributing then to the increasing intensity of $HNO_3(H_2O)_{(k-1)}H^+$. Our spectra would indicate that the threshold size for the exchange reaction would be $k \geq 4$.

To probe the neutral cluster size distribution more directly, we have employed the Na pickup technique combined with photoionization and TOFMS because this technique is believed to provide essentially fragmentation-free mass spectra.[23,29] To our surprise, no signal was observed at the HNO_3 mole fraction exceeding approximately 1%! Figure 2a illustrates this situation for expansion of 10.5% HNO_3 mole fraction in the vapor (65% nitric acid). The observed mass peaks are mostly nitrogen and oxygen from poor background subtraction (in Figure 2d, one can see that these background peaks are negligible with respect to the beam signals). The solvated electron can be detached from the water cluster with energies of 3−4 eV, and here, we used photon energies of 3.44 (360 nm) and 4.03 eV (308 nm) with essentially the same results. Only at lower concentrations below 1% do the $(H_2O)_nNa^+$ mass peaks start to appear, as illustrated in Figure 2b, and become more intense with lowering concentration, Figure 2c. No mixed $(HNO_3)_m(H_2O)_nNa^+$ clusters have been detected!

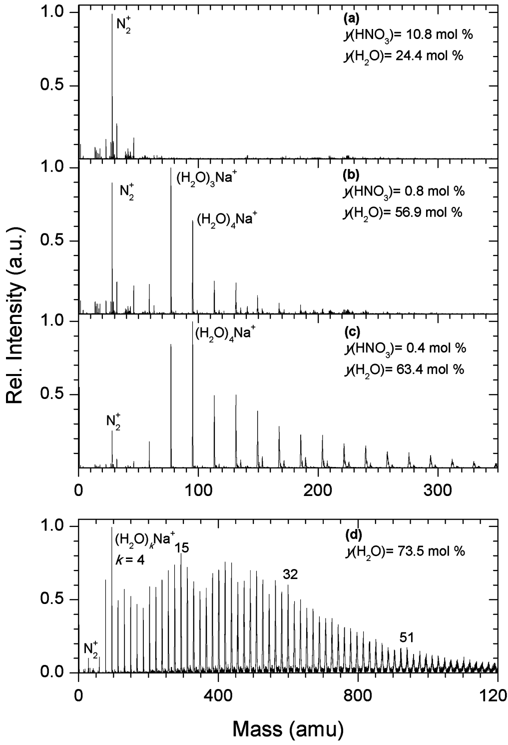

Figure 2. Photoionization mass spectra after Na pickup. (a−c) Decreasing HNO_3 mole fraction in the vapor coexpanding with He; (d) pure water in the He expansion for comparison (note different mass scale). The background N_2^+ peak and the major water spectra peaks are labeled (see text). See also Figure 3 for a schematic representation of the ionization method.

It is important to note that the Na pickup is a sensitive method to measure the pure water clusters.[25] To illustrate this, Figure 2d shows the mass spectrum of water clusters generated under the conditions corresponding to panel (b) but with pure water. We can clearly see the strong $(H_2O)_nNa^+$ mass peak progression extending to cluster sizes well over 50 molecules. Therefore, if there were some pure water clusters generated in the beam upon the expansion of the concentrated acid vapors, the corresponding mass peaks would appear in the spectra. We can conclude that pure water clusters are not produced in the expansions from nitric acid vapor at a mole fraction of $y(HNO_3) \geq 1\%$.

On the other hand, from our electron ionization spectra above, we know that expansions from concentrated nitric acid vapors undoubtedly produce clusters resulting in the $(HNO_3)_m(H_2O)_nH^+$ mass peaks (including the $m = 0$ series). We expect the same clusters to be generated in photoionization and electron ionization experiment because we transferred our nozzle from Prague to Göttingen to ensure the same expansion conditions. Thus, from the combination of these experiments, we can conclude that (i) the series of $(H_2O)_kH^+$ mass peaks in the electron ionization experiments originates from the mixed clusters from which HNO_3 molecules have evaporated upon ionization and (ii) the mixed $(HNO_3)_m(H_2O)_n$ clusters are not detected by the Na doping method.

The observation of evaporation of HNO_3 from the $HNO_3(H_2O)_n$ cluster upon ionization can be supported by predissociation vibrational spectroscopy,[31,32] showing that $HNO_3(H_2O)_nH^+$ cluster ions for $n \geq 3$ are hydronium ion−water aggregates weakly bound to HNO_3, which can be easily evaporated. Conclusion (i) also means that there are essentially no clusters without HNO_3 molecules present in our beam generated in the expansions of concentrated nitric acid vapors despite prevailing water content in the vapor. It implies that the nucleation in the supersonic expansions starts with the HNO_3 molecule.

Conclusion (ii) can be justified assuming the charge-transfer (CT) reaction $Na + HNO_3 \rightarrow Na^+ + HNO_3^-$. This reaction is feasible when the difference between the ionization potential of Na, IP(Na) $\approx$ 5.1 eV, and the HNO_3 electron affinity, EA(HNO_3) $\approx$ 0.6 eV,[33,34] is balanced by the Coulombic attraction of the two charges separated by a distance $R[\text{Å}] = 14.363/(\text{IP} - \text{EA})[\text{eV}]$. This condition is fulfilled for $R \approx 3.2$ Å. This simple electrostatic model estimate assuming just the point charges is backed by our ab initio calculation supporting the spontaneous CT process leading to Na^+ and stable HNO_3^-. We also show that the Na atom can approach the HNO_3 molecule at a closer distance. These calculations are outlined in some more detail in the Supporting Information (SI) supplied with this paper. It is worth noting that HNO_3 is exceptional with its positive electron affinity, and a similar mechanism cannot be expected for, for example, water[23,25−27] or acetic acid[28,29] clusters; the electron attachment to the majority of

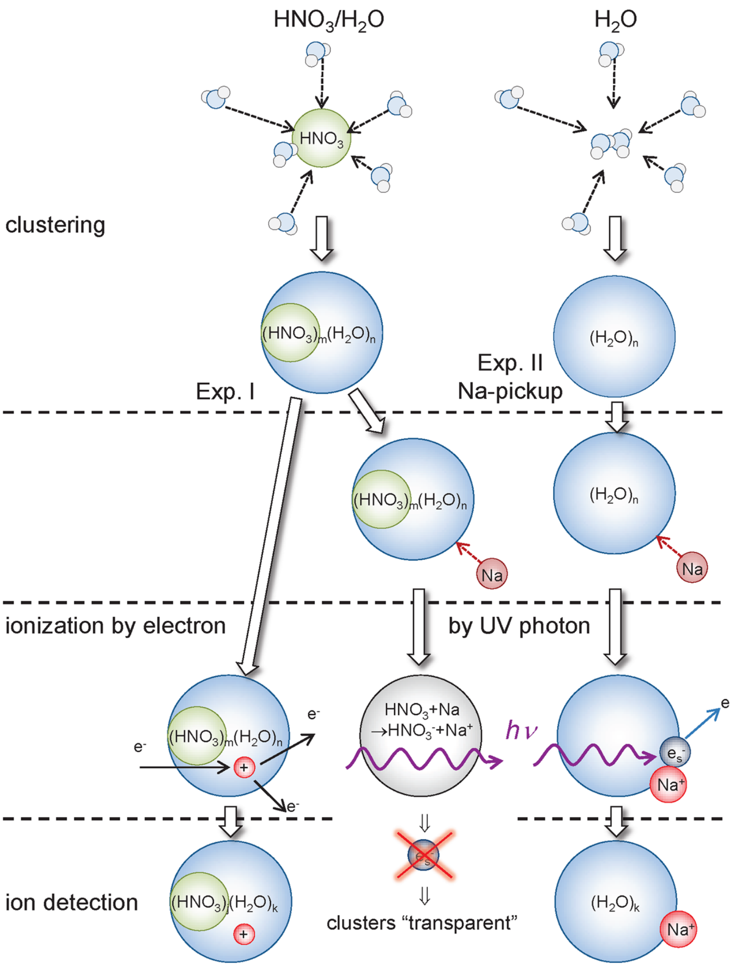

Figure 3. Schematic illustration of processes observed in the present cluster experiments.

neutral molecules leads only to metastable anionic states.[35] The ionization potential of this structure is around 7.5 eV, far above our photon energies (see the SI); therefore, we cannot ionize the clusters in which this reaction has occurred and detect any clusters with nitric acid by the Na doping experiment.

Figure 3 illustrates schematically the processes occurring in our experiments. First, the clusters are generated in supersonic expansions. In a nitric acid−water mixture, the HNO_3 molecule serves as the nucleation center, and the mixed $(HNO_3)_m(H_2O)_n$ clusters are generated. In the electron ionization experiment, their ionization can be accompanied by evaporation of some cluster constituents, and the ionized fragments $(HNO_3)_j(H_2O)_kH^+$ are then detected. In the doping experiment, Na is picked up by the cluster, and $Na^+{-}e_s^-$ is generated in pure water clusters. The solvated electron e_s^- is then ejected from the cluster by the UV radiation, resulting in the detected $(H_2O)_kNa^+$ ions. The pickup of Na on the mixed $(HNO_3)_m(H_2O)_n$ clusters leads to the quick CT reaction. Thus, the solvated electron is not available in the cluster for ionization when the photon arrives and the clusters are "transparent" and not detectable in this experiment.

This shows that the Na doping method cannot be employed for measurements of a certain important class of atmospherically relevant aerosol particles, in which the constituent molecules can react with sodium. However, this is not necessarily "bad news" because in turn, it offers the possibility to exploit the Na doping method for detection of species in clusters with an electron affinity for which the CT process proceeds with Na. It is interesting to note that sodium reacts vividly with water in the bulk, yet in clusters, it reacts much slower and rather produces the solvated electron, which can be then easily photodetached. On the other hand, a molecule with some electron affinity such as HNO_3 seems to react via fast CT with Na to generate an ion pair in the cluster.

In summary, several major conclusions can be drawn. The nitric acid molecule seems to be acidically dissociated in $HNO_3(H_2O)_n$ clusters with $n = 4$ water molecules; in supersonic expansions of vapors with a HNO_3 mole fraction of $\geq 1\%$, generation of clusters starts with the acid molecule; the Na doping method cannot be used generally for the detection of a certain type of clusters; and the Na doping in combination with electron ionization provides a new tool to study reactivity in some neutral clusters.

■ EXPERIMENTAL SECTION

The experiments have been performed on two different apparatuses. The CLUB apparatus in Prague has been comprehensively described in ref 36, except for the new TOF spectrometer employed in the present study; it is a custom-built[37] double-stage reflectron system with Wiley−McLaren ion extraction. Clusters are ionized by a pulsed electron gun at a frequency of 10 kHz, and electron energies are tunable between ∼5 and 90 eV with a resolution of ∼0.7 eV. Qualitatively, the mass spectra recorded at various electron energies do not differ significantly from the present spectra measured at 70 eV. Calibration measurements have shown that clusters of masses up to 5×10^3 amu could be measured without discrimination with a resolution of $M/\Delta M \approx 4 \times 10^3$. The Na doping experiment in Göttingen has been described in detail previously.[23−27]

The expansion conditions were identical on both apparatuses; the same divergent conical nozzle with a 100 μm diameter and 33° full opening angle was used. The nitric acid mole fraction in the vapor was controlled by heating the reservoir with the nitric acid−water mixture (65%), and the buffer gas (Ar or He) carried the vapor to the nozzle heated independently to a somewhat higher temperature (usually by 5−10 °C) to avoid condensation. Reservoir temperatures between 50 and 110 °C and buffer gas pressures between 1 and 3 bar were exploited. The qualitative features of the mass spectra reported here were reproduced at all conditions exploited here. The highly diluted vapors were obtained by adding water to the reservoir in the experiments with Na doping.

■ ASSOCIATED CONTENT

Supporting Information

Further details concerning the theoretical ab initio calculation of the CT process in the Na−HNO_3 system (also solvated with water molecules). This material is available free of charge via the Internet at http://pubs.acs.org.

■ AUTHOR INFORMATION

Corresponding Author

*Phone: +420 (0)2 6605 3206. Fax: +420 (0)2 8658 2307. E-mail: michal.farnik@jh-inst.cas.cz.

Notes

The authors declare no competing financial interest.

¶Also at the Department of Physical Chemistry, Institute of Chemical Technology, Technická 5, 166 28 Prague 6, Czech Republic.

§Also at the Department of Surface and Plasma Science, Faculty of Mathematics and Physics, Charles University, V Holešovičkách 2, 180 00 Prague 8, Czech Republic.

■ ACKNOWLEDGMENTS

Support of the Grant P208/11/0161 and Grant 203/09/0422 of the Grant Agency of the Czech Republic is acknowledged. J.L. acknowledges the support by the Deutsche Forschungsgemeinschaft for his stay in Göttingen during measurements of the present experiments. T.Z. thanks funding by the Deutsche Forschungsgemeinschaft (GRK 782, Grant ZE 890-1-1). Fruitful discussions of the present results with U. Buck are highly appreciated.

■ REFERENCES

(1) Peter, T. Microphysics and Heterogeneous Chemistry of Polar Stratospheric Clouds. *Annu. Rev. Phys. Chem.* **1997**, *48*, 785−822.

(2) Solomon, S. Stratospheric Ozone Depletion: A Review of Concepts and History. *Rev. Geophys.* **1999**, *37*, 275−316.

(3) Finlayson-Pitts, B. J.; Pitts, J. N. *Chemistry of the Upper and Lower Atmosphere*; Academic Press: San Diego, CA, 2000.

(4) Ravishankara, A. R. Heterogeneous and Multiphase Chemistry in the Troposphere. *Science* **1997**, *276*, 1058−1065.

(5) Prenni, A. J.; Tolbert, M. A. Studies of Polar Stratospheric Cloud Formation. *Acc. Chem. Res.* **2001**, *34*, 545−553.

(6) Dickens, D. B.; Sloan, J. J. The Nucleation and Freezing of Dilute Nitric Acid Aerosols. *J. Phys. Chem. A* **2002**, *106*, 10543−10549.

(7) Stetzer, O.; Möhler, O.; Wagner, R.; Benz, S.; Saathoff, H.; Bunz, H.; Indris, O. Homogeneous Nucleation Rates of Nitric Acid Dihydrate (NAD) at Simulated Stratospheric Conditions — Part I: Experimental Results. *Atmos. Chem. Phys.* **2006**, *6*, 3023−3033.

(8) Lengyel, J.; Kočišek, J.; Poterya, V.; Pysanenko, A.; Svrčková, P.; Fárník, M.; Zaouris, D.; Fedor, J. Uptake of Atmospheric Molecules by Ice Nanoparticles: Pickup Cross Sections. *J. Chem. Phys.* **2012**, *137*, 034304.

(9) Leopold, K. R. Hydrated Acid Clusters. *Annu. Rev. Phys. Chem.* **2011**, *62*, 327−349.

(10) McCurdy, P. R.; Hess, W. P.; Xantheas, S. S. Nitric Acid−Water Complexes: Theoretical Calculations and Comparison to Experiment. *J. Phys. Chem. A* **2002**, *106*, 7628−7635.

(11) Sedo, G.; Doran, J. L.; Leopold, K. R. Partial Proton Transfer in the Nitric Acid Trihydrate Complex. *J. Phys. Chem. A* **2009**, *113*, 11301−11310.

(12) Escribano, R.; Couriero, M.; Gómez, P. C.; Carrasco, E.; Moreno, M. A.; Herrero, V. J. The Nitric Acid Hydrates: Ab Initio Molecular Study, and RAIR Spectra of the Solids. *J. Phys. Chem. A* **2003**, *107*, 651−661.

(13) Bianco, R.; Wang, S.; Hynes, J. T. Theoretical Study of the Dissociation of Nitric Acid at a Model Aqueous Surface. *J. Phys. Chem. A* **2007**, *111*, 11033−11042.

(14) Mishra, H.; Enami, S.; Nielsen, R. J.; Hoffmann, M. R.; Goddard, W. A., III; Colussi, A. J. Anions Dramatically Enhance Proton Transfer Through Aqueous Interfaces. *Proc. Natl. Acad. Sci. U.S.A.* **2012**, *109*, 10228−10232.

(15) Poterya, V.; Fárník, M.; Slavíček, P.; Buck, U.; Kresin, V. V. Photodissociation of Hydrogen Halide Molecules on Free Ice Nanoparticles. *J. Chem. Phys.* **2007**, *126*, 071101.

(16) Ončák, M.; Slavíček, P.; Poterya, V.; Fárník, M.; Buck, U. Emergence of Charge-Transfer-to-Solvent Band in the Absorption Spectra of Hydrogen Halides on ice Nanoparticles: Spectroscopic Evidence for Acidic Dissociation. *J. Phys. Chem. A* **2008**, *112*, 5344−5353.

(17) Poterya, V.; Fedor, J.; Pysanenko, A.; Tkáč, O.; Lengyel, J.; Ončák, M.; Slavíček, P.; Fárník, M. Photochemistry of HI on Argon and Water Nanoparticles: Hydronium Radical Generation in $HI\cdot(H_2O)_n$. *Phys. Chem. Chem. Phys.* **2011**, *13*, 2250−2258.

(18) Ončák, M.; Slavíček, P.; Fárník, M.; Buck, U. Photochemistry of Hydrogen Halides on Water Clusters: Simulations of Electronic Spectra and Photodynamics, and Comparison with Photodissociation Experiments. *J. Phys. Chem. A* **2011**, *115*, 6155−6168.

(19) Kay, B. D.; Hermann, V.; Castleman, A. W. Studies of Gas-Phase Clusters: The Solvation of HNO_3 in Microscopic Aqueous Clusters. *Chem. Phys. Lett.* **1981**, *80*, 469−474.

(20) Zhang, X.; Mereand, E. L.; Castleman, A. W. Reactions of Water Cluster Ions with Nitric Acid. *J. Phys. Chem.* **1994**, *98*, 3554−3557.

(21) Gilligan, J. J.; Castleman, A. W. Acid Dissolution by Aqueous Surfaces and Ice: Insight from a Study of Water Cluster Ions. *J. Phys. Chem. A* **2001**, *105*, 5601−5605.

(22) D'Auria, R.; Turco, R.; Houk, K. N. Effects of Hydration on the Properties of Protonated-Water−Nitric Acid Clusters. *J. Phys. Chem. A* **2004**, *108*, 3756−3765.

(23) Bobbert, C.; Schütte, S.; Steinbach, C.; Buck, U. Fragmentation and Reliable Size Distributions of Large Ammonia and Water Clusters. *Eur. Phys. J. D* **2002**, *19*, 183−192.

(24) Steinbach, C.; Buck, U. Ionization Potentials of Large Sodium Doped Ammonia Clusters. *J. Chem. Phys.* **2005**, *122*, 134301.

(25) Forck, R. M.; Dauster, I.; Schieweck, Y.; Zeuch, T.; Buck, U.; Ončák, M.; Slavíček, P. Observation of two Classes of Isomers of

Hydrated Electrons in Sodium−Water Clusters. *J. Chem. Phys.* **2010**, *132*, 221102.

(26) Forck, R. M.; Dieterich, J. M.; Pradzynski, C. C.; Huchting, A. L.; Mata, R. A.; Zeuch, T. Structural Diversity in Sodium Doped Water Trimer. *Phys. Chem. Chem. Phys.* **2012**, *14*, 9054−9057.

(27) Pradzynski, C. C.; Forck, R. M.; Zeuch, T.; Slavíček, P.; Buck, U. A Fully Size-Resolved Perspective on the Crystallization of Water Clusters. *Science* **2012**, *337*, 1529−1532.

(28) Forysinski, P. W.; Zielke, P.; Luckhaus, D.; Corbett, J.; Signorell, R. Photoionization of Small Sodium-Doped Acetic Acid Clusters. *J. Chem. Phys.* **2011**, *134*, 094314.

(29) Yoder, B. L.; Litman, J. H.; Forysinski, P. W.; Corbett, J. L.; Signorell, R. Sizer for Neutral Weakly Bound Ultrafine Aerosol Particles Based on Sodim Doping and Mass Spectrometric Detection. *J. Phys. Chem. Lett.* **2011**, *2*, 2623−2628.

(30) Moro, R.; Heinrich, J.; Kresin, V. V. Electric Dipole Moments of Nitric Acid−Water Complexes Measured by Cluster Beam Deflection. 2009, arXiv:0910.1630v1 [physics.atm-clu].

(31) Cao, Y.; Choi, J.-H.; Haas, B.-M.; Okumura, M. Spectroscopic Studies of Intracluster Hydration Reaction of NO_2. *J. Phys. Chem.* **1994**, *98*, 12176−12185.

(32) Choi, J.-H.; Kuwata, K. T.; Cao, Y.-B.; Haas, B.-M.; Okumura, M. Protonation of Chlorine Nitrate and Nitric Acid: Identification of Isomers by Vibrational Spectroscopy. *J. Phys. Chem. A* **1997**, *101*, 6753−6760.

(33) Mathur, B. P.; Rothe, E. W.; Tang, S. Y.; Mahajan, K.; Reck, G. P. Negative Gaseous Ions from Nitric Acid. *J. Chem. Phys.* **1976**, *64*, 1247−1248.

(34) Paulson, J. F.; Dale, F. Reactions of $OH^-{\cdot}H_2O$ with NO_2. *J. Chem. Phys.* **1982**, *77*, 4006−4008.

(35) Simons, J. Molecular Anions. *J. Phys. Chem. A* **2008**, *112*, 6401−6511.

(36) Fárník, M. *Molecular Dynamics in Free Clusters and Nanoparticles Studied in Molecular Beams*; ICT Prague Press: Institute of Chemical Technology Prague: Prague, Czech Republic, 2011; ISBN: 978-80-7080-781-1.

(37) Built by Stefan Kaesdorf, Geräte für Forschung und Industrie, Munich, Germany.

THE JOURNAL OF PHYSICAL CHEMISTRY Letters

Letter

pubs.acs.org/JPCL

Reactivity of Hydrated Electron in Finite Size System: Sodium Pickup on Mixed N_2O−Water Nanoparticles

Daniela Šmídová,[†,‡] Jozef Lengyel,[†] Andriy Pysanenko,[†] Jakub Med,[‡] Petr Slavíček,*[,‡]
and Michal Fárník*[,†]

[†]J. Heyrovský Institute of Physical Chemistry v.v.i., The Czech Academy of Sciences, Dolejškova 3, 18223 Prague 8, Czech Republic
[‡]Department of Physical Chemistry, University of Chemistry and Technology, Technická 5, Prague 6, Czech Republic

S *Supporting Information*

ABSTRACT: We investigate the reactivity of hydrated electron generated by alkali metal deposition on small water particles with nitrous oxide dopant by means of mass spectrometry and ab initio molecular dynamics simulations. The mixed nitrous oxide/water clusters were generated in a molecular beam and doped with Na atoms in a pickup experiment, and investigated by mass spectrometry using two different ionization schemes: an electron ionization (EI), and UV photoionization after the Na doping (NaPI). The NaPI is a soft-ionization nondestructive method, especially for water clusters provided that a hydrated electron e_s^- is formed in the cluster. The missing signal for the doped clusters indicates that the hydrated electron is not present in the N_2O containing clusters. The simulations reveal that the hydrated electron is formed, but it immediately reacts with N_2O, forming first N_2O^- radical anion, later O^-, and finally an $OH^\bullet$ and OH^- pair.

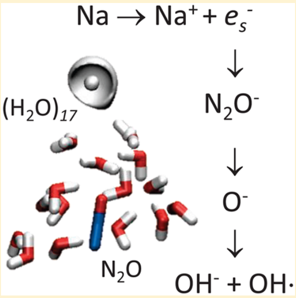

Hydrated electron is an important short-lived reactive species that is formed during water photolysis and radiolysis.[1] Its structure and reactivity has attracted attention ever since its identification in 1960s,[2] focusing both on the electron solvated in liquid water and finite-size analogues of the hydrated electron.[3] Solvated electrons are on one hand the simplest chemical species, even simpler than hydrogen atoms. On the other hand, they owe their very existence to complex interactions with solvent molecules so that their modeling becomes cumbersome; a general consensus on their structure has not yet been reached.[4,5]

Experimentally, the solvated electron was first prepared by Humphry Davy in 1807−1809 by dissolving alkali metals in liquid ammonia. The same approach cannot be used in liquid water, as alkali metals and water react immediately. Hydrated electron is, however, formed on the surface of finite size water particles, providing that only a single alkali atom is deposited on the cluster.[6−8] With such an arrangement, we can observe the reactivity of hydrated electron in water clusters doped with the N_2O quencher.

Hydrated electron formed via the alkali atom deposition on molecular clusters is recently increasingly used for characterization of aerosols and crystalline particles in nanometer size range.[9−11] For water clusters, the sodium pickup process results in generating Na^+ and a hydrated electron e_s^-. Note that in finite size solid clusters the hydrated electron typically resides near the cluster surface.[12−14] The hydrated electrons are weakly bound to the cluster (the binding energy converges to 3.2 eV for large clusters[15]) and can be detached by UV photons of relatively low energies. The remaining $(H_2O)_N \cdot Na^+$ cluster ions can be then detected by a mass spectrometer. The method (NaPI) is essentially fragmentation-free at low photon energies close to the ionization threshold of 3.2 eV, and thus the mass spectra reflect the original neutral cluster size distributions. This was first shown for water clusters by Buck et al.[9] and later on suggested by Signorell et al. as a "sizer for weakly bound ultrafine aerosol particles",[16] and demonstrated for different clusters.[11,17,18] Several articles and recent reviews from Buck's and Zeuch's group describe the method in detail and also show its applications in vibrational spectroscopy.[6,15,19,20]

The sodium pickup method, therefore, represents a very powerful technique for a characterization of aerosols. This is a very important aspect, since water droplets, ice, and aerosol particles in the nanometer size range are key players in atmospheric processes,[21,22] yet these small particles are difficult to investigate. In this respect, we should focus on mixed aerosols, particularly those containing nitrogen compounds. We have recently demonstrated, however, that the hydrated electron can strongly interact with molecules other than water in the mixed clusters, in particular HNO_3.[23] In this work, we combine photoionization (NaPI) and electron ionization (EI) techniques together with ab initio molecular dynamics simulations to reveal the nature of the interaction between hydrated electron and mixed N_2O/H_2O clusters. The goal of the study is twofold: first, we reveal details of the hydrated electron quenching reactions; second, we point to the limitations of sodium pickup technique for the investigation of small aerosols.

Received: June 15, 2015
Accepted: July 6, 2015

DOI: 10.1021/acs.jpclett.5b01269
J. Phys. Chem. Lett. 2015, 6, 2865−2869

Figure 1 compares the NaPI and EI mass spectra. The top row shows the NaPI spectra of $(H_2O)_N$ clusters generated in expansions of pure He through the water reservoir using three different He pressures: 5, 6, and 7 bar, panels Ia, Ib, and Ic, respectively. The spectra are composed of $(H_2O)_NNa^+$ mass peaks and reflect the neutral cluster size distributions;[9,24] in all three cases the mean cluster size corresponds to $\bar{N} \approx 17$. The middle row shows the mass spectra where the coexpansion was done with 5% mixture of N_2O in He. At P_0 = 5 bar, the $(H_2O)_NNa^+$ mass peaks were present. The spectrum extends to even larger cluster sizes than in the case of pure He. This can be justified by N_2O acting as a buffer gas at low concentrations, cooling the expansion more efficiently than He, and thus even larger $(H_2O)_N$ clusters were generated than in pure helium expansions. However, the signal weakened significantly at 6 bar and disappeared at 7 bar. Does the presence of more N_2O in the expansion at the higher stagnation pressure inhibit cluster generation? To answer this question, we recorded the mass spectra under the same conditions (including Na-doping) using the EI (bottom). This series clearly shows that clusters are generated in the mixed $He/N_2O/H_2O$ expansions. The observed charged fragments in the mass spectra are smaller due to the large fragmentation after EI compared to NaPI.[24] Nevertheless, these spectra proved that even larger clusters were generated in the mixed expansions at 7 bar than at 5 bar, yet these clusters were not detected by the NaPI method.

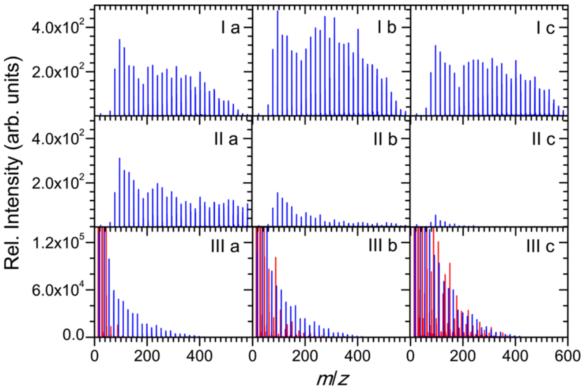

Figure 1. Mass spectra measured at different expansion conditions (water reservoir T_R = 328 K, nozzle temperature T_0 = 343 K). Top row corresponds to NaPI spectra with pure He as the buffer gas at P_0 = 5, 6, and 7 bar, (Ia−c). Middle and bottom rows correspond to the spectra obtained with 5% N_2O/He mixture as the buffer gas (P_0 as above): series II and III correspond to NaPI and EI spectra, respectively. Red bars label the mixed fragments containing some N_2O molecules and their fragments.

The EI spectra also exhibit mixed N_2O/H_2O fragment ions, which are labeled (red) in Figure 1. The detailed analysis can be found in the Supporting Information (SI) where the mixed N_2O/H_2O mass peak series are assigned. However, important for the present conclusions is the qualitative observation that the spectra at 5 bar are dominated by pure protonated water $(H_2O)_nH^+$ fragments (blue), while the mixed peaks (red) grow in intensity with the stagnation pressure, i.e., overall N_2O concentration in the expansion. The spectra show unambiguously that the mixed $(N_2O)_M{\cdot}(H_2O)_N$ clusters are generated and their concentration and size increased with P_0, while the relative concentration of pure $(H_2O)_N$ clusters in the expansions decreased. The fact that the signal intensity decreased in Figure 1 IIa−c demonstrates that the NaPI method is sensitive only to the pure $(H_2O)_N$ clusters. On the other hand, the universal EI method detects (but also fragments) all the clusters, and their abundances increased in Figure 1 IIIa−c.

This explanation opens another question: Why is the NaPI method insensitive to the mixed N_2O containing clusters? An obvious answer is a reaction of N_2O with Na prior to the photoionization. The cluster detection with the low-energy photons in the NaPI method requires that the ion pair Na^+ with solvated electron e_s^- is generated prior to the photoionization; then the photodetachment of the e_s^- weakly bound to the cluster leaves behind the molecular cluster doped by Na^+. However, if a reaction with a solvated electron takes place in the cluster, the above-mentioned e_s^- detachment mechanism cannot occur.

The experimental results thus strongly suggest that the hydrated electron is involved in the subsequent reaction and disappears from the system. To reveal the nature of this process, we have employed ab initio simulations. The pure $(H_2O)_N$ mass spectra yielded the mean cluster size $\bar{N} \approx 17$. At P_0 = 7, bar almost all the generated clusters contained some N_2O molecules, since we could not detect them by the NaPI method. Therefore, we performed our calculations for the $Na{\cdot}(H_2O)_{15}{\cdot}N_2O$ cluster as a representative system for our experiment. We observe in our simulations a cascade of reactions. The reaction starts with the formation of a hydrated electron paired with the sodium cation:

$$Na \xrightarrow{(H_2O)_N} Na^+ + e_s^- \tag{1}$$

The solvated electron then almost immediately reacts with N_2O dopant:

$$N_2O + e_s^- \rightarrow N_2O^- \tag{2}$$

This step can easily be observed visually in the simulations because the N_2O is linear molecule, while the N_2O^- anion has a broken structure. In the next step, the radical anion releases the nitrogen molecule, forming an O^- radical anion:

$$N_2O^- \rightarrow N_2 + O^- \tag{3}$$

The nascent radical anion is rather reactive, and it further reacts with water in the cluster to generate OH^- anion and $OH^\bullet$ radical pair:

$$O^- + H_2O \rightarrow OH^\bullet + OH^- \tag{4}$$

Figure 2 shows the ionization energies (IEs) and Mulliken charges on several atoms along a selected trajectory, starting with unsolvated Na atom near the cluster surface. We observe both from the Mulliken charges and spin densities that at the beginning, the unpaired electron is connected to the sodium atom. The IE is close to the one of the sodium atom, yet in less than a picosecond, the IE falls down to about 3 eV. This evolution corresponds to a sodium solvation and the formation of an $e_s^-{\cdot}Na^+$ pair.[12] At this moment, the unpaired electron is still close to the sodium atom. In the next step, the charge transfer process (eq2) takes places. This reaction is reflected by a sharp increase of the IE to ≈8 eV. Already at this step, the NaPI experiment becomes blind to the clusters. The dynamical processes, however, continue. The formation of the oxygen radical anion (eq3) leads to a further increase in the IE (≈11 eV); in our sample trajectory this process takes

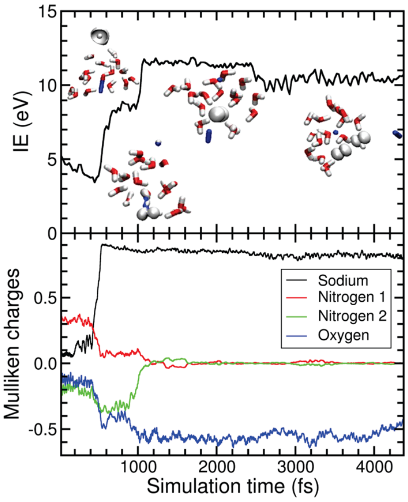

Figure 2. Reactions taking place in the $\mathrm{Na\cdot(H_2O)_{15}\cdot N_2O}$ complex for a selected trajectory. Upper panel shows ionization energies along the BLYP-based MD trajectory recalculated at the BMK/6-31++g** level together with spin densities at four different time instants. The lower panel displays Mulliken atomic charges for different atoms along the trajectory.

place at the time of 1 ps. The final step (eq4) of the whole cascade, the formation of the OH^- anion and $OH^\bullet$ radical, leads to certain decrease in the IE. The formation of the $OH^\bullet$ radical is not without interest, as the powerful reductive species, hydrated electron, is transformed into a strong oxidative agents, hydroxyl radical, which plays an important role both in the chemistry of the atmosphere and in radiation chemistry.

Figure 3 shows the evolution of the IEs for all simulated trajectories together with the probabilities for the distinct reaction steps. We observe that the whole reaction series is on average almost completed within the 5 ps duration of our simulations. The sodium solvation and formation of equilibrated hydrated electron is rather fast, while the subsequent reaction steps can take a longer time. It ought to be mentioned that the kinetics can be somewhat different, depending on the electronic structure method used (see also SI). The robust observation here is that even the first product formed is characterized by a significantly increased ionization energy.

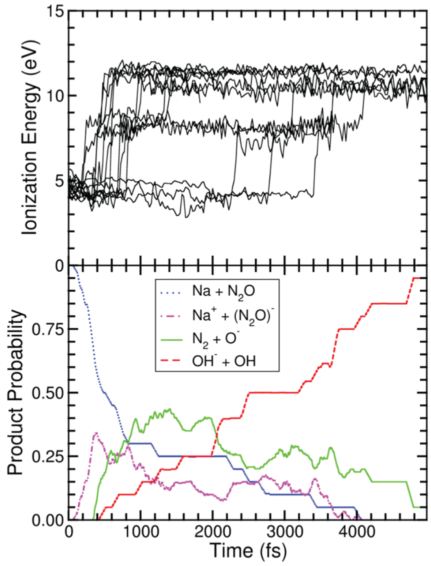

Figure 3. Upper panel shows ionization energies along the BLYP-based MD trajectories recalculated at the BMK/6-31++g** level for 20 trajectories. The lower panel displays the time evolution of probability for the formation of different species.

The observed reaction products are generally in accord with the known facts on reactivity of N_2O in the condensed phase. The nitrous oxide is being used as a hydrated electron scavenger, with the rate constant close to its diffusion limit.[25] The reaction of an electron with N_2O in liquid water was recently studied theoretically using dielectric continuum model, and only a small barrier was found for this reaction.[26,27] In finite size systems, the reaction seems to proceed essentially without any barrier. The mechanism of the subsequent reactions was a subject of some discussion. Originally, the N_2O^- was considered as a relatively stable intermediate. Later its fast dissociation was established.[28] Both $(H_2O)_nO^-$ and $(H_2O)_nOH^-$ products were observed from reactions of negatively charged water clusters with N_2O.[29,30] The oxygen radical anion should be relatively stable in the aqueous phase.[31] Our simulations, on the other hand, suggest that the oxygen radical anion quickly accepts a proton from a neighboring water molecule (see SI for the possible role that a self-interaction error of the GGA BLYP functional may play in the enhanced reactivity of the oxygen radical anion). The reactivity of an oxygen radical anion in liquid water and in finite size clusters can be different for physical reasons. The oxygen radical anion has a very high solvation energy[32] due to the long-range polarization of the solvent. In small water particles, however, the oxygen radical anion is much less stabilized, which leads to decreasing of the reaction barrier for the reaction of the radical anion with water.

We have combined different mass spectrometry techniques with ab initio dynamical simulations to investigate the mechanism of hydrated electron quenching by N_2O. While the hydrated electron is formed upon a deposition of sodium atom on small water clusters, no hydrated electron is detected by the NaPI method for the N_2O containing clusters. This indicates fast reactions forming species with high ionization energies. Ab initio molecular dynamics simulation have revealed the chain of reactions forming subsequently N_2O^-, O^-, and $OH^\bullet$ and OH^- pair. The whole sequence occurs on a picosecond time scale for the finite size clusters investigated in our simulations. Already the first reaction step leads to the formation of species with more tightly bound electrons and therefore an increase in the ionization energy. In the future, experiments should be designed to experimentally detect the OH^- or $OH^\bullet$ radical products that have been observed theoretically in this work.

■ EXPERIMENTAL AND THEORETICAL METHODS

The present experiments were performed on our versatile CLUster Beam apparatus (CLUB) apparatus.[33−35] In this study we have exploited the reflectron time-of-flight mass spectrometer (RTOF) using two different ionization methods, EI and NaPI described recently.[24] The RTOF was described in details elsewhere.[36,37] The expansion conditions and some measurement details are outlined in the SI. The theoretical simulations of the reaction between the sodium atom and the $N_2O(H_2O)_{15}$

clusters was modeled with ab initio molecular dynamics approach using the CP2K program package.[38,39] The energies and forces were calculated at the density functional (DFT) level, using the BLYP functional.[40,41] All the details and procedures are given in the SI.

■ ASSOCIATED CONTENT

Ⓢ Supporting Information

Details of the experiment and theoretical calculations and further results. The Supporting Information is available free of charge on the ACS Publications website at DOI: 10.1021/acs.jpclett.5b01269.

■ AUTHOR INFORMATION

Corresponding Authors

*E-mail: petr.slavicek@vscht.cz.
*Phone: +420 (2)6605 3206. Fax: +420 (2)8658 2307. E-mail: michal.farnik@jh-inst.cas.cz.

Notes

The authors declare no competing financial interest.

■ ACKNOWLEDGMENTS

This work has been supported by the Grant Agency of the Czech Republic project No.: 14-08937S.

■ REFERENCES

(1) Garrett, B. C.; Dixon, D. A.; Camaioni, D. M.; Chipman, D. M.; Johnson, M. A.; Jonah, C. D.; Kimmel, G. A.; Miller, J. H.; Rescigno, T. N.; Rossky, P. J.; et al. Role of Water in Electron-Initiated Processes and Radical Chemistry: Issues and scientific advances. *Chem. Rev.* **2005**, *105*, 355−389.

(2) Hart, E.; Boag, J. Absorption Spectrum of Hydrated Electron in Water and in Aqueous Solutions. *J. Am. Chem. Soc.* **1962**, *84*, 4090−4095.

(3) Young, R.; Neumark, D. Dynamics of Solvated Electrons in Clusters. *Chem. Rev.* **2012**, *112*, 5553−5577.

(4) Larsen, R.; Glover, W.; Schwartz, B. Does the Hydrated Electron Occupy a Cavity? *Science* **2010**, *329*, 65−69.

(5) Herbert, J.; Jacobson, L. Nature's Most Squishy Ion: The Important Role of Solvent Polarization in the Description of the Hydrated Electron. *Int. Rev. Phys. Chem.* **2011**, *30*, 1−48.

(6) Steinbach, C.; Buck, U. Reaction and Solvation of Sodium in Hydrogen Bonded Solvent Clusters. *Phys. Chem. Chem. Phys.* **2005**, *7*, 986−990.

(7) Mundy, C.; Hutter, J.; Parrinello, M. Microsolvation and Chemical Reactivity of Sodium and Water Clusters. *J. Am. Chem. Soc.* **2000**, *122*, 4837−4838.

(8) Bobbert, C.; Schulz, C. Solvation and Chemical Reaction of Sodium in Water Clusters. *Eur. Phys. J. D* **2001**, *16*, 95−97.

(9) Bobbert, C.; Schütte, S.; Steinbach, C.; Buck, U. Fragmentation and Reliable Size Distributions of large Ammonia and Water Clusters. *Eur. Phys. J. D* **2002**, *19*, 183−192.

(10) Schütte, S.; Buck, U. Strong Fragmentation of Large Rare Gas Clusters by High Energy Electron Impact. *Int. J. Mass Spectrom.* **2002**, *220*, 183−192.

(11) Forysinski, P.; Zielke, P.; Luckhaus, D.; Corbett, J.; Signorell, R. Photoionization of Small Sodium-Doped Acetic Acid Clusters. *J. Chem. Phys.* **2011**, *134*, 094314.

(12) Forck, R. M.; Dauster, I.; Schieweck, Y.; Zeuch, T.; Buck, U.; Ončák, M.; Slavíček, P. Observation of Two Classes of Isomers of Hydrated Electrons in Sodium-Water Clusters. *J. Chem. Phys.* **2010**, *132*, 221102.

(13) West, A.; Yoder, B.; Luckhaus, D.; Saak, C.; Doppelbauer, M.; Signorell, R. Angle-Resolved Photoemission of Solvated Electrons in Sodium-Doped Clusters. *J. Phys. Chem. Lett.* **2015**, *6*, 1487−1492.

(14) Signorell, R.; Yoder, B.; West, A.; Ferreiro, J. J.; Saak, C. Angle-Resolved Valence Shell Photoelectron Spectroscopy of Neutral Nanosized Molecular Aggregates. *Chem. Sci.* **2014**, *5*, 1283−1295.

(15) Zeuch, T.; Buck, U. Sodium Doped Hydrogen Bonded Clusters: Solvated Electrons and Size Selection. *Chem. Phys. Lett.* **2013**, *579*, 1−10.

(16) Yoder, B. L.; Litman, J. H.; Forysinski, P. W.; Corbett, J. L.; Signorell, R. Sizer for Neutral Weakly Bound Ultrafine Aerosol Particles Based on Sodim Doping and Mass Spectrometric Detection. *J. Phys. Chem. Lett.* **2011**, *2*, 2623−2628.

(17) Litman, J. H.; Yoder, B. L.; Schläppi, B.; Signorell, R. Sodium-Doping as a reference to study the influence of intracluster chemistry on the Fragmentation of Weakly-Bound Clusters Upon Vacuum Ultraviolet Photionization. *Phys. Chem. Chem. Phys.* **2013**, *15*, 940−949.

(18) Schläppi, B.; Ferreiro, J. J.; Litman, J. H.; Signorell, R. Sodium-Sizer for Neutral Nanosized Molecular Aggregates: Quantitative Correction of Size-Dependence. *Int. J. Mass Spectrom.* **2014**, *372*, 13−21.

(19) Buck, U.; Pradzynski, C. C.; Zeuch, T.; Dieterich, J. M.; Hartke, B. A Size Resolved Investigation of Large Water Clusters. *Phys. Chem. Chem. Phys.* **2014**, *16*, 6859−6871.

(20) Pradzynski, C. C.; Forck, R. M.; Zeuch, T.; Slavíček, P.; Buck, U. A Fully Size-Resolved Perspective on the Crystallization of Water Clusters. *Science* **2012**, *337*, 1529−1532.

(21) Finlayson-Pitts, B. J.; Pitts, J. N. *Chemistry of the Upper and Lower Atmosphere*; Academic Press: San Diego, CA, 2000.

(22) Kulmala, M.; Kontkanen, J.; Junninen, H.; Lehtipalo, K.; Manninen, H. E.; Nieminen, T.; Petäjä, T.; Sipilä, M.; Schobesberger, S.; Rantala, P.; et al. Direct Observations of Atmospheric Aerosol Nucleation. *Science* **2013**, *339*, 943−946.

(23) Lengyel, J.; Pysanenko, A.; Kočišek, J.; Poterya, V.; Pradzynski, C.; Zeuch, T.; Slavíček, P.; Fárník, M. Nucleation of Mixed Nitric Acid-Water Ice Nanoparticles in Molecular Beams that Starts with a HNO_3 Molecule. *J. Phys. Chem. Lett.* **2012**, *3*, 3096−3101.

(24) Lengyel, J.; Pysanenko, A.; Poterya, V.; Kočišek, J.; Fárník, M. Extensive Water Cluster Fragmentation After Low Energy Electron Ionization. *Chem. Phys. Lett.* **2014**, *612*, 256−261.

(25) Takahashi, K.; Ohgami, S.; Koyama, Y.; Sawamura, S.; Marin, T. W.; Bartels, D. M.; Jonah, C. D. Reaction Rates of the Hydrated Electron with N_2O in High Temperature Water and Potential Surface of the N_2O^- Anion. *Chem. Phys. Lett.* **2004**, *383*, 445−450.

(26) Kryachko, E.; Vinckier, C.; Nguyen, M. Another Look at the Electron Attachment to Nitrous Oxide. *J. Chem. Phys.* **2001**, *114*, 7911−7917.

(27) Uhlig, F.; Jungwirth, P. Embedded Cluster Models for Reactivity of the Hydrated Electron. *Z. Phys. Chem.* **2013**, *227*, 1583−1593.

(28) Zehavi, D.; Rabani, J. Pulse Radiolytic Investigation of O_{aq}^- Radical Ions. *J. Phys. Chem.* **1971**, *75*, 1738−1744.

(29) Arnold, S. T.; Morris, R. A.; Viggiano, A. A.; Johnson, M. A. Thermal Energy Reactions of Size-Selected Hydrated Electron Clusters $(H_2O)_n^-$. *J. Phys. Chem.* **1996**, *100*, 2900−2906.

(30) Balaj, O. P.; Siu, C.-K.; Balteanu, I.; Beyer, M. K.; Bondybey, V. E. Free Electrons, the Simplest Radicals of Them All: Chemistry of Aqueous Electrons as Studied by Mass Spectrometry. *Int. J. Mass Spectrom.* **2004**, *238*, 65−74.

(31) Buxton, G.; Greenstock, C.; Helman, W.; Ross, A. Critical-Review of Rate Constants for Reactions of Hydrated Electrons, Hydrogen-Atoms and Hydroxyl Radicals ($\cdot OH/\cdot O^-$) in Aqueous Solution. *J. Phys. Chem. Ref. Data* **1988**, *17*, 513.

(32) Marcus, Y. Thermodynamics of Solvation Ions, Part 5.-Gibbs Free Energies of Hydration at 298.15 K. *J. Chem. Soc., Faraday Trans.* **1991**, *87*, 2995−2999.

(33) Poterya, V.; Lengyel, J.; Pysanenko, A.; Svrčková, P.; Fárník, M. Imaging of Hydrogen Halides Photochemistry on Argon and Ice Nanoparticles. *J. Chem. Phys.* **2014**, *141*, 074309.

(34) Poterya, V.; Kočišek, J.; Pysanenko, A.; Fárník, M. Caging of Cl Atoms from Photodissociation of CF_2Cl_2 in Clusters. *Phys. Chem. Chem. Phys.* **2014**, *16*, 421−429.

(35) Lengyel, J.; Pysanenko, A.; Poterya, V.; Slavíček, P.; Fárník, M.; Kočišek, J.; Fedor, J. Irregular Shapes of Water Clusters Generated in Supersonic Expansions. *Phys. Rev. Lett.* **2014**, *112*, 113401.

(36) Kočišek, J.; Lengyel, J.; Fárník, M.; Slavíček, P. Energy and Charge Transfer in Ionized Argon Coated Water Clusters. *J. Chem. Phys.* **2013**, *139*, 214308.

(37) Kočišek, J.; Lengyel, J.; Fárník, M. Ionization of Large Homogeneous and Heterogeneous Clusters Generated in Acetylene-Ar Expansions: Cluster Ion Polymerization. *J. Chem. Phys.* **2013**, *138*, 124306.

(38) VandeVondele, J.; Krack, M.; Mohamed, F.; Parrinello, M.; Chassaing, T.; Hutter, J. QUICKSTEP: Fast and accurate density functional calculations using a mixed Gaussian and plane waves approach. *Comput. Phys. Commun.* **2005**, *167*, 103−128.

(39) VandeVondele, J.; Hutter, J. Gaussian Basis Sets for Accurate Calculations on Molecular Systems in Gas and Condensed Phases. *J. Chem. Phys.* **2007**, *127*, 114105.

(40) Becke, A. Density-Functional Exchange-Energy Approximation with Correct Asymptotic-Behavior. *Phys. Rev. A: At., Mol., Opt. Phys.* **1988**, *38*, 3098−3100.

(41) Lee, C.; Yang, W.; Parr, R. Development of the Colle-Salvetti Correlation-Energy Formula into a Functional of the Electron-Density. *Phys. Rev. B: Condens. Matter Mater. Phys.* **1988**, *37*, 785−789.

Eur. Phys. J. D (2015)
DOI: 10.1140/epjd/e2015-60532-6

THE EUROPEAN
PHYSICAL JOURNAL D

Regular Article

Sodium doping and reactivity in pure and mixed ice nanoparticles*

Jozef Lengyel, Andriy Pysanenko, Peter Rubovič, and Michal Fárník[a]

J. Heyrovský Institute of Physical Chemistry v.v.i., The Czech Academy of Sciences, Dolejškova 3, 18223 Prague, Czech Republic

Received 22 September 2015 / Received in final form 19 October 2015

Abstract. Doping of clusters by sodium atoms and subsequent photoionization (NaPI) is used as a fragmentation-free cluster ionization method. Here we investigate different clusters using NaPI and electron ionization (EI) with a reflectron time-of-flight mass spectrometer (RTOF). The mass spectra of the same clusters ionized by NaPI and EI reveal significant differences which point to Na reactivity in the clusters. First, we discuss mixed $X_M{\cdot}(H_2O)_N$ ($X = HNO_3$, N_2O) clusters where reactions between Na and molecules X leads to the "cluster invisibility" for the NaPI method. Second, mixed $(NH_3)_M{\cdot}(H_2O)_N$ clusters are observed by both methods, but they reveal different cluster compositions, and the mass spectra suggest that neither the EI nor the NaPI spectrum corresponds exactly to the neutral cluster distribution. Finally, we discuss the reactions of Na in pure water clusters as a function of the number of Na atoms doped into the clusters. In summary, we present experimental evidence that the NaPI method in the present cases does not reveal the size and composition of the neutral clusters. A detailed understanding of Na reactivity in the clusters is needed for its application as a fragmentation-free cluster ionization method. Besides, we introduce the combination of NaPI and EI as a new tool to investigate the sodium reactivity in clusters and aerosol particles.

1 Introduction

Various mass spectrometric methods represent indispensable tools for the characterization of clusters, free nanoparticles and aerosol particles especially in atmospherically relevant investigations [1–3]. They can provide an insight into the size, structure and chemical composition of the studied species. A major drawback of mass spectrometry is the necessity of cluster ionization which often leads to significant fragmentation, especially in the case of weakly bound cluster species. In 2002 the group of Buck introduced Na-doping and subsequent photoionization (NaPI) as a fragmentation-free cluster ionization method for large water and ammonia clusters [4]. Applying this ionization method, mass spectrometry revealed the original neutral cluster size distributions of water and ammonia clusters. The essential idea in this method was that an Na atom releases an electron generating an Na^+ ion and a so-called *solvated electron* e_s^- in the cluster. The binding energy of the solvated electron was approximately 3.2 eV and 1.8 eV in large water and ammonia clusters, respectively [5,6]. Thus low energy UV photons could be used to photodetach e_s^- from these clusters while this photodetachment did not lead to any significant cluster fragmentation. The same group also obtained essentially fragmentation-free mass spectra of rare gas clusters by Na-doping [7]. In this case, however, the ionization mechanism did not involve any solvated electrons – the Na atoms with low ionization energy of approximately 5.1 eV were ionized directly in the clusters by 193 nm (6.1 eV) photons.

Later on, the group of R. Signorell proposed the NaPI method as a "sizer for weakly bound ultrafine aerosol particles" due to the fragmentation-free ionization [3,8]. They have implemented the method to investigate different large homogeneous clusters [9–11]. They have also revealed the nature of the solvated electron in various clusters using photoelectron velocity map imaging after Na-doping [12,13]. The group of Zeuch used Na-doping for investigating the vibrational spectroscopy of size selected large clusters [14–17]. More details about the NaPI and its different aspects and applications can be found in two recent comprehensive reviews [6,18].

The majority of previous studies investigated only homogeneous clusters by the NaPI [3–5,7–11]. An important class of atmospheric aerosols includes mixed species, e.g., HNO_3 containing ices which form polar stratospheric clouds (PSC) and play a pivotal role in ozone depletion processes [19–23]. Therefore we implemented Na-doping to probe the mixed HNO_3-water clusters in laboratory experiments [24]. We investigated these clusters using electron ionization (EI) mass spectrometry combined with NaPI measurements which we performed in Zeuch's group. These experiments revealed a surprising result. The NaPI method was completely "blind" to the mixed clusters containing HNO_3 molecules, which was interpreted by

---

* Contribution to the Topical Issue "Advances in Positron and Electron Scattering", edited by P. Limao-Vieira, G. Garcia, E. Krishnakumar, J. Sullivan, H. Tanuma and Z. Petrovic.

[a] e-mail: `michal.farnik@jh-inst.cas.cz`

accompanying theoretical calculations to be due to a fast reaction between the Na and HNO_3 molecule.

Subsequently, we extended our experimental apparatus in Prague with NaPI method [25]. A unique combination of NaPI and EI applied to a single molecular beam allows for investigations of Na reactivity in clusters: while EI ionizes all cluster species, the NaPI requires the presence of solvated electrons which are lost if a molecule reacts in the cluster with an Na atom or with a solvated electron. Here we demonstrate a few cases, especially of mixed clusters, where the NaPI method cannot provide a real picture of the neutral cluster size distribution and composition. A detailed understanding of the underlying processes is necessary in order to implement the NaPI method for studying the mixed clusters representing atmospheric aerosols.

First, we discuss mixed $X_M{\cdot}(H_2O)_N$ (X = HNO_3, N_2O) clusters where reactions between Na and the molecule X lead to the "cluster invisibility" for the NaPI method. Second, mixed $(NH_3)_M{\cdot}(H_2O)_N$ clusters are observed by both the NaPI and EI method, however, they both reveal quite different cluster compositions, which cannot be assigned to the neutral cluster composition. Finally, we discuss the reactions of Na in pure water clusters doped with several Na atoms.

2 Experiment

The experiments were carried out on the CLUster Beam (CLUB) apparatus which is a versatile molecular beam setup devoted to photodissociation, mass spectrometry and pickup experiments with various clusters namely of atmospheric relevance [25–28]. In the present study we exploited a high resolution reflectron time-of-flight mass spectrometer (RTOF) with the two above mentioned ionization options: (1) photoionization with UV photons at 315 nm (3.94 eV), and (2) electron ionization using a variable energy high frequency electron gun. The clusters were doped with Na-atoms in both the cases to probe identical cluster beam, however, EI is an all-purpose method ionizing all clusters with and without sodium, while the photoionization only works for Na-doped clusters, as will be discussed in Section 3.2.

The cluster beam was generated in supersonic expansions through conical nozzles into vacuum. Pure water clusters were produced in water vapor expansions without seeding gas. Mixed $(NH_3)_M{\cdot}(H_2O)_N$ clusters were produced expanding 15% NH_3 in He through a reservoir filled with water vapor. The expansion conditions are summarized in Table 1.

Table 1. Nozzle parameters: diameter d, opening angle $\alpha = 30°$, length $l = 2$ mm. The source reservoir filled with water heated to the temperature T_R and H_2O vapor is coexpanded with the gas given in the table through the nozzle at the temperature T_N. The stagnation pressures in the source is P_0. Temperatures of the pickup Na-oven: reservoir T_{Na} and cap T_{C}.

Clusters	$(H_2O)_N$	$(NH_3)_M{\cdot}(H_2O)_N$
Cluster source:		
gas	–	15%NH_3/He
d (μm)	100	55
P_0 (bar)	2.63	1.5–7.0
T_R/T_0 (K)	403/428	333/343
Na-oven:		
T_{Na} (K)	473–583	503
T_{C} (K)	453–523	483

The cluster beam was skimmed and passed through differentially pumped chambers before Na-doping. The clusters were doped by Na atoms evaporated in an oven kept at temperatures $T_{\mathrm{Na}}/T_{\mathrm{C}}$, where T_{Na} was the sodium oven temperature and T_{C} was the temperature of the cap where the sodium condensed. The sodium oven was the same as described elsewhere [4,7], and it was surrounded by a cold aluminium box to prevent any diffusion of Na from the oven to the surrounding vacuum. After passing through the pickup oven the cluster beam passed through another differentially pumped chamber and entered a mass spectrometer chamber with the RTOF mounted perpendicularly to the beam. This mass spectrometer offers several ionization options [29–31].

In the present study we used EI with 70 eV electrons (exploiting an electron gun with 10 kHz repetition frequency and tunable electron energy up to 90 eV with 0.7 eV resolution), and photoionization at 315 nm (3.94 eV) wavelength (using a tunable UV laser system with 10 Hz repetition frequency and 10 ns pulse width described below). The ions were extracted perpendicularly to the beam and accelerated to the final kinetic energy of 8 kV. After passing the effective flight path of 0.95 m length, the ions were detected on the Photonics MCP detector in the Chevron configuration, 40 mm in diameter. The mass spectra were recorded with a resolution of $M/\Delta M \geq 5 \times 10^3$.

Laser radiation at 315 nm was produced by frequency doubling output of the dye laser at 630 nm (LAS) pumped with the second harmonics 532 nm of the Nd:YAG laser (Spectra Physics, GCR-4). The typical UV energy at the chamber entrance was 3.7 mJ/pulse focused by $f =$ 400 mm lens through a fused silica window into the ionization region of the mass spectrometer. Attention was paid to avoid ionization by electrons emitted from electrodes by UV radiation.

3 Results and discussion

3.1 Charge transfer in mixed clusters

First, we briefly summarize the major results of our previous investigations of mixed clusters [24,32] obtained by using the NaPI method which motivated the present study of the mixed water-ammonia clusters. These investigations are important for understanding the present results.

The generation of mixed clusters in our molecular beam was proved by the presence of $(HNO_3)_m{\cdot}(H_2O)_nH^+$ cluster ion fragments after 70 eV EI. Surprisingly, no evidence of any clusters was found when using the NaPI method under the same expansion conditions. Only after significant nitric acid dilution with water in the reservoir some pure water clusters were generated and $(H_2O)_nNa^+$ cluster ions started to appear in the NaPI mass spectra. The fact that the mixed clusters, although clearly present in the beam, were not observed by NaPI was attributed to a fast charge transfer (CT) reaction between the Na and HNO_3 molecule in the clusters:

$$\mathrm{Na} + \mathrm{HNO_3} \rightarrow \mathrm{Na^+} + \mathrm{HNO_3^-} \quad (1)$$

possibly followed by further reactions of the HNO_3^- ion in the cluster. These experiments and the corresponding calculations have been described in detail in reference [24].

Several questions arose: Is the nitric acid in clusters the only exception which cannot be detected by the NaPI method? Is NaPI an all-purpose method for aerosol detection? These questions motivated our further experiments with mixed N_2O-water clusters [32]. In this case again, the mixed $(N_2O)_M{\cdot}(H_2O)_N$ clusters were not detected by the NaPI method but their generation was proved by the EI spectra. Theoretical simulations of the dynamics in the mixed Na-doped clusters revealed that the solvated electron is generated at first but reacts immediately with an N_2O molecule to form an N_2O^- anion, which makes it unavailable for the cluster ionization by electron photodetachment. A further chain of reactions was suggested:

$$\mathrm{N_2O^-} \rightarrow \mathrm{N_2} + \mathrm{O^-}, \quad (2)$$

$$\mathrm{O^-} + \mathrm{H_2O} \rightarrow \mathrm{OH^-} + \mathrm{OH}. \quad (3)$$

Preliminary experiments with other NO_x species give similar results suggesting that the "invisibility" of these clusters for the NaPI method is quite a general phenomenon for molecules with sizable electron affinity. These examples suggest that NaPI is not a general method for aerosol ionization, especially not for the mixed species.

3.2 Mixed water-ammonia clusters

At this point we pose the question: Can any mixed clusters be detected by the NaPI method? Obvious candidates are mixed water-ammonia clusters, since both water and ammonia support solvated electrons and their clusters were detected by the NaPI method [4]. Figure 1 shows the mass spectra of mixed clusters generated in supersonic expansion of 15% NH_3 in He with water vapor (T_R = 333 K, T_0 = 343 K, P_0 = 7 bar). Detailed resolved parts of the spectra are shown, illustrating the mixed species, and the insets show the overall spectra. The NaPI spectrum (Fig. 1a), shows $(NH_3)_m{\cdot}(H_2O)_n{\cdot}Na^+$ ions with $m = 0$–2, while the EI spectrum (Fig. 1b), contains $(NH_3)_m{\cdot}(H_2O)_n{\cdot}H^+$ ions with $m = 0$–5. The maximum peak in the NaPI spectra is always the $m = 0$ one, while in the EI spectra it shifts from $m = 1$ to 2 with increasing cluster size. Different detailed sections are displayed for NaPI and EI to illustrate the mixed species because the peaks corresponding to $m = 2$ are not present at lower masses in the NaPI spectrum (a), and, on the other hand, the signal-to-noise is smaller and the spectrum more congested at higher masses for the EI spectrum (b).

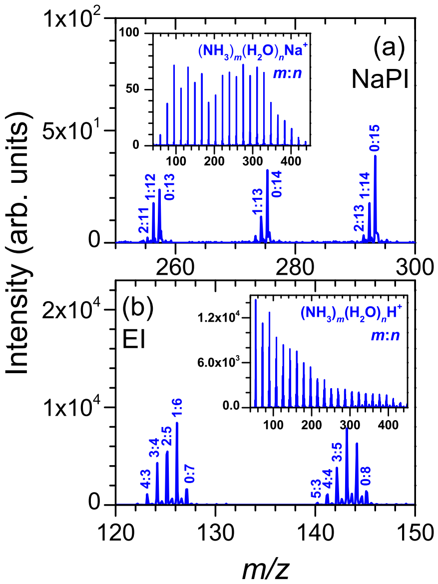

Fig. 1. (a) Part of the NaPI mass spectrum of clusters generated in supersonic expansion of 15% NH_3 in He with water vapor (T_R = 333 K, T_0 = 343 K, P_0 = 7 bar). (b) The spectrum of identical clusters obtained by EI with 70 eV energy electrons. The mass peaks are labelled by the ratio $m : n$ of NH_3:H_2O molecules in the detected ions. The insets show the entire mass spectra.

Different expansion conditions were exploited and similar spectra were also recorded under lower expansion pressure P_0 = 6 bar; on the other hand, using lower NH_3/He mix concentrations of 5% and 10% did not yield any mixed clusters for stagnation pressures up to 7 bar. It should be noted, that in the NaPI and especially in the EI spectra smaller peaks at fractional mass units are observed corresponding to metastable ions fragmenting in the reflectron TOF region [33,34]. One of the possible sources of these metastable ions might be some intracluster ion-molecule reactions which will be discussed further below.

Thus for ammonia-water system the mixed clusters are observed by both the NaPI and the EI method. However, both the methods show clearly different cluster compositions. The overall spectra (insets) suggest more fragmentation upon EI, as expected [25]. Nevertheless, the EI spectra exhibit fragments richer with NH_3 molecules. This could be explained, if these fragments in the EI spectra originated from some much larger neutral precursors containing significant amount of NH_3 and fragmenting upon EI to these ammonia-rich fragments. However, there is no evidence of such large NH_3-rich clusters in the NaPI spectrum (Fig. 1a), which was assumed to represent neutral cluster distribution. There are only $(NH_3)_m{\cdot}(H_2O)_n{\cdot}Na^+$ ions with $m \leq 2$ in the NaPI spectrum up to the largest observed clusters. It ought to be stressed also that this cannot be due to a mass discrimination of the larger clusters in our RTOF. The spectrometer has been calibrated to work discrimination-free up to masses $m/z \approx 1000$. The present spectra extend only to masses $m/z \leq 500$. If there were any larger fragments, they would be present in the spectra.

Thus the NaPI spectrum is clearly less fragmented than the EI one, and yet, there are $(NH_3)_m{\cdot}(H_2O)_n^+$ fragments in the EI spectrum with significantly more NH_3 molecules m than in the NaPI spectrum which cannot originate from some larger ammonia-rich clusters. There are two possible explanations: either the clusters fragment upon NaPI ionization, or the NaPI and EI sample different subsets of clusters from the molecular beam. The former explanation questions the “softness” of the NaPI process, since some of the NH_3 molecules must evaporate from the clusters during photoionization to yield the fragment ions with a smaller m than yielded by EI.

The latter scenario assumes that different species are probed by the EI and NaPI method. The cluster beam contains both $(NH_3)_M{\cdot}(H_2O)_N$ and $(NH_3)_M{\cdot}(H_2O)_N{\cdot}Na$ species after the Na-doping process. Indeed, the NaPI method probes only the Na-doped clusters, while EI ionizes all species in the beam indifferently. At the relatively low $T_{Na} = 563$ K temperatures used here for single doping, the majority of the clusters in the beam will be presumably $(NH_3)_M{\cdot}(H_2O)_N$ clusters without Na. Thus the mass spectra can reflect the fact that the Na-doped clusters contain less NH_3 molecules than the undoped ones. Either, the NH_3 containing clusters are less efficient in picking up Na atoms in the oven than the ones with less NH_3, or the NH_3 molecules selectively evaporate from the clusters after the Na-doping while water remains. The former possibility seems unlikely, since both the water and ammonia clusters had previously been efficiently doped with Na [4]. Thus we concentrate on the mechanism which would lead to selective ammonia evaporation during NaPI.

Both, the differences in the cluster ionization as well as in the Na-doping, can contribute to NH_3 evaporation. The proposed scenario is depicted schematically in the right-hand column of Figure 2. The Na pickup presumably leads to solvated electron generation located in the water part of the cluster since the ionization energy of Na-doped clusters is larger for water (3.2 eV) than for ammonia (1.8 eV) [6,35]. The generation of e_s^- and Na^+ in the water part can lead to selective NH_3 evaporation. In the ionization process, the e_s^- is detached by a UV photon and the structural rearrangement of water around the remaining Na^+ can lead to further NH_3 evaporation. Selective NH_3 evaporation in these processes would be consistent with the lower binding energy (300 meV in large ammonia clusters [4]) compared to that of H_2O (480 meV in large water clusters [4]).

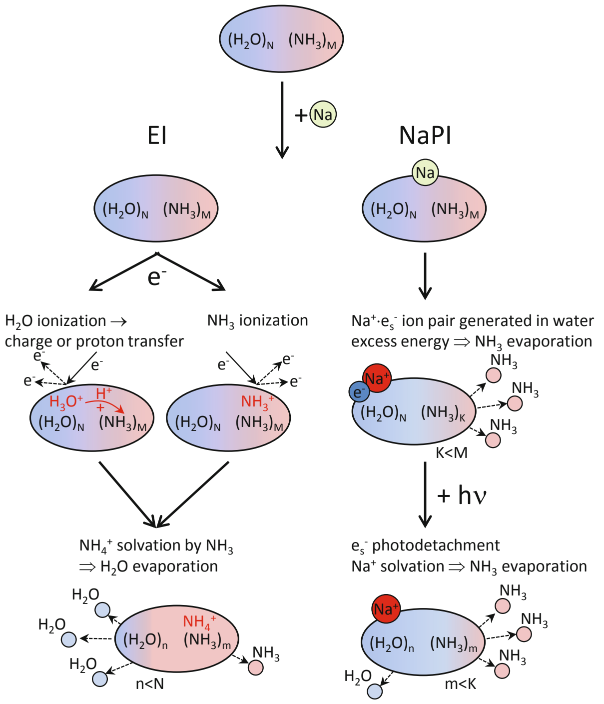

Fig. 2. Schematic picture of the mixed cluster $(NH_3)_M{\cdot}(H_2O)_N$ ionization and fragmentation processes (see text for explanation).

On the other hand, EI probes all clusters in the beam which are probably dominated by the pure $(NH_3)_M{\cdot}(H_2O)_N$ species. Since these clusters did not undergo the Na-doping process and NH_3 evaporation, they are still richer in ammonia. Upon electron ionization they fragment evaporating both H_2O and NH_3 molecules. Due to a lower ionization potential of NH_3 (10.0 eV) compared to that of H_2O (12.6 eV) the charge will be localized on the ammonia: either NH_3 is ionized by the electron directly, or first water is ionized which is followed by a charge or proton transfer reaction from H_2O^+ or H_3O^+ to NH_3. All these reactions occur readily between the isolated molecules in the gas phase [36]:

$$H_2O^+ + NH_3 \to NH_3^+ + H_2O, \tag{4}$$

$$H_2O^+ + NH_3 \to NH_4^+ + OH, \tag{5}$$

$$H_3O^+ + NH_3 \to NH_4^+ + H_2O. \tag{6}$$

Even a hydrogen transfer from an H_2O molecule to an NH_3^+ ion is a highly exoergic reaction (2.4 eV) occurring in the gas phase [36]:

$$NH_3^+ + H_2O \to NH_4^+ + OH. \tag{7}$$

Therefore it can be expected that after the mixed cluster ionization the charge finally localizes on an ammonia molecule generating an NH_4^+ ion. The neighbouring NH_3 molecules are attached tightly to the NH_4^+ by polarization forces. Thus ammonia will not evaporate from the charged clusters so easily leading to the appearance of fragments with a larger ammonia content in the spectra than in the case of Na-doping. The presence of metastable peaks in Figure 1b can be consistent with some slow ion-molecule reactions occurring in the clusters on the microsecond time-scale after the EI. The above mentioned processes are depicted schematically in the left column of Figure 2.

Further theoretical investigations are needed to prove (or disprove) our current hypothesis and fully understand the underlying processes. Nevertheless, in any case the NaPI method does not reveal the real neutral cluster composition for the mixed ammonia-water clusters.

3.3 Pure water clusters with multiple Na pickup

The key to understanding the above mentioned processes in the Na-doped clusters is sodium reactivity. Therefore we focused on this phenomena also in pure $(H_2O)_N$ clusters. This issue has been partly covered previously, starting with the pioneering work of Hertel's group [37,38] and further investigated in more detail [5,39,40]. We add here further insight provided by EI applied to the Na doped water clusters.

Sodium is well-known to react violently with water by a famous, highly exoergic, explosive reaction:

$$2\mathrm{Na} + 2\mathrm{H_2O} \rightarrow 2\mathrm{NaOH} + \mathrm{H_2}. \quad (8)$$

The molecular level mechanism of that reaction in bulk water has been recently revealed [41]. But the fact that at least two Na atoms are needed to produce NaOH products in this reaction was recognised in previous cluster studies [5]. Therefore the Na chemistry in pure water clusters can only start with a multiple pickup of several Na atoms.

Figure 3a shows detail of the NaPI mass spectrum obtained in pure water vapor expansion at $T_0 = 428$ K and $T_R = 403$ K which corresponds to $P_0 = 2.6$ bar. The mean size of water clusters produced under these conditions corresponds to $\bar{N} = 190$ [4]. It ought to be mentioned that the pickup of Na by water clusters is not a very efficient process. In our experiment the pickup cross sections can be determined from accurate cluster velocity measurements [42–44]. However, for Na pickup the exact pickup cross sections could not be obtained, since these measurements were hampered by a large experimental error due to an uncertainty in Na pressure. However, the cross sections were clearly smaller than the geometrical cross sections of the corresponding water clusters, i.e. the Na pickup and sticking to water clusters are rather inefficient processes. Nevertheless, several Na atoms are picked up by the clusters at the Na-oven temperature $T_{\mathrm{Na}} = 556$ K and $T_{\mathrm{C}} = 523$ K, as is demonstrated by the presence of $(\mathrm{NaOH})_m{\cdot}(\mathrm{H_2O})_n{\cdot}\mathrm{Na}^+$ peaks with $m = 2$ and 4 in the mass spectrum, Figure 3a. The dependence of these mass spectra on Na-pickup pressure (determined by T_{Na}) was measured. Even number m fragments were observed up to $m = 8$ at the highest temperatures $T_{\mathrm{Na}}/T_{\mathrm{C}} = 583/523$ K.

These experimental observations are fully consistent with the previous measurements by Steinbach and Buck [5]. In their paper they outlined a reaction mechanism leading to the NaOH generation proposed by theoretical simulations [45]. This reaction mechanism is more subtle than the general reaction (8): first a sodium atom is solvated and its valence electron is delocalized over the cluster. Then a sodium dimer binding to the cluster leads to charge separation to an Na^- and a solvated Na^+. The Na^- attracts a proton yielding NaH intermediate which subsequently reacts with water to NaOH and $\mathrm{H_2}$. In this process the delocalised valence electrons of the solvated sodium can be regarded as a catalyst. In total two Na atoms are needed to generate two NaOH products and a third Na atom must be present on the cluster to produce the solvated electron so that the cluster can be finally detected by the NaPI.

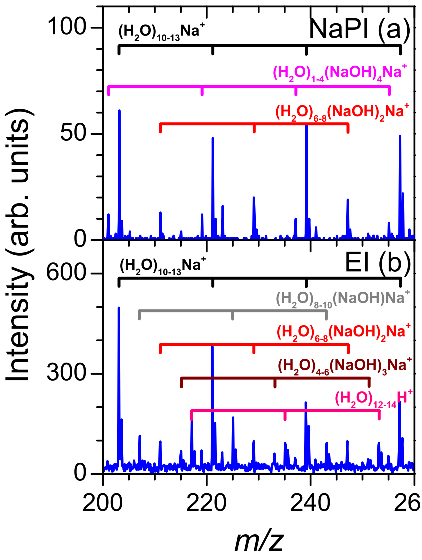

Fig. 3. (a) Part of the NaPI mass spectrum of clusters generated in supersonic expansion of pure water vapor ($T_R = 403$ K, $T_0 = 428$ K, $P_0 = 2.6$ bar). (b) The spectrum of identical clusters obtained by EI with 70 eV energy electrons.

On the other hand, in the EI spectrum of the same clusters in Figure 3b both even and odd values of m are observed. It is also worth noting, that the spectrum is dominated by $(\mathrm{H_2O})_n{\cdot}\mathrm{Na}^+$ fragments just as the NaPI spectrum, whilst the EI spectra of pure water clusters without Na contain always only protonated water peaks $(\mathrm{H_2O})_n\mathrm{H}^+$. They are significantly smaller in the present spectrum of clusters doped by several Na atoms.

The reaction (8) is, indeed, fast in liquid water, but it is not obvious that it should proceed readily in a frozen ice nanoparticle at about 100 K (the temperature of large water clusters [46]). Therefore one can ask the question if UV excitation in the NaPI experiments cannot initiate the reaction. Both NaPI and EI spectra contain mainly ions of essentially the same composition $(\mathrm{NaOH})_m{\cdot}(\mathrm{H_2O})_n{\cdot}\mathrm{Na}^+$. This suggests that the NaOH products are generated by the ground state chemical reactions and not only after the excitation. Since the UV photon and electron ionization represent quite different excitation processes they would probably yield a different kind of ions. The reason why the odd m clusters are not ionized by NaPI has been briefly explained above and discussed in detail elsewhere [5]. On the other hand, all-purpose EI can ionize clusters with any number of picked up Na atoms. If there are two Na atoms picked up yielding two NaOH products, the EI can lead to OH fragmentation yielding $(NaOH)\cdot(H_2O)_n\cdot Na^+$. Analogically the other odd m ions in the EI spectra can be generated. Thus the observation of the odd m ions in the EI spectra is consistent with the larger fragmentation after electron ionization compared to photoionization [25].

The main conclusion from this section concerns applicability of the NaPI method to the neutral cluster size determination. The method has indeed been proven to deliver reliable results for water and other homogeneous clusters [3–5,7–11,25]. Nevertheless, great attention must be paid to a single Na atom doping, since in case of multiple doping the above mentioned Na reactions with water release significant energy (reaction (8) is by 8.9 eV exoergic) which can lead to substantial cluster decay.

4 Conclusions

Cluster doping with sodium atoms and subsequent photoionization is a relatively new method of fragmentation-free ionization used in cluster mass spectrometry [3–5,7–11,25]. All these previous studies investigated homogeneous clusters. Nevertheless atmospheric aerosols are mostly heterogeneous species. Therefore we have concentrated on mixed clusters, combining NaPI with EI for RTOF mass spectrometry. We have provided experimental evidence that a presence of a single impurity molecule can make the cluster undetectable by the NaPI, if Na atoms or the solvated electrons react with the cluster molecules [24,32]. Here we present an example of mixed ammonia-water clusters which are detected by NaPI method but the mass spectra do not correspond to the neutral cluster size and composition. We also show that attention must be paid to single cluster doping in NaPI due to the sodium reactivity. In summary, the NaPI method is relatively well established, yet detailed understanding of Na reactivity is necessary for its practical application.

Several particular conclusions can be outlined:

(1) The NaPI method has been demonstrated to be "blind" to mixed HNO_3-water and N_2O-water clusters where reactions between Na atoms and cluster constituents occur. This is suggested to be a general pattern for molecules which are able to accept electrons.

(2) Mixed ammonia-water clusters have been detected by both NaPI and EI, but each method revealed a different cluster composition. Surprisingly, the EI spectra exhibited clusters with higher ammonia content, thus the differences cannot be simply attributed to larger fragmentation upon EI compared to NaPI. Therefore the NaPI method does not provide the real neutral cluster composition for these mixed clusters. The possible scenarios of cluster fragmentation in the NaPI process have been discussed.

(3) Sodium reactivity in pure water clusters doped with several Na atoms has been observed in accordance with previous studies [5,45], and the combination of NaPI and EI confirms the reactions occurring in the electronically ground state on ice nanoparticles. Sodium reactions in clusters lead to substantial energy release and subsequently to cluster fragmentation. Therefore, attention must be paid to single doping if NaPI is used for cluster size analysis.

(4) The combination of the NaPI and EI methods represents a new tool for investigating Na reactivity in clusters and laboratory systems mimicking atmospheric aerosol particles and ices.

Currently, we are extending our investigations and preliminary results point to several further systems with similar behavior as outlined in point (1): "invisibility" of the clusters for NaPI. Concerning point (2), we have presented a hypothesis to substantiate the experimental observations: selective evaporation of NH_3 molecules in both Na-pickup and ionization process yields ions with less NH_3 in NaPI, while a generation of ionized ammonia core leads to a loss of less NH_3 molecules from clusters in case of EI. Further theoretical investigations are needed to confirm this hypothesis and fully understand the underlying processes. Such studies are currently being carried out in our laboratory and collaborating theoretical groups.

We dedicate this article to Prof. Michael Allan, who has been a great inspiration for many from our Czecho-Slovak community of chemical-physicists. This work was supported by the Czech Science Foundation Project No. 14-08937S. P. Rubovič acknowledges the support from Vakuum Praha. We thank P. Slavíček for fruitful discussions.

References

1. R.S. MacTaylor, A.W. Castleman, J. Atmos. Chem. **36**, 23 (2000)
2. A. Laskin, J. Laskin, S. Nizkorodov, Environ. Chem. **9**, 163 (2012)
3. B.L. Yoder, J.H. Litman, P.W. Forysinski, J.L. Corbett, R. Signorell, J. Phys. Chem. Lett. **2**, 2623 (2011)
4. C. Bobbert, S. Schütte, C. Steinbach, U. Buck, Eur. Phys. J. D **19**, 183 (2002)
5. C. Steinbach, U. Buck, Phys. Chem. Chem. Phys. **7**, 986 (2005)
6. T. Zeuch, U. Buck, Chem. Phys. Lett. **579**, 1 (2013)
7. S. Schütte, U. Buck, Int. J. Mass Spectrom. **220**, 183 (2002)
8. B. Schläppi, J.J. Ferreiro, J.H. Litman, R. Signorell, Int. J. Mass Spectrom. **372**, 13 (2014)
9. P. Forysinski, P. Zielke, D. Luckhaus, J. Corbett, R. Signorell, J. Chem. Phys. **134**, 094314 (2011)
10. J.H. Litman, B.L. Yoder, B. Schläppi, R. Signorell, Phys. Chem. Chem. Phys. **15**, 940 (2013)
11. B. Schläppi, J.H. Litman, J.J. Ferreiro, D. Stapfer, R. Signorell, Phys. Chem. Chem. Phys. **17**, 25761 (2015)
12. A.H. West, B.L. Yoder, R. Signorell, J. Phys. Chem. A **113**, 13326 (2013)
13. A.H. West, B.L. Yoder, D. Luckhaus, C.M. Saak, M. Doppelbauer, R. Signorell, J. Phys. Chem. Lett. **6**, 1487 (2015)
14. R.M. Forck, I. Dauster, Y. Schieweck, T. Zeuch, U. Buck, M. Ončák, P. Slavíček, J. Chem. Phys. **132**, 221102 (2010)

15. R.M. Forck, C.C. Pradzynski, S. Wolff, M. Ončák, P. Slavíček, T. Zeuch, Phys. Chem. Chem. Phys. **9**, 3004 (2012)
16. C.C. Pradzynski, R.M. Forck, T. Zeuch, P. Slavíček, U. Buck, Science **337**, 1529 (2012)
17. R.M. Forck, J.M. Dieterich, C.C. Pradzynski, A.L. Huchting, R.A. Mata, T. Zeuch, Phys. Chem. Chem. Phys. **14**, 9054 (2012)
18. U. Buck, C.C. Pradzinski, T. Zeuch, J.M. Dieterich, B. Hartke, Phys. Chem. Chem. Phys. **16**, 6859 (2014)
19. C.R. Webster, R.D. May, D.W. Toohey, L.M. Avallone, J.G. Anderson, P. Newman, L. Lait, M.R. Schoeberl, J.W. Elkins, K.R. Chan, Science **261**, 1130 (1993)
20. M.J. Molina, T.L. Tso, L.T. Molina, F.C.Y. Wang, Science **238**, 1253 (1987)
21. T. Peter, Ann. Rev. Phys. Chem. **48**, 785 (1997)
22. A.J. Prenni, M.A. Tolbert, Acc. Chem. Res. **34**, 545 (2001)
23. A. Bogdan, M.J. Molina, H. Tenhu, E. Mayer, T. Loerting, Nat. Chem. **2**, 197 (2010)
24. J. Lengyel, A. Pysanenko, J. Kočišek, V. Poterya, C. Pradzynski, T. Zeuch, P. Slavíček, M. Fárník, J. Phys. Chem. Lett. **3**, 3096 (2012)
25. J. Lengyel, A. Pysanenko, V. Poterya, J. Kočišek, M. Fárník, Chem. Phys. Lett. **612**, 256 (2014)
26. M. Fárník, V. Poterya, Front. Chem. **2**, 4 (2014)
27. V. Poterya, J. Kočišek, J. Lengyel, P. Svrčková, A. Pysanenko, D. Hollas, P. Slavíček, M. Fárník, J. Phys. Chem. A **118**, 4740 (2014)
28. P. Svrčková, A. Pysanenko, J. Lengyel, P. Rubovič, J. Kočišek, V. Poterya, P. Slavíček, M. Fárník, Phys. Chem. Chem. Phys. **17**, 25734 (2015)
29. J. Kočišek, J. Lengyel, M. Fárník, J. Chem. Phys. **138**, 124306 (2013)
30. J. Lengyel, R. Gorejová, Z. Herman, M. Fárník, J. Phys. Chem. A **117**, 11225 (2013)
31. J. Kočišek, J. Lengyel, M. Fárník, P. Slavíček, J. Chem. Phys. **139**, 214308 (2013)
32. D. Šmidová, J. Lengyel, A. Pysanenko, J. Med, P. Slavíček, M. Fárník, J. Phys. Chem. Lett. **6**, 2865 (2015)
33. S.Q. Wei, A.W. Castleman, Int. J. Mass Spectrom. Ion Process. **131**, 233 (1994)
34. L. Belau, K.R. Wilson, S.R. Leone, M. Ahmed, J. Phys. Chem. A **111**, 10075 (2007)
35. C. Steinbach, U. Buck, J. Chem. Phys. **122**, 134301 (2005)
36. W.T. Huntress, Astrophys. J. Suppl. Series **33**, 495 (1977)
37. C.P. Schulz, R. Haugstätter, H.U. Tittes, I.V. Hertel, Phys. Rev. Lett. **57**, 1703 (1986)
38. I.V. Hertel, Hüglin, C. Nitsch, C.P. Schulz, Phys. Rev. Lett. **67**, 1767 (1991)
39. U. Buck, C. Steinbach, J. Phys. Chem. A **102**, 7333 (1998)
40. C. Bobbert, C.P. Schulz, Eur. Phys. J. D **16**, 95 (2001)
41. P.E. Mason, F. Uhlig, V. Vaněk, T. Buttersack, S. Bauerecker, P. Jungwirth, Nat. Chem. **7**, 250 (2015)
42. J. Fedor, V. Poterya, A. Pysanenko, M. Fárník, J. Chem. Phys. **135**, 104305 (2011)
43. J. Lengyel, J. Kočišek, V. Poterya, A. Pysanenko, P. Svrčková, M. Fárník, D. Zaouris, J. Fedor, J. Chem. Phys. **137**, 034304 (2012)
44. J. Lengyel, A. Pysanenko, V. Poterya, P. Slavíček, M. Fárník, J. Kočišek, J. Fedor, Phys. Rev. Lett. **112**, 113401 (2014)
45. C. Mundy, J. Hutter, M. Parrinello, J. Am. Chem. Soc. **122**, 4837 (2000)
46. N. Gimelshein, S. Gimelshein, C.C. Pradzynski, T. Zeuch, U. Buck, J. Chem. Phys. **142**, 244305 (2015)

Appendix C

Photochemistry of molecules on ice nanoparticles

THE JOURNAL OF CHEMICAL PHYSICS **141**, 074309 (2014)

Imaging of hydrogen halides photochemistry on argon and ice nanoparticles

V. Poterya,[a] J. Lengyel,[b] A. Pysanenko, P. Svrčková,[b] and M. Fárník[c]
J. Heyrovský Institute of Physical Chemistry v.v.i., Academy of Sciences of the Czech Republic,
Dolejškova 3, 18223 Prague, Czech Republic

(Received 29 May 2014; accepted 28 July 2014; published online 18 August 2014)

The photodissociation dynamics of HX (X = Cl, Br) molecules deposited on large Ar_N and $(H_2O)_N$, $\bar{N} \approx 10^2$–10^3, clusters is investigated at 193 nm using velocity map imaging of H and Cl photofragments. In addition, time-of-flight mass spectrometry after electron ionization complemented by pickup cross section measurements provide information about the composition and structure of the clusters. The hydrogen halides coagulate efficiently to generate smaller $(HX)_n$ clusters on Ar_N upon multiple pickup conditions. This implies a high mobility of HX molecules on argon. On the other hand, the molecules remain isolated on $(H_2O)_N$. The photodissociation on Ar_N leads to strong H-fragment caging manifested by the fragment intensity peaking sharply at zero kinetic energy. Some of the Cl-fragments from HCl photodissociation on Ar_N are also caged, while some of the fragments escape the cluster directly without losing their kinetic energy. The images of H-fragments from HX on $(H_2O)_N$ also exhibit a strong central intensity, however, with a different kinetic energy distribution which originates from different processes: the HX acidic dissociation followed by H_3O neutral hydronium radical formation after the UV excitation, and the slow H-fragments stem from subsequent decay of the H_3O. The corresponding Cl-cofragment from the photoexcitation of the $HCl \cdot (H_2O)_N$ is trapped in the ice nanoparticle. © *2014 AIP Publishing LLC*. [http://dx.doi.org/10.1063/1.4892585]

I. INTRODUCTION

In this article, we focus on the photochemistry of hydrogen halides HX (X = Cl, Br) deposited on argon clusters and ice nanoparticles in molecular beams. The ice particles, hydrogen halides, and ultraviolet (UV) photons belong to the major ingredients in the stratospheric ozone depletion process. The HCl molecule is an inert form of chlorine present in the stratosphere. However, the Cl yield due to the direct photodissociation of gaseous HCl is negligible because of a small actinic flux around 150 nm near the HCl first absorption band maximum. The major activation route of Cl from HCl is the heterogeneous reaction of HCl with $ClONO_2$ on ice particles in polar stratospheric clouds (PSC). This reaction produces the active chlorine in the form of Cl_2 which can be readily photolyzed to the ozone destroying Cl radical.[1–4] Similar schemes were also proposed for Br radical.[4]

Therefore, many studies were carried out to investigate the HX on bulk ice, and a comprehensive review can be found in Huthwelker *et al.*[5] The HX chemistry starts with the uptake of the molecule by the ice surface: it was investigated in dependence on the surface temperature, thickness, and morphology, and on the HCl partial pressure and incident energy. The HCl molecules are adsorbed on the ice efficiently up to a single monolayer of coverage under the PSC conditions. Molecular beam studies[6,7] showed that the HCl has the sticking coefficient of ≈1 at thermal incident energies. The molecules form strong hydrogen bonds with the surface H_2O molecules, and are incorporated into the surface layer. The surface properties play crucial role for the reactivity.

The obviously possible reaction is the water induced acidic dissociation of HX to form the ion pair X^- and H_3O^+. Numerous experimental and theoretical studies were devoted to the question of hydrogen halide acidic dissociation in water clusters and bulk ice surfaces.[8–22] The HCl and HBr solvated by four to five water molecules form the stable zwitterionic structures.[11–15,23] The theoretical modeling of dissociation dynamics of hydrogen halides on the ice surfaces revealed that the preferential position to trigger the ionic mechanism was the one where HX replaced the surface water molecule and was subjected to at least three hydrogen bonds bridging the dangling H and O water sites.[17] The photodissociation of covalently bound hydrogen halides on ice was investigated in detail theoretically.[24,25]

The experimental studies of the HCl reaction with $ClONO_2$ on ice suggest that the reaction is very likely assisted by the ion pair formation.[26] The heterogeneous reactions of HCl with $ClONO_2$ proceeds via Cl^- attacking the chlorine atom of $ClONO_2$, forming Cl_2. To facilitate this reaction on ice, the Cl^- fragment has to move freely on the ice surface.

In our laboratory, we focus on similar experiments with hydrogen halides and other atmospherically relevant molecules on large $(H_2O)_N$ cluster (ice nanoparticles). Recently, we have investigated the uptake of atmospheric molecules including hydrogen halides by ice nanoparticles:

---

[a] Author to whom correspondence should be addressed. Electronic mail: poterya@jh-inst.cas.cz

[b] Also at Department of Physical Chemistry, Institute of Chemical Technology, Technická 5, 16628 Prague 6, Czech Republic.

[c] Author to whom correspondence should be addressed. Electronic mail: michal.farnik@jh-inst.cas.cz

these experiments have revealed that the cluster pickup cross sections can exceed the geometrical ones,[27] and that the large clusters assume quite irregular shapes.[28] To address the question of acidic dissociation in ice nanoparticles, we have performed a series of experiments with photodissociation of hydrogen halide molecules deposited on large water clusters $(H_2O)_N$, $\bar{N} \approx 10^2$–10^3.[29–32] These experiments accompanied by theoretical investigations revealed the hydrogen halide acidic dissociation in the ground state and H_3O radical formation after the UV excitation into a state of charge-transfer-to-solvent (CTTS) character.[23,33,34] The understanding of our results was largely facilitated by a comparison with previous studies of HX on rare gas clusters, namely, Ar_N.[35–41]

The inert environment of rare gas clusters allows to investigate the mechanical processes of the fragment *caging* and *direct exit*.[37] While the previous studies were done by the time-of-flight (TOF) methods, here we present the first investigations of the $HX \cdot (H_2O)_N$ and $HX \cdot Ar_N$ systems using up-to-date velocity map imaging (VMI) technique. The caging processes have been reported in various clusters investigated by VMI as "central blobs" in the images.[42–44] First, in this work we demonstrate that the "central blob" generated by the H-fragment caging from HX photodissociation on Ar_N is quite different in character from the "central blob" formed by the H-fragments from HX photodissociation on $(H_2O)_N$, which is a fingerprint of the acidic dissociation and subsequent H_3O dissociation.

Second, we extend our previous studies of HCl on Ar_N and $(H_2O)_N$ to monitor also the Cl fragments of dissociating HCl molecules. The VMI detection is utilized for the detection of both H and Cl photofragments. One of the atmospherically relevant questions addressed here is: Can the Cl atom escape the ice nanoparticle after the photoexcitation?

Third, in addition to the investigation of photochemistry, we performed other experiments to characterize the studied systems, i.e., electron ionization mass spectrometry of the clusters, and pickup cross section measurements. These measurements reveal an interesting dynamics of the molecules after their uptake by the cluster concerning their mobility and coagulation to $(HX)_n$ on the clusters.

II. EXPERIMENT

In this study, we combine various methods available on our versatile CLUster Beam apparatus (CLUB): (i) the photofragment VMI, (ii) the electron ionization time-of-flight mass spectrometry, and (iii) the velocity measurements to determine the pickup cross sections. The unique combination of these different techniques in one apparatus can provide a detailed insight into the studied cluster species and processes. This combination has been exploited in a parallel study of CF_2Cl_2 for the first time.[45] Fig. 1 shows the schematic overview of the CLUB apparatus experiments. A general description of the apparatus can be found elsewhere,[46] and recent extensions with the VMI system and a new reflectron time-of-flight mass spectrometer (RTOF) are outlined below.

The Ar_N and $(H_2O)_N$ clusters were produced under different expansion conditions summarized in Table I. For the argon expansions and pure water vapour expansions, the cluster size distributions were measured and well characterized previously.[47–51] The reliable mean cluster sizes $\bar{N}$ calculated using Hagena's and Buck's formulas are outlined in Table I. The applied formulas can be found explicitly in our recent publication.[52]

The cluster beam passes through a skimmer and two differentially pumped chambers into the VMI chamber where the photodissociation of molecules in clusters is investigated. Our VMI system was first implemented on our other Apparatus for IMaging (AIM) and is described in detail elsewhere.[43,53] The design of the ion lens system approximately follows the original velocity map imaging of Eppink and Parker.[54] The detector consists of two multichannel

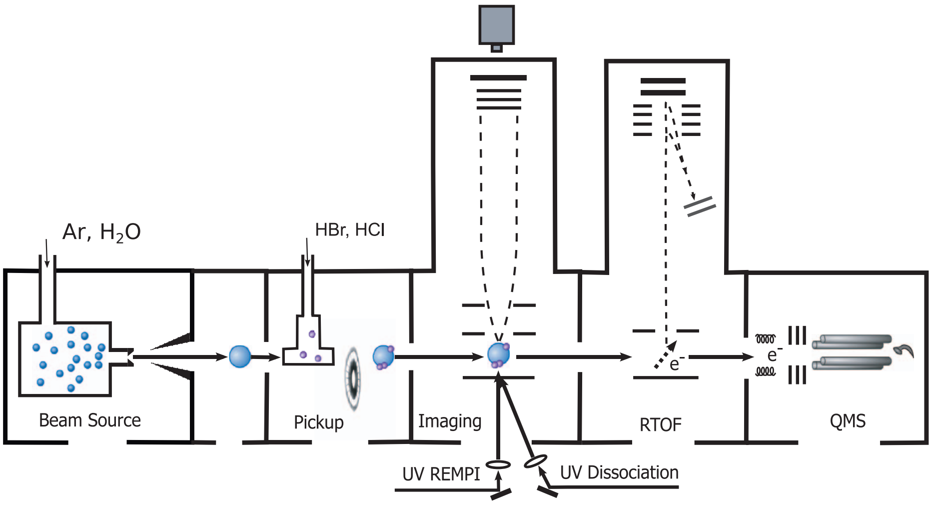

FIG. 1. Schematic drawing of the CLUster Beam (CLUB) apparatus outlining the present experiments. Adapted from Ref. 45.

TABLE I. The expansion conditions exploited in the present work. Nozzle parameters: diameter 55 μm for HCl and rare gas expansions, and 100 μm for water; divergence angle 30° and thickness 2 mm for all expansions. Expansion conditions: nozzle temperature T_0, and stagnation pressure P_0; for water vapour P_0 was determined by the water reservoir temperature T_R. The mean cluster sizes $\bar{N}$ for argon and water clusters were calculated using Hagena's and Buck's formulas.[47–52]

Expansion gas	Source temperature T_0/T_R (K)	Pressure P_0 (bar)	Generated species	Mean size $\bar{N}$	Pickup pressure p_{HX} (10^{-4} mbar)
HCl	313	0.5–1.0	HCl molecule	1	...
HBr	313	0.5–1.0	HBr molecule	1	...
Ar	213–233	5.0–8.0	Ar_N	200–450	0.1–5.5
H_2O	428–443/403–433	3.5–7.0	$(H_2O)_N$	200–750	0.1–5.5

plates in chevron configuration with active diameter 41 mm (TOPAG) in combination with P43 phosphor screen. It can be operated in continuous or gated mode which enables imaging of single ion mass. To record the images we use a CCD camera (Unibrain Fire-i 702b) with imaging lens (25 mm, *f*/1.6). The images were processed using the inverse Abel transform for reconstructing the images.[55] In addition, the results were checked using the Hankel and iterative inversion methods.[55]

In the interaction point, the molecular beam is crossed with two laser beams: the photodissociation 193.3 nm ArF/F_2-Excimer laser, and the tunable ionization laser. All the photodissociation experiments reported here were performed at 193.3 nm. For the resonance enhanced multiphoton ionization (REMPI) of H and Cl($^2P_{3/2}$) fragments, the laser system was tuned to 243.07 nm and 235.336 nm, respectively. The tunable UV radiation was generated by sum frequency mixing of the fundamental 1064 nm from the Nd:YAG laser (Spitlight 1500, Innolas) with the doubled output of the tunable dye laser (Pulsare-S, Lioptec) pumped by the Nd:YAG second harmonics (532 nm). The pulsed lasers were crossed under the mutual angle of 17.5° and operated at 10 Hz frequency in nanosecond regime. Their time overlap was adjusted with delay generator (BNC) and space overlap and system alignment was tested with well known images of HBr molecule.[43]

The next vacuum chamber after the VMI is hosting the RTOF mass spectrometer mounted orthogonally to the molecular beam. The spectrometer was custom built on the basis of our specifications,[56] and has been described in detail recently.[52,57] The clusters were ionized by electrons at 10 kHz repetition frequency, and the mass spectra were recorded with the resolution of $\frac{M}{\Delta M} \approx 10^4$. The electron energy of 70 eV was used in this work.

Finally, the quadrupole mass spectrometer at the end of the machine can be used for the velocity measurements. The cluster beam is interrupted with a pseudorandom chopper after the pickup process, and the time-of-flight is recorded after the clusters are ionized by electrons in a separated quadrupole ion source, and a particular ion fragment is detected. The cluster velocity can be accurately evaluated from the flight time on the 151 cm flight path. Measuring the cluster velocity as a function of the gas pressure in the pickup chamber allows for evaluation of the cluster cross section for the pickup of molecules. The velocity measurements and cluster cross section determination methods have been outlined in detail elsewhere.[27,28,58]

III. RESULTS AND DISCUSSION

A. Photodissociation of HX molecule

First, we briefly reveal the VMI of photodissociation dynamics for isolated HCl and HBr molecules for comparison with the photodissociation of these molecules deposited on the large Ar_N and $(H_2O)_N$ clusters. Besides, the molecular data provide the calibration energies for the investigations of H and Cl photofragments released from the clusters. Fig. 2 shows the images from 193 nm photodissociation of (a) HBr, and (b)–(c) HCl molecules. The panels (a) and (b) correspond to H-fragment imaging (243 nm REMPI) from HBr and HCl, respectively, and (c) corresponds to Cl-fragment (235 nm REMPI) from HCl. The corresponding KEDs are evaluated in Fig. 3. The open squares and blue line in panel (a) shows the H-fragment KED from the isolated HBr molecule

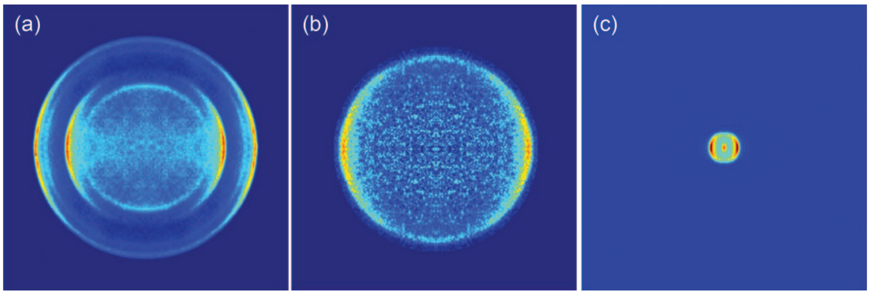

FIG. 2. The images from VMI of 193 nm photodissociation of hydrogen halide molecules: (a) H-fragment (243 nm REMPI) from HBr molecule; (b) H from HCl; (c) Cl (235 nm REMPI) from HCl.

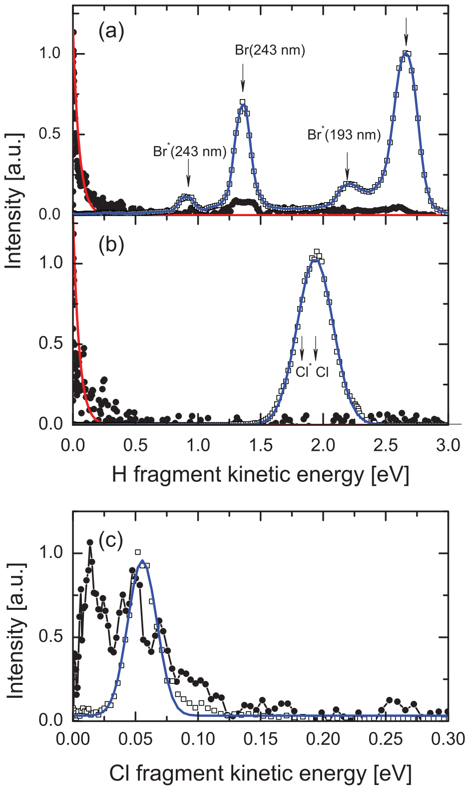

FIG. 3. The fragment KEDs from the photodissociation of hydrogen halide molecules isolated (open symbols) and deposited on large Ar_N clusters (closed symbols): (a) H-fragment from HBr; (b) H from HCl; and (c) Cl from HCl. The KEDs correspond to the images in Fig. 2.

photodissociation. There are two fragment states populated: the ground state $Br(^2P_{3/2})$ and spin-orbit excited state $Br^*(^2P_{1/2})$; the corresponding doublets are labeled by arrows: the one at 0.88 eV and 1.34 eV corresponds to the photodissociation with the "ionization" laser at 243 nm; while the 193 nm photodissociation leads to the higher energies 2.18 eV and 2.65 eV. The HCl molecule dissociates only at the 193 nm generating the H-fragments with kinetic energies around 1.9 eV, Fig. 3(b): two closely spaced Cl-fragment spin-orbit states correspond to the kinetic energies 1.94 eV and 1.83 eV for Cl and Cl*, respectively. The Cl* is populated by about 40%.[59] The corresponding kinetic energy of Cl fragment is very small due to HCl high mass $m(\mathrm{HCl}) = 35$ compared to hydrogen $m(\mathrm{H}) = 1$

$$E_{kin}(\mathrm{Cl}) = \Delta E \cdot \frac{m(\mathrm{H})}{m(\mathrm{HCl})}, \tag{1}$$

where $\Delta E = 1.99$ eV is the total kinetic energy released for Cl ground state. Thus, the $E_{kin}(\mathrm{Cl})$ peaks at 0.055 eV, Fig. 3(c). The Cl* exhibited essentially the same behavior, just a weaker signal. These features have already been discussed in previous investigations of isolated molecules,[60–63] therefore we do not go into more details and rather focus on the changes in the photodissociation dynamics upon the molecule deposition on clusters.

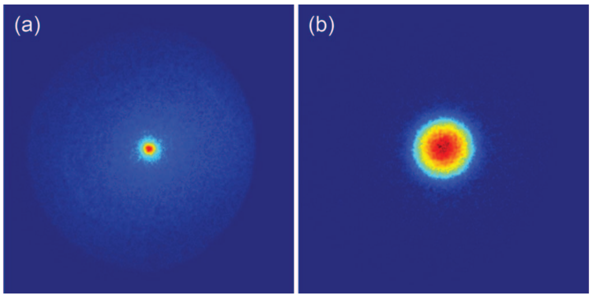

FIG. 4. The H-fragment images of HBr photodissociation at 193 nm (a) on Ar_N, $\bar{N} \approx 250$, and (b) on $(H_2O)_N$, $\bar{N} \approx 500$ clusters.

B. Photodissociation of HX on Ar_N

The photodissociation dynamics changes completely upon adsorption of HX molecules on large Ar_N clusters where it is dominated by the strong *caging* of the H-fragment. This is demonstrated in Fig. 4(a) for HBr molecule adsorbed on Ar_N, $\bar{N} \approx 250$, which exhibits essentially only a strong central intensity. The images of H and Cl fragments from HCl photodissociation on Ar_N are also dominated by the central peak. They are very similar to Fig. 4(a) and therefore not shown. The evaluated KEDs are represented by the solid circles in Fig. 3. The zero kinetic energy peaks were fitted by exponential decrease, red lines in Figs. 3(a) and 3(b). Similar KEDs were obtained in the previous studies of HBr and HCl on Ar_N clusters using the TOF technique.[35–39,41] The strong peak with maximum at 0 eV is the fingerprint of the *cage effect*.[37,43] However, it will be argued below that the strong central "blob" in images does not always point necessarily to the fragment *caging*, and can stem from a much more complex photochemistry, as in the case of hydrogen halides on water clusters.

It has been suggested in the previous TOF studies and accompanied theoretical calculations that the hydrogen halides deposited on the surface of large argon clusters sit most likely half solvated in the outer surface shell with the H-atom pointing into the cluster.[38,39,41] Therefore, after photodissociation the H-fragment departs right into the cluster where it is slowed down in many inelastic collisions with Ar-atoms. The cluster decays during the process and leaves behind the free H-fragment with zero kinetic energy. Indeed, any anisotropy of the velocity distribution which is present in the electronic transition of the free molecule is smeared out in these collisions.

Due to the HX libration motion some of the H-fragments can escape with their energy unperturbed, *direct exit*. The present spectra show some very small intensities at the positions of the molecular peaks for HBr, Fig. 3(a); for HCl this contribution cannot be resolved within the present signal-to-noise ratio, Fig. 3(b). The theoretical simulations comparing the pickup process of hydrogen halides on rare gas clusters showed that HCl had the tendency to sink deeper into the Ar_N surface than HBr. The HCl matched almost perfectly with the Ar position of the outer shell and slightly penetrated into the second shell, while the larger HBr molecule did not fit the position of an Ar atom and stick slightly out from the cluster.[39,41] This also resulted in no cage exit for $\mathrm{HCl} \cdot Ar_N$ around

$\bar{N} \approx 140$,[39] while for HBr the libration motion of the molecule can lead to some direct exit.[38,41] Thus, the present measurements confirm the previous TOF results with the VMI technique.

The entirely new result is the observation of the Cl-fragment from the photodissociation of HCl on Ar_N: Fig. 3(c), black symbols and line, shows the corresponding KED. The Cl-fragment kinetic energy from isolated HCl molecule (open squares) is 0.055 eV (Eq. (1) above). The Cl signal observed from the HCl on Ar_N was very low in the present cluster experiment. Yet, a peak near 0.05 eV can be clearly distinguished in the KED. This agrees with the peak from the isolated molecule, and thus it is suggested to correspond to the direct exit.

However, the energy partitioning between the fragments on Ar cluster should be different from the isolated molecule: the Cl fragment is not dissociating only against the light H atom on the Ar cluster. The dissociation against the heavy cluster would result in the deposition of a larger fraction of the total available energy ΔE into the kinetic energy of the Cl fragment E_{kin}(Cl) according to Eq. (1). However, the Cl kinetic energy E_{kin}(Cl) from the cluster does not extend to much higher values than the peak from the photodissociation of isolated HCl molecule in Fig. 3(c). This suggests that the hydrogen co-fragment is very loose in the Ar_N cluster and the departure of Cl fragment proceeds in a similar manner as from the photodissociation of a free HCl molecule. In other words, the classical momentum conservation can be considered for H and Cl fragments and the H fragment moves freely within the Ar_N cluster (until it eventually collides with an Ar atom).

The other maximum in KED around ≈0.02 eV corresponds to the fragments which have lost their energy in collisions with Ar. These collisions can lead to very effective energy transfer due to the comparable Cl and Ar masses. Therefore, even a single collision can slow down the Cl fragment significantly.

These observations complement the picture obtained from the H-fragment dynamics, namely, that the HCl molecules are deposited in the outer Ar layer oriented with Cl atoms pointing out of the cluster, otherwise the direct Cl-fragment exit would not be observed. Nevertheless, at the same time some Cl-fragments lose at least part of their kinetic energy suggesting that they are partly buried in the surface layer and the fragments collide with Ar atoms upon exit.

Similar results were obtained for various cluster sizes outlined in Table I. Also a range of HCl pickup pressures was exploited ranging from a single molecule pickup to $(HCl)_n$, $n \geq 10$, cluster generation on Ar_N. The great advantage of our present setup is that we can characterize the clusters by independent RTOF mass spectrometry with high mass range and resolution. Fig. 5 demonstrates the generation of $(HCl)_n$ clusters on Ar_N, $\bar{N} \approx 230$. At the low pickup pressure of $p_{HCl} = 0.1\times10^{-4}$ mbar the spectrum (a) is dominated by Ar_N^+ fragment ions accompanied by $Ar_N \cdot HCl^+$ series. Besides, there are Cl^+ and HCl^+ monomer peaks, and some evidence for HCl dimers: the protonated monomer $HClH^+$ and dimer $(HCl)_2^+$ ions. At the higher pressure $p_{HCl} = 3.0\times10^{-4}$ mbar (b) the $(HCl)_k^+$ ions dominate the spectrum; the $Ar_N \cdot HCl^+$ series is weaker and pure Ar_N^+ series is strongly suppressed.

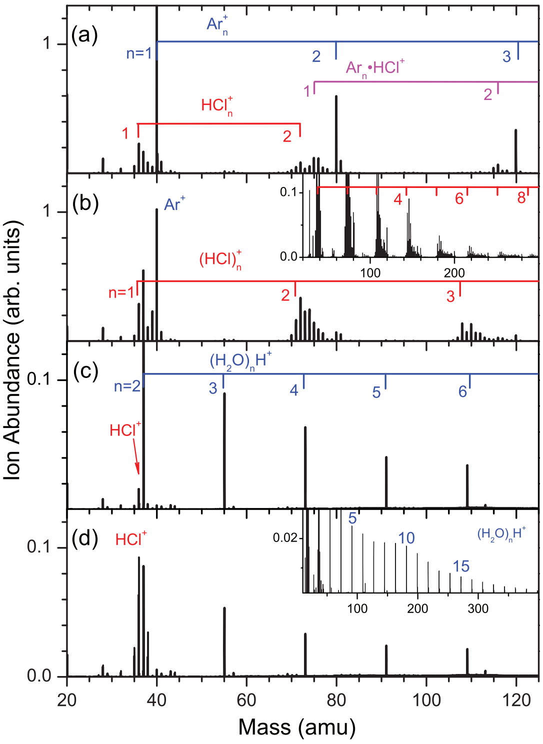

FIG. 5. The RTOF mass spectra after 70 eV electron ionization of Ar_N, $\bar{N} \approx 230$, clusters with adsorbed HCl molecules at different pickup pressures: (a) $p_{HCl} = 0.1\times10^{-4}$ mbar; (b) $p_{HCl} = 3.0\times10^{-4}$ mbar. (c) Pickup of HCl on $(H_2O)_N$, $\bar{N} \approx 700$ clusters at (d) $p_{HCl} = 0.7\times10^{-4}$ mbar; (e) $p_{HCl} = 2.5\times10^{-4}$ mbar.

The cluster ions up to $k = 8$ can be seen in the inset. This demonstrates that quite a few HCl molecules can be adsorbed on the Ar_N cluster and coagulate into the $(HCl)_n$ clusters.

It is interesting to note that the molecules must remain highly mobile to meet and recombine on the Ar_N cluster. The presence of mixed $Ar_N \cdot HCl^+$ fragments in the spectra suggests that the Ar_N cluster does not evaporate completely upon the HCl aggregation. The dissociation energy of HCl dimer of 54 meV was determined experimentally.[64] For the larger clusters the attachment of an additional HCl releases about 150 meV with the values for trimer and tetramer being somewhat larger as calculated theoretically.[65] Thus, approximately 1500 meV energy is released upon the coagulation of $n = 10$ HCl molecules to $(HCl)_n$. The energy needed to evaporate an Ar atom from Ar_N, $N = 200$, cluster is approximately 60 meV.[66] Therefore, about 25 Ar atoms can be evaporated upon the coagulation of 10 HCl molecules which is still much less than the mean argon cluster size. Therefore, $(HCl)_n \cdot Ar_N$ clusters are clearly generated in our experiments at the higher pickup pressures.

We have not considered that the kinetic energy of the adsorbed molecule is transferred into the internal heating of the cluster, rather that the momentum of the molecule is transferred to the change of the whole cluster momentum. This assumption has been tested previously in our pickup experiments[27,28,58] where the slowing down of the clusters by uptake of the molecules was measured. Nevertheless, even if this kinetic energy is considered, it corresponds to approximately 40 meV at the measured cluster velocity of 480 ms^{-1} and it can be spread over all ($3N - 6$) degrees of freedom of the cluster. This would correspond to the cluster heating only by about 1.2 K, which is not sufficient for any appreciable melting of the solid Ar_N cluster. The cluster temperature is known to be $\approx$37 K.[67] However, if the energy was spread over a limited number of degrees of freedom, some increase of temperature and melting of the cluster could be achieved locally, even if only a fraction of the kinetic energy was deposited into the cluster heating. Could this "local heating" caused by the collisions facilitate the coagulation of HCl molecules on Ar cluster? Molecular dynamic simulations for uptake of HBr molecule by Ar_N cluster of the size $N = 130$ showed melting-like process of the whole cluster on the timescale of 10 ns and reconstruction of the icosahedral structure after 50 ns.[38]

Relevant to this discussion is also the study of H+Cl association reaction in Ar clusters[68] where for the temperatures $T \geq 45$ K the cluster was liquid-like and the reaction probability was high, while for $T \leq 40$ K the cluster was solid-like and there was no reactivity. The present study can induce theoretical investigations of the uptake and coagulation processes of the molecules in clusters which can elucidate the molecular details of our experimental observations. This would be highly desirable especially in the view of the differences observed for analogical processes on the water clusters below.

In addition, the pickup cross section measurements outlined in Sec. II have been performed to elucidate the uptake and coagulation processes. The pickup cross section for HCl on Ar_N for $\bar{N} \approx 230$ has been determined $\sigma \approx 950$ Å^2. The number n_p of adsorbed molecules at the pickup pressure p_{HCl} is

$$n_p = \sigma \cdot L_p \cdot \frac{p_{HCl}}{k_B T}, \qquad (2)$$

where $L_p = 17$ cm is the pickup chamber length, k_B is Boltzmann constant, and $T \approx 300$ K is the pickup gas temperature. Thus, $n_p \approx 11$ for $p_{HCl} = 3 \times 10^{-4}$ mbar. The charged $(HCl)_k^+$ fragments up to $k \approx 10$ are discernible in the mass spectra under these conditions, and thus k and n_p from mass spectrometry and pickup measurements, respectively, are consistent. This suggests that the majority of HCl molecules adsorbed on the Ar_N cluster coagulate to $(HCl)_n$.

Nevertheless, the character of images and corresponding KEDs did not change significantly (within our signal to noise ratio) whether a single molecule has been adsorbed on Ar_N or more molecules coagulated to $(HX)_n$ clusters on Ar_N surface. This rises interesting questions: What is the structure of the HX clusters on Ar_N? How do they dissociate on Ar_N? The small isolated $(HX)_n$ clusters have cyclic structures. The photodissociation of the free $(HBr)_n$ clusters yielded a significant contribution of fast H-fragments even for $\bar{n} \geq 10$.[62,69,70] Since no such significant contribution of fast fragments is observed from the $(HBr)_n$ photodissociation on Ar_N, their structure and/or their photodissociation mechanism have to be different on argon compared to free $(HBr)_n$. Theoretical calculations would be needed to answer these questions. Further, we focus on the hydrogen halides on ice nanoparticles.

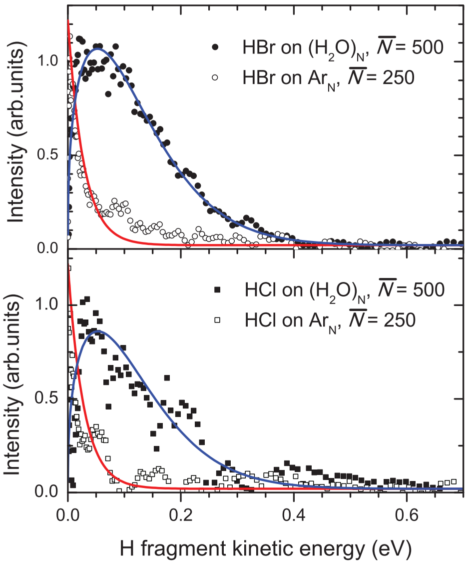

FIG. 6. The H-fragment KEDs from 193 nm photodissociation of (a) HBr and (b) HCl on $(H_2O)_N$, $\bar{N} \approx 500$, clusters. The KEDs from photodissociation of these molecules on Ar_N, $\bar{N} \approx 250$, are shown for comparison.

C. Photodissociation of HX on $(H_2O)_N$

The H-fragment image from 193 nm photodissociation of HBr molecule adsorbed on $(H_2O)_N$, $\bar{N} \approx 500$, is shown in Fig. 4(b). The images of H-fragments from HCl photodissociation were very similar with somewhat lower signal (not shown). It ought to be mentioned that no hydrogen signal from pure water clusters contributes to the data. These images from water clusters exhibit essentially only the strong intensity around the center similar to the case of argon. However, the evaluated KEDs plotted in Fig. 6 show a clear difference between the photodissociation on argon and on water. Since there is no direct exit from HX molecule on $(H_2O)_N$ at the higher kinetic energies, we focus on the energies below 0.7 eV. Here, it is clear that the cage effect in Ar_N corresponds to the peak at 0 eV with nearly exponential decrease in intensity, while the photochemistry on the ice yields rather slow fragments with a KED peaking at $\approx$0.05 eV. The KED extends to $\approx$0.5 eV well beyond the exponential decrease of the fragments from Ar_N. Although the signal for HCl is lower than for HBr, both systems yield very similar picture. It should be noted that our previous TOF investigations of these systems – i.e., HX (X = Cl, Br, and I) on ice nanoparticles – delivered essentially the same KEDs.[29–32] Thus, the present VMI experiments nicely confirm the previous TOF results.

In our previous investigations,[29–32] it was shown that the H-fragments originated from a H_3O neutral hydronium radical. The generation of H_3O upon the UV-excitation in HCl-water clusters was proposed already by earlier theoretical calculations of Sobolewski and Domcke.[23,33,34] We have brought the most direct evidence for the H_3O generation by experiments with the deuterated species comparing $HX \cdot (H_2O)_N$, $DX \cdot (H_2O)_N$, and $HX \cdot (D_2O)_N$ systems. Assuming the hydronium radical generation, we expect to generate H_3O, H_2DO, and D_2HO in these clusters, respectively. Thus, the H-atom signal ratio from these species was expected to be 3:2:1 (assuming the same clusters, expansion and pickup conditions, and observing only the H-signal, not D). This ratio has been confirmed for all three studied hydrogen halides (see Table 5 in Ref. 32). Besides the absorption cross section calculations combined with our experiments showed that the molecules were acidically dissociated on the ice nanoparticle prior to their UV excitation.[30,31] Thus, the following picture arises for the HX photochemistry on ice nanoparticles: HX acidically dissociates upon deposition on $(H_2O)_N$ in the ground state to a localized ion pair structure. This is UV excited to a CTTS state, from where it relaxes to a biradical state, and the hydrogen is released from the H_3O radical. Subsequently, an evidence for the H_3O radical has also been found in time resolved experiments.[71]

The mass spectra for HCl molecules adsorbed on $(H_2O)_N$, $\bar{N} \approx 700$, at $p_{HCl} = 0.7\times10^{-4}$ mbar and 2.5×10^{-4} mbar are shown in Figs. 5(c) and 5(d), respectively. The spectra show the series of protonated water clusters $(H_2O)_NH^+$ typical for the large water cluster ionization and the Cl^+ and HCl^+ mass peaks corresponding to the HCl molecule. There is no evidence for $(HCl)_n$ cluster generation on $(H_2O)_N$ as opposed to $(HCl)_n$ on Ar_N. Similar spectra with the evidence for HCl monomer only were recorded for all the experimental conditions (cluster sizes and pickup pressures) outlined in Table I. It should be noted that any background due to the HCl molecules diffused from the pickup chamber into the ionization region has been carefully subtracted. Thus, the HCl^+ signal corresponds to the molecules which are adsorbed on the $(H_2O)_N$ clusters and carried to the ionization region. These mass spectra and the H-fragment images from HCl molecules prove that the molecules are present on the $(H_2O)_N$ clusters. Yet, these molecules do not generate $(HCl)_n$ clusters even upon elevated pickup pressure corresponding to the multiple pickup.

We could again support our evidence for uptake of several HCl molecules on $(H_2O)_N$ by the pickup cross sections measured previously.[27,28] The pickup cross section of $(H_2O)_N$, $\bar{N} \approx 260$, was $\sigma \approx 690$ Å^2 and 560 Å^2 for HCl and HBr, respectively.[27] Considering the size dependence $\propto N^{1/3}$ proposed by Vigué *et al.*[72] we can extrapolate the pickup cross section for HCl and HBr to 960 Å^2 and 780 Å^2 at $\bar{N} \approx 700$. This corresponds to about 10 HCl molecules adsorbed on the $(H_2O)_N$ cluster of the size $N = 700$ at the pressure $p_{HCl} = 2.5\times10^{-4}$ mbar in the pickup chamber. Recently, we have shown by measuring the pickup cross section size dependence for H_2O on $(H_2O)_N$ that the cross section for $N \geq 400$ departs from the $N^{1/3}$ dependence and can be significantly larger.[28] Thus, the above estimate represents rather the lower limit, and the actual number of molecules adsorbed on the cluster can be more than twice larger.

Several reasons can be discussed why these molecules do not coagulate on $(H_2O)_N$ while they aggregate strongly on Ar_N. First, the HCl molecule is obviously more strongly bound on water than on argon. The binding energy of $HCl\cdots H_2O$ dimer was measured 165 meV,[73] which is about 10-times larger than the binding energy of $HCl\cdots Ar$.[74] In the larger clusters, the binding energies increase, e.g., the calculated physisorption energy of HCl on hexagonal ice surface corresponds to 300 meV.[75] Nevertheless, the difference between water and argon persists. Therefore, the HCl molecules cannot move on the ice surface as freely as on argon where they are not so strongly bound. The $HCl\cdots H_2O$ bond (165 meV)[73] is even three times stronger than $HCl\cdots HCl$ (54 meV),[64] and also stronger than the $H_2O\cdots H_2O$ bond (137 meV).[73] Therefore, the HCl molecule would rather bind to H_2O than to another HCl, and there would be no propensity for HCl clustering on the water cluster. If this trend persists to larger clusters, it remains to be confirmed by theoretical investigations.

In addition, our previous studies have shown that the HCl molecule dissociates acidically and forms a local ion pair $H_3O^+\cdot Cl^-$ on the water clusters.[30–32] If this process happens before the next HCl molecule is adsorbed on the cluster, the clustering of unperturbed HCl molecules is inhibited. The average delay between successive collisions of the cluster with HCl molecules in the pickup chamber at elevated pressures is of the order of 10 μs. Thus, if acidic dissociation happens faster than that the HCl clusters cannot be generated.

Our previous experiments have also shown that the $H_3O^+\cdot Cl^-$ ion pair is of rather local nature, and no proton transfer takes place along the hydrogen bond network within the cluster on the time-scale of ∼1 ms. The evidence for that was the absence of H/D exchange in the clusters upon the acidic ionization. This was clearly demonstrated by the signal ratios: there was 10^3-times more H-atoms in $HX\cdot(H_2O)_n$ clusters with $n \approx 500$ than in $HX\cdot(D_2O)_n$. Yet, the H-signal ratio from these two systems was about 3:1, while rather a ratio of 10^3:1 would be expected if the H/D atoms in these clusters were all equivalent (statistical scrambling). Thus, the proton in H_3O^+ remained immobile in the cluster at least for the flight time of the cluster from the pickup cell (where the HX adsorption and acidic dissociation occur) to the photoexcitation region which was approximately 1 ms.

From this point of view it is interesting to compare our results to the ice surface studies of Kang's group.[76–80] They observed that the proton can be stabilized at the pure ice surface as a hydronium ion by an activation barrier.[80] On the other hand, a very efficient H/D exchange of surface water molecules was observed upon adsorption of HCl onto ice films[77] suggesting that the proton transfer can occur easily on the ice surface with a negligible barrier. They also investigated the temperature dependent transition of HCl from molecular to ionically dissociated form.[76,78,79] This transition occurred between 90 K and 120 K. Since we have presented an evidence for the ionically dissociated molecules on clusters,[30–32] the present cluster temperature probably exceeds 90 K. This is quite in agreement with the cluster temperatures around 100 K suggested by recent spectroscopy experiments.[81]

The 193 nm and 157 nm photodissociation of water ice films dosed with HCl was also investigated.[82] Dependence on surface temperature and morphology was discussed. There has been a recent evidence on the cluster morphology from our group,[28] namely, that the large clusters assume highly irregular shapes. Also the aforementioned spectroscopic investigation[81] found an evidence for a hexagonal ice core in these clusters. However, a direct comparison of the surface study[82] with our results is difficult. In the surface experiments, the hydrogen atoms from water photodissociation contributed to the results, while they have been avoided in our experiments. In addition, much higher HCl coverages were used in the surface experiments. Some slow H-fragments were observed from the surfaces upon dosing with HCl, however, the hydronium radical mechanism was not considered in their interpretation. No Cl fragments from the ice surfaces were observed at 193 nm in agreement with our cluster results (below). However, the Cl-fragments from surfaces were detected at 157 nm, and they were interpreted as coming from the covalently bound (not ionically dissociated) HCl molecules.

Our mass spectrometry experiments also provide some evidence for non-dissociated HCl molecules on $(H_2O)_N$, namely, the HCl^+ ion fragment. It is possible that our photodissociation and electron ionization experiments are sensitive to different species: due to the shift in the HCl absorption spectrum after the acidic dissociation[30–32] the ionically dissociated species are excited much more efficiently at 193 nm. On the other hand, the non-dissociated HCl molecules can be ionized by the electrons (or charge transfer from the ionized water) more efficiently than the $Cl^- \cdot H_3O^+$ ion pair. Therefore, the photodissociation experiment probes the ionically dissociated $Cl^- \cdot H_3O^+$, while the mass spectrometry probes the remaining covalently bound HCl molecules on $(H_2O)_N$ yielding the Cl^+ and HCl^+ ions in essentially the same ratio as the gas phase HCl ionization. This mechanism remains to be elucidated in more detail by theory and further experiments.

One of the most important results of the present investigation is that we do not observe any Cl fragments from the photoexcitation of the $HCl \cdot (H_2O)_N$ system. Despite the fact that the $(HCl)_n$ clusters are not generated on $(H_2O)_N$ there is no doubt, that the HCl molecules stay on the ice nanoparticles and are photoexcited via the H_3O generation mechanism – this is evidenced by the observed strong H-fragment signal. The H-signal from $HCl \cdot (H_2O)_N$ is significantly stronger than from $HCl \cdot Ar_N$ under comparable conditions (cluster sizes and pickup pressures). In addition, the Cl signal has been observed from $HCl \cdot Ar_N$ system. Therefore, it is rather surprising on the first sight that no measurable Cl-fragment signal has been observed from $HCl \cdot (H_2O)_N$.

What is the fate of the Cl fragment after the photoexcitation? Why is it not detected? This observation is actually consistent with the above H_3O mechanism: the $HCl \cdot (H_2O)_N$ cluster undergoes the acidic dissociation to $Cl^- \cdot H_3O^+ \cdot (H_2O)_{N-1}$, and subsequent UV excitation to the CTTS state leads to the biradical generation $Cl \cdot H_3O \cdot (H_2O)_{N-1}$ from which the observed H fragment is released.[23,29–34] The Cl radical is generated in the excitation process, however, the energy released by the relaxation to the biradical state is relatively low and mostly carried away by the released H-fragment. The theoretical calculations[34] suggest that this energy corresponds to about 0.5 eV. The high energy tail of KEDs in Fig. 6 extends to 0.5 eV. Therefore, there is probably not enough energy to release also the heavy Cl fragment from the cluster, and the water cluster is not decaying after the excitation process. This is different from the HCl dissociation on Ar_N where the Cl fragment is also very slow, however, the weakly bound rare gas cluster decays during the process. This is confirmed by the observation of the zero kinetic energy H-fragments, which have been slowed down by the collisions with Ar atoms to 0 eV, yet they remain free and are detected in our experiment. These processes on Ar_N and $(H_2O)_N$ are schematically depicted in Fig. 7.

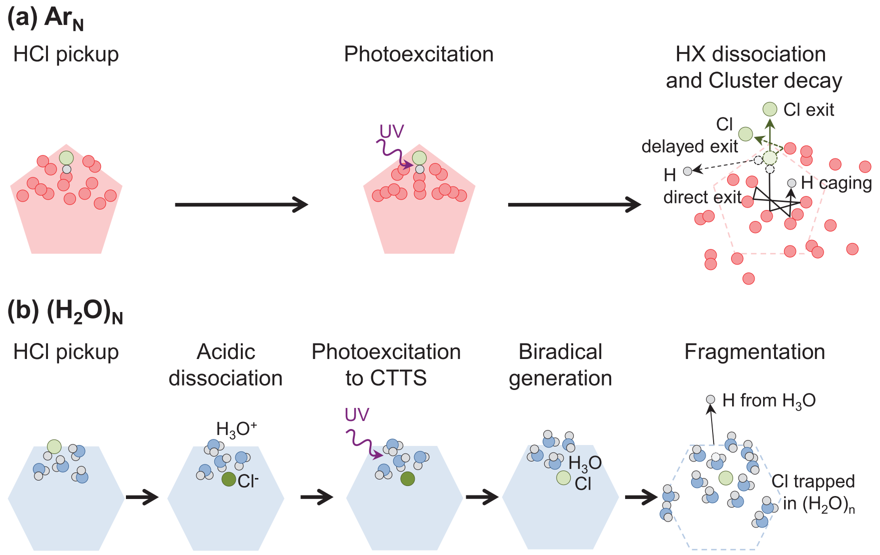

FIG. 7. The schematic picture of the reaction mechanism: (a) on Ar_N the H-fragment is mostly caged by the cluster to zero kinetic energy, but the cluster decays during the process and the fragment is detected; the Cl-fragment exits directly or loses some kinetic energy in collisions with Ar. (b) On $(H_2O)_N$ the HCl undergoes the acidic dissociation in the ground state; $Cl^- \cdot H_3O^+ \cdot (H_2O)_{N-1}$ is UV excited to a state of charge-transfer-to-solvent (CTTS) character; barrierless transition to the biradical state $Cl \cdot H_3O \cdot (H_2O)_{N-1}$ follows; the observed H fragment is released while the Cl fragment remains caged in the remaining cluster.

Even though the detailed mechanism of Cl fragment caging should be the subject of further theoretical studies, it remains a clear experimental fact that the Cl fragments from $HCl\cdot(H_2O)_N$ are not observed. This can have atmospheric consequences: In our previous TOF studies, we have argued that the acidic dissociation of hydrogen halides on ice nanoparticles shifts the absorption spectrum to the region where there is significantly higher photon flux by several orders of magnitude.[30,32] This could enhance the photodissociation of HCl when deposited on ice nanoparticles in the stratosphere with respect to the gas phase photodissociation. Nevertheless, the present study shows that this enhancement will not contribute to the Cl radical yield in the stratosphere since the Cl is not released from the ice nanoparticles.

As the last remark it is worth to mention our very recent investigation of CF_2Cl_2 deposited on argon and water clusters.[45] Several results have been remarkably similar to the present case: e.g., $(CF_2Cl_2)_n$ clusters were generated on large Ar_N clusters upon multiple pickup of CF_2Cl_2 molecules, while only isolated CF_2Cl_2 molecules were detected on $(H_2O)_N$; Cl fragments from CF_2Cl_2 on $(H_2O)_N$ were also trapped in the remaining water cluster and not detected, although the photodissociation mechanism of CF_2Cl_2 was, indeed, different from acidically dissociated HCl. Thus, the difference in molecule mobility on argon and water clusters, and the heavy fragment trapping in water cluster seems to be a general common feature of these systems.

IV. CONCLUSIONS

Photodissociation dynamics of HCl and HBr molecules deposited on large Ar_N and $(H_2O)_N$ clusters has been investigated in VMI experiment. In addition, the TOF mass spectrometry after electron ionization complemented by pickup cross section measurements have revealed information about the composition and structure of the species generated by uptake of the hydrogen halide molecules on the clusters.

Although the photodissociation of hydrogen halides on rare gas and water clusters has been investigated before,[29–32,35–41] new results are presented here:

- the first VMI images for HBr and HCl on large Ar_N and $(H_2O)_N$;
- the Cl-fragment dynamics from HCl on Ar_N and $(H_2O)_N$ has been investigated for the first time;
- it has been revealed that "central blobs" in VMI can point to different dynamics: namely, *caging* versus H_3O dynamics in the present case;
- the combination of mass spectrometry and pickup cross section measurements showed interesting effects of mobility, binding, and coagulation of HX molecules on the clusters.

These points are detailed below.

First, the experiments demonstrated that upon multiple pickup conditions the hydrogen halides coagulate efficiently to generate $(HX)_n$ clusters on the large Ar_N clusters. This implies a high mobility of HX molecules on argon. On the other hand, the HX molecules remain isolated on the ice nanoparticles. This is consistent with the stronger bonding of HX to water than to Ar and with the acidic dissociation of HX on $(H_2O)_N$.

Photodissociation of HX on Ar_N leads to strong H-fragment caging for all investigated cluster sizes $\bar{N} = 200$–450 and up to $\bar{n} \approx 1$–10 HX molecules deposited and coagulated on Ar_N. The H caging is manifested by a peak of exponential character with the maximum at 0 eV. The Cl-fragments from the photodissociation are also partly caged. However, some Cl-atoms escape the cluster directly without losing any kinetic energy. Their KED suggests that they dissociate against the light H-atom and not against the whole Ar_N cluster. This points to a weak and floppy binding of the HCl molecule to the argon cluster.

On the other hand, the H-fragments from HX on $(H_2O)_N$ exhibit quite different dynamics. The KEDs obtained from the present VMI experiments confirm the previous TOF measurements.[29–32] They were shown previously to originate from HX acidic dissociation on $(H_2O)_N$ and UV excitation into a CTTS state and subsequent relaxation to a biradical state, where the hydrogen is released from the H_3O radical.[23,29–34] An important message from the present investigations is that the images from $HX\cdot(H_2O)_N$ system exhibit strong central "blob" usually attributed to *caging* in the literature. However, upon closer inspection and analysis it is revealed that it actually reflects quite different photodynamics.

The corresponding Cl-cofragment from the HCl photodissociation on $(H_2O)_N$ is not observed and is presumably lost in the ice nanoparticle. This can be important result for atmospheric chemistry, and the possible atmospheric consequences of this process are briefly discussed.

ACKNOWLEDGMENTS

This work has been supported by the Grant Agency of the Czech Republic Project No. 14-14082S. We also thank J. Kočišek for valuable discussions. J. Lengyel acknowledges the Gordon F. Kirkbright bursary award by the Association of British Spectroscopists (ABS) Trust.

[1] S. Solomon, R. R. Garcia, F. S. Rowland, and D. J. Wuebbles, Nature (London) **321**, 755 (1986).

[2] M. J. Molina, T. L. Tso, L. T. Molina, and F. C. Y. Wang, Science **238**, 1253 (1987).

[3] M. A. Tolbert, M. J. Rossi, R. Malhotra, and D. M. Golden, Science **238**, 1258 (1987).

[4] S. Solomon, Rev. Geophys. **37**, 275, doi:10.1029/1999RG900008 (1999).

[5] T. Huthwelker, M. Ammann, and T. Peter, Chem. Rev. **106**, 1375 (2006).

[6] M. J. Isakson and G. O. Sitz, J. Phys. Chem. A **103**, 2044 (1999).

[7] P. U. Andersson, M. B. Någård, and J. B. C. Pettersson, J. Phys. Chem. B **104**, 1596 (2000).

[8] K. Ando and J. T. Hynes, J. Phys. Chem. B **101**, 10464 (1997).

[9] L. Delzeit, K. Powell, N. Uras, and J. P. Devlin, J. Phys. Chem. B **101**, 2327 (1997).

[10] D. A. Estrin, J. Kohanoff, D. H. Laria, and R. O. Weht, Chem. Phys. Lett. **280**, 280 (1997).

[11] S. Re, Y. Osamura, Y. Suzuki, and H. F. Schaefer, J. Chem. Phys. **109**, 973 (1998).

[12] B. Gertner, G. Peslherbe, and J. Hynes, Isr. J. Chem. **39**, 273 (1999).

[13] A. Milet, C. Struniewicz, R. Moszynski, and P. E. S. Wormer, J. Chem. Phys. **115**, 349 (2001).

[14] S. M. Hurley, T. E. Dermota, D. P. Hydutsky, and A. W. Castleman, Science **298**, 202 (2002).

[15] S. M. Hurley, T. E. Dermota, D. P. Hydutsky, and A. W. Castleman, J. Chem. Phys. **118**, 9272 (2003).

[16] V. Buch, J. Sadlej, N. Aytemiz-Uras, and J. P. Devlin, J. Phys. Chem. A **106**, 9374 (2002).
[17] J. P. Devlin, N. Uras, J. Sadlej, and V. Buch, Nature (London) **417**, 269 (2002).
[18] M. Weimann, M. Fárník, and M. A. Suhm, Phys. Chem. Chem. Phys. **4**, 3933 (2002).
[19] A. Al-Halabi, R. Bianco, and J. T. Hynes, J. Phys. Chem. A **106**, 7639 (2002).
[20] M. Fárník, M. Weimann, and M. A. Suhm, J. Chem. Phys. **118**, 10120 (2003).
[21] J. P. Devlin, M. Fárník, M. Suhm, and V. Buch, J. Phys. Chem. A **109**, 955 (2005).
[22] T. E. Dermota, D. P. Hydutsky, N. J. Bianco, and A. W. Castleman, J. Chem. Phys. **123**, 214308 (2005).
[23] A. L. Sobolewski and W. Domcke, J. Phys. Chem. A **107**, 1557 (2003).
[24] S. Woittequand, C. Toubin, B. Pouilly, M. Monnerville, S. Briquez, and H. D. Meyer, Chem. Phys. Lett. **406**, 202 (2005).
[25] S. Woittequand, D. Duflot, M. Monnerville, B. Pouilly, C. Toubin, S. Briquez, and H. D. Meyer, J. Chem. Phys. **127**, 164717 (2007).
[26] S. Lee, D. C. Leard, R. Zhang, L. T. Molina, and M. J. Molina, Chem. Phys. Lett. **315**, 7 (1999).
[27] J. Lengyel, J. Kočišek, V. Poterya, A. Pysanenko, P. Svrčková, M. Fárník, D. Zaouris, and J. Fedor, J. Chem. Phys. **137**, 034304 (2012).
[28] J. Lengyel, A. Pysanenko, V. Poterya, P. Slavíček, M. Fárník, J. Kočišek, and J. Fedor, Phys. Rev. Lett. **112**, 113401 (2014).
[29] V. Poterya, M. Fárník, P. Slavíček, U. Buck, and V. V. Kresin, J. Chem. Phys. **126**, 071101 (2007).
[30] M. Ončák, P. Slavíček, V. Poterya, M. Fárník, and U. Buck, J. Phys. Chem. A **112**, 5344 (2008).
[31] V. Poterya, J. Fedor, A. Pysanenko, O. Tkáč, J. Lengyel, M. Ončák, P. Slavíček, and M. Fárník, Phys. Chem. Chem. Phys. **13**, 2250 (2011).
[32] M. Ončák, P. Slavíček, M. Fárník, and U. Buck, J. Phys. Chem. A **115**, 6155 (2011).
[33] A. L. Sobolewski and W. Domcke, Phys. Chem. Chem. Phys. **4**, 4 (2002).
[34] A. L. Sobolewski and W. Domcke, Phys. Chem. Chem. Phys. **9**, 3818 (2007).
[35] R. Baumfalk, N. H. Nahler, and U. Buck, Faraday Discuss. **118**, 247 (2001).
[36] R. Baumfalk, N. H. Nahler, and U. Buck, Phys. Chem. Chem. Phys. **3**, 2372 (2001).
[37] U. Buck, J. Phys. Chem. A **106**, 10049 (2002).
[38] N. H. Nahler, R. Baumfalk, U. Buck, H. Vach, P. Slavíček, and P. Jungwirth, Phys. Chem. Chem. Phys. **5**, 3394 (2003).
[39] N. H. Nahler, M. Fárník, U. Buck, H. Vach, and R. B. Gerber, J. Chem. Phys. **121**, 1293 (2004).
[40] P. Slavíček, P. Jungwirth, M. Lewerenz, N. H. Nahler, M. Fárník, and U. Buck, J. Chem. Phys. **120**, 4498 (2004).
[41] M. Fárník, N. H. Nahler, U. Buck, P. Slavíček, and P. Jungwirth, Chem. Phys. **315**, 161 (2005).
[42] L. Rubio-Lago, D. Zaouris, Y. Sakellariou, D. Sofikitis, T. N. Kitsopoulos, F. Wang, X. Yang, B. Cronin, A. L. Devine, G. A. King *et al.*, J. Chem. Phys. **127**, 064306 (2007).
[43] J. Fedor, J. Kočišek, V. Poterya, O. Votava, A. Pysanenko, L. Lipciuc, T. N. Kitsopoulos, and M. Fárník, J. Chem. Phys. **134**, 154303 (2011).
[44] P. Glodic, A. Kartakoullis, M. Fárník, P. C. Samartzis, and T. N. Kitsopoulos, J. Chem. Phys. **137**, 154306 (2012).
[45] V. Poterya, J. Kočišek, J. Lengyel, P. Svrčková, A. Pysanenko, D. Hollas, P. Slavíček, and M. Fárník, J. Phys. Chem. A **118**, 4740 (2014).
[46] M. Fárník, *Molecular Dynamics in Free Clusters and Nanoparticles Studied in Molecular Beams* (ICT Prague Press, Institute of Chemical Technology, Prague, 2011).
[47] O. F. Hagena, Surf. Sci. **106**, 101 (1981).
[48] O. F. Hagena, Z. Phys. D **4**, 291 (1987).
[49] O. F. Hagena, Rev. Sci. Instrum. **63**, 2374 (1992).
[50] U. Buck and R. Krohne, J. Chem. Phys. **105**, 5408 (1996).
[51] C. Bobbert, S. Schütte, C. Steinbach, and U. Buck, Eur. Phys. J. D **19**, 183 (2002).
[52] J. Kočišek, J. Lengyel, M. Fárník, and P. Slavíček, J. Chem. Phys. **139**, 214308 (2013).
[53] V. Poterya, J. Kočišek, A. Pysanenko, and M. Fárník, Phys. Chem. Chem. Phys. **16**, 421 (2014).
[54] A. T. J. B. Eppink and D. H. Parker, Rev. Sci. Instrum. **68**, 3477 (1997).
[55] B. Whitaker, *Imaging in Molecular Dynamics* (Cambridge University Press, Cambridge, 2003).
[56] See http://www.kaesdorf.de/ for time-of-flight spectrometers by S. Kaesdorf, Geräte für Forschung und Industrie.
[57] J. Lengyel, A. Pysanenko, J. Kočišek, V. Poterya, C. Pradzynski, T. Zeuch, P. Slavíček, and M. Fárník, J. Phys. Chem. Lett. **3**, 3096 (2012).
[58] J. Fedor, V. Poterya, A. Pysanenko, and M. Fárník, J. Chem. Phys. **135**, 104305 (2011).
[59] J. Zhang, M. Dulligan, and C. Wittig, J. Chem. Phys. **107**, 1403 (1997).
[60] Z. Xu, B. Koplitz, and C. Wittig, J. Phys. Chem. **92**, 5518 (1988).
[61] T. Kinugawa and T. Arikawa, J. Chem. Phys. **96**, 4801 (1992).
[62] R. Baumfalk, U. Buck, C. Frischkorn, N. H. Nahler, and L. Hüwel, J. Chem. Phys. **111**, 2595 (1999).
[63] T. P. Rakitzis, P. C. Samartzis, R. L. Toomes, L. Tsigiridas, M. Coriou, D. Chestakov, A. T. J. B. Eppink, D. H. Parker, and T. N. Kitsopoulos, Chem. Phys. Lett. **364**, 115 (2002).
[64] H. Ni, J. M. Serafin, and J. J. Valentini, J. Chem. Phys. **113**, 3055 (2000).
[65] R. C. Guedes, P. C. do Couto, and B. J. C. Carbal, J. Chem. Phys. **118**, 1272 (2003).
[66] A. V. Malakhovskii and M. Ben-Zion, Chem. Phys. **264**, 135 (2001).
[67] J. Farges, M. F. de Feraudy, B. Raoult, and G. Torchet, Surf. Sci. **106**, 95 (1981).
[68] B. Schmidt and B. Gerber, J. Chem. Phys. **101**, 343 (1994).
[69] R. Baumfalk, U. Buck, C. Frischkorn, S. R. Gandhi, and C. Lauenstein, Chem. Phys. Lett. **269**, 321 (1997).
[70] R. Baumfalk, U. Buck, C. Frischkorn, S. R. Gandhi, and C. Lauenstein, Ber. Bunsenges. Phys. Chem. **101**, 606 (1997).
[71] D. P. Hydutsky, N. J. Bianco, and A. W. Castleman, Chem. Phys. Lett. **476**, 15 (2009).
[72] J. Vigué, P. Labastie, and F. Calvo, Eur. Phys. J. D **8**, 265 (2000).
[73] A. K. Samanta, L. C. Ch'ng, and H. Reisler, Chem. Phys. Lett. **575**, 1 (2013).
[74] D. E. Woon, K. A. Peterson, and T. H. Dunning, J. Chem. Phys. **109**, 2233 (1998).
[75] G.-J. Kroes and D. C. Clary, J. Phys. Chem. **96**, 7079 (1992).
[76] H. Kang, T. H. Shin, S. C. Park, I. K. Kim, and S. J. Han, J. Am. Chem. Soc. **122**, 9842 (2000).
[77] S.-C. Park, K.-H. Jung, and H. Kang, J. Chem. Phys. **121**, 2765 (2004).
[78] S. C. Park and H. Kang, J. Phys. Chem. B **109**, 5124 (2005).
[79] H. Kang, Acc. Chem. Res. **38**, 893 (2005).
[80] J. Y. E.-S. Moon and H. Kang, J. Chem. Phys. **133**, 044709 (2010).
[81] C. C. Pradzynski, R. M. Forck, T. Zeuch, P. Slavíček, and U. Buck, Science **337**, 1529 (2012).
[82] A. Yabushita, D. Kanda, N. Kawanaka, and M. Kawasaki, J. Chem. Phys. **127**, 154721 (2007).

THE JOURNAL OF PHYSICAL CHEMISTRY A

Article

pubs.acs.org/JPCA

Clustering and Photochemistry of Freon CF_2Cl_2 on Argon and Ice Nanoparticles

Viktoriya Poterya,[†] Jaroslav Kočišek,[†] Jozef Lengyel,[†,‡] Pavla Svrčková,[†,‡] Andriy Pysanenko,[†] Daniel Hollas,[‡] Petr Slavíček,[†,‡] and Michal Fárník*,[†]

[†]J. Heyrovský Institute of Physical Chemistry, v.v.i., Academy of Sciences of the Czech Republic, Dolejškova 3, 182 23 Prague 8, Czech Republic

[‡]Department of Physical Chemistry, Institute of Chemical Technology Prague, Technická 5, 166 28 Prague 6, Czech Republic

S *Supporting Information*

ABSTRACT: The photochemistry of CF_2Cl_2 molecules deposited on argon and ice nanoparticles was investigated. The clusters were characterized via electron ionization mass spectrometry, and the photochemistry was revealed by the Cl fragment velocity map imaging after the CF_2Cl_2 photodissociation at 193 nm. The complex molecular beam experiment was complemented by ab initio calculations. The $(CF_2Cl_2)_n$ clusters were generated in a coexpansion with Ar buffer gas. The photodissociation of molecules in the $(CF_2Cl_2)_n$ clusters yields predominantly Cl fragments with zero kinetic energy: caging. The CF_2Cl_2 molecules deposited on large argon clusters in a pickup experiment are highly mobile and coagulate to form the $(CF_2Cl_2)_n$ clusters on Ar_N. The photodissociation of the CF_2Cl_2 molecules and clusters on Ar_N leads to the caging of the Cl fragment. On the other hand, the CF_2Cl_2 molecules adsorbed on the $(H_2O)_N$ ice nanoparticles do not form clusters, and no Cl fragments are observed from their photodissociation. Since the CF_2Cl_2 molecule was clearly adsorbed on $(H_2O)_N$, the missing Cl signal is interpreted in terms of surface orientation, possibly via the so-called halogen bond and/or embedding of the CF_2Cl_2 molecule on the disordered surface of the ice nanoparticles.

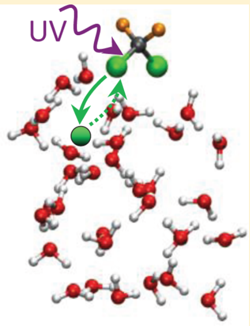

INTRODUCTION

The usage of chlorofluorocarbons (CFC) as refrigerants and foam propellants released a significant load of these molecules into the atmosphere where they affect the atmospheric chemistry.[1−3] In the troposphere, CFCs act as greenhouse gases. They absorb efficiently the radiation in the atmospheric window and have a high global warming potential.[2,4] The CFC molecules are preserved for decades, as relatively inert gases, and they slowly diffuse into the stratosphere, where they can finally be destroyed by solar ultraviolet (UV) radiation. The Cl radical released in the CFC photodissociation initiates the well-known catalytic decomposition of ozone, first proposed by Molina and Rowland.[5] In the present study, we focus on the interaction and photodynamics of dichlorodifluoromethane CF_2Cl_2 (CFC-12) with nanoparticles.

Many of the important stratospheric processes take place on the surface of ice particles in the polar stratospheric clouds (PSC).[1,6] It is therefore relevant to ask whether the photochemistry of CFCs can be controlled by their adsorption on ice surfaces. The CFC molecules adsorbed on ice have also received a significant attention in connection with reactions of presolvated electron. The dissociative electron attachment to CFC-12 in the gas phase[7] increases by several orders of magnitude upon the adsorption on ice for electrons with near-zero kinetic energy, as reported by Lu et al.[8,9] This mechanism has been proposed as an additional potential source of Cl radicals in the stratosphere.[10,11] Interestingly in the context of the present work, the high-energy resonances associated with the excited states of CFCs disappear upon the transition from the gas phase to a polar solvent.[12,13]

To the best of our knowledge, no experiment on the UV-photodissociation of CF_2Cl_2 on ice has been reported so far. Similar chlorine containing molecules, such as $CFCl_3$, have been studied, and their photodissociation dynamics revealed by the time-of-flight (TOF) spectroscopy of Cl fragments released from the ice surface.[14,15] Chemical reactions of CFC-12 in water ice films have been investigated upon X-ray or electron irradiation of the ice.[16,17]

A CF_2Cl_2 molecule absorbs UV-photons with wavelengths below $\lambda \approx 225$ nm and undergoes a direct photodissociation of a single C−Cl bond:

$$CF_2Cl_2 \rightarrow CF_2Cl\cdot + Cl\cdot \tag{1}$$

Photodissociation dynamics of CFC-12 in the gas phase at 193 nm was investigated previously,[18−20] and the quantum yield measurements were reported by Taketani et al.[21] Recently, we have implemented the up-to-date velocity map imaging (VMI) technique to study the detailed photodissociation dynamics of CF_2Cl_2[22] and compared our results with the previous TOF measurements of Baum and Huber[19] and Yen et al.[20] Within the same work, we have investigated the CFC-12 photodissociation embedded in rare gas clusters.[22] Here we extend

Received: April 23, 2014
Revised: June 3, 2014
Published: June 9, 2014

dx.doi.org/10.1021/jp503983x | *J. Phys. Chem. A* 2014, 118, 4740−4749

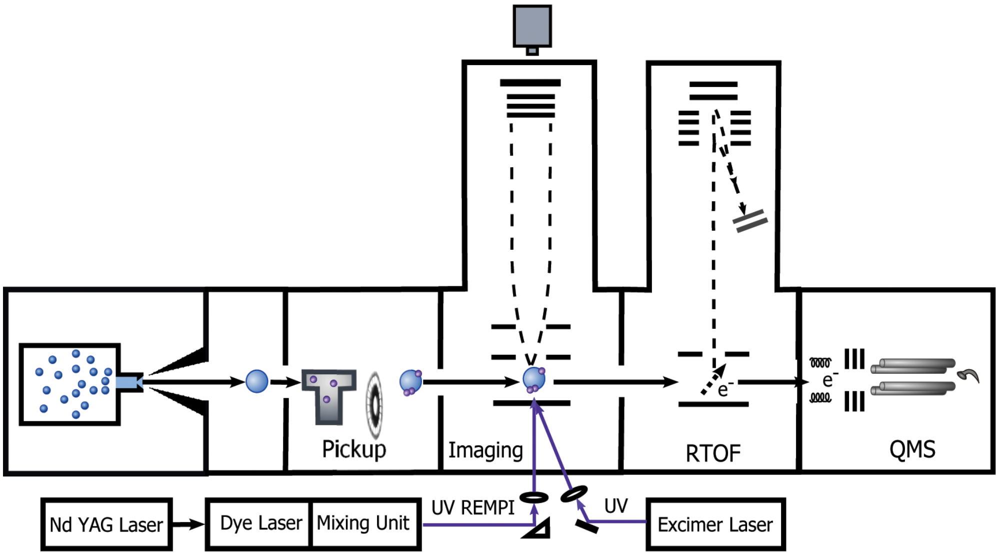

Figure 1. Schematic drawing of the CLUster Beam (CLUB) apparatus outlining the experiments exploited in this paper.

Table 1. Expansion Conditions: Nozzle Diameter was 55 μm for CFC-12 and Ar Expansions, and 100 μm for Water; Divergence Angle was 30° and Thickness 2 mm for all Expansions; Nozzle Temperature, and Stagnation Pressure P_0 [for Water P_0 was Determined by the Water Reservoir Temperature (T_R)]^a

expansion gas	source temperature T_0/T_R (°C)	pressure P_0 (bar)	generated species	mean size $\bar{N}$	pickup P_{CFC} (10^{-4}mbar)
CFC-12	+40	0.5−1.7	CF_2Cl_2	1	−
CFC-12/Ar	+40	0.5−1.7	$(CF_2Cl_2)_n$	1−16	−
Ar	−60 − −40	5.0−8.0	Ar_N	200−450	0.1−5.5
H_2O	+155−170/130−160	3.5−7.7	$(H_2O)_N$	200−750	0.1−5.5

^{a}Mean cluster sizes $\bar{N}$ for Ar_N and $(H_2O)_N$ clusters were calculated using Hagena's and Buck's formulas.[41−45] For $(CF_2Cl_2)_n$ clusters, the range of the observed fragments in the mass spectra is given.

our previous studies to the systems where the CFC-12 molecules were deposited on surfaces of large Ar_N clusters, and on atmospherically relevant ice nanoparticles.

In the present study, we continue in our long-term effort to understand how the environment affects the photoinduced processes. They can range from purely mechanical trapping of the molecular fragments formed within the photodissociation, cage effect,[22−24] to complex processes involving reactions of the dopant with the surface.[25−28] The CFC-12 molecule represents an interesting example in this context. The photodissociated Cl fragment can dissipate its kinetic energy efficiently because of its higher mass comparable to the cluster constituents. Thus, it is a more sensitive probe of the interactions in the excited state than the hydrogen fragment investigated in our previous studies. The CFC-12 molecule is also anisotropic. We might ask whether and how the molecule is oriented on the ice surface. The preferential orientation could be mediated by the so-called halogen bond[29] between the CF_2Cl_2 and water, C−X···OH_2 (X = Cl and F).

The experimental arrangement used for the study is unique since it combines several experimental tools in one apparatus: (1) well-defined production of relatively large clusters (nanoparticles);[30] (2) investigation of the photodissociation dynamics with the velocity map imaging (VMI) method;[22,24] (3) high-resolution mass spectrometry after electron ionization for the cluster composition determination;[31,32] and (4) pickup experiment for cluster size determination.[33−35] In the present work, we have combined all these methods for the first time to deliver a complex picture of the investigated cluster species and processes in their environment.

■ EXPERIMENTAL AND THEORETICAL METHODS

Experiment. Figure 1 shows the schematic overview of the present experiments. The general description of our CLUster Beam apparatus (CLUB) can be found elsewhere.[30,36] Recently, the experiment has been extended with the velocity map imaging (VMI) technique and a reflectron time-of-flight mass spectrometer (RTOF). The combination of these techniques within one apparatus can provide a detailed insight into the studied cluster species and processes.

Various clusters were produced under different expansion conditions, which are summarized in Table 1. The expansion was skimmed ~25 mm downstream from the nozzle, and the beam passed about 1 m through two differentially pumped chambers into the detection VMI chamber where the photodissociation of molecules in clusters was investigated. The VMI system is perpendicular to the beam axis, and the design is identical to our other apparatus for imaging (AIM) described in more detail elsewhere.[22,24,37] For the position sensitive detection, we used chevron multichannel plate (TOPAG) with an active diameter of 41 mm in combination with P43 phosphor screen and CCD camera (Unibrain Fire-i 702b) with imaging lens (25 mm, $f/1.6$). To process the images the inverse Abel transform was performed. We used the Hankel method for reconstructing the images,[38] and also the Iterative Inversion method[38] was implemented to check the consistency of our results.

In the interaction point, the molecular beam was crossed with two laser beams: the photodissociation 193.3 nm ArF-Excimer laser and 235.336 nm laser to REMPI ionize the Cl($^2P_{3/2}$) photofragments. The tunable UV radiation around 235 nm is generated by sum frequency mixing of the fundamental 1064 nm from the Nd:YAG laser (Spitlight 1500, Innolas) with the doubled output of the tunable dye laser (Pulsare-S, Lioptec) pumped by the Nd:YAG second harmonics (532 nm). The pulsed lasers were crossed under the mutual angle of 17.5° and operated at a 10 Hz frequency in the nanosecond regime.

The next vacuum chamber was hosting the RTOF mounted orthogonally to the molecular beam. It was custom-built on the basis of our specifications[39] and described in detail in our recent studies.[32,40] The clusters were ionized by electrons at 10 kHz repetition frequency, and the mass spectra of the ionized product were recorded with the resolution of $(M/\Delta M) \approx 10^4$. The present spectra were recorded at the electron energy of 70 eV.

Finally, the quadrupole mass spectrometer at the end of the machine was used for the velocity measurements. The cluster beam was interrupted with a pseudorandom chopper after the pickup process, and the time-of-flight was recorded after the clusters were ionized by electrons in the quadropole ion source and a particular ion fragment detected. The cluster velocity was evaluated from the flight time. Measuring the cluster velocity as a function of the gas pressure in the pickup chamber allowed for the evaluation of the cluster cross section for the pickup of molecules. The velocity measurements and cluster cross section determination methods have been outlined in detail in our recent publications.[33−35]

This has been the very first study performed on our CLUster Beam (CLUB) apparatus in which we combined the different experiments: (i) the high resolution time-of-flight mass spectrometry, (ii) the photofragment velocity imaging, and (iii) the pickup cross-section measurements.

Theory. The interpretation of our measurements has been assisted by ab initio calculations. We have calculated the geometries of the participating molecules and structures of the respective binary complexes between CFC-12, water, and argon. The structures of the complexes were optimized at the MP2 level with cc-PVTZ basis. The counterpoise correction of Boys and Bernardi was employed during the optimization.[46] Such a combination has been shown to provide highly accurate geometries for van der Waals complexes.[47] The binding energies were then calculated within a supramolecular approach at the CCSD(T)/CBS level. The procedure was as follows. First, the MP2/CBS energy was obtained by extrapolating the aug-cc-pVTZ- and aug-cc-PVQZ-based calculations to the complete basis set limit using the n^{-3} formula. The HF energy was not extrapolated but taken from the calculation with the aug-cc-pVQZ basis set. The CCSD(T) correction to the MP2 result was computed with the aug-cc-pVDZ basis and added to the MP2/CBS energy. The final energy expression thus reads:

$$E_{\mathrm{CBS}}^{\mathrm{CCSD}(T)} = E_{\mathrm{aug-pVQZ}}^{\mathrm{HF}} + E_{\mathrm{CBS}}^{\mathrm{RI-MP2}} + E_{\mathrm{aug-pVDZ}}^{\mathrm{CCSD}(T)} - E_{\mathrm{aug-pVDZ}}^{\mathrm{MP2}} \quad (2)$$

This scheme has been shown to be of a comparable accuracy to more costly direct extrapolation of CCSD(T) energies.[48] The counterpoise correction was also used for the binding energy calculations.

We have also investigated the excited states of the CFC molecule in the gas phase and in the binary complexes. The high-level estimates of the excitation energies and corresponding oscillatory strengths were performed with the EOM-CCSD method, using aug-cc-pVTZ basis set. The mapping of the excited state potential energy surface along the C−Cl dissociation coordinate was performed with multi reference configuration interaction (MRCI) method with single and double excitations. The CI treatment was performed on the complete active space self consistent fields (CASSCF) wave function defined by 8 electrons distributed in 5 active orbitals. This choice has provided a consistent description of the potential energy surface (PES) of both isolated CFC and CFC complexed with water and argon.

Most of the calculations were performed in Molpro, version 2010.[49,50] The optimization of the binary complexes with the counterpoise correction was done in Gaussian09.[51]

■ RESULTS AND DISCUSSION

Our major target was the atmospherically relevant photochemistry of CF_2Cl_2 on ice nanoparticles. To meet this aim, we have investigated the photodissociation gradually proceeding from the isolated molecule to the photodissociation in the environment of $(CF_2Cl_2)_n$ and rare gas clusters and finally in $(H_2O)_N$. This section is structured as follows: first, we demonstrate (namely by mass spectrometry) and discuss the generation of the different clusters in our experiment; second, the VMI results of photodissociation experiment are presented and discussed; and third, the surprising disappearance of Cl fragment from photodissociation on ice nanoparticles is discussed and justified in more detail.

Nature of Generated Clusters Species. *Coexpansion with Ar.* The CF_2Cl_2 molecules do not generate clusters in pure expansions: figure 2a shows an example of the mass spectrum measured at P_0 = 1.7 bar CF_2Cl_2 expansion pressure and T_0 = 50 °C nozzle temperature exhibiting only fragments of isolated CF_2Cl_2 molecule. Figure 2b corresponds to the expansion of 10% CFC in Ar under the same stagnation conditions. The inset shows that ionized fragments of $(CF_2Cl_2)_n$ clusters even for $n \geq 16$ have been observed. There are three groups of cluster fragment ions corresponding to each size n: $(CF_2Cl_2)_n^+$ cluster ions composed of nonfragmented molecules, and $CFCl_2(CF_2Cl_2)_{n-1}^+$ and $CF_2Cl(CF_2Cl_2)_{n-1}^+$ cluster ions where F or Cl atom, respectively, was missing. The individual mass peaks in each group correspond to various combinations of ^{35}Cl and ^{37}Cl isotopes as confirmed by their intensity ratios. Indeed, these fragment ions can originate from any neutral cluster size $\geq n$. Since no mixed CF_2Cl_2/Ar fragments were observed in the coexpansion mass spectra, we propose that pure $(CF_2Cl_2)_n$ clusters were generated. This will be contrasted to CF_2Cl_2 deposited on the Ar_N surface discussed below. Additional spectra showing the expansion pressure dependence are shown in the Supporting Information.

The fact that no clusters were generated in the pure CF_2Cl_2 expansions demonstrates that the molecule itself is very inefficient for cooling the expansion. On the other hand, the $(CF_2Cl_2)_n$ clusters were readily generated in the coexpansion with Ar. We can briefly discuss the cluster formation in terms of the calculated binding energies of binary complexes summarized in Table 2. The $CF_2Cl_2\cdots CF_2Cl_2$ binding energy is higher than for the $CF_2Cl_2\cdots Ar$ and $Ar\cdots Ar$ complexes. Thus, argon

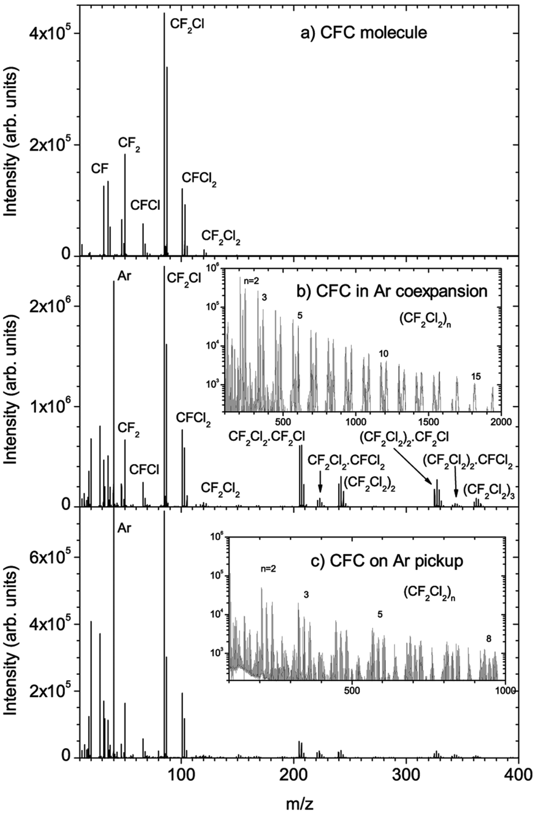

Figure 2. Electron ionization (70 eV) mass spectra (TOFMS): (a) pure CF_2Cl_2 molecule expansion P_0 = 1.7 bar, T_0 = 50 °C, and molecular fragments indicated. (b) Expansion of 10% CFC in Ar, P_0 = 1.7 bar, T_0 = 50 °C, and fragments of $(CF_2Cl_2)_n$ clusters indicated; the inset shows clusters from n = 2 up to 17 (note the logarithmic scale). (c) Pickup of CF_2Cl_2 molecules on Ar_N, $\bar{N}$ = 330, expansion conditions: P_0 = 7.5 bar, T_0 = −50 °C, and CF_2Cl_2 pressure in the pickup chamber $P_{CFC} = 5.2 \times 10^{-4}$ mbar; the inset shows clusters from n = 2 up to 8.

atoms serve as an efficient cooling medium in the expansion; they take away the excess energy released upon the CF_2Cl_2 aggregation and do not bind to the clusters.

Pickup on Large Ar Clusters. In the second series of experiments, pure Ar_N clusters were generated and the CF_2Cl_2 molecules were deposited on them in the pickup chamber. It ought to be mentioned that pure rare gas expansions were investigated in great detail previously,[41−44] and the cluster size distributions are well-known. In our experiments, the species were probed more than a meter downstream from the source, where the molecular beam was well-defined, and the clusters were stabilized after almost 1 ms flight-time in vacuum. Different expansion conditions were exploited corresponding to different cluster sizes and also different CF_2Cl_2 pressures in the pickup cell. The conditions and corresponding cluster sizes are summarized in Table 1. At lower pickup pressures, the spectra were dominated by the Ar_N^+ series. Increasing the CF_2Cl_2 pressure yielded $(CF_2Cl_2)_n$ clusters built after multiple CF_2Cl_2 pickup on Ar_N clusters. Figure 2c shows the mass spectrum at a high pickup pressure $P_{CFC} = 5.2 \times 10^{-4}$ mbar, where the mass peaks corresponding to $(CF_2Cl_2)_n$ clusters dominate over Ar_N^+. Further spectra illustrating the pressure dependence can be found in the Supporting Information.

The spectrum in Figure 2c is similar to the spectrum obtained in the coexpansion (b). Yet, closer inspection reveals some differences, namely the presence of the mixed CF_2Cl_2/Ar ions in (c). This is demonstrated in Figure 3, where a detailed part of the (a) coexpansion spectrum is compared to the (b) pickup spectrum at somewhat lower pickup pressure of $P_{CFC} = 7.4 \times 10^{-5}$ mbar to show clearly the Ar-series mass peaks. The spectrum is dominated by Ar_N^+ and exhibits the mixed mass peaks Ar_NCl^+, $Ar_NCF_2Cl^+$, and $Ar_NCFCl_2^+$, in addition to the CF_2Cl_2 cluster series: $(CF_2Cl_2)_n^+$, $CFCl_2(CF_2Cl_2)_{n-1}^+$, and $CF_2Cl(CF_2Cl_2)_{n-1}^+$.

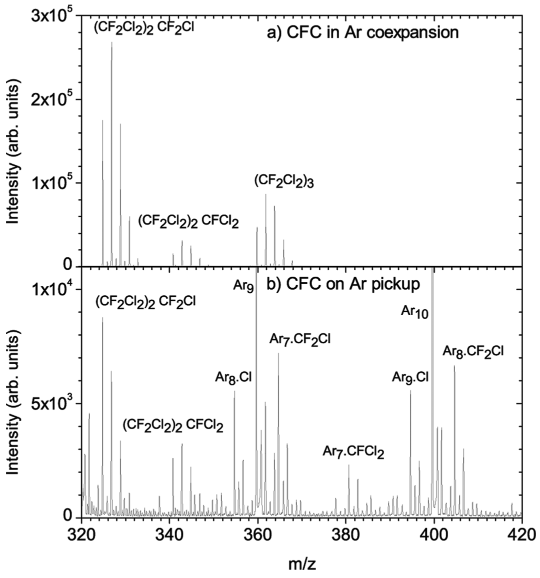

Figure 3. Detailed section of the mass spectrum from (a) expansion of CFC mixture in Ar (P_0 = 1.7 bar, T_0 = 57 °C), in comparison with (b) pickup of CF_2Cl_2 molecules on Ar_N clusters (P_0 = 8 bar, T_0 = −59 °C, $P_{CFC} = 7.4 \times 10^{-5}$ mbar).

These spectra recorded in the pickup experiment under various conditions have provided the experimental evidence that CF_2Cl_2 molecules are adsorbed and coagulate to the $(CF_2Cl_2)_n$ clusters on the Ar_N clusters. The Ar_N cluster absorbs the CF_2Cl_2 binding energy, subsequently disposing it by the Ar evaporation. The binding energy of $(CF_2Cl_2)_2$ dimer is approximately 90 meV, according to our calculations. Presumably, CF_2Cl_2 will be bound by somewhat higher energy in larger clusters: four-times the dimer energy can be assumed as the upper boundary (i.e., ~360 meV). From the mass spectra, $n \leq 10$ corresponds to the largest size of the $(CF_2Cl_2)_n$ cluster generated on the Ar_N at the highest pickup pressure.

Table 2. Calculated Binding Energies of Various Binary Complexes at the Estimated CCSD(T)/CBS Level

complex	$CF_2Cl_2\cdots CF_2Cl_2$	$CF_2Cl_2\cdots H_2O$	$CF_2Cl_2\cdots Ar$	$H_2O\cdots H_2O$	$Ar\cdots Ar$
ΔE_{int} (meV)	87	88	35	218[53]	12[54]

Therefore, the total energy of ~3600 meV can be released by the CFC-12 coagulation at most. The binding energy of Ar to Ar_N is approximately 60 meV for $N = 200$.[52] Thus, the CFC-12 coagulation evaporates less than 60 Ar atoms. This number is smaller than the smallest investigated mean Ar_N cluster size $\bar{N} \approx 200$. Therefore, in the pickup experiments, small $(CF_2Cl_2)_n$ clusters were generated on the surface of large Ar_N clusters, where n ranges from 1 (single molecule pickup) to ~10 and $N > 10 \times n$.

In this case, argon again represented an efficient heat bath promoting the CF_2Cl_2 aggregation. In the pickup process, the energy released by the CF_2Cl_2 clustering was not sufficient to evaporate the large argon cluster and mixed $(CF_2Cl_2)_n{\cdot}Ar_N$ species were generated. It is interesting to note that the CF_2Cl_2 molecules must be highly mobile on the argon surface to coagulate after the uptake.

Pickup on Ice Nanoparticles. In the last series of experiments, we deposit the CF_2Cl_2 molecules on large water clusters $(H_2O)_N$ generated in water vapor expansion. As for argon clusters, the water cluster size distributions were investigated and characterized in great detail, in this case even with our present cluster source.[45] The present experiments were done with different mean water cluster sizes between $\bar{N} \approx 200$ and 750 and various CF_2Cl_2 pickup pressures, as in the case of Ar_N clusters (Table 1). Figure 4 shows an example mass spectrum for $\bar{N} \approx 750$ with the series of protonated clusters $(H_2O)_NH^+$ typical for the water cluster ionization. The only ions corresponding to CF_2Cl_2 molecules identified in the spectra were the strong CF_2Cl^+ peak and substantially weaker, yet discernible, CF_2Cl^+ and CF_2^+. There was no evidence for CF_2Cl_2 clusters nor for mixed CF_2Cl_2/H_2O fragments under any exploited conditions.

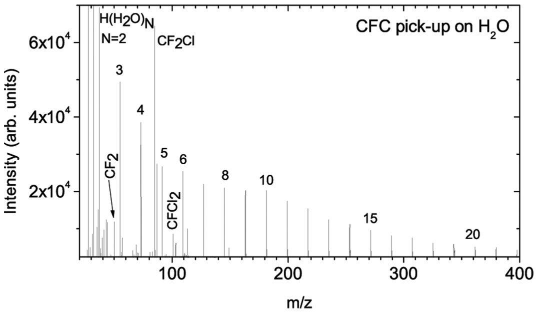

Figure 4. Mass spectrum from pickup of CF_2Cl_2 molecules on $(H_2O)_N$, $\bar{N} \approx 750$ clusters, $P_{CFC} = 2.5 \times 10^{-4}$ mbar.

It ought to be stressed that the background spectrum of any diffused CF_2Cl_2 molecules was carefully subtracted, and the relatively strong CF_2Cl^+ peak appeared only due to the ionization of the CF_2Cl_2 molecules arriving to the mass spectrometer with the $(H_2O)_N$ clusters. Since there is no evidence for $(CF_2Cl_2)_n$ clusters on $(H_2O)_N$, the CF_2Cl_2 molecules were either less mobile on the ice than on argon or did not bind even if they met on the $(H_2O)_N$ surface, or there were fewer molecules adsorbed on ice than on argon. The two former options are supported by our calculations. The $CF_2Cl_2{\cdots}H_2O$ interaction is much stronger than the corresponding $CF_2Cl_2{\cdots}Ar$ interaction. The mobility of the molecule is thus limited. At the same time, the $CF_2Cl_2{\cdots}CF_2Cl_2$ interaction is weaker than for $CF_2Cl_2{\cdots}H_2O$. Thus, there is no reason for a preferential coagulation of the CF_2Cl_2 molecules on the ice surface.

To answer the question if there are less CF_2Cl_2 molecules deposited on the ice nanoparticles than on Ar_N, we have performed an additional experiment: the pickup cross-section measurements. The geometrical size of the investigated water and argon clusters was comparable. The radius of the clusters can be estimated as $R = R_0{\cdot}N^{1/3}$, where the parameter R_0 can be evaluated from the density ρ as $R_0 = [(3/4\pi)(m/\rho N_A)]^{1/3}$, m is the molar mass, and N_A is Avogadro's constant. Solid argon and water ice densities yield $R_0 = 2.09$ and 1.93 Å, respectively. This implies that $M/N \approx 1.3$ for $(H_2O)_M$ and Ar_N clusters of the same radius. We investigated clusters from the corresponding size range, however, the sticking of the CF_2Cl_2 molecules to $(H_2O)_M$ and Ar_N clusters can be different. In the present experiments, we determine the pickup cross section $\sigma \approx 1000$ Å^2 for CF_2Cl_2 molecules on Ar_N, $\bar{N} = 330$, using our recently developed method based on cluster velocity measurements.[33−35] The measured cross section corresponds to approximately 20 CF_2Cl_2 molecules deposited on Ar_N at the highest exploited pressure $P_{CFC} = 5.2 \times 10^{-4}$ mbar (the mass spectra exhibited ionized fragments up to about $n \approx 10$). The measured pickup cross section for the CF_2Cl_2 molecules on $(H_2O)_M$, $\bar{M} = 430$, was about 4 times smaller. Nevertheless, multiple pickup of about 5 CF_2Cl_2 molecules is still expected on $(H_2O)_M$ under the same conditions as for Ar. Even more adsorbed molecules is expected on the larger clusters (up to $\bar{M} \approx 750$), which we investigated. Yet, a possible evaporation of CF_2Cl_2 molecules should be considered as discussed below.

In all cases, the presence of the CF_2Cl_2 peak in the mass spectra proved that the ice nanoparticles arrive into the photodissociation region with one or more nonclustered CF_2Cl_2 molecules.

Photodissociation in Clusters. Here we present the VMI results for the different cluster species, which were produced as

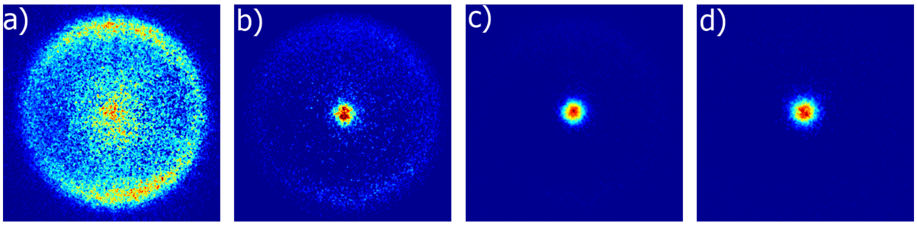

Figure 5. Cl-fragment images from 193 nm photodissociation of CF_2Cl_2 in various environments (laser polarization vertical): (a) isolated CF_2Cl_2 molecules; (b) $(CF_2Cl_2)_n$ clusters generated in CFC/Ar expansion at $P_0 = 1.4$ bar, and (c) 1.7 bar; (d) CF_2Cl_2 molecules deposited on large Ar_N clusters.

outlined in the previous section. Figure 5 shows the Cl fragment images for the various cases.

CF_2Cl_2 Molecule. The image in Figure 5a corresponds to the photodissociation of the isolated CF_2Cl_2 molecule. Similar images have been recorded in expansions of pure CFC-12 and also in expansions of CFC/Ar mixtures below 1 bar stagnation pressure. These images agree with our recent study[22] performed on AIM and were analyzed in detail there. Here we repeat only the major conclusions for the sake of completeness. The underlying reason for the lower signal-to-noise ratio in the present image is a very long (>1 m) flight path from the source to the laser interaction region in CLUB compared to AIM (~10 cm). The long flight path reduces the monomer intensity, yet it brings advantages for large cluster studies. The kinetic energy distribution (KED) shown in Figure 6 is dominated by the fast fragments at $E_{\mathrm{kin}}(\mathrm{Cl}) = 0.97$ eV originating from the direct Cl–CF_2Cl bond fission at 193 nm. Additionally, there are some slower fragments below ~0.5 eV, which were also identified in the earlier work of Yen et al.[20] These slow fragments can be formed in the concerted dissociation of the two Cl atoms from CF_2Cl_2; in the secondary CF_2Cl dissociation; or due to multiphoton processes. For the discussion see our previous study;[22] here, we concentrate on how the dynamics of the process changes in the clusters.

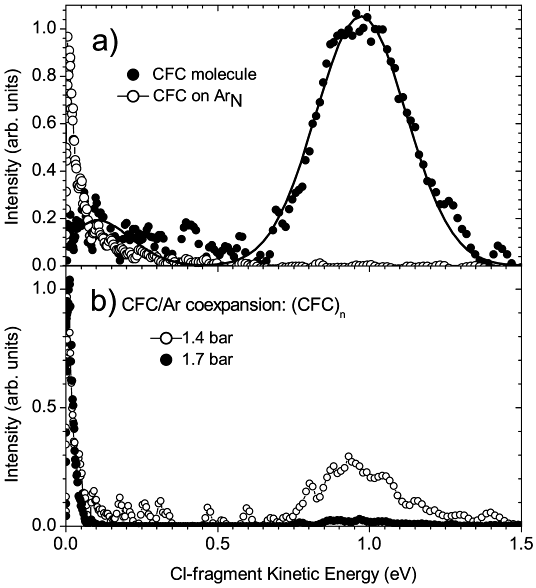

Figure 6. Cl-fragment KEDs: (a) isolated CF_2Cl_2 molecules (●) and CF_2Cl_2 molecules deposited on large Ar_N clusters (○); (b) $(CF_2Cl_2)_n$ clusters generated in CFC/Ar expansion at 1.4 bar (○) and 1.7 bar (●).

$(CF_2Cl_2)_n$. First, we probed pure $(CF_2Cl_2)_n$ clusters generated in mixed expansions. The images in Figure 5, (panels b and c) show an increasing contribution of the caged Cl fragments (in the middle) compared to the fast Cl-fragments, corresponding to the direct exit from clusters. The fast fragments disappeared almost entirely at the higher expansion pressure of $P_0 = 1.7$ bar; see also the corresponding KEDs in Figure 6b. Even for the larger $(CF_2Cl_2)_n$ clusters where the caging strongly dominates, some direct exit fragments are still discernible in the KED (Figure 6b). The rapid disappearance of the fast velocity component with increasing cluster size reflects the efficient dissipation of energy of the dissociated chlorine fragment. Several collisions suffice to essentially stop the chlorine atom. The caging is thus rather efficient even in medium-sized $(CF_2Cl_2)_n$ clusters. In contrast, caging of the hydrogen atom in hydrogen halide clusters of similar sizes[55−57] was less pronounced.

The pattern corresponding to the fast fragments in the images from clusters exhibited slightly lower anisotropy than the fast fragments from isolated molecules. The more isotropic distribution could be caused by the elastic scattering of the Cl fragments in the cluster. Yet, the differences in the anisotropy parameter β were within the error bars of the limited signal intensities. Thus, we cannot determine unambiguously whether the fast fragments in the cluster images originated from the clusters or unclustered molecular fraction in the beam.

$(CF_2Cl_2)_n{\cdot}Ar_N$. Figure 5d shows an example of the image from Ar_N clusters with the CF_2Cl_2 molecules deposited on their surface. The corresponding KED is compared to the molecular spectrum in Figure 6a. At lower pickup pressures (where the mass spectra indicated that only a single CF_2Cl_2 molecule was deposited on the Ar_N cluster), a weaker Cl signal corresponding to Cl caging is still clearly observed. However, its low intensity prevents to unambiguously distinguish any faster fragments at the position of the direct exit peak from the background. Thus, essentially only the caged Cl fragments were observed from the CF_2Cl_2 photodissociation on Ar_N. On the other hand, for the H-fragment from hydrogen halides deposited on rare gas clusters, some cage exit has been observed previously.[23,58−61] The mass of the argon atom is close to the mass of the chlorine fragment, and thus it very efficiently slows the chlorine upon collisions.

$CF_2Cl_2{\cdot}(H_2O)_N$. Finally, we performed the photodissociation experiment on the large water clusters with the CF_2Cl_2 molecules deposited on them by the pickup. Despite the fact that we observed the CF_2Cl_2 molecules deposited on the $(H_2O)_N$ clusters in the mass spectrometry experiment (as outlined in the previous section), we did not obtain any Cl signal from its photodissociation under any exploited experimental conditions (Table 1). It is a negative yet important result, and we discuss it in more detail in the next section.

Rationalization of the Chlorine Fragment Disappearance. In this section, we discuss the possible explanations for the lack of the chlorine signal upon the photodissociation of the CF_2Cl_2 molecule on the surface of ice nanoparticles. Several options can be outlined: (1) the CF_2Cl_2 molecule is not present in the photodissociation region in sufficient quantity, (2) the molecule is not photoexcited at 193 nm, or (3) the excitation does not yield the free chlorine radical.

(1). Small Amount of CF_2Cl_2. The trivial reason for the lack of the signal could be the small amount of CF_2Cl_2 molecules adsorbed on the $(H_2O)_N$ clusters. It has been reported previously[62] that CFC-12 begin to desorb from the ice surface at temperatures above approximately 100 K, but they can be trapped inside the ice film up to the temperature of about 150 K. The temperature of the water clusters is typically estimated to be around 100 K; however, the exact value is not known and a range of temperatures between 80 and 150 K can be found in the literature.[63−65] The desorption from finite size clusters should be considered in the context of time available between the pickup and photodissociation. The desorption rate constant can be estimated as

$$k = \nu \exp(-E_a/k_BT) \qquad (3)$$

where E_a is the activation barrier which can be in first approximation identified with the binding energy. The attempt frequency ν is typically considered 10^{12} s^{-1}.[66] If a binding energy of the CFC-12 on ice[67] is around 0.3 eV, the desorption lifetime is in the order of minutes for 100 K. This is well above the ≈0.6 ms time interval between the pickup and the photodissociation events. The CFC-12 molecule should stay on the ice particle for the time required even at 150 K. This conclusion is consistent with the relatively strong CF_2Cl^+ peak in the mass spectra, which can be only due to the molecules arriving with the clusters to the detector, as argued above. The pickup cross section measurements above suggest that there are less CF_2Cl_2 molecules adsorbed on $(H_2O)_N$ than on Ar_N. Yet, the signal from the pickup on Ar_N was relatively strong, and the signals more than an order of magnitude lower would still be distinguished from the background.

(2). Shift in the Absorption Spectra. The water solvent molecules could influence the CF_2Cl_2 photoabsorption cross section on the ice nanoparticle. Blue shift of the spectrum could lead to a lower probability of the absorption at 193 nm (6.41 eV). Our calculations showed, however, little influence of the water solvent on the CF_2Cl_2 absorption cross section. For example, the first excitation energy in the optimal gas phase geometry (MP2/cc-pVTZ level) of the CF_2Cl_2 molecule is 7.32 eV (oscillatory strength 0.0176) and it shifts to 7.41 eV (0.0178) in the $CF_2Cl_2\cdots H_2O$ complex and to 7.34 eV (0.0171) in the $CF_2Cl_2\cdots Ar$ complex. In addition, the CFC-12 photodissociation cross section is still large enough in the environment of $(CF_2Cl_2)_n$ and Ar_N clusters. Therefore, we exclude the shift in the photoabsorption cross section as the reason for the missing Cl-fragments.

(3). Cl Fragment Disappearance. If CF_2Cl_2 is present and photolyzed on the cluster, the missing fragment has to disappear in the water cluster or recombine. The first option is that the chlorine radical reacts with water molecules. The reaction $Cl + H_2O \rightarrow HCl + OH$ is endoergic by ≤0.8 eV;[68,69] the HCl formed can further acidically dissociate, decreasing thus the overall reaction energy. The Cl-fragment kinetic energy of ≈1.0 eV after the direct CF_2Cl_2 photodissociation can facilitate this reaction as suggested by theoretical calculations.[70] Yet, in this case we would still expect some of the generated fast Cl fragments to leave the cluster and escape the reaction. Therefore, we can also exclude the Cl reaction. The more probable scenario is that the Cl-fragment is trapped in the ice nanoparticle. The water clusters are more strongly bound compared to the argon clusters. For argon, the deposited energy causes the cluster decay during the dissociation process and the Cl-fragment is released even when it has been slowed to zero energy. On the other hand, the slow chlorine atom cannot be released from the water cluster which remains bound (at least within the duration of the experiment). The third possibility would be a very efficient geminate recombination taking place upon population transfer into the ground electronic state. This again requires an efficient draining of the kinetic energy from the dissociated chlorine atom so that the radical would stay within the first solvation shell and subsequently recombine.

All three scenarios for the fragment disappearance (i.e., the reaction between the chlorine atom and water, chlorine atom trapping, and CF_2Cl_2 recombination) are based on the assumption that there are no dangling C−Cl bonds in the cluster. If the dangling C−Cl bonds were present, the Cl-fragment would be released because the water cluster does not affect the bond. This is demonstrated in Figure 7, showing the energy profiles for the ground state and the first excited state of the $CF_2Cl_2\cdots H_2O$ complex. The dissociation along (a) the dangling C−Cl bond is characterized by a rapid decrease in energy and fast free dissociation is thus expected. The total excess energy upon the photoabsorption of the 193 nm photon corresponds to 2.9 eV.[19−21] Note that out of this excess energy, only ≈1.0 eV ends up in the form of kinetic energy of the chlorine fragment.[22] The dissociation along (b) the C−Cl···O bond for the C−Cl bond connected to the solvent water molecule (considering the lowest energy structure) is quite different. First, the excess energy is much smaller (∼1.9 eV). Second, the chlorine kinetic energy is transferred into the water molecule. It leaves the static chlorine atom in the proximity of the CF_2Cl radical in a vibrationally highly excited state. Such an arrangement enables a geminate recombination and chlorine atom trapping.

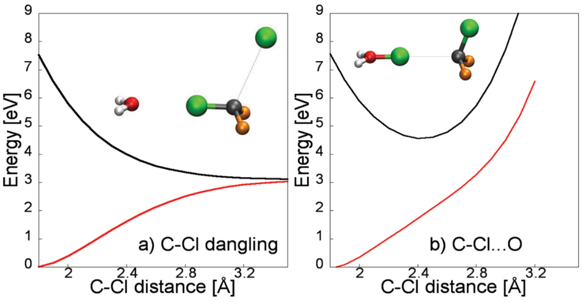

Figure 7. Energy profile along the (a) dangling C−Cl bond and (b) C−Cl···O bond. Ground state (red line) and first singlet excited state (black line) are shown. The calculations were performed at the MR-CI level with a 6-31+g* basis set.

If the CF_2Cl_2 molecule freely rotated on the surface of the spherical ice cluster, dangling C−Cl bonds would be provided and some free Cl fragments would be released. Since such fragments were not observed, we further consider two possibilities: the CF_2Cl_2 molecule is either oriented on the surface with the Cl atoms pointing into the cluster or is embedded inside the cluster. These options are discussed below.

Orientation of CF_2Cl_2 on the Surface. The possible preferential orientation of the CF_2Cl_2 molecule with respect to water particles was tested by computing the structures and relative energies for the various $CF_2Cl_2\cdots H_2O$ arrangements. The rich conformational space of the dimer $CF_2Cl_2\cdots H_2O$ can be divided into 3 distinct binding motifs: halogen bond, hydrogen bond, and dispersion-bound complexes. The representative structures of each motif with the lowest energies are shown in Figure 8. All calculated structures and their energetics can be found in the Supporting Information. The global minimum is represented by a complex in the C−Cl···O arrangement of a halogen bond type (structure **1**). This bond is not nominated a halogen bond accidentally; it displays the major features of halogen bond definition:[71] it is a linear bond with the C−Cl···O bond (3.05 Å) shorter than the sum of van der Waals radii of the Cl (1.75 Å) and O (1.52 Å) atoms. On the other hand, the analogous arrangement of the C−F···O type is almost unbound at the CCSD(T)/CBS level

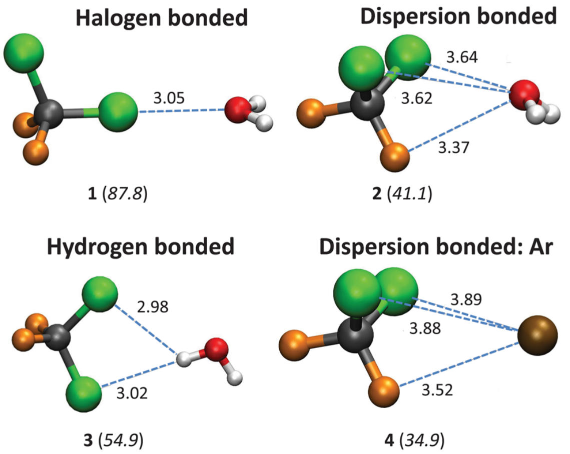

Figure 8. Structures with the highest interaction energies for three distinct $CF_2Cl_2 \cdots H_2O$ motifs (**1**, **2**, **3**) and the $CF_2Cl_2 \cdots Ar$ complex (**4**): interaction energies in millielectron volts (in parentheses), distances in Å. The geometries were obtained at the MP2/cc-pVTZ level; at each minimum, the energies are recalculated at the CCS$_2$D(T) level in an estimated complete basis set limit. All calculated structures and their energetics can be found in the Supporting Information.

(interaction energy 6 meV, see Figure SI4 of the Supporting Information). This is in line with the general observation that fluorine atoms usually do not form halogen bonds.[29] The halogen bond arrangement should support the orientation of the CFC molecules toward the water surface. The chlorine atom can also act as a hydrogen bond acceptor, which gives rise to the second type of isomers (**3**). The hydrogen-bonded complexes are energetically less favorable by about 40 meV (i.e., half of the interaction energy). Finally, the complexes can be arranged in a structure maximizing dispersion energy (**2**). Such an arrangement is energetically comparable to the hydrogen-bonded complexes. Analogous arrangement, however, represents a global minimum for the $CF_2Cl_2 \cdots Ar$ complex. Here, the argon atom resides in the center of the ClClF face of the $CFCl_2$ tetrahedron (structure **4**). Only the halogen bond specifically orients the chlorine atoms toward water. We conclude that CF_2Cl_2 could be preferentially oriented on the surface of ice particles. The preference is, however, not very strong, and it is questionable to what extent the halogen bond plays a role on the disordered ice surface.

Embedding of CF_2Cl_2 Inside the Cluster. CF_2Cl_2 is a large molecule, relatively weakly bound to water. Considering the strong hydrogen bonding between water molecules, the direct incorporation of CF_2Cl_2 after the uptake seems unlikely. However, we have recently shown that the shape of the large ice nanoparticles produced in the supersonic expansion is highly irregular and nonspherical.[35] CF_2Cl_2 deposited on the surface can attempt to maximize its interactions, which would position it in the encapsulated sites on the cluster. The photodissociated chlorine atoms would be then efficiently stopped in such an arrangement. Note that, on the other hand, the measurements for argon clusters were found to agree with the spherical nanoparticle shape.

Perspective of Other Experiments. The present analysis of the negative result can be also supported by the comparison with our recent experiments on the photodissoaciation of HCl on water and argon clusters. We have investigated the photodissociation of HCl and other hydrogen halides deposited on Ar_N and $(H_2O)_N$ previously[25,26,28] and repeated these experiments within the present work with the VMI system.

First, the HCl experiments support our claim that the CF_2Cl_2 molecules are, indeed, deposited on $(H_2O)_N$: The mass spectra for HCl pickup on water have similar features to the CF_2Cl_2 case: relatively strong mass peaks corresponding to the molecule and no evidence for $(HCl)_n$ clusters and no mixed HCl/H_2O species. The mass spectra are also similar for the pickup on Ar_N: strong HCl clustering upon multiple pickup (some of the mass spectra can be found in our recent review[30]). We have, however, an independent and unambiguous evidence for the presence of the HCl molecule on the cluster: a strong H-fragment signal from the photodissociation of HCl on $(H_2O)_N$. This analogy shows that the molecules can be deposited on the ice nanoparticles, even though only the molecular peaks are observed in the mass spectra. It is worth mentioning that HCl is not the only additional example, and we have recently studied other molecules which exhibit very similar patterns (e.g., aniline).

There is even a closer analogy between HCl and CF_2Cl_2. Although we detected a strong H-fragment signal from HCl on ice, the corresponding Cl fragments were not observed (both H and Cl fragments were observed from Ar_N). The photodissociation mechanism of HCl on ice clusters is different from the CF_2Cl_2; it proceeds via the photolysis of acidically dissociated HCl with a subsequent formation of H_3O and Cl radicals upon the excitation, as we have shown by series of experiments and theoretical calculations.[25−28] This process can only produce slow Cl fragments, which cannot react with H_2O in the endothermic reaction. Therefore, the Cl fragments are more likely caged mechanically in the nondecaying water clusters. This means that the missing Cl signal can be essentially explained by an immediate production of slow Cl atoms. The geminate recombination between the CF_2Cl and Cl radicals or chlorine reaction with water can take place, such steps are, however, not necessary for the explanation of the experimental observations.

■ CONCLUSIONS

We have studied CF_2Cl_2 molecule photodynamics on argon and water ice nanoparticles in the complex molecular beam experiment using the velocity map imaging technique. The particle composition was probed by mass spectrometry. The discussion of the results was supported by high-level ab initio calculations. The CF_2Cl_2 photodissociation was explored in different cluster environments: (i) $(CF_2Cl_2)_n$ clusters produced in the coexpansions with Ar buffer gas; (ii) individual CF_2Cl_2 molecules and $(CF_2Cl_2)_n$ clusters deposited on large Ar_N clusters by pickup and coagulation of CF_2Cl_2 molecules; and (iii) CF_2Cl_2 molecules on ice nanoparticles $(H_2O)_N$.

The experimental observations can be summarized as follows: (1) Although the CF_2Cl_2 molecules do not cluster in neat expansions, they readily form $(CF_2Cl_2)_n$ clusters in the coexpansion with Ar buffer gas. (2) The CF_2Cl_2 molecules deposited on large rare gas clusters after multiple pickup coagulate efficiently to $(CF_2Cl_2)_n$ clusters generating $(CF_2Cl_2)_n \cdot Ar_N$ species ($n \approx 1-10$, $N > 10 \times n$). (3) On the other hand, the CF_2Cl_2 molecules do not generate clusters on the $(H_2O)_N$ ice nanoparticles and are adsorbed less efficiently than on argon. (4) Cl fragments from the photodissociation of the CF_2Cl_2 molecules in $(CF_2Cl_2)_n$ clusters are efficiently caged, yet some small direct exit is observed if smaller clusters are formed. (5) Photodissociation of CF_2Cl_2 adsorbed on Ar_N

yields only caged Cl fragments. (6) No Cl fragments have been observed from the photodissociation of the CF_2Cl_2 molecules on ice nanoparticles.

From these observations, we emphasize the remarkable energy dissipation observed for the C−Cl dissociation already in $(CF_2Cl_2)_n$ and Ar_N clusters and eventually in $(H_2O)_N$. The rapid slow-down of the chlorine atoms, as opposed to hydrogen fragments, is caused by a comparable mass of the chlorine atoms and the cluster constituents.

Although we proved experimentally that the ice nanoparticles with the CF_2Cl_2 molecules are detected by our mass spectrometer, the lack of the Cl-fragment signal from the photodissociation can still partly be due to the less efficient pickup of CF_2Cl_2 on ice nanoparticles than on Ar_N. In addition, the loss of Cl-fragments on ice nanoparticles can be interpreted by the strong caging: they efficiently loose their kinetic energy in collisions with the cluster constituents, and the slow fragments get trapped in the water cluster which does not decay since it is relatively strongly bound compared to the argon clusters. The almost complete disappearance of the chlorine fragment suggests that CF_2Cl_2 has no dangling C−Cl bonds on the ice surface. This can be explained either by a strong orientation of the adsorbed molecule (possibly via a halogen bond) on the surface or its encapsulation within a cluster of a highly irregular shape.

■ ASSOCIATED CONTENT

Ⓢ Supporting Information

Further experimental mass spectra and calculated complex structures and energies. This material is available free of charge via the Internet at http://pubs.acs.org.

■ AUTHOR INFORMATION

Corresponding Author

*E-mail: michal.farnik@jh-inst.cas.cz. Tel: +420 (0)2 6605 3206. Fax: +420 (0)2 8658 2307.

Notes

The authors declare no competing financial interest.

■ ACKNOWLEDGMENTS

This work has been supported by the Czech Grant Agency project no.: 14-08937S. The authors thank J. Fedor and M. Allan from the University of Fribourg for fruitful discussions and providing CF_2Cl_2 for our experiments.

■ REFERENCES

(1) Solomon, S. Stratospheric Ozone Depletion: A Review of Concepts and History. *Rev. Geophys.* **1999**, *37*, 275−316.

(2) Jacob, D. J. *Introduction to Atmospheric Chemistry*; University Press: Princeton, 1999.

(3) Finlayson-Pitts, B. J.; Pitts, J. N. *Chemistry of the Upper and Lower Atmosphere*; Academic Press: San Diego, 2000.

(4) Lu, Q.-B. Cosmic-Ray-Driven Reaction and Greenhouse Effect of Halogenated Molecules: Culprits for Atmospheric Ozone Depletion and Global Climate Change. *Int. J. Mod. Phys.* **2013**, *27*, 1350073.

(5) Molina, M. J.; Rowland, F. S. Stratospheric Sink for Chlorofluoromethanes: Chlorine Atom-Catalysed Destruction of Ozone. *Nature* **1974**, *249*, 810.

(6) Solomon, S.; Garcia, R. R.; Rowland, F. S.; Wuebbles, D. J. On the Depletion of Antarctic Ozone. *Nature* **1986**, *321*, 755.

(7) Graupner, K.; Haughey, S. A.; Field, T. A.; Mayhew, C. A.; Hoffmann, T. H.; May, O.; Fedor, J.; Allan, M.; Fabrikant, I. I.; Illenberger, E.; et al. Low-Energy Electron Attachment to the Dichlorodifluoromethane (CCl_2F_2) Molecule. *J. Phys. Chem. A* **2010**, *114*, 1474−1484.

(8) Lu, Q.-B.; Madey, T. E. Giant Enhancement of Electron-Induced Dissociation of Chlorofluorocarbons Coadsorbed with Water or Ammonia Ices: Implications for Atmospheric Ozone Depletion. *J. Chem. Phys.* **1999**, *111*, 2861.

(9) Lu, Q.-B.; Sanche, L. Effects of Cosmic Rays on Atmospheric Chlorofluorocarbon Dissociation and Ozone Depletion. *Phys. Rev. Lett.* **2001**, *87*, 078501.

(10) Lu, Q.-B. Cosmic-Ray-Driven Electron-Induced Reactions of Halogenated Molecules Adsorbed on Ice Surfaces: Implications for Atmospheric Ozone Depletion and Global Climate Change. *Phys. Rep.* **2010**, *487*, 141−167.

(11) Bertin, M.; Meyer, M.; Stähler, J.; Gagl, C.; Wolf, M.; Bovensiepen, U. Reactivity of Water-Electron Complexes on Crystalline Ice Surfaces. *Faraday Discuss.* **2009**, *141*, 293−307.

(12) Lu, Q.-B.; Sanche, L. Enhanced Dissociative Electron Attachment to CF_2Cl_2 by Transfer of Electrons in Precursors to the Solvated State in Water and Ammonia Ice. *Phys. Rev. B* **2001**, *63*, 153403.

(13) Lu, Q.-B.; Sanche, L. Dissociative Electron Attachment to CF_4, CFCs and HCFCs Adsorbed on H_2O Ice. *J. Chem. Phys.* **2004**, *120*, 2434.

(14) Yabushita, A.; Inoue, Y.; Senga, T.; Kawasaki, M.; Sato, S. Photodissociation of Chlorine Molecules Adsorbed on Amorphous and Crystalline Water Ice Films. *J. Phys. Chem. B* **2002**, *106*, 3151−3159.

(15) Yabushita, A.; Kawasaki, M.; Sato, S. Ultraviolet Photodissociation Dynamics of Cl_2 and $CFCl_3$ Adsorbed on Water Ice Surfaces. *J. Phys. Chem. A* **2003**, *107*, 1472−1477.

(16) Perry, C. C.; Wolfe, G. M.; Wagner, A. J.; Torres, J.; Faradzev, N. S.; Madey, T. E.; Fairbrother, D. H. Chemical Reactions in CF_2Cl_2/Water (Ice) Films Induced by X-ray Radiation. *J. Phys. Chem. B* **2003**, *107*, 12740−12751.

(17) Perry, C. C.; Faradzev, N. S.; Fairbrother, D. H.; Madey, T. H. Electron Stimulated Reactions of Halogenated Compounds in Condensed Phases: Effects of Solvent Matrices on Reaction Dynamics and Kinetics. *Int. Rev. Phys. Chem.* **2004**, *23*, 289−340.

(18) Matsumi, Y.; Tonokura, K.; Kawasaki, M.; Inoue, G.; Satyapal, S.; Bersohn, R. Fine Structure Branching Ratios and Doppler Spectroscopy of Chlorine Atoms from the Photodissociation of Alkyl Chlorides and Chlorofluoromethanes at 157 and 193 nm. *J. Chem. Phys.* **1991**, *94*, 2669.

(19) Baum, G.; Huber, J. R. Photodissociation of CF_2Cl_2 at 193 nm Investigated by Photofragment Spectroscopy. *Chem. Phys. Lett.* **1993**, *203*, 261.

(20) Yen, M.; Johnson, P. M.; White, M. G. The Vacuum Ultraviolet Photodissociation of the Chlorofluorocarbons. Photolysis of CF_3Cl, CF_2Cl_2, and $CFCl_3$ at 187, 125, and 118 nm. *J. Chem. Phys.* **1993**, *99*, 126.

(21) Taketani, F.; Takahashi, K.; Matsumi, Y. Quantum Yields for $Cl(^2P_j)$ Atom Formation from the Photolysys of Chlorofluorocarbons and Chlorinated Hydrocarbons at 193.3 nm. *J. Phys. Chem. A* **2005**, *109*, 2855.

(22) Poterya, V.; Kočišek, J.; Pysanenko, A.; Fárník, M. Caging of Cl Atoms from Photodissociation of CF_2Cl_2 in Clusters. *Phys. Chem. Chem. Phys.* **2014**, *16*, 421−429.

(23) Fárník, M.; Nahler, N. H.; Buck, U.; Slavíček, P.; Jungwirth, P. Photodissociation of HBr on the Surface of Ar_n Clusters at 193 nm. *Chem. Phys.* **2005**, *315*, 161.

(24) Fedor, J.; Kočišek, J.; Poterya, V.; Votava, O.; Pysanenko, A.; Lipciuc, L.; Kitsopoulos, T. N.; Fárník, M. Velocity Map Imaging of HBr Photodissociation in Large Rare Gas Clusters. *J. Chem. Phys.* **2011**, *134*, 154303.

(25) Poterya, V.; Fárník, M.; Slavíček, P.; Buck, U.; Kresin, V. V. Photodissociation of Hydrogen Halide Molecules on Free Ice Nanoparticles. *J. Chem. Phys.* **2007**, *126*, 071101.

(26) Ončák, M.; Slavíček, P.; Poterya, V.; Fárník, M.; Buck, U. Emergence of Charge-Transfer-to-Solvent Band in the Absorption Spectra of Hydrogen Halides on Ice Nanoparticles: Spectroscopic

Evidence for Acidic Dissociation. *J. Phys. Chem. A* **2008**, *112*, 5344−5353.

(27) Poterya, V.; Fedor, J.; Pysanenko, A.; Tkáč, O.; Lengyel, J.; Ončák, M.; Slavíček, P.; Fárník, M. Photochemistry of HI on Argon and Water Nanoparticles: Hydronium Radical Generation in HI·$(H_2O)_N$. *Phys. Chem. Chem. Phys.* **2011**, *13*, 2250−2258.

(28) Ončák, M.; Slavíček, P.; Fárník, M.; Buck, U. Photochemistry of Hydrogen Halides on Water Clusters: Simulations of Electronic Spectra and Photodynamics, and Comparison with Photodissociation Experiments. *J. Phys. Chem. A* **2011**, *115*, 6155−6168.

(29) Metrangolo, P.; Neukirch, H.; Pilati, T.; Resnati, G. Halogen Bonding Based Recognition Processes: A World Parallel to Hydrogen Bonding. *Acc. Chem. Res.* **2005**, *38*, 386−395.

(30) Fárník, M.; Poterya, V. Atmospheric Processes on Ice Nanoparticles in Molecular Beams. *Front. Chem.* **2014**, *2*, 4.

(31) Lengyel, J.; Pysanenko, A.; Kočišek, J.; Poterya, V.; Pradzynski, C.; Zeuch, T.; Slavíček, P.; Fárník, M. Nucleation of Mixed Nitric Acid-Water Ice Nanoparticles in Molecular Beams that Starts with a HNO_3 Molecule. *J. Phys. Chem. Lett.* **2012**, *3*, 3096.

(32) Kočišek, J.; Lengyel, J.; Fárník, M.; Slavíček, P. Energy and Charge Transfer in Ionized Argon Coated Water Clusters. *J. Chem. Phys.* **2013**, *139*, 214308.

(33) Fedor, J.; Poterya, V.; Pysanenko, A.; Fárník, M. Cluster Cross Sections from Pickup Measurements: Are the Established Methods Consistent? *J. Chem. Phys.* **2011**, *135*, 104305.

(34) Lengyel, J.; Kočišek, J.; Poterya, V.; Pysanenko, A.; Svrčková, P.; Fárník, M.; Zaouris, D.; Fedor, J. Uptake of Atmospheric Molecules by Ice Nanoparticles: Pickup Cross Sections. *J. Chem. Phys.* **2012**, *137*, 034304.

(35) Lengyel, J.; Pysanenko, A.; Poterya, V.; Slavíček, P.; Fárník, M.; Kočišek, J.; Fedor, J. Irregular Shapes of Water Clusters Generated in Supersonic Expansions. *Phys. Rev. Lett.* **2014**, *112*, 113401-1−113401-5.

(36) Fárník, M. *Molecular Dynamics in Free Clusters and Nanoparticles Studied in Molecular Beams*; ICT Prague Press: Prague, 2011.

(37) Fárník, M.; Poterya, V.; Kočišek, J.; Fedor, J.; Slavíček, P. Short Review on the Acetylene Photochemistry in Clusters: Photofragment Caging and Reactivity. *Mol. Phys.* **2012**, *110*, 2817.

(38) Whitaker, B. *Imaging in Molecular Dynamics: Technology and Applications*; Cambridge University Press: Cambridge, 2003.

(39) Kaesdorf, S. *Geräte für Forschung und Industrie*; Wiley: Munich, 2011.

(40) Kočišek, J.; Lengyel, J.; Fárník, M. Ionization of Large Homogeneous and Heterogeneous Clusters Generated in Acetylene-Ar Expansions: Cluster Ion Polymerization. *J. Chem. Phys.* **2013**, *138*, 124306.

(41) Hagena, O. F. Nucleation and Growth of Clusters in Expanding Nozzle Flows. *Surf. Sci.* **1981**, *106*, 101.

(42) Hagena, O. F. Condensation in Free Jets: Comparison of Rare Gases and Metals. *Z. Phys. D* **1987**, *4*, 291.

(43) Hagena, O. F. Cluster Ion Sources. *Rev. Sci. Instrum.* **1992**, *63*, 2374.

(44) Buck, U.; Krohne, R. Cluster Size Determination from Diffractive He Atom Scattering. *J. Chem. Phys.* **1996**, *105*, 5408.

(45) Bobbert, C.; Schütte, S.; Steinbach, C.; Buck, U. Fragmentation and Reliable Size Distributions of Large Ammonia and Water Clusters. *Eur. Phys. J. D* **2002**, *19*, 183−192.

(46) Boys, S.; Bernardi, F. The Calculation of Small Molecular Interactions by the Differences of Separate Total Energies. Some Procedures with Reduced Errors. *Mol. Phys.* **1970**, *19*, 553−566.

(47) Řezáč, J.; Riley, K. E.; Hobza, P. Evaluation of the Performance of Post-Hartree-Fock Methods in Terms of Intermolecular Distance in Noncovalent Complexes. *J. Comput. Chem.* **2012**, *33*, 691−694.

(48) Řezáč, J.; Riley, K. E.; Hobza, P. S66: A Well-Balanced Database of Benchmark Interaction Energies Relevant to Biomolecular Structures. *J. Chem. Theory Comput.* **2011**, *7*, 2427−2438.

(49) Werner, H.-J.; Knowles, P. J.; Knizia, G.; Manby, F. R.; Schütz, M. Molpro: a General-Purpose Quantum Chemistry Program Package. *Wiley Interdiscip. Rev.: Comput. Mol. Sci.* **2012**, *2*, 242−253.

(50) Werner, H.-J.; Knowles, P. J.; Knizia, G.; Manby, F. R.; Schütz, M.; et al. *MOLPRO*, version 2010.1, A Package of Ab Initio Programs; 2010 (http://www.molpro.net).

(51) Frisch, M. J. et al. *Gaussian 09*, revision A.1. Gaussian Inc.: Wallingford, CT, 2009.

(52) Malakhovskii, A. V.; Ben-Zion, M. Temporal Evolution of an Argon Cluster During the Process of its Evaporation. *Chem. Phys.* **2001**, *264*, 135−143.

(53) Temelso, B.; Archer, K. A.; Shields, G. C. Benchmark Structures and Binding Energies of Small Water Clusters with Anharmonicity Corrections. *J. Phys. Chem. A* **2011**, *115*, 12034−12046.

(54) Ogilvie, J. F.; Wang, F. Y. H. Potential-Energy Functions of Diatomic Molecules of the Noble Gases I. Like Nuclear Species. *J. Mol. Struct.* **1992**, *273*, 277.

(55) Baumfalk, R.; Buck, U.; Frischkorn, C.; Gandhi, S. R.; Lauenstein, C. UV Photolysis of $(HBr)_n$ Clusters with Known Size Distribution. *Chem. Phys. Lett.* **1997**, *269*, 321.

(56) Baumfalk, R.; Buck, U.; Frischkorn, C.; Gandhi, S. R.; Lauenstein, C. Photodissociation and Size Analysis of $(HBr)_n$ Clusters. *Ber. Bunsenges. Phys. Chem.* **1997**, *101*, 606.

(57) Baumfalk, R.; Nahler, N. H.; Buck, U. Vibrational Excitation and Caging Following the Photodissociation of Small HBr Clusters in and on Large Ar Clusters. *Phys. Chem. Chem. Phys.* **2001**, *3*, 2372.

(58) Buck, U. Photodissociation of Hydrogen Halide Molecules in Different Cluster Environments. *J. Phys. Chem. A* **2002**, *106*, 10049.

(59) Nahler, N. H.; Baumfalk, R.; Buck, U.; Vach, H.; Slavíček, P.; Jungwirth, P. Photodissociation of HBr in and on Ar_n Clusters: The Role of the Position of the Molecule. *Phys. Chem. Chem. Phys.* **2003**, *5*, 3394.

(60) Nahler, N. H.; Fárník, M.; Buck, U.; Vach, H.; Gerber, R. B. Photodissociation of HCl and Small $(HCl)_m$ Complexes in and on Large Ar_n Clusters. *J. Chem. Phys.* **2004**, *121*, 1293.

(61) Slavček, P.; Jungwirth, P.; Lewerenz, M.; Nahler, N. H.; Fárník, M.; Buck, U. Photodissociation of HI on the Surface of Large Argon Clusters: The Orientation of Librational Wavefunction and the Scattering from the Cluster Cage. *J. Chem. Phys.* **2004**, *120*, 4498.

(62) Lu, Q.-B.; Madey, T. E.; Parenteau, L.; Weik, F.; Sanche, L. Structural and Temperature Effects on Cl-Yields in Electron-Induced Dissociation of CF_2Cl_2 Adsorbed on Water Ice. *Chem. Phys. Lett.* **2001**, *342*, 1−6.

(63) Jansen, R.; Wysong, I.; Gimelshein, S.; Zeifman, M.; Buck, U. Non-equilibrium Numerical Model of Homogeneous Condensation in Argon and Water Vapour Expansions. *J. Chem. Phys.* **2010**, *132*, 244105.

(64) Pradzynski, C. C.; Forck, R. M.; Zeuch, T.; Slavíček, P.; Buck, U. A Fully Size-Resoved Perspective on the Crystallization of Water Clusters. *Science* **2012**, *337*, 1529−1532.

(65) Buck, U.; Pradzynski, C. C.; Zeuch, T.; Dieterich, J. M.; Hartke, B. A Size Resolved Investigation of Large Water Clusters. *Phys. Chem. Chem. Phys.* **2014**, *16*, 6859−6871.

(66) Biham, O.; Furman, I.; Pirronello, V.; Vidali, G. Master Equation for Hydrogen Recombination on Grain Surfaces. *Astrophys. J.* **2001**, *553*, 595−603.

(67) This energy has been estimated approximately as 3−4 times the calculated binding energy of $CF_2Cl_2 \cdots H_2O$.

(68) Sinha, A.; Thoemke, J. D.; Crim, F. F. Controlling Bimolecular Reactions: Mode and Bond Selected Reaction of Water with Translationally Energetic Chlorine Atoms. *J. Chem. Phys.* **1992**, *96*, 372−376.

(69) Thoemke, J. D.; Pfeiffer, J. M.; Metz, R. B.; Crim, F. F. Mode- and Bond-Selective Reactions of Chlorine Atoms with Highly Vibrationally Excited H_2O and HOD. *J. Phys. Chem.* **1995**, *99*, 13748−13754.

(70) Rougeau, N. Planar Study of $H_2O + Cl \rightarrow HO + HCl$ Reactions. *Phys. Chem. Chem. Phys.* **2007**, *9*, 2113−2120.

(71) Desiraju, G. R.; Ho, P. S.; Kloo, L.; Legon, A. C.; Marquardt, R.; Metrangolo, P.; Politzer, P.; Resnati, G.; Rissanen, K. Definition of the Halogen Bond. *Pure Appl. Chem.* **2013**, *85*, 1711−1713.

Appendix D

Nucleation and growth of ice nanoparticles

THE JOURNAL OF CHEMICAL PHYSICS **135**, 104305 (2011)

Cluster cross sections from pickup measurements: Are the established methods consistent?

J. Fedor,[a] V. Poterya, A. Pysanenko, and M. Fárník[b]
J. Heyrovský Institute of Physical Chemistry v.v.i., Academy of Sciences of the Czech Republic, Dolejškova 3, 18223 Prague, Czech Republic

(Received 21 July 2011; accepted 16 August 2011; published online 8 September 2011)

Pickup of several molecules, H_2O, HBr, and CH_3OH, and Ar atoms on free Ar_N clusters has been investigated in a molecular beam experiment. The pickup cross sections of the clusters with known mean sizes, $\bar{N} \approx 150$ and 260 were measured by two independent methods: (i) the cluster beam velocity decrease due to the momentum transfer of the picked up molecules to the clusters, and (ii) Poisson distribution of a selected cluster fragment ion as a function of the pickup pressure. In addition, the pickup cross sections were calculated using molecular dynamics and Monte Carlo simulations. The simulations support the results of the velocity measurements. On the other hand, the Poisson distributions yield significantly smaller cross sections, inconsistent with the known Ar_N cluster sizes. These results are discussed in terms of: (i) an incomplete coagulation of guest molecules on the argon clusters when two or more molecules are picked up; and (ii) the fragmentation pattern of the embedded molecules and their clusters upon ionization on the Ar cluster. We conclude that the Poisson distribution method has to be cautiously examined, if conclusions should be drawn about the cluster cross section, or the mean cluster size $\bar{N}$, and the number of picked up molecules. © *2011 American Institute of Physics*. [doi:10.1063/1.3633474]

I. INTRODUCTION

The pickup technique was introduced in mid 1980s for doping clusters with foreign molecules.[1] Since then it has been developed into a very powerful tool in the cluster science: especially numerous experiments with large helium clusters use this technique[2–4] to study the spectroscopy of molecules[5–10] and their reactions[11–15] in the cold superfluid environment of the helium nanodroplets. Here we focus on the pickup to argon clusters which was also exploited in many studies, e.g., for cluster isolated chemical reactions on large Ar clusters in the group of Mestdagh[16,17] and others.[18] The pickup to argon and various other clusters was also employed for studies of photochemistry of molecules in cluster environment,[19–22] and in general for investigation of various mixed molecular clusters.[23,24] Despite these widespread applications of the pickup technique and the earlier studies of this process,[2–4] many questions remain opened concerning the mechanism of the pickup process itself, and sticking, migration and coagulation of the molecules on/in the host clusters – especially for other cluster species than helium nanodroplets. This paper contributes to the detailed understanding of this technique by investigating the pickup process of various molecules (HBr, H_2O, CH_3OH) and argon atoms on large argon clusters.

The second crucial aspect of our paper concerns the pickup cross section and the corresponding cluster size determination. One of the original motivations for cluster studies has been to investigate the evolution of certain properties or processes as a function of the system size.[25] Therefore the cluster size determination has been one of the pivotal issues in the cluster science, which is not a straightforward task for the neutral clusters. Generally, due to the strong fragmentation upon ionization of the weakly bound species, mass spectrometry is of little help here.[26–28] For the small clusters $N \lesssim 10$ the scattering method of Buck and Meyer[26,27] can be exploited to measure the neutral cluster sizes. For the large and medium sizes ($N \sim$10–10^3) several other methods have been developed, e.g., electron diffraction,[29–32] cluster beam scattering by a buffer gas,[33] pickup of sodium atoms and photoionization,[34] and helium atom diffraction on clusters.[35]

Here we are concerned with two methods for the mean cluster size determination using the pickup process: (1) The first method consists in measuring the variations of the average beam velocity with the pickup pressure.[36] (2) The second one relies on measuring the Poisson distributions of the picked up molecules.[37] Their common feature is that in order to evaluate the cluster mean size $\bar{N}$ from the measured data, the pickup cross section σ has to be determined independently – generally, the geometrical cross section of a hard-sphere was assumed. We assess the two methods by inverting the procedure, i.e., by preparing cluster beam with known mean size $\bar{N}$, evaluating the pickup cross sections σ and comparing them.

We utilized large argon Ar_N clusters with known mean cluster sizes $\bar{N} = 150$ and 260. The argon clusters have been selected as cluster archetypes for several reasons. First, their size distributions were studied in great detail by various methods[35,38–40] and well characterized by Hagena's scaling law.[35,39] Therefore the cluster sizes determined by the

---

[a] Author to whom correspondence should be addressed. Electronic mail: juraj.fedor@unifr.ch. Present address: Department of Chemistry, University of Fribourg, Chemin du Musée 9, CH-1700 Fribourg, Switzerland.

[b] Author to whom correspondence should be addressed. Electronic mail: michal.farnik@jh-inst.cas.cz.

expansion conditions are well known. Further advantage of Ar_N clusters is, that a fair amount of work exists on the pickup of the present molecules in particular: HBr,[41] H_2O,[37] CH_3OH.[18] This facilitates a critical comparison of the present data obtained by two different methods. Finally, the interaction of Ar-clusters with pickup molecules and atoms can be described by relatively simple potentials and the pickup can be modelled by molecular dynamics and Monte Carlo methods. The theoretically calculated cross sections provide useful references for the assessment of the two experimental methods. Surprisingly the two experimental methods delivered different results. We conclude that the results from velocity measurements are close to the real cross sections while the Poisson distribution method is biased by an incomplete coagulation of the host molecules on the cluster and fragmentation pattern of the host embedded clusters upon the ionization. Also a combination of the two methods is proposed which, in principle, would allow to determine $\bar{N}$ and σ from the experimental data independently without any assumptions of their analytical relation.

II. EXPERIMENT

The principle of the experiment can be briefly summarized as follows: clusters are doped with the guest molecules in a pickup chamber and two characteristics of the cluster beam are measured as a function of the pickup gas pressure – the neutral beam velocity and the fragment ion mass spectra. Our complex cluster beam apparatus was described in detail elsewhere,[42,43] therefore only the parts of the machine relevant for the present experiment are described here and shown in Fig. 1.

The argon clusters were generated in the source chamber S1 by supersonic expansion through a conical nozzle (diameter $d = 50\ \mu$m, length 2 mm, and opening angle $\alpha = 30^\circ$). The nozzle was cooled to a constant temperature of $T_0 = 223$ K and the size of the clusters was controlled by varying the stagnation pressure of argon p_0. The resulting mean cluster size can be determined according to the empirical formulas,[35,39]

$$\bar{N} = K\left(\frac{\Gamma^*}{1000}\right)^{\zeta}, \quad \Gamma^* = \frac{p_0[\mathrm{mbar}]\,d_e[\mu\mathrm{m}]^{0.85}}{T_0[\mathrm{K}]^{2.2875}}K_c, \tag{1}$$

where $K = 38.4$ and $\zeta = 1.64$ were determined from the diffractive He atom scattering on large Ar_N clusters,[35] $K_c = 1646$ is a characteristic constant of the expanding gas for Ar, and $d_e = \frac{d}{\tan(\alpha/2)}$ is the equivalent nozzle diameter. The applicability of these formulas for rare gas clusters were proved by several experiments,[35,38–40] some of which were done in Göttingen[35] using the cluster source implemented in the present experiments. The two values of stagnation pressure applied in the present experiments $p_0 = 5$ and 7 bars correspond to the mean cluster sizes $\bar{N} = 150$ and 260, respectively.

The Ar cluster beam passed through a skimmer with 1 mm opening before entering the differentially pumped scattering chamber SC. This chamber served as a pickup cell filled with the gas to dope the clusters with molecules. The effective capture length was $L = 17$ cm.[44] The pressure in the chamber was monitored by Bayard-Alpert ionization gauge (Varian type 571), which was calibrated for the specific gases by comparing the measured pressures to the values of a capacitance gauge pressure (Pfeiffer CMR 365). The background pressure in the pickup chamber was $\leq 1 \times 10^{-6}$ mbar, and the pressure with the pickup gas went up to 7×10^{-4} mbar.

For the velocity measurements the cluster beam was modulated by a pseudorandom mechanical chopper[45] (PRC) in the next differentially pumped chopper chamber CC. The chopper contained two pseudorandom sequences of 127 elements and its rotation with frequency of 492.1 Hz corresponded to a single opening time window of 8 μs. After the chopper the beam passed the flight path of 955 mm through the photodissociation chamber PDC (not used in the present experiments) to the ion source of a quadrupole mass spectrometer (QMS) with an electron multiplier detector at the end. The arrival time to the detector was measured. The total flight time was properly corrected for the time spent by the ion fragment in the quadrupole and for any electronic delay of the trigger signals and converted to the beam velocity distribution. The velocity distribution was evaluated from the measured data by the cross-correlation mathematical method.[45] Usually the quadrupole mass spectrometer was set on the major ionization fragment of Ar clusters which is the dimer Ar_2^+ ($m/z = 80$ amu). The maximum velocity of the Ar clusters (without any pickup gas) measured at the nozzle temperature $T_0 = 223$ K was 490 ms^{-1} with a speed-ratio of $S = 35$. This

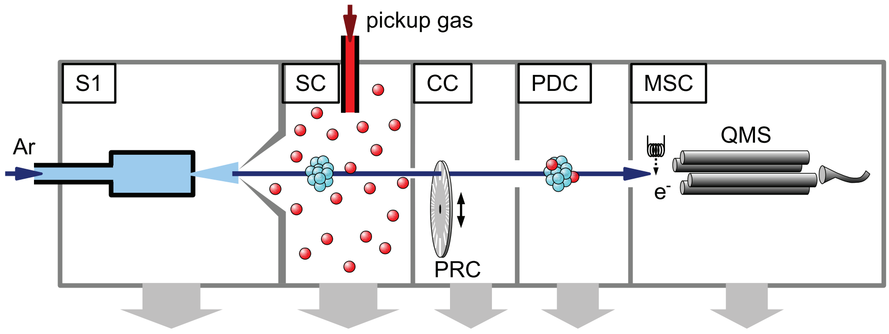

FIG. 1. Schematic picture of the experiment.

corresponds to the theoretical maximum beam velocity,[46]

$$v_\infty = \sqrt{\frac{2k_B T_0}{m}\frac{\gamma}{\gamma-1}}, \tag{2}$$

where k_B is the Boltzmann constant and γ is the adiabatic index ($\gamma = 5/3$ for a monoatomic ideal gas), i.e., $v_\infty = 481\ \mathrm{ms}^{-1}$. The slightly higher measured beam velocity can be due to the condensation effect which provides an additional heating of the beam during the expansion.

In addition to the beam velocities, the fragment ion mass spectra of the doped clusters were recorded as a function of the pickup gas pressure. The ionizing electron energy was 70 eV. The quadrupole mass spectrometer transmittance was calibrated using the known spectrum of mass calibrant FC-43.

III. PICKUP DYNAMICS AND STATISTICS

Since the argon clusters have a solid-like character,[29,30,32] the molecules do not penetrate the cluster upon the pickup and stay in the outer solvation shell,[47–49] and the clusters in the beam are slowed down by the pickup due to the momentum transfer. The velocity change increases with the number of guest molecules.

Let us assume an Ar_N cluster of a size N with an initial velocity v_i colliding with k stationary molecules in the pickup cell which stick to the cluster. Then the momentum conservation yields for the cluster final velocity v_f the equation,

$$N m_{\mathrm{Ar}} v_i = (N m_{\mathrm{Ar}} + k m_X) v_f, \tag{3}$$

where m_{Ar} is Ar atom mass and m_X is the mass of the guest molecule. It assumes that no considerable evaporation of cluster constituents occurs upon the pickup. This assumption has been justified by the molecular dynamics simulations outlined in Sec. V. The simulations also show that the molecule remains on the cluster if a considerable momentum transfer between the molecule and the cluster occurs. Thus this simple model describes the final velocity dependence sufficiently well (see Sec. V).

The number of picked up molecules along the path-length L in a gas at a pressure p (corresponding to the number density $n_g = p/k_B T$) can be expressed as

$$k = n_g \sigma_e L = \frac{p}{k_B T}\sigma_e L, \tag{4}$$

where σ_e is the pickup cross section. The measured effective cross section σ_e incorporates the velocity-averaging correction factor[46,50,51] into the cross section $\sigma_e = \sigma_0\, F_{a0}(\infty, x)$. Combining Eqs. (3) and (4), the relative change in the cluster velocity is directly proportional to pickup cell pressure,

$$\frac{\Delta V}{V} \equiv \frac{v_i - v_f}{v_f} = \frac{m_X}{N m_{Ar}} \frac{L\sigma_e}{k_B T} p. \tag{5}$$

Thus, from the slope of the relative velocity change dependence on the pressure the pickup cross section σ_e can be evaluated.

Since the pickup of the kth molecule is assumed to be a random process independent of the previous $(k-1)$ events, its probability follows the Poisson distribution:[2]

$$P_k(p) = \frac{1}{k!}(\sigma_e L n_g)^k e^{-\sigma_e L n_g} = \frac{1}{k!}\left(\frac{\sigma_e L}{k_B T} p\right)^k e^{-\frac{\sigma_e L}{k_B T} p}. \tag{6}$$

Thus the pickup cross section σ_e can be obtained by measuring the dependence of a fragment ion intensity (corresponding to, e.g., pickup of $k = 1$ molecule) on the pickup pressure, and fitting this dependence with the corresponding Poisson distribution.[3]

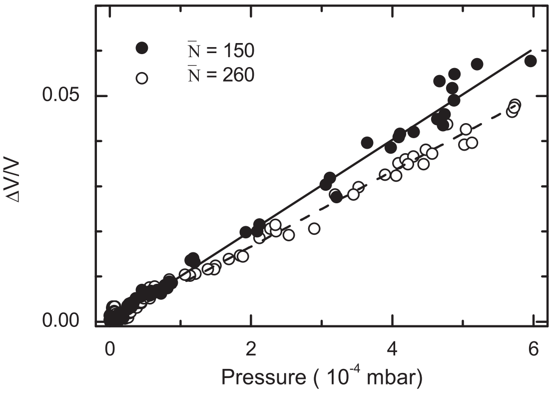

FIG. 2. Relative decrease in the cluster beam velocity as a function of the pickup gas pressure (lines, Eq. (5)) for the pickup of H_2O on Ar_N clusters with $\bar{N} = 150$ and 260.

IV. EXPERIMENTAL RESULTS

A. Velocity measurements

Water H_2O, methanol CH_3OH, hydrogen bromide HBr, and argon Ar were used as pickup gases. According to Eq. (5) the relative change in the cluster beam velocity is directly proportional to the pickup gas pressure. This linear dependence is demonstrated in Fig. 2 for the pickup of H_2O on Ar_N, $\bar{N} = 150$ and 260. The somewhat larger scatter of the data for $\bar{N} = 150$ corresponds to the smaller signals measured for the smaller clusters. Nevertheless, both data sets can be fitted by straight lines with high confidence, in accordance with the previous experiments.[36] Similar dependence was measured for the other pickup species. The pickup cross sections σ_e were derived from the slopes of the linear fits and are summarized in Table I. The error in the velocity measurement is smaller than 1%; however, the uncertainty due to the pressure calibration can be up to 10%.

The quantity that is evaluated directly from the experimental data is the effective cross section,

$$\sigma_e = \sigma_0 \cdot F_{a0}(\infty, x), \tag{7}$$

which incorporates the velocity-averaging correction factor F_{a0} due to the velocity distribution of the target molecules.[46,50,51] Label ∞ denotes the hard sphere potential approximation, and $x = v_i/\alpha_g$ where v_i is the cluster beam velocity and α_g is the most probable velocity

TABLE I. Pickup cross sections for two mean Ar_N cluster sizes $\bar{N} = 150$ and 260 obtained by various methods: velocity measurements, Poisson distribution measurements, and molecular dynamics simulations. The experimental error of σ_e obtained from the velocity measurements was estimated $\lesssim 10\%$. The Poisson distribution cross section was obtained by fitting the experimental data by $P_1(p)$, Eq. (6), and does not have a real physical meaning as argued in the text. The corrected cross sections σ_0 were evaluated from the experimental σ_e obtained from the velocity measurements divided by the velocity correction factors $F_{a0}(\infty, x)$ (see the text). Correction R_0 to the hard sphere geometrical cross section was evaluated from the simulated cross sections.

Molecule	$\bar{N}$	Velocity σ_e (Å^2)	F_{a0} (∞, x)	σ_0 (Å^2)	Detected ion mass (amu)	Poisson σ_e (Å^2)	Simulations σ_e (Å^2)	R_0 (Å)
HBr	150	672	1.133	593	Br^+ (81)	500	748	4.3
	260	836		738		352	...	
H_2O	150	848	1.545	549	H_2O^+ (18)	528	928	6.1
	260	1083		701		408	...	
CH_3OH	150	1041	1.329	783	CH_3O^+ (31)	561	...	
	260	1523		1146		522	...	
Ar	150	708	1.267	559	...	...	824	5.1
	260	1080		852	...	...	...	

in the Maxwellian distribution of the scattering gas. These correction factors were tabulated in the literature[50,51] and are summarized together with the evaluated σ_0 in Table I.

B. Poisson distributions

Generally the mass spectra of Ar_N clusters doped with the above molecules exhibit three groups of mass peaks: (i) the most pronounced is the sequence of Ar_n^+ peaks; (ii) the ion fragments of the guest molecules and ion fragments of the formed guest clusters; (iii) in some cases there are mixed cluster ions containing Ar-atom(s) and the picked up molecule or its fragment.

When methanol is introduced into the pickup chamber characteristic peaks at $m/z = 31$ amu (CH_2OH^+) and 29 amu (COH^+) appear in the mass spectra. At elevated methanol pressures new peaks raise due to the methanol cluster generation on Ar cluster: 33 amu ($(CH_3OH)H^+$) and 63 amu ($CH_3OH{\cdot}CH_2OH^+$) which can be generated from the methanol dimer and larger clusters $(CH_3OH)_k$, $k \geq 2$; 65 amu ($(CH_3OH)_2H^+$) and 95 amu ($(CH_3OH)_2{\cdot}CH_2OH^+$) which indicate the presence of $k \geq 3$ host clusters; and 97 amu ($(CH_3OH)_3H^+$) fragmenting from $k \geq 4$. There was no evidence for $Ar_n(CH_3OH)_m{}^+$ fragments. Similar spectra were measured for methanol pickup on Ar clusters in other experiments.[18]

From the earlier studies [52–55] of hydrogen bonded clusters, it was found that a fast proton transfer reaction follows the cluster ionization. Thus the major ionization channel results in the protonated fragments with the abstraction of one or more monomer units. The ions below the monomer mass are usually expected to originate from the ionization of a single molecule on the cluster. The intensities of the following ion peaks were plotted against the pressure in the pickup chamber and analysed with the Poisson statistics, see Fig. 3: COH^+ and CH_2OH^+ monitoring the pickup of $k = 1$ molecule; $(CH_3OH)H^+$ and $(CH_3OH)CH_2OH^+$ monitoring $k = 2$ pickup, and $(CH_3OH)_2H^+$ for $k = 3$. This assumes the coagulation of molecules upon pickup on the cluster and the following fragmentation upon ionization:

$$\begin{aligned}&CH_3OH \rightarrow COH^+, CH_2OH^+,\\&(CH_3OH)_2 \rightarrow (CH_3OH)H^+, (CH_3OH)CH_2OH^+,\\&(CH_3OH)_3 \rightarrow (CH_3OH)_2H^+,\end{aligned}$$

i.e., no population of these fragments from larger clusters. We argue in the discussion that our data indicate that these assumptions are not fulfilled completely.

The capture of water molecules results in the observation of peaks at $m/z = 18$ amu (H_2O^+) and 58 amu ($Ar{\cdot}H_2O^+$) presumably from the monomer; 19 amu (H_3O^+) and 59 amu ($Ar{\cdot}H_3O^+$) which can originate from $k \geq 2$; and 55 amu ($(H_2O)_3H^+$) from $k \geq 4$ (the fragment $(H_2O)_2H^+$ at 37 amu indicative of $k \geq 3$ was obscured by the nearby strong Ar^+ peak at 40 amu). It is interesting to note that here, unlike in the methanol case, the ion fragments containing Ar are observed. Again we measure the pickup pressure dependence of

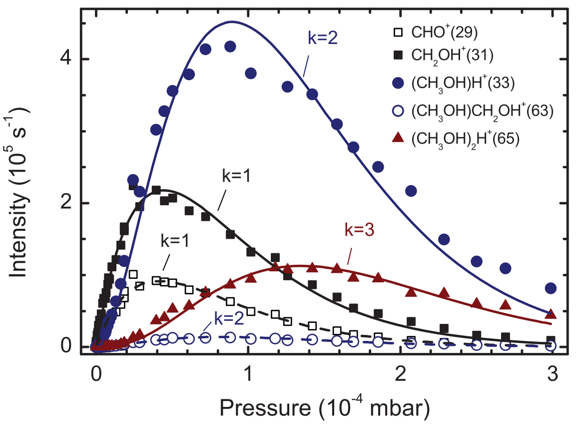

FIG. 3. Intensity of fragment ion peaks in the mass spectra as a function of pickup pressure of CH_3OH. The lines correspond to the Poisson fits P_k, Eq. (6). Detected ions (mass in amu): COH^+ (29) and CH_3OH^+ (31) fitted with $k = 1$; $(CH_3OH)H^+$ (33) and $(CH_3OH)CH_2OH^+$ (63) fitted with $k = 2$; and $(CH_3OH)_2H^+$ (65) fitted with $k = 3$.

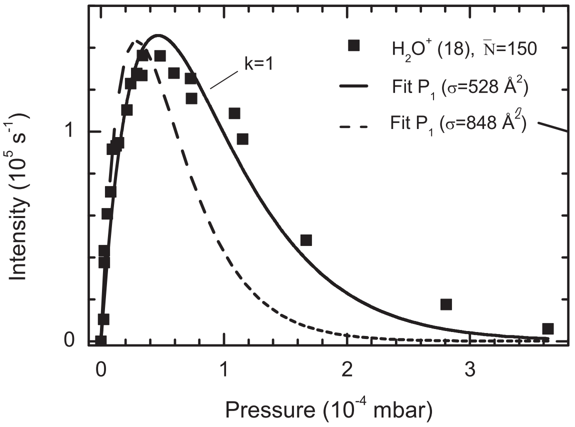

FIG. 4. Intensity of monomer fragment ion peak ($m/z = 18$ amu) in the mass spectrum as a function of water pressure in the pickup chamber. Solid line represents the Poisson distribution fit (Eq. (6)) with $k = 1$ and σ_e as a fitting parameter ($\Rightarrow \sigma_e = 528$ Å^2). The dashed line corresponds to the Poisson distribution with $\sigma_e = 848$ Å^2 obtained from the velocity measurement.

H_2O^+ to monitor $k = 1$ pickup and $(H_2O)H^+$ for $k = 2$, and fit these dependencies with the corresponding Poisson statistics.

Finally for HBr pickup the necessity of a higher mass resolution (to resolve various fragments with ^{79}Br and ^{81}Br isotopes) limited the monitored mass range of our quadrupole below the mass of 150 amu. Due to this reason the HBr cluster ion peaks were not measured. However, an appreciable signal from $H^{81}BrH^+$ at m/z = 83 amu manifests the presence of $(HBr)_k$ clusters with $k \geq 2$. We have monitored ^{81}Br for the molecule $k = 1$ pickup and $H^{81}BrH^+$ peak for $k = 2$ capture. The intensity at 81 amu has been corrected for a contribution from $H^{79}BrH^+$. This could be done since the ^{81}Br:^{79}Br = 0.973 ratio is known and the $^{81}HBrH^+$ peak was measured.

The experimental data can be illustrated by the example in Fig. 4 which shows the H_2O^+ ion intensity dependence on the water pickup pressure. The solid line corresponds to the Poisson distribution fit to the data using Eq. (6) with $k = 1$ and σ_e as a fitting parameter. However, the obtained cross section $\sigma_e \approx 528$ Å^2 is significantly smaller than 848 Å^2 obtained for the same clusters from the velocity measurements. If the later value was used for Poisson fit with $k = 1$ (dashed line in Fig. 4), the experimental data could not be fitted adequately. Similar results were obtained for the other picked up molecules and the obtained cross sections are summarized in Table I. They will be further discussed in Sec. VI.

Figure 5 shows several examples of pickup data for HBr (top) and H_2O (bottom) molecules. Here the data are fitted by a sum of Poisson distributions with constant cross section σ_e (Eq. (6)) fixed to the value obtained from the velocity measurements. The fitting parameter was the number m of added $P_k(p)$, $k = 1, \ldots, m$. This is further discussed in Sec. VI.

V. MOLECULAR DYNAMICS AND MONTE CARLO SIMULATIONS

In order to support the experimental data we have performed molecular dynamics (MD) and Monte Carlo (MC) simulations of the pickup process. The simulations were performed in the coordinate system in which the cluster is initially at rest and the projectiles were shot at the cluster with the mean velocity corresponding to the experimental cluster beam velocity (490 ms^{-1}). The simulations were performed for the Ar_N cluster size N= 150 for three projectiles: Ar, HBr, and H_2O.

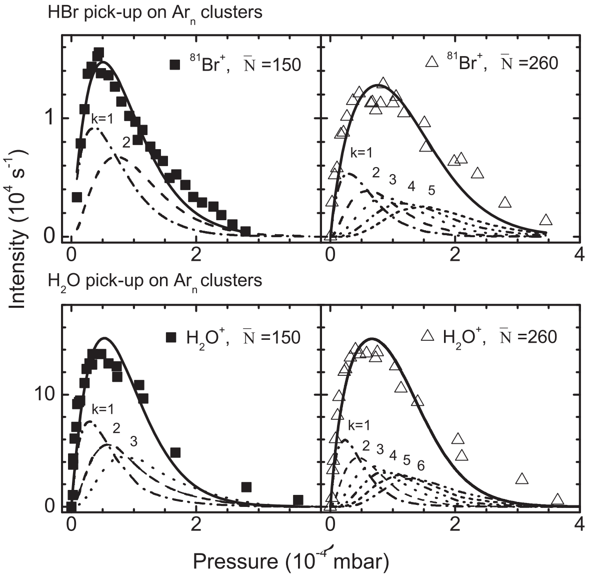

FIG. 5. Intensity of monomer fragment ion peaks in the mass spectra as a function of the pickup chamber pressure. The detected ions were Br^+ (m/z = 81 amu) and H_2O^+ (m/z = 18 amu) for HBr and H_2O pickup, respectively. The solid lines represent the fits to the data with a sum of Poisson distributions (see Eq. (12)).

The Lennard-Jones (LJ) potential of the form

$$V_{LJ}(r) = 4\varepsilon\left(\left(\frac{\rho}{r}\right)^{12} - \left(\frac{\rho}{r}\right)^{6}\right) \qquad (8)$$

has been used for the description of Ar-Ar, HBr-Ar, and H_2O-Ar interactions. The parameters ε and ρ of the potential are listed in Table II. The parameters for Ar-Ar interaction have been obtained in Ref. 49 by fitting the correct pairwise potential of Aziz and Slaman.[56] It has been shown, that the LJ parameters usually used for simulation of liquids and solids cannot be used for simulations of cryogenic clusters.[49] Both HBr and H_2O were represented as united atom. The parameters for HBr-Ar potential were obtained in Ref. 48 by averaging the three body potential of Hutson[57] over all possible HBr orientations. The isotropic potential for H_2O-Ar has been successfully used to model argon-water ice collisions.[58,59] The parameters for H_2O-Ar potential were taken from Ref. 58. The use of isotropic potential is a relatively crude approximation; however, it has been applied previously for MD simulation of pickup of hydrogen halides on rare gas clusters and yielded good agreement with experiments.[47,48] As seen below, the present simulations agree very well with the experiment also for the H_2O-Ar_N system, which justifies the use of the isotropic potential also in this case. Because of the relative complexity of the CH_3OH molecule, the simulation of the

TABLE II. Lennard-Jones potential parameters used for molecular dynamics simulations.

	ρ (Å)	ε (K)
Ar-Ar	3.35	143.2
HBr-Ar	3.55	174
H_2O-Ar	3.0	174

methanol-Ar_N collisions is beyond the scope of the present mostly experimental paper.

We have used the Verlet's algorithm with a time step of 1 fs to integrate Newton's equation of motion. Simulation of one trajectory went as follows: The icosahedral structure of Ar_{150} cluster was assumed with coordinates taken from Cambridge cluster database.[60] The temperature of the cluster was assumed to be 32 K (Ref. 29) and the cluster was equilibrated for 10 ps. Then the cluster was randomly oriented and the projectile was shot at the cluster with a certain impact parameter. The impact velocity was sampled from the Maxwell-Boltzmann distribution of projectile gas at 300 K centered around 490 ms^{-1}. For each trajectory, the simulation lasted for 1 ns. After the simulation was finished, it was determined whether the projectile remained on the cluster, how many argon atoms were evaporated from the cluster, and the velocity of the cluster after the collision.

In order to calculate the pickup cross section, 2500 projectile trajectories were generated with random impact parameters and the cross section was evaluated from the ratio of sticking to nonsticking trajectories. This approach is illustrated in Fig. 6. The normally constant maximal impact parameter at which the collision is sticking has been diffused by the fact, that the projectiles have also transversal velocities sampled from the Maxwell-Boltzmann distribution. The pickup cross sections obtained from these simulations are listed in Table I.

In addition to the pickup cross section, the simulations addressed two questions that justify evaluation of the experimental data according to Eq. (5): (i) Are collisions with the gas in the pickup cell elastic or inelastic? (ii) Does the collision lead to an effective evaporation of cluster constituents? The bottom panel of Fig. 6 shows the histogram of simulated final cluster velocities for sticking and nonsticking collisions. The plot demonstrates that a considerable momentum transfer between the projectile and the cluster occurs only in the case of sticking collisions, i.e., in inelastic events. Also, the mean value of the final cluster beam velocity distribution is in excellent agreement with Eq. (3). No evaporation from the cluster was observed on the timescale of the simulation (1 ns).

We have addressed one more question using the simulations: If two HBr molecules are picked up on the Ar_{150} cluster, what is the probability that they coagulate, i.e., form the HBr dimer? The simulation was done as follows: the first HBr projectile was shot at the cluster with a random impact parameter (within the sticking range) and the system was simulated for 500 ps. Then the second HBr projectile was shot at this cluster with a random impact parameter and the system was simulated for 1 ns. The distance between the two HBr atoms was monitored and if the average distance was less than 5 Å the coagulation was considered to occur (in all cases when the dimer was formed it did not dissociate till the end of the simulation). Total 2500 simulations were run and the coagulation occurred in 22.6% of cases. The mean time of dimer formation was 93 ps after the impact of the second projectile on the cluster.

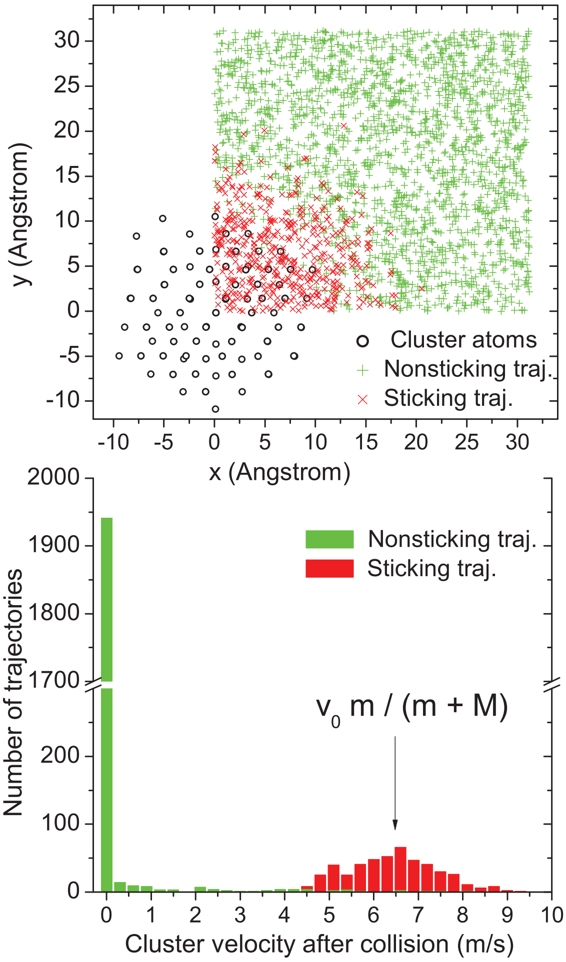

FIG. 6. Results of MD simulations for Ar_{150}-HBr collisions. Top: Map of sticking and nonsticking trajectories used to evaluate effective cross section. Bottom: Histogram for cluster velocities after the collisions. In the simulations the HBr projectiles were shot at the cluster initially in rest with the velocity corresponding to the experimental velocity of the cluster beam. The vertical arrow indicates the velocity shift according to Eq. (3) in excellent agreement with the simulations.

The HBr-HBr interaction has been approximated by the isotropic hard-core Lennard-Jones (HCLJ) potential of Hurly,[61]

$$V_{HCLJ}(r) = 4\varepsilon\left(\left(\frac{\rho - 2a}{r - 2a}\right)^{12} - \left(\frac{\rho - 2a}{r - 2a}\right)^{6}\right) \tag{9}$$

with the parameters $\varepsilon = 533.45$ K, $\rho = 3.44$ Å, and $a = 0.526$ Å. This potential approximates the HBr dimer by a diatomic-like molecule with isotropic interaction. We are aware of the crudeness of such approximation – the present results do not properly describe the behaviour of two HBr molecules on Ar cluster. A proper interpretation of the simulation is that it describes the behaviour of two picked up atom-like objects that have the same binding energy as the HBr dimer. Nonetheless, results of such simulation – coagulation only in about 23% of cases – are helpful to understand the discrepancy in the experimental methods (see the discussion in Sec. VI A).

VI. DISCUSSION

A. Capture cross sections

The major point to be discussed here is the comparison of the pickup cross sections summarized in Table I. First, we focus on the effective cross sections σ_e evaluated from the velocity measurements which are in a good agreement with the simulated ones: in all cases the calculated cross sections exceed the measured ones by about 10% for HBr and H_2O and by 14% for Ar. The agreement between the velocity measurements and simulations suggests that the cross sections determined by this method are close to the real values.

It is interesting to note that σ_0 is consistent for all the molecules except methanol; i.e., $\sigma_0 \approx 570$ Å^2 for $\bar{N} = 150$ with all the values within 4%, and $\sigma_0 \approx 775$ Å^2 for $\bar{N} = 260$ with all the values within 10%. For methanol significantly larger σ_0 were obtained which could be caused by the fact that velocity correction factors corresponding to the hard sphere potential approximation is not valid for this large molecule with internal structure and many degrees of freedom. It should be also noted that the simulated cross sections were calculated in a way that mimics the experiment, thus they correspond to the effective cross section σ_e, i.e., the velocity correction factors F_{a0} are implicitly included. Both, in the experiment and simulations the cross sections are obtained on the assumption, that the projectile is a point-like particle, i.e., the size of the incoming molecule is neglected, or more precisely included in the obtained σ_e. This may add a small relative shift, especially for molecules like methanol.

We also compare the obtained cross sections to the simple geometrical cross sections. To determine the cluster mean size $\bar{N}$ by any of the two methods exploited here a certain analytical relationship between the cross section σ and N had to be assumed. Both Cuvellier *et al.*[36] and Macler and Bae,[3] assumed a geometrical pickup cross sections when introducing their methods for the mean cluster size determination, i.e.,

$$\sigma_g = \pi R_N^2, \quad R_N = \left(\frac{3a^3}{16\pi}N\right)^{1/3}, \tag{10}$$

where $a = 5.34$ Å is the lattice parameter of Ar clusters.[29] The geometrical cross sections corresponding to the present mean cluster sizes $\bar{N} = 150$ and 260 are $\sigma_g = 390$ Å^2 and 560 Å^2, respectively. Cuvellier *et al.*[36] used collision dynamics simulations to account for a more realistic attractive interaction of the molecule with the cluster and modified the geometrical cross section formula to

$$\sigma_{g0} = \pi(R_N + R_0)^2. \tag{11}$$

The value $R_0 = 3$ Å was determined by the simulations of Ar-Ar_{125} system. This yields the geometrical cross section $\sigma_{g0} = 620$ Å^2 and 840 Å^2 for the present mean cluster sizes $\bar{N} = 150$ and 260, respectively.

Clearly the simple hard sphere cross sections σ_g (Eq. (10)) are strongly underestimated. Adopting the approach of Cuvellier *et al.*[36] we can modify σ_g by the contribution R_0 due to the interaction between the cluster and the projectile to σ_{g0} (Eq. (11)). Thus from comparison of the simulated cross sections with σ_g, the parameter R_0 can be evaluated (Table I). Note, that the comparison was made with the calculated σ_e value which implicitly includes also the velocity dependence (F_{a0}) thus R_0 is in principle velocity dependent. Since this parameter is due to the interaction between the species, it should correlate with the potential parameters in Table II. It is interesting to note that R_0 increases with the decreasing parameter ρ of LJ potential.

The most striking observation is the significantly smaller cross sections evaluated from the Poisson distributions. The Poisson statistics is frequently used to determine the number k of particles picked up by the cluster.[2,7,16,19] Generally the good quality of the Poisson distribution fit to the experimental data is regarded as the justification for using such analysis to obtain k, $\bar{N}$, or σ values. The present measurements show that, although high quality fits could be obtained, the evaluated cross sections still differ significantly from the real values. An indication that the σ_e values are wrong is the fact that they are larger for the smaller clusters in all cases.

Also the second order $k = 2$ Poisson distributions were fitted to the corresponding signals for all three studied molecules, e.g., at masses $m/z = 19$ amu [H_2OH^+], 33 amu [$(CH_3OH)H^+$], and 83 amu [$HBr^{81}H^+$]. However, even smaller cross sections were obtained from these fits than from the $k = 1$ fragments. The quality of these fits was somewhat worse with evident broadening in the high pressure region.

Below several factors are addressed that complicate the emergence of the Poisson statistics and could explain why the analysis yields the lower cross sections. We argue that some of these factors (i.e., non-sticking collisions, evaporation, and scattering from the beam) do not contribute to present discrepancy, while other factors (i.e., coagulation and fragmentation upon ionization) can contribute.

The first possible reason for the discrepancy could be the *non-sticking* collisions. If the sticking coefficient of a molecule is $s < 1$, only a fraction of the total number of collisions will actually result in the capture of the molecule on the cluster. On the other hand, the cluster can be slowed down even in an inelastic collision, which does not result in complete momentum transfer and the sticking of the molecule to the cluster. However, as is demonstrated in Fig. 6, the simulations suggest that the measured velocity decrease is caused almost exclusively by the sticking collisions, and thus the cross sections obtained by both methods should be the same.

Further effect can be an *evaporation* of the Ar cluster atoms due to the energy transfer in the sticking collision. This effect would lower the cross section for each subsequent pickup event, since $\sigma \propto \bar{N}^{2/3}$. The molecular dynamics simulations did not show any evaporation within 1 ns after the pickup. The large clusters are efficient thermal baths for energy dissipation and a significant evaporation on longer timescale is not expected. The following energy arguments can be also used. For the binding energy of a single Ar atom to the Ar_N cluster $N = 150$ a model calculation[62] as well as our estimate based on the LJ potential yield ∼80 meV. The binding energy of an HBr molecule to the cluster can be estimated from the Ar-Ar_N binding energy and the comparison of the LJ potentials for Ar-Ar and HBr-Ar interactions (Table II), i.e., the HBr-Ar_N energy would correspond to ∼100 meV. Upon the pickup of a single HBr molecule this binding energy plus the heat due to collision inelasticity (∼100 meV) are transferred to the cluster, i.e., total about 200 meV which would be sufficient to evaporate only two Ar atoms. This effect could not explain the observed cross section decrease.

The *scattering* of clusters on molecules in the pickup cell can deflect the smaller clusters out of the beam to a greater extent than the large ones, and thus shift the mean cluster size to a larger value. This effect could make the observed capture cross section larger which, however, is not the case.[63] Additionally, this effect would influence both experimental methods simultaneously.

One explanation of the observed difference concerns the *coagulation* of the embedded molecules. It was discussed in detail for He clusters,[2–4] however, the present case of solid-like argon clusters might differ significantly from the superfluid helium nanodroplets. The coagulation on Ar clusters will be controlled by a competition between the polarization forces attracting the molecules towards each other and the forces binding the molecules to the cluster and hindering their diffusion on the surface. This issue has been also addressed with our MD simulations (Sec. V) for two HBr-like objects picked up by the cluster. The coagulation (i.e, the formation of HBr dimer on the cluster surface) occurred only in 22.6% out of 2500 simulations. If the picked up molecules do not coagulate, even the pickup of $k \geq 2$ molecules will contribute to the signal assigned to the monomer. This signal is, however, fitted with $k = 1$ distribution $P_k(p)$. Thus the ion signal dependence corresponding to the monomer will be a composition of several independent events where $k = 1,2,...$ molecules are picked up by the cluster. Figure 5 shows the experimental data fitted with a sum of Poisson distributions,

$$P(p) = A_0 \sum_{k=1}^{m} P_k(p). \tag{12}$$

In the nonlinear least-squares fit procedure the number m of P_k distributions (Eq. (6)) was varied while the parameter σ was fixed to the value obtained from the velocity experiment. From these fits it would follow that Ar clusters of size $\bar{N} = 150$ can accommodate up to $m = 3$ water molecules without coagulation. The distribution for larger clusters is even broader with up to $m = 6$ water molecules. This would imply very poor migration of the guest molecule on the Ar cluster.

Yet another important issue is the *fragmentation* of the host molecule or cluster upon the ionization. The assumption that we measure the Poisson distribution for the pickup of k molecules X can be only valid if we detect a fragment which corresponds exclusively to the ionization of $\mathrm{X_k}$ species, i.e., for P_1 distribution we have to choose the fragment which corresponds exclusively to the monomer ionization and not to the ionization of an $\mathrm{X}_{k\geq 2}$ cluster. However, the fragmentation dynamics can be more complicated and affected by the Ar cluster. For example, the accepted fast proton transfer reaction as a main fragmentation channel for the hydrogen bonded clusters after ionization can be quenched by the cluster environment as observed for the methanol clusters on larger Ar clusters.[18] Thus, even if the molecules coagulate and form the dimer, upon ionization the dimer fragment can contribute to P_1 distribution and the fit will yield erroneous result for the cross section.

In summary, due to incomplete coagulation and ionization fragmentation dynamics the pickup of $k \geq 2$ molecules can still contribute to the measured intensity of the fragment assigned to the pickup of a single molecule. The dependence of the fragment intensity on the pickup pressure will thus extend to higher pressures which will result in smaller fitted σ_e if the fit with a single Poisson ($k = 1$) distribution is used. It ought to be mentioned that in some cases dependencies with clearly enhanced intensity at higher pressures have been measured. Thus the pickup cross section evaluated from the Poisson distribution fit will be smaller than the real cross section.

B. Implications for cluster size determination

Two methods for the mean cluster size determination based on the pickup process were examined in our study.[36,37] Since the cluster mean size $\bar{N}$ and the pickup cross section σ cannot be determined independently by these methods, both methods assumed a certain analytical relationship between these two quantities which was the geometrical cross section of a hard sphere. Our original motivation for these measurements was that by combining Eqs. (5) and (6), both quantities σ and $\bar{N}$ could be determined by simultaneous measurements of velocity and Poisson distributions. This would present a new method for determining the mean cluster size in a beam without the geometrical cross section assumption.

However, as seen above, in the course of our pickup measurements we have discovered that the two methods actually provide inconsistent results. The reason is that in the Poisson distribution measurements, incomplete coagulation of molecules on the cluster surface and their fragmentation patterns complicate the fitting procedure. Since these processes are not always obvious, it has to be cautiously examined which species are actually detected in the Poisson distribution measurements, if the cluster size or cross section are to be determined from such data. In other words, if the mean cluster size or cluster cross section is based solely on the Poisson distribution $P_k(p)$ measurement of a certain fragment after the pickup process, the result can be wrong, unless the measured fragment ion is assigned unambiguously to the pickup of k molecules and any contribution from pickup of more than k molecules is excluded.

VII. CONCLUSIONS

We report here the capture cross sections σ_e for pickup of several gas molecules (HBr, H_2O, CH_3OH) and Ar atoms on Ar_N clusters of the mean sizes $\bar{N} \approx 150$ and 260. Two different methods proposed in the literature[36,37] were employed in the present measurements and σ_e was evaluated from

1. the decrease in the cluster beam velocity due to the momentum transfer of the picked up molecules;
2. the Poisson distribution fit of a selected cluster fragment ion intensity dependence on the pickup pressure.

In addition, the pickup cross sections were calculated with molecular dynamics and Monte Carlo simulations. The simulations support the results of the velocity measurements. On the other hand, the Poisson distributions yield significantly smaller cross sections, which are also inconsistent with the dependence on the cluster size. The reasons for the inconsistency of the results based on the Poisson distributions are discussed in terms of (i) an incomplete coagulation of guest molecules on the argon clusters when $k \geq 2$ molecules are picked up, and (ii) the fragmentation pattern of the embedded molecules and their clusters upon ionization on the Ar cluster.

The general message from this paper is that the Poisson distribution method has to be cautiously examined, if conclusions should be drawn about the cluster mean size $\bar{N}$, or the cross section σ, or the number k of picked up molecules.

It is also important to note that both the velocity measurements as well as the MC simulations show that the simple geometrical cross sections are significantly smaller than the real values and therefore not a good approximation for the cluster pickup cross section.

ACKNOWLEDGMENTS

This work has been supported by the Grant Agency of the Czech Republic Project Nos. 203/09/0422 and P208/11/0161, and the Academy of Sciences of the Czech Republic Project No. KJB400400902. J. Fedor acknowledges the support of the Grant No. 235414 "IPhoN" within FP7-MC-IEF. We gratefully acknowledge discussing our results with Udo Buck.

[1] T. E. Gough, M. Mengel, P. A. Rowntree, and G. Scoles, J. Chem. Phys. **83**, 4958 (1985).
[2] M. Lewerenz, B. Schilling, and J. P. Toennies, J. Chem. Phys. **102**, 8191 (1995).
[3] M. Macler and Y. K. Bae, J. Chem. Phys. **106**, 5785 (1997).
[4] M. Lewerenz, B. Schilling, and J. P. Toennies, J. Chem. Phys. **106**, 5787 (1997).
[5] M. Hartmann, R. E. Miller, J. P. Toennies, and A. F. Vilesov, Phys. Rev. Lett. **75**, 1566 (1995).
[6] S. Grebenev, J. P. Toennies, and A. F. Vilesov, Science **279**, 2083 (1998).
[7] M. Behrens, R. Fröchtenicht, M. Hartmann, J. G. Siebers, and U. Buck, J. Chem. Phys. **111**, 2436 (1999).
[8] G. Scoles and K. K. Lahmann, Science **287**, 2429 (2000).
[9] J. P. Toennies and A. F. Vilesov, Angew. Chem., Int. Ed. **43**, 2622 (2004).
[10] M. Y. Choi, G. E. Douberly, T. M. Falconer, W. K. Lewis, C. M. Lindsay, J. M. Merritt, P. L. Stiles, and R. E. Miller, Int. Rev. Phys. Chem. **25**, 15 (2006).
[11] E. Lugovoj, J. P. Toennies, and A. F. Vilesov, J. Chem. Phys. **112**, 8217 (2000).
[12] M. Fárník and J. P. Toennies, J. Chem. Phys. **122**, 014307 (2005).
[13] J. M. Merritt, S. Rudić, and R. E. Miller, J. Chem. Phys. **124**, 084301 (2006).
[14] S. Denifl, F. Zappa, I. Mähr, F. Ferreira da Silva, A. Aleem, A. Mauracher, M. Probst, J. Urban, P. Mach, A. Bacher, O. Echt, T. D. Märk, and P. Scheier, Angew. Chem., Int. Ed. **121**, 9102 (2009).
[15] A. Gutberlet, G. Schwaab, O. Birer, M. Masia, A. Kaczmarek, H. Forbert, M. Havenith, and D. Marx, Science **324**, 1545 (2009).
[16] J. M. Mestdagh, M. A. Gaveau, C. Gée, O. Sublemontier, and J. P. Visticot, Int. Rev. Phys. Chem. **16**, 215 (1997).
[17] M.-A. Gaveau, E. Glogauen, P.-R. Fournier, and J.-M. Mestdagh, J. Phys. Chem. A **109**, 9494 (2005).
[18] M. Ehbrecht, M. Stemmler, and F. Huisken, Int. J. Mass. Spectrom. **123**, R1 (1993).
[19] U. Buck, J. Phys. Chem. A **106**, 10049 (2002).
[20] V. Poterya, M. Fárník, P. Slavíček, U. Buck, and V. V. Kresin, J. Chem. Phys. **126**, 071101 (2007).
[21] V. Poterya, O. Votava, M. Fárník, M. Ončák, P. Slavíček, U. Buck, and B. Friedrich, J. Chem. Phys. **128**, 104313 (2008).
[22] V. Poterya, J. Fedor, A. Pysanenko, O. Tkáč, J. Lengyel, M. Ončák, P. Slavíček, and M. Fárník, Phys. Chem. Chem. Phys. **13**, 2250 (2011).
[23] C. Nitsch, C. P. Schulz, A. Gerber, W. Zimmermann-Edling, and I. V. Hertel, Z. Phys. D: At., Mol. Clusters **22**, 651 (1992).
[24] M. Ahmed, C. J. Apps, C. Hughes, N. E. Watt, and J. C. Whitehead, J. Phys. Chem. A **101**, 1250 (1997).
[25] H. Haberland, *Clusters of Atoms and Molecules* (Springer, Berlin, 1994).
[26] U. Buck and H. Meyer, Phys. Rev. Lett. **52**, 109 (1984).
[27] U. Buck and H. Meyer, J. Chem. Phys. **84**, 4854 (1986).
[28] T. D. Märk, in *Linking the Gaseous and Condensed Phases of Matter*, edited by L. G. Christopherou (Plenum, New York, 1994), p. 155.
[29] J. Farges, M. F. de Feraudy, B. Raoult, and G. Torchet, Sur. Sci. **106**, 95 (1981).
[30] J. Farges, M. F. de Feraudy, B. Raoult, and G. Torchet, J. Chem. Phys. **78**, 5067 (1983).
[31] G. Torchet, P. Schwartz, J. Farges, M. F. de Feraudy, and B. Raoult, J. Chem. Phys. **79**, 6196 (1983).
[32] J. Farges, M. F. de Feraudy, B. Raoult, and G. Torchet, J. Chem. Phys. **84**, 3491 (1986).
[33] A. D. Martino, M. Benslimane, M. Châtelet, C. Crozes, F. Padère, and H. Vach, Z. Phys. D: At., Mol. Clusters **27**, 185 (1993).
[34] C. Bobbert, S. Schütte, C. Steinbach, and U. Buck, Eur. Phys. J. D **19**, 183 (2002).
[35] U. Buck and R. Krohne, J. Chem. Phys. **105**, 5408 (1996).
[36] J. Cuvellier, P. Meynadier, P. de Pujo, O. Sublemontier, J.-P. Visticot, J. Berlande, A. Lallement, and J.-M. Mestdagh, Z. Phys. D: At., Mol. Clusters **21**, 265 (1991).
[37] M. Macler and Y. K. Bae, J. Phys. Chem. A **101**, 145 (1997).
[38] O. F. Hagena, Surf. Sci. **106**, 101 (1981).
[39] O. F. Hagena, Z. Phys. D: At., Mol. Clusters **4**, 291 (1987).
[40] O. F. Hagena, Rev. Sci. Instrum. **63**, 2374 (1992).
[41] R. Baumfalk, N. H. Nahler, U. Buck, M. Y. Niv, and R. B. Gerber, J. Chem. Phys. **113**, 329 (2000).
[42] R. Baumfalk, U. Buck, C. Frischkorn, S. R. Gandhi, and C. Lauenstein, Ber. Bunsenges. Phys. Chem. **101**, 606 (1997).
[43] M. Fárník, *Molecular Dynamics in Free Clusters and Nanoparticles Studied in Molecular Beams* (ICT Prague Press, Institute of Chemical Technology Prague, 2011).
[44] The experiments were also performed with a small pickup cell of $L = 5$ cm length placed in the next vacuum chamber. Since the capture probability is proportional to L and the pickup gas pressure p, using the chamber with longer pickup path allowed to lower the pressure p resulting in a more precise pressure control and consequently better characterization of the pickup process. The results using the two different chambers were consistent within the experimental error.
[45] D. J. Auerbach, in *Atomic and Molecular Beam Methods*, edited by G. Scoles (Oxford University Press, New York, 1988), Vol. I, p. 362.
[46] H. Pauly, *Atom, Molecule and Cluster Beams* (Springer, Berlin, 2000).
[47] M. Fárník, N. H. Nahler, U. Buck, P. Slavíček, and P. Jungwirth, Chem. Phys. **315**, 161 (2005).
[48] N. H. Nahler, R. Baumfalk, U. Buck, H. Vach, P. Slavíček, and P. Jungwirth, Phys. Chem. Chem. Phys. **5**, 3394 (2003).

[49] P. Slavíček, P. Jungwirth, M. Lewerenz, N. H. Nahler, M. Fárník, and U. Buck, J. Chem. Phys. **120**, 4498 (2004).

[50] K. Berling, R. Belbing, K. Kramer, H. Pauly, C. Schlier, and P. Toschek, Z. Phys. **166**, 406 (1962).

[51] N. C. Lang, H. V. Lilenfeld, and J. L. Kinsey, J. Chem. Phys. **55**, 3114 (1971).

[52] U. Nagashima, H. Shinohara, N. Nishi, and H. Tanaka, J. Chem. Phys. **84**, 209 (1986).

[53] S. Morgan and A. W. Castleman, J. Phys. Chem. **93**, 4544 (1989).

[54] F. Huisken and M. Stemmler, Z. Phys. D: At., Mol. Clusters **24**, 277 (1992).

[55] U. Buck and M. Winter, Z. Phys. D: At., Mol. Clusters **31**, 291 (1994).

[56] R. A. Aziz and M. J. Slaman, Mol. Phys. **58**, 679 (1986).

[57] J. M. Hutson, J. Chem. Phys. **91**, 4455 (1989).

[58] K. Bolton, M. Svanberg, and J. B. C. Pettersson, J. Chem. Phys. **110**, 5380 (1999).

[59] P. U. Andersson, M. B. Någård, K. Bolton, M. Svanberg, and J. B. C. Pettersson, J. Phys. Chem. A **104**, 2681 (2000).

[60] D. J. Wales, J. P.K. Doye, A. Dullweber, M. P. Hodges, F. Y. Naumkin, F. Calvo, J. Hernández-Rojas, and T. F. Middleton, *The Cambridge Cluster Database*, available from http://www-wales.ch.cam.ac.uk/CCD.html.

[61] J. J. Hurly, Int. J. Thermophys. **21**, 805 (2000).

[62] K. Hansen and E. E.B. Cambell, Int. J. Mass. Spectrom. **233**, 215 (2004).

[63] We attempted to correct the data for the beam attenuation by using an exponential fit to observed decrease of the total pressure in the detector chamber. This results in somewhat larger evaluated cross sections, yet still not in agreement with the velocity measurements. Since only the small clusters can be deflected enough to escape the detection, the estimated error of the obtained cross sections due to this effect could be $\lesssim$10%.

THE JOURNAL OF CHEMICAL PHYSICS **137**, 034304 (2012)

Uptake of atmospheric molecules by ice nanoparticles: Pickup cross sections

J. Lengyel,[1,a)] J. Kočišek,[1,b)] V. Poterya,[1] A. Pysanenko,[1] P. Svrčková,[1,a)] M. Fárník,[1,c)] D. K. Zaouris,[2] and J. Fedor[3,c)]
[1] *J. Heyrovský Institute of Physical Chemistry v.v.i., Academy of Sciences of the Czech Republic, Dolejškova 3, 18223 Prague, Czech Republic*
[2] *School of Chemistry, University of Bristol, Bristol BS8 1TS, United Kingdom*
[3] *Department of Chemistry, University of Fribourg, Chemin du Musée 9, CH-1700 Fribourg, Switzerland*

(Received 21 May 2012; accepted 22 June 2012; published online 17 July 2012)

Uptake of several atmospheric molecules on free ice nanoparticles was investigated. Typical examples were chosen: water, methane, NO_x species (NO, NO_2), hydrogen halides (HCl, HBr), and volatile organic compounds (CH_3OH, CH_3CH_2OH). The cross sections for pickup of these molecules on ice nanoparticles $(H_2O)_N$ with the mean size of $\bar{N} \approx 260$ (diameter ~2.3 nm) were measured in a molecular beam experiment. These cross sections were determined from the cluster beam velocity decrease due to the momentum transfer during the pickup process. For water molecules molecular dynamics simulations were performed to learn the details of the pickup process. The experimental results for water are in good agreement with the simulations. The pickup cross sections of ice particles of several nanometers in diameter can be more than 3 times larger than the geometrical cross sections of these particles. This can have significant consequences in modelling of atmospheric ice nanoparticles, e.g., their growth. © *2012 American Institute of Physics*. [http://dx.doi.org/10.1063/1.4733987]

I. INTRODUCTION

Small ice nanoparticles and aerosols play an important role in physics and chemistry of Earth atmosphere.[1] Perhaps the most important example is the ozone hole above Antarctica: some of the key reactions which lead to the ozone depletion process proceed on ice particles in polar stratospheric clouds (PSCs) as proposed by Solomon *et al.* in 1980s.[2] The physics and chemistry of PSC particles has been investigated in great details ever since and covered by a number of articles and reviews, e.g., Refs. 3–5.

All these processes start with the formation and growth of the nanoparticles via homogeneous or heterogeneous nucleation and uptake of various molecules on the particles. In this study we focus on the uptake processes. The initial steps in the ice particle generation are the collisions of water monomers with small water clusters, which prevail under the conditions where there are many more monomers than clusters.[6] Therefore, we focus especially on the pickup of water molecules by the large water clusters. Besides, the pickup of some other typical atmospheric molecules is investigated. These include methane CH_4 as one of the most influential greenhouse gases; NO_x species represented by NO and NO_2; hydrogen halides HCl and HBr important in the ozone depletion process; and volatile organic compounds (VOCs) represented by methanol CH_3OH and ethanol CH_3CH_2OH.

The atmospheric pure ice nanoparticles and pickup processes can be mimicked in the laboratory with large $(H_2O)_N$ clusters in molecular beams. If the beam is passed through a chamber (pickup cell) filled with a particular gas, the molecules can collide with the nanoparticles and stick to the surface. The efficiency of this process is reflected by the *pickup cross section*. Recently, we have examined two methods for determining these cross sections with Ar_N cluster beams.[7] Our measurements were based on two approaches proposed for determination of the mean clusters size in molecular beams: (i) velocity decrease due to the pickup of molecules by the cluster;[8] (ii) Poisson distribution measurements.[9] We concluded that only the first method yielded the correct and reliable results.[7]

This method utilizes the fact that the mean cluster size $\bar{N}$ in supersonic expansions is known and can be controlled by the cluster source conditions.[10–13] We determine the cross section from variation of the beam velocity with the pickup pressure as outlined in Sec. II. Since the relation between $\bar{N}$ and the expansion conditions is well established also for water clusters,[14] the method can be extended also to these atmospherically important species.

In the present paper we determine experimentally the cross sections of the ice nanoparticles with the mean size $\bar{N} = 260$ for the atmospheric molecules mentioned above. For pickup of water molecules we have also performed molecular dynamics simulations, which allow a detailed insight into the molecular mechanism of the pickup process.

[a)] Also at Department of Physical Chemistry, Institute of Chemical Technology Prague, Technická 5, 16628 Prague 6, Czech Republic.
[b)] Also at Department of Surface and Plasma Science, Faculty of Mathematics and Physics, Charles University, V Holešovičkách, 18000 Prague, Czech Republic.
[c)] Authors to whom correspondence should be addressed. Electronic addresses: michal.farnik@jh-inst.cas.cz and juraj.fedor@unifr.ch.

0021-9606/2012/137(3)/034304/7/$30.00

II. EXPERIMENT

A. Experimental setup

The pickup experiment and cluster cross section measurements have been described in detail in our recent publication.[7] Therefore, only a brief account of the method will be given here.

The general and comprehensive description of our complex cluster beam apparatus can be found in Refs. 15 and 16. The water clusters were generated in the source chamber by supersonic expansion of a neat water vapor through a conical nozzle (diameter $d = 90$ μm, length 2 mm, and opening angle $\alpha = 30°$). The vapor pressure P_0 was determined by heating the reservoir filled with water to a constant temperature T_R. The nozzle was heated to somewhat higher temperature T_0 to prevent the water condensation. The size of the clusters was controlled by varying the source conditions and the resulting mean cluster sizes could be determined according to the empirical formulas:[14]

$$\bar{N} = D \cdot \left(\frac{\Gamma^*}{1000}\right)^a, \; \Gamma^* = \frac{\Gamma}{K_c} = \frac{n_0 \cdot d_e^q \cdot T_0^{q-3}}{K_c}, \tag{1}$$

where parameters $D = 11.6$, $a = 1.886$, and $q = 0.634$ were determined from fitting the measured size distributions of large $(H_2O)_N$ clusters.[14] The reduced scaling parameter Γ^* was introduced by Hagena[12] to classify various clustering conditions, and for water clusters this parameter and cluster size distributions were studied in Buck's group.[14] The characteristic constant of the expanding gas $K_c = (r_c \cdot T_c)^{q-3}$ for water was evaluated from $r_c = 3.19$ Å and $T_c = 5684$ K. The equivalent nozzle diameter $d_e = \frac{d}{\tan(\alpha/2)}$ was given by $d = 90$ μm and opening angle $\alpha = 30°$. The water vapor density in the source was calculated from the reservoir temperature T_R and pressure P_0 as $n_0 = \frac{P_0}{k_B T_0}$ (k_B is the Boltzmann constant). The stagnation pressure of $P_0 = 3.2$ bar and nozzle temperature $T_0 = 428$ K result in the mean cluster size $\bar{N} = 260$. The water cluster size distribution produced in the supersonic expansions has a log-normal character with a width $\Delta N \approx \bar{N}$ as determined in the previous experiments[14] with our present cluster source.

The cluster beam passed through a skimmer with 1 mm opening before entering the differentially pumped scattering chamber. This chamber served as a pickup cell filled with the gas to dope the clusters with various molecules. The effective capture length was $L = 170$ mm is limited on the other side by a 5 mm orifice to the next chamber. Thus the chamber length is well defined and a possible error of ±5% due to the gas streaming out of the orifices and pressure inhomogeneity was included in the evaluation of the cross section error bars.

The pressure in the chamber was monitored by Bayard-Alpert ionization gauge (Varian type 571). The background pressure in the pickup chamber was $\leq 1 \times 10^{-6}$ mbar, and the pressure with the pickup gas increased up to 6×10^{-4} mbar. The measured pressures for various gasses were divided by the correction factor suggested in the gauge instruction manual. Since the pickup pressure is a critical parameter for the cross section evaluation, great attention was paid to its measurement. The ionization gauge was also calibrated independently for the various gases by comparing the measured pressures to the values of a capacitance gauge pressure (Pfeiffer CMR 365) and the calibration values were found in good agreement with the values proposed in the instruction manual. The measurements for the various gases were performed repeatedly on different days to avoid any memory effects of the gauge. In each individual measurement, ample time was allowed for stabilization of each pressure step. The cross section measurements for all gases were tested for consistency against a test system (methanol) always before and after each day of measurement. The data for various gases were collected repeatedly over the time period of approximately half a year. The error bars on the measured cross sections include all the effects which appeared to influence the present data.

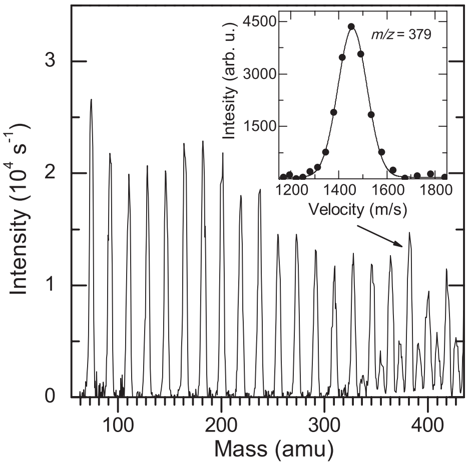

FIG. 1. Fragment ion mass spectrum of $(H_2O)_N$ $\bar{N} = 260$ clusters. The inset shows an example of the measured velocity distribution for the *m/z* = 379 amu mass peak with the Gaussian fit (line).

For the velocity measurements the cluster beam was modulated by a pseudorandom mechanical chopper[17] in the next differentially pumped chamber. The chopper contained two pseudorandom sequences of 127 elements and its rotation with frequency of 492.1 Hz corresponded to a single opening time window of 8 μs. After the chopper the beam passed the flight path of 955 mm through another differentially pumped chamber to the ion source of a quadrupole mass spectrometer with an electron ionizer and channeltron detector. The clusters were ionized with 70 eV electrons. Figure 1 shows an example of the measured fragment mass spectrum. The mass range of our quadrupole mass spectrometer was limited to cluster fragments $(H_2O)_kH^+$ with $k \leq 25$. However, Bobbert *et al.*[14] have demonstrated a significant water cluster fragmentation upon electron ionization in direct comparison with Na doping and subsequent photoionization which is essentially fragmentation-free method. Thus also the larger clusters from our size distribution contribute to the present mass peaks, and since the cluster velocity after supersonic expansion is almost independent of their size (within less than 10%), it can be measured on the small fragment mass peaks in the spectrum.

The arrival time to the detector was measured. The total flight time was properly corrected for the time spent by the ion fragment in the quadrupole and for any electronic delay of the trigger signals and converted to the beam velocity distribution. The velocity distribution was evaluated from the measured data by the cross-correlation mathematical method.[17] The beam velocity was measured for several water cluster fragments and the values were carefully checked for consistency. Typically the velocity dependence on pickup pressure was measured for at least two masses, e.g., on a strong fragment mass peak of $(H_2O)_kH^+$ $k = 10$ at $m/z = 181$ amu, and at the end of the measured fragment mass range for $k = 21$ at $m/z = 379$ amu. The maximum velocity of the water clusters (without any pickup gas) measured at the nozzle temperature $T_0 = 428$ K was $v_0 = 1450 \pm 10$ ms^{-1}, and the speed-ratio $S = 2\sqrt{ln(2)}\frac{v_0}{\Delta_{FWHM} v_0} \approx 17$. The inset in Fig. 1 shows an example of the measured TOF distribution at the $m/z = 379$ amu mass peak.

B. Pickup cross section

We have discussed the pickup cross-section determination in detail in our recent publication.[7] The method is based on the assumption that water clusters in the beam are slowed down by the pickup due to the momentum transfer, and the velocity change increases with the number of guest molecules. Let us assume cluster of a size N with an initial velocity v_i colliding with k stationary molecules in the pickup cell which stick to the cluster. Then the momentum conservation yields for the cluster final velocity v_f the equation:

$$N m_C \cdot v_i = (N m_C + k m_X) \cdot v_f, \tag{2}$$

where m_C is the cluster constituent mass (H_2O) and m_X is the mass of the picked-up species.

This formula has two important assumptions: (i) the collision is inelastic, i.e., molecule sticks to the cluster if a considerable momentum transfer between the molecule and the cluster occurs and (ii) no considerable evaporation of cluster occurs upon the pickup. Both assumptions are confirmed for H_2O pickup by molecular dynamics simulations outlined in Sec. IV. The previous investigations[7,8] showed that this simple model described the final velocity dependence very accurately for argon clusters.

The number of picked-up molecules along the path-length L in a gas at a pressure p (corresponding to the number density $n_g = \frac{p}{k_B T}$) can be expressed as

$$k = n_g \sigma_e L = \frac{p}{k_B T} \sigma_e L, \tag{3}$$

where σ_e is the pickup cross section. Combining Eqs. (2) and (3), the relative change in the cluster velocity is directly proportional to the pickup cell pressure

$$\frac{\Delta V}{V} \equiv \frac{v_i - v_f}{v_f} = \frac{m_X}{N m_C} \frac{L \sigma_e}{k_B T} \cdot p. \tag{4}$$

Thus, we plot the relative velocity change as a function of the pressure and fit a linear dependence $\frac{\Delta V}{V} = \alpha \cdot p$. From the slope α the pickup cross section σ_e can be evaluated as

$$\sigma_e = \alpha \cdot \frac{m_C N}{m_X} \cdot \frac{k_B T}{L}. \tag{5}$$

The quantity that is evaluated directly from the experimental data is the effective cross section

$$\sigma_e = \sigma_0 \cdot F_{a0}(\infty, x), \tag{6}$$

which incorporates the velocity-averaging correction factor F_{a0} due to the velocity distribution of the target molecules.[18–20] Label ∞ denotes the hard sphere potential approximation, and $x = \frac{v_i}{\alpha_g}$, where v_i is the cluster beam velocity and α_g is the most probable velocity in the Maxwellian distribution of the scattering gas. These correction factors were tabulated in the literature.[18,19]

III. EXPERIMENTAL RESULTS

Figure 2 shows examples of the measured relative velocity dependencies on the pickup gas pressure p for several molecules (H_2O, NO, NO_2) on $(H_2O)_N$ clusters $\bar{N} = 260$. Such dependencies were measured repeatedly on various days over a long time period to confirm the reproducibility of our data. The figure documents the high quality of the linear fit to the relative velocity change dependence on pickup pressure. A possible source of error in the pickup cross section determination can be the pressure correction factor used for various gases. Therefore, the ion gauge was also calibrated independently with the capacitance gauge, yet the later does not cover the entire measurement pressure range. Thus, the error bars on the pickup cross sections reflect not only the reproducibility of our data which was high, but rather the possible uncertainty in the pressure determination. It ought to be mentioned that the raw data not corrected by the pressure correction factor are shown in Fig. 2.

The measured cross sections are summarized in Fig. 3 and Table I. The geometrical cross section of the water clusters is indicated by the horizontal line. It was evaluated from the water molecule van der Waals radius $r_w = 1.6$ Å, i.e., the cluster volume corresponds to the volume of N spheres with r_w radius multiplied by a factor $\frac{\sqrt{18}}{\pi}$ accounting for the hexagonal close packing of the hard spheres. Thus, the geometrical cross section was calculated as

$$\sigma_g = \pi R_N^2, \quad R_N = r_w \cdot \left(\frac{\sqrt{18}}{\pi} \cdot N \right)^{1/3}, \tag{7}$$

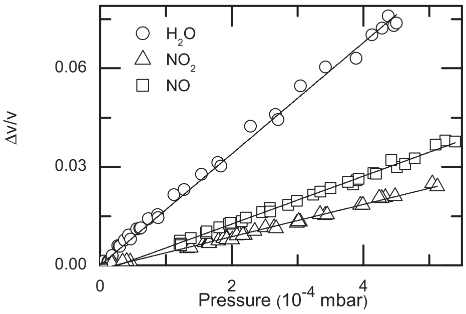

FIG. 2. The relative velocity dependence on the pickup gas pressure p for H_2O (circles), NO (squares), and NO_2 (triangles) molecules on $(H_2O)_N$ clusters $\bar{N} = 260$ with the linear fits (lines).

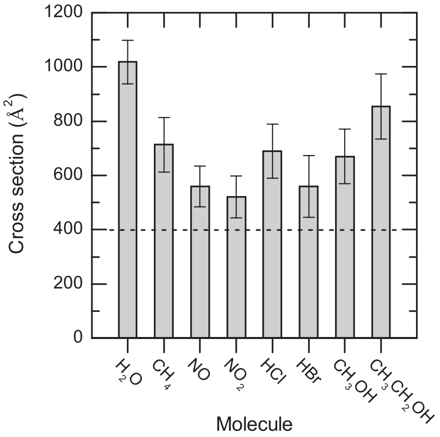

FIG. 3. The pickup cross sections for atmospheric molecules H_2O , CH_4, NO, NO_2, HCl, HBr, CH_3OH, and CH_3CH_2OH on $(H_2O)_N$ clusters $\bar{N}$ = 260. Horizontal line represents the geometrical cross section.

giving the geometrical cross section $\sigma_g \approx 400$ Å^2 for N = 260.

IV. THEORETICAL CROSS SECTIONS FOR WATER PICKUP

Of the presented experimental cross sections, we focus on the pickup of water molecules, because of its significance for build-up of the ice particles in the initial stages of nucleation. To provide support for the experimental findings, we have performed molecular dynamics (MD) simulations for the $(H_2O)_N$–H_2O collisions. Simulations provide a value of the cross section that can be compared with the experimental number. Furthermore, by repeating simulations for several cluster sizes, we are able to extend the experimental findings and formulate more general conclusions.

Simulations were done in the coordinate system where the $(H_2O)_N$ cluster is initially in rest and the H_2O molecule is shot at it with the velocity corresponding to experimental cluster beam velocity. In this section we thus call the picked-up molecule a projectile. Each cross section was determined from an ensemble of trajectories with varying impact parameters, where each trajectory was obtained from the MD simulation. The cross section was then evaluated from the maximum impact parameter that leads to the momentum transfer assumed in Eq. (2) used in evaluation of the experimental data. All simulations were done with our own (fortran) code.

The H_2O–H_2O interaction was described by the TIP3P model.[21] The model has positive charges on the hydrogens ($q_H = +0.417e$) and negative charge on oxygen ($q_O = -0.834e$). The potential between two water molecules is a sum of electrostatic Coulomb interaction between all intermolecular pairs and a single Lennard-Jones term between oxygen atoms. The water molecules were not considered rigid, the vibration of intramolecular bonds was treated within harmonic approximation with frequencies matching the experimental frequencies of the normal vibrational modes. This approach is rather unusual—the molecules within the water model are usually kept rigid. We have decided for the present model due to simpler implementation of the trajectory integrating code (no need for a constrain algorithm). Additionally, Zamith *et al.*[22,23] have recently shown that dynamical processes on a short time scale influence sticking properties of charged water clusters. Of course, the explicit treatment of the intramolecular motion brings the necessity of a short numerical time step. For integrating the trajectories, Verlet algorithm with the timestep of 0.2 fs was used. For the largest cluster simulated ($N = 520$) the algorithm conserved the total energy within 0.5% for the simulation length of 20 ps.

The initial cluster structure was obtained by starting with the $(H_2O)_{21}$ cluster with coordinates taken from Cambridge Cluster Database,[24] adding water molecules to this structure one by one and simultaneous cooling of the structure. The whole cluster was heated once more to 300 K and slowly cooled down to 90 K. This was repeated several times and different cluster structures were obtained. The cluster structure obtained this way is certainly not a global minimum of the potential energy surface. As was pointed out in a review by Buch *et al.*,[25] the search for a global energetic minimum in water clusters has plethora of difficulties, including a "rugged energy landscape," i.e., a multitude of local minima separated by high barriers. However, the quantity investigated here: the calculated pickup cross section is primarily influenced by the long-range interaction between water molecules, thus does not depend on the exact structural conformation of the cluster. This was confirmed by repeating the simulations for several cluster structures. The resulting values of cross section differed by less than 10% for different structures. Moreover, for all cluster sizes, the mean geometrical cross section of the obtained structures (as determined from the radial distribution function from the cluster's centre of mass) was in very good agreement with the approximative geometrical cross section, Eq. (7).

The simulation of one projectile trajectory proceeded as follows: first the cluster was equilibrated for 5 ps. The cluster temperature was assumed to be 90 K—this was chosen as a compromise between 70 and 100 K as estimated in Ref. 26 for a cluster source identical to ours. Then the cluster was randomly rotated and the H_2O projectile was shot at the cluster with a certain impact parameter and velocity of 1450 ms^{-1}, equal to velocity of cluster beam in the experiment. The whole system was simulated for 20 ps. After the simulation, it was

TABLE I. Cross sections for pickup of several molecules on $(H_2O)_N$, $\bar{N}$ = 260. The corresponding geometrical cross section is $\sigma_g \approx 400$ Å^2, and the simulated cross section for water molecules was $\sigma_s \approx 946$ Å^2.

Molecule	H_2O	CH_4	NO	NO_2	HCl	HBr	CH_3OH	CH_3CH_2OH
σ_e(Å^2)	1018 ± 80	713 ± 80	560 ± 75	520 ± 77	690 ± 100	560 ± 114	670 ± 100	855 ± 120

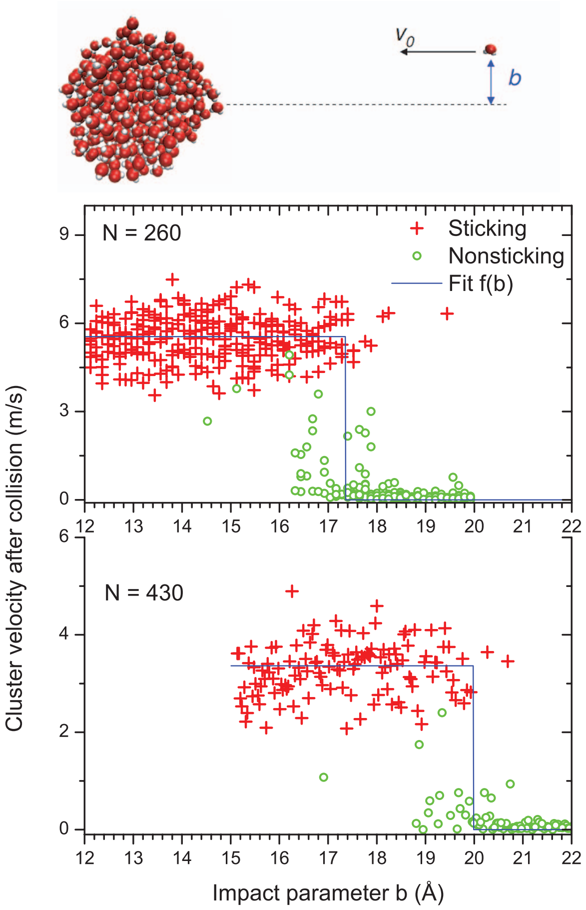

FIG. 4. (Top panel) The MD simulation geometry for one trajectory. (Graphs) The calculated cluster velocity after the collision as a function of the projectile impact parameter. The individual trajectories are categorized as sticking (crosses) or nonsticking (open circles). The line is a fit of the step function *f*(*b*) determining the maximum impact parameter b_{max}, Eq. (8).

determined whether the collision was sticking or nonsticking and the final cluster velocity was calculated.

In total 250 such trajectories were generated with impact parameter ranging from 12 to 22 Å. The results of simulations: the cluster velocity after the collision vs. the impact parameter of the projectile are plotted in Fig. 4. The momentum transfer follows the expected result: only the sticking trajectories lead to a considerable momentum transfer to the cluster. The data can be approximated by the function (line in Fig. 4)

$$f(b) = v_c\,[1 - \Theta(b - b_{max})]\,. \qquad (8)$$

Here v_c is the cluster velocity after collision according to momentum conservation, Eq (2). $\Theta(x)$ is the Heaviside step function. The maximum impact parameter b_{max} is determined from one-parameter fit of the function *f*(*b*) to the experimental data. The corresponding cross section is then

$$\sigma = \pi b_{max}^2. \qquad (9)$$

The calculated cross section for $N = 260$ is 946 Å^2 which is in good agreement with the experimental value of (1018 ± 80) Å^2 and it provides support for the experimental finding that the pickup cross section is significantly larger than just the geometric cross section of the cluster. Figure 4 confirms the basic assumption used in evaluating the experimental data [Eq. (2)]—only sticking collisions lead to considerable momentum transfer between the projectile and cluster.

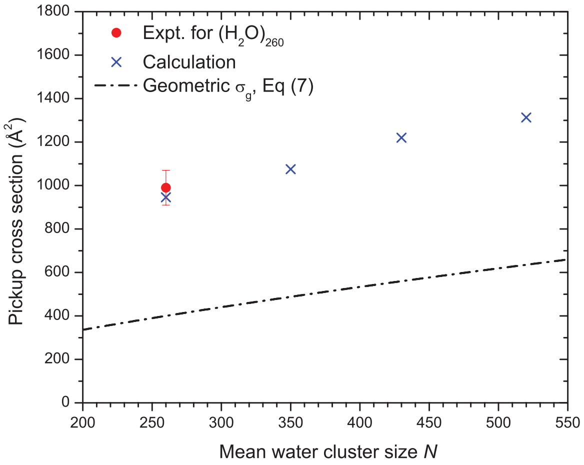

FIG. 5. Cross sections for the pickup of H_2O molecules on $(H_2O)_N$. The full circle is the experimental value for $\bar{N} = 260$, the crosses are calculated values for four different sizes of water cluster. The line indicates the corresponding geometrical cross sections calculated from van der Waals radius of H_2O, Eq. (7).

We have repeated the cross section calculation for several cluster sizes, $\bar{N} = 260, 350, 430, 520$, in order to observe the general trend. The calculated cross sections are summarized in Fig. 5.

V. DISCUSSION

The pickup cross sections measured for various molecules on $(H_2O)_N$, $\bar{N} \approx 260$ nanoparticles vary between 520 Å^2 for NO_2 and 1018 Å^2 for H_2O and are larger than the geometrical cross section of 400 Å^2. We have observed the variation of the pickup cross section for various molecules already previously for argon clusters.[7] The pickup cross section is determined by the strength and extent of the interaction potential between the picked-up molecule and the cluster constituents and also by the mass of the molecule and relative velocity. The later issue is discussed below.

The experimental cross section for the pickup of water molecules (1018 ± 80 Å^2) is within the experimental error in agreement with the value obtained from the molecular dynamics simulations (946 Å^2). The measured cross section is by factor of 2.5 larger than the simple geometrical cross section of the nanoparticle. The calculated cross sections for several cluster sizes shown in Fig. 5 suggest that this is a general trend—the calculated values are consistently higher by approximately factor of 2.2. The range of cluster sizes in the graph is not sufficient to see the $N^{2/3}$ dependence in full extent. The question arises, whether the actual pickup cross section will follow the size dependence of the geometrical cross section. The effect of long-range forces in the cluster-molecule collision has been theoretically investigated by Vasilev and

Reiss,[27,28] for water droplets and by Vigué *et al.*[29] for argon clusters. The later work has shown that the capture cross section for Ar_N clusters (which is also larger than the geometrical cross section) scales as $N^{2/3}$ for $N \gtrsim 10^3$. The cluster-molecule potential for water cluster–water molecule interaction is different than the VB potential used by Vigué *et al.* and Fig. 5 suggests, that for water clusters the $N^{2/3}$ scaling sets on already at the present size range.

An important point which should be discussed is the velocity dependence. The attractive potential between the particle and molecule will pull the slower molecule from a larger distance towards the cluster than the faster one. Thus the pickup cross section will increase with decreasing relative velocity. In the present experiment the cluster velocity is determined by the nozzle temperature which could not be changed significantly enough to observe any effect on the measured cross sections. The cluster velocity corresponds essentially to the relative velocity since it is significantly higher than the thermal velocity of the molecules. The temperature dependence can be estimated from Eq. (6): e.g., for water molecule $x = \frac{v_i}{\alpha_g} \approx 2.75$ giving $F_{a0} = 1.066$ (tabulated in Refs. 18 and 19) which yields $\sigma_0 = 955$ Å^2. At atmospheric conditions, i.e., in a thermal equilibrium, $v_i = \alpha_g$ giving $F_{a0} = 1.47$ and the corresponding effective cross section $\sigma_e \approx 1400$ Å^2. This value is larger than the geometrical cross section by factor of 3.5.

Our cross sections can be compared to the attachment cross section of water molecules on mass selected protonated water clusters.[22,23] The experimentally measured cross sections of Zamith *et al.*[22,23] for $N = 250$ are approximately 800 Å^2 (for 33 eV kinetic energy in the lab frame) which is close to our measured and simulated values. Nevertheless the authors report that their cross sections are smaller than the geometrical ones. The major reason for the discrepancy is the different geometrical cross sections reported in the work of Zamith *et al.* compared to our work. We calculate the geometrical cross section according to Eq. (7) considering the water molecule van der Waals radius of $r_w = 1.6$ Å. On the other hand Zamith *et al.* derive their geometrical cross section from the molecular radius of 2.25 Å, deduced from the density of bulk ice of about 2 Å. Our simulations suggest that the $(H_2O)_N$ cluster structure for $N = 260$ is far from hexagonal ice lattice structure at least at the temperatures of 90 K considered in our experiments. Besides, it has been also shown by other theoretical calculations[25] that the cluster structures do not correspond to the hexagonal ice lattice structure at least in the mid-size region investigated in our experiments. They assume rather the structure of amorphous solid water, and the cluster radius of 10–13 Å, can be estimated from Fig. 8 in Ref. 25 for the cluster consisting of 293 water molecules which is good agreement with our radius of 11.3 Å, for $N = 260$ obtained from our Eq. (7) using the van der Waals radius of 1.6 Å. In addition, our simulated cluster diameter (and subsequently its geometrical cross section 400 Å^2) is also in good agreement with Eq. (7) using the radius of 1.6 Å. This suggests that the geometrical cross section in the work of Zamith *et al.* is overestimated.

The effective integral collision cross sections of small water clusters $N = 4$–8 have also been measured by beam attenuation in various gasses to be ∼100–300 Å^2.[30] However, a direct comparison to the present data is difficult due to the different methods and different evaluated quantities.

The agreement of the measured cross section with the simulated one for water molecules and our previous investigations of Ar-cluster cross sections[7] both suggest high reliability of the present experimental method. The present water cluster cross sections for other molecules range from $\sigma_e \approx (520 \pm 77)$ Å^2 for NO_2 to (855 ± 120) Å^2 for ethanol. All the measured values are significantly larger than the geometrical cross sections, and can be expected to be even larger at the thermal equilibrium conditions in the atmosphere in analogy to the above discussion of water molecule pickup.

One possible effect which could lead to overestimation of the observed sticking cross section (essentially by factor of two) would be the head-on elastic collision. The performed MD simulations have not revealed any such events for water molecules where the cross section is the largest one. Besides our previous measurements and simulations of Ar cluster pickup cross sections[7] have not revealed such effect for Ar_n which are more rigid compared to the water clusters and the interactions of the molecules with them are much weaker. Despite that we have observed in the simulations mostly sticking collisions—no elastic scattering—and the cross sections were in good agreement with the experiment. Therefore, we conclude that the effects of elastic scattering cannot dominate in the present experiments.

VI. CONCLUSIONS

We have measured the pickup cross sections of ice nanoparticles for several typical atmospheric molecules in the laboratory experiment with molecular beams. For water molecules the pickup cross sections were also calculated in a molecular dynamics simulation of the pickup process. The agreement between the experimental and calculated cross section values underscores the reliability of our measurements, and the simulations provide detailed insight into the pickup process dynamics.

The measured pickup cross sections for all molecules starting from $\sigma_e(NO_2) \approx 520$ Å^2 are larger than the geometrical cross section $\sigma_g = 400$ Å^2. The largest measured cross section for water was 1018 ± 80 Å, by factor of 2.5 larger than the geometrical value. The values measured at the beam velocity of 1450 ms^{-1} can be extrapolated to the thermal equilibrium atmospheric conditions where the pickup cross sections will be even larger. In particular, for water the corresponding effective cross section will be ≈1400 Å^2, i.e., by factor of 3.5 larger than σ_g.

These findings can have consequences in modelling the formation and growth of atmospheric ice nanoparticles. Atmospheric nanoparticle formation consists of a complicated set of processes that include the production of nanometer-size clusters from gaseous vapors, the growth of these clusters to larger sizes, and their simultaneous removal by coagulation with the pre-existing particle population.[31] Considerable effort is devoted to the modelling of initial stages of the particle growth and cluster formation (e.g., Refs. 6 and 32). In these models, when considering the formation (or evaporation) of clusters, the geometrical cross section of the cluster is used in the expressions for the dynamical rate constants and the collision rates are taken to be hard sphere collision rates. The present data show that the more realistic cross sections should be used instead.

ACKNOWLEDGMENTS

This work has been supported by the Grant Agency of the Czech Republic Project Nos. 203/090422 and P208/110161 and by the Swiss National Science Foundation Project No. PZ00P2_1323571. J. Kočišek and D. Zaouris acknowledge the Grant No. 238671 "ICONIC" within FP7-MC-ITN and D.Z. also acknowledges the support of Professor N. M. R. Ashfold. We gratefully acknowledge discussing our results with Professor U. Buck.

[1] B. J. Finlayson-Pitts and J. J. N. Pitts, *Chemistry of the Upper and Lower Atmosphere* (Academic, San Diego, 2000).

[2] S. Solomon, R. R. Garcia, F. S. Rowland, and D. J. Wuebbles, Nature (London) **321**, 755 (1986).

[3] T. Peter, Ann. Rev. Phys. Chem. **48**, 785 (1997).

[4] A. J. Prenni and M. A. Tolbert, Acc. Chem. Res. **34**, 545 (2001).

[5] A. Bogdan, M. J. Molina, H. Tenhu, E. Mayer, and T. Loerting, Nat. Chem. **2**, 197 (2010).

[6] H. Vehkamäki, M. J. McGrath, T. Kurtén, J. Julin, K. E. J. Lehtinen, and M. Kulmala, J. Chem. Phys. **136**, 094107 (2012).

[7] J. Fedor, V. Poterya, A. Pysanenko, and M. Fárník, J. Chem. Phys. **135**, 104305 (2011).

[8] J. Cuvellier, P. Meynadier, P. de Pujo, O. Sublemontier, J.-P. Visticot, J. Berlande, A. Lallement, and J.-M. Mestdagh, Z. Phys. D **21**, 265 (1991).

[9] M. Macler and Y. K. Bae, J. Phys. Chem. A **101**, 145 (1997).

[10] O. F. Hagena, Surf. Sci. **106**, 101 (1981).

[11] O. F. Hagena, Z. Phys. D **4**, 291 (1987).

[12] O. F. Hagena, Rev. Sci. Instrum. **63**, 2374 (1992).

[13] U. Buck and R. Krohne, J. Chem. Phys. **105**, 5408 (1996).

[14] C. Bobbert, S. Schütte, C. Steinbach, and U. Buck, Eur. Phys. J. D **19**, 183 (2002).

[15] R. Baumfalk, U. Buck, C. Frischkorn, S. R. Gandhi, and C. Lauenstein, Ber. Bunsenges. Phys. Chem. **101**, 606 (1997).

[16] M. Fárník, *Molecular Dynamics in Free Clusters and Nanoparticles Studied in Molecular Beams* (ICT Press, Prague, 2011).

[17] D. J. Auerbach in *Atomic and Molecular Beam Methods*, edited by G. Scoles (Oxford University Press, New York, Oxford, 1988), Vol. I, p. 362.

[18] K. Berling, R. Belbing, K. Kramer, H. Pauly, C. Schlier, and P. Toschek, Z. Phys. **166**, 406 (1962).

[19] N. C. Lang, H. V. Lilenfeld, and J. L. Kinsey, J. Chem. Phys. **55**, 3114 (1971).

[20] H. Pauly, *Atom, Molecule and Cluster Beams* (Springer, Berlin, 2000).

[21] W. L. Jorgensen, J. Chandrasekhar, J. D. Madura, R. W. Impey, and M. L. Klein, J. Chem. Phys. **79**, 926 (1983).

[22] S. Zamith, P. Feiden, P. Labastie, and J.-M. L'Hermite, Phys. Rev. Lett. **104**, 103401 (2010).

[23] S. Zamith, P. Feiden, P. Labastie, and J.-M. L'Hermite, J. Chem. Phys. **133**, 154305 (2010).

[24] D. J. Wales, J. P. K. Doye, A. Dullweber, M. P. Hodges, F. Y. Naumkin, F. Calvo, J. Hernández-Rojas, and T. F. Middleton, The Cambridge Cluster Database, see http://www-wales.ch.cam.ac.uk/CCD.html.

[25] V. Buch, S. Bauerecker, J. P. Devlin, U. Buck, and J. K. Kazimirski, Int. Rev. Phys. Chem. **23**, 375 (2004).

[26] J. Brudermann, P. Lohbrandt, U. Buck, and V. Buch, J. Phys. Chem. **112**, 11038 (2000).

[27] O. V. Vasilev and H. Reiss, J. Chem. Phys. **105**, 2946 (1996).

[28] O. V. Vasilev and H. Reiss, Phys. Rev. E **54**, 3950 (1996).

[29] J. Vigué, P. Labastie, and F. Calvo, Eur. Phys. J. D **8**, 265 (2000).

[30] Z. Sternovsky, M. Horányi, and S. Robertson, Phys. Rev. A **64**, 023203 (2001).

[31] M. K. V.-M. Kerminen, Atmos. Res. **90**, 132 (2008).

[32] M. Kulmala, Atmos. Res. **98**, 201 (2010).

PRL **112,** 113401 (2014) PHYSICAL REVIEW LETTERS week ending 21 MARCH 2014

Irregular Shapes of Water Clusters Generated in Supersonic Expansions

J. Lengyel,* A. Pysanenko, V. Poterya, P. Slavíček,* and M. Fárník†
J. Heyrovský Institute of Physical Chemistry v.v.i., Academy of Sciences of the Czech Republic, Dolejškova 3, 18223 Prague, Czech Republic

J. Kočišek, and J. Fedor‡
Department of Chemistry, University of Fribourg, Chemin du Musée 9, CH-1700 Fribourg, Switzerland

(Received 10 October 2013; published 18 March 2014)

We report cross sections for pickup of guest molecules on neutral argon and water clusters with the mean sizes in the range from $\bar{N} = 50$ to 600. The experiments are supported by molecular dynamics simulations and analytical models based on the interaction potentials. The cross sections for argon clusters are consistent with their assumed spherical shape and follow approximately the theoretically justified $N^{1/3}$ dependence. On the other hand, the cross sections of water clusters depart from this dependence and are considerably larger starting from $\bar{N} \geq 300$. We interpret this increase of cross section by the occurrence of highly irregular shapes of water clusters produced in the supersonic expansion of water vapor under the conditions of the large cluster generation.

DOI: 10.1103/PhysRevLett.112.113401 PACS numbers: 36.40.Mr, 34.20.Gj, 36.40.Jn

Recent years have witnessed growing interest in the morphology of unsupported submicrometer systems. This interest, sparked to a large degree by technological advances in imaging techniques, led to characterization of aerosol particles [1], biological systems [2], or large rare-gas clusters [3]. In this Letter we focus on the morphology of clusters produced in supersonic expansion of water vapor.

Such clusters are widely used as a laboratory model system that mimics a variety of environments. For example, water clusters are often used to probe the transition of biologically relevant molecules from the gas phase to bulk. Another broad area of experiments involves atmospherically relevant systems where the clusters represent aerosols or atmospheric ice nanoparticles. The initial steps of such nanoparticle nucleation—successive pickup of water molecules on the initial cluster—can be probed in the laboratory by passing the neutral cluster beam [4,5] or mass selected water cluster ions [6,7] through a pickup chamber filled with water vapor. Such experiments deliver pickup cross sections which, apart from providing an understanding of the growth process, reflect also structural properties of the clusters themselves.

A lot of effort has been put into finding a global energy minima of small [8] and even large isolated water clusters [9]; however, little is known about the actual morphology of clusters produced in the expansions [10]. The spherical or close-to-spherical shapes are often assumed to occur *a priori* since they correspond to the lowest-energy arrangement [9]. This assumption represents a basis for analysis of many cluster experiments [6,11,12]. Here we report evidence that the water clusters with mean size $\bar{N} \geq 300$ considerably differ from such spherical or close-to-spherical structures. This conclusion is based on the measured anomalously large cross sections of such clusters which are not consistent with their spherical shape. To verify the experimental method and support the conclusions, we have also performed the pickup experiments for argon ($\mathrm{Ar}_N + \mathrm{Ar}$). In this case the measured cross sections of Ar clusters agree with the spherical model very well.

Experiment.—The experimental method has been described previously [4,5]. The clusters are generated by supersonic expansion of either argon gas or heated water vapor through a conical nozzle. The mean cluster size is controlled by the cluster source conditions (stagnation pressure, temperature, and geometrical nozzle parameters). It is determined using well-established empirical scaling formulas [13–16]. We point out that the applicability of the formulas has been demonstrated by Buck's group in Göttingen [13,14] with the same cluster sources that are used in the present experiments.

The skimmed cluster beam passes through a chamber filled with pickup gas. The gas pressure in the pickup chamber is controlled by two independent capacitance and ionization pressure gauges. The velocity distribution of the cluster beam is measured by modulating the beam with a pseudorandom mechanical chopper and measuring the time of flight into the detector. In the detector the clusters are ionized by electron impact, and fragment ions selected by the quadrupole analyzer are detected. The arrival time to the detector is measured and converted to the velocity distribution. Upon introducing the gas with molecular mass m_X at temperature T ($= 300$ K) and pressure p into the pickup chamber the clusters are slowed down due to momentum transfer. The relative decrease of their velocity $\Delta v/v = (m_X/Nm_C)(L\sigma/k_BT)p$, is directly proportional

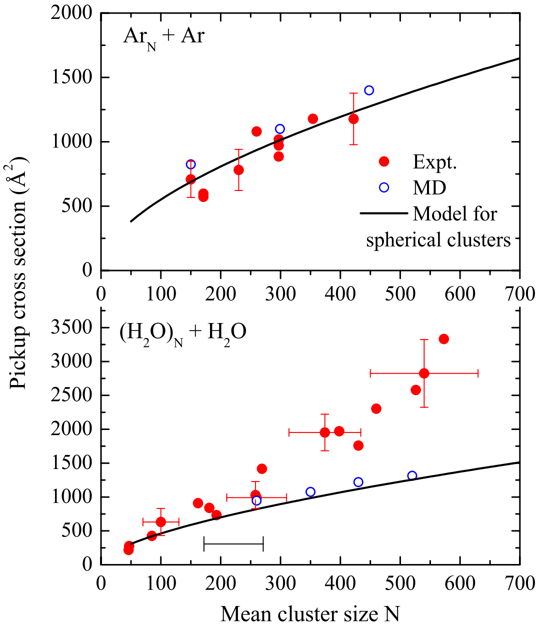

FIG. 1 (color online). Cross sections for pickup of argon atoms on argon clusters (top) and water molecules on water clusters (bottom) as a function of the mean cluster size.

to the pressure in the pickup cell (N is the cluster size and m_C its constituent mass) [4]. The pickup cross section is then evaluated from the slope of this dependence.

We have measured the cross sections for each cluster size repeatedly over an extensive period to avoid experimental artifacts. The vertical error bars in Fig. 1 include the spread of different measurements as well as the experimental uncertainties, e.g. in the pickup-cell pressure measurement (see Refs. [4,5]). The horizontal error bars placed on data points reflect the uncertainty in the mean cluster size determination—they were obtained in Ref. [13] and reflect the spread of $\bar{N}$ determined by various experiments. The black horizontal error bar reflects the spread of the cluster size distribution (FWHM) centered around size 219 [13].

This experimental approach substitutes the cluster size distribution by its mean value and, additionally, it contains two important assumptions: (i) that the clusters are slowed down only by sticking collisions and (ii) that no fragmentation or evaporation of clusters occurs upon the pickup event. For the present data—pickup of argon atoms on argon clusters and pickup of water molecules on water clusters—both assumptions were verified by molecular dynamics (MD) simulations. (i) The statistical weight of inelastic scattering collisions is much smaller than that of pickup events and (ii) the evaporation rate of clusters due to the released binding energy is negligible.

MD simulations.—The simulations provide independent cross sections for comparison. In the simulations we send the guest molecules toward the stationary cluster with velocities corresponding to the experiment and vary the impact parameter. The pickup cross section is obtained from an ensemble of trajectories by finding the mean impact parameter which leads to the momentum transfer assumed in the evaluation of the experimental data [5]. The interaction between argon atoms was described by using the Lennard-Jones (LJ) potential; the interaction between two water molecules was described by a TIP3P model [17], modified by explicitly including intramolecular motion. The initial structure of water clusters was obtained by adding individual H_2O molecules to a small cluster core with subsequent heating and cooling of the cluster. This procedure resulted in close-to-spherical structures with diameters in good agreement with previous simulations [18].

Spherical cluster model.—Another reference can be provided by an analytical model based on the average potential between a spherical cluster and the projectile. If the projectile interacts with the cluster constituents via LJ potential $V_1 = 4\varepsilon[(\sigma/r)^{12} - (\sigma/r)^6]$ then the interaction of a sphere of evenly distributed LJ centers with the projectile can be described by the Gspann-Vollmar potential [19,20]

$$V_N(r) = N4\varepsilon\sigma^{12}\frac{r^6 + \frac{21}{5}r^4r_0^2 + 3r^2r_0^4 + \frac{1}{3}r_0^6}{(r^2 - r_0^2)^9} - N\frac{4\varepsilon\sigma^6}{(r^2 - r_0^2)^3}. \qquad (1)$$

Here, $r_0 = r_w(N^{1/3} - 1)$, where r_w is the effective radius of the cluster constituent. The pickup cross section is then $\sigma = \pi b_{\mathrm{max}}^2$, where b_{max} is the maximal impact parameter which fulfills the condition that the kinetic energy of the projectile is smaller than the centrifugal barrier in the effective potential $V_N + (1/2)m_{\mathrm{red}}v_0^2(b^2/r^2)$. For argon clusters the validity of such an approach was thoroughly verified even at finite cluster temperatures by Vigue, Labastie, and Calvo [21]. The parameters used in the potential (1) are $\varepsilon = 143.2$ K, $\sigma = 3.34$ Å, and $r_w = 2.08$ Å [21].

For water, the anisotropic interaction of two molecules has a complicated functional form [22] but the use of the potential (1) can be advocated by the fact that the final constituent-projectile potential will result from Keesom-like averaging which has also $1/r^6$ long-range behavior. We have used LJ parameters obtained from H_2O-H_2O molecular beam scattering: [23] $\varepsilon = 390$ K, $\sigma = 2.75$ Å. For r_w in water clusters the literature reports values between 1.7 and 2.2 Å [7]. Here we use the value of $r_w = 2.2$ Å to demonstrate that even the largest r_w does not account for large measured cross sections. The resulting potential (1) agrees very well with projectile-cluster potential obtained from MD simulations. It should be noted that the use of the present potential has been previously suggested in theoretical work to describe growth of water droplets [24] or ammonia clusters [25].

Results and discussion.—The top panel of Fig. 1 shows the cross sections for pickup of an argon atom on argon clusters. Cross sections obtained from MD simulations and the spherical cluster model both agree very well with the experiment. It was pointed out by Vigue, Labastie, and Calvo [21] that the Gspann-Vollmar potential implies that the size scaling of the cross section is closer to $N^{1/3}$ than to $N^{2/3}$ expected from the simple geometrical scaling. The present results are the first direct experimental evidence of this fact.

The bottom panel of Fig. 1 shows that up to the mean water cluster size $\bar{N} \approx 300$ the experimental cross sections agree with both the MD simulations and the spherical cluster model. For the larger clusters the experimental cross sections are consistently higher than the theoretical ones, for the largest achievable mean cluster sizes the data exceed the calculated value by a factor of 2.2–2.5.

A number of remarks can be made to this finding with respect to its possible cause. Starting from cluster size of ≈ 280 the crystallization features are observable in the infrared spectra of water clusters [26]. The transition from an amorphous cluster structure to a crystalline one is accompanied by a slight increase of the geometrical size of the cluster due to the density decrease. However, even if all the molecules in the cluster undergo the transition to a crystalline arrangement (hexagonal ice), the corresponding increase of the cross section is $\approx 6\%$, much less than the presently observed increase. Thus the divergence of the data from the model cannot be inscribed to the change in the cluster density alone.

Another reason for the observed increase in the cross section could be an unspecified increase of long-range forces, e.g., if the large clusters were formed with an additional dipole moment. It has been suggested that such spontaneous dipole formation in cryogenic amorphous water ice grains enhances grain-grain adhesion which may increase the planet formation rate in protoplanetary nebulae [26]. However, we are not aware of a physical reason why clusters with such large net dipole moments should be formed in the expansion, or of any experimental evidence of such effect.

If a number of elastic head-on collisions for some reason increased with the cluster size, it would lead to a larger momentum transfer than assumed in the evaluation and corresponding increase of the evaluated cross section. Such attachment probability variation due to processes on a short time scale has been suggested by Zamith *et al.* [6] to influence the cross sections of protonated water clusters. However, our MD simulations revealed a negligible amount of such collisions (their eventual occurrence was the main reason for using a model with nonrigid intramolecular bonds). The present low center-of-mass collision energy ($\approx$0.2 eV) leads to long collision time, the excess energy is redistributed among the internal degrees of freedom and the collision is sticking. The lowest collision energy in the experiments of Zamith and co-workers was 6 eV.

Thus, the most probable reason for the disagreement of the experimental data with MD simulations and the spherical-cluster model is the actual morphology of clusters. Soler *et al.* [27] have shown that large clusters are formed by coagulation of smaller clusters rather than successive capture of monomers. Also, Buck *et al.* [13] observed the cluster size distributions with a bimodal character for large water clusters, and suggested that the large clusters are generated by coagulation of the smaller clusters. The resulting shape of the coagulated cluster depends on the internal energy of the colliding species. If they are sufficiently vibrationally hot the cluster will rearrange to close-to-spherical shape and the binding energy will be released by evaporation monomers. However, if the partners are vibrationally cold, they will merely stick together and the formed cluster will have a twin shape. A succession of such cold coagulation events may form aggregates with various morphology. Evidence for the cluster sticking collisions and generation of twin shapes has been provided recently [3].

In order to probe the influence of the cluster shape on the resulting cross section we have performed MD simulations with several irregular shapes of the $((H_2O)_{520}$ cluster shown in Fig. 2. The structures (b) "twinned," (c) "tripled," and (d) "sixtupled" were created by a slow collision of smaller equal-size clusters. The highly irregular structures (e) and (f) were created by a fast cooling of a diffuse arrangement of water molecules. For twinned and tripled clusters the cross sections increases only slightly—cluster orientations with large maximal pickup impact parameters are counterbalanced by orientations with small maximal pickup impact parameter. However, more irregular structures show a considerable increase of the cross section.

The experimental value corresponding to the mean water cluster size of 520 is $\approx$2400 Å^2. This suggests that the actual clusters have highly irregular shapes; from the shown structures only those in (e) and (f) show comparably high cross sections. Such structures are of course far from the

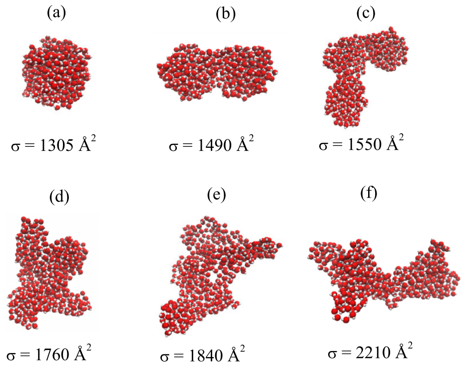

FIG. 2 (color online). Various structures of the$(H_2O)_{520}$ cluster and the corresponding cross sections evaluated from MD simulations.

optimal energy arrangement and, thus, the question of their stability arises. This depends on the cluster temperature: Brudermann *et al.* [28] determined the vibrational temperature to be in the range 69–101 K. At the temperature of 100 K, the present structure with the largest cross section (f) was stable in the whole time range of the MD simulations (1 ns).

One option to explain the high experimental value is a very high fraction of irregular structures such as shown in Figs. 2(e) or 2(f). An alternative explanation would be a smaller fraction of even more diffuse structures. The candidates for highly diffuse species could be fractal structures. The fast cooling in the expansion causes the onset of crystallization for cluster sizes larger than 280 molecules [26]. The crystallization could lead to a formation of *nanosnowflakes*. The generation of protosnowflakes in a supersonic flow has been proposed based on electron-diffraction experiments [29]. Those experiments probed clusters with sizes down to 24 nm (more than 10 000 molecules), the present finding concerns much smaller clusters.

Reference can be made to several recent works concerning nanoparticle morphology. Rupp *et al.* [3] have probed xenon clusters in supersonic expansion by single-shot free-electron-laser x-ray scattering and found that 10% to 30% of clusters had twin configuration [similar to Fig. 2(b)]. The authors do not directly report more complicated structures, but it should be noted that in their analysis twin structures were assumed *a priori*. Additionally, water due to the strong hydrogen bonds and its anisotropic nature probably forms more complicated structures than the rare gas xenon.

On the other hand, Wyslouzil and co-workers performed a series of experiments on supersonic expansion of water in Laval nozzles (e.g., Ref. [30]) and observed evidence of liquid droplet formation and subsequent liquid-solid nucleation, which leads to spherical clusters. However, their experiment differs considerably from the present one which uses conical nozzles more than 100 times smaller and with a much larger difference between stagnation pressure and pressure in the expansion chamber. The higher pressure gradient, together with the fact that our measured velocities (1400 ms^{-1}) are much higher than those of Wyslouzil *et al.* ($\sim$400 ms^{-1}), suggests a faster cooling rate in our experiments which leads to different clustering conditions. In this respect it might be useful to review the time scales of our experiment: the pickup events (i.e., the probing of the morphology) occur between 17 and 130 μs after the beam has left the nozzle throat. The simulations of cluster formation in water vapor expansion from a nozzle similar to ours [31] suggest that the cluster formation occurs in the first 100–300 μm behind the nozzle throat, which corresponds to nanoseconds. These simulations were performed for conditions of small cluster generation ($\bar{N} = 7$–10), the present much higher stagnation pressures suggest even faster cooling and cluster formation.

A useful comparison can also be made with the mobility measurements of large aerosol particles of controlled morphology [32], which found the dynamic shape factor (DSF) of compact agglomerates to be 1.3 to 1.4. DSF reflects the increased drag on a particle due to nonspherical shape and is approximately proportional to the particle diameter [33]. Our cross sections are proportional to square of particle diameter, i.e., the square of the corresponding DSF. The cross section increase by a factor of 2–2.5 compared to the spherical cluster model agrees nicely with the second power of the aerosol DSF ($\approx 1.4^2$).

Conclusions.—The cross sections for argon clusters are consistent with MD simulations and the analytical model that assumes their close-to-spherical shape. The cross sections for water clusters are considerably larger starting from $\bar{N} \approx 300$. Such high cross sections can be explained by production of highly irregular cluster shapes in the supersonic expansion of water vapor. One option for the morphology of these clusters are nanometer-sized protosnowflakes. This hypothesis can be directly confirmed by imaging experiments with a single-particle resolution. This surprising finding should be taken into account in a range of experiments: there are numerous studies [6,11,12] and whole experimental approaches [34,35] that are based on spherical or regular shapes of clusters. Also, the present findings may open new possibilities in cluster science. For instance, in addition to well-studied size-dependent phenomena, new shape-dependent effects may emerge, e.g., connected to the larger surface-to-volume ratio of the irregular structures.

This work has been supported by the SNSF Project No. PZ00P2_132357/1, the SCIEX program and the GACR Projects No. P208/11/0161 and 14-08937S. The authors thank M. Lattuada, Fribourg, and J. Kolafa, Prague, for fruitful discussions.

---

[*] Also at Department of Physical Chemistry, Institute of Chemical Technology, Technická 5, 16628 Prague, Czech Republic.

[†] michal.farnik@jh-inst.cas.cz

[‡] juraj.fedor@unifr.ch

[1] N. D. Loh *et al.*, Nature (London) **486**, 513 (2012).
[2] M. M. Siebert *et al.*, Nature (London) **470**, 78 (2011).
[3] D. Rupp *et al.*, New J. Phys. **14**, 055016 (2012).
[4] J. Fedor, V. Poterya, A. Pysanenko, and M. Fárník, J. Chem. Phys. **135**, 104305 (2011).
[5] J. Lengyel, J. Kočišek, V. Poterya, A. Pysanenko, P. Svrčková, M. Fárník, D. K. Zaouris, and J. Fedor, J. Chem. Phys. **137**, 034304 (2012).
[6] S. Zamith, P. Feiden, P. Labastie, and J.-M. L'Hermite, Phys. Rev. Lett. **104**, 103401 (2010).
[7] S. Zamith, G. de Tournadre, P. Labastie, and J. M. L'Hermite, J. Chem. Phys. **138**, 034301 (2013).
[8] J. Brudermann, U. Buck, and V. Buch, J. Phys. Chem. A **106**, 453 (2002).

[9] V. Buch, S. Bauerecker, J. P. Devlin, U. Buck, and J. K. Kazimirski, Int. Rev. Phys. Chem. **23**, 375 (2004).

[10] C. C. Pradzynski, R. M. Forck, T. Zeuch, P. Slavíček, and U. Buck, Science **337**, 1529 (2012).

[11] J. V. Coe, Int. Rev. Phys. Chem. **20**, 33 (2001).

[12] A. E. K. Sunden, S. Stochkel, S. Panja, U. Kadhane, P. Hvelplund, S. B. Nielsen, H. Zettergren, B. Dynefors, and K. Hansen, J. Chem. Phys. **130**, 224308 (2009).

[13] C. Bobbert, S. Schütte, C. Steinbach, and U. Buck, Eur. Phys. J. D **19**, 183 (2002).

[14] U. Buck and R. Krohne, J. Chem. Phys. **105**, 5408 (1996).

[15] O. F. Hagena, Surf. Sci. **106**, 101 (1981).

[16] O. F. Hagena, Z. Phys. D **4**, 291 (1987).

[17] W. L. Jorgensen, J. Chandrasekhar, J. D. Madura, R. W. Impey, and M. L. Klein, J. Chem. Phys. **79**, 926 (1983).

[18] V. Buch, S. Bauerecker, J. P. Devlin, U. Buck, and J. K. Kazimirski, Int. Rev. Phys. Chem. **23**, 375 (2004).

[19] J. Gspann and H. Vollmar, in *Rarefield Gas Dynamics*, edited by R. Campargue (CEA, Paris, 1979), p. 1193.

[20] Considering only the attractive part of the potential yielded basically the same cross sections which confirms that the determining factors are the long-range forces.

[21] J. Vigué, P. Labastie, and F. Calvo, Eur. Phys. J. D **8**, 265 (2000).

[22] R. Bukowski, K. Szalewski, G. C. Groenenboom, and A. van der Avoird, J. Chem. Phys. **128**, 094313 (2008).

[23] R. W. Bickes, G. Duquette, C. J. N. van den Meijdenberg, A. M. Rulis, G. Scoles, and K. M. Smith, J. Phys. B **8**, 3034 (1975).

[24] O. V. Vasilev and H. Reiss, J. Chem. Phys. **105**, 2946 (1996).

[25] Y. Okada, S. Yamaguchi, and K. Takeuchi, J. Aerosol Res. **18**, 47 (2003).

[26] H. Wang, R. C. Bell, M. J. Iedema, A. A. Tsekouras, and J. P. Cowin, Astrophys. J. **620**, 1027 (2005).

[27] J. M. Soler, N. García, O. Echt, K. Sattler, and E. Recknagel, Phys. Rev. Lett. **49**, 1857 (1982).

[28] J. Brudermann, P. Lohbrandt, U. Buck, and V. Buch, J. Chem. Phys. **112**, 11038 (2000).

[29] L. S. Bartell and P. J. Lennon, J. Chem. Phys. **130**, 084303 (2009).

[30] A. Manka, H. Pathak, S. Tanimura, J. Wölk, R. Strey, and B. E. Wyslouzil, Phys. Chem. Chem. Phys. **14**, 4505 (2012).

[31] R. Jansen, I. Wysong, S. Gimelshein, M. Zeifman, and U. Buck, J. Chem. Phys. **132**, 244105 (2010).

[32] A. Zelenyuk, Y. Cai, and D. Imre, Aerosol Sci. Technol. **40**, 197 (2006).

[33] P. F. DeCarlo, J. G. Slowik, D. R. Worsnop, P. Davidovits, and J. J. Jimenez, Aerosol Sci. Technol. **38**, 1185 (2004).

[34] M. Macler and Y. K. Bae, J. Phys. Chem. A **101**, 145 (1997).

[35] J. Cuvellier, P. Meynadier, P. de Pujo, O. Sublemontier, J.-P. Visticot, J. Berlande, A. Lallement, and J.-M. Mestdagh, Z. Phys. D **21**, 265 (1991).

THE JOURNAL OF PHYSICAL CHEMISTRY A
Article
pubs.acs.org/JPCA

Lack of Aggregation of Molecules on Ice Nanoparticles

Andriy Pysanenko,[†] Alena Habartová,*[,‡] Pavla Svrčková,[†,§] Jozef Lengyel,[†,§] Viktoriya Poterya,[†] Martina Roeselová,[‡] Juraj Fedor,*[,†] and Michal Fárník*[,†]

[†]J. Heyrovský Institute of Physical Chemistry v.v.i., Czech Academy of Sciences, Dolejškova 3, 18223 Prague 8, Czech Republic
[‡]Institute of Organic Chemistry and Biochemistry v.v.i., Czech Academy of Sciences, Flemingovo nám. 2, 16610 Prague 6, Czech Republic

Supporting Information

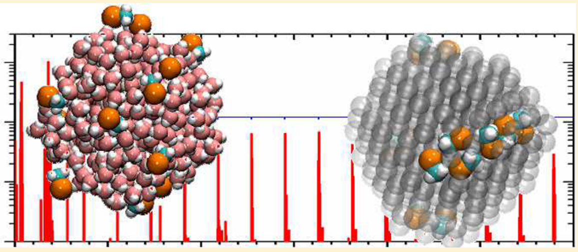

ABSTRACT: Multiple molecules adsorbed on the surface of nanosized ice particles can either remain isolated or form aggregates, depending on their mobility. Such (non)-aggregation may subsequently drive the outcome of chemical reactions that play an important role in atmospheric chemistry or astrochemistry. We present a molecular beam experiment in which the controlled number of guest molecules is deposited on the water and argon nanoparticles in a pickup chamber and their aggregation is studied mass spectrometrically. The studied molecules (HCl, CH_3Cl, $CH_3CH_2CH_2Cl$, C_6H_5Cl, CH_4, and C_6H_6) form large aggregates on argon nanoparticles. On the other hand, no aggregation is observed on ice nanoparticles. Molecular simulations confirm the experimental results; they reveal a high degree of aggregation on the argon nanoparticles and show that the molecules remain mostly isolated on the water ice surface. This finding will influence the efficiency of ice grain-mediated synthesis (e.g., in outer space) and is also important for the cluster science community because it shows some limitations of pickup experiments on water clusters.

INTRODUCTION

Heterogeneous chemistry of molecules adsorbed on ice particles with nano- to micrometer dimensions plays a central role in several environments. An obvious example is photochemistry of halogenated species on polar stratospheric clouds and other ice particles in the atmosphere, where the presence of such nanoparticles triggers globally important chemical changes (ozone hole).[1] Also, it is believed that in outer space, where molecular density is very low, molecular ice particles (water ice in particular) represent "sponges" where guest molecules are adsorbed and meet other molecules yielding reactions, often assisted by high-energy radiation.[2,3]

One factor that will strongly influence both the photochemistry and ice-assisted synthesis is whether molecules remain isolated on the particle surface or form aggregates prior to the triggering radiation event. It can result in a dramatically different outcome of the subsequent reaction. The examples include the change in photochemistry of HCl in complexes when compared to that of monomers,[4] or cosmic-ray-induced glycine synthesis from simpler molecules on extraterrestrial ices.[3] The aggregation will be influenced by the molecules' mobility and migration upon their uptake on the particle. Surprisingly, few data about the molecular mobility on ice surfaces exists even for bulk ices.[5,6]

In laboratory experiments, the environments mentioned above are often mimicked by large water clusters (ice nanoparticles) with guest molecules adsorbed on their surface. The pickup technique that is used to adsorb the guest molecules on the clusters was introduced in 1980s by Gough et al.[7] A subsequent aggregation of adsorbed/embedded molecules has been exploited extensively for large superfluid helium nanodroplets[8−14] and to limited extent for argon nanoparticles.[4,15−19] We are not aware of any study addressing the question of aggregation on the surface of ice nanoparticles.

In this paper, we examine the aggregation of guest molecules on ice nanoparticles [water clusters $(H_2O)_N$, where $\bar{N} = 10^2$–10^3]. These particles have diameters in a nanometer range and possess low temperatures; as discussed in Computational Methods, we assume a temperature of ≈100 K. We successively dope the nanoparticles with a controlled number of guest molecules by pickup[20−22] and probe them mass spectrometrically. Surprisingly, no aggregation of guest molecules is observed. To examine the reliability of our technique and to provide a chemically inert reference, we perform analogous experiments with Ar_N clusters. In this case, strong aggregation of guest molecules is observed, in spite of the lower particle temperature of ≈37 K.[23] The experimental results are confirmed by molecular dynamics (MD) simulations. As the guest molecules, we study mainly Cl-containing species because of their atmospheric relevance. To probe different types of bonding, we proceed from diatomic HCl to chloroalkanes with various chain lengths (CH_3Cl and $CH_3CH_2CH_2Cl$) and to

Received: June 5, 2015
Revised: July 19, 2015
Published: July 27, 2015

DOI: 10.1021/acs.jpca.5b05368
J. Phys. Chem. A 2015, 119, 8991−8999

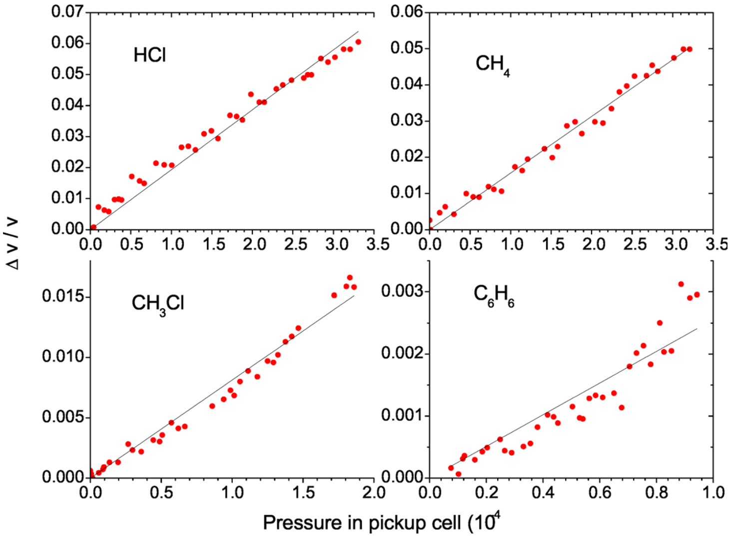

Figure 1. Dependence of the relative velocity decrease of the beam $\Delta v/v$ on pressure. Pickup on $(H_2O)_N$, $\bar{N} \approx 430$.

Table 1. Maximal Aggregate Fragment Sizes Observed in the Mass Spectra ($m_{\max}$), Mean Numbers of Adsorbed Molecules (m_p) at Pressure p, and Maximal Aggregate Sizes from MD Simulations (m_{cal})[a]

		Ar_N			$(H_2O)_N$		
	p ($\times 10^{-4}$ mbar)	m_p	$m_{\max}$	m_{cal}	m_p	$m_{\max}$	m_{cal}
HCl	3.0	17(3)	11(2)	8(3)	17(5)	1	1
CH_4	3.3	22(2)	3(1)	2(1)	18(4)*	1	1
CH_3Cl	1.7	10(3)	7(2)	5(1)	4(2)	1	2(1)
C_3H_7Cl	0.9	7(1)	7(2)	4(1)	3(1)	1	3(1)
C_6H_6	0.9	4(2)**	9(1)	5(1)	1(1)**	1	2(1)
C_6H_5Cl	0.7	3(2)**	7(1)	5(1)	1(1)**	1	2(1)

[a] The numbers in parentheses correspond to standard deviations. The m_p value for methane on ice nanoparticles (one asterisk) is judged to be overestimated, and for benzene and chlorobenzene (two asterisks), both argon and ice have lower confidence levels (see the text).

aromatic compound C_6H_5Cl that can bind via π interactions. For comparison, nonpolar CH_4 and C_6H_6 molecules are also considered.

■ EXPERIMENTAL METHODS

The experiments were performed on the CLUster Beam apparatus (CLUB), which is a versatile molecular beam setup allowing for a range of experiments, including photochemistry, mass spectrometry, and pickup experiments with clusters and nanoparticles.[18,19,22,24] The Ar_N and $(H_2O)_N$ nanoparticles are generated in continuous supersonic expansion of Ar and water vapor, respectively, through a conical nozzle into the vacuum. The mean cluster size is controlled by the source conditions (stagnation pressure, temperature, and geometrical nozzle parameters). The present mean sizes are $\bar{N} \approx 330$ and 430 for Ar_N and $(H_2O)_N$, respectively. They correspond approximately to the same geometrical cross section of nanoparticles ($\sigma_g \approx 660$ Å^2), estimated assuming a spherical particle shape and density of the corresponding solid. The mean cluster size determination and calculation of geometrical cross section are described in the Supporting Information. The cluster beam is skimmed and passes through a differentially pumped chamber where the guest molecules are introduced.

In the first type of measurement, we determine the amount of picked up guest molecules from deceleration of the beam after it passes the pickup chamber. For this purpose, the beam velocity is determined by modulating the beam with a pseudorandom mechanical chopper and measuring its time of flight. The chopper is located in the next differentially pumped chamber after the pickup chamber, and the flight time is measured on a subsequent 151 cm path into a detector. There the clusters are ionized by 70 eV electrons, and ions selected by quadrupole analyzer are detected. The arrival time to the detector is measured and converted to the velocity distribution. Assuming that the cluster with the mass $\bar{N}M_C$ is slowed by picking up m_p guest molecules, the relative change of the cluster velocity is

$$\frac{\Delta v}{v} = \frac{M_M}{\bar{N}M_C} m_p \tag{1}$$

where M_M and M_C are masses of the guest molecule and cluster constituent, respectively. Despite the simplified assumptions (sticking collisions), this formula has been proven to deliver reliable results confirmed by molecular dynamics simulations of the pickup process for several species previously.[20−22] m_p is linearly dependent on the pickup cell pressure p, and consequently, $\Delta v/v = \alpha p$. Figure 1 shows typical pressure dependences of the relative deceleration $\Delta v/v$. The linear dependence was verified for each guest molecule, and m_p during subsequent mass spectrometry measurement (performed at a fixed p) was determined from measured slope α.

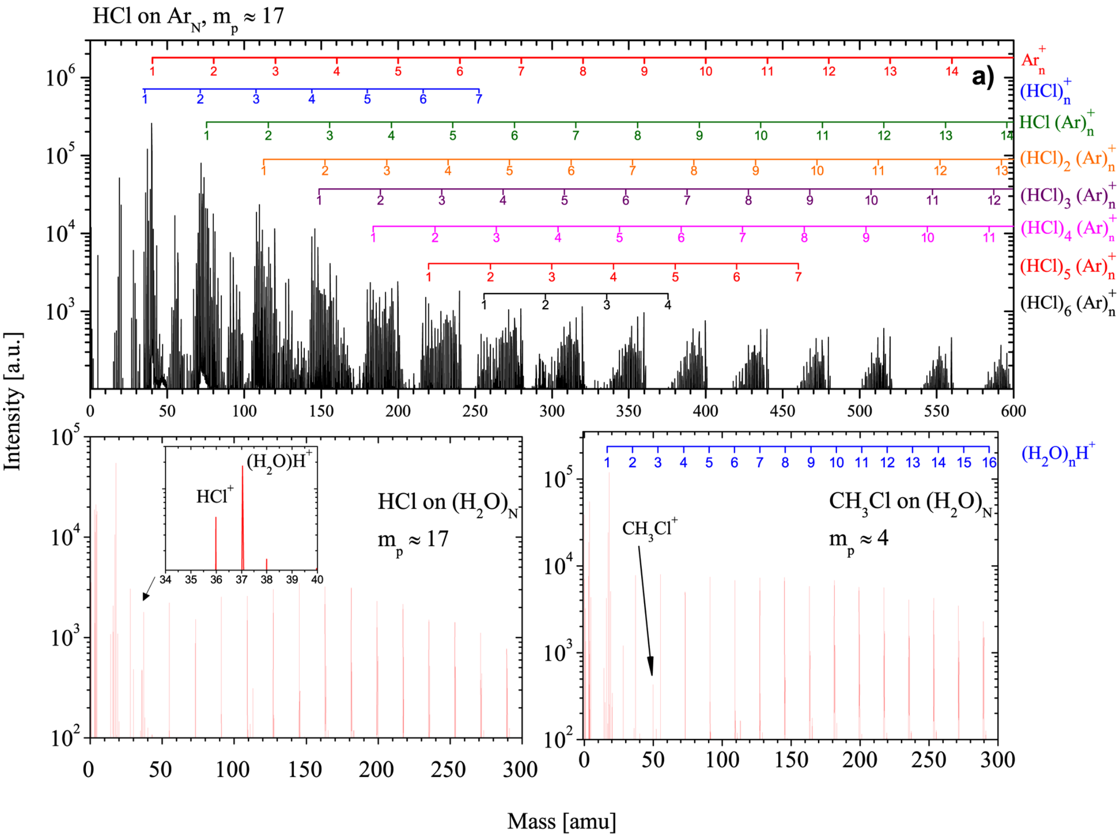

Figure 2. Representative time-of-flight mass spectra. The top panel shows HCl molecules adsorbed on argon nanoparticles with $\bar{N}$ ≈ 330. The bottom panels show HCl and CH_3Cl molecules adsorbed on water ice nanoparticles with $\bar{N}$ ≈ 430.

Pressure p was monitored with a Bayard-Alpert ionization gauge (Varian type 571). The measured pressures for various gases were divided by the correction factor listed in the gauge instruction manual. Because this is a crucial factor for m_p determination, we have calibrated the ionization gauge independently with a capacitance manometer (Pfeiffer CMR 365) and the absolute pressures were found to be in very good agreement with the corrected pressures based on the ionization gauge manual. The uncorrected pressure limit of the ionization gauge is 5×10^{-4} mbar, which for benzene and chlorobenzene leads to very low calibrated pressures (shown in Table 1) where the determination of α (and consequently of m_p) is subject to a relatively large error.

In the second type of measurement, the beam is not chopped, and we measure the mass spectra of the doped nanoparticles in another differentially pumped chamber with a high-resolution reflectron time-of-flight mass spectrometer (RTOF).[25−27] The RTOF is mounted orthogonally to the molecular beam. The clusters are ionized by 70 eV electrons at a 10 kHz repetition frequency, and the mass spectra are recorded with a resolution of $M/\Delta M \approx 5 \times 10^3$. In the perpendicular arrangement, attention must be paid to the mass discrimination because of the different cluster energies along the beam direction. The transmission of the spectrometer was checked with perfluorotributylamine (FC-43) and known spectra of large Ar$_N$ clusters so that no discrimination occurs in the mass range up to ~10^3 amu.

COMPUTATIONAL METHODS

To provide further insight, we simulated motion of several guest molecules on both types of nanoparticles. Spherical nanoparticles consisting of 300 Ar atoms or H_2O molecules were carved out from a previously simulated liquid argon ($T \approx$ 100 K)/liquid water ($T \approx$ 300 K) system. Each nanoparticle was then placed in the center of a cubic simulation cell with an edge size of 80 Å (the diameters of the argon and water nanoparticles were ~30 Å). To equilibrate the nanoparticles to the known target temperature of 37 K (for argon)[23] and 100 K (for water),[28,29] 50 ns isochoric−isothermal (NVT) simulations were performed. The temperatures correspond to the experimental conditions. For argon nanoparticles created in supersonic expansion, the commonly accepted value is 37 K as measured by electron diffraction.[23] For water nanoparticles, a range of temperatures has been put forward: 180 ± 20 K was reported by electron diffraction experiment for N < 200,[30] temperatures between 50 and 100 K were estimated in a recent perspective,[29] and vibrational spectroscopy of size-selected nanoparticles with 200−500 molecules reported temperatures of 90−115 K.[31] We therefore assume a nanoparticle temperature of ≈100 K.

Subsequently, 12 identical molecules from the list of studied pickup species were added to the simulation cell. The molecules were initially evenly (pseudorandomly) distributed around the argon/amorphous ice nanoparticle several angstroms from the surface. The entire system was again shortly equilibrated (≈10 ps) at the respective experimental temperature. During that period, most of the molecules landed on the surface, and the resulting configurations of the argon/amorphous ice nanoparticle with 12 adsorbed molecules were used as initial conditions for the subsequent production runs. The systems were propagated for 50 ns in the *NVT* simulation at the experimental temperatures given above to sample structural characteristics. Periodic boundary conditions were applied in all three dimensions. For each combination of the argon nanoparticle and the pickup species, five different initial configurations of molecules around the argon nanoparticle were created and the simulations were propagated independently. Close contacts of picked up molecules were considered as an aggregate (cluster) when no molecule of argon/H_2O was found between them.

Interaction Potentials. Water molecules were described using the TIP4P/2005 model,[32] while for argon, the OPLS parameters[33] were used. Topologies for the pickup molecules were obtained from the Automated Topology Builder,[34] and the general Amber force field (GAFF) parameter set[35] was employed to describe their interactions. Chemical bonds were kept intact during the simulations, including that in HCl (i.e., no acidic dissociation of molecular HCl on the clusters was considered, which will be discussed below). The atomic partial charges were calculated by the RESP method.[36] For CH_3Cl and C_6H_6, these charges were enhanced by factors of 1.7[37] and 1.24,[38] respectively. Further details of the theoretical simulations and the atomic partial charges and topologies of studied molecular species are attached as itp files in the Supporting Information.

■ RESULTS

Mass Spectra of Doped Nanoparticles. *Pickup on Ice Nanoparticles.* Bottom panels in Figure 2 show example mass spectra following the pickup of HCl and CH_3Cl on H_2O nanoparticles. Further spectra for all studied molecules are presented in the Supporting Information. The peak progression corresponds to protonated water cluster ions $(H_2O)_NH^+$. No ions corresponding to aggregates of guest molecules (either pure or mixed water−guest aggregates) were observed; only the monomer ions and their fragments are present in the spectra.

We are certain that these peaks originate from species deposited on the nanoparticles as the background signals measured with the blocked beam were carefully subtracted. The presence of molecules on ice nanoparticles was confirmed in some cases by our previous photodissociation studies[19,39,40] where features corresponding to nanoparticle−guest interactions (acidic dissociation) clearly dominate the spectra. Further evidence comes from the measured velocities shown in Figure 1. The increasing relative deceleration $\Delta v/v$ with pressure shows that the clusters are slowed by a momentum transfer from multiple guest molecules. Additionally, in a similar experiment, Ahmed and co-workers[41−43] reported sticking of a number of similar organic molecules on the surface of water clusters.

Pickup on Argon Nanoparticles. Mass spectra following pickup of guest molecules on argon nanoparticles are shown in the top panel of Figure 2 for HCl and in Figure 3 for CH_4, CH_3Cl, and $CH_3CH_2CH_2Cl$. Because of overlap of multiple spectra, a detailed analysis based on isotope ratios was required to assign all the mass peaks unambiguously. This analysis, as well as the mass spectra corresponding to the pickup of other guest molecules, is shown in the Supporting Information.

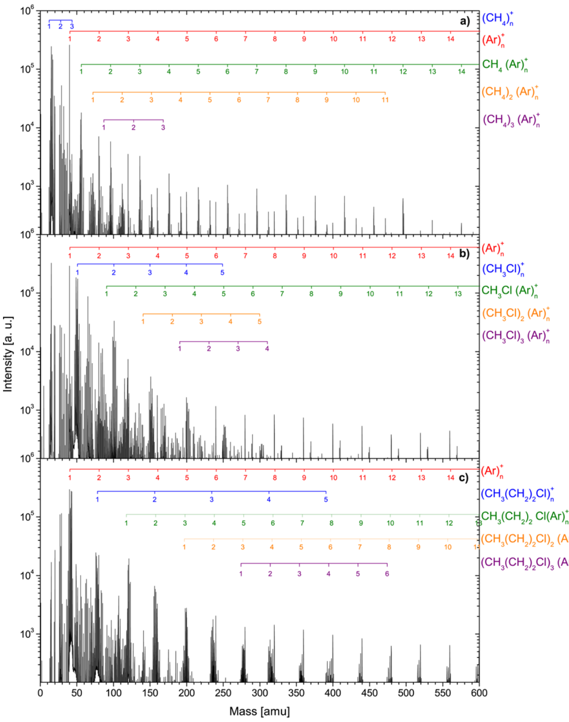

Figure 3. Mass spectrum of Ar_N, $\bar{N} = 330$, clusters after the pickup of (a) CH_4 at $p = 2.0 \times 10^{-4}$ mbar, (b) CH_3Cl at $p = 1.0 \times 10^{-4}$ mbar, and (c) $CH_3CH_2CH_2Cl$ at $p = 0.6 \times 10^{-4}$ mbar. The series corresponding to the different cluster ion fragments are labeled.

As opposed to the ice nanoparticles, relatively large aggregate ions of the adsorbed molecules were observed on Ar_N: the mass spectra exhibited M_m^+ with $m \geq 10$ as well as mixed species $Ar_n \cdot M_k^+$. Figure 4 summarizes the mass peak intensities corresponding to M_m^+ cluster ions generated on Ar_N at the highest exploited pickup pressures. We denote the largest detected molecular cluster size as m_{max}. For the ice nanoparticles, $m_{max} = 1$ for all guest molecules. The results are summarized in Table 1.

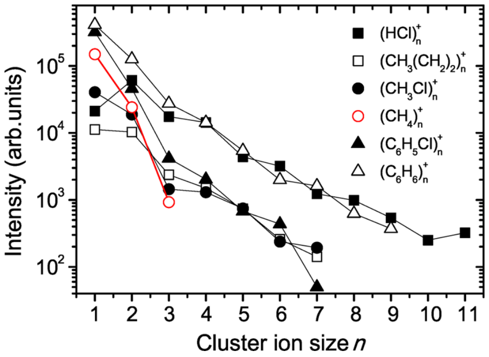

Figure 4. Mass peak intensities corresponding to M_n^+ aggregate ions following pickup of M on Ar_N nanoparticles ($\bar{N} \approx 330$).

For HCl, the mass spectra showed evidence of $(HCl)_m^+$ clusters up to the maximal cluster fragment size (m_{max}) of 11. For chloromethane also, relatively large $(CH_3Cl)_m^+$ cluster ions with $m_{max} = 7$ were observed. On the other hand, the clustering

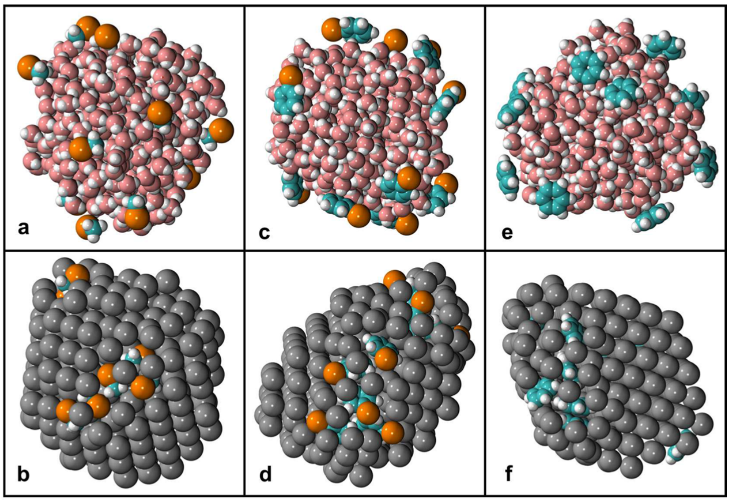

Figure 5. Last snapshots of the 50 ns MD simulation of ice (top) and argon (bottom) nanoparticles with 12 adsorbed pickup molecules: chloromethane (a and b), chlorobenzene (c and d), and benzene (e and f). Color coding: chlorine in orange, carbon in cyan, and hydrogen in white.

of a methane molecule on Ar_N was inefficient. Cluster fragments $(CH_4)_m^+$ were observed, but the maximal cluster size was only $m_{max} = 3$. This is nonetheless an interesting result. The fact that on the argon surface methane forms aggregates that do not decay completely upon the electron ionization opens experimental possibilities that are addressed in the Conclusions.

To investigate the influence of hydrocarbon chain length on molecule coagulation, we have studied the pickup of chloropropane where again the spectra exhibited large $(CH_3CH_2CH_2Cl)_m^+$ cluster ions up to $m_{max} = 7$. Because the linear chain length of the adsorbed molecule did not have any significant influence on the clustering on Ar_N, we exploited aromatic molecules chlorobenzene (C_6H_5Cl) and benzene (C_6H_6), if the interaction of the ring π electrons would change the coagulation behavior. However, the spectra exhibit essentially the same clustering as the linear molecules described above: large $(C_6H_6)_m^+$ fragments with $m_{max} = 9$ for benzene and $(C_6H_5Cl)_m^+$ with $m_{max} = 7$ for chlorobenzene.

MD Simulations. The MD simulations were performed for 50 ns to visualize possible coagulation of 12 individual molecules of the tested molecules on Ar_N or $(H_2O)_N$ ($N = 300$) nanoparticles. Within the first 10 ps, the guest molecules were adsorbed on the nanoparticle surfaces. Once adsorbed, they remained so on argon or ice for the entire simulation run. The only exceptions were the molecules of HCl and methane, which underwent desorption/absorption cycles on amorphous ice. In a 50 ns period, an isolated molecule of HCl desorbed approximately four times while an isolated CH_4 molecule desorbed ~200 times. However, for HCl, one has to consider that the molecule acidically dissociates on the ice nanoparticles, which has not been taken into account in simulations presented here (see Discussion). All the other adsorbed molecules were moving on the nanoparticle surface roughly for the first 10 ns. During this period, molecular aggregates were formed and submerged, and a practically final orientation of the molecules took place. For the next 40 ns, the molecules remained mostly fixed, except for benzene aggregates being submerged in the argon nanoparticle. Figure 5 shows several snapshots at the end of the simulation (see the Supporting Information for further snapshots and videos).

Coagulation on Argon. All studied molecules formed aggregates on argon (Figure 5). To eliminate the influence of the initial conditions, for each molecular species several separate simulations were run and the maximal cluster size was determined from the last snapshot. HCl molecules created molecular chains with an average maximal size of eight molecules. Methyl chloride and propyl chloride generated on average clusters of five and four molecules, respectively. Benzene (without a dipole moment) and chlorobenzene (dipole moment of 2.1 D) coagulate to the same extent (average maximal size $m_{cal} = 5$ molecules). This points to the dominant role of π interaction of aromatic rings. The largest aggregates of methane consisted on average of only two molecules (Table 1). Interestingly, chloromethanes, chlorobenzenes, and benzenes were submerged in argon nanoparticles, while chloropropanes remained localized more at the surface. Chlorine atoms of both chloropropane and chlorobenzene were mostly oriented outside of the argon cluster.

Coagulation on Ice. We observe mostly individual molecules on the $(H_2O)_N$ ice nanoparticles because the picked up molecules do not aggregate. Only chloromethane, benzene, and chlorobenzene formed in each simulation one dimer, and chloropropane formed one trimer. The nonaggregation on the ice particles results from a combination of kinetic and thermodynamic effects. The interaction of guest molecules with polar water molecules inhibits their mobility. They generally remain at the position of the first contact with the surface and merely reorient themselves with respect to the closest water molecules (kinetic effect). A similar finding has been observed experimentally for chloroform ($CHCl_3$) molecules that remain immobile on the bulk ice surface up to the desorption temperature.[5] Additionally, the amorphous surface layer effectively solvates the guest molecule, and in some cases, this solvation prevents aggregation of guest molecules in spite of their physical proximity (thermodynamic effect).

■ DISCUSSION

The unambiguous experimental observation is that while large aggregate ions of guest molecules M are detected from argon nanoparticles, both pure M_n^+ and mixed $M_n{\cdot}Ar_m^+$ ions, only the monomer ions are detected from the ice nanoparticles. To be certain that this observation leads to the conclusion outlined in the title of this paper, several issues have to be addressed. First, we have to consider the possibility of electron-induced aggregate fragmentation. Generally, the electron impact ionization in the gas phase leads to strong fragmentation, which allows speculation that molecular aggregates on ice particles could be formed but are decomposed in the ionization process. Even though we cannot fully exclude a certain amount of fragmentation, there is a strong evidence that ionization is much softer when the aggregate is on the surface of a nanoparticle. This is clearly experimentally demonstrated in this work in the case of argon nanoparticles upon comparison of m_p and $m_{\max}$ in Table 1. The number of picked up molecules (m_p) corresponds to the cluster ion size observed on Ar_N. This shows that molecules coagulate efficiently into their aggregates and a certain fraction of these aggregates does not fragment upon ionization. The reason is that the nanoparticle serves as an efficient heat bath and can dissipate the excess energy upon ionization, e.g., via evaporation of Ar atoms. Second, the ionization on nanoparticles is less destructive, because it can proceed via ionization of an argon atom and a subsequent charge transfer process to the guest molecule with release of much less excess energy than a direct ionization.[26,27] It should be noted that the mass peak intensities in Figure 4 do not follow a Poisson distribution, which describes the number of picked up molecules.[20] This points to a certain degree of fragmentation. However, the mass peak intensities are determined not only by the eventual fragmentation but also by the aggregate size distribution before the ionization event, i.e., degree of coagulation, which is difficult to predict.

We are aware of only one experimental confirmation of soft ionization for molecules deposited on ice nanoparticles: Moro et al.[44,45] reported almost negligible fragmentation of amino acids after they were picked up on water clusters, in contrast to rich fragmentation patterns of these molecules in the gas phase. The excess energy transfer to the water solvent can be even more efficient than in the argon case because the water molecules pose internal degrees of freedom, where the energy can be transferred. Besides, a lower ionization energy of water compared to that of argon leads to less excess energy in case of the host molecule/cluster ionization by charge transfer from water or argon. In addition, relatively soft proton transfer ionization is possible in $(H_2O)_N$. It is thus reasonable to assume soft ionization of aggregates on the surface of ice nanoparticles.

Another critical factor is the number of picked up molecules (m_p). Its determination relies on two assumptions about the deceleration of nanoparticles in the pickup chamber: (i) the sticking collisions during which guest molecules land on the surface are the dominant contributor to the momentum transfer, and (ii) guest molecules do not spontaneously desorb. We have previously shown[20−22] by extensive Monte Carlo simulations that assumption (i) is fulfilled for both argon and water particles; the statistical weight of nonsticking scattering events is much smaller than that of the sticking events. The relatively low collision energies (undisturbed beam velocities being 1450 ms^{-1} for H_2O and 490 ms^{-1} for Ar particles) lead to "soft landing" on the particle surface. Assumption (ii) is verified in the MD simulations presented here. The guest molecules, once adsorbed, remained on the surface of both argon or ice for the entire simulation run, with two exceptions, HCl and CH_4, as described above. Therefore, the m_p value for methane can be overestimated. This is also suggested by the negligible intensity of the methane peaks in the mass spectra (Supporting Information). The situation is different for HCl, which has been shown experimentally to undergo acidic dissociation to the $Cl^-{\cdot}H_3O^+$ ion pair on ice nanoparticles.[19,39,40,46] A simulation of this process goes beyond the MD model presented here, in which the chemical bonds were kept intact. Acidic dissociation will prohibit desorption of HCl from the surface and probably further inhibit the aggregation of the guest molecules. Thus, the determination of the m_p for HCl is reliable. As for the possible desorption of other guest molecules, it should be noted that MD simulations probe a time scale that is approximately 5 orders of magnitude shorter than the experimental time window and thus do not fully exclude the possibility of desorption in the experiment. However, in our previous systematic investigation of chloroalkanes at liquid water interfaces, we have shown that the free energy profiles have minima at the water−vapor interface and molecules prefer to stay adsorbed on the water surface even at 300 K.[37] The present, much lower temperature will only decrease the desorption probability.

For benzene and chlorobenzene on argon nanoparticles, the m_p values are lower than $m_{\max}$. This is possible because m_p is a mean number of picked up molecules; their actual number follows a Poisson distribution[20] and can be larger. However, we consider these m_p values to be underestimated; no other molecule shows $m_{\max} > m_p$, and the pickup chamber pressures for these two molecules are low because of high correction factors. All pressures in Table 1 correspond to the maximal reliable pressure of the ionization gauge of 5×10^{-4} mbar. The slope determination of the $\Delta v/v$ pressure dependence (described in the Supporting Information) at these low pressures has large error bars.

These MD simulations were actually inspired by the experimental results and were performed to account for the main uncertainty in the experimental interpretation, whether the lack of observation of aggregate ions in the mass spectra on ice nanoparticle can be interpreted as the lack of neutral aggregates prior to the ionization. As described in Results, they fully support this interpretation. Again, the shorter time scale of the simulations when compared with that of the experiment comes into question. The degree of aggregation would be strongly influenced by a time scale if it were limited solely by the mobility of guest molecules on the particle. However, the low mobility on the ice surface is only part of the reason for the nonaggregation. We have observed a number of trajectories in which two guest molecules came into physical proximity of each other on the ice surface but did not form dimers because they were solvated by water molecules. The important role of binding of guest molecules to water has been pointed out by Ahmed and co-workers.[42,43] The fact that the guest molecules remain on the surface and are not submerged in the nanoparticle can be attributed to the fact that guest−H_2O interaction is weaker than H_2O−H_2O interaction. On the other hand, the guest−H_2O and guest−guest interaction energies have similar magnitudes, which leads to surface solvation of the guest molecules. The detailed analysis of energetics and the temperature dependence of the mobility and aggregation process will be a subject of a separate theoretical publication.

■ CONCLUSIONS

In conclusion, we have shown experimentally that adsorption of multiple molecues on the surface of water ice nanoparticles and the subsequent ionization do not lead to formation of any aggregate ions. MD simulations confirm that the molecules stay mostly isolated and do not form aggregates in spite of their physical proximity. This is in strong contrast with their behavior on the surface of argon nanoparticles, where they are mobile and coagulate efficiently. In the mass spectra, this is reflected in a rich progression of either pure aggregate or mixed aggregate−argon ions. Even methane after adsorption on argon and ionization forms pure aggregates $(CH_4)_n^+$ up to $n = 3$. Methane is known to be a difficult gas to cluster in co-expansions probably due to its small c_p/c_v ratio.[47] The use of argon nanoparticles as a cold support could represent a way to generate interesting methane-containing aggregates, e.g., clathrates. An additional interesting result for doped argon nanoparticles is shown by MD simulations: while some of the aggregates are submerged into the nanoparticle (chloromethanes, chlorobenzenes, and benzenes), some remain on its surface (methane and chloropropane). Chloropropane and chlorobenzene are oriented with chlorine atoms pointing out of the surface. These two findings will have consequences for the amount of caging observed in future photodissociation studies.

With respect to the implications in astro- and atmospheric chemistry outlined in the Introduction, it is important to note that the present findings apply to water ices with temperature around 100 K and an amorphous surface layer.[48] Naturally occurring nano- to microsized ices encompass a range of temperatures in different regions. The time scales should also not be overlooked: experimentally, we probed processes on a millisecond time scale, theoretically on a nanosecond time scale, while for example, the interstellar chemistry often requires millions of years. Present results are also of fundamental interest to the cluster physics research. Rare gas nanoparticles or helium nanodroplets are often used as a support for forming cold clusters of picked-up molecules. This will be apparently difficult with water clusters. Several research groups have envisioned the use of water clusters as a supporting microsolvation system, e.g., for providing support for Watson−Crick pair formation by successive pickup of nucleobases. The low mobility and nonaggregation of guest molecules can represent an obstructive factor for such approach. A more promising way to generate such species would be co-expansion with the water vapor instead of the pickup, which has been demonstrated for a number of biomolecules.[49−51] However, in such a case, the molecules are generally incorporated into the bulk water and composition of the resulting nanoparticles (number of water molecules vs number of "guest" molecules) is difficult to control.

■ ASSOCIATED CONTENT

Ⓢ Supporting Information

The Supporting Information is available free of charge on the ACS Publications website at DOI: 10.1021/acs.jpca.5b05368.

Detailed description of the experiment, expansion conditions, geometrical cross sections, and detailed analysis of mass spectra (PDF)
Topology files used in MD simulations (ZIP)
Video with the final configuration of chloropropane on Ar nanoparticle (MPG)
Video with the final configuration of chlorobenzene on Ar nanoparticle (MPG)
Video with the final configuration of benzene on Ar nanoparticle (MPG)
Video with the final configuration of chloromethane on Ar nanoparticle (MPG)
Video with the final configuration of methane on Ar nanoparticle (MPG)
Video with the final configuration of HCl on Ar nanoparticle (MPG)
Video with the final configuration of chloropropane on ice nanoparticle (MPG)
Video with the final configuration of chlorobenzene on ice nanoparticle (MPG)
Video with the final configuration of benzene on ice nanoparticle (MPG)
Video with the final configuration of chloromethane on ice nanoparticle (MPG)
Video with the final configuration of methane on ice nanoparticle (MPG)
Video with the final configuration of HCl on ice nanoparticle (MPG)

■ AUTHOR INFORMATION

Corresponding Authors

*E-mail: alena.habartova@marge.uochb.cas.cz.
*E-mail: juraj.fedor@jh-inst.cas.cz.
*E-mail: michal.farnik@jh-inst.cas.cz.

Present Address

[§]P.S. and J.L.: Department of Physical Chemistry, University of Chemistry and Technology, Technická 5, 16628 Prague 6, Czech Republic.

Notes

The authors declare no competing financial interest.

■ ACKNOWLEDGMENTS

This work has been supported by Czech Science Foundation Projects 15-12386S and 13-06181S. We thank Prof. Pavel Jungwirth, Prague, for fruitful discussions.

■ REFERENCES

(1) Peter, T. Microphysics and Heterogeneous Chemistry of Polar Stratospheric Clouds. *Annu. Rev. Phys. Chem.* **1997**, *48*, 785−822.

(2) Herbst, E.; van Dishoeck, E. F. Complex Organic Interstellar Molecules. *Annu. Rev. Astron. Astrophys.* **2009**, *47*, 427−480.

(3) Holtom, P. D.; Bennett, C. E.; Osamura, Y.; Mason, N. J.; Kaiser, R. I. A Combined Experimental and Theoretical Study on the Formation of the Amino Acid Glycine and its Isomer in Extraterrestrial Ices. *Astrophys. J.* **2005**, *626*, 940−952.

(4) Nahler, N. H.; Fárník, M.; Buck, U.; Vach, H.; Gerber, R. B. Photodissociation of HCl and Small $(HCl)_m$ Complexes in and on Large Ar_n Clusters. *J. Chem. Phys.* **2004**, *121*, 1293−1302.

(5) Grecea, M.; Backus, E.; Fraser, H.; Pradeep, T.; Kleyn, A.; Bonn, M. Mobility of Haloforms on Ice Surfaces. *Chem. Phys. Lett.* **2004**, *385*, 244−248.

(6) Park, S. C.; Moon, K. S.; Kang, H. Some Fundamental Properties and Reactions of Ice Surfaces at Low Temperatures. *Phys. Chem. Chem. Phys.* **2010**, *12*, 12000−12011.

(7) Gough, T. E.; Mengel, M.; Rowntree, P. A.; Scoles, G. Infrared Spectroscopy at the Surface of Clusters: SF_6 on Ar. *J. Chem. Phys.* **1985**, *83*, 4958−4961.

(8) Lewerenz, M.; Schilling, B.; Toennies, J. P. Successive Capture and Coagulation of Atoms and Molecules to Small Clusters in Large Liquid Helium Clusters. *J. Chem. Phys.* **1995**, *102*, 8191−8207.

(9) Behrens, M.; Fröchtenicht, R.; Hartmann, M.; Siebers, J. G.; Buck, U.; Hagemeister, F. C. Vibrational Spectroscopy of Methanol and Acetonitrile clusters in Cold Helium Droplets. *J. Chem. Phys.* **1999**, *111*, 2436−2443.

(10) Scoles, G.; Lahmann, K. K. Nanomatrices are Cool. *Science* **2000**, *287*, 2429−2430.

(11) Toennies, J. P.; Vilesov, A. F. Superfluid Helium Droplets: A Uniquely Cold Nanomatrix for Molecules and Molecular Complexes. *Angew. Chem., Int. Ed.* **2004**, *43*, 2622−2648.

(12) Choi, M.; Miller, R. Infrared Laser Spectroscopy of Imidazole Complexes in Helium Nanodroplets: Monomer,Dimer, and Binary Water Complexes. *J. Phys. Chem. A* **2006**, *110*, 9344−9351.

(13) Denifl, S.; Zappa, F.; Mähr, I.; da Silva, F. F.; Aleem, A.; Mauracher, A.; Probst, M.; Urban, J.; Mach, P.; Bacher, A.; et al. Ion−Molecule Reactions in Helium Nanodroplets Doped with C_{60} and Water Clusters. *Angew. Chem.* **2009**, *121*, 9102−9105.

(14) Lehnig, R.; Sebree, J. A.; Slenczka, A. Structure and Dynamics of Phthalocyanine-Argon$_n$ (n = 1−4) Complexes Studied in Helium Nanodroplets. *J. Phys. Chem. A* **2007**, *111*, 7576−7584.

(15) Huisken, F.; Stemmler, M. Infrared Spectroscopy of Methanol Clusters Adsorbed on Large Ar_x Host Clusters. *J. Chem. Phys.* **1993**, *98*, 7680.

(16) Ehbrecht, M.; Stemmler, M.; Huisken, F. Enhanced Production of Unprotonated Hydrogen-bonded Cluster Ions. *Int. J. Mass Spectrom. Ion Processes* **1993**, *123*, R1.

(17) Fedor, J.; Kočišek, J.; Poterya, V.; Votava, O.; Pysanenko, A.; Lipciuc, L.; Kitsopoulos, T. N.; Fárník, M. Velocity Map Imaging of HBr Photodissociation in Large Rare Gas Clusters. *J. Chem. Phys.* **2011**, *134*, 154303.

(18) Poterya, V.; Kočišek, J.; Lengyel, J.; Svrčková, P.; Pysanenko, A.; Hollas, D.; Slavíček, P.; Fárník, M. Clustering and Photochemistry of Freon CF_2Cl_2 on Argon and Ice Nanoparticles. *J. Phys. Chem. A* **2014**, *118*, 4740−4749.

(19) Poterya, V.; Lengyel, J.; Pysanenko, A.; Svrčková, P.; Fárník, M. Imaging of Hydrogen Halides Photochemistry on Argon and Ice Nanoparticles. *J. Chem. Phys.* **2014**, *141*, 074309.

(20) Fedor, J.; Poterya, V.; Pysanenko, A.; Fárník, M. Cluster Cross Sections from Pickup Measurements: Are the Established Methods Consistent? *J. Chem. Phys.* **2011**, *135*, 104305.

(21) Lengyel, J.; Kočišek, J.; Poterya, V.; Pysanenko, A.; Svrčková, P.; Fárník, M.; Zaouris, D.; Fedor, J. Uptake of Atmospheric Molecules by Ice Nanoparticles: Pickup Cross Sections. *J. Chem. Phys.* **2012**, *137*, 034304.

(22) Lengyel, J.; Pysanenko, A.; Poterya, V.; Slavíček, P.; Fárník, M.; Kočišek, J.; Fedor, J. Irregular Shapes of Water Clusters Generated in Supersonic Expansions. *Phys. Rev. Lett.* **2014**, *112*, 113401.

(23) Farges, J.; de Feraudy, M. F.; Raoult, B.; Torchet, G. Structure and Temperature of Rare Gas Clusters in a Supersonic Expansion. *Surf. Sci.* **1981**, *106*, 95.

(24) Poterya, V.; Kočišek, J.; Pysanenko, A.; Fárník, M. Caging of Cl Atoms from Photodissociation of CF_2Cl_2 in Clusters. *Phys. Chem. Chem. Phys.* **2014**, *16*, 421−429.

(25) Lengyel, J.; Pysanenko, A.; Kočišek, J.; Poterya, V.; Pradzynski, C.; Zeuch, T.; Slavíček, P.; Fárník, M. Nucleation of Mixed Nitric Acid-Water Ice Nanoparticles in Molecular Beams that Starts with a HNO_3 Molecule. *J. Phys. Chem. Lett.* **2012**, *3*, 3096−3109.

(26) Kočišek, J.; Lengyel, J.; Fárník, M. Ionization of Large Homogeneous and Heterogeneous Clusters Generated in Acetylene Ar Expansions: Cluster Ion Polymerization. *J. Chem. Phys.* **2013**, *138*, 124306.

(27) Kočišek, J.; Lengyel, J.; Fárník, M.; Slavíček, P. Energy and Charge Transfer in Ionized Argon Coated Water Clusters. *J. Chem. Phys.* **2013**, *139*, 214308.

(28) Jansen, R.; Wysong, I.; Gimelshein, S.; Zeifman, M.; Buck, U. Nonequilibrium Numerical Model of Homogeneous Condensation in Argon and Water Vapor Expansions. *J. Chem. Phys.* **2010**, *132*, 244105.

(29) Buck, U.; Pradzynski, C. C.; Zeuch, T.; Dieterich, J. M.; Hartke, B. A Size Resolved Investigation of Large Water Clusters. *Phys. Chem. Chem. Phys.* **2014**, *16*, 6859−6871.

(30) Torchet, G.; Schwartz, P.; Farges, J.; de Feraudy, M. F.; Raoult, B. Structure of Solid Water Clusters Formed in a Free Jet Expansion. *J. Chem. Phys.* **1983**, *79*, 6196−6202.

(31) Pradzynski, C. C.; Forck, R. M.; Zeuch, T.; Slavíček, P.; Buck, U. A Fully Size-Resolved Perspective on the Crystallization of Water Clusters. *Science* **2012**, *337*, 1529−1532.

(32) Abascal, J. L. F.; Vega, C. A General Purpose Model for the Condensed Phases of Water: TIP4P/2005. *J. Chem. Phys.* **2005**, *123*, 234505.

(33) Kaminski, G. A.; Friesner, R. A.; Tirado-Rives, J.; Jorgensen, W. L. Evaluation and Reparametrization of the OPLS-AA Force Field for Proteins via Comparison with Accurate Quantum Chemical Calculations on Peptides. *J. Phys. Chem. B* **2001**, *105*, 6474−6487.

(34) Malde, A. K.; Zuo, L.; Breeze, M.; Stroet, M.; Poger, D.; Nair, P. C.; Oostenbrink, C.; Mark, A. E. An Automated Force Field Topology Builder (ATB) and Repository: Version 1.0. *J. Chem. Theory Comput.* **2011**, *7*, 4026−4037.

(35) Wang, J.; Wolf, R. M.; Caldwell, J. W.; Kollman, P. A.; Case, D. A. Development and Testing of a General Amber Force Field. *J. Comput. Chem.* **2004**, *25*, 1157−1174.

(36) Bayly, C. I.; Cieplak, P.; Cornell, W.; Kollman, P. A. A Well-Behaved Electrostatic Potential Based Method Using Charge Restraints for Deriving Atomic Charges: the RESP Model. *J. Phys. Chem.* **1993**, *97*, 10269−10280.

(37) Habartová, A.; Valsaraj, K. T.; Roeselová, M. Molecular Dynamics Simulations of Small Halogenated Organics at the Air-Water Interface: Implications in Water Treatment and Atmospheric Chemistry. *J. Phys. Chem. A* **2013**, *117*, 9205−9215.

(38) Vácha, R.; Jungwirth, P.; Chen, J.; Valsaraj, K. Adsorption of Polycyclic Aromatic Hydrocarbons at the Air-Water Interface: Molecular Dynamics Simulations and Experimental Atmospheric Observations. *Phys. Chem. Chem. Phys.* **2006**, *8*, 4461−4467.

(39) Poterya, V.; Fárník, M.; Slavíček, P.; Buck, U.; Kresin, V. V. Photodissociation of Hydrogen Halide Molecules on Free Ice Nanoparticles. *J. Chem. Phys.* **2007**, *126*, 071101.

(40) Poterya, V.; Fedor, J.; Pysanenko, A.; Tkáč, O.; Lengyel, J.; Ončák, M.; Slavíček, P.; Fárník, M. Photochemistry of HI on Argon and Water Nanoparticles: Hydronium Radical Generation in HI·$(H_2O)_n$. *Phys. Chem. Chem. Phys.* **2011**, *13*, 2250−2258.

(41) Ahmed, M.; Apps, C. J.; Hughes, C.; Whitehead, J. C. The Adsorption of Methanol on Large Water Clusters. *Chem. Phys. Lett.* **1995**, *240*, 216−219.

(42) Ahmed, M.; Apps, C. J.; Hughes, C.; Watt, N. E.; Whitehead, J. C. Adsorption of Organic Molecules on Large Water Clusters. *J. Phys. Chem. A* **1997**, *101*, 1250−1253.

(43) Ahmed, M.; Apps, C. J.; Buesnel, R.; Hughes, C.; Hillier, I. H.; Watt, N. E.; Whitehead, J. C. Adsorption of NxOy-Based Molecules on Large Water Clusters: An Experimental and Theoretical Study. *J. Phys. Chem. A* **1997**, *101*, 1254−1259.

(44) Moro, R.; Rabinovitch, R.; Kresin, V. V. Amino-acid and Water Molecules Adsorbed on Water Clusters in a Beam. *J. Chem. Phys.* **2005**, *123*, 074301.

(45) Moro, R.; Rabinovitch, R.; Kresin, V. V. Pickup Cell for Cluster Beam Experiments. *Rev. Sci. Instrum.* **2005**, *76*, 156104.

(46) Ončák, M.; Slavíček, P.; Fárník, M.; Buck, U. Photochemistry of Hydrogen Halides on Water Clusters: Simulations of Electronic Spectra and Photodynamics, and Comparison with Photodissociation Experiments. *J. Phys. Chem. A* **2011**, *115*, 6155−6168.

(47) Ding, A.; Cassidy, R. A.; Futrell, J. H.; Cordis, L. Ion−molecule Reactions within Methane Clusters Initiated by Photoionization. *J. Phys. Chem.* **1987**, *91*, 2562−2568.

(48) Buch, V.; Bauerecker, S.; Devlin, J. P.; Buck, U.; Kazimirski, J. K. Solid Water Clusters in the Size Range of Tens-Thousands of H_2O: a Combined Computational/Spectroscopic Outlook. *Int. Rev. Phys. Chem.* **2004**, *23*, 375−433.

(49) Kim, S. K.; Lee, W.; Herschbach, D. R. Cluster Beam Chemistry: Hydration of Nucleic Acid Bases; Ionization Potentials of Hydrated Adenine and Thymine. *J. Phys. Chem.* **1996**, *100*, 7933−7937.

(50) Belau, L.; Wilson, K. R.; Leone, S. R.; Ahmed, M. Vacuum-Ultraviolet Photoionization Studies of the Microhydration of DNA Bases (Guanine, Cytosine, Adenine, and Thymine). *J. Phys. Chem. A* **2007**, *111*, 7562−7568.

(51) Nosenko, Y.; Kunitski, M.; Riehn, C.; Harbach, P. H. P.; Dreuw, A.; Brutschy, B. The Structure of Adenine Monohydrates Studied by Femtosecond Multiphoton Ionization Detected IR Spectroscopy and Quantum Chemical Calculations. *Phys. Chem. Chem. Phys.* **2010**, *12*, 863−870.

Appendix E

Essential building blocks of biomolecules

PCCP

PAPER

View Article Online
View Journal | View Issue

Cite this: *Phys. Chem. Chem. Phys.*, 2015, **17**, 25004

Photodissociation of aniline N–H bonds in clusters of different nature†

Viktoriya Poterya,[a] Dana Nachtigallová,*[b] Jozef Lengyel[a] and Michal Fárník*[a]

Received 30th July 2015,
Accepted 29th August 2015

DOI: 10.1039/c5cp04485e

www.rsc.org/pccp

We investigated the solvent effects on the N–H bond photodisociation dynamics of aniline ($PhNH_2$) in clusters using velocity map imaging (VMI). The VMI experiment was accompanied by a time-of-flight mass spectrometry after electron ionization to reveal the cluster nature. The H-fragment images were recorded at 243 nm in various expansion regimes corresponding to different species: isolated molecules; small $(PhNH_2)_N$, $N \leq 3$, clusters; larger $(PhNH_2)_N$, $N \geq 10$; small mixed $PhNH_2{\cdot}(H_2O)_N$, $N \leq 10$, clusters; and individual $PhNH_2$ molecules deposited on large $(H_2O)_N$, $\bar{N} = 430$. The H-fragment kinetic energy distributions exhibit fast fragments around 0.8 eV (A) assigned previously to a direct dissociation along a repulsive $\pi\sigma^*$ state potential, and slow statistical fragments peaking near 0.2 eV (B). In the aniline clusters the contribution of fast fragments (A) decreases relatively to (B) with increasing cluster size. A similar effect is observed when aniline is solvated with water molecules. The experimental data are interpreted with *ab initio* calculations. Cluster structures were calculated with both N–H bonds of an aniline molecule participating in hydrogen bonding, as well as the ones with free N–H bonds. The latter ones yield preferentially the fast fragments as the isolated molecule. For N–H engaged in hydrogen bonding a barrier increased along the N–H coordinate on the dissociative $\pi\sigma^*$ state potential surface, and also the energy of $\pi\sigma^*/S_0$ conical intersection increased. Thus the fast dissociation channel was closed stabilizing the molecule in clusters. The population could be funnelled through other conical intersections into the hot ground state which decayed statistically, yielding the slow H-fragments.

1 Introduction

The photophysical behavior of heteroaromatic systems, incuding phenol, pyrrole, and aniline, has been the subject of numerous experimental and theoretical papers covered in recent reviews.[1,2] Special attention has been paid to the non-radiative relaxation mechanism which utilizes the dissociative $\pi\sigma^*$ channel with the σ^* orbital localized on the X–H bond (X = O, N). This channel has been suggested to provide an effective relaxation route *via* $\pi\sigma^*/S_0$ conical intersection (CI) leading either to X–H bond fission or to the original species in the ground state.[3]

In this work we concentrate on the N–H bond dissociation in aniline ($PhNH_2$) at 243 nm and investigate the photochemistry of aniline solvated in various clusters. Small heteroaromatic molecules represent essential building blocks of larger biomolecules and act as ultraviolet (UV) chromophores in these biomolecules. Therefore the investigations of photodissociation behavior of the small heteroaromatic molecules in the gas phase can contribute to the understanding of biomolecule photostability. Aniline, in particular, represents a model system for investigations of photochemistry in the purine derived DNA bases, guanine and adenine.[2,4] Studying the photodissociation in clusters provides a molecular-level insight into the solvent effects, which is a step towards understanding these processes in bulk.

Several recent experimental and computational studies on aniline photodynamics were reported.[4–12] These studies concentrated mainly on the role of the $^1\pi\sigma^*$ channel in the excited state dissociation dynamics. Similar to phenol, in the vertical Franck–Condon (vFC) region this state is of Rydberg character and it is located energetically between the first and second bright singlet states of $\pi\pi^*$ character. Details of the aniline dissociation are still a subject of discussion, in particular, various scenarios of the $\pi\sigma^*$ state population were suggested as discussed below.

Nevertheless, all previously reported experimental studies agreed that the excited $S_3(2^1\pi\pi^*)$ state is populated at the wavelengths $\leq$240 nm.[4–8] At these energies, a fast dissociation is observed *via* the sequence $2^1\pi\pi^*/1^1\pi\pi^*$, $1^1\pi\pi^*/^1\pi\sigma^*$ and $^1\pi\sigma^*/S_0$ CIs. Recently, Sala *et al.* reported the existence of a three-state CI of $2^1\pi\pi^*$, $1^1\pi\pi^*$ and $1^1\pi\sigma^*$ states which can utilize the

---

[a] *J. Heyrovský Institute of Physical Chemistry v.v.i., Czech Academy of Sciences, Dolejškova 3, 18223 Prague, Czech Republic. E-mail: michal.farnik@jh-inst.cas.cz; Fax: +420 2 8658 2307; Tel: +420 2 6605 3206*

[b] *Institute of Organic Chemistry and Biochemistry v.v.i., Czech Academy of Sciences, Flemingovo nám. 2, 16610 Prague 6, Czech Republic. E-mail: dana.nachtigallova@marge.uochb.cas.cz*

† Electronic supplementary information (ESI) available: Aniline monomer VMI and further calculation results. See DOI: 10.1039/c5cp04485e

N–H bond fission,[13] and these theoretical calculations have also been confirmed experimentally.[12] The corresponding CIs can occur also in the out-of-plane coordinates of a complex potential energy surface which can be found in Fig. 3 of ref. 4.

Some disagreements exist on the excited state population in the intermediate regime of 269.5–240 nm. King *et al.*[5] claim that at the wavelengths corresponding to the origin of the $S_2(3s/\pi\sigma^*)$ state (at the wavelengths $\leq$269.5 nm) the quasibound vibrational level along the N–H coordinate is populated, while further wavelength lowering results in the excitation into the $S_1(1^1\pi\pi^*)$ state followed by an internal conversion to the $S_2(^1\pi\sigma^*)$ state. The internal conversion was also attributed to the H-fragment signal observed by Stavros *et al.* at the wavelengths shorter than 250 nm.[4] Contrary to this, Montero *et al.*[6] and Fielding *et al.*[7,8] saw no evidence of the S_1 state in the photoelectron imaging experiment and predicted a direct S_2 state population. They showed[7,12,13] that at all measured wavelengths (269–238 nm) the $^1\pi\sigma^*$ state is populated directly and it decays by the two different pathways: one *via* the coupling to the $^1\pi\pi^*$ state through CI in the vFC region with subsequent population transfer to the S_0 state, and the second where the population develops on the $^1\pi\sigma^*$ state followed by dissociation or transition to the S_0 state. Time-resolved photoelectron imaging of Thompson *et al.*[9] suggested a simultaneous population of S_1 and S_2 states in the region 273–266 nm and recently confirmed this result also at a wavelength of 250 nm.[11] The most recent discussion of the photoelectron spectra from aniline can be found elsewhere.[12] Although the exact dynamics of the excited aniline is still not determined it is unambiguous that the $^1\pi\sigma^*$ state plays a crucial role providing the fast H-atoms.

The slow statistical H atom channel was also observed experimentally. This channel was detected in a wide range of excitation wavelengths in H-photofragment imaging experiments resulting in a broad Boltzmann-like component of H-fragment kinetic energy spectra.[4,5] Several processes were suggested to be responsible for these slow H-fragments: (i) fast multiphoton processes, *e.g.*, dissociative ionization producing H^+ directly; (ii) statistical unimolecular decay of the vibrationally hot S_0 ground state populated *via* appropriate CIs. Roberts *et al.*[4] identified three $1^1\pi\pi^*/S_0$ CIs on the PES and also suggested a possible cascade process *via* $1^1\pi\pi^*/^1\pi\sigma^*$ and $^1\pi\sigma^*/S_0$ CIs. Although, they have not seen strong evidence for S_0 repopulation on the time scales shorter than 100 ps, it can occur at later times.

The important consequences of the $\pi\sigma^*$ state character appear when the heteroaromatic molecule is complexed with other solvating species. Possible reaction channels are available in the excited states including (i) dissociation of hydrogen into free space, (ii) hydrogen transfer between the heterocyclic unit and the solvating molecule, (iii) a reaction channel leading to puckered CI, and (iv) coupled electron–proton transfer.[14] The mechanism of the photodissociation process in an isolated molecule depends on the relative energy position of the $\pi\pi^*$ and $\pi\sigma^*$ states which can be influenced by the presence of the solvent.[1] Different effects on the mechanism of the photodisociation *via* $\pi\sigma^*$ channel were reported for phenol[3,15] and indole[16,17] as compared to pyrrole[18] solvated by ammonia. In the vFC region, these heteroaromatic species exhibit different relative ordering of the $\pi\sigma^*$ and $\pi\pi^*$ states with $\pi\sigma^*$ located above the $\pi\pi^*$ state for phenole and indole, and below the $\pi\pi^*$ state for pyrrole, respectively.

Combined experimental and computational studies performed on pyrrole and phenol clusters showed that the direct $\pi\sigma^*$ dissociative channel along the N–H coordinate yielding the fast H-fragments was closed. On the contrary, the presence of solvent molecule had a little influence on the valence states resulting from the $\pi \rightarrow \pi^*$ electronic transition.[14,19,20]

Here we focus on aniline clusters and mixed clusters of aniline with water. The aniline dimer and trimer structures were investigated in the ground and excited states previously.[21–23] The N–H site in the amino group of aniline can form a hydrogen bond with a lone pair of the nitrogen atom of another aniline or with the π electrons of its benzene ring. The neutral structure of the aniline dimer shows relative stability for both conformers: the stacked complexes with a N–π type hydrogen bond and N–H···N bonding with head-to-tail orientation.[21,22] Analogical structures were found for the trimers.[22]

To reveal the solvent effects on the photochemistry of aniline we vary the size and composition of the complexes from isolated molecules and small $(PhNH_2)_N$, $N \leq 3$, clusters to larger $(PhNH_2)_N$, $N \geq 10$. More about the generation of different aniline clusters in supersonic expansions under various conditions can be found in our recent publication.[24] Water can act as an effective quencher in photochemical reactions and is an important biological solvent. Therefore we investigate also aniline in water clusters from small mixed $PhNH_2{\cdot}(H_2O)_N$, $N \leq 10$, species to $PhNH_2$ molecules deposited on large $(H_2O)_N$, $\bar{N} = 430$ (ice nanoparticles). The structure of neutral aniline–water clusters has not been investigated previously, however, it was studied for cluster ions $[PhNH_2{\cdot}(H_2O)_n]^+$, $n \leq 12$, exhibiting a strong hydrogen bond formation among water molecules with a ring-like structure around aniline molecules.[25]

2 Experiment

The present experiments were carried out on two experimental setups: CLUster Beam (CLUB) apparatus and Apparatus for IMaging (AIM). The AIM is a velocity map imaging (VMI) apparatus[26,27] used in the present experiments mainly to confirm the results for isolated molecules. The CLUB is a complex and versatile molecular beam setup specialized in molecular clusters,[27–31] where the photodissociation dynamics and mass spectrometry of different aniline clusters were investigated. The CLUB experiments will be briefly outlined below, further details of the apparatus can be found in our recent publications.[24,28,32,33]

A specially designed temperature controlled nozzle setup with a built in reservoir for solid and liquid samples inside the vacuum chamber was used to generate various aniline species from single molecules to large aniline $(PhNH_2)_N$ clusters and mixed clusters of aniline complexed with water $(PhNH_2)_N{\cdot}(H_2O)_M$. To generate the beam composed mostly of aniline monomers the He carrier gas under 1 bar stagnation pressure

Table 1 Expansion conditions: stagnation pressure P_0 and reservoir temperature T_R (the nozzle temperature T_0 was higher typically by 10 K). Sizes n denote the largest $(PhNH_2)_n^+$ or $PhNH_2{\cdot}(H_2O)_n^+$ ion fragment discernible in the mass spectra (neutral cluster size $N \geq n$). Nozzle parameters: diameter 50 μm (90 μm for $(H_2O)_N$), opening angle 30°, length 2 mm

Buffer gas	P_0 (bar)	T_R (K)	Species	Size
He	0.8	303	Molecule	
He	2	323–373	$(PhNH_2)_N$	$n \leq 3$
Ar	2–4	323–373	$(PhNH_2)_N$	$n \geq 10$
H_2O/He	2–6	313–343	$PhNH_2{\cdot}(H_2O)_N$	$n \leq 10$
H_2O	4.6	423	$PhNH_2{\cdot}(H_2O)_N$	$\bar{N} \approx 430$

passed through the reservoir with aniline at room temperature. Increasing the reservoir temperature and using Ar carrier gas allowed generation of larger clusters. To produce mixed clusters with water, the He gas passed over a $PhNH_2/H_2O$ mixture in a ratio of 1 : 5 by volume. To deposit aniline molecules on large water clusters, the pickup technique was used.[34] Pure water clusters $(H_2O)_N$, $\bar{N} \approx 430$, were generated with a different water cluster source[29] and aniline vapour was introduced into a separated pickup chamber by means of an external inlet system with heated aniline samples. The water clusters passing through the pickup cell uptake aniline molecule(s). The neutral $(H_2O)_N$ cluster mean size $\bar{N} \approx 430$ was derived using Bucks' formula.[35,36] Table 1 summarizes the expansion conditions.

It ought to be mentioned that we use continuous expansions through conical nozzles in the CLUB experiments. This is especially important for the cluster generation, since pulsed nozzles provide different clustering conditions at the different phases of valve opening[26] and often a pulse-to-pulse reproducibility in cluster distribution is poor. On the contrary, the continuous expansions provide very reproducible and stable cluster size distributions which we could verify on CLUB for various clusters by several different mass spectrometric techniques.[29]

The skimmed cluster beam passed through two differentially pumped chambers before entering the chamber hosting the VMI assembly perpendicular to the beam axis. The molecules and clusters interacted with the laser in the center of the electrostatic lens system which extracted the ionic photoproducts towards a position sensitive detector. The original VMI design of Eppink and Parker[37] was used for the extraction electrostatic lens. Gating the detector enabled discriminating of other ions apart from H^+. The images were recorded using a 16-bit greyscale CCD camera (unibrain Fire-i 780b) with an imaging lens (25 mm, *f*/1.6). The recorded images were analysed using the Hankel reconstruction algorithm.[38] From the integrated radial velocity distributions the final kinetic energy distributions (KEDs) and angular distributions were calculated. The calibration of velocity was achieved through photodissociation of HBr at 243 nm, which produces H-atoms with known velocities.[26]

The H-fragments were photoionized *via* a (2 + 1) REMPI process at 243.12 nm, and aniline was photodissociated at the same wavelength in a one-color experiment. The UV laser was scanned over the entire Doppler profile of the resonant transition to record the images. The tunable radiation at around 243.1 nm was generated by frequency summing 315 nm with the fundamental 1064 nm of the Nd:YAG laser (Spitlight 1500, Innolas). The tunable 315 nm radiation was produced by doubling a 630 nm output of a dye laser (Pulsare-S, Lioptec) pumped by the second harmonics (532 nm) of the Nd:YAG laser. The lasers were operated at 10 Hz frequency with a pulse width of 7 ns. The laser radiation was polarized so that the electric field vector of the radiation was parallel to the molecular beam, *i.e.* perpendicular to the imaging TOF axis.

The photodissociation experiments were accompanied by simultaneous mass spectral measurements using a reflectron time-of-flight mass spectrometer (RTOFMS), which provided information about the species in the molecular beam. After the VMI chamber the molecular beam entered the mass spectrometer chamber with RTOFMS mounted perpendicularly to the beam. This mass spectrometer offers several ionization options.[29,36,39,40] In the present study we used electron ionization with an electron gun with 10 kHz repetition frequency and an electron energy of 70 eV. The aniline cluster mass spectrometry has been investigated in detail by our recent study where also a more detailed description of our RTOFMS can be found.[24]

3 Theoretical methods

The experiments were complemented by *ab initio* calculations. The ground state equilibrium geometries of aniline molecules and $(PhNH_2)_{2,3}$ clusters were optimized using the density functional method employing the ωB97XD functional which includes empirical dispersion[41] and the 6-311G* basis set. The interaction of $PhNH_2$ with a large water cluster (ice nanoparticles) was modelled by a cluster which consists of 50 water molecules. These clusters were taken from the previous ice surface simulation studies as described elsewhere.[42] They were calculated with the B97-D functional[43] and the TZVP basis set.[44] The interaction energies were corrected for basis set superposition error (BSSE). This approach has been successfully used for the description of the aromatic species with the ice surface previously.[42]

The calculations of the vertical excitation energies were obtained at the DFT level employing the long-range corrected LC-ωPBE functional[45–47] and the aug-cc-pVTZ basis set. The structures at conical intersections on the S_0/S_1 crossing seam have been obtained using the SA-CASSCF method.[48–50] To obtain the energetic profiles of all considered stationary points and CI the excitation energies of the resulting geometries were obtained using the LC-ωPBE functional. The effectiveness of the CIs was evaluated based on the calculations of linear interpolation curves (LIICs) performed with LC-ωPBE functional. The Gaussian09[51] and Columbus[52] program packages were used to perform the calculations at the DFT and SA-CASSCF levels, respectively.

4 Experimental results

4.1 Isolated aniline and small aniline clusters

Our measured H-fragment KED from 243 nm aniline molecule photodissociation is in good agreement with the previously reported spectra.[4] Besides, it is essentially identical to the KED

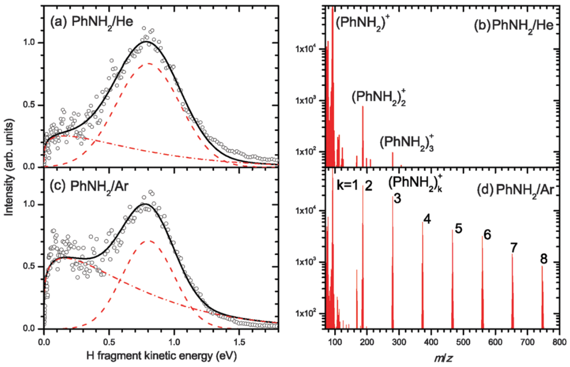

Fig. 1 (a) KED spectrum obtained from the photodissociation of small aniline clusters generated in coexpansion with He at stagnation pressure P_0 = 2 bar and reservoir temperature T_R = 343 K; the corresponding mass spectrum (b) exhibits ions up to $(PhNH_2)_3{}^+$. (c) KED spectrum obtained from the photodissociation of larger aniline clusters generated in coexpansion with Ar at stagnation pressure P_0 = 2 bar and reservoir temperature T_R = 323 K, and the corresponding mass spectrum (d).

obtained for the small aniline clusters shown in Fig. 1(a) (our isolated molecule KED is shown in the accompanying ESI†). The KED is decoupled into two components: (A) a Gaussian peak of fast fragments centered at 0.8 eV originating from the direct N–H bond fission along the $^1\pi\sigma^*$ surface; and a statistical distribution (B) peaking at low energies around 0.1–0.2 eV with a tail extending towards 1.5 eV assigned to the decay of the hot S_0 ground state populated through the CI($^1\pi\sigma^*/S_0$).[4,5]

The images were also processed to evaluate the angular distribution of the departing H atom. Integrating the image over the higher kinetic energy region corresponding to the direct dissociation process (A) around 0.8 eV yielded an anisotropy parameter $\beta \approx -0.7 \pm 0.2$ in agreement with the previously reported $\beta = -0.5$.[5] This implies that the excitation is of perpendicular character and the dissociation dynamics is fast compared to the molecular rotation. The anisotropy is apparent from the image in the ESI.†

Our main focus is on the photodissociation in clusters. Small aniline clusters were formed already in He expansions at the elevated He-pressure P_0 = 2 bar and reservoir temperatures T_R = 323–373 K. The mass spectra in Fig. 1(b) exhibit peaks up to the trimer ion. Due to expected cluster fragmentation upon electron ionization, presumably neutral dimers and trimers are populated significantly in the beam apart from the monomers. The H-fragment signal in the images increased due to the higher particle densities in the beam at the higher T_R. However, the images did not differ significantly from the aniline monomer. The corresponding KED shown in Fig. 1(a) is essentially identical to the KED of isolated molecules in the ESI.† Thus the photodissociation dynamics in these small clusters (dimers and trimers) is not significantly affected by the solvation.

4.2 Large aniline clusters

To generate a beam dominated by aniline clusters we used Ar as the buffer gas. The mass spectrum in Fig. 1(d) exhibits aniline cluster ions $(PhNH_2)_n{}^+$, and clusters larger than $n \geq 10$ are observed. We have shown in our recent detailed mass spectrometric study[24] that under the present conditions pure aniline clusters $(PhNH_2)_N$ were generated.

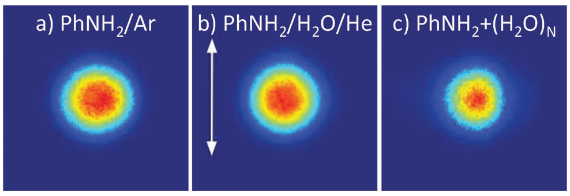

Fig. 2 The H-fragment images from 243 nm photodissociation of aniline clusters generated in PhNH$_2$/Ar expansions (a), $PhNH_2{\cdot}(H_2O)_n$ clusters (b), and $PhNH_2$ molecule deposited on large $(H_2O)_N$ clusters (c). The vertical arrow indicates laser polarization.

There are some differences in the H-fragment images from these large aniline clusters, shown in Fig. 2(a), compared to the images from isolated molecules shown in the ESI.† The cluster image is quite isotropic with $\beta \approx 0$ for the fast fragments (A). This is due to the elastic scattering of the fast H-fragments with the cluster constituents in which they are redirected from their original flight path after the dissociation but do not lose their kinetic energy. Although the H-fragment KED from the larger clusters in Fig. 1(c) resembles the ones from the isolated molecules and small clusters, Fig. 1(a), the slow fragment portion is enhanced in the larger clusters significantly. Numerous similar spectra recorded under various conditions with Ar buffer gas confirmed this trend.

4.3 Aniline–water clusters

The mixed species were generated by coexpansion of $PhNH_2$ and water vapour from a 1 : 5 liquid volume mixture in the reservoir. The mass spectrum in Fig. 3(b) shows several progressions of peaks: $(PhNH_2)_n{}^+$, $(H_2O)_nH^+$, $PhNH_2{\cdot}(H_2O)_n{}^+$ and $PhNH_2{\cdot}(H_2O)_nH^+$. The $(H_2O)_nH^+$ ions can originate from pure $(H_2O)_N$ clusters in the beam. However, any significant contribution from the pure water clusters to the present VMI could be excluded since a H signal from pure water clusters at 243 nm can originate only after multiphoton absorption.[53] In the present study the photon flux was kept lower to avoid these multiphoton processes. The processes observed in our

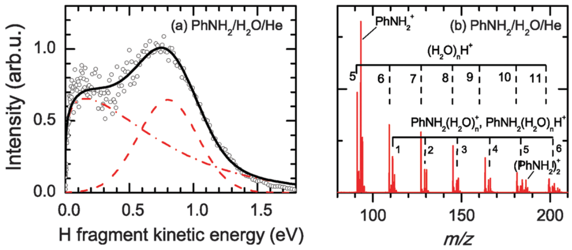

Fig. 3 The KED obtained after photodissociation of aniline–water clusters produced in expansion of $PhNH_2$ and water vapour mixture (1 : 5 liquid volume ratio) in He P_0 = 2 bar and T_R = 313 K (a). The corresponding mass spectrum (b).

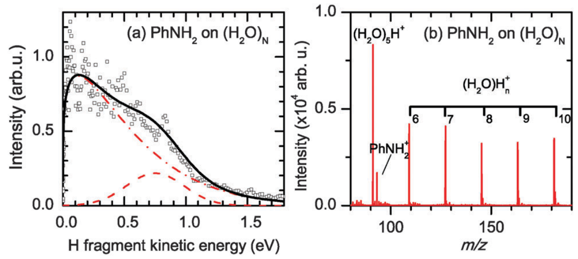

Fig. 4 The KED obtained after photodissociation of aniline picked up on large $(H_2O)_N$, $\bar{N} \approx 430$, clusters produced in pure water vapour expansion $P_0 = 4.6$ bar, $T_R = 423$ K (a). The corresponding TOF mass spectrum (b).

previous study[53] of $(H_2O)_N$ were 5-photon processes: 2-photon dissociation and (2 + 1) H-fragment REMPI. The present processes require essentially 4-photons, since a single-photon dissociation is involved. Therefore, the 5-photon processes could be suppressed at the lower photon fluxes as proved by no H-fragment signal from pure water clusters. Also pure aniline clusters exhibit only a small contribution in the mass spectra. There is a strong monomer $PhNH_2^+$ peak, nevertheless, the image in Fig. 2(b) and KED in Fig. 3(a) differ from the isolated molecule: the image is more isotropic, and the KED contains significantly more slow statistical fragments. Thus the H-fragments must originate mostly from the mixed $PhNH_2{\cdot}(H_2O)_N$ clusters. They again exhibit an enhanced slow component (B) compared to the fast one (A).

Finally, we investigated the aniline photodissociation in the extreme case of the individual molecules embedded on the surface of large water clusters $(H_2O)_N$, $\bar{N} \approx 430$. Fig. 4(b) shows the corresponding mass spectrum with the protonated water peaks and $PhNH_2^+$ peak. This suggests that even in the case of multiple molecule pickup, the aniline molecules remain isolated on the water clusters. We have recently observed this lack of coagulation for various molecules deposited on ice nanoparticles.[28,32,34] In this case the KED in Fig. 4(a) is strongly dominated by the slow statistical component. The fast hydrogen fragments are still present but their fraction is significantly suppressed compared to the aniline and smaller aniline–water clusters.

5 Calculation results

5.1 Isolated aniline

First, we calculate isolated aniline molecules to reference our method to the previously published aniline studies. The results of vertical excitation energies of the three lowest excited states calculated at the TD-LC-ωPBE are compared in the ESI† with the previously reported computational results. In comparison to the experimentally observed vertical excitation energy to the $1^1\pi\pi^*$ state of 4.4 eV,[54] the calculated absorption energy is overestimated by approximately 0.6 eV, giving a larger error than results obtained with TD-CAM-B3LYP and EOM-CCSD(T).[4] However, we focus here on the clusters, for which the high level calculations are not feasible, and thus the above difference of 0.6 eV provides a rough estimate how the present calculation results can be scaled for a comparison with the experiment.

The optimization of CI($1^1\pi\sigma^*/S_0$) performed at the MS-CASSCF level resulted in the structure with the N–H bond distances of the corresponding bond fission of 1.832 Å, and this structure was placed 5.06 eV above the energy of the ground state equilibrium structure. The linear interpolation curves of the PESs of the ground and first three excited states with respect to the N–H bond fission between the vFC region and this CI (shown in ESI†) suggest the previously reported scenario:[4] a direct barrierless path from the $2^1\pi\pi^*$ towards the $1^1\pi\sigma^*/S_0$ CI, leading to the formation of fast hydrogen atoms. The additional paths would include tunneling through the barrier. Based on our results this barrier appeared at the structure with a N–H bond distance of 1.337 Å. The wavefunctions of first two excited states were characterized by mixing of $\pi \rightarrow \pi^*$ and $\pi \rightarrow \sigma^*$. Based on the energy values obtained from the linear interpolation curve, this barrier was 0.16 eV above the vertical excitation energy of $2^1\pi\pi^*$. The optimization of the relevant point with the N–H bond kept fixed resulted in reducing of the energy barrier by 0.20 eV, *i.e.* below the $2^1\pi\pi^*$ vertical excitation energy and, thus, made a direct reaction channel from $2^1\pi\pi^*$ towards the $1^1\pi\sigma^*/S_0$ CI feasible.

5.2 Aniline dimers

The structure of the two most stable aniline dimer clusters $(PhNH_2)_2$-I and of $(PhNH_2)_2$-II is shown in Fig. 5(a) and (c), respectively. In the former structure the monomers possess the stacked head-to-tail orientation which is stabilized by hydrogen bonding towards π-aromatic systems, while the latter structure is stabilized by the hydrogen bonding between NH_2 groups. In agreement with previously reported results of *ab initio* calculations[22] the energy difference between these two dimer structures is 1.54 kcal mol^{-1}. Note that in the latter structure two types of

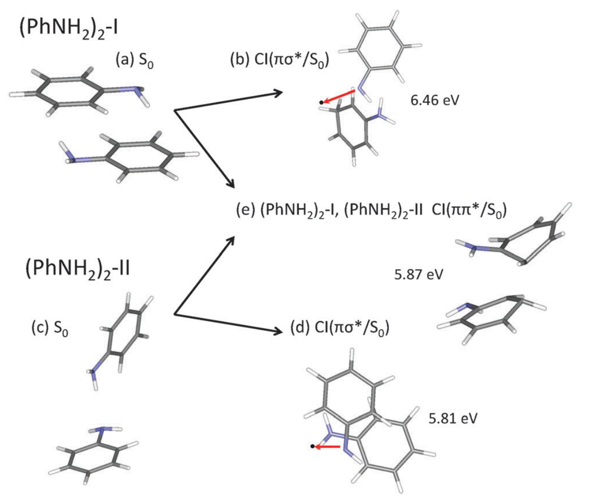

Fig. 5 The optimized aniline dimer structures. Top $(PhNH_2)_2$-I: (a) ground state equilibrium structure, (b) CI($1^1\pi\sigma^*/S_0$). Bottom $(PhNH_2)_2$-II: (c) ground state, (d) CI($1^1\pi\sigma^*/S_0$). Middle structure (e) CI($\pi\pi^*/S_0$).

hydrogen can be identified, those involved in hydrogen bonding and those directed towards a free space. The vertical excitation energies are given in the ESI.† The structures of four energetically lowest structures of $PhNH_2$ trimers are also shown in the ESI.† These results show that also in the trimers the two types of hydrogen atoms of the amino group can be identified, *i.e.* the ones involved in the hydrogen bonding, and free space pointing hydrogens.

The geometry of CI($1^1\pi\sigma^*/S_0$) of $(PhNH_2)_2$-I which corresponds to the hydrogen dissociation is shown in Fig. 5(b). In this structure the dissociative hydrogen is attached to the aromatic ring of the second molecule. The energy of this CI is, however, 6.46 eV above the ground state minimum structure. This is above the experimental excitation energy. The CI relevant to the hydrogen dissociation in the $(PhNH_2)_2$-II dimer is shown in Fig. 5(d). This structure is characterized by a complex in which the dissociative hydrogen interacts with both nitrogens. Linear interpolation curves (LIICs) between the vFC region and the CI($1^1\pi\sigma^*/S_0$) structure are shown in the ESI,† Fig. S3. This CI is located 5.81 eV above the ground state minimum and it is, thus, energetically slightly above the experimental value (considering the scaling factor between the experimental and calculated results discussed in Section 5.1). Taking into account that the description at the DFT level gives only an approximate value due to its multi-configurational character we can assume that this CI is accessed in the current experiment. However, the LIIC connecting the vFC region and this CI is characterized by a barrier of about 6.6 eV. Based on the experience on the constrained optimization of the barrier height on the hydrogen dissociation channel (see Sections 5.1 and 5.3), lowering of the barrier below the experimental excitation energy is not expected.

Fig. 5(e) illustrates the CI which can be reached after excitation of both $(PhNH_2)_2$-I and $(PhNH_2)_2$-II dimers. This structure is characterized by a strong distortion of both aromatic rings and it is located energetically 5.87 eV above the ground state minimum. This CI is assumed to be accessible in the current experiment using the same argumentation about the description of CI within the DFT method as given in the previous paragraph. As in the previous case the height of the barrier on the LIIC was calculated to be 6.5 eV. A constrained optimization of the point on the LIIC corresponding to the top of the barrier with fixed carbon atoms leads to a lowering of this barrier below the initial excitation energy and, thus, makes this CI effective.

5.3 Aniline–water clusters

To describe the photodissociation in aniline–water clusters two models were considered, Fig. 6(a) and (d), in which one ($PhNH_2\cdot(H_2O)_2$-I) or both ($PhNH_2\cdot(H_2O)_2$-II) hydrogen atoms of the amino group interact with the water molecules. The excitation energies in the vFC region are given in the ESI.†

The structures of optimized CI($1^1\pi\pi^*/S_0$) and CI($1^1\pi\sigma^*/S_0$) are shown in Fig. 6(b) and (c) for $PhNH_2\cdot(H_2O)_2$-I, and in Fig. 6(e) and (f) for $PhNH_2\cdot(H_2O)_2$-II, respectively. The character of hydrogen bonding remains unchanged in both excited state minima. The $1^1\pi\pi^*/S_0$ conical intersections are characterized by a distortion of the benzene ring. They are placed by about 5.7 eV above the ground state minima, and thus accessible within our experiment.

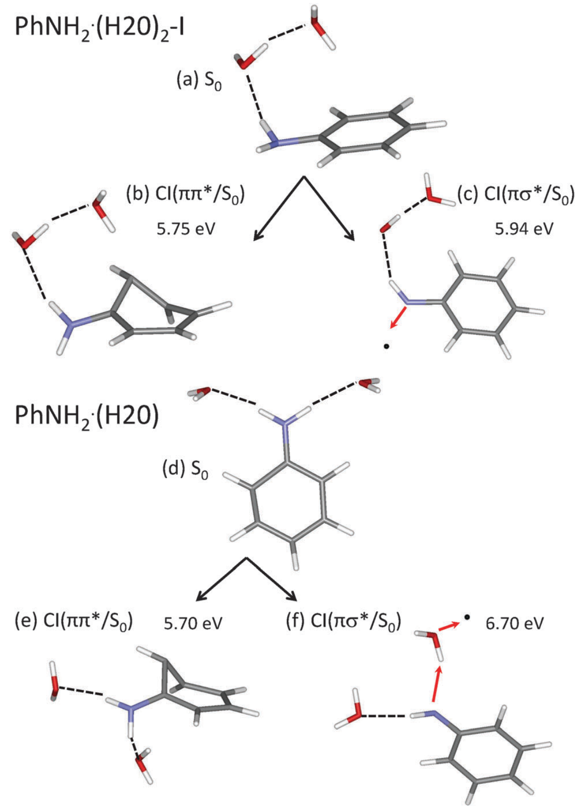

Fig. 6 The optimized structures of $PhNH_2\cdot(H_2O)_2$ clusters. Top $PhNH_2\cdot(H_2O)_2$-I: (a) ground state, (b) CI($1^1\pi\pi^*/S_0$), (c) CI($1^1\pi\sigma(NH)^*/S_0$). Bottom $PhNH_2\cdot(H_2O)_2$-II: (d) ground state, (e) CI($1^1\pi\pi^*/S_0$), (f) CI($1^1\pi\sigma(OH)^*/S_0$).

CI($\pi\sigma^*/S_0$) in Fig. 6(c) which corresponds to the dissociation of the hydrogen towards the free space is located energetically slightly above the experimental excitation energy. As in the case of previously described CI we can predict that this CI can be accessible in our experiment, because of the errors due to a single-reference description at the DFT level. Similar to isolated aniline, the optimization resulted in the planarization of NH_2 which is accompanied by rearrangement of clustering water molecules. The calculated LIIC between the vFC region and CI($1^1\pi\sigma^*/S_0$) calculated for the $PhNH_2\cdot(H_2O)_2$-I cluster is shown in the ESI,† Fig. S5. The barrier on the relevant reaction path is about 0.5 eV higher compared to the experimentally used excitation energy. As in the case of a monomer the optimization of the highest point on the potential energy surface leads to the lowering of this barrier by about 0.4 eV making this CI very likely efficient for the hydrogen dissociation. In the CI($\pi\sigma^*/S_0$) of $PhNH_2.(H_2O)_2$-II, Fig. 6(f), the hydrogen dissociating from the amino group is attached to the clustering water followed by dissociation of hydrogen from there. This structure is, however, about 1.6 eV above the excitation energy used in the experiment, and thus not accessible for the relaxation process.

Finally, we have calculated the optimized structures of large water clusters with aniline $PhNH_2{\cdot}(H_2O)_{50}$ interacting *via* a single or both hydrogen bonds formed between the NH_2 group and oxygen atoms of the water molecules. The BSSE corrected interaction energies obtained at the ωB97D functional calculated for these structures are −17.92 kcal mol^{-1} and −22.18 kcal mol^{-1}, respectively. Thus the double hydrogen bonded structure is more stable by 4.26 kcal mol^{-1}. The structures are presented in the ESI.†

6 Discussion

6.1 Aniline clusters

The KEDs of H-fragments from small $(PhNH_2)_N$, $N \leq 3$, clusters closely resemble the spectra of isolated molecules with the fast hydrogens (A) and the slow statistical fragments (B). According to the previous experiments and theoretical calculations for isolated molecules[2,4,5] the excitation at 243 nm should be above the $^1\pi\sigma^*$ transition origin and above the $\pi\pi^*/^1\pi\sigma^*$ CI, and can even reach the $2^1\pi\pi^*$ state. Although the absolute position of these states seems to be somewhat shifted towards higher energies in our calculations, their relative spacing is in good agreement with the previous experiments.[5,55,56]

Based on the comparison of excitation energies, the first and second pairs of states of the $\pi\pi^*$ character of the dimer correspond to the $1^1\pi\pi^*$ and $2^1\pi\pi^*$ states of the monomer, respectively. For both structures, the oscillator strengths of the more intense state corresponding to the monomer $2^1\pi\pi^*$ state are 3–4 times larger than the oscillator strengths of states corresponding to the monomer $1^1\pi\pi^*$ state. Similarly, the transitions to the Rydberg states are less intense, with 15 and 7 times smaller oscillator strengths for $(PhNH_2)_2$-I and $(PhNH_2)_2$-II, respectively. In this case the dynamics will involve sequential decay through several CIs $2^1\pi\pi^*/1^1\pi\pi^*$, $^1\pi\pi^*/^1\pi\sigma^*$, and $^1\pi\sigma^*/S_0$. The previous experimental measurements of the time constant for H atom elimination at $\lambda \leq 240$ nm showed very fast dynamics with $\tau \approx 155$ fs proving very efficient population transfer from the $2^1\pi\pi^*$ to $^1\pi\sigma^*$ state.[4] This dynamics yields the fast (A) fragments. The slow fragments (B) were also observed in a wide range of excitation wavelengths[4,5] generated by a statistical decay of the hot ground state S_0 populated *via* available CIs ($^1\pi\sigma^*/S_0$, $^1\pi\pi^*/S_0$).

In the larger clusters (generated in Ar expansions), the slow contribution increases. This observation is similar to the case of pyrrole, pyrazole, imidazole, and phenol studied in clusters previously.[14,19,20,57–59] The pathway along the hydrogen bonding N–H coordinate towards the $^1\pi\sigma^*/S_0$ CI and thus towards the fast channel closes by complexation in clusters. However, in the case of aniline there are two N–H bonds and, if the other one remains free, it can still be dissociated. Thus in aniline the cluster effect is not as pronounced as in the case of the molecule with a single N–H bond and sets on for the larger clusters.

It is worth noting that our one-color experiment probes only the H-fragments generated within the time window of a single laser pulse of ≈7 ns. The slow H-atoms born through statistical decay are likely to continue to form beyond this time-window. Thus the fast fragment peak (A) might be somewhat enhanced with respect to the slow peak (B) in the present spectra. A similar effect is evident in the differences between the kinetic energy spectra from Rydberg-tagging TOF[5] and time-resolved VMI[4] at 240 nm. This can be especially true in the clusters where the dynamics of statistical decay can be significantly slowed down, as we have demonstrated previously for acetylene clusters.[60]

As discussed above, our calculations revealed that in dimers there are two types of hydrogen atoms in the amino group, those directed into a free space and those involved in the hydrogen bonding. The former type of hydrogen exists in the optimized ground state and S_1 minimum structures, as well as $\pi\sigma^*/S_0$ CI of $(PhNH_2)_2$-II, Fig. 5(c) and (d). The latter type of hydrogen atom correspond to those bound either by interaction with the π system or with the amino group of the surrounding molecule in the cluster, as found for $(PhNH_2)_2$-I and $(PhNH_2)_2$-II, Fig. 5.

The free N–H bonds resemble the monomer behaviour, *i.e.* they provide both fast and slow H-fragments. The prevailing fast ones result from a direct dissociation. The slow hydrogens result from the statistical decay of the vibrationally hot S_0 ground state populated *via* $\pi\pi^*/S_0$ and $\pi\sigma^*/S_0$ CIs. Indeed such CIs were found in our calculations for the dimer, and were energetically available with our excitation energy. On the other hand, the hydrogen bonding blocks the dissociative channels and, thus, the hydrogens from the N–H bonds engaged in the hydrogen bonding cannot contribute to the formation of the fast fragments, but they may be funnelled *via* available CIs into the population of the slow statistical ones.

Our calculated trimer structures (see ESI,† Fig. S4) resemble the bonding motifs discussed here for the dimers. Therefore we expect similar photochemical behaviour also in small aniline clusters beyond the dimers. Presumably, in significantly larger clusters the number of free N–H bonds decreases with respect to the ones engaged in the hydrogen bonding, and thus the fast fragments decrease relative to the slow ones.

Since our experiment is not completely size-selective and a certain cluster size distribution determined by expansion conditions is generated in the beam, we cannot exclude the presence of isolated monomers even in the beam of larger clusters. Therefore an alternative explanation of our experimental results can be that the fast fragments stem from the isolated monomers. However, two experimental observations suggest that this is not the case entirely: the image isotropy and the mass spectra. The images from large clusters were isotropic, Fig. 2(a), with the anisotropy parameter $\beta \approx 0$ integrated over the fast fragment region at around 0.8 eV. This suggests that the fast H-fragments undergo elastic collisions within the cluster and are scattered isotropically upon leaving the clusters. Such behaviour was observed previously upon photodissociation in clusters.[61,62] In the present case the fast fragments strongly overlap with the slow ones distributed isotropically. Yet, since the isolated molecule photodissociation anisotropy is relatively large $\beta \approx -0.7$, at least some anisotropy would be preserved if the fast H-fragments would originate entirely from the isolated molecules in the beam. Also the relatively large ion fragments $(PhNH_2)_n^+$ with $n \geq 10$ in the mass spectra suggest significantly larger neutral precursors with log-normal distribution.[29] Therefore the monomer contribution is not expected to prevail in the beam. Even though these observations suggest that the fast fragments do not originate only from the monomers in the beam, this possibility cannot be disproved unambiguously and is left opened as a possible – although less likely – interpretation of our present results.

In addition, some of the slow fragments may originate from the fragmentation of the ionic clusters generated in multiphoton ionization of aniline clusters. We have tried to avoid this contribution in our experiment by lowering the photon flux as outlined in the ESI.† The VMI experiments were performed under the conditions where no aniline cluster ion signal from direct multiphoton ionization was observed. This suggests that the H^+ contribution from direct multiphoton ionization of aniline clusters was not overwhelming.

6.2 Mixed clusters with water

The VMI images and KEDs corresponding to the small mixed clusters resemble closely the pure large aniline clusters. According to the mass spectra, here the contribution from isolated molecules in the beam can be more significant than in the case of a large aniline cluster discussed above. Therefore the fast H-atoms could still originate from the photodissociation of the isolated molecules. However, in this case we would expect the anisotropy observed for the isolated molecule photodissociation as discussed above. Again, the images exhibit isotropic distribution with $\beta \approx 0$ for the fast fragments suggesting that they originate mostly from the clusters. The mass spectra also demonstrate that there are no large pure $(PhNH_2)_N$ clusters generated in the $PhNH_2$:H_2O/He expansions. Thus the fast H-fragments arise from the mixed $PhNH_2{\cdot}(H_2O)_N$ clusters.

Similar to aniline clusters, solvation of aniline by water can lead to the formation of clusters in which only one or both hydrogen atoms of the NH_2 group are involved in hydrogen bonds with water molecules, Fig. 6. In the former case the calculations predict the existence of a direct dissociation along the free N–H bond leading to the fast and slow H fragments with the same relaxation mechanisms as was suggested for isolated aniline. This situation can be applied to structural motifs observed in $PhNH_2{\cdot}(H_2O)_2$-I. In the second type, $PhNH_2{\cdot}(H_2O)_2$-II, only the bonded hydrogen atoms are available. The evaluation of the relative energies of CI shows that these bonding motifs block the direct dissociation pathways.

When the aniline molecule is deposited on a large $(H_2O)_N$ cluster, we observe quite a decrease of the fast H-fragments compared to the slow statistical ones. This can be explained if the structures with two hydrogen bonds dominate among the $PhNH_2{\cdot}(H_2O)_N$ clusters over the single-bond structures (see Fig. S6 in the ESI†). The former structures are by 4.26 kcal mol^{-1} more stable than the latter ones. The water cluster temperature on which the aniline is adsorbed in the molecular beam is about 100 K.[63] Thus it is reasonable to assume that the more stable structure will be stabilized on the cluster. Anchoring the molecules with two N–H bonds pointing towards the cluster surface will efficiently close the direct $\pi\sigma^*$ dissociation channel.

Finally, it is worth noting that no strong zero-kinetic-energy peak was observed from the large clusters (neither from the large pure aniline clusters nor from aniline deposited on the ice nanoparticles). Usually a very narrow and pronounced maxima in VMI images and KEDs provide evidence for fragment *caging* in clusters[61,62,64,65] as observed, *e.g.*, in photodissociation of hydrogen halides[26,28] and freons[27,32] on/in Ar clusters, or most recently in photodissociation of ethanethiol clusters.[33] We have also demonstrated that this narrow maximum should not be confused with a ''central blob'' of slow fragments in images which can point to quite different dynamics.[28,33] Thus in the present case, there is no *caging* (in Bucks' sense[64]) of the H-fragments in the aniline clusters. Either, the clusters are not large enough to slow down the H-fragments to zero kinetic energy, although the mass spectra show evidence for clusters with more than 10 molecules, or the fragment caging is inefficient in these clusters. On the other hand, the isotropic distribution in the fast H fragments demonstrates the elastic collisions of leaving hydrogens with the cluster constituents.

7 Conclusions

We have investigated the 243 nm photodissociation dynamics of N–H bonds in aniline in different complex cluster environments: from isolated molecules to small $(PhNH_2)_N$, $N \leq 3$, and larger $(PhNH_2)_N$, $N \geq 10$, clusters, and from small mixed $PhNH_2{\cdot}(H_2O)_N$, $N \leq 10$, clusters to individual $PhNH_2$ molecules deposited on large $(H_2O)_N$, $\bar{N} = 430$, clusters. The main conclusions of the complementary experimental and theoretical investigations can be summarized as follows:

- For isolated aniline molecules we have confirmed the previous experimental and theoretical results and supported the proposed dynamical scenarios for the fast and slow H-fragment generation by further theoretical investigations.
- Small clusters $(PhNH_2)_N$, $N \leq 3$, exhibit very similar behavior to the isolated molecules mainly due to the presence of the free N–H bonds in these clusters.
- Large clusters $(PhNH_2)_N$, $N \geq 10$, exhibit increasing contribution of slow statistical fragments compared to the fast ones. This is rationalized based on our calculations by closing the direct N–H dissociation channel. This closing drives the population towards other coordinates which eventually funnel the population through available CIs onto the hot ground state decaying statistically.
- Small mixed $PhNH_2{\cdot}(H_2O)_N$, $N \leq 10$, clusters show similar behavior with the increased contribution of slow statistical fragments. Our calculations support a similar scenario as above, closing of the direct N–H dissociation channel. The calculations show also free N–H bonds in the $PhNH_2{\cdot}(H_2O)_N$ clusters which yield the fast fragment contribution. Based on the relative energies of the relevant CI we predict that the generation of slow statistical fragments is slightly preferred.

- The individual $PhNH_2$ molecules dissociated on a surface of ice nanoparticles yield the slow fragments almost exclusively, which the calculations rationalize by a more stable structure of the $PhNH_2\cdot(H_2O)_{50}$ cluster with two hydrogen bonds, thus closing the direct dissociation pathways for both N–H bonds.

The general pattern observed not only here but also in our previous investigations of heteroaromatic molecule photodissociation in clusters[14,19,20,59] can be formulated intuitively: the engagement of the dissociation of N–H bonds into hydrogen bonds with solvating molecules closes the direct dissociation along the repulsive $\pi\sigma^*$ potential yielding the fast hydrogen fragments and funnels the population into the slow hydrogens from a statistical decay of the vibrationally hot ground state instead. However, the present combination of VMI experiment and *ab initio* calculations offers a more detailed insight into the influence of the solvent – water molecules, in particular – on the photodissociation dynamics of the N–H bond in aniline, illustrating the complexity of the solvent effects even in this relatively simple system.

Acknowledgements

This work was supported by the Czech Science Foundation project no. 14-14082S.

References

1 M. N. R. Ashfold, B. Cronin, A. L. Devine, R. N. Dixon and M. G. D. Nix, *Science*, 2006, **312**, 1637.

2 G. M. Roberts and V. G. Stavros, *Chem. Sci.*, 2014, **5**, 1698–1722.

3 A. Sobolewski, W. Domcke, C. Dedonder-Lardeux and C. Jouvet, *Phys. Chem. Chem. Phys.*, 2002, **4**, 1093.

4 G. M. Roberts, C. A. Williams, J. D. Young, S. Ullrich, M. J. Patterson and V. G. Stavros, *J. Am. Chem. Soc.*, 2012, **134**, 12578–12589.

5 G. A. King, T. A. A. Oliver and M. N. R. Ashfold, *J. Chem. Phys.*, 2010, **132**, 214307.

6 R. Montero, A. P. Conde, V. Ovejas, R. Martínez, F. Castaño and A. Longarte, *J. Chem. Phys.*, 2011, **135**, 054308.

7 R. Spesyvtsev, O. M. Kirkby and H. H. Fielding, *Faraday Discuss.*, 2012, **157**, 165–179.

8 R. Spesyvtsev, O. M. Kirkby, M. Vacher and H. H. Fielding, *Phys. Chem. Chem. Phys.*, 2012, **14**, 9942–9947.

9 J. O. F. Thompson, R. A. Livingstone and D. Townsend, *J. Chem. Phys.*, 2013, **139**, 034316.

10 F. Wang, S. P. Neville, R. Wang and G. A. Worth, *J. Phys. Chem. A*, 2013, **117**, 7298.

11 J. O. F. Thompson, L. Saalbach, S. W. Crane, M. J. Paterson and D. Townsend, *J. Chem. Phys.*, 2015, **142**, 114309.

12 O. M. Kirkby, M. Sala, G. Balerdi, R. de Nalda, L. Bañares, S. Guérin and H. H. Fielding, *Phys. Chem. Chem. Phys.*, 2015, **17**, 16270–16276.

13 M. Sala, O. M. Kirkby, S. Guérin and H. H. Fielding, *Phys. Chem. Chem. Phys.*, 2014, **16**, 3122.

14 P. Slavíček and M. Fárník, *Phys. Chem. Chem. Phys.*, 2011, **13**, 12123.

15 G. Pino, A. N. Oldani, E. Marceca, M. Fujii, S.-I. Ischiuchi, M. Miyazaki, M. Broquier, C. Dedonder and C. Jouvet, *J. Chem. Phys.*, 2010, **133**, 124313.

16 H. Lippert, V. Stert, C. P. Schulz, I. V. Hertel and W. Radloff, *Phys. Chem. Chem. Phys.*, 2004, **6**, 2718.

17 A. L. Sobolewski and W. G. Domcke, *J. Phys. Chem. A*, 2007, **111**, 11725.

18 L. Rubio-Lago, G. A. Amaral, A. N. Oldani, J. D. Rodríguez, M. G. Gonzáles, G. A. Pino and L. Bañares, *Phys. Chem. Chem. Phys.*, 2011, **13**, 1082.

19 V. Poterya, V. Profant, M. Fárník, P. Slavíček and U. Buck, *J. Chem. Phys.*, 2007, **127**, 064307.

20 V. Poterya, L. Šištík, P. Slavíček and M. Fárník, *Phys. Chem. Chem. Phys.*, 2012, **14**, 8936–8944.

21 J. H. Yeh, T. L. Shen, D. G. Nocera, G. E. Leroi, I. Suzuka, H. Ozawa and Y. Namuta, *J. Phys. Chem.*, 1996, **100**, 4385–4389.

22 D. Schemmel and M. Schütz, *J. Chem. Phys.*, 2010, **132**, 174303.

23 D. Schemmel and M. Schütz, *J. Chem. Phys.*, 2010, **133**, 134307.

24 J. Lengyel, V. Poterya and M. Fárník, *J. Mass Spectrom.*, 2015, **50**, 643–649.

25 M. Alauddin, J. K. Song and S. M. Park, *Int. J. Mass Spectrom.*, 2012, **314**, 49–56.

26 J. Fedor, J. Kočišek, V. Poterya, O. Votava, A. Pysanenko, L. Lipciuc, T. N. Kitsopoulos and M. Fárník, *J. Chem. Phys.*, 2011, **134**, 154303.

27 V. Poterya, J. Kočišek, A. Pysanenko and M. Fárník, *Phys. Chem. Chem. Phys.*, 2014, **16**, 421–429.

28 V. Poterya, J. Lengyel, A. Pysanenko, P. Svrčková and M. Fárník, *J. Chem. Phys.*, 2014, **141**, 074309.

29 J. Lengyel, A. Pysanenko, V. Poterya, J. Kočišek and M. Fárník, *Chem. Phys. Lett.*, 2014, **612**, 256–261.

30 J. Lengyel, A. Pysanenko, V. Poterya, P. Slavíček, M. Fárník, J. Kočišek and J. Fedor, *Phys. Rev. Lett.*, 2014, **112**, 113401.

31 M. Fárník and V. Poterya, *Front. Chem.*, 2014, **2**, 4.

32 V. Poterya, J. Kočišek, J. Lengyel, P. Svrčková, A. Pysanenko, D. Hollas, P. Slavíček and M. Fárník, *J. Phys. Chem. A*, 2014, **118**, 4740–4749.

33 P. Svrčková, A. Pysanenko, J. Lengyel, P. Rubovič, J. Kočišek, V. Poterya, P. Slavíček and M. Fárník, *Phys. Chem. Chem. Phys.*, 2015, DOI: 10.1039/c5cp00367a.

34 A. Pysanenko, A. Habartová, P. Svrčková, J. Lengyel, V. Poterya, M. Roeselová, J. Fedor and M. Fárník, *J. Phys. Chem. A*, 2015, **119**, 8991–8999.

35 C. Bobbert, S. Schütte, C. Steinbach and U. Buck, *Eur. Phys. J. D*, 2002, **19**, 183–192.

36 J. Kočišek, J. Lengyel, M. Fárník and P. Slavíček, *J. Chem. Phys.*, 2013, **139**, 214308.

37 A. T. J. B. Eppink and D. H. Parker, *Rev. Sci. Instrum.*, 1997, **68**, 3477.

38 B. Whitaker, *Imaging in Molecular Dynamics*, Cambridge University Press, Cambridge, 2003.

39 J. Kočišek, J. Lengyel and M. Fárník, *J. Chem. Phys.*, 2013, **138**, 124306.

40 J. Lengyel, R. Gorejová, Z. Herman and M. Fárník, *J. Phys. Chem. A*, 2013, **117**, 11225–11232.

41 J.-D. Chai and M. Head-Gordon, *Phys. Chem. Chem. Phys.*, 2008, **10**, 6615–6620.

42 D. Heger, D. Nachtigallová, F. Surman, J. Krausko, B. Magyarová, M. Brumovský, M. Rubeš, I. Gladich and P. Klán, *J. Phys. Chem. A*, 2011, **115**, 11412–11422.

43 S. Grimme, *J. Comput. Chem.*, 2006, **27**, 1787–1799.

44 A. Schäfer, C. Huber and R. Ahlrichs, *J. Chem. Phys.*, 1994, **100**, 5829.

45 O. A. Vydrov and G. E. Scuseria, *J. Chem. Phys.*, 2006, **125**, 234109.

46 O. A. Vydrov, J. Heyd, A. Krukau and G. E. Scuseria, *J. Chem. Phys.*, 2006, **125**, 074106.

47 O. A. Vydrov, G. E. Scuseria and J. P. Perdew, *J. Chem. Phys.*, 2007, **126**, 154109.

48 H. Lischka, M. Dallos and R. Shepard, *Mol. Phys.*, 2004, **100**, 1647.

49 H. Lischka, M. Dallos, P. G. Szalay, D. R. Yarkony and R. Shepard, *J. Chem. Phys.*, 2004, **120**, 7322.

50 M. Dallos, H. Lischka, R. Shepard, D. R. Yarkony and P. G. Szalay, *J. Chem. Phys.*, 2004, **120**, 7330.

51 M. J. Frisch, G. W. Trucks, H. B. Schlegel, G. E. Scuseria, M. A. Robb, J. R. Cheeseman, G. Scalmani, V. Barone, B. Mennucci, G. A. Petersson, H. Nakatsuji, M. Caricato, X. Li, H. P. Hratchian, A. F. Izmaylov, J. Bloino, G. Zheng, J. L. Sonnenberg, M. Hada, M. Ehara, K. Toyota, R. Fukuda, J. Hasegawa, M. Ishida, T. Nakajima, Y. Honda, O. Kitao, H. Nakai, T. Vreven, J. A. Montgomery, Jr., J. E. Peralta, F. Ogliaro, M. Bearpark, J. J. Heyd, E. Brothers, K. N. Kudin, V. N. Staroverov, R. Kobayashi, J. Normand, K. Raghavachari, A. Rendell, J. C. Burant, S. S. Iyengar, J. Tomasi, M. Cossi, N. Rega, J. M. Millam, M. Klene, J. E. Knox, J. B. Cross, V. Bakken, C. Adamo, J. Jaramillo, R. Gomperts, R. E. Stratmann, O. Yazyev, A. J. Austin, R. Cammi, C. Pomelli, J. W. Ochterski, R. L. Martin, K. Morokuma, V. G. Zakrzewski, G. A. Voth, P. Salvador, J. J. Dannenberg, S. Dapprich, A. D. Daniels, O. Farkas, J. B. Foresman, J. V. Ortiz, J. Cioslowski and D. J. Fox, *Gaussian 09 Revision D*, Gaussian Inc., Wallingford CT, 2009.

52 H. Lischka, R. Shepard, I. Shavitt, R. M. Pitzer, M. Dallos, T. Mller, P. G. Szalay, F. B. Brown, R. Ahlrichs, H. J. Bhm, A. Chang, D. C. Comeau, R. Gdanitz, H. Dachsel, C. Ehrhardt, M. Ernzerhof, P. Hchtl, S. Irle, G. Kedziora, T. Kovar, V. Parasuk, M. J. M. Pepper, P. Scharf, H. Schiffer, M. Schindler, M. Schler, M. Seth, E. A. Stahlberg, J.-G. Zhao, S. Yabushita, Z. Zhang, M. Barbatti, S. Matsika, M. Schuurmann, D. R. Yarkony, S. R. Brozell, E. V. Beck, J.-P. Blaudeau, M. Ruckenbauer, B. Sellner, F. Plasser and J. J. Szymczak, *COLUMBUS, an ab initio* electronic structure program, release 7.0, 2012.

53 V. Poterya, M. Fárník, M. Ončák and P. Slavíček, *Phys. Chem. Chem. Phys.*, 2008, **10**, 4835.

54 K. Kimura and S. Nafakura, *Mol. Phys.*, 1965, **9**, 117.

55 W. E. Sinclair and D. W. Pratt, *J. Chem. Phys.*, 1996, **105**, 7942.

56 T. Ebata, C. Minejima and N. Mikami, *J. Phys. Chem. A*, 2002, **106**, 11070.

57 L. Rubio-Lago, D. Zaouris, Y. Sakellariou, D. Sofikitis, T. N. Kitsopoulos, F. Wang, X. Yang, B. Cronin, A. L. Devine, G. A. King, M. G. D. Nix and M. N. R. Ashfold, *J. Chem. Phys.*, 2007, **127**, 064306.

58 M. L. Lipciuc, F. Wang, X. Yang, T. N. Kitsopoulos, G. S. Fanourgakis and S. S. Xantheas, *ChemPhysChem*, 2008, **9**, 1838.

59 V. Poterya, V. Profant, M. Fárník, L. Šištík, P. Slavíček and U. Buck, *J. Phys. Chem. A*, 2009, **113**, 14583.

60 M. Fárník, V. Poterya, O. Votava, M. Ončák, P. Slavíček, I. Dauster and U. Buck, *J. Phys. Chem. A*, 2009, **113**, 7322.

61 P. Slavíček, P. Jungwirth, M. Lewerenz, N. H. Nahler, M. Fárník and U. Buck, *J. Chem. Phys.*, 2004, **120**, 4498.

62 M. Fárník, N. H. Nahler, U. Buck, P. Slavíček and P. Jungwirth, *Chem. Phys.*, 2005, **315**, 161.

63 N. Gimelshein, S. Gimelshein, C. C. Pradzynski, T. Zeuch and U. Buck, *J. Chem. Phys.*, 2015, **142**, 244305.

64 U. Buck, *J. Phys. Chem. A*, 2002, **106**, 10049.

65 N. H. Nahler, M. Fárník, U. Buck, H. Vach and R. B. Gerber, *J. Chem. Phys.*, 2004, **121**, 1293.

Research article

Journal of MASS SPECTROMETRY

Received: 4 November 2014 Revised: 9 December 2014 Accepted: 12 January 2015

(wileyonlinelibrary.com) DOI 10.1002/jms.3572

Proton transfer and isotope-induced reaction in aniline cluster ions

Jozef Lengyel,[a,b]* Viktoriya Poterya[a] and Michal Fárník[a]*

The proton transfer (PT) and other intraclusters reactions occurring after electron ionization of aniline clusters $(PhNH_2)_N$ are investigated by the time-of-flight mass spectrometry. The mass spectra are recorded for different expansion conditions leading to the generation of different cluster sizes. Several fragment ions are shown to originate from intracluster reactions, namely, $[Ph]^+$, $[PhNH_3]^+$ and $[Ph–N–Ph]^+$. Reaction schemes are proposed for these ions starting with the PT process. The mass region beyond the monomer mass is dominated by cluster ions $(PhNH_2)_n^+$ accompanied by satellites with ±H and +2H. In experiments with deuterated species, new fragment ions are identified. The aniline isotopomer d_5-$PhNH_2$ yields the fragment ions $(PhNH_2)_n{\cdot}(N–Ph–NH_2)^+$. Analogical series is observed in experiments with d_7-$PhND_2$, and additional fragments occur corresponding to $(PhND_2)_n{\cdot}(D_2N–ND–Ph–ND–ND_2)^+$ ions. The possible reaction pathways to these ions and the unusual isotope effects are discussed. Copyright © 2015 John Wiley & Sons, Ltd.

Additional supporting information may be found in the online version of this article at the publisher's web site.

Keywords: isotope effect; intracluster reaction; electron ionization

Introduction

The proton transfer (PT) processes induced by electron ionization in molecular clusters represent an active research area.[1] These processes play an essential role, e.g. in biological systems,[2–5] and the detailed elucidation of their mechanisms at the molecular level can be assisted by molecular beam studies in clusters containing the building blocks of biomolecules.[6,7] While the PT process was investigated in many systems containing O–H bonds,[8–13] the studies of PT from N–H bond were more limited.[14–16] The simplest amine on which the previous studies of PT in N–H bonded systems focused was ammonia, where the ionization of its clusters led to the generation of $(NH_3)_n\,NH_4^+$ cluster ions.[14–16] To understand the dynamics of biological processes, it is necessary to extend such studies towards more complex systems with the interplay of different intermolecular interactions, e.g. N–H···N hydrogen bond, N–H···π interaction and π···π stacking. Such system can be represented by the aniline clusters.

Aniline ($PhNH_2$) is the simplest aromatic amine in which the amino group is connected to the benzene ring. The hydrogen bonding motif of aromatic amines is present in many biological molecules, including the DNA bases adenine, guanine and cytosine. The amino group of $PhNH_2$ can act both as the proton donor and proton acceptor. Moreover, the aromatic ring can serve as the proton acceptor via the delocalized π-electron system. Therefore, the aforementioned different bonding motifs can play a role in the aniline-containing clusters.

Various spectroscopy methods accompanied by theoretical calculations investigated the structure of small aniline clusters. Recently, quantum mechanical calculations[17] revealed that the interaction energy in aniline dimer was dominated by the van der Waals dispersion of the N–H···π interaction. It corresponds to the head-to-tail sandwich structure between two aniline molecules. These theoretical results supported earlier findings by infrared depletion spectroscopy[18] where the detected frequencies were attributed to the head-to-tail conformation with double N–H···π bonds. The aniline dimer head-to-tail isomer was also found as the most stable structure by the hole-burning spectroscopy and *ab initio* calculations.[19] The larger neutral aniline clusters were not studied to a large extent: The quantum mechanical calculations predicted the global minimum of the aniline trimer corresponding to the N–H···N hydrogen bonding arrangement.[17]

The structures of the dimer and trimer cations were also studied experimentally.[20,21] For the dimer, two stable isomers with N–H···N and N–H···π bonding were observed. The density functional theory predicted the most stable structure for the N–H···N-type conformation.[22] The experimental studies of the trimer aniline ion revealed that the cluster is stabilized by the hydrogen bond of N–H N-type between proton of one aniline and nitrogen of neutral aniline.[21] It was suggested also that the stability of the trimer could be enhanced by the N–H···π bond between two neutral aniline molecules.

Recently, we have investigated the PT dynamics in the O–H hydrogen bonded system represented by homonuclear phenol cluster ions, where the intracluster rearrangement via formation of water molecule and diphenyl ether as the reaction driving force was identified.[13] Here, we focus on the N–H dissociation and the

---

* *Correspondence to: Jozef Lengyel, J. Heyrovský Institute of Physical Chemistry v.v.i., Academy of Sciences of the Czech Republic, Dolejškova 3, 18223 Prague, Czech Republic. E-mail: jozef.lengyel@jh-inst.cas.cz*

* *Correspondence to: Michal Fárník, J. Heyrovský Institute of Physical Chemistry v.v.i., Academy of Sciences of the Czech Republic, Dolejškova 3, 18223 Prague, Czech Republic. E-mail: michal.farnik@jh-inst.cas.cz*

a *J. Heyrovský Institute of Physical Chemistry v.v.i., Academy of Sciences of the Czech Republic, Dolejškova 3, 18223 Prague, Czech Republic*

b *Department of Physical Chemistry, University of Chemistry and Technology, Technická 5, 16628 Prague, Czech Republic*

dynamics of PT reaction in the aniline cluster ions induced by electron ionization and leading to the subsequent intracluster rearrangement. An unexpected effect of the isotopic H/D substitution on the intracluster reactions is revealed.

Experiment

The experiment was performed on our cluster beam (CLUB) apparatus. It is a complex molecular beam setup devoted to the investigations of photochemistry and other processes in clusters and nanoparticles in molecular beams.[23,24] The apparatus has recently been extended with a reflectron time-of-flight (RTOF) mass spectrometer allowing for various mass spectrometric studies of clusters using different methods of ionization, e.g. electron ionization (EI),[12,13,25–27] photoionization and a special method of Na doping.[25,27] The clusters were generated in the expansion of aniline (≥99.5%, Sigma-Aldrich) in helium (99.999%, Messer) or argon (99.998%, Messer) buffer gas through a divergent conical nozzle into the vacuum. For the experiments with deuterated species, the following substances were used: aniline-2,3,4,5,6-d$_5$ (d_5-$PhNH_2$) in which the five hydrogens of the ring were replaced by deuterium (98 atom % D, Aldrich) and aniline-d_7 (d_7-$PhND_2$) where all hydrogens of the molecule were replaced by deuterium (98 atom % D, Aldrich). The aniline was filled to a temperature controlled reservoir inside the vacuum chamber that was connected directly to the nozzle. The nozzle was heated independently to a slightly higher temperature (usually by 10 °C) to prevent condensation in the nozzle. At a given stagnation pressure, the buffer gas carried the aniline molecules through the nozzle expansion. Different conditions were exploited resulting in different cluster sizes and compositions: The reservoir temperatures varied between 50 and 180 °C, and buffer gas pressures between 1 and 6 bar. In addition, two different nozzles were used with the throat diameters of 55 and 100 µm; both nozzles were 2 mm long and had a full opening angle of 33°.

After passing through a skimmer, the cluster beam passes through two differentially pumped vacuum chambers and enters an ultrahigh-vacuum chamber with a perpendicularly mounted RTOF MS. Here, the clusters are ionized by electrons. The custom-built mass spectrometer has been described recently in more detail elsewhere.[25,26] The aniline clusters are ionized in the extraction region of the mass spectrometer using a pulsed electron gun operated at 10 kHz frequency with electron energies of 70 eV. The ions are accelerated to the final kinetic energy of 8 kV. After passing the effective flight path of 0.95 m, the ions are detected by the Photonics microchannel plate detector in the chevron configuration. This instrument was calibrated using perfluorotributylamine (Supelco Analytical) as a standard material and also by large Ar_n^+ clusters for the higher masses. The mass spectra were measured with a resolution of $M/\Delta M \approx 4 \times 10^3$ and in the mass range up to 5×10^3 amu without mass discrimination.

Result and discussion

Aniline molecule and cluster spectra

Figure 1 shows the comparison of the mass spectra measured after 70 eV EI in pure $PhNH_2$ expansion (a), $PhNH_2$ in He (b) and $PhNH_2$ in Ar expansion (c). These conditions correspond to an isolated molecule, small $(PhNH_2)_N$ clusters and large species, respectively, as will be discussed later. The mass spectra are normalized to the major molecular fragment ion $[C_5H_6]^+$ at $m/z = 66$.

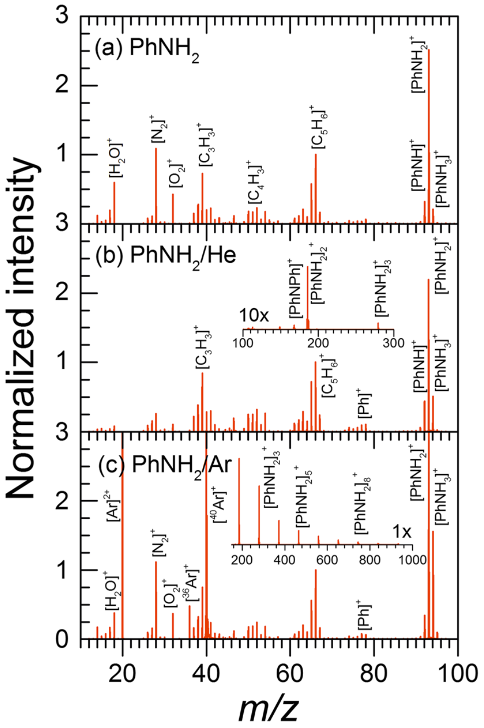

Figure 1. Mass spectra of $PhNH_2$ molecule and clusters obtained under various expansion conditions: (a) pure $PhNH_2$ molecule, (b) small $(PhNH_2)_n^+$ clusters ($n \leq 3$) and (c) large $(PhNH_2)_n^+$ clusters ($n \leq 10$) (see text for details).

In the mass spectrum of the molecular $PhNH_2$ as shown in Fig. 1 (a), the typical fragmentation pattern was observed, where the major fragment ions at $m/z = 39$, 65 and 66 appeared. The metastable decay of the aniline parent ion, $m/z = 93$, is well known and has been described in detail previously.[28,29] The ion decays by the loss of HNC to yield the $[C_5H_6]^+$ ion, $m/z = 66$, with the subsequent secondary fragmentation. This mechanism of molecular fragmentation is analogous to CO loss from phenols.[13,28] Our measured mass spectrum of molecular $PhNH_2$ shows a good agreement with published data.[28,29]

For production of small $(PhNH_2)_N$ clusters, coexpansion with helium buffer gas was used. Under these conditions, only small $(PhNH_2)_n^+$ cluster ions ($n \leq 3$) were observed as can be seen in Fig. 1 (b). However, these can originate from somewhat larger $N > n$ neutral precursors. Much larger clusters are produced in coexpansion with argon buffer gas. It is important to note that, under different expansion conditions, different cluster species could be generated in terms of size, and also composition. These included the mixed aniline–argon species as outlined in the Supporting information. However, here, we concentrate on the pure aniline clusters.

The typical mass spectrum obtained under the conditions corresponding to large pure $(PhNH_2)_N$ clusters is shown in Fig. 1(c). This spectrum exhibits only the peaks corresponding to $(PhNH_2)_n^+$ ions and their fragments; there are no Ar-containing peaks apart from Ar^+ and Ar^{2+}. Each $(PhNH_2)_n^+$ cluster ion mass peak in the spectra is accompanied by several satellite peaks of lower intensities, which are displaced by mass distances of ±1 amu. These peaks are clearly discernible in Fig. S2 in the Supporting information. These peaks

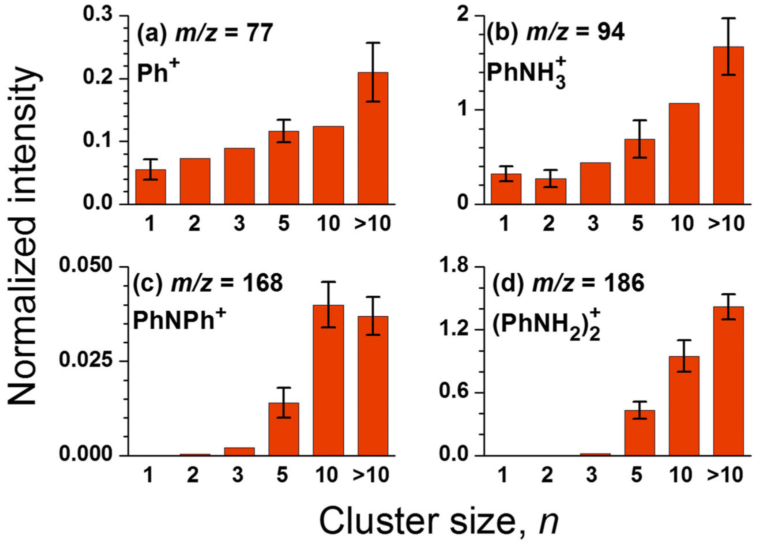

Figure 2. Dependence of different fragment ions relative intensities on the cluster sizes n. The intensities are normalized to the major molecular aniline fragment ion $[C_5H_6]^+$ ($m/z = 66$). The cluster sizes n correspond to the maximum $(PhNH_2)_n^+$ ion peaks clearly discernible in the corresponding mass spectra.

correspond to the $[(PhNH_2)_nH_k]^+$ ions with $k = 1–3$, i.e. to the addition of one, two or three hydrogen atoms from another aniline unit, which broke off the cluster upon the ionization. On the other hand, the satellite peaks correspond to the $[(PhNH_2)n{-}1PhNH]^+$ and $[(PhNH_2)n{-}1PhN]^+$, i.e. they correspond to the one and two H-atom fragmentation, respectively, from the cluster upon the ionization. For the larger cluster fragments $n \geq 3$, the $[(PhNH_2)n - 1PhN]^+$ satellite peaks tend to disappear, which suggests that only one single H-atom breaks off from the cluster upon ionization. This is consistent with the cluster structure where the neutral $(PhNH_2)_N$ precursors generate cyclic structures for $N \geq 3$[17] and the hydrogen abstraction from these structures upon ionization is more difficult than from the monomers and from the sandwiched dimer structures.

To analyze the fragmentation of large aniline clusters, we first discuss the molecular parts of the mass spectra up to the mass $m/z = 100$, which are presented in Fig. 1. All the measured mass spectra are similar in this region; however, there are some fragments that strongly depend on the cluster size, namely, $m/z = 77$ and 94 corresponding to phenyl $[Ph]^+$ and protonated aniline $[PhNH_3]^+$ ions, respectively. The intensities dependence of these fragments on the cluster size is shown in Fig. 2. The labeled cluster sizes n correspond to the maximum $(PhNH_2)_n^+$ ion peaks clearly discernible in the corresponding mass spectra.

The phenyl $[Ph]^+$ ion (Fig. 2(a)), $m/z = 77$, intensity increases with the cluster size. It cannot be generated by a simple dissociation of the single C–N bond in $PhNH_2$, where the aromatic ring decomposition by HNC loss is the energetically preferred channel.[28] The observed increase of $[Ph]^+$ ion intensity can be explained by the PT between two aniline units, as proposed in Scheme 1 for the aniline $(PhNH_2)_2^+$ dimer cation. The reaction starts with the formation of $[PhNH{\cdot}PhNH_3]^+$ ion, $m/z = 186$, by PT. Afterwards, the release of the neutral $[PhNH]^{\cdot}$ leads to the protonated phenol $[PhNH_3]^+$, $m/z = 94$. Finally, $[PhNH_3]^+$ deactivates the ring and dissociates to the neutral NH_3 and $[Ph]^+$ ion. The similarity between the cluster-size dependency of $[Ph]^+$ (Fig. 2(a)) and $[PhNH_3]^+$ (Fig. 2(b)) supports this mechanism. A similar effect was measured after protonation of aniline by an electrospray ionization where the relative intensity of the $m/z = 77$ and $m/z = 94$ increased simultaneously in the collision-induced dissociation.[30] Thus the formation of the $[Ph]^+$ fragment points to the PT reaction after the cluster ionization.

Figure 2(c) shows the cluster-size dependency of the peak intensity at $m/z = 168$ that corresponds to the diphenylamine ion without a hydrogen atom $[PhNPh]^+$. The $[PhNPh]^+$ ion exhibits the most pronounced cluster-dependent ion intensity. In the mass spectra of small $(PhNH_2)_n^+$ cluster ions ($n \leq 3$), its intensity is negligible. For the larger $(PhNH_2)_N$ clusters, the intensity strongly increases with the cluster size. The cluster-size dependency of the aniline dimer ion $[PhNH_2]_2^+$ in Fig. 2(d) is very similar to the $[PhNPh]^+$ dependence with the strong increase for $n > 3$. As shown in Scheme 1, the $[PhNHPh]^+$ ion as well as $[PhNPh]^+$ originates from the dimer

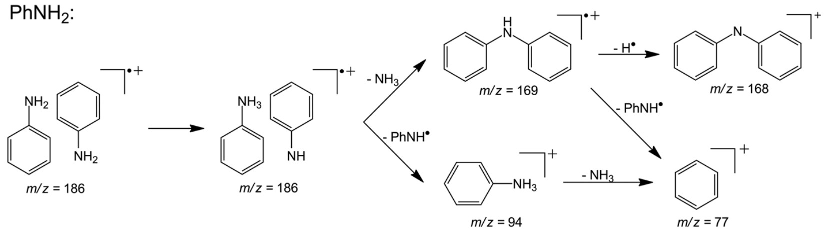

Scheme 1. Intracluster rearrangement in the aniline dimer ions.

$[PhNH_2]_2^+$ ion. Furthermore, the $[PhNHPh]^+$ ion may also contribute to the $[Ph]^+$, $m/z = 77$, ion intensity.

It is interesting to compare the present aniline cluster fragmentation with our previous study of phenol clusters.[13] The aniline cluster fragmentation product $[PhNPh]^+$ at $m/z = 168$ is analogical to the diphenyl ether $[PhOPh]^+$ observed in the phenol clusters, as shown in Scheme 2. However, the equivalent intracluster reaction, which leads to $[PhOPh]^+$ in phenol clusters, would yield the diphenyl amine $[PhNHPh]^+$ ion in the aniline case. It corresponds to a minor peak in the mass spectra, i.e. an intermediate step. Thus, the hydrogen from the $[PhNHPh]^+$ probably transfers to $PhNH_2$ in larger clusters forming the $PhNH_3$, which leaves the cluster.

Isotope effect in aniline clusters

Next we used the deuterium labeling to further elucidate the intracluster reaction mechanisms after the ionization. Two isotopes were used to investigate these effects: d_5-$PhNH_2$ with the deuterated aniline ring and fully deuterated d_7-$PhND_2$. Figure 3(a) and (b) shows the mass spectra recorded with these two isotopes under the same expansion conditions as the corresponding non-deuterated $PhNH_2$ spectrum in Fig. 1(c). These spectra are dominated by the $(PhNH_2)_n^+$ cluster ion series as the normal aniline cluster spectra earlier. These series are, indeed, shifted by mass $\Delta m = n \times 5$ amu and $n \times 7$ amu for $(d_5\text{-}PhNH_2)_n^+$ and $(d_7\text{-}PhND_2)_n^+$ clusters, respectively, with respect to the normal aniline $(PhNH_2)_n^+$ mass peaks. These shifts confirm the majority of the deuterated species in our sample.

Nevertheless, the $(PhNH_2)_n^+$ ions are again accompanied by the satellites displaced by $\Delta m = \pm 1$ amu even in the fully deuterated sample d_7-$PhND_2$. It points to some H/D exchange probably in the source reservoir. This effect has been minimized by rinsing the reservoir with pure D_2O prior to introducing the deuterated aniline. Yet it could not be eliminated completely. Nevertheless, the position of the major mass peaks at the correct masses corresponding to the deuterated species suggests that the H/D exchange is not substantial and that the deuterated species dominate the cluster beam.

Although the spectra of deuterated clusters are very similar to the ones of the normal aniline on the first sight, there are new series discernible upon a closer inspection in the intermediate positions between the $(PhNH_2)_n^+$ peaks. In the spectrum of d_5-$PhNH_2$, there is a series of peaks displaced by $\Delta m = +12$ amu from the major $(PhNH_2)_n^+$ peaks. These peaks are labeled in Fig. 3(a). The same series is also identified in d_7-$PhND_2$ spectrum in Fig. 3(b). In addition, there is a series displaced by $\Delta m = +48$ amu in d_7-$PhND_2$ spectrum in Fig. 3(b). Note also that the intensities in Fig. 3 are in logarithmic scale and normalized to the intense aniline monomer peak.

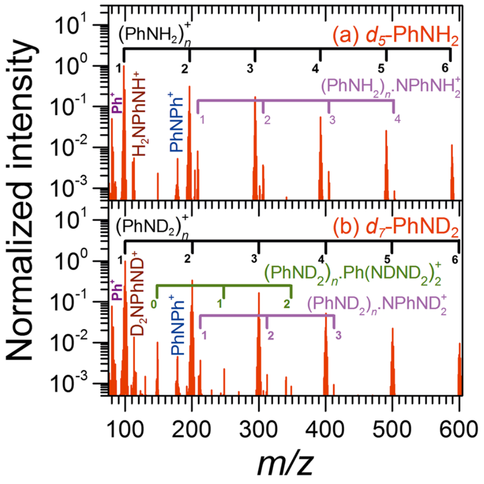

Figure 3. The mass spectra of deuterated species (a) d_5-$PhNH_2$ and (b) d_7-$PhND_2$. The relative intensities are scaled to the same maximum ($m/z = 98$ and 100, respectively).

It is worth noting that the peaks corresponding to the $[Ph]^+$ and $[PhNPh]^+$ ions discussed earlier are clearly discernible and labeled in both deuterated spectra as well. They appear at $m/z = 82$ and 178, respectively, corresponding to the fully deuterated phenol rings. Thus, the analogical PT reactions outlined in Scheme 1 occur in the deuterated clusters representing the major pathway of ion-molecule reaction also in deuterated clusters.

Scheme 3 outlines the intracluster reaction channels for the d_5-$PhNH_2$ dimer. The major PT reaction channel leading to the dominant $(PhNH_2)_n^+$ molecular cluster ion series is shown schematically at the top (**I**). Later, two possible ion intracluster rearrangements are proposed leading to the weaker $\Delta m = +12$ amu series in d_5-$PhNH_2$ spectra. The first peak assigned to this series occurs at $m/z = 111$ amu, i.e. displaced by $\Delta m = +13$ amu from the monomer. We assume that the reactions can occur either on the site of the nitrogen or on the ring. First, we propose the reaction to take place on the N-site leading to the formation of 'phenyldiazene-like' structure $[Ph{-}N{=}NH]^+$ with loss of the molecular hydrogen (**IIa**). Thus, the product ion gains NH ($\Delta m = +15$ amu) and loses H_2 ($\Delta m = -2$ amu); i.e. it appears shifted by $\Delta m = +13$ amu from the molecular ion $[PhNH_2]^+$. The second possibility is that the reaction proceeds on the ring yielding the 'iminoaniline-like' structure $[NH{-}Ph{-}NH_2]^+$ (**IIb**). Formally, this pathway corresponds to the exchange of $D^\bullet$ in the ring ($\Delta m = -2$ amu) with NH ($\Delta m = +15$ amu) resulting in the same total mass shift of $\Delta m = +13$ amu.

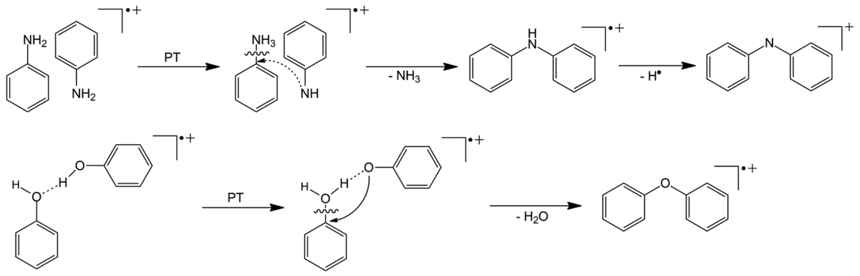

Scheme 2. Proton transfer with subsequent intracluster rearrangement in aniline dimer leading to the $Ph{-}N{-}Ph^+$ ion and analogical process observed in phenol clusters.[13]

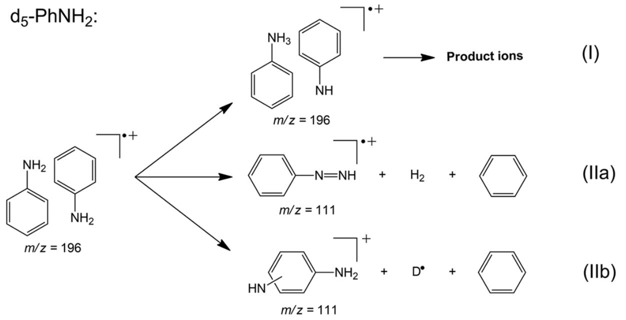

Scheme 3. The intracluster rearrangement in d_5-PhNH$_2$ dimer ions: (top) PT represents the major reaction channel leading to the $(\mathrm{PhNH_2})_n^+$ cluster ion series (**I**); (bottom) two possible reaction channels (**IIa**) and (**IIb**) leading to the product masses observed in the mass spectra of the isotopically labeled clusters d_5-PhNH$_2$.

In general, the nitrogen atom of aniline is most likely to lose the hydrogen[31] that would favor the first proposed reaction channel (**IIa**) in Scheme 3. On the other hand, the head-to-tail structure of aniline dimer in the ground state prefers the second reaction route (**IIb**). Also, the shift $\Delta m = +12$ for the larger clusters supports the later mechanism, as well as the experiment with fully deuterated d_7-PhND$_2$. Both these later arguments are outlined later.

The smaller shift $\Delta m = +12$ for the larger $(d_5\text{-PhNH}_2)_n^+$ clusters $n \geq 2$ can be justified by the cyclic structure of these clusters where a single hydrogen is 'shared' between the molecules in the hydrogen bond. These structures are illustrated in Scheme 4 for the dimer (b) and trimer (c) ions, as generated from trimer and tetramer precursors, respectively. However, they can originate from the larger neutral precursors as well. The cluster fragmentation by evaporation of further monomer(s) has no influence on the proposed reaction pathways and therefore is not discussed here. The cluster reaction can be formally described as N → D exchange: D in one aniline unit is exchanged for N from the other unit, and the donor of N atom is evaporated, while the rest of the cluster remains charged. (Indeed, this reaction can be accompanied by evaporation of more than one aniline molecule from the cluster ion.) This reaction is analogical to the channel (**IIb**) in Scheme 3. Building the structures assuming the generation of Ph–N=NH moiety in analogy to the channel (**IIa**) in Scheme 3 would be more complicated, supporting the proposed simple N → D exchange mechanism.

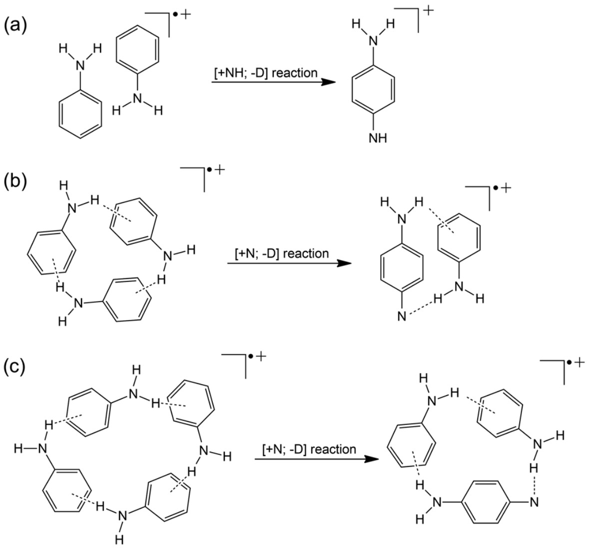

Scheme 4. The proposed cluster reactions in d_5-PhNH$_2$ clusters: From the dimer, the $[\mathrm{HN{-}Ph{-}NH_2}]^+$ ion is generated by the reaction pathway (**IIb**) in Scheme 3; an analogical process in the larger cyclic clusters yields the N–Ph–NH$_2$ moiety, i.e. $(\mathrm{PhNH_2})_n{\cdot}(\mathrm{N{-}Ph{-}NH_2})^+$ cluster ions.

Finally, we used the fully deuterated aniline d_7-PhND$_2$ for the isotope substitution to further elucidate the aforementioned reactions. The fragmentation of d_7-PhND$_2$ clusters upon EI results again in the $\Delta m = +12$ amu series of ion progression (Fig. 3(b)). This shift is consistent with the previously proposed N → D exchange reaction mechanism. On the other hand, the other reaction path leading to the Ph–N=NH structure would yield the shift of only $\Delta m = +10$ amu, because this reaction would be formally N → H$_2$ exchange in the case of d_5-PhNH$_2$, and N → D$_2$ exchange in the case of d_7-PhND$_2$. Thus, the $\Delta m = +12$ amu series is assigned to the series $(d_5\text{-PhNH}_2)_n{\cdot}(\mathrm{N{-}Ph{-}NH_2})^+$ and $(d_7\text{-PhND}_2)_n{\cdot}(\mathrm{N{-}Ph{-}ND_2})^+$ in the d_5-PhNH$_2$ and d_7-PhND$_2$ spectra, respectively.

The two mechanisms outlined in Scheme 3 could in principle be distinguished also at the peaks near the monomer mass. For the d_5-PhNH$_2$ isotopomer, both pathways (**IIa**) and (**IIb**), i.e. (+NH; −H$_2$) and (+NH; −D), yield $\Delta m = +13$ amu. However, for the d_7-PhND$_2$ isotopomer, the analogical reactions are (+ND; −D$_2$) and (+ND; −D) leading to $\Delta m = +12$ amu and $\Delta m = +14$ amu, respectively. The peak at $\Delta m = +14$ amu is stronger than the one at $\Delta m = +12$ amu. However, an unambiguous analysis in this region is somewhat obscured by a relatively strong background peak at $m/z = 113$ amu that exceeds the small intensities at $m/z = 112$ and 114 amu (and $m/z = 111$ in d_5-PhNH$_2$) even after the background subtraction (note that signals 10^2–10^3 times smaller than the major cluster peaks are analyzed here). Another complication can arise from the aforementioned H/D exchange in the source. Thus, the main support for the N → D exchange mechanism comes from the larger cluster masses as outlined earlier where the peaks are mostly isolated and no ambiguity exists concerning the $\Delta m = +12$ amu series.

There is another weaker series present only in the fully deuterated aniline shifted by $\Delta m = +48$ amu from the corresponding $(d_7\text{-PhND}_2)_n^+$ peaks. We assign this series to the 'phenyldihydrazine-like' structure that can be formally written as $(d_7\text{-PhND}_2)_n{\cdot}(\mathrm{D_2N{-}ND{-}Ph{-}ND{-}ND_2})^+$. The generation of this structure is in principle possible by elimination of three benzene rings, as depicted in Scheme 5. Although this structure is speculative and cannot be further proved within the present mass spectrometric experiment, the experimental observations of these mass peak series are quite unambiguous. For clarity, Fig. 4 shows the previously discussed series isolated from the mass spectra: the major peak intensities as

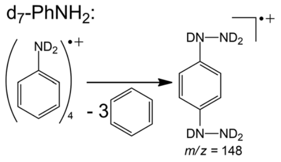

Scheme 5. The generation of the $D_2N–ND–Ph–ND–ND_2$ in d_7-PhND$_2$ clusters.

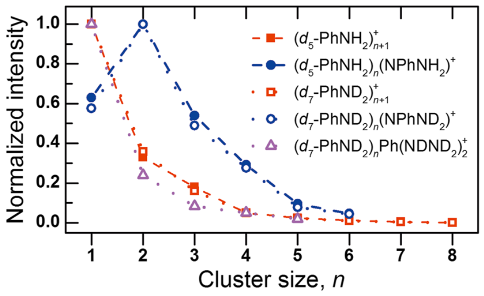

Figure 4. The main series peak intensities isolated from the mass spectra as functions of cluster ion size n evaluated from Fig. 3. All the intensities are normalized to the maximum peak in the series.

functions of cluster ion size n. The intensities are normalized to the maximum peaks in the series. The major molecular ion series $(PhNH_2)_n^+$ is almost identical for d_5-PhNH$_2$ and d_7-PhND$_2$, as well as the $(PhNH_2)_n{\cdot}(N–Ph–NH_2)^+$ series. It is important to point out that no analogic series corresponding to $(PhNH_2)_n{\cdot}(N–Ph–NH_2)^+$ and $(PhNH_2)_n{\cdot}(H_2N–NH–Ph–NH–NH_2)^+$ could be identified in the normal aniline.

Conclusions

The clusters of aniline molecules were investigated by the RTOF mass spectrometry after the EI, and the spectra were recorded for aniline clusters of various sizes. The spectra dependencies on the cluster size point to several fragments that originate from the intracluster ion-molecule reactions, namely, $[Ph]^+$, $[PhNH_3]^+$ and $[Ph–N–Ph]^+$ ions. Reaction schemes have been proposed for these ion fragments starting with the PT process in the aniline clusters. The cluster mass spectra are dominated by the molecular $(PhNH_2)_n^+$ cluster ion peaks accompanied by satellites corresponding mainly to the clusters with ±H and +2H.

The deuterated aniline isotopomers were used to further elucidate the intracluster reactions. The deuteration seems to open new channels leading to the new fragment ions that were not identified in the normal aniline: $(PhNH_2)_n{\cdot}(N–Ph–NH_2)^+$ in d_5-PhNH$_2$ and analogical $(PhND_2)_n{\cdot}(N–Ph–ND_2)^+$ in d_7-PhND$_2$, and $(PhND_2)_n{\cdot}(D_2N–ND–Ph–ND–ND_2)^+$ only in d_7-PhND$_2$. The reaction mechanisms are proposed to explain the occurrence of these ions, which involve entirely new reaction steps of N ↔ D and NH ↔ D exchange between the aniline subunits within the cluster. To our best knowledge, such reactions have not been reported yet for these clusters. However, because of the mass effect, the reactions with deuterium are usually slower than their hydrogen analogues. Thus, the possible explanation for observing these products with the deuterated species is that the proposed reactions are intermediate steps in a more complex intracluster chemistry that ultimately leads to the major $(PhNH_2)_n^+$ cluster ions ($\pm k{\cdot}H$) observed in normal aniline with hydrogen. The deuterium can slow down some of the reaction steps in the deuterated species, so that the proposed intermediates occur in the mass spectra. It ought to be noted that these effects are not very strong: The additional series observed in deuterated species are about two orders of magnitude weaker than the main molecular series. Yet, these effects are unambiguous and very interesting and can stimulate theoretical research to fully understand the ion-molecule reactions in the ionized aniline clusters.

Acknowledgements

Financial support by the grant no. 14-14082S of the Czech Science Foundation and from specific university research (MSMT no. 20/2014) is acknowledged. J.L. also acknowledges the Journal of Mass Spectrometry Award by the John Wiley and Sons Ltd. and the International Mass Spectrometry Foundation.

References

[1] J. T. Hynes, J. P. Klinman, H. H. Limbach, R. L. Schowen. *Hydrogen Transfer Reactions*. WILEY-VCH: Weinheim, **2007**.
[2] C. A. Rice-Evans, N. J. Miller, G. Paganga. Structure-antioxidant activity relationships of flavonoids and phenolic acids. *Free Radical Biol Med* **1996**, *20*, 933.
[3] G. Litwinienko, K. U. Ingold. Solvent effects on the rates and mechanisms of reaction of phenols with free radicals. *Acc Chem Res* **2007**, *40*, 222.
[4] T. J. Meyer, M. H. V. Huynh, H. H. Thorp. The possible role of proton-coupled electron transfer (PCET) in water oxidation by photosystem II. *Angew Chem Int Ed* **2007**, *46*, 5284.
[5] A. Migliore, N. F. Polizzi, M. J. Therien, D. N. Beratan. Biochemistry and theory of proton-coupled electron transfer. *Chem Rev* **2014**, *114*, 3381.
[6] B. Brutschy. The structure of microsolvated benzene derivatives and the role of aromatic substituents. *Chem Rev* **2000**, *100*, 3891.
[7] V. Poterya, O. Tkáč, J. Fedor, M. Fárník, P. Slavíček, U. Buck. Mass spectrometry of hydrogen bonded clusters of heterocyclic molecules: electron ionization vs. photoionization. *Int J Mass Spectrom* **2010**, *290*, 85.
[8] A. W. Castleman, B. D. Kay, V. Hermann, P. M. Holland, T. D. Märk. Studies of the formation and structure of homomolecular and heteromolecular clusters. *Surf Sci* **1981**, *106*, 179.
[9] B. D. Kay, A. W. Castleman. Molecular-beam electric deflection study of the hydrogen-bonded clusters $(H_2O)_N$, $(CH_3OH)_N$, and $(C_2H_5OH)_N$. *J Phys Chem* **1985**, *89*, 4867.
[10] M. S. El-Shall, C. Marks, L. W. Sieck, M. Meot-Ner. Reactions and thermochemistry of protonated methanol clusters produced by electron-impact ionization. *J Phys Chem* **1992**, *96*, 2045.
[11] S. Y. Lee, D. N. Shin, S. G. Cho, K. H. Jung, K. W. Jung. Proton-transfer reactions within ionized methanol clusters: mass-spectrometric and molecular-orbital studies. *J Mass Spectrom* **1995**, *30*, 969.
[12] J. Kočišek, J. Lengyel, M. Fárník, P. Slavíček. Energy and charge transfer in ionized argon coated water clusters. *J Chem Phys* **2013**, *139*, 214308.
[13] J. Lengyel, R. Gorejová, Z. Herman, M. Fárník. Proton transfer in hydrogen-bonded network of phenol molecules: intracluster formation of water. *J Phys Chem A* **2013**, *117*, 11225.
[14] C. Bobbert, S. Schütte, C. Steinbach, U. Buck. Fragmentation and reliable size distributions of large ammonia and water clusters. *Eur Phys J D* **2002**, *19*, 183.
[15] K. Stephan, J. H. Futrell, K. I. Peterson, A. W. Castleman, H. E. Wagner, N. Djuric, T. D. Märk. An electron-impact study of ammonia clusters in a supersonic molecular-beam: appearance potentials of NH_4^+, $(NH_3)_2^+$, $(NH_3)_2H^+$, $(NH_3)_3H^+$ and $(NH_2NH_3)^+$. *Int J Mass Spectrom Ion Process* **1982**, *44*, 167.
[16] A. Pelc, L. Michalak. Electron ionization study of ammonia microclusters. *Rapid Commun Mass Spectrom* **2000**, *14*, 1455.
[17] D. Schemmel, M. Schütz. Molecular aniline clusters. I. The electronic ground state. *J Chem Phys* **2010**, *132*, 174303.
[18] K. Sugawara, J. Miyawaki, T. Nakanaga, H. Takeo, G. Lembach, S. Djafari, H. D. Barth, B. Brutschy. Infrared depletion spectroscopy of the aniline dimer. *J Phys Chem* **1996**, *100*, 17145.

[19] N. Yamamoto, K. Hino, K. Mogi, K. Ohashi, Y. Sakai, H. Sekiya. Hole-burning spectroscopy and ab initio calculations for the aniline dimer. *Chem Phys Lett* **2001**, *342*, 417.

[20] K. Ohashi, Y. Inokuchi, H. Izutsu, K. Hino, N. Yamamoto, N. Nishi, H. Sekiya. Electronic and vibrational spectra of aniline-benzene hetero-dimer and aniline homo-dimer ions. *Chem Phys Lett* **2000**, *323*, 43.

[21] K. Ohashi, Y. Inokuchi, N. Nishi, H. Sekiya. Intermolecular interactions in aniline-benzene hetero-trimer and aniline homo-trimer ions. *Chem Phys Lett* **2002**, *357*, 223.

[22] N. Yamamoto, K. Ohashi, K. Hino, H. Izutsu, K. Mogi, Y. Sakai, H. Sekiya. Density functional studies on aniline dimer cations. *Chem Phys Lett* **2001**, *345*, 532.

[23] M. Fárník. *Molecular Dynamics in Free Clusters and Nanoparticles Studied in Molecular Beams*. ICT Prague Press: Prague, **2011**.

[24] M. Fárník, V. Poterya. Atmospheric processes on ice nanoparticles in molecular beams. *Front Chem* **2014**, *2*, 4.

[25] J. Lengyel, A. Pysanenko, J. Kočišek, V. Poterya, C. C. Pradzynski, T. Zeuch, P. Slavíček, M. Fárník. Nucleation of mixed nitric acid-water ice nanoparticles in molecular beams that starts with a HNO_3 molecule. *J Phys Chem Lett* **2012**, *3*, 3096.

[26] J. Kočišek, J. Lengyel, M. Fárník. Ionization of large homogeneous and heterogeneous clusters generated in acetylene–Ar expansions: cluster ion polymerization. *J Chem Phys* **2013**, *138*, 124306.

[27] J. Lengyel, A. Pysanenko, V. Poterya, J. Kočišek, M. Fárník. Extensive water cluster fragmentation after low energy electron ionization. *Chem Phys Lett* **2014**, *612*, 256.

[28] J. H. Gross. *Mass Spectrometry: A Textbook*. 1st. Springer: Heildelberg, **2004**.

[29] M. N. Eberlin, D. Vasconcellos Augusti, R. Augusti. Mass spectrometry and gas-phase chemistry of anilines. In *The Chemistry of Anilines*, Z. Rappoport (Ed). John Wiley & Sons Ltd: Chichester, **2007**, 293–346.

[30] P. M. Lalli, B. A. Iglesias, H. E. Toma, G. F. de Sa, R. J. Daroda, J. C. Silva, J. E. Szulejko, K. Araki, M. N. Eberlin. Protomers: formation, separation and characterization via travelling wave ion mobility mass spectrometry. *J Mass Spectrom* **2012**, *47*, 712.

[31] M. T. Nguyen. General and theoretical aspects of anilines. In *The Chemistry of Anilines*, Z. Rappoport (Ed). John Wiley & Sons Ltd: Chichester, **2007**, 75–166.

Supporting information

Additional supporting information may be found in the online version of this article at the publisher's web site.

THE JOURNAL OF
PHYSICAL CHEMISTRY A
Article
pubs.acs.org/JPCA

Proton Transfer in Hydrogen-Bonded Network of Phenol Molecules: Intracluster Formation of Water

Jozef Lengyel,*,† Radka Gorejová, Zdeněk Herman, and Michal Fárník*

J. Heyrovský Institute of Physical Chemistry, v.v.i., Academy of Sciences of the Czech Republic, Dolejškova 3, 18223 Prague, Czech Republic

ABSTRACT: Electron ionization and time-of-flight mass spectrometry was used to investigate the phenol clusters $(PhOH)_n$ of different size from single molecule to large clusters: in coexpansion with He, the dimers $n = 2$ are mostly generated; in Ar, large species of $n \geq 10$ also occur. Besides $[(PhOH)_n]^{+\bullet}$ cluster ion series, hydrated phenol cluster ions $[(PhOH)_n{\cdot}xH_2O]^{+\bullet}$ with up to $x = 3$ water molecules and dehydrated phenol clusters $[(PhOH)_n{-}H_2O]^{+\bullet}$ were observed. The hydrated phenol series exhibits minima and maxima that are interpreted as evidence for proton transfer between the hydrogen bonded cluster ions of cyclic structures. The proton transfer leads to a water generation within the clusters, and subsequent elimination of the diphenyl ether molecule(s) from the cluster yields the hydrated phenol cluster ions. Alternatively, a water molecule release yields a series of dehydrated phenols, among which the diphenyl ether ion $[PhOPh]^{+\bullet}$ ($n = 2$) constitutes the maximum.

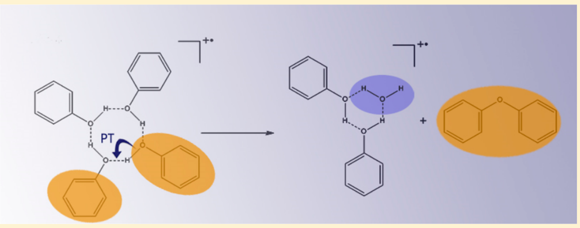

1. INTRODUCTION

The proton-transfer reactions represent the central topic in various chemical and biological processes. This can be demonstrated on phenol, the simplest aromatic alcohol, wherein the proton transfer plays a crucial role in many natural processes. For example, the proton transfer in the phenol derivate tyrosine leads to the photostability in plants (in Photosystem II).[1] Phenol also belongs to an important class of molecules exhibiting antioxidant activity and free-radical scavenging properties: tocopherols and flavonoids[2−5] inhibit oxidative degradation of organic and biological materials.

Detailed pathways of the antioxidant activity have long been discussed, yet the hypotheses have not been experimentally confirmed at the molecular level. In general, the phenolic antioxidants are believed to trap the damaging peroxy radicals ($ROO^\bullet$) via three independent mechanisms based on the hydrogen and proton transfer.[2,6−8] The single step of the reactive radical termination by phenolic antioxidants is the hydrogen atom transfer (HT) mechanism, where the O−H bond is homolytically broken. However the other two reactions are two-step heterogeneous dissociations of the O−H bond: either the initial electron transfer is followed by the proton transfer or the electron is coupled to the initial proton transfer. Moreover, the proton transfer and coupled electron−proton transfer reactions were suggested as the light-driven reactions leading to the water oxidation in Photosystem II.[9] While the gas-phase experiments favor the HT mechanism, the proton-transfer mechanisms can be preferred in bulk chemistry, as it represents a closer analogy to the natural environment in living organisms. Detailed understanding necessarily brings out a question: What effects does the solvent environment have on the particular mechanisms? Despite numerous experimental and theoretical studies[10−15] of the intermolecular proton-transfer mechanism of phenol in different environments (e.g., water, methanol or ammonia), the answer to the above question is not straightforward.

Sato and Mikami[10] studied the intracluster proton-transfer reaction occurring in the hydrogen-bonded network of mixed $[PhOH{\cdot}(H_2O)_n]^+$ ($n = 1{-}4$) clusters using trapped ion photodissociation (TIP) spectroscopy. The experiments revealed that at least three water molecules are needed for the proton transfer from the phenol molecule. This hypothesis was confirmed also by IR photodissociation spectroscopy.[11] Analogous results were found by IR photodissociation after resonant ionization,[12] where no proton transfer was observed in mixed cations with one or two water molecules. These observations are in agreement with the theoretical calculations,[13] which predicted that the critical size for the proton transfer is $n = 3$ for $[PhOH{\cdot}(H_2O)_n]^+$ and $n = 1$ for $[PhOH{\cdot}(NH_3)_n]^+$ clusters. The proton transfer in $[PhOH{\cdot}(NH_3)]^+$ clusters was experimentally observed by mass-analyzed threshold ionization (MATI).[14] Although the hydrogen-bonded structures and proton transfer in mixed $(PhOH)_m{\cdot}(H_2O)_n$ or $(PhOH)_m{\cdot}(NH_3)_n$ clusters have been extensively investigated, studies of analogous processes in pure phenol clusters were rather neglected.

Phenol consists of the benzene ring condensed with the hydroxyl group; that is, it may be regarded, on the one hand, as a derivate of benzene and, on the other hand, as a derivate of water. The hydroxyl group of phenol determines its acidity as proton donor, whereas the benzene ring characterizes its basicity. In

Received: July 9, 2013
Revised: August 26, 2013
Published: October 14, 2013

general, the geometry of the neutral phenol clusters is governed by the interplay among different interactions: the hydrogen bond formed between the OH groups, the H−π interaction between the OH group and the aromatic ring, and the π−π interaction between the aromatic rings.[16] The O−H···O hydrogen-bond interaction prevails in small phenol clusters and leads to their closed-ring structures, as calculated theoretically and observed experimentally.[15,17−19]

In the work of Ebata et al.,[17] the OH stretching vibration of phenol dimers and trimers was measured by IR−UV double-resonance and stimulated Raman-UV double-resonance spectroscopies. They found evidence of cyclization of phenol molecules to the hydrogen-bonded network in a large red shift of the OH stretching vibrations in the trimer. Later on, they reported their findings in a comprehensive review[18] and extended their study to heteronuclear clusters of phenol with water and methanol. The cyclic structures were also confirmed in a theoretical study by ab initio and DFT calculations.[15] The dominant effect of the hydrogen bond in the cluster formation was observed in experiments of Tubaro et al.[20] with binary solutions of benzene−phenol using the atmospheric pressure photoionization (APPI).

We have studied the dynamics of hydrogen transfer in phenol clusters previously in a photodissociation experiment.[19] In the experiments presented in this communication, we use new mass spectrometry tools recently implemented on our experimental setup[21,22] to address the question of the O−H dissociation and proton transfer in phenol clusters after electron ionization. This approach provides complementary information to our previous cluster photochemistry studies[19] concerning the elementary proton and hydrogen-transfer processes.

2. EXPERIMENT

The experiments have been performed on the CLUster Beam (CLUB) apparatus described elsewhere[23] with a new reflectron time-of-flight mass spectrometer (RTOFMS) recently implemented on our apparatus.[21,22] The clusters were produced in supersonic expansions of phenol (redistilled 99+%, Sigma-Aldrich) and buffer gas (argon or helium) through a divergent conical nozzle of 100 μm diameter, 2 mm long, and 33° full opening angle into the vacuum. The molecular beam flow and the clustering conditions were controlled by heating the phenol reservoir and by the stagnation pressure of the buffer gas (Ar or He). The buffer gas carried the phenol vapor to the nozzle heated independently to a somewhat higher temperature (usually by 10 °C) to avoid condensation. Different expansion conditions were exploited: reservoir temperatures between 50 and 100 °C and buffer gas pressures between 1 and 4 bar, resulting in different mean cluster sizes, as discussed later.

Because one of the findings of the present paper is water generation in phenol clusters upon ionization and phenol is a highly hygroscopic substance, great attention must be paid to the purity of the used phenol. Otherwise, the absorbed moisture could be misinterpreted for the water generated in pure phenol clusters. Therefore, we used a new phenol bottle for each experiment and introduced phenol from the reservoir through the nozzle both placed in the high vacuum source chamber ($<10^{-6}$ mbar background pressure) and heated (>50 °C) overnight (>12 h) before the measurements were started. High-purity buffer gases He (99.996%, Messer) and Ar (99.998%, Messer) were used.

The cluster beam was skimmed and passed through two differentially pumped chambers before entering the ion source of the perpendicularly mounted RTOFMS. The spectrometer was custom-built[24] and has been described recently in more detail elsewhere. The phenol clusters were ionized using a 70 eV pulsed electron gun at 10 kHz frequency in the extraction region of the mass spectrometer. Ions formed were extracted by a 10 kV pulse and accelerated to the final kinetic energy of 8 kV. After passing the effective flight path of 0.95 m length, the ions were detected on the Photonics MCP detector in the Chevron configuration. The instrument was calibrated using perfluorotributylamine (Supelco Analytical) as a standard material. The calibration measurements showed that clusters of masses up to 5×10^3 amu could be measured with a resolution of $M/\Delta M \approx 4 \times 10^3$, and the signal has not been limited by any mass discrimination.

3. RESULTS AND DISCUSSION

Figure 1 shows the electron ionization mass spectra measured in pure PhOH expansion (a), PhOH in He expansion (b), and PhOH in Ar expansion (c). All mass spectra in Figure 1 have been normalized to the most intense molecular phenol fragment ion $[C_5H_6]^+$ (m/z = 66).

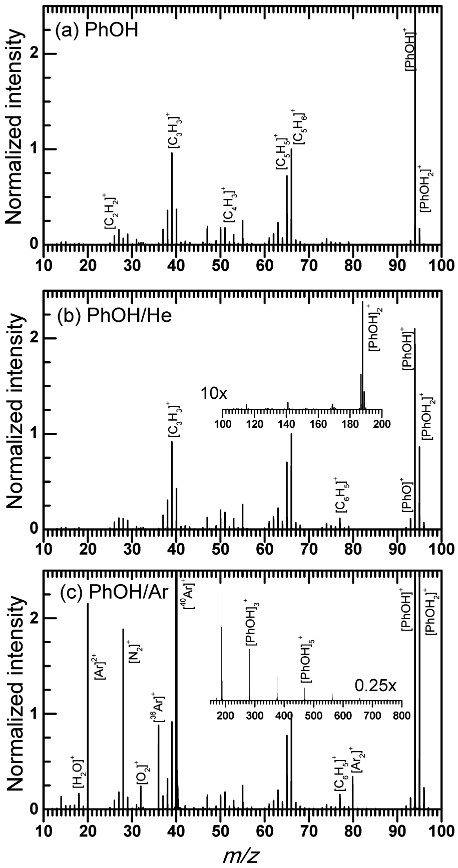

Figure 1. Mass spectra of phenol molecule and clusters obtained under various expansion conditions: (a) pure phenol molecule, (b) small clusters generated in coexpansion with He at 2 bar, and (c) large clusters generated in 2 bar coexpansion with Ar (for details see text).

3.1. Fragmentation of the Phenol Molecular Ion.

Figure 1a shows the mass spectrum of the monomer phenol molecule upon electron ionization. Analogous spectra were measured previously,[2,25,26] and the present mass spectrum also agrees with

Scheme 1. Fragmentation Pathways of Phenol Molecular Ion

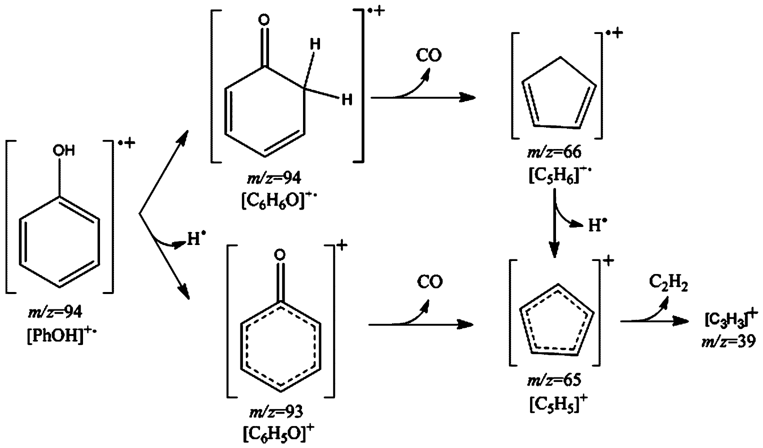

the standard NIST spectrum.[27] In the following, we summarize the monomer fragmentation pathways for the sake of the cluster mass spectra analysis below.

The spectrum is dominated by the intense peak of the molecular parent ion $[PhOH]^{+\bullet}$ ($m/z = 94$). The fragmentation pathways of phenol upon electron ionization are outlined in Scheme 1. The phenol isomer 2,4-cyclohexadienone $[C_6H_6O]^{+\bullet}$ ion is generated after the electron excitation via keto−enol tautomerization.[25] The fragmentation of the 2,4-cyclohexadienone ion is energetically favored over the O−H bond cleavage and leads to the C−C bond cleavage followed by decarbonylation, resulting in the formation of the major fragment, the cyclopentadiene ion $[C_5H_6]^{+\bullet}$ ($m/z = 66$). In the other reaction path the hydrogen-elimination process leads to the phenoxy ion $[PhO]^+$ ($m/z = 93$), which further fragments by decarbonylation to the cyclopentadienyl ion ($m/z = 65$). This fragment can also be formed from the cyclopentadiene by hydrogen-atom elimination. Further fragmentation of $[C_5H_5]^+$ to $[C_3H_3]^+$ ion ($m/z = 39$) and acetylene ($m/z = 26$) occurs. This scheme explains the typical fragmentation pattern and formation of the major fragment ions at $m/z = 39$, 65, and 66 observed in the EI mass spectra of phenol.[2,25]

3.2. Cluster Fragments. The major focus of the present study is on the phenol clusters. They were generated in coexpansion with the buffer gases helium and argon, as indicated in the insets of Figure 1b,c, respectively. Here we show the spectra recorded at the reservoir temperature of 373 K, nozzle temperature of 383 K, and the buffer gas pressure of 2 bar. Other conditions were exploited, too, and they gave similar results.

In the expansion with helium, only a certain amount of the phenol dimer ion was observed, as shown in the inset in Figure 1 b. However, the dimer ion can originate from larger neutral clusters due to cluster fragmentation, often very strong.[28] The expansion with Ar generally leads to much larger clusters due to a more effective collisional cooling. The inset in Figure 1c shows $[PhOH]_n^{+\bullet}$ ions up to $n = 8$. They were accompanied by series of satellite peaks corresponding to hydrated phenol clusters $[(PhOH)_n{\cdot}xH_2O]^{+\bullet}$ with up to $x = 3$ water molecules and dehydrated species $[(PhOH)_n{-}H_2O]^{+\bullet}$, that is, $[(PhOH)_{n\text{-}2}{\cdot}PhO{\cdot}Ph]^{+\bullet}$. This is illustrated in Figure 2. The $[PhOH]_n^{+\bullet}$, $[(PhOH)_n{+}xH_2O]^{+\bullet}$, and $[(PhOH)_n{-}H_2O]^{+\bullet}$ ions were each accompanied by series of ions spaced by one hydrogen mass. Similar mass spectra were recorded in our previous photoionization study of phenol cluster focused on photodissociation dynamics.[19] Our present findings suggest that water formation in the phenol cluster ions is an intrinsic process due to intracluster rearrangements or intracluster reactions, as discussed in the following.

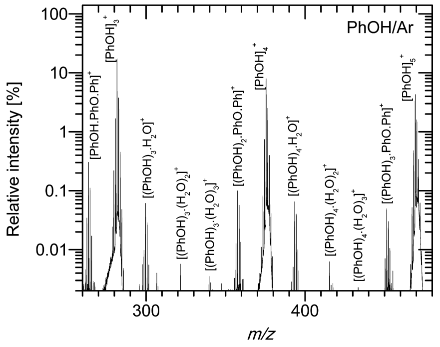

Figure 2. Mass spectrum section of phenol cluster ions between the trimer and pentamer illustrating the presence of $[PhOH]_n^{+\bullet}$ cluster ions, hydrated ions $[(PhOH)_n{\cdot}xH_2O]^{+\bullet}$ with up to $x = 3$, and dehydrated fragment ions $[(PhOH)_n{-}H_2O]^{+\bullet}$ (i.e., $[(PhOH)_{n\text{-}2}{\cdot}PhO{\cdot}Ph]^{+\bullet}$).

All mass spectra in Figure 1 are nearly identical in the region of molecular fragments below $m/z = 94$. However, there are a few fragments in this region that depend strongly on the clustering. The dependence on the cluster size is shown in Figure 3. It should be noted that the numbers N labeling the abscissa do not correspond to the true neutral cluster sizes: $N = 1$ refers to the monomer beam; $N = 2$ denotes the He expansions, where a small abundance of the dimer ion showed in the spectra (Figure 1b); that is, a certain amount of small clusters was present in the beam. $N = 10$ corresponds to Ar expansions where $[PhOH]_n^{+\bullet}$ cluster ion series up to $n = 15$ were observed upon favorable clustering conditions. (Figure 1c shows ions up to $n = 8$.) The cluster size of the neutral precursor cannot be unambiguously determined from the mass spectra. In addition, there is no single cluster size but a size distribution generated in the expansion. In general, the distribution has an exponential character for small clusters and log-normal character for large clusters.[29] Thus $N = 2$ in Figure 3 indicates that neutral dimers are present, although the beam is presumably still dominated by monomers, while in the Ar expansions the mean cluster size generated may actually be larger

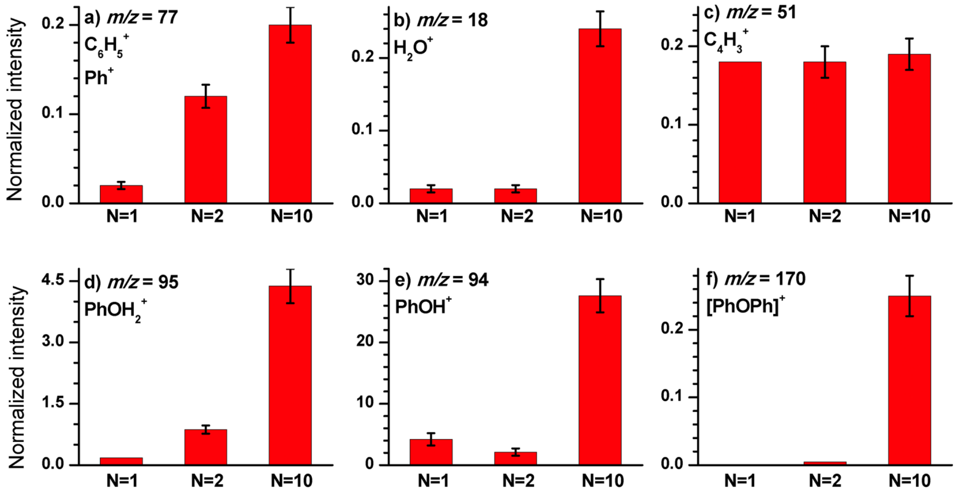

Figure 3. Dependence of intensities of different fragment ions on cluster sizes. (See the text for an explanation of *N* labels.) Normalized intensities as in Figure 1.

Scheme 2. Intracluster Rearrangement of Phenol Dimer Cluster Ions

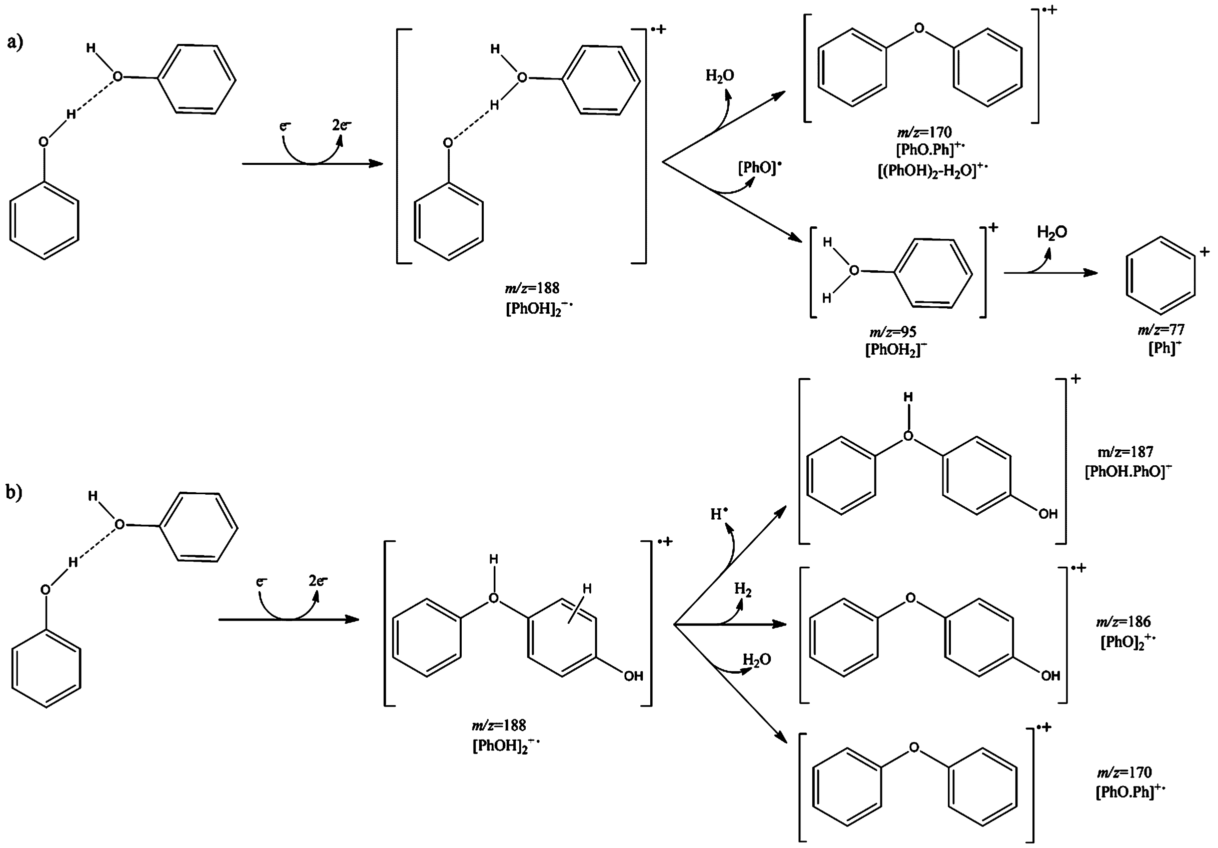

than $N = 10$ (although the distribution presumably still preserves the exponential character).

The phenyl ion $[C_6H_5]^+$ ($m/z = 77$), Figure 3a, exhibits the most pronounced cluster-dependent ion intensity. In the $N = 1$ spectrum, its intensity corresponds to the reference NIST spectrum[27] (normalized to $m/z = 66$); then, it strongly increases with the cluster size. Thus it cannot be generated by a simple dissociation of the C–O bond of the monomer. The observed significant increase already for $N = 2$ can be explained by proton transfer within the dimer cation, as proposed in Scheme 2a: Ionization of the dimer and internal rearrangement results in establishing a water within the cluster, and subsequent

Scheme 3. Intracluster Rearrangement of Phenol Trimer Cluster Ions

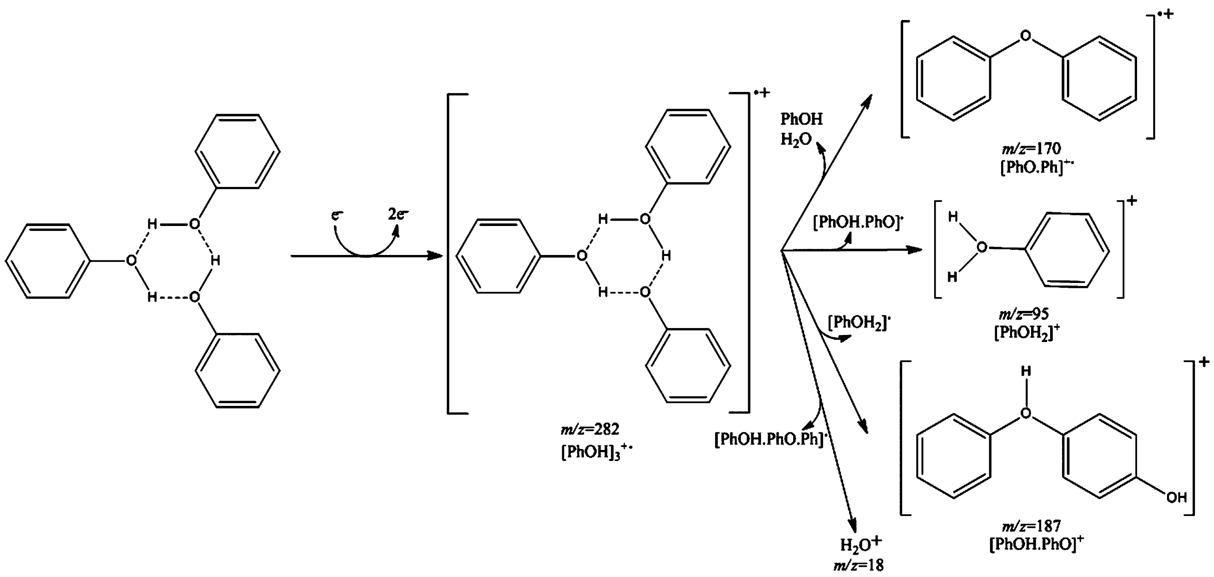

dissociation of neutral $[PhO]^{\bullet}$ leads to the protonated phenol $[PhOH_2]^+$ (m/z = 95). Then, the bond between water and the aromatic ring is dissociated, yielding the $[C_6H_5]^+$ ion. Because proton transfer between two phenol molecules is unlikely in the ground state of the neutral dimer, this process evidently occurs in the ionized species. Therefore, this fragmentation is more efficient than the C−O bond dissociation in the isolated phenol.

Figure 3b shows the cluster size dependence of $[H_2O]^{+\bullet}$ m/z = 18 peak intensity. ($[OH]^+$ m/z = 17 shows essentially the same dependence with intensities five times lower.) The $[H_2O]^{+\bullet}$ and $[OH]^+$ signals could be misinterpreted as the presence of moisture in the phenol and ionization of water molecules. Therefore, water impurities have been carefully removed from the phenol samples, as outlined in the Experimental Section. The monomer spectrum and the N = 2 spectrum exhibit very similar intensities of $[H_2O]^{+\bullet}$, only for large clusters (N = 10) its intensity increases significantly. The water molecule can be formed by intracluster rearrangements within the phenol dimer via the proton/hydrogen transfer, as outlined in Scheme 2a. Let us consider two decay channels of ionized phenol dimer: (1) leading to water ion $[H_2O]^{+\bullet}$, neutral phenyl radical $Ph^{\bullet}$, and neutral phenoxy radical $PhO^{\bullet}$ (reaction enthalpy ΔH_0 = 1355 kJ/mol)[30] and (2) formation of phenyl ion $[Ph]^+$, neutral water molecule H_2O, and phenoxy radical $PhO^{\bullet}$ (ΔH_0 = 950 kJ/mol).[30] Channel (2) is energetically preferable, and this is why there is no increase in the $[H_2O]^{+\bullet}$ signal in the regime where clusters larger than the phenol dimer are not populated significantly, while the formation of the phenyl ion $[Ph]^+$ increases (Figure 3a). The water ion signals increase only for the larger clusters (N = 10), as discussed later on.

In contrast with the cluster-size dependence of $[Ph]^+$ and $[H_2O]^{+\bullet}$, the intensity of $[C_4H_3]^+$ (m/z = 51) is independent of the cluster size (Figure 3c). This behavior clearly indicates its origin in the fragmentation of the ionized monomer phenol.

The protonated phenol $[PhOH_2]^+$ (m/z = 95) is involved in the decomposition pathways leading to the phenyl ion $[Ph]^+$ (m/z = 77) of the ionized dimer (Scheme 2a). The cluster size dependence of $[PhOH_2]^+$ in Figure 3d is similar to that of $[Ph]^+$ in Figure 3a. The $[PhOH_2]^+$ fragment ion may be stabilized when originating from larger clusters, where the excess energy can be better dissipated. Therefore, the increase in its intensity for N = 10 is somewhat steeper compared with that of the phenyl ion $[Ph]^+$. The dependence on the cluster size of the protonated phenol $[PhOH_2]^+$ can be contrasted with that of the phenol ion $[PhOH]^{+\bullet}$ (m/z = 94) in Figure 3e. This ion presumably originates only from larger clusters. Its normalized intensity for N = 2 agrees with the standard spectrum of the monomer,[27] suggesting that $[PhOH]^{+\bullet}$ is not generated by the dimer fragmentation.[31]

There is a strong increase in the intensity of the diphenyl ether ion $[PhOPh]^{+\bullet}$ (m/z = 170) and of its protonated analogue with clustering, especially for larger clusters; see Figure 3f. The diphenyl ether ion can be formed from the phenol dimer ion by dehydration, as outlined in Scheme 2a. However, an alternative pathway is proposed in Scheme 2b. First, an ion of m/z = 188 is generated upon ionization with a structure that promotes further fragmentation. It can release either a hydrogen molecule or a H atom, leading to 4-phenoxyphenol (m/z = 186) or its protonated analogue (m/z = 187), respectively. Alternately, a dehydration process is possible via intracluster hydrogen transport in the ionized complex, and this leads to the formation of diphenyl ether ion $[PhOPh]^{+\bullet}$. The dependence of intensities of m/z = 186 and 187 on cluster size follows the dependence of the diphenyl ether ion $[PhOPh]^{+\bullet}$, thus favoring the pathway proposed in Scheme 2b. However, the major contribution to m/z = 170 comes from the larger clusters, and Scheme 3 suggests a pathway for generating this ion from the phenol trimer.

3.3. Proton Transfer and Intracluster Processes.

In this part, we concentrate on water generation and other processes in the larger clusters (N = 10). The neutral phenol clusters beyond the dimer exhibit cyclic structures, as outlined in the Introduction.

Figure 4 shows the intensities of the major cluster ions formed upon ionization of phenol cluster from coexpansion with Ar as a function of the number of phenol molecules in cluster ions, n. Note that all peaks were normalized to the maximum of the series because there are orders of magnitude differences in their intensities in the mass spectra. Similar spectra were recorded

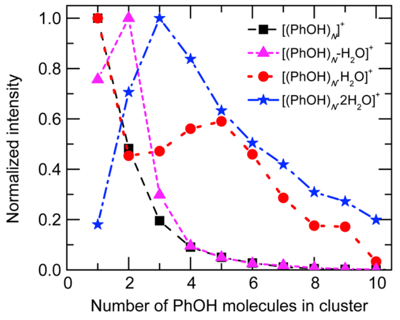

Figure 4. Spectra analysis, distinguishing the different groups of ion intensities in coexpansion with Ar. Phenol cluster ions $[(\mathrm{PhOH})_n]^{+\bullet}$, black squares; hydrated clusters $[(\mathrm{PhOH})_n{\cdot}\mathrm{H_2O}]^{+\bullet}$ and $[(\mathrm{PhOH})_n{\cdot}2\mathrm{H_2O}]^{+\bullet}$, red circles and blue stars, respectively; and dehydrated clusters $[(\mathrm{PhOH})_n{-}\mathrm{H_2O}]^{+\bullet}$ (i.e., $[(\mathrm{PhOH})_{n\text{-}2}{\cdot}\mathrm{PhO{\cdot}Ph}]^{+\bullet}$), magenta triangles.

under different conditions (corresponding to the large cluster generation), namely by changing the phenol concentration in the vapor by varying the reservoir and nozzle temperatures and changing the buffer gas pressure. The intensities changed with the varying conditions, yet the general features exhibited by maxima and minima in Figure 4 remained essentially unchanged.

The fact that the character of the intensities was essentially independent of the experimental conditions suggested that this behavior was due to intrinsic cluster properties. An attractive explanation is that these shapes are indicative of some rather abrupt chemical transformation such as ion pair formation within the neutral clusters, as demonstrated in the previous work on acidic dissociation of HNO_3 in water clusters.[21,32] However, the acidic dissociation of phenol in the ground state is improbable, and this holds for the dimer and presumably for the larger clusters, too. The acidic dissociation is of importance in excited clusters, as discussed later. Therefore, we suggest below that the reason behind the observed features is the proton-transfer

Scheme 4. Intracluster Rearrangement of Phenol Cluster Ions

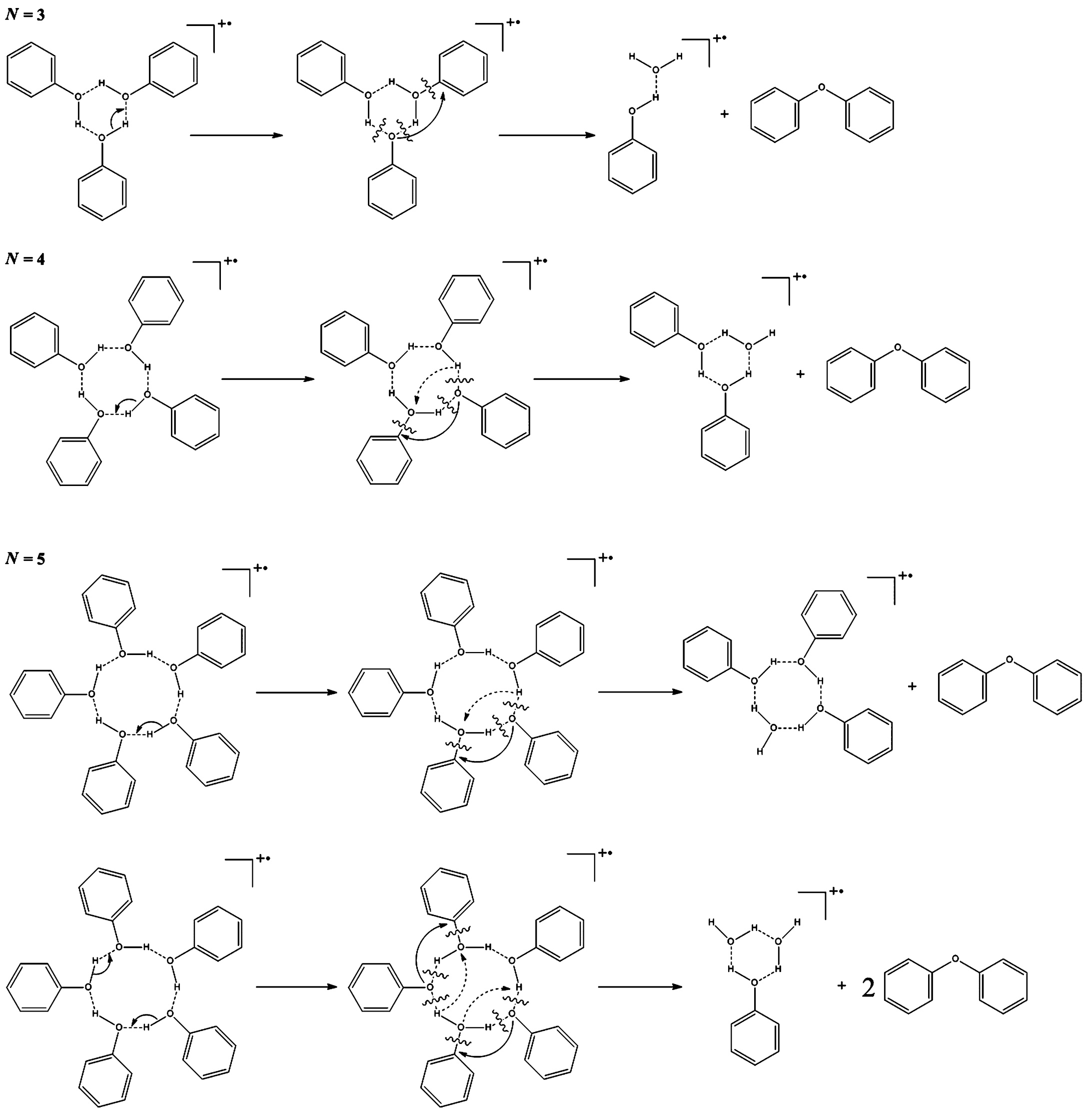

process within the cluster in the ionic state and the stability of the clusters (neutral or ionic) against the fragmentation.

The phenol cluster ions $[(PhOH)_n]^{+\bullet}$ (black squares in Figure 4) exhibit an exponential decay typical for cluster fragmentation. In the present case, even in the regime of the "large" clusters their mean neutral size is not significantly larger than $n \approx 10$, which means that their neutral size distribution is not yet of the log-normal character but rather exponential. This in combination with the strong cluster fragmentation upon ionization leads to the typical exponential character of the dependence of $[(PhOH)_n]^{+\bullet}$ fragment ion abundance on n.

The intensity of the dehydrated clusters $[(PhOH)_n{-}H_2O]^{+\bullet}$ (magenta triangles in Figure 4) first increases from $n = 1$ to 2; then, it falls off exponentially. This behavior can be understood if one realizes that this ion for $n = 2$ corresponds to the diphenyl ether ion $[PhOPh]^{+\bullet}$ ($m/z = 170$), a rather stable molecular ion. The generation of this ion from phenol dimers and trimers has been previously discussed and suggested in Schemes 2 and 3, respectively. Higher stability of this ion against fragmentation as compared with the cluster ions $[(PhOH)_{n-2}\cdot PhO\cdot Ph]^{+\bullet}$ for $n > 2$ leads to its higher abundance in the spectra.

The most peculiar behavior exhibits the hydrated phenol cluster ions $[(PhOH)_n\cdot H_2O]^{+\bullet}$ (red circles in Figure 4): their intensity first decreases to a minimum for $n = 2$ to 3, followed by an increase to a maximum at $n \approx 5$. This dependence will be discussed in connection with the weak intensity series of the doubly hydrated phenol cluster ions $[(PhOH)_n\cdot 2H_2O]^{+\bullet}$ (blue stars in Figure 4), the dependence of which increases significantly from $n = 1$, reaching a maximum at $n = 3$ and decreasing afterward.

In Scheme 4, $N = 3$, we propose the generation of the hydrated phenol ion $[(PhOH)_n\cdot H_2O]^{+\bullet}$ from the phenol trimer: we propose that the water is generated by the proton transfer from one phenol unit to another and that the subsequent cluster rearrangement leads to the evaporation of the stable neutral diphenyl ether molecule PhOPh. An analogous pathway may be proposed for the tetramer and pentamer, resulting in $[(PhOH)_n\cdot H_2O]^{+\bullet}$ $n = 2$ and 3, respectively, as shown in Scheme 4. There is yet another pathway that may be suggested for the generation of the doubly hydrated phenol ion $[(PhOH)\cdot 2H_2O]^{+\bullet}$ from the pentamer. In this pathway (Scheme 4, bottom), the proton transfer proceeds at two different sites within the hydrogen-bonded ring; then, two diphenyl ether molecules dissociate subsequently to form the fragment ion $[(PhOH)\cdot 2H_2O]^{+\bullet}$. This pathway requires the transfer of two protons in the singly charged cluster. However, this process may be facilitated by the $H^+\cdots PhO^-$ ion-pair formation from one phenol. Although phenol is not a strong acid in the ground state, its acidity increases in the excited states,[33] and thus the proposed pathway may be feasible after the electron ionization, when a substantial amount of excitation energy is likely to be deposited in the cluster ion. Analogous pathways can be drawn for larger phenol cluster ions for the formation of hydrated $[(PhOH)_n\cdot H_2O]^{+\bullet}$ and doubly hydrated $[(PhOH)_n\cdot 2H_2O]^{+\bullet}$ (and even triply hydrated) phenol cluster ions following dissociation of diphenyl ether neutral molecules.

Assuming this model, the maxima of intensities of $[(PhOH)_5\cdot H_2O]^{+\bullet}$ and $[(PhOH)_3\cdot 2H_2O]^{+\bullet}$ in Figure 4 should originate from the same neutral precursor: the phenol heptamer $(PhOH)_7$. Similarly, the threshold of the doubly hydrated series at $[PhOH\cdot 2H_2O]^{+\bullet}$ and the minimum of the singly hydrated series at $[(PhOH)_3\cdot H_2O]^{+\bullet}$ should both correspond to the same neutral precursor $(PhOH)_5$.[34] This observation suggests that the proton-transfer process and the subsequent neutral diphenyl ether evaporation from the ionized cluster start to proceed efficiently from the threshold size of the neutral precursor cluster $(PhOH)_t$, $t \approx 4$ to 5. Above this size, the feasibility of the proton-transfer process in the cluster increases. Therefore, the intensity of the hydrated ion fragments increases for the neutral precursor size above $t \approx 4$ to 5, that is, for hydrated and doubly hydrated phenol cluster ions for $n > 2$ to 3 and $n > 1$, respectively.

The appearances of the maxima for $n = 5$ and 3 for the hydrated and doubly hydrated phenol cluster ions, respectively, correspond to the same neutral $(PhOH)_7$ precursor. Beyond this cluster size the decrease in abundance of the neutral precursors in the beam overweighs the increasing feasibility of the proton transfer process, and thus the intensities of the hydrated fragments begin to decrease again.

4. CONCLUSIONS

Phenol clusters of various sizes from the single molecule to clusters of more than 10 molecules were investigated using electron ionization and time-of-flight mass spectrometry.

The phenyl ion $[Ph]^+$ ($m/z = 77$) is the major ion fragment in the mass region of molecular fragments originating from the clusters. The mechanism of its generation by water elimination from the protonated phenol $[PhOH_2]^+$ ($m/z = 95$) is proposed in clusters beginning from the dimer. This mechanism starts with the proton-transfer process in the ionized clusters. Further cluster fragments in the molecular mass region are $[H_2O]^{+\bullet}$ and $[OH]^+$ formed from larger clusters. Their generation can be explained by a similar mechanism starting with the proton-transfer process in the ionized clusters of $n \geq 3$.

The generation of the stable diphenyl ether ion $[PhOPh]^{+\bullet}$ at $m/z = 170$ and its protonated analogue was observed with clustering, especially for the larger clusters, and a mechanism was proposed for generation of this molecular ion from phenol dimers and larger clusters. In the spectra of the large clusters, the dehydrated phenol cluster ions $[(PhOH)_n{-}H_2O]^{+\bullet}$, that is, $[(PhOH)_{n-2}\cdot PhO\cdot Ph]^{+\bullet}$, were observed. The series exhibits a maximum for $n = 2$, which corresponds to the above stable diphenyl ether ion $[PhOPh]^{+\bullet}$.

Perhaps the most interesting is the observation of the hydrated phenol clusters $[(PhOH)_n{+}xH_2O]^{+\bullet}$ with up to $x = 3$ water molecules. The intensities of these species exhibit features (minima, maxima) essentially independent of the clustering conditions. We propose schemes for intracluster rearrangements that lead to the observed fragments and are consistent with the experimental observations. We suggest that the proton transfer between phenol units leads to water generation, and subsequent evaporation of the diphenyl ether molecule(s) from the cluster yields the observed hydrated phenol cluster ions.

■ AUTHOR INFORMATION

Corresponding Authors

*E-mail: jozef.lengyel@jh-inst.cas.cz.
*Phone: +420 (0)2 6605 3206. Fax: +420 (0)2 8658 2307. E-mail: michal.farnik@jh-inst.cas.cz

Present Address

[†]Department of Physical Chemistry, Institute of Chemical Technology, Technická 5, 16628 Prague, Czech Republic.

Notes

The authors declare no competing financial interest.

■ ACKNOWLEDGMENTS

This work has been supported by the Grant Agency of the Czech Republic project No.: 203/09/0422. J.L. acknowledges the financial support by MSMT grant No. 21/2013.

■ REFERENCES

(1) Siegbahn, P. E. M.; Blomberg, M. R. A. Important Roles of Tyrosines in Photosystem II and Cytochrome Oxidase. *Biochim. Biophys. Acta* **2004**, *1655*, 45−50.

(2) Rappoport, Z., *The Chemistry of Phenols*; John Wiley & Sons, Ltd.: Chichester, U.K., 2003; p 1506.

(3) Klein, E.; Lukeš, V.; Ilčin, M. DFT/B3LYP Study of Tocopherols and Chromans Antioxidant Action Energetics. *Chem. Phys.* **2007**, *336*, 51−57.

(4) Vagánek, A.; Rimarčík, J.; Lukeš, V.; Klein, E. On the Energetics of Homolytic and Heterolytic O−H Bond Cleavage in Flavonoids. *Comput. Theor. Chem.* **2012**, *991*, 192−200.

(5) Lengyel, J.; Rimarčík, J.; Vagánek, A.; Klein, E. On the Radical Scavenging Activity of Isoflavones: Thermodynamics of O−H Bond Cleavage. *Phys. Chem. Chem. Phys.* **2013**, *15*, 10895−10903.

(6) Litwinienko, G.; Ingold, K. U. Solvent Effects on the Rates and Mechanisms of Reaction of Phenols with Free Radicals. *Acc. Chem. Res.* **2007**, *40*, 222−230.

(7) Klein, E.; Lukeš, V. Study of Gas-Phase O−H Bond Dissociation Enthalpies and Ionization Potentials of Substituted Phenols - Applicability of *Ab Initio* and DFT/B3LYP Methods. *Chem. Phys.* **2006**, *330*, 515−525.

(8) Klein, E.; Lukeš, V. DFT/B3LYP Study of the Substituent Effect on the Reaction Enthalpies of the Individual Steps of Single Electron Transfer-Proton Transfer and Sequential Proton Loss Electron Transfer Mechanisms of Phenols Antioxidant Action. *J. Phys. Chem. A* **2006**, *110*, 12312−12320.

(9) Meyer, T. J.; Huynh, M. H. V.; Thorp, H. H. The Possible Role of Proton-Coupled Electron Transfer (PCET) in Water Oxidation by Photosystem II. *Angew. Chem., Int. Ed.* **2007**, *46*, 5284−5304.

(10) Sato, S.; Mikami, N. Size Dependence of Intracluster Proton Transfer of Phenol-$(H_2O)_n$ ($n = 1−4$) Cations. *J. Phys. Chem.* **1996**, *100*, 4765−4769.

(11) Sawamura, T.; Fujii, A.; Sato, S.; Ebata, T.; Mikami, N. Characterization of the Hydrogen-Bonded Cluster Ions [Phenol-$(H_2O)_n$]$^+$ ($n = 1−4$), $(\mathrm{Phenol})_2^+$, and (Phenol-Methanol)$^+$ as Studied by Trapped Ion Infrared Multiphoton Dissociation Spectroscopy of Their OH Stretching Vibrations. *J. Phys. Chem.* **1996**, *100*, 8131−8138.

(12) Kleinermanns, K.; Janzen, C.; Spangenberg, D.; Gerhards, M. Infrared Spectroscopy of Resonantly Ionized $(\mathrm{Phenol})(H_2O)_n^+$. *J. Phys. Chem. A* **1999**, *103*, 5232−5239.

(13) Sobolewski, A. L.; Domcke, W. Photoinduced Electron and Proton Transfer in Phenol and Its Clusters with Water and Ammonia. *J. Phys. Chem. A* **2001**, *105*, 9275−9283.

(14) Kim, H.; Kapral, R. Solvation and Proton Transfer in Polar Molecule Nanoclusters. *J. Chem. Phys.* **2006**, *125*, 234309.

(15) Parthasarathi, R.; Subramanian, V.; Sathyamurthy, N. Hydrogen Bonding in Phenol, Water, and Phenol-Water Clusters. *J. Phys. Chem. A* **2005**, *109*, 843−850.

(16) Kołaski, M.; Kumar, A.; Singh, N. J.; Kim, K. S. Differences in Structure, Energy, and Spectrum Between Neutral, Protonated, and Deprotonated Phenol Dimers: Comparison of Various Density Functionals with *Ab Initio* Theory. *Phys. Chem. Chem. Phys.* **2011**, *13*, 991−1001.

(17) Ebata, T.; Watanabe, T.; Mikami, N. Evidence for the Cyclic Form of Phenol Trimer - Vibrational Spectroscopy of the OH Stretching Vibrations of Jet-Cooled Phenol Dimer and Trimer. *J. Phys. Chem.* **1995**, *99*, 5761−5764.

(18) Ebata, T.; Fujii, A.; Mikami, N. Vibrational Spectroscopy of Small-Sized Hydrogen-Bonded Clusters and Their Ions. *Int. Rev. Phys. Chem.* **1998**, *17*, 331−361.

(19) Poterya, V.; Šištík, L.; Slavíček, P.; Fárník, M. Hydrogen Bond Dynamics in the Excited States: Photodissociation of Phenol in Clusters. *Phys. Chem. Chem. Phys.* **2012**, *14*, 8936−8944.

(20) Tubaro, M.; Marotta, E.; Seraglia, R.; Traldi, P. Atmospheric Pressure Photoionization Mechanisms. 2. The Case of Benzene and Toluene. *Rapid Commun. Mass Spectrom.* **2003**, *17*, 2423−2429.

(21) Lengyel, J.; Pysanenko, A.; Kočišek, J.; Poterya, V.; Pradzynski, C. C.; Zeuch, T.; Slavíček, P.; Fárník, M. Nucleation of Mixed Nitric Acid-Water Ice Nanoparticles in Molecular Beams that Starts with a HNO_3 Molecule. *J. Phys. Chem. Lett.* **2012**, *3*, 3096−3101.

(22) Kočišek, J.; Lengyel, J.; Fárník, M. Ionization of Large Homogeneous and Heterogeneous Clusters Generated in Acetylene−Ar Expansions: Cluster Ion Polymerization. *J. Chem. Phys.* **2013**, *138*, 124306.

(23) Fárník, M. *Molecular Dynamics in Free Clusters and Nanoparticles Studied in Molecular Beams*; ICT Prague Press: Prague, 2011; p 98.

(24) Kaesdorf, S. Gerate für Forschung und Industrie, Munich, Germany. http://www.kaesdorf.de/.

(25) Gross, J. H. *Mass Spectrometry: A Textbook*, 1st ed.; Springer: Heidelberg, 2004.

(26) Fahmey, M. A.; Zayed, M. A.; Keshk, Y. H. Comparative Study on the Fragmentation of Some Simple Phenolic Compounds Using Mass Spectrometry and Thermal Analyses. *Thermochim. Acta* **2001**, *366*, 183−188.

(27) NIST Standard Reference Database 69. NIST WebBook Chemie. http://webbook.nist.gov/chemistry/.

(28) Poterya, V.; Tkáč, O.; Fedor, J.; Fárník, M.; Slavíček, P.; Buck, U. Mass Spectrometry of Hydrogen Bonded Clusters of Heterocyclic Molecules: Electron Ionization *vs.* Photoionization. *Int. J. Mass Spectrom.* **2010**, *290*, 85−93.

(29) Bobbert, C.; Schütte, S.; Steinbach, C.; Buck, U. Fragmentation and Reliable Size Distributions of Large Ammonia and Water Clusters. *Eur. Phys. J. D* **2002**, *19*, 183−192.

(30) Lias, S. G.; Bartmess, J. E.; Liebman, J. F.; Holmes, J. L.; Levin, R. D.; Mallard, W. G. Gas-Phase Ion and Neutral Thermochemistry. *J. Phys. Chem. Ref. Data* **1988**, *17*, 1−861.

(31) The slightly higher intensity of $[\mathrm{PhOH}]^{+\bullet}$ for $N = 1$ compared with $N = 2$ is within error limits; however, it could also be justified by the spectra normalization to the intensity of $m/z = 66$. If the dimers contribute directly to this fragment, the normalized intensity of the $[\mathrm{PhOH}]^{+\bullet}$ peak in the corresponding dimer spectrum would be slightly underestimated.

(32) Kay, B. D.; Hermann, V.; Castleman, A. W. Studies of Gas-Phase Clusters - The Solvation of HNO_3 in Microscopic Aqueous Clusters. *Chem. Phys. Lett.* **1981**, *80*, 469−474.

(33) Pang, Y.; Chen, W. Excited-State Intramolecular Proton Transfer in 2-(2′-Hydroxyphenyl)Benzoxazole. In *Hydrogen Bonding and Transfer in the Excited State*; Han, K. L., Zhao, G. J., Eds.; John Wiley & Sons, Ltd: Chichester, U.K., 2011; Vol. 2, pp 747−761.

(34) Note that the actual minimum of the hydrated series is $n = 2$, which would actually correspond to the tetramer precursor $(\mathrm{PhOH})_4$; however, from this cluster, doubly hydrated phenol ion cannot be generated (see Scheme 4).